Swansea University
Prifysgol Abertawe

The Thermo-Mechanical Properties of novel MAX phase Ceramics

By

Stephen Counsell

College of Engineering,

Swansea University, UK

Submitted to Swansea University in fulfilment of the requirements for the Degree of Doctor of Philosophy

2022

Acknowledgements

For the financial support given in support of this work I would like to thank the Engineering & Physical Science Research Council (EPSRC). Special thanks must be given to my two primary supervisors when writing this work, Prof George Fourlaris and Prof Soran Birosca. George was the person that encouraged me to start this PhD, and his help in starting the project and the discussions in those early days were invaluable. Soran deserves a special thanks in particular for taking me on after George left the university, and I greatly enjoyed our discussions and his support throughout the project. I would also like to thank my secondary supervisors, Prof Dave Penney and Dr Karen Perkins for taking me on after Soran left the University and helping me navigate the year of Covid-19 and thesis submission.

Writing a materials engineering thesis such as this would be impossible without the use of microscopy equipment, and I would like to thank the Materials Research Centre of the College of Engineering and AIM for the use of their SEM facilities. Special praise in particular must be paid to Peter Davies, who has helped me countless times with the SEM and EBSD.

I would like to extend my thanks to my fellow PhD students that I've had the privilege of working with during my time in Swansea, especially Daryl for his invaluable help with the troublesome Gleeble; Mark for his material prep skills; and Liu, Diween, Ali and Rebecca for their help and discussions regarding all things EBSD.

Finally, and most importantly, I would like to thank my family – my parents, Brian and Gillian; my step father, Gary; my brothers, Dan and Mat; and my grandparents. Without their love, support and encouragement this work would simply not have been possible.

Abstract

The main focus of this research work was to investigate the high-temperature mechanical performance of the electrically conductive Ti_2AlC and Ti_3SiC_2 MAX phases. Using microscopy techniques, it was found that Ti_2AlC had a grain size approximately 4 times larger than the Ti_3SiC_2 material. Secondary phases were also found to be present in both materials. Electron backscatter diffraction analysis revealed that both materials appeared to have a random texture.

A Gleeble 3500 was used to test each materials response to high-strain rate, high-temperature uniaxial compression testing. Ti_3SiC_2 was found to generally have higher ultimate compressive strengths for each test condition and thereby validating a Hall-Petch relationship. For Ti_2AlC, the slower the strain rate, the lower the ultimate compressive stress and also, for each strain rate, the higher the temperature, the lower the ultimate compressive stress. The behaviour of Ti_3SiC_2 was more incoherent, although generally followed a trend of increasing ductility as the temperature was increased and strain rate decreased. Both MAX phases were thermally shocked while being subjected to a compressive load from either 1000°C or 1200°C. For the 1000°C samples, there was a slight increase in the ultimate compressive stress when the compressive load was increased, while the for the 1200°C samples the change in compressive loads under quenching had no significant effect on the mechanical properties.

The microstructure of the thermo-mechanically tested samples revealed substantial deformation in the form of intergranular and transgranular cracking, kinking, delaminations, voids and grain bending. The ductile samples saw a deformation ‘dead zone’ at the edges that had been closest to the compression anvil. The EBSD analysis revealed that the primary phase in samples tested at slower strain rates orientated favourably to the [0001] direction. These samples also showed evidence of low angle grain boundaries. A GND analysis of both materials was also undertaken and revealed higher GND densities with increasing strain rate and temperature for Ti_3SiC_2 samples, with the opposite being true of Ti_2AlC samples.

Declaration

This work has not previously been accepted in substance for any degree and is not being concurrently submitted in candidature for any degree.

Signed .....[redacted]

Date ..... 11/04/2022.....

STATEMENT 1

This thesis is the result of my own investigations, except where otherwise stated.

Other sources are acknowledged by footnotes giving explicit references. A bibliography is appended.

Signed .....[redacted]

Date ..... 11/04/2022.....

STATEMENT 2

I hereby give my consent for my work, if relevant and accepted, to be available for photocopying and for inter-library loan, and for the title and summary to be made available to outside organisations.

Signed ....[redacted]

Date ..... 11/04/2022.....

Table of Contents

The Thermo-Mechanical Properties of novel MAX phase ceramics

Chapter 1 - Introduction

The main focus of this research work is to investigate the high temperature mechanical properties of high-density MAX phase electrically conductive ceramics. Particular attention has been paid to the Ti_2AlC and Ti_3SiC_2 MAX phases. Several tests of these materials' mechanical properties have been investigated following thermo-mechanical testing in a Gleeble 3500 thermomechanical simulation unit. The following chapter will give a short introduction to the MAX phase ceramics and their structure, properties, and applications. This chapter will also touch upon the synthesis, fabrication techniques and applications of the MAX phase ceramics.

The MAX phases are a class of layered ternary compounds with the general formula $M_{n+1}AX_n$, where M is an early transition metal, A is a group A element, X is either Carbon or Nitrogen and n is a value between 1 and 3[1]. They were first discovered in powder form by Jeitschko and Nowotny in the 1960's, where they termed what was to become the 211 class, as a H-phase [2–11]. More than 60 ternary carbides and nitrides have been identified since those early discoveries [12]. The value of n determines the custom of referring to the M_2AX, M_3AX_2 and M_4AX_3 phases as 211, 312 and 413 phases respectively. It should be noted that there is also experimental evidence for the existence of higher order MAX phases such as 514, 615 and 716 [13]. Although not studied in great detail in this work, the MAX phases also have the ability to form substitutional solid solutions in each of the M, A and X elements [1]. However, this work will predominantly focus on the M_2AX and M_3AX_2 phases.

All of the MAX phases have a layered hexagonal structure with a space group of $P6_3/mmc$ with two formula units per unit cell. This hexagonal crystal structure consists of edge sharing M_6X octahedron interleaved with A layers. The structures of the 211, 312 and 413 phases have one major difference in the number of M layers in between every two A layers. There are two in 211, three in 312 and four in 413 [1-13]. This layering is of great importance when it comes to understanding the general properties of the MAX phases, and has been discussed in more detail in later chapters.

A major characteristic of the MAX phase ceramics is their highly unusual properties. They combine the advantageous attributes of both metallic and ceramic materials in possessing the good electrical and thermal conductivity, high damage tolerance, readily machineability and thermal shock resistance of metallic materials with the high temperature resistance, high elastic moduli and good oxidation and corrosion resistance of ceramic materials. It is these unusual properties that have led to some publications terming this class of materials as 'metallic ceramics'. As previously stated, the layered structure has a significant effect on the properties of the MAX phases. This layered structure, with the predominantly metallic nature of the exceptionally strong MX bonds together with the somewhat weaker MA bonds, give the characteristic properties of the MAX phases. The layering has particular importance to the mechanical properties of the MAX phases, the primary interest of this work [1,12–15].

One of the primary MAX phase ceramics investigated in this work was in the Ti-Al-C system, namely the 211 phase, Ti_2AlC. This is one of the most researched MAX phases and according to Web of Science, around 600 papers have been published on this MAX phase alone. It is one of the few MAX phases to be synthesized in fully dense bulk forms [16]. Ti_2AlC was first synthesized in powder form by a group of Russian scientists in the 1970's, although their microhardness results are very different to modern findings. Nowotny et al, who is credited as having discovered the MAX phases first reported on Ti_2AlC in 1980 [2–11]. Like most known MAX phases, Ti_2AlC is known to possess good electrical and thermal conductivity, with an electrical conductivity of around $3.0x10^6 \Omega^{-1}.m^{-1}$ at 300K and a thermal conductivity of 46 W/mK. The mechanical properties of this MAX phase are also indicative of most MAX phases in that it has good thermal shock resistance and is damage tolerant while also possessing high compressive strengths and a hardness value around 4 GPa [1,17–21].

Ti_3SiC_2 is the other MAX phase which has been investigated in this work. Ti_3SiC_2 was the first MAX phase to have its structure determined and was also the first MAX phase that was synthesized by Nowotny in the early discoveries of the MAX phases. However, due to the difficulties in fabricating single phase, bulk, polycrystalline samples, its potential to be used for structural high temperature material was not fully realised [1,2,15,22]. Like Ti_2AlC, those early problems of fabricating a fully dense, bulk samples have been overcome and Ti_3SiC_2 can also now be purchased in various bulk forms [16]. Ti_3SiC_2 also possesses a better thermal and

electrical conductivity than titanium metal, with values of 43 W/mK and $4.5x10^{6}\Omega^{-1}m^{-1}$ respectively. It is also quite resistant to thermal shock and with a hardness of 4 GPa that is anonymously low for a carbide. Like most MAX phases it is also readily machinable [22]. A simple search for research papers online shows that Ti_3SiC_2 is the most extensively studied MAX phase so far.

The properties of both MAX phases will be discussed in further detail in the following chapters, but it should be apparent just from this short introduction that these properties make the MAX phases suitable for a variety of applications. Some applications involve utilising the high temperature capabilities of the MAX phases, such as aerospace engines. The MAX phases also have potential applications in areas such as substitution for machinable ceramics, kiln furniture, wear and corrosion protection, low friction applications and electrodes.

It is due to these plethora of potential applications that investigating the reaction of the MAX phases to extreme conditions such as the high strain rate, high temperature tests is of great interest. While there have been several studies on the effect of similar conditions, this work has attempted to combine the results of thermomechanical testing with the subsequent microscopic and crystallographic analysis of samples into a cohesive report to understand the mechanisms behind the failure of the MAX phases and their potential suitability for high temperature applications. Crystallographic analysis techniques such as EBSD and GND have also been employed to identify and understand such mechanisms, with these methods not having been fully utilised in previous studies.

Chapter 2 - Aims

The aims of the project are as follows:

- To complete a literature review investigating MAX phase ceramics, with particular focus on their mechanical properties and performance after being subjected to high temperatures and uniaxial compression.

- To carry out a study on the original microstructure of the two MAX phase ceramics, Ti_2AlC and Ti_3SiC_2.

- To undertake an experimental study simulating the high temperature thermos-mechanical performance of the MAX phase ceramics, using the Gleeble 3500 thermomechanical simulation unit. At high temperatures, different heating ‘regimes’ will be simulated. This will be performed by modifying various parameters in the testing, such as the temperature, amount of strain and amount of strain rate.

- To undertake thermal shock tests on the MAX phase ceramics while subjected to mechanical loads.

- To perform an investigation to characterise the deformation damage using scanning electron microscopy techniques, including EDS and EBSD instruments.

Chapter 3 - Literature Review

3.1 Introduction to the Literature Review

This study is principally investigating the high temperature thermos-mechanical performance of MAX phase ceramics. It is therefore necessary to compile a detailed literature review on the MAX phases and their properties. The following chapter has been split into a few overarching sections, with the first section reviewing the fundamentals of the MAX phases such as the terminology, crystal structure and an introduction to other aspects and their properties.

The second and third parts will go into detail on the two MAX phases which will be studied and tested for this work, Ti_2AlC and Ti_3SiC_2. How these materials are synthesized, their microstructure and thermal and electrical properties will just be a few of the topics discussed here.

The following section will concentrate on what this work is predominantly based around, the mechanical properties of all MAX phases and in particular Ti_2AlC and Ti_3SiC_2. The primary aim for this section is to review literature on the high temperature mechanical properties, with uniaxial compression, strain rates, resistance to thermal shock and deformation mechanisms being of notable interest. Other related properties including the room temperature properties and the residual effects of applying stress in areas such as electrical and thermal properties will also be investigated.

High strain-rate testing of aerospace components will be touched upon in the following section, as well as introducing the main piece of equipment to be used for the PhD, the Gleeble 3500 thermomechanical simulation unit. The penultimate section will then evaluate some of the high temperature applications of the MAX phases, with particular emphasis on the aerospace applications. The main findings of the literature review will be summarised in the final section, which will also outline potential areas where further research and experimentation could be taken.

3.2 The MAX phases: terminology, crystal structure, existing phases and physical properties

The MAX phases were first synthesized by Jeitchko and Nowotny in the 1960's. They have been defined as a family of nanolaminated ternary nitrides and carbides. As the name suggests, they possess a general formula of $M_{n+1}AX_n$, with the value of n being between 1 and 3, M being an early transition metal, A being a group A element and X being either Carbon or Nitrogen. Among the early discoveries in the 1960's was that these phases possessed a $P6_3/mmc$ space group and a hexagonal crystal structure. *Figure 3.1* shows a periodic table with the location of the M, A and X elements that go into forming the MAX phases [1,2,11,23,3–10].

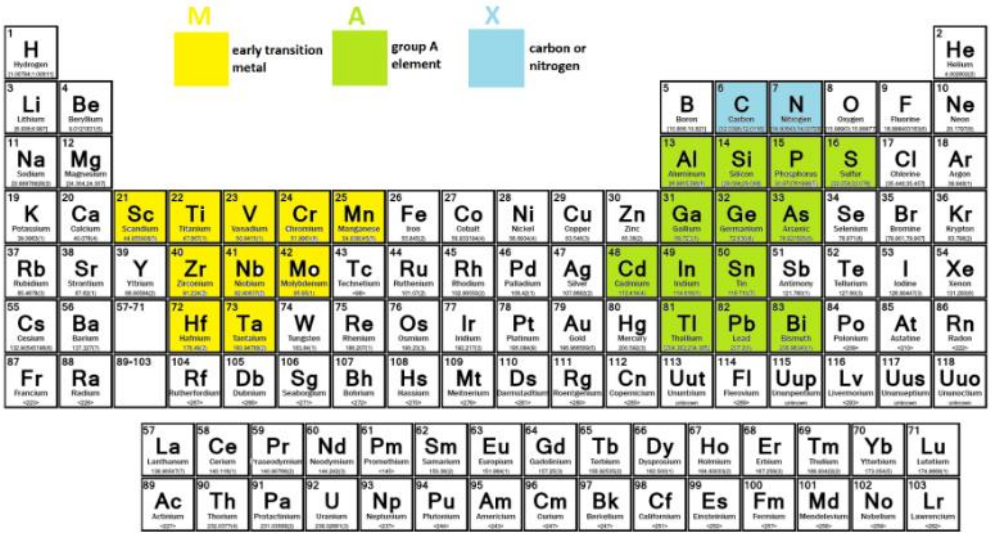

Figure 3.1: *Location of the M, A and X elements that form the MAX phases in the periodic table.[23]*

Shown in *Figure 3.*2 (a) are the unit cells of the M_2AX (211) and M_3AX_2 (312) phases, the phases that are being studied for this work. To complete the picture, the unit cell of the 3rd most understood class of MAX phases in M_4AX_3 (413) phase is shown in *Figure 3.2 (b).* It has been noted that each structure consists of edge sharing M_6X octahedra which is interleaved with A layers. This is identical to that found in the rock salt structure of the MX binaries [15]. The main difference between each unit cell shown in *Figure 3.1* is, as the terminology suggests, in the number of M layers separating the A layers, meaning that there are two M layers separating the A layers in the 211 MAX phases, three in the 312's and four in the 413's. This observation can be seen in the cross section of the M_2AX, M_3AX_2 and M_4AX_3 phases alongside

the unit cells in *Figure 3.2*, which appears similar to published HRTEM micrographs [14,24,25].

As the MAX phases investigated for this work are Ti_2AlC and Ti_3SiC_2, the 211 and 312 unit cells are of more interest than the 413. Applying the figure to Ti_2AlC, the red M circles correspond to Ti, the white A circles Al and the grey circles C, meaning that the structure consists of two adjacent Ti-C-Ti chains sharing one Al atom. Similarly, for Ti_3SiC_2, there are two adjacent Ti-C-Ti-C-Ti chains sharing one Si (A) atom. It can also be seen that the 413 system also follows the same trend, with an extra layer of the M and X layers between each row of A atoms. A well-known example of the 413 phases is Ti_4AlN_3 [1].

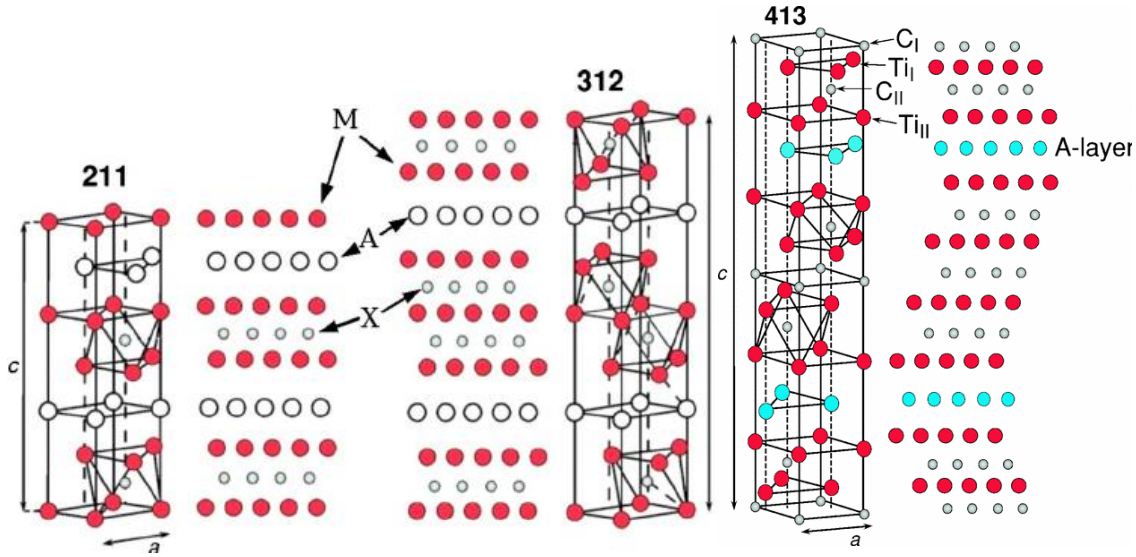

Figure 3.2: (a) *Unit cells for the 211 and 312 MAX phases with cross sections.* ***(b)*** *Unit Cell for 413 MAX phase with cross section.* [24,25]

Barsoum and others have so far reported that more than 60 MAX phases and solid solutions have either been experimentally synthesized, calculated or predicted. The 211 phases are by far the most common type of MAX phase, with some reports suggesting over 50. Since 2001, when Barsoum compiled the first comprehensive review of the MAX phases and found only three 312 phases and one 413 phase, synthesizing methods have improved and changed and now the number in both classes has more than doubled. *Figure 3.3* shows a table of the existing MAX phases split into their different classes and sorted by stoichiometry and valence electron configuration of M and A elements [12,23].

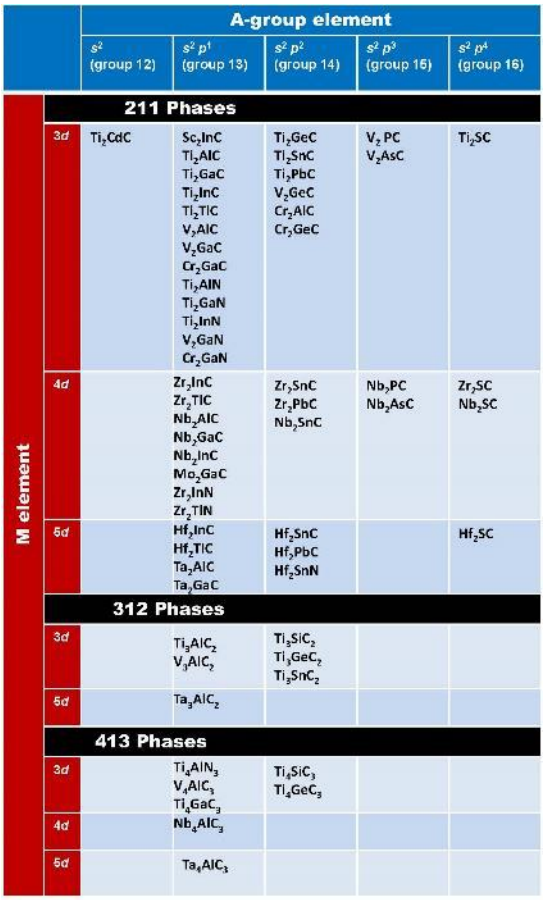

		A-group element				
		s^2 (group 12)	$s^2 p^1$ (group 13)	$s^2 p^2$ (group 14)	$s^2 p^3$ (group 15)	$s^2 p^4$ (group 16)
M element	**211 Phases**					
	3d	Ti_2CdC	Sc_2InC Ti_2AlC Ti_2GaC Ti_2InC Ti_2TlC V_2AlC V_2GaC Cr_2GaC Ti_2AlN Ti_2GaN Ti_2InN V_2GaN Cr_2GaN	Ti_2GeC Ti_2SnC Ti_2PbC V_2GeC Cr_2AlC Cr_2GeC	V_2PC V_2AsC	Ti_2SC
	4d		Zr_2InC Zr_2TlC Nb_2AlC Nb_2GaC Nb_2InC Mo_2GaC Zr_2InN Zr_2TlN	Zr_2SnC Zr_2PbC Nb_2SnC	Nb_2PC Nb_2AsC	Zr_2SC Nb_2SC
	5d		Hf_2InC Hf_2TlC Ta_2AlC Ta_2GaC	Hf_2SnC Hf_2PbC Hf_2SnN		Hf_2SC
	312 Phases					
	3d		Ti_3AlC_2 V_3AlC_2	Ti_3SiC_2 Ti_3GeC_2 Ti_3SnC_2		
	5d		Ta_3AlC_2			
	413 Phases					
	3d		Ti_4AlN_3 V_4AlC_3 Ti_4GaC_3	Ti_4SiC_3 Ti_4GeC_3		
	4d		Nb_4AlC_3			
	5d		Ta_4AlC_3			

Figure 3.3: *Table of the existing $M_{n+1}AX_n$ phases compiled by Barsoum and his team. Table is sorted by stoichiometry and valence electron configuration for the M and A elements.*

It has already been touched upon that the main reason for the interest in MAX phases is that they exhibit remarkable properties when compared to conventional ceramics and metals. The reason for these unusual properties is due to the nanolayered structure through the mostly metallic, with covalent and ionic contributions, nature of the exceptionally strong MX bonds which are interleaved with A layers through the weak MA bonds. There are several published articles and reports with tables and diagrams comparing the mechanical properties of all the MAX phases that have been synthesized, together with some predicted and calculated results of phases that have yet to be successfully synthesized. The MAX phases combine the virtues of both metals and ceramics to give a class of materials that couldn't be more different mechanically from the physically similar MX ceramics. For example, like metals, they are readily machinable, damage tolerant, relatively soft at 1-5 GPa, resistant to thermal shock and deform plastically at elevated temperatures. As well as these mechanical properties, they are both thermally and electrically conductive. Like conventional ceramics, MAX phases are

known to be oxidation resistant, relatively stiff, resistant to chemical attack and have a relatively low coefficient of thermal expansion. Their impressive mechanical properties above high temperatures has enhanced interest in the potential applications for the MAX phases with aerospace being perhaps the most exciting area. These potential applications will be discussed in greater detail later in this chapter [1,12,15]

3.3 Ti_2AlC - Introduction

Of all the MAX phases that have been discovered, Ti_2AlC is one of the most studied and most promising. First discovered by Jeitschko and Nowotny in the 1960's, the interest in this particular layered ternary carbide stems from the ability to tailor their properties, which is due to the fact that there are two distinct but structurally related ternary phases in the Ti-Al-C system, Ti_2AlC and Ti_3AlC_2 [4,20]. The density of Ti_2AlC is also relatively low at 4.11 g/cm^3, which is especially beneficial when it is used as a structural material for aerospace applications or as a reinforcement for polymers and metals [17,18]

Crystallising in a $P6_3/mmc$ space group, the location of the atoms are at the following Wyckoff positons: Ti at 4*f,* Al at 2*c* and C at 2*a.* The lattice parameters have been calculated as a=3.04 Å and c=13.60 Å with two formulae per unit cell [17]. An example of the same unit cell as Ti_2AlC can be found in *Figure 3.2*, with Ti occupying the red M dots, Al the white A dots and C the grey X dots.

Ab initio calculations conducted at the turn of the century indicated that the chemical bonding of Ti_2AlC was metallic-covalent-ionic in nature. Zhou and Sun found that there was metallic bonding in the Ti and Al layers. The Ti-C interaction was noted to be very strong and covalent in nature, while the bonding between Ti and C was found to be ionic due to C being more electronegative compared to Ti. Ionic bonding was also found between Ti and Al due to the more electropositive nature of Al [21]. It is this bonding that provides Ti_2AlC with its unusual physical and mechanical properties. The metallic bonding is responsible for the good electrical conductivity while the high strength, modulus and melting points has been credited to the covalent and ionic bonding of Ti-C [15,21].

3.3.1 Synthesis

The production of ceramics is usually carried out using a process called sintering. This method involves heating a powder compact at an elevated temperature which is below its melting point. This causes the particles to fuse together and the voids between the particles to decrease until eventually a dense, solid body is attained. Sintering technology has been used for thousands of years and is well known for the manufacture of bricks and porcelain ware. Sintering is still used today, but the technology has improved considerably and a number of different types have been developed. The sum of the surface-free energy of a powder compact is not at its minimum and therefore not in equilibrium.

When the system is heated, it tries to decrease its surface-free energy by decreasing its total surface area and therefore forcing the powder particles to join together. The excess surface-free energy of the powder compact has been noted to be the driving force of sintering. The sintering process improves the physical and mechanical properties of the material [26].

Since the pioneering work conducted by Jeitschko and Nowotny in the early 1960's in discovering Ti_2AlC, numerous methods have been developed to prepare this ternary carbide. One technique that has been explored significantly is that of hot isostatic pressing (HIP) or the very similar hot pressing (HP). In 1976, a two step method involving first the synthesis of powders and then the subsequent sintering of grounded powders was undertaken by Ivchenko *et al.* These compacts were recorded as being of 90 to 92 pct dense and their properties were measured, however the results have do not compare well with later studies (ie. Hardness values of >20 GPa compared to more recent studies which suggest a hardness of ~4.5 GPa) [19,27,28]. Wang and Zhou believed this could be explained by the nominal Ti_2AlC containing significant amount of a TiC_x phase [19]. It took over two decades before Barsoum *et al* were able to produce high purity bulk samples of Ti_2AlC. In 1997, using the HP process they hot pressed powders of Ti, Al_4C_3 and graphite at 1600°C for 4 hours under a pressure of 40 MPa and a heating rate of 10°C/min. Under closer inspection using an SEM, it was discovered that the material produced was fully dense Ti_2AlC [18]. Later, in 2000, Barsoum *et al* employed the HIP technique to mix Ti, Al_4C_3 and graphite powders to form Ti_2AlC. Increasing the amount of time while the material was subjected to a pressure of 40 MPa at 1300°C led to a decrease in the amount of the unwanted secondary phases of TiC_{1-x} and Ti_3AlC_2 until 30 hours, where

Ti_2AlC was the only remaining phase. The first high purity Ti_2AlC was developed by Barsoum using these techniques [17]. Dense polycrystalline Ti_2AlC was also synthesized by Bai *et al* when they used self-propagating high-temperature synthesis (SHS) with the pseudo-HIP process. The phase purity was noted to be highly dependent on the raw powders molar ratio. After the SHS reaction, Ti_2AlC was densified by applying pressure [29,30].

The spark plasma sintering (SPS) method has also been utilised by Zhou *et al* to prepare high purity Ti_2AlC. This process has advantages over HP and HIP by allowing sintering at both shorter soaking times and lower temperatures. When treated at 1100°C under a 30 MPa pressure for 1 hour, high purity Ti_2AlC was obtained [31].

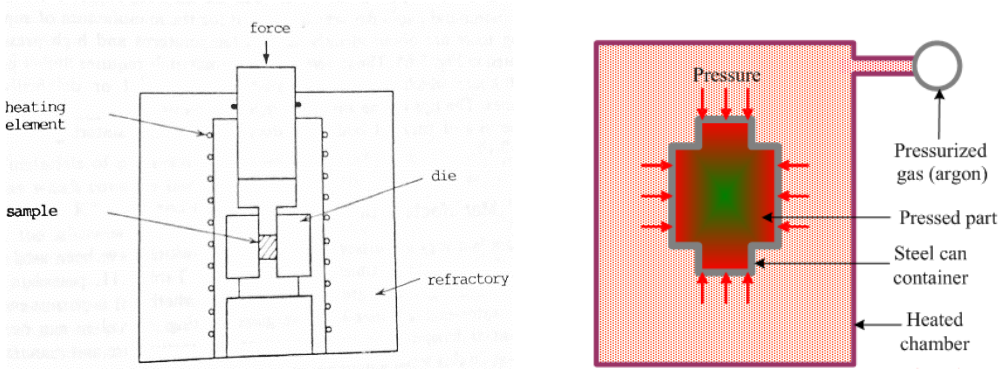

Figure 3.4: (a) *Schematic diagram of hot pressing. Hot pressing involves compacting a powder in a die and pressed uniaxially while heated to high temperatures* ***(b)*** *Schematic diagram of hot isostatic pressing. This process differs as an inert gas such as Ar is used as a pressurisation medium and sinters in a high temperature, high pressure vessel. Powders are then compacted in container in a similar manner to HP* [26,30]

Combustion synthesis is also a common technique employed to produce Ti_2AlC. Another name for the SHS process, this method was used by Lopacinski *et al* in their attempt to synthesize Ti_2AlC. A direct reaction between Ti, Al and C was performed, which was indicated to be strongly exothermic and resulted in the binary carbides of TiCa and Al_4C_3 forming in a partially molten state. The combustion temperature was significantly reduced when they adopted TiAl as the source of Al, resulting in the formation of ternary titanium aluminium phases [32]. Zhou *et al.* reported difficulties in obtaining Ti_2AlC from the SHS process, with some minor phases along with Ti_2AlC being seen. However, they were eventually able to produce single phase Ti_2AlC_{1-x} when the carbon level was deficient with respect to the ratio 3Ti/1.5Al/C or

2Ti/Al/0.7C [33]. A number of other papers have been written on the topic of using the SHS process to produce Ti_2AlC, but while improvements and breakthroughs have been made it should not go unnoticed that samples prepared by combustion synthesis are never dense. A post densification process associated with pressure is required to obtain dense samples. [28,34–38]

Despite the HP, HIP and SPS methods being able to successfully produce dense, high phase pure Ti_2AlC in bulk form, there are drawbacks to these techniques. Major shortcomings include the inefficiency that derives from pressure needing to be utilised during the process and the difficulty of mass producing, particularly mechanical parts with complex shapes. Pressureless sintering (PS) involves sintering the material from a green compact of powders without mechanical pressure. Attempts to pressureless sinter Ti_2AlC were made by Hashimoto *et al*. When they sintered Ti_2AlC without additives, the relative density was recorded as 94.2%. Several oxides, including Al_2O_3, Y_2O_3, MgO, Cao, or TiO_2 of 5 wt pct were mixed in with the Ti_2AlC powders to improve densification, yielding a density of 96.0% when the sample mixed with 5 wt pct of Al_2O_3 was tested [39].

It should now be apparent that there are a number of ways producing Ti_2AlC. Some of these methods have been touched upon once again when discussing the production of the Ti_3SiC_2 MAX phase. Despite only focussing on two of the MAX phases, these methods can generally be applied to most other MAX phases, as evidenced by the studies on the other MAX phase in the Ti-Al-C system, Ti_3AlC_2. Using similar composition of elemental powders and under similar sintering conditions to Ti_2AlC, researchers have been able to synthesize Ti_3AlC_2.

The Ti_2AlC MAX phase that was used for this thesis was produced by Kanthal, a subsidiary of the Sandvik group, under the product name of Maxthal 211. In collaboration with Drexel University, two patents were lodged by the group on the production of the MAX phases. These patents suggest that the material used was manufactured using combustion synthesis [22,40,41].

3.3.2 General information and microstructure

As is established, small changes in heat treatment conditions or starting materials can lead to different microstructures and different materials. As with any material, the microstructure has a pivotal role to play in its properties, including their physical, chemical and mechanical properties. As such, this section will review the works done on characterising the microstructure of Ti_2AlC.

Lin *et al.* undertook a comprehensive investigation of Ti_2AlC as a monolithic ceramic material with microstructural features. Before this, it had been well established that Ti_2AlC formed as a precipitate in the Ti-Al alloys when carbon was added, leading to the enhancement of mechanical properties [42,43]. For their work, Lin *et al.* prepared Ti_2AlC by the solid-liquid reaction/in situ HP method and discussed the microstructural characterisations of hexagonal Ti_2AlC and the crystallographic relationships of Ti_3AlC_2, TiC and TiAl with Ti_2AlC [28]. As has already been established with results from powder XRD and using selected area electron diffraction (SAED) patterns, high-resolution transmission electron microscopy (HRTEM) and their corresponding images, it was found to crystallise in the $P6_3/mmc$ space group. The high temperature properties of polycrystalline ceramics are primarily determined by the grain boundaries. The HRTEM images taken for that study can be found in *Figure 3.5*. From these images, especially *Figure 3.5a*, it was observed that most of the grain boundaries in Ti_2AlC are large angle and also that grains with misorientation of a few degrees are present. *Figure 3.5(a)* is HRTEM image of a Ti_2AlC grain boundary and shows the absence of any secondary glass phase. It has been noted the excellent high temperature oxidation resistance of Ti_2AlC might be due to this absence. The crystalline grain boundary may also provide this carbide with its high temperature strength [43].

Lin *et al.* also discovered, using HRTEM imaging and energy dispersive spectroscopy (EDS) analysis, intergrowth of Ti_3AlC_2 and Ti_2AlC, and TiC and Ti_2AlC in the otherwise single phase sample. A lattice image of intergrowth of Ti_2AlC and Ti_3AlC_2 is shown in *Figure 3.5(b).* According to image simulations, the white columns correspond to Al layers while the grey columns correspond to Ti layers. It was realised that every three or two Ti layers were separated by Al layers in the same grain. This observation, together with the fact the structurers of Ti_3AlC_2 and Ti_2AlC are so that the number of Ti layers separated by Al layers is three in

Ti_3AlC_2 and two in Ti_2AlC, led them to the conclusion that intergrowth of Ti_3AlC_2 with Ti_2AlC was present. In addition to Ti_3AlC_2, TiC has also been seen to intergrow with Ti_2AlC, as shown in the HRTEM image in *Figure 3.5(c).* The orientation relationships between Ti_2AlC and TiC were revealed to be $(0001)Ti_2AlC//(111)TiC$ and $[11\bar{2}0]Ti_2AlC//[1\bar{1}0]TiC$. Compositional analysis using a high-angle annular dark-field detector (HAADF) in the scanning TEM also confirmed this intergrowth. The HAADF image is shown in *Figure 3.6(a)* while the EDS line scan profiles along the line are shown in *Figure 3.6(b).* As is evident from the figure, the results show that the thin platelet is rich in I and lacking in Al. Lin *et al*. concluded that when combined with the HRTEM image, that the thin platelet is TiC and that TiC can intergrow with Ti_2AlC. It was determined that the presence of the Ti_2AlC-Ti_3AlC_2-Ti_2AlC and Ti_2AlC-TiC-Ti_3AlC_2 intergrown structures was due to the local segregation of Ti and lack of Al [44].

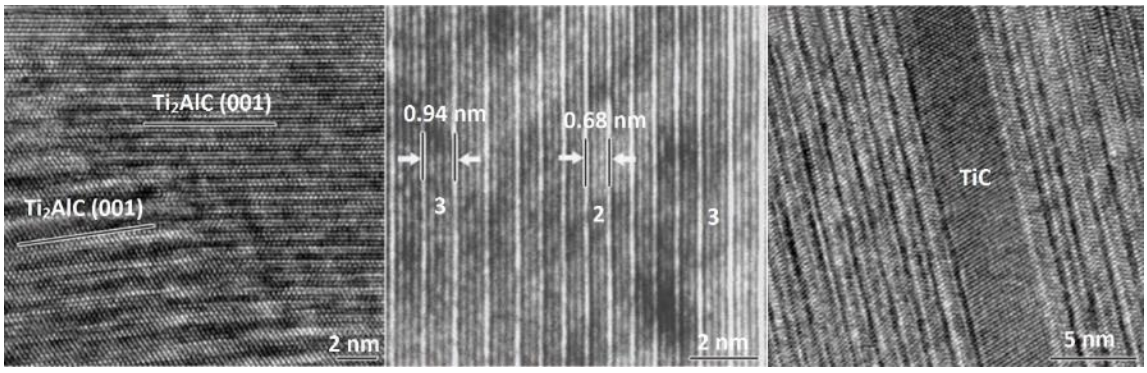

Figure 3.5: (a) *Typical HRTEM image taken at a Ti_2AlC grain boundary. Note that no amorphous grain boundary phase is observed;* ***(b)*** *Lattice image showing intergrowth of Ti_3AlC_2 with Ti_2AlC;* ***(c)*** *Intergrowth of TiC with Ti_2AlC [44]*

Wang *et al*. found that TiAl was an intermediate phase when they synthesised Ti_2AlC from elemental powders using a novel solid-liquid reaction synthesis and simultaneous densification method [28]. Due to the transformation from TiAl to Ti_2AlC not being fully understood, Lin *et al*. hot pressed the elemental powder compact for 30 minutes at 1400°C and studied the microstructure. Using XRD, they found that the as prepared sample was similar to the single-phase (Ti_2AlC) sample. They found a minor contribution from the TiAl (111) reflection in the as-prepared sample. However, due to the weak intensity of the reflections of TiAl it was determined that the TiAl content is small. A fine and uniform lamellar structure was identified in the as-prepared sample using TEM. SAED analysis revealed that these lamellar structures consisted of TiAl twins, while linear diffusion streaks suggested significant amounts of two-dimensional defects. A HRTEM image of the TiAl twin boundaries showed the Ti_2AlC thin

platelet forms uniformly along the twinned Ti-Al laths and at the TiAl twin boundaries, countering what had been reported by Chien *et al* [45]. Lin *et al* found that significant amounts of TiAl twin boundaries and two dimensional defects provide rapid diffusion paths for carbon. They also noted that large amounts of carbon helped accelerate the dissolution of TiAl laths, leading to rapid formation of Ti_2AlC [44].

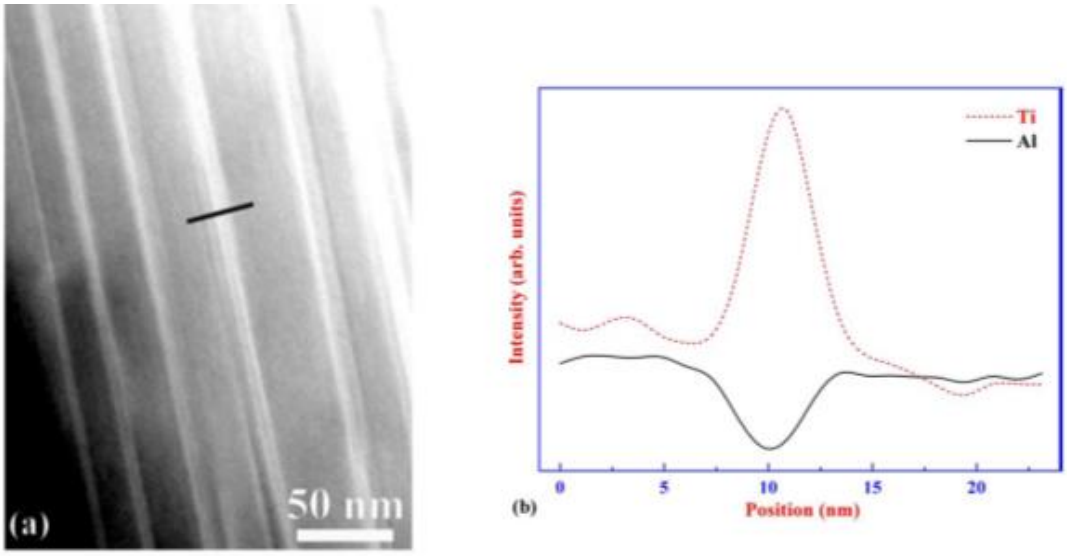

Figure 3.6: (a) *HAADF image showing presence of thin platelets in Ti_2AlC;* ***(b)*** *EDS line-scanning profiles along the line shown in (a). [43]*

3.4 Ti_3SiC_2 - Introduction

Ti_3SiC_2 is perhaps the most important MAX phase in the history of the layered ternary compounds. It was this phase that was first synthesised by Jeitschko and Nowotny in the 1960's via a chemical reaction between TiH_2, Si and graphite at 2000°C. Nickl *et al.* were the first to realise that Ti_3SiC_2 was atypical when they worked on chemically vapour deposited, CVD, single crystals. Their work showed that Ti_3SiC_2 was anomalously soft for a carbide. It was also found that the despite this, the hardness was quite anisotropic and the hardness normal to the basal place about 3 times that of the parallel to them [46]. Like most other MAX phases, Ti_3SiC_2 combines the prominent properties of both metals and ceramics. However, the main stumbling block that hindered conclusive investigations into the properties was the difficulty in synthesising monolithic-bulk-dense Ti_3SiC_2. However, the recent breakthroughs in synthesis has allowed these properties to be more intensively examined.

Barsoum *et al* recorded a relatively low density of 4.52 g/cm^3, making it one of the least dense MAX phases. This, like Ti_2AlC, allows it to be considered for use as a structural material. Like every MAX phase, Ti_3SiC_2 crystallises with the $P6_3/mmc$ space group in a hexagonal structure and lattice parameters of a=0.3068 nm and c=1.7669 nm [22]. An example of the Ti_3SiC_2 crystal structure can be found in *Figure 3.2(b).* There are two formula units per unit cell, with the Wyckoff positions of Ti corresponding to 2a and 4f, Si to 2b and C to 4f. Similar to other MAX phases in its 312 class, the structure of Ti_3SiC_2 can be described as two edge-shared Ti_6 octahedron layers linked by a two-dimensional closed packed Si layer.

Many, including Zhang *et al*, found that the properties were strongly related to their bonding characteristics and the layered microstructures. The fundamental relationship of "microstructure-property" can be examined in greater detail using this exceptional material [47].

3.4.1 Synthesis

Single-phase Ti_3SiC_2 is notoriously difficult to be synthesized with the purity of a finished sample depending on the processing parameters. Early attempts at synthesising Ti_3SiC_2 involved chemical vapour deposition (CVD) or the reaction of gaseous reactant at temperatures as high as 2273K [2]. There are several problems with these methods however, with the formation of the TiC, SiC, Ti_5Si_3 and $TiSi_2$ impurity phases among them. Of these, TiC is the main impurity and die to the close structural relationship between TiC and Ti_3SiC_2 is difficult to remove.

As previously stated, a popular early method for synthesising Ti_3SiC_2 was to use CVD. This method has been popularly used be several research groups, including Nickl *et al*, who synthesised it first in 1972. When investigating the $TiCl_4$-$SiCl_4$-CCl_4-H_2 system, they found a deposition ternary diagram at T=1473K and $p=10^5$ Pa. However, the conditions favourable to the deposition of pure Ti_3SiC_2 were very narrow, particularly in terms of initial molar fraction CCl_4. As was later confirmed by Goto *et al*, the final product was more often than not Ti_3SiC_2 with TiC, SiC, $TiSi_2$, Ti_5Si_3 or two of these binary compounds [46,48].

Like Ti_2AlC, Ti_3SiC_2 was also synthesised using SHS by Lis *et al* in a series of papers. When employed with hot isostatic pressing of Ti_3SiC_2-based powders, the SHS prepared specimens were found to be dense and polycrystalline. They found the bulk material to possess a high stiffness of E=350 GPa, a relatively low Vickers hardness of between 2 to 6 GPa, a high fracture toughness close to 10 $MPa.m^{1/2}$, a pseudo-ductile character at room temperature, plastic behaviour at elevated temperatures and high chemical and corrosion resistance. However, Ti_3SiC_2 tended to transform into cubic TiC when subjected to high temperatures and high pressures [49]. The influence that high energy mechanical alloying has on the SHS of Ti_3SiC_2 was investigated by Riley *et al*. They concluded that the mechanical alloying pre-treatments improved the SHS process, enabling the synthesis of higher purity Ti_3SiC_2. They also found a beneficial relationship between milling time and ignition temperature: increasing homogeneity of reactants improved purity or Ti_3SiC_2; (2) as the overall enthalpy of the reaction remained constant, lowering the ignition temperature potentially decreased the combustion temperature, and then reduced reactant losses through vapourisation; (3) greater densities of nucleation sites promoted a more uniform combustion reaction, reducing thermal and concentration profiles across the sample [50].

Arc melting involves using a furnace that heats charged material by means of an electric arc. This method in relation to Ti_3SiC_2 was first comprehensively studied by Arunajatesan *et al*, where they synthesised bulk Ti_3SiC_2 using arc melting and post annealing. Using Ti, Si and C as starting materials they investigated the effect of various parameters on the phase purity of Ti_3SiC_2, including the starting compositions, compaction techniques, arc melting of the samples and annealing temperatures and time. Slightly Si-deficient and C-rich starting compositions yielded their best bulk sample, containing a TiC second phase of approximately 2 vol. pct. They concluded that Ti_3SiC_2 existed over a range of compositions, such as in the C-deficient, C-rich and Si-deficient regions [51]. Abu *et al*. later also attempted to synthesise high purity Ti_3SiC_2 from elemental powders using the arc melting method. They found that samples sintered at 80 s and arced at 30 A produced a near single phase of Ti_3SiC_2 (99.2 wt%) with a relative density of 88.9%, these results being dependent on the formation of macropores in bulk samples and micropores in TiC_x grains. They proposed that the Ti_3SiC_2 might be formed from TiC_x + Si, $Ti_5Si_3C_x$ + C, and $Ti_5Si_3C_x$ + TiC_x at early arcing times while at between 15 and 80 s TiC_x + $TiSi_2$ takes place. After 80 s, decomposition of Ti_3SiC_2 into TiC_x, $TiSi_2$ and C was observed [52].

Synthesis of Ti_3SiC_2 was notoriously difficult due to the normally solid-solid reaction that was involved in the formation of Ti_3SiC_2. Zhimei *et al*. found that the formation of a liquid phase in the Ti-Si-C was favourable for the formation of Ti_3SiC_2. NaF was added at elevated temperatures to the powder mixtures and formed a liquid phase, dramatically increasing the amount of the as-prepared Ti_3SiC_2 [53]. Following this, Zhou *et al*. proposed using the in-situ hot pressing/solid liquid reaction synthesis using elemental Ti, Si and graphite powders as the initial materials. Their best results came from heating at 1550°C for 1 h under the pressure of 38 MPa. The solid-solid reaction process was changed to become the solid-liquid reaction process by optimising the processing parameters, namely by melting Si and Ti-Si intermediate phases and through the exothermic reaction during the formation of Ti_3SiC_2. This had the positive effect of significantly promoting the reaction rate and decreasing the synthesising time, while the liquid phase increased the relative density of as-prepared samples to more than 98.8%. This method not only exhibits itself with excellent recorded mechanical properties but also the ability to form large-scale samples [54].

HIP was employed by Barsoum *et al*. when they fabricated bulk polycrystalline Ti_3SiC_2 by mixing 3Ti/2C/1SiC powders. The powders were cold pressed at 180 MPa and then hot pressed at 1600°C for 4 h under a pressure of 40 MPa. XRD and SEM analysis was then utilised and found that there was less than 2 vol. pct SiC and TiC in the final sample but no porosity. The as-prepared samples were subjected to a variety of tests to determine their properties. They recorded a compressive strength at room temperature of 600 MPa, which dropped to 260 MPa a 1300°C. However, the mechanical response changed from brittle failure at room temperature to a more plastic behaviour at high temperature [22].

The similar hot pressing method was used by Luo *et al*. when they synthesised Ti_3SiC_2 from mixtures of Ti, Si and active carbon powders. Like the process used in hot isostatic pressing, the starting materials were firstly cold pressed at 100 MPa before the green compacts were hot pressed at 1500 to 1700°C under a pressure of 25 MPa in flowing argon. They recorded a Ti_3SiC_2 content of higher than 99 wt pct [55].

The similar spark plasma sintering (SPS) and pulse discharge sintering (PDS) methods have also been used to synthesise bulk Ti_3SiC_2. Gao *et al*. rapidly synthesised and simultaneously consolidated Ti_3SiC_2 from a starting mixture of Ti/Si/2TiC using the SPS technique. Within the 1250-1300°C sintering temperature range and depending on the applied pressure and dimension of the sample, Ti_3SiC_2 with 2 wt.% TiC_x was produced. Using XRD, they also detected preferential grain growth of Ti_3SiC_2 along the crystallographic basal place. The anisotropic hardness of the material was due to the platelet grains tending to align perpendicular to the loading surface [56]. The PDS technique was employed by Zhang *et al* when they subjected Ti/SiC/TiC powders to temperatures of between 1250 and 1450°C to synthesise bulk Ti_3SiC_2. The purity and density of the resulting Ti_3SiC_2 was as high as 98 vol.% and 99% respectively when the sintering temperatures were above 1350°C. Three microstructures were observed, *i.e.* fine, coarse and duplex grains [57,58].

Li *et al.* investigated the pressureless sintering process of Ti_3SiC_2 by subjecting the mechanically alloyed elemental Ti, Si and C powder mixture starting materials to temperatures of about 1500°C. At 1100°C, the mechanically alloyed elemental powders converted to Ti_3SiC_2, with densification occurring after increasing the sintering temperatures up to 1500°C. The as-prepared sample possessed a density of over 98% and purity of nearly 80%, with a secondary TiC_x phase. They found that the properties were similar to that of hipped Ti_3SiC_2 [59].

3.4.2 General information and Microstructure

The reaction processes to form Ti_3SiC_2 are numerous and varying, with small alterations in the starting materials resulting in a potentially totally different reaction process to form Ti_3SiC_2. In the first of their two-part study investigating the processing and mechanical properties of Ti_3SiC_2, El-Raghy and Barsoum used XRD and SEM techniques to identify TiC_x and $Ti_5Si_3C_x$ as the intermediate phases that form in the HIP production of Ti_3SiC_2 from Ti/SiC/C powders after about 1200°C [60]. Wu *et al.* later further confirmed this when they used the in-situ neutron powder diffraction to form Ti_3SiC_2 [61,62].

As is the case with many materials, the effect of time and temperature has a significant effect on the microstructure of the material. *Figure 3.7* shows this effect in the form of XRD patterns. At 1200°C and no soak time only small peaks of Ti_3SiC_2 are visible, with the main phases being TiC_x, $Ti_5Si_3C_x$ and some unreacted Ti. At 1400°C and no soak time, Ti_3SiC_2 is the major phase, while a minor TiC_x phase is also visible. The presence of $Ti_5Si_3C_x$ is also visible in SEM micrographs, fulfilling the mass balance criteria that requires a secondary phase with silicon present. El-Raghy and Barsoum produced a micrograph (*Figure 3.8*) which shows the 1400°C sample etched in HF. They noted that the HF dissolves the $Ti_5Si_3C_x$, suggesting that nucleation and growth of Ti_3SiC_2 occurs within the $Ti_5Si_3C_x$ phase. At 1600°C and between 2 to 4 h soak time, the small amount of unreacted TiC_x is removed and predominantly phase pure, fully dense samples are now produced [60].

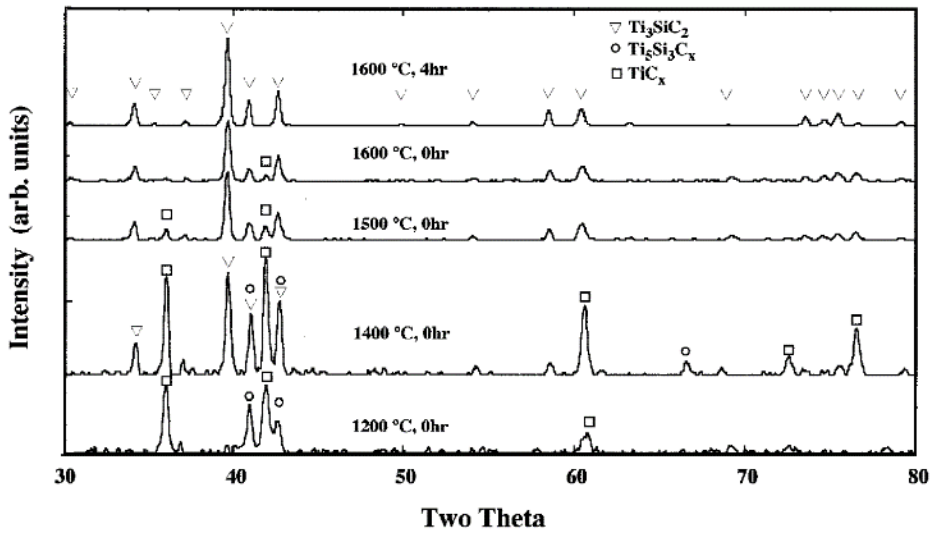

Figure 3.7: *XRD patterns of reaction products after hipping as a function of reaction temperatures and times [60]*

The reaction sequence of Ti_3SiC_2 was outlined in the appendix of El-Raghy and Barsoum's study, along with the reaction formulas. The reaction for synthesising Ti_3SiC from Ti/SiC/C powders was described by the following equation:

$$3Ti + SiC + C = \frac{4}{3}TiC_X + \frac{1}{3}Ti_5Si_3C_y + \frac{6-4x-y}{3}C = Ti_3SiC_2$$

The thermal stability of Ti_3SiC_2 was also explored in El-Raghy and Barsoum's study. They noted that some previous studies claimed that Ti_3SiC_2 dissociates at temperatures as low as

1450°C. However, by using two different annealing experiments and with the confirmation of XRD they were able to dispel those earlier theories, finding that Ti_3SiC_2 is the only phase present after those heat treatments. Some samples were even fabricated at 1700°, confirming that Ti_3SiC_2 is stable at that temperature.

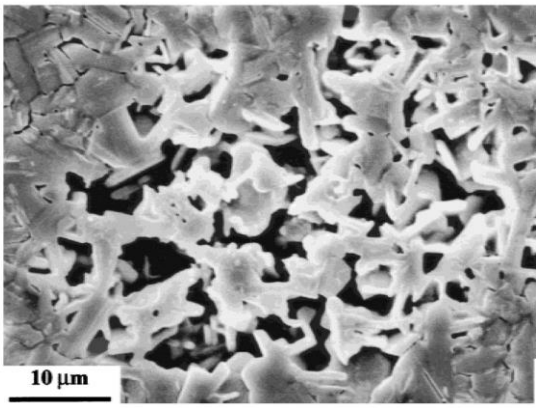

Figure 3.8: *SEM micrograph of sample heated to 1400°C and furnace cooled and etched in a solution for 10 s. A 'lighter' $Ti_5Si_3C_x$ phase has leached out, leaving only the dark Ti_3SiC_2 phase [60].*

Their microstructural evolution study of Ti_3SiC_2 was conducted in the 1450-1600°C temperature range. Three micrographs (*Figure 3.9*) were produced showing the effect of soaking time on the microstructure. In general, it was seen that the higher the temperatures and the longer the soak time, the coarser grained the microstructure. The microstructures in the *Figure 3.9* were described as small (3-5 μm), large (~200 μm) and duplex grains, which is large (100-200 μm) Ti_3SiC_2 grains embedded in a much finer matrix. They postulated that the microstructural evolution is determined by 3 dominant factors, namely: (i) unreacted phases such as predominantly TiC_x inhibiting grain growth; (ii) a large anisotropy in growth rates along the *c* and *a* directions (growth normal to the basal planes is approximately an order of magnitude smaller than that parallel to these planes at 1450°C, while at 1600°C the ratio is 4) and; (iii) the impingement of grains.

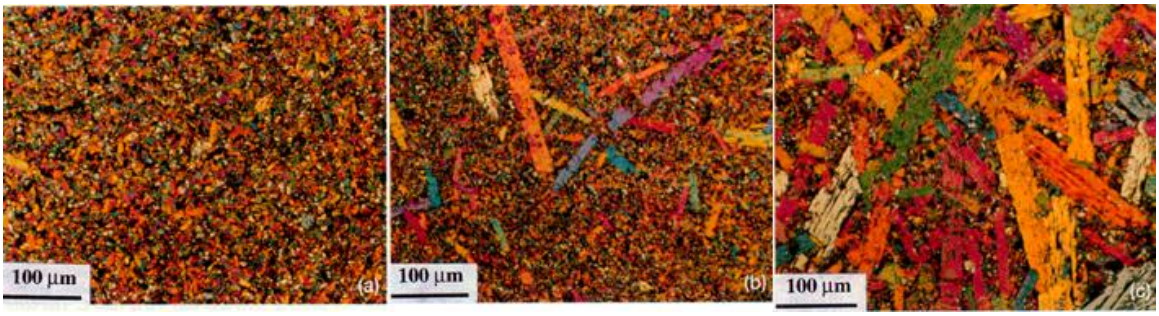

Figure 3.9: *Optical micrographs of polished and etched samples hipped samples at 1450°C for (a) 8, (b) 16 and (c) 24 h [60].*

3.5 Electrical and thermal properties

3.5.1 Electrical properties

One of the aspects that makes the MAX phases so promising is their electrical properties. As will be further explained later, in order to test the mechanical properties in the Gleeble 3500 a material must have thermocouples attached to it, therefore requiring a decent electrical conductivity. Conventional electrically insulating ceramics are unable to be tested in this manner. This is what makes the MAX phases almost unique amongst ceramics and why they are thought of so highly.

The resistivity, ρ, of the MAX phases decreases linearly with decreasing temperatures, as has been plotted in *Figure 3.10* for 3 'AlC' containing ternaries. Barsoum *et al* represented this in an equation:

$$\rho = \rho_0[1 + \alpha(T - T_{ref})]$$

Where ρ_0, α and T are, respectively, the resistivity at the reference temperature, T_{ref}, the temperature coefficient of resistivity, and the temperature in degree Kelvin. One of the reasons that the MAX phases are sometimes classed as 'metallic ceramics' derives from the metal-like conduction from the large density of states at the Fermi level $N(E_F)$ of the compounds. Theoretical results have demonstrated that the Ti d-orbitals dominates the $N(E_F)$ with these properties being comparable to their transition metal Ti [63]. In an earlier study, Barsoum *et al*. tested the resistivities of the Ti-containing ternaries, with the scatter in ρ and dρ/dt being narrow, indicating that these exist over a narrow range of stoichiometry and are therefore line compounds [1,64].

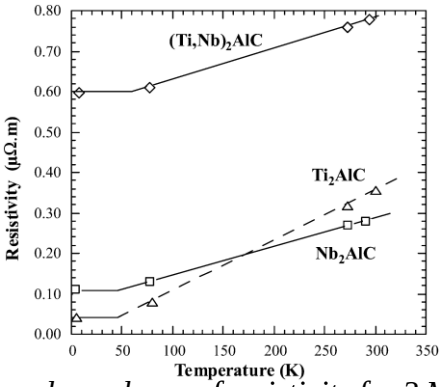

Figure 3.10: (a) *Temperature dependence of resistivity for 3 MAX phases in the range of 4.2-300 K [64].*

Ti_3SiC_2 is one such MAX phase that possesses a relatively high conductivity in comparison to other MAX phases in the same 312 class. In one of the first papers that took a comprehensive look at the electrical properties, Barsoum *et al* measured the electrical resistance using a microohmeter, from which they were able to calculate the electrical conductivity as 4.5 x 10^6 $\Omega^{-1}m^{-1}$ at room temperature [22]. Li *et al.*, among others, later confirmed this high room temperature conductivity with a similar value of 4.8 x 10^6 $\Omega^{-1}m^{-1}$. At 800°C and similar to the earlier study, they found an electrical conductivity of 1.1 x 10^6 $\Omega^{-1}m^{-1}$, showing that, like metals, Ti_3SiC_2 shows decreasing electrical conductivity with increasing temperature [65]. When Barsoum *et al* undertook a study of the Ti_3AlC_2, Ti_4AlN_3 and Ti_3SiC_2 MAX phases, they found that Ti_3SiC_2 had the highest conductivity of those tested [66]. In their earlier study they also found that the temperature coefficient of resistivity in the 50-300 K temperature range was $0.019°C^{-1}$. This, together with the fact that the electrical conductivity of Ti_3SiC_2 is higher than either pure Ti or TiC led Barsoum *et al* to conclude that delocalised electrons parallel to the Si planes are contributing to the overall conductivity [22].

The room temperature electrical resistivity of bulk Ti_2AlC was also determined by a microohmeter, and it was found that the resistivity is different depending on the synthetisation route. Bai *et al.* recorded that synthesis by the SHS/PHIP process yielded a resistivity of 0.40 ± 0.03 x 10^{-6} Ω·m, this was comparable to that recorded for HIP (0.36 x 10^{-6} Ω·m) but substantially higher than the resistivity recorded after the HP process (0.23 x 10^{-6} Ω·m). This compares relatively favourably to pure Ti, which has a resistivity of 0.45 ± 0.05 x 10^{-6} Ω·m. It was initially believed that the reason that HIP process employed by Barsoum *et al.* was higher than the HP process used by Wang *et al.* was the presence of the Al_2O_3 impurity, something

that was dispelled in the work of Bai *et al* [1,28,66,67]. Bai *et al.* concluded that Ti_2AlC synthesized by SHS/PHIP was nonstoichiometric, which would indicate many lattice defects [29]. Calculating the reciprocal of the resistivities of hipped Ti_2AlC gave an electrical conductivity of 2.7 x $10^6(\Omega m)^{-1}$, similar to the 2.5 x $10^6(\Omega m)^{-1}$ given by the SHS/PHIP process, while the sample that was hot pressed by Wang *et al* yielded a conductivity of 4.3 x $10^6(\Omega m)^{-1}$ [17]. The coefficient of thermal expansion (α) of Ti_2AlC synthesized by SHS/PHIP process was calculated to be 0.00200 K^{-1}, lower than the samples prepared by hipping (0.0035 K^{-1}) and HP (0.00295 K^{-1}). Bai *et al* determined that this was related to the high electrical resistivity due to lattice defects (C vacancies). [1,67].

Before examining the mechanisms of electronic transport in the MAX phases, it is helpful to look at the mechanisms of transition metals such as Ti. Hettinger *et al* derived a similar Bloch-Grüneisen expression to Kulikov of the resistivity of the transition metals:

$$\rho \propto \frac{1}{n\tau} \propto \frac{N(E_F)\lambda\Theta}{n}\left(\frac{T}{\Theta}\right)^5 J_5\left(\frac{\Theta}{T}\right)$$

where τ is the scattering time, $N(E_f)$ the density of states at the Fermi level, λ the electron-phonon coupling factor, $J_5(x)$ the Grüneisen integral, and Θ the Debye temperature. This equation, according to Hettinger *et al.* and assuming Matthiessen's rule, $\mu(T=0) \propto \lambda(RRR-1)/N(E_F)$ where (RRR-1) relates to the intrinsic resistivity. Hettinger *et al.* plotted the electronic mobilities at 5K as a function of $(RRR-1)/N(E_F)$ for the compounds they tested, along with reported corresponding values of other MAX phases. They found a linear relationship which would indicate that the electron-phonon coupling is essentially constant for all materials. The graphs of these can be found in *Figure 3.11* [68,69].

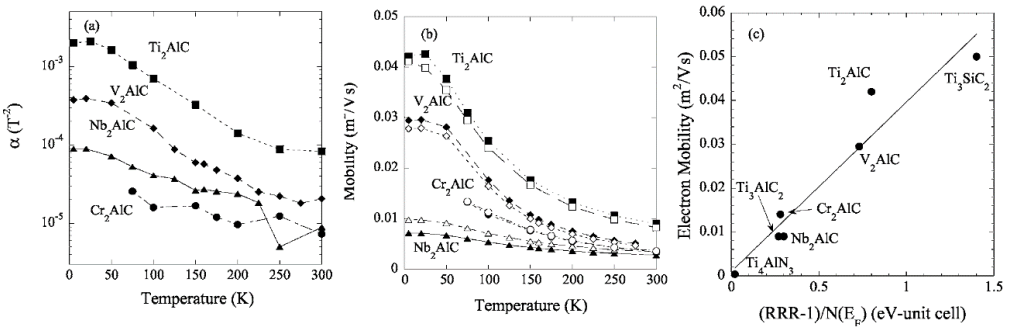

Figure 3.11: (a) *Semilogarithmic plot of α as a function of temperature for several M_2AlC materials,* ***(b)*** *Temperature dependence of electron (solid shapes) and hole (open shapes) mobilities,* ***(c)*** *Electron mobilities at 4K against $(RRR-1)/N(E_F)$. Linear relationship indicating that the electron-phonon coupling is similar to all MAX phases studied to date [68]*

The mechanisms of electronic transport in the MAX phases can be determined by analysing the magnetotransport and electrotransport results. The Hall coefficient, R_H is typically measured when attempting to determine the concentrations and sign of the majority charge carriers. The mobility is determined from the conductivity values using this information [70]. To explain the results, a temperature dependent Hall number requires at least a two-band model to explain the results. Within this two-band framework, an expression to describe the Hall number R_H is used:

$$R_H = \frac{(\mu_p^2 p - \mu_n^2 n)}{e(\mu_p p + \mu_n p)^2}$$

The unknows in the above expression are as follows: μ_p = hole mobility, μ_n= electron mobility, p= hole concentration, n=electron concentration. Three additional constraints are required to solve each unknown. In the two-band model, the magnetoresistance $\Delta\rho/\rho$=[$\rho(H)$-$\rho(H=0)/\rho(H=0)$] and the electrical conductivity σ are given by:

$$\frac{\Delta\rho}{\rho} = \alpha B^2 = \frac{\mu_n \mu_p np(\mu_n + \mu_p)^2}{(n\mu_n + p\mu_p)^2} B^2$$

$$\sigma = \frac{1}{\rho} = e(n\mu_n + p\mu_p)$$

However, to solve the problem an additional constraint is required. Hettinger *et al*. found that unlike most other metallic conductors, the MAX phases they tested (Ti_2AlC, Cr_2AlC and V_2AlC) possessed small Seebeck and Hall coefficients, making the reasonable assumption to choose carrier concentrations that are temperature independent and as important, based on existing previous work, roughly equal numbers for the densities of the electrons and holes. In solving the above expressions, and assuming that $n=p$, it was found that at all temperatures for the three materials with negative Hall coefficients (including Ti_2AlC), $\mu_p \sim 0.8\text{-}0.9\mu_n$. The temperature dependence of R_H *is* embedded in the mobility. Hettinger *et al.* recorded the carrier concentration of Ti_2AlC to be 1.0 x 10^{27}, comparing well with the more researched M_3AX_2 compounds Ti_3SiC_2 and Ti_3GeC_2 (≈2.0 x 20^{27}) [68]. They surmised that the electronic properties of the MAX phases were dominated by the *d* orbitals of the M elements and that these properties were comparable to those of transition metals. Typically, the sign of the

Seebeck voltage is used to qualitatively determine the sign of the dominant charge carrier. Taking this into consideration, it was expected that the Seebeck voltage would loosely follow the sign and shape of R_H as a function of temperature. However, it became clear to Hettinger *et al* that when they compared the Hall and Seebeck coefficients, as can be seen from *Figures 3.12(a) and (b),* that there were no obvious correlations between them. Three of the MAX phases, including Ti_2AlC show a noticeable change in signs of the Seebeck voltage with no corresponding changes in R_H, providing additional evidence that these compounds are nearly compensated [1,44,64,68].

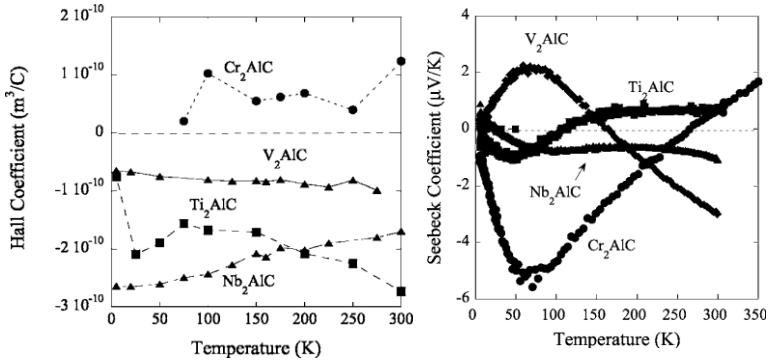

Figure 3.12: (a) *Temperature dependence of Hall coefficients. Note Ti_2AlC being negative. Temperature dependencies also tend towards zero as temperature is lowered, with a few points on the Ti_2AlC line not keeping to the trend.* ***(b)*** *Plot of Seebeck coefficients as a function of temperature. In general, the temperature dependencies are low, tending to fluctuate around zero and changing sign with increasing temperatures. [68]*

Over two papers, Barsoum *et al* measured the electrical conductivity, Hall effect and thermopower of Ti_3AlC_2, Ti_4AlN_3 and Ti_3SiC_2 [66,71]. The paper on only Ti_3SiC_2 investigated the electromotive force or absolute thermopower, itself a function of temperature, of the material. Over the 300-850 K temperature range they estimated that the thermopower as $\Theta = 0.18 \pm 0.22\ \mu V\ K^{-1}$, showing that Θ is practically zero within $\pm 0.22\ \mu V\ K^{-1}$. The reason for this is unclear, however it is known that in some transition metals such as Ti, both electrons and holes are involved in the transport properties and that only be having oppositely charged particles can Θ disappear. The thermoelectric contributions by electrons and holes delicately cancel each other out over the wide temperature range. They also found that the Hall coefficient of Ti_3SiC_2 fluctuates around 0 too, suggesting that the concentration, mobility and heat of transport values of electrons are identical to those of the holes over temperature range investigated [71]. The near-zero thermopower of Ti_3SiC_2 lends itself to be used as electrodes during thermopower measurements of other compounds.

3.5.2 Thermal properties

Due to the MAX phases being candidates for high-temperature applications, it is necessary to understand their thermal properties, including their thermal conductivities, heat capacities and thermal expansion coefficients. They are generally described as being good thermal conductors because they are good electronic conductors. However, before considering the conductivity and thermal expansion coefficients it is useful to examine the specific heat of Ti_2AlC.

As Ti_2AlC is a metallic-like conducting material, at temperatures up to 10 K, the low temperature heat capacity, c_p, can be approximated using the relationship:

$$c_p \approx c_v = \gamma T + \beta T^3$$

Where γ and β are coefficients of electronic and lattice heat capacities, respectively and c_v is the heat capacity at constant volume, which is assumed to be c_v. According to Scabarozi *et al*, this relationship should yield plots of c_p/T vs T^2 which should give straight lines with slopes β and intercepts γ [72].

The thermal properties of Ti_3SiC_2 were measured by Barsoum *et al* in their early paper on the synthesis and characterisation of the material. The thermal conductivity and specific heat capacity of a sample of density of 4.48 gcm^{-1} were recorded as 43 W/(mk) and 588 J/(kgK), being of similar value to pure Ti (31 W/(mk) and 523 J/(kgK) respectively. The similar values strongly indicate that the thermal properties are dominated by the Ti atoms. They also measured the thermal expansion coefficient in the temperature range 25-1000°C. The samples were covered in TiC powder and the runs carried out under Ar in order to avoid oxidation. With a calculated value of $10 \pm 1 \times 10^{-6}$ $°C^{-1}$, this value is slightly lower than that of pure TiC [22].

When it comes to thermal properties, the MAX phases share much in common with the similar MX binaries. As previously stated, they are good thermal conductors because they are good electrical conductors. Most MAX phases with the 'A' elements heavier than S are poor phonon conductors because the combination of the rattling effect of the A-group element together with enhanced mass, renders the A layers potent phonon scatters. However, the TiAlC phases are

an exception to the rule due to the Al atoms appearing to behave less as rattlers than the heavier A atoms. Phonon conductivities are also quite sensitive to the presence of defects.

The atomic displacement parameters (ADPs) are seen to increase with temperature, albeit still being relatively low. The rattler nature is further confirmed when studying the A layers' atomic displacements, which are high than those of the other atoms in the structure, the displacements also being found to be anisotropic and tending to favour the basal planes. The density functional theory (DFT) calculations of the phonon DOS also predicted that vibrations of the A elements along the basal planes should occur more readily than along [0001].

As a first approximation, the heat capacities at a constant pressure c_ps of the MAX phases was assumed to be (n+1) times the c_p of their corresponding MAX phases. The DFT calculations can predict the heat capacities over a relatively wide temperature range reasonably well, but only if the experimentally derived values of γ are included. It was found that beyond 800˚C the theoretical and experimental values for heat capacity diverge. The body of work surrounding thermal properties was further confirmed when the Debye temperatures were calculated from the low temperature c_p, with the results agreeing with those calculated from the velocity of sound and from the ADPs. It was determined that the discrepancy between the DFT-calculated density of states (DOS) and those derived from low-temperature heat capacity measurements was most probably down to electron-phonon coupling, λ_{ep}, with most MAX phases possessing a λ_{ep} value of around 0.4.

From room temperature to around 1000˚C, the thermal expansion coefficients of most MAX phases lie in the relatively narrow range of 6-10 x 10^{-6}. The thermal decomposition of the MAX phases generally occurs by the loss of the A element and formation of higher n-containing MAX phases and/or MX. The MAX phases are only kinetically stable in most environments, with their decomposition temperatures depending on their morphology (powder vs bulk) state of surface oxidation, or whether a reaction product prevents the escape of the A-group element [15]. As has been established, Ti_3SiC_2 was first synthesised in powder form in 1967 by Jeitshko and Nowotny when they chemically reacted TiH_2, Si and graphite at 2000˚C, suggesting that this material must have been stable up to at least that temperature [2]. Barsoum *et al* later

confirmed this to some degree and challenged the findings of others that it decomposed at 1400˚C, attributing this low temperature to impurity contamination. They found that under the right conditions, pure Ti_3SiC_2 is stable up to at least 1700˚C [22,60]. With regards to Ti_2AlC, Barsoum *et al* determined that under certain conditions that this MAX phase was thermodynamically stable at 1600˚C [18].

3.6 Mechanical Properties

One of the primary reasons for the interest in the MAX phases is their mechanical behaviour. As outlined previously, the MAX phases possess properties of both ceramics and metals, leading some to define them as 'metallic ceramics'. This definition becomes more logical when you consider that MAX phases are in the middle ground between metals, with their 5+ independent slip systems, and structural ceramics, including the relatively similar MX phases, with effectively no slip systems. This middle ground sees the MAX phases perform differently at both high and low temperatures. Generally, at higher temperatures, pseudo-plastic behaviour is observed as the MAX phases are in constrained deformation modes and possess a highly-orientated microstructure. However, at lower temperatures and in unstrained deformation, thin form and especially in tension, the MAX phases behave in a brittle manner.

Among the many definitions of the MAX phases is that it is a 'Layered Carbide'. The Other similar 'layered solids' include ice and graphite which are, by definition, plastically anisotropic. This means that they lack the five independent slip systems needed for ductility. Therefore, when polycrystalline layered solids are loaded, these solids quickly develop large internal stresses and uneven states of stress [73,74]. The soft grains which are favourably orientated deform by glide of basal plane dislocations, which rapidly transfers load to hard grains which are not favourably oriented to the applied stress. The formation of kink bands is also another important consequence of plastic anisotropy.

In this section, some of the mechanical properties of the MAX phases studied in the literature have been reported, including some mechanical properties that have been further explored and studied in this thesis. One of the main avenues of work for this thesis is to investigate the high temperature thermo-mechanical performance of the MAX phases, with much of the work

focusing on Ti_2AlC and Ti_3SiC_2, although similar phases such as Ti_3AlC_2 have also been reported. As the majority of mechanical testing carried out for this work utilises a Gleeble 3500 thermomechanical simulation unit, research papers that utilise this machine or similar machines have been reviewed. Alongside this, some of the other mechanical properties will be explored, including the thermal shock characteristics, something closely aligned with the high temperature thermo-mechanical performance and room temperature compression testing of the MAX phases and the residual stress following testing. Some other mechanical properties of the MAX phases have also been touched upon in this section.

3.6.1 Deformation Mechanisms and Dislocations

The next few sections will deal with both the room temperature and high temperature mechanical properties of the MAX phases. However, before reviewing these properties, the main deformation mechanisms should be understood, including the formation of kink bands (KBs). Despite KB formation being quite ubiquitous in nature, the KBs in the MAX phases are different in that they are dislocation-based.

Dislocations and stacking faults are the two primary types of defects within the microstructure of the MAX phases. By utilising a TEM, both Wang *et al* and Barsoum *et al* were able to observe dislocations in both as-received and deformed samples [75,76]. Barsoum *et al* discovered that the Ti_3SiC_2 microstructure possessed a high density of perfect $\{0001\}$ basal-plane dislocations with a Burgers vector of $1/3\langle 11\bar{2}\,0\rangle$, this being ascribed to the very anisotropic structure of the MAX phases. Due to the dislocations being confined to the basal planes, they are arranged in either arrays (pile-ups), where the dislocations exist on identical slip planes, or in dislocation walls normal to the arrays. Due to the fact that the low angle kink boundaries are mobile, Farber *et al* referred to them as mobile dislocation walls (MDWs). As the walls consisted of both tilt and twist components, the boundary was interpreted to be composed of parallel, alternating, mixed, perfect dislocations. They also noted that two different burgers vectors lay in the basal plane 120° relative to one another [77]. In their study, Barsoum *et al* found that shear deformation is caused by the arrays propagating across the entire grains and also that the walls form due to KB formation [76].

It is thus important to understand KB formation in the MAX phases, something which Barsoum *et al* have dedicated a significant amount of work to achieve [1,15,78]. First proposed by Orowan in 1942, the mechanism of kinking was expanded upon by first Hess and Barrett and then Frank and Stroh. They derived an expression for the critical remote shear stress (CRSS) using a Griffith-like approach, where a subcritical KB will become critical and rapidly grow, similar to a crack, if the stress is above the CRSS. In their model, which was later expanded upon and related to the MAX phases by Barsoum *et al*, when a critical remote applied shear stress is exceeded, pairs of dislocations of opposite signs nucleate and grow at the tip of a thin elliptical kink. MDWs are formed when the continuing stress forces the walls to part. This wall formation process can then be repeated which results in the creation of more MDWs. A kink boundary can then be formed following the collapse of the component dislocations in successive walls. As can be seen in *Figure 3.13(d)*, this collapse can occur sequentially from one end of the kink boundary to the other. It was thus determined that accumulation of several MDWs in a relatively narrow region results in a kink boundary. Frank and Stroh suggested that the reason for this accumulation was due to successive changes of lattice direction causing each wall to make a different angle to the external load, causing the increase in the shear stress for each successive MDW formed moving faster [15,79].

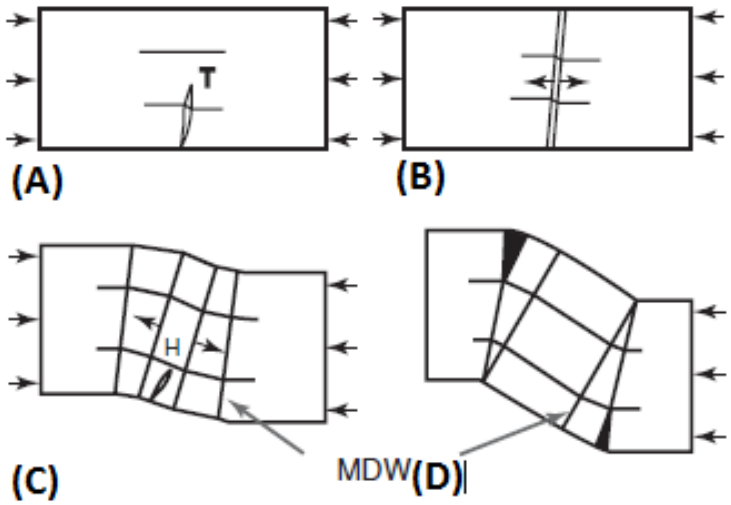

Figure 3.13: *Schematic of kind band formation according to Frank and Stroh. (a) Kink band initiation at tip of narrow kink T (b) The walls move apart in opposite directions after the intersection of T with free surface removes the attractive energy between them (c, d) The same process is repeated, which creates more MDWs, which ultimately become kink boundaries [16]*

The concept of incipient kink bands (IKBs) was invoked by Barsoum *et al* to describe the behaviour of the MAX phases, and Ti_3SiC_2 in particular when subjected to hysteretic nonlinear elastic behaviour upon loading. Hysteretic stress strain loops were generated after repeatedly and cyclically compressing Ti_3SiC_2 under stresses up to 1 GPa [79]. They found that the loops generated were independent of strain rate. Nested loops were obtained with a single loading trajectory when the samples were cycled to progressively larger stresses. One test Barsoum *et al* attempted was to eliminate microcracking as a possible mechanism by cycling a fine grained (FG) sample 100 times to 700 MPa. Upon comparing the first and last loops, it was noted that the last loop was slightly stiffer, excluding microcracking as the origin of the loops. The coarse grained (CG) samples showed similar behaviour to the FG loops, as shown in *Figure 3.14* [15,78,80]. Represented by hysteresis loop areas in *Figure 3.15(c),* the dissipated energy per unit volume per cycle, W_d was found to increase as the square of the maximum applied stress with a threshold stress. Grain size also had a strong impact on W_d, with the larger grains dissipating significantly more energy at the same stresses. Barsoum *et al* also noted that the W_d appeared higher for porous solids than for fully dense ones [81–83].

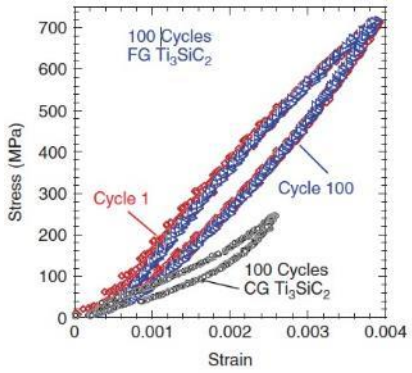

Figure 3.14: *Cyclic compressive spontaneously reversible stress/strain loop in coarse grained (CG) and fine grained (FG) Ti_3SiC_2. Both were cycled 100 times, with the FG sample to 700 MPa and the CG to 250 MPa [80]*

An IKB consists of multiple, coaxial, parallel dislocation loops separated from each horizontal slip plane by a distance D. Barsoum *et al* defined the IKB as a KB whose dislocation walls, for whatever reason, remain attached at its ends in a lenticular shape and do not dissociate into MDWs. If the walls separate then they can then be defined as KBs instead. This important difference is necessary to understand due to the belief that the production and annihilation of IKBs is a reversible process, while that of KBs is an irreversible one [78].

The realisation that the behaviour witnessed in cyclically compressing Ti_3SiC_2 was due the IKB micromechanism led to Barsoum *et al* labelling such solids as kinking nonlinear elastic (KNE). Elastic due to the absence of plastic deformation, nonlinear because the stress-strain curves were clearly nonlinear, and kinking because it was the formation of dislocation based IKBs that were responsible for the dissipation of energy [78]. In a later paper, Barsoum *et al* determined that plastic anisotropy where the c/a ratio was higher than 1.4 in hexagonal crystals would be sufficient condition for a solid to be KNE. It was found that most MAX phases can be classified as KNE solids [84].

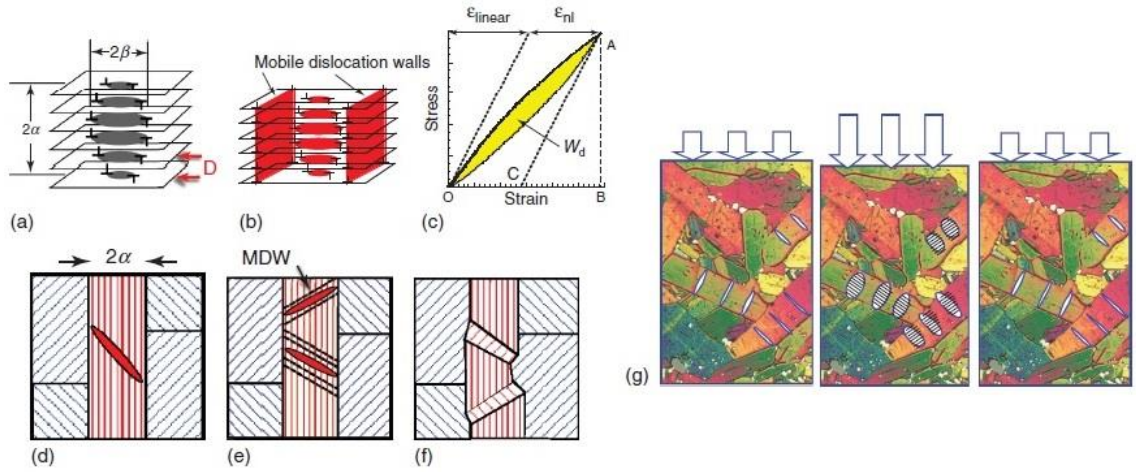

***Figure 3.15**: **(a)** Schematic showing an IKB with a length of 2α and a width 2β. The distance between the horizontal slip planes is denoted by D. **(b)** Same as (a) but also showing the presence of MDWs. **(c)** Typical stress-strain loop with the definitions of nonlinear strain ε_{NL} and W_d. **(d)** Formation of an IKB within a grain. The IKB extends to the grain boundaries where it is subsequently halted. **(e)** The IKBs can devolve into MDWs at higher stresses and/or temperatures. **(f)** Kink bands and boundaries can form due to the formation and collapse of several MDWs. **(g)** Schematic showing how an IKB can form in a polycrystalline sample. IKBs are nucleated at a threshold stress. Increasing this stress results in the IKBs growing 'fatter' and showing an increase in 2β. The IKBs shrink upon the removal of the load, resulting in their ultimate annihilation [15, 78].*

Figure 3.15(c) shows an example of a stress-strain curve with a large hysteretic loop, a consequence of deforming KNE solids. The total strain ε_{tot} at a stress σ can be calculated by additively decomposed into two parts, nonlinear strain (ε_{NL}) and linear strain (ε_l). The latter can be calculated from Hooke's law, where $\varepsilon_l=\sigma/E$ and E is the Young's modulus of the material. Generally, and in the absence of phase transitions and/or microcracking, the nonlinear fully reversible strain ε_{NL} is made up of two components: ε_{IKB} and ε_{DP}, which are due to IKBs and

dislocation pile-ups respectively. Even though both strains are in principle fully reversible due to dislocation loops being confined to parallel planes, Barsoum *et al* generally only dealt with ε_{IKB}, assuming that if ε_{DP} was present, that it would be small and increase linearly with stress: [84]

$$\varepsilon_{tot} = \frac{\sigma}{E} + \varepsilon_{IKB} + \varepsilon_{DP}$$

As was described earlier, Frank and Stroh were one of the first to expand the knowledge on the mechanism of kinking. In an equation that was later modified by Barsoum *et al* for polycrystalline materials loaded axially with a load equivalent to a remote axial stress σ_t, they considered an elliptic KB, with a length 2α and a width 2β, where $\alpha >> \beta$ (*Figure 3.15(a)),* demonstrating in the process that the remote critical shear stress τ_c needed to render such a subcritical KB unstable is given by:

$$\tau > \tau_c \approx \frac{\sigma_t}{M} = \sqrt{\frac{4G^2 b\gamma_c}{\pi^2 2\alpha} ln\frac{b}{w\gamma_c}}$$

where M is the Taylor factor relating σ_t to τ_c, *G* is the shear modulus and *b* is the burgers vector *b* and *w* is the dislocation core width [79, 80, 85]. For MAX phases, 2α can be considered as the grain dimension along the c-axis [84 - 86]. The dislocation core width, *w,* can be determined by assuming that M=3 and by measuring the threshold stress (σ_t), a parameter that is otherwise quite difficult to measure. The final remaining variable in the equation is the critical kinking angle, γ_c, which can be calculated using the following equation: [79]

$$\gamma_c = \frac{b}{D} \approx \frac{3\sqrt{3}(1-v)\tau_{loc}}{2G}$$

Where *v* is the Poisson's ratio, τ_{loc} is the local shear stress required to nucleate a pair of dislocation and *D* is the distance between dislocation loops 2α, as seen in *Figure 3.15(a).*

As can be seen in *Figure 3.15(a),* an IKB consists of multiple parallel dislocation loops. Zhou *et al* at first approximated that each loop would be made up of two edge and two screw dislocation segments with lengths $2\beta_x$ and $2\beta_y$, respectively. These are related to the applied stress σ and 2α assuming the following expression, which are modified from the original Frank and Stroh paper to account for the polycrystalline nature of the materials tested [79,85].

$$2\beta_x \approx \frac{2\alpha(1-v)}{G\gamma_c}\frac{\sigma}{M} \text{ and } 2\beta_y \approx \frac{2\alpha}{G\gamma_c}\frac{\sigma}{M}$$

There are two stages in the formation of an IKB: nucleation and growth [86,87]. As nucleation is not that well understood, the model put forward by Barsoum *et al* only concerns the growth of IKBs from $2\beta_{xc}$ and β_{yc} to $2\beta_x$ and $2\beta_y$, respectively. The dislocation segment lengths of an IKB nucleus, $2\beta_{xc}$ and $2\beta_{yc}$ are assumed to either pre-exist, or to nucleate during pre-straining. It follows that the nuclei grow for $\sigma > \sigma_t$. The IKB induced axial strain resulting from their growth is assumed to be given by :[79,86,88]

$$\varepsilon_{IKB} = \frac{\Delta V N_k \gamma_c}{k_1} = \frac{N_k \gamma_c 4\pi\alpha\left(\beta_x\beta_y - \beta_{cx}\beta_{cy}\right)}{3k_1}$$

$$= \frac{4\pi(1-v)N_k\alpha^3}{3k_1 G^2\gamma_c M^2}(\sigma^2 - \sigma_t^2) = m_1(\sigma^2 - \sigma_t^2)$$

where m_1 is the coefficient before the term in brackets in the fourth term, N_k is the number of IKBs per unit volume, ΔV is the IKB volume change. The volume fraction of the material that is kinked is given by the product VxN_k. The factor k_1 relates the volumetric strain caused by the IKBs to the axial strain along the loading direction. N_k can be estimated using the above equation once m_1 has been determined experimentally.

Barsoum *et al* and Zhou *et al* developed an expression for energy dissipated per unit volume per cycle, W_d, resulting from the growth of IKBs from β_{ic} to β_i and back to β_{ic} again [84,86]

$$W_d = \frac{4\Omega\pi N_k\alpha}{D}\left(\beta_x\beta_y - \beta_{xc}\beta_{yc}\right) = \frac{4\pi(1-v)N_k\alpha^3}{G^2\gamma_C M^2}\frac{\Omega}{b}(\sigma^2\sigma_t^2) = m_2(\sigma^2 - \sigma_t^2)$$

where Ω is the energy dissipated by a dislocation line sweeping a unit area, with Ω/b being proportional, if not equal, to the CRSS of an IKB dislocation loop. When the two previous equations are combined, it gives rise to a new equation:

$$W_d = 3k_1\frac{\Omega}{b}\varepsilon_{IKB} = \frac{m_2}{m_1}\varepsilon_{IKB}$$

In their equation, Barsoum *et al* assumed for simplicities sake that the IKBs are cylinders with a mean radius β_{av} – where $\beta_{av} = (\beta_x + \beta_y)/2$ – then the ρ_{rev}, or reversible dislocation density due to the IKBs is given by [84]:

$$\rho_{rev}\frac{2\pi N_k 2\alpha\beta_{av}}{D} = \frac{4\pi N_k \alpha\beta_{av}\gamma_c}{b}$$

In the two previous equations, m_1, m_2, σ_t and $3k_1$ (Ω/b) can be determined experimentally, while to estimate Ω/b, only knowledge of k_1 in the above equation is required and N_k can be determined from the equation to calculate ε_{IKB} as long as k_1 and M are known.

After nested loops are obtained from hysteresis curves, m_1 and σ_t can be determined from the slopes of plots of ε_{nl} versus σ^2. Similarly, m_2 and σ_t can be determined from W_d versus σ^2 plots, while $3k_1(\Omega/b)$ can be determined from plotting W_d against $\varepsilon_{nl.}$ It was therefore determined, that if the assumptions made by Barsoum *et al* were correct, and that the micromechanism causing the dependence of ε_{nl} on σ is identical to the one responsible for W_d, then the ratio m_2/m_1 should equal $3k_1(\Omega/b)$. This can otherwise be described as that if both expressions give the same values for Ω/b, then the same micromechanism that results in the parabolic dependence of σ on ε_{nl}, is the one responsible for W_d as well [15,78,84,86].

In review, it was found that large grains, less rigid solids and higher stresses all have an effect in increasing W_d. The large grains and less rigid solids do this by reducing the threshold stresses needed for IKB formation while the higher stresses increases the diameters of the dislocation loops formed. Spontaneous collapse of the IKBs is the consequence of the removal of a load. The energy dissipated, or damping, results from the friction associated with the back and forth motion of IKB dislocations.

3.6.2 Room Temperature Compression Testing

Before examining the high temperature mechanical characteristics of the MAX phases, it would be prudent to discuss their room temperature properties. Papers published at the turn of the century started to investigate the mechanical properties of the MAX phases in much more detail. In their paper on the processing and characterisation of Ti_2AlC from 2000, Barsoum *et al* tested its room temperature compressive deformation, yielding a compressive stress result of 540 ± 21 MPa . They discovered that at room temperature the failure was quasi-plastic, something which they noted had previously been associated with the formation of a shear band

at 45 degrees to the direction of the applied load. This shear band cut across grains and was bridged by full or partial grains that had rotated or kinked [17,74]. The following year a more comprehensive study into the mechanical properties of Ti_2AlC was undertaken by Zhou *et al*. They recorded a higher room temperature compressive stress of 763 MPa with the sample, like in the previous study, maintaining its integrity. *Figure 3.16* shows an SEM image of the sample, when they examined these images it was noted that the main crack propagated along ~45 degrees off the axis of the cylinder, or the loading direction and that the damage was confined to the vicinity of the crack. Void and cavity formation, branching and deflecting of the main cracks, Ti_2AlC grain pull-out and bridging of two halves of the sample by laminated Ti_2AlC grains were all seen in the SEM micrographs. The micro-scale deformation of Ti_2AlC is shown in *Figure 3.16(b),* where kinking and delaminating of Ti_2AlC grains are obvious in the figure. The break-up of laminated grains was also noted, as marked by A in the figure. Evidence that Ti_2AlC could confine the damage, as indicated by the delaminating crack that was confined within the laminated Ti_2AlC grains was also noted. Using the SEM observations, they deduced that kinking, delaminating and pull-out of Ti_2AlC grains, cavity formation and crack branching were the main contributions to the room temperature deformation and damage confinement of Ti_2AlC [20].

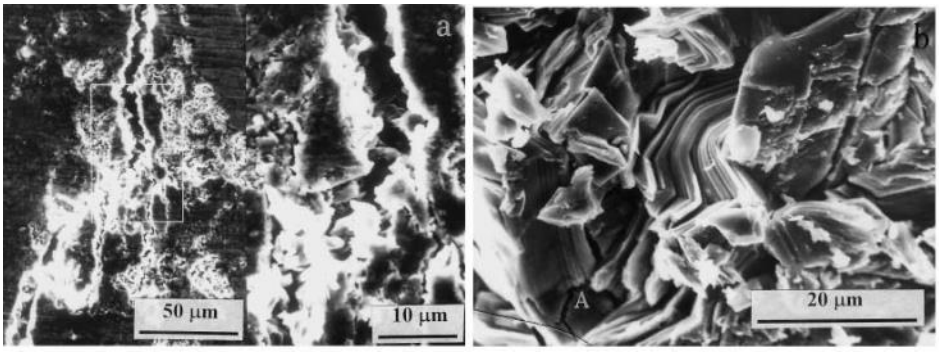

Figure 3.16: (a) *SEM micrograph of sample surface after room temperature compressive test* ***(b)*** *SEM micrograph showing microscale deformation due to kinking and delaminating of laminated Ti_2AlC grains [20].*

Barsoum *et* al conducted room temperature mechanical properties tests on Ti_3SiC_2 in one of their early papers on this MAX phase. They recorded a compressive strength of 580 ± 20 MPa, although noted that these values should be considered to be in a lower band due to the conditions of the test [22]. In a later study, when testing the effect of grain size and deformation temperature on Ti_3SiC_2, El-Raghy *et al* found that fine-grained samples produced a

compressive stress of 1050 MPa, significantly higher than the 720 MPa value of the coarse-grained samples. Incidentally, this figure is close to the value of compressive stress for Ti_2AlC calculated by Zhou *et al*. At a strain rate of 5 x 10^{-3} s^{-1}, the failure was noted as brittle [20,89]. In a similar study on the room temperature ductile carbides, Barsoum *et al* loaded large-grained, oriented, polycrystalline samples of Ti_3SiC_2 in compression at room temperature before interrupting the tests before the samples failed. They carried out tests along the x- and z-axis (*Figure 3.17),* with tests along the x direction yielding a higher maximum yield stress than along the z-axis, followed by a region of strain softening. They concluded that when basal planes were orientated in such a way that allowed for slip, deformation occurs by formation of shear bands. When the slip planes were parallel to applied load, a situation where it's impossible for ordinary glide to arise, deformation occurs by a combination of delamination of, and kink band formation in, individual grains, as well as shear band formation. The material therefore deforms plastically in any arbitrary orientation due to this unique multiplicity of deformation modes [90].

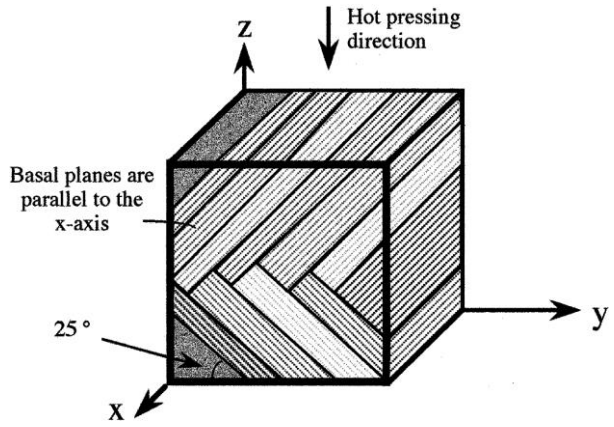

Figure 3.17: *Schematic of grain orientation relative to loading directions. Basal planes are for the most part parallel to the x-axis. Hot pressing direction it vertical [90]*

Zhou *et al* also investigated the room temperature compression behaviour of Ti_3SiC_2. With the help of scanning electron micrographs (*Figure 3.18*) of shear fractured samples, where, like the test conducted on Ti_2AlC, the crack was orientated ~45 deg to loading direction, they were able to determine a number of features. Although the sample cracked, it did not break into a number of small pieces. *Figure 3.18(a(ii))* shows a high magnifcation image of voids and cavities that are bridged by laminated Ti_3SiC_2 grains. *Figure 3.18(b)* shows a micrograph after breaking the shear fractured specimen into two parts, where two noticable features were

identified: The shear deformation characeristic from the laminated Ti_3SiC_2 grains and the laminated Ti_3SiC_2 grains consisting of a stack of the hexagonal slices with the nanometer size. The deformation region from the fracture surface was the subject of *Figure 3.18(c)*. This *Figure* shows the kinking and delamination of individual grains together with intergranular fracture contributing to deformation of polycrystalline Ti_3SiC_2 under compression [54].

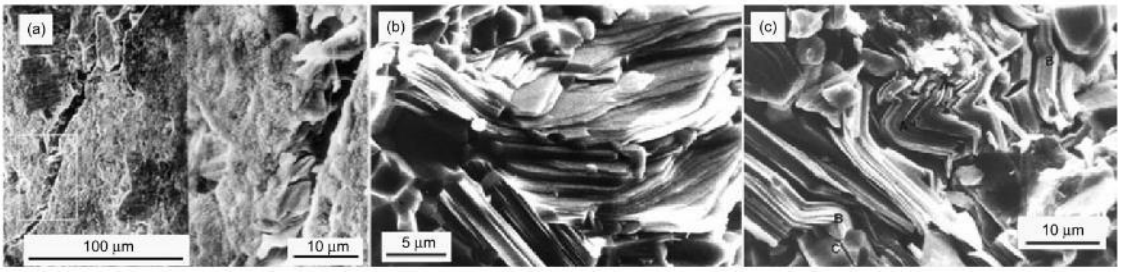

Figure 3.18: *Scanning electron micrographs of typical fracture surfaces of Ti_3SiC_2 after compressive loading at room temperature and under a strain rate of $1x10^{-4}s^{-1}$* [54]

To generalise, it has been found that the ultimate compressive stresses (UCSs) of the MAX phases are a function of grain size, with CG Ti_3SiC_2 samples being weaker than FG [75,89]. Compressive failure modes have also been studied in the literature, with them being realised to be a function of grain size, loads at failure and strain rates. When FG samples were loaded at high strain rates they tended to fail suddenly in a brittle manner, especially when the UCSs are 1.0 GPa or higher [18]. As was described earlier, not all of the MAX phases fail suddenly, with some, especially the CG 211 and 312 phases, exhibiting graceful-failure behaviour with stress-displacement gurves such as those seen in *Figure 3.19(a)* being closer to an inverted shalow V than a sharp drop at the UCS [17,91].

Graceful failure, like the kind Tzenov and Barsoum set out in their paper, usually occurs along a plane that is inclined ≈20-40° to the loading axis. The angle of shear fracture, θ_c, upon compression is typically in the range of 23-35°, deviating substantially from the maximum shear stress plane of ~45° in behaviour that was noted to be reminiscent of Ice and other brittle solids. Zhang and Sun noted that the appropriate failure criteria to use is the Mohr-Coulomb criterion. The failure occurs when:

$$\tau_n + \mu\sigma_n \geq \tau_c$$

where τ_c is the critical shear fracture stress, μ is an effective friction coefficient across the shear plane, σ_n and τ_n are the normal and shear stresses on the shear plane, given by:

$$\sigma = \sigma sin^2\theta$$

$$\tau_n = \sigma sin\theta cos\theta$$

where θ is the angle between the stress axis and the shear plane. By combining the 3 above equations and by determining the minimum with respect θ it can be shown that:

$$\mu = \frac{cos2\theta}{sin2\theta}$$

and also:

$$\tau_c = \sigma_f sin\theta_c(cos\theta_c - \mu sin\theta_c)$$

where σ_f is the normal stress at failure. If one knows σ_f and θ_c from experiment then τ_c can be calculated, which represents the resistance to shear of a polycrystalline sample in the absence of friction [17,18,87].

A number of papers that subjected compression results of a select number of MAX phases to Mohr-Coulomb analysis have been published. In general, these results showed that τ_c is a function of grain size, with smaller values of τ_c resulting from larger grains and also that μ is within the range of 0.2 to ≈1.0 [17,87,90,92,93].

An example of a typical shear band can be seen inset of *Figure 3.19(b).* The extent of damage to the grain boundaries can be seen in the higher magnification micrograph, where the typical MAX phase energy absorbing mechanisms such as grain bending, grain decohesion, grain pull-out and push in, crack deflections at the grain boundaries and KBs are all evident. It was assumed that the grain deformation played an important part in the sudden loss in load bearing capability, which was demonstrated in the stress-displacement curves in *Figure 3.19(a)* [15,17,91]. These tests were undertaken at room temperature and a strain rate of 5×10^{-3}/s.

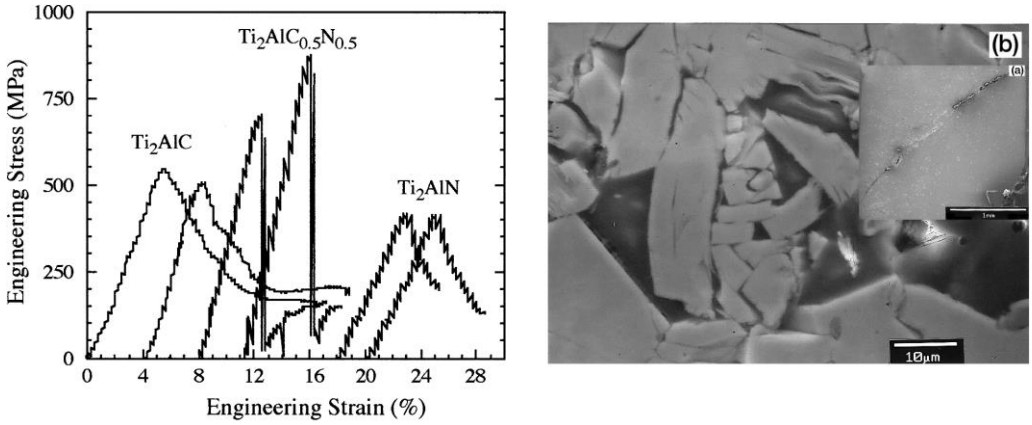

Figure 3.19: (a) *Characteristic room temperature stress-displacement curves obtained upon loading CG Ti_2AlX samples in compression at a strain rate of 5×10^{-3}/s. Curves shifted to the right for the sake of clarity [17].* ***(b)*** *High magnification SEM micrograph showing a shear band formed when a CG Ti_3AlC_2 sample was compressively loaded [91]*

The effect of strain rates at ambient temperatures is not as well understood as it is for high temperatures. However, a test on the effect of strain rates on the compressive stress-strain curves of Nb_2AlC and TiNbAlC was undertaken. The stress-displacement curves can be seen in *Figure 3.20,* which show that Nb_2AlC behaves in a manner similar to that of MAX phases subjected to higher temperatures in that decreasing the strain rate increases the ductility but at the expense of the ultimate compressive strength. Salama *et al* were surprised when they found that the TiNbAlC solid solution behaved differently in that decreasing the strain rates resulted in an increase in the ultimate compressive strengths and a slight increase in ductility, something which they could not explain [93].

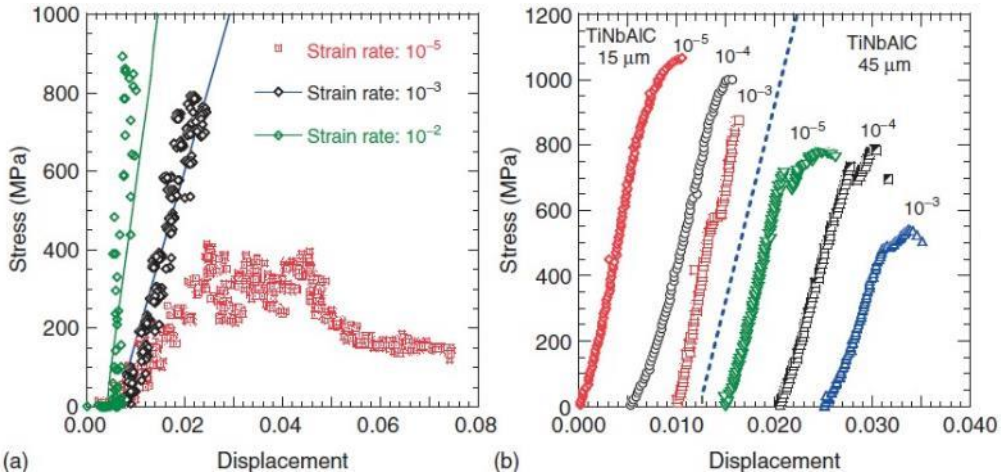

Figure 3.20: (a) *Effect of strain rate on room temperature compressive stress-displacement curve of Nb_2AlC,* ***(b)*** *Effect of strain rates on room temperature compressive stress-displacement curve of TiNbAlC with two different grain sizes and the curves shifted to the right for clarities sake [15, 93]*

3.6.3 Effect of temperature, amount of strain and strain rate

A key consideration when choosing materials for structural applications is their mechanical behaviour at elevated temperatures. One potential area for the application of the MAX phases, and the Al containing ones in particular, is in the field of aerospace, where the MAX phases have been put forward as possible materials in turbines, where high temperatures and high strains are present [94]. This is just one of many applications for the MAX phases but is perhaps the most relevant for this thesis, which concentrates on the mechanical properties at high temperatures.

To understand the high temperature mechanical properties of the MAX phases, one must understand the nature of the brittle-to-plastic transition temperature (BPTT/BDTT) that these phases go through. Unsurprisingly, the BPTT of each MAX phase is different, but for many of the Al-containing phases, including Ti_2AlC and also Ti_3SiC_2, it is between 1000 and 1100°C [17,89].

Some of the investigations undertaken by Barsoum *et al* in their early studies on the MAX phases included testing the compressive strength of Ti_3SiC_2 in air at 1300°C using a crosshead displacement rate of 0.0033mm/s. They recorded a compressive strength of 260 ± 5 MPa, with their load-displacement curves indicating substantial yield at 1300°C [22]. Barsoum *et al* later performed similar tests on Ti_2AlC and Ti_3GeC_2 at 1150 and 1300°C. They noted that the 312 phases have higher yield points, around 250 MPa at 1300°C and 550 MPa at 1150°C than the 211 phases, which yielded at 250 MPa at 1150°C. All phases were also found to deform plastically as opposed to the brittle failure at room temperature [18].

In their paper on the effect of grain size and deformation temperature on the mechanical properties of Ti_3SiC_2, El-Raghy *et al* used a servohydraulic testing machine to test the compressive properties of the material. Using a strain rate of 5×10^{-3} s^{-1}, they found that below 1200°C, the stress-strain curve was linear to failure, with a failure stress that decreases with increasing grain size. At 1200°C, there was not much difference between the FG and CG samples with regards to the strains to failure, which were recorded at being around 2.5%. At 1300°C, significant levels of plastic strain were attained, with the stress-strain response

exhibiting three stages: i) an elastic regime, ii) a transient 'hardening' regime and iii) a distinct softening regime. At all temperatures, the FG material was found to be stronger than the CG samples with a substantial decrease in strength at around 1200°C for both the FG and CG samples. They determined that the inelastic deformation in Ti_3SiC_2 was assisted by damage formation in the form of grain boundary cracks, kinking, and delamination of grains. Damage initiation does not result in catastrophic failure because Ti_3SiC_2 has a capacity to confine the spatial extent of the damage. The recorded UCS values at 1300°C were 330 MPa for high purity and 270 MPa for low purity samples [89]. Barsoum *et al* (of the same research group as El-Raghy *et al*) performed similar tests on Ti_2AlX MAX phases, where, as would be expected, deformation was more plastic at high temperatures. Similar to the Ti_3SiC_2 samples tested earlier by El-Raghy *et al*, the stress-strain curves exhibited four regimes: a linear regime, followed by a hardening regime, then a region of distinct softening before finally a second hardening regime, something which was not seen in the earlier study. The UCS of Ti_2AlC was found to be 340 MPa at 1200°C and 270 MPa at 1300°C for FG samples, comparable to those results found for Ti_3SiC_2 [17].

Sun *et al* were one of several groups that subsequently performed similar compression tests on the MAX phases, with their paper investigating the deformation and fracture behaviour at different temperatures. They found that the fracture stress decreases monotonically with increasing temperature and like the previous tests, confirmed that above 1123 K (~850°C) plastic deformation was observed, with pseudo-strain-hardening followed by strain softening. Also, when tested above this temperature, many microcracks form homogenously on the sample surfaces during compression. *Figure 3.21* shows the multiple mechanisms by which Ti_3SiC_2 deform under compressive loading, including basal plane slipping, kink band formation, grain buckling, fracture of layers and delamination of the layered structure. They confirmed that kink band formation was a common deformation mode especially at high temperatures for Ti_3SiC_2 [95].

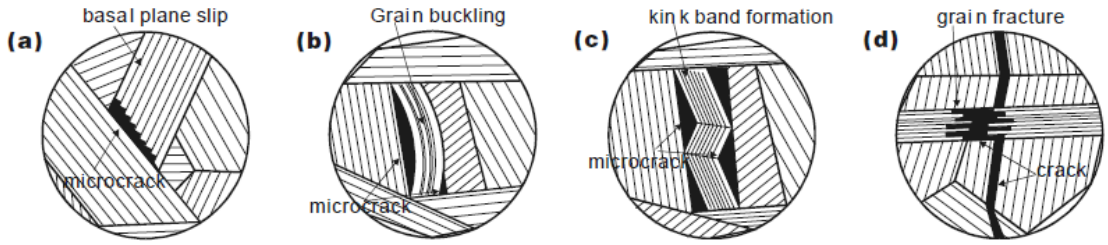

Figure 3.21: *Schematic showing the mechanisms by which Ti_3SiC_2 deform under compressive loading:* ***(a)*** *Basal plane slip and the formation of a microcrack at the grain boundary,* ***(b)*** *grain buckling and the induced microcracks,* ***(c)*** *Formation of kink bands and the associated cracking* ***(d)*** *Grain fracture as a result of crack propagation and grain pullout formation [95]*

As was touched upon in the section on kink bands earlier in this review, Barsoum *et al* published an article on the cyclic compressive deformation of FG and CG Ti_3SiC_2 at different temperatures and strain rates. At high temperatures, they found that stress-strain hysteresis loops were open and strongly dependent on strain rate and loading history, with cyclic hardening observed. The loops continue to expand upon the removal of load. This phenomenon was attributed to the IKBs dissociating and coalescing to form regular irreversible kink bands [78]. Zhen *et al*, of the same research group as Barsoum, performed a further test of the cyclic compressive loading of Ti_3SiC_2 when they investigated the effects of temperature, strain rate and grain size on its compressive properties. At temperatures of over 1000°C, they found very similar results to the earlier paper, with the hardening being explained by kink bands and dislocation arrays interacting to form deformation cells that are smaller than the original grains [80].

3.6.3.1 Split Hopkinson Pressure Bar testing

A number of papers have seen the use of the Split Hopkinson Pressure Bar (SPHB) to test the compressive properties of the MAX phases. With regards to thermo-mechanical testing, this equipment has its faults in that it is not as easy to accurately control and record a samples response to high temperature, high strain rate testing as other methods but it can generally give a good picture of the high strain-rate response of materials. The technique works by applying a stress-wave to a specimen that is sandwiched between two long bars. A key advantage of this method is that it a dynamic experiment, in contrast to the quasi-static servo-hydraulic testing machines that most of the previous papers have based their results upon. The SPHB was utilised

by Bhattacharya *et al* to investigate the high strain-rate response and deformation mechanism of Ti_2AlC, albeit at lower temperatures, they found that at very high strain rates (up to ~4700 s^{-1}) this MAX phase showed significant inelastic deformation and strain softening before fracture. Maximum compressive strains as high as 7.5% were found from the constitutive stress-strain response before any macroscopic cracks were formed. This paper also references some impact design requirements for the SPHB technique with regards to ceramics [96].

Parrikar *et al* further developed the SPHB technique to test the mechanical response of Ti_2AlC under extreme thermo-mechanical dynamic loading conditions. They realised that part of the appeal of the MAX phases is their performance in extreme environments. By utilising coiled induction loops around the specimen, they were able to subject the samples to temperatures of up to 1200°C and strain rates of 10^{-4} s^{-1} and 500 s^{-1}. As laid out in *Figure 3.22*, the dynamic compressive peak stresses were always higher than under static loading conditions. Like previous tests, the UCS decreases with increasing temperature, with the decrease being more pronounced above the BPTT under both testing conditions. The BPTT was, however, found to be higher in dynamic loading conditions than in quasi-static conditions for 200-300°C. The BPTT under quasi-static conditions was in the range 800-900°C, with plastic strains exceeding 25% recorded above that temperature. Under dynamic conditions, however, the BPTT was observed in the 1000-1100°C temperature range, with samples still failing in a predominantly brittle manner even as high as 1200°C (strains to failure of less than 1.5%). The high UCSs they reported prior to the BPTT under both conditions were amongst the highest ever recorded for Ti_2AlC, with this being attributed to finer grain size used than in previous studies. After the BPTT, however, the UCS decreases rapidly with increasing temperature, reaching a value of 853 MPa at 1200°C from a peak of 1645 MPa at room temperature. With regards to the strain rate sensitivity, they found that the material shows positive strain rate sensitivity exhibiting a higher UCSs with increasing strain rate. In general, high temperatures and low strain rates were seen to promote plastic behaviour of FG Ti_2AlC [97].

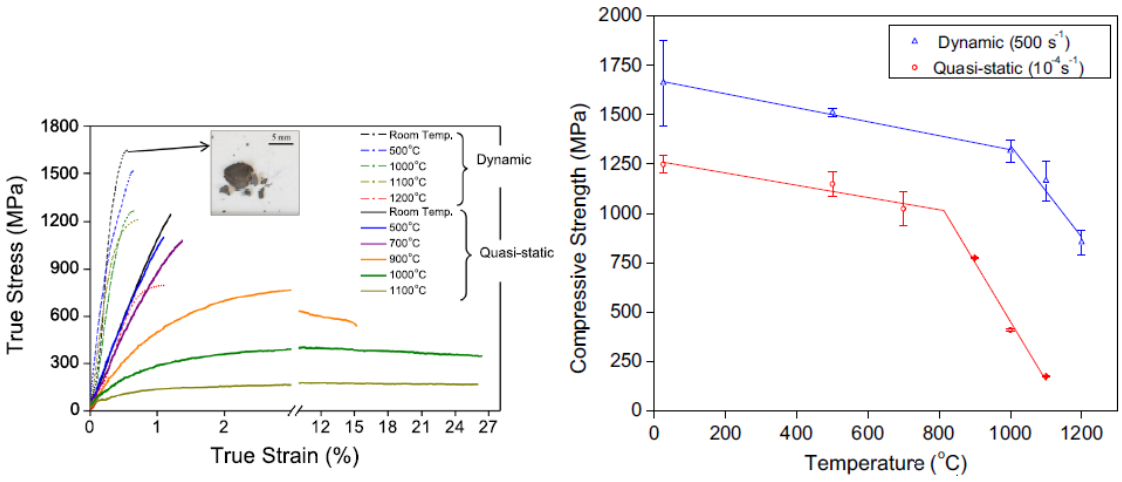

Figure 3.22: (a) *True compressive stress-strain curve of Ti_2AlC at various temperatures under both quasi-static (strain rate = 10^{-4} s^{-1}) and dynamic (strain rate = 500 s^{-1}) loading conditions.* ***(b)*** *Effect of temperature on the compressive strength of both dynamic and quasi-static tests [97]*

A follow-up test on the effect of grain size under similar conditions was undertaken by Parrikar *et al*. They again found that compressive strength was related to grain sizes at a given temperature in a Hall-Petch type relationship. The Hall-Petch relationship is a common one witnessed within materials science. This relationship describes materials with a finer grain size usually having a higher strength than materials with a coarser grains size. The reason for this is that during plastic deformation, slip or dislocation motion must take place across a common grain boundary, with this grain boundary acting a barrier to dislocation motion. Due to there being more grains and therefore more grain boundaries in fine grained materials, these materials have a larger total grain boundary area than the coarse grain size materials. The higher total grain boundary area acts in impeding dislocation motion and thereby leading to higher strengths in fine grained materials [98]. The relationship is described by an equation, where yield strength is σ_y, d is grain diameter and σ_0 and k_y are constants for a particular material:

$$\sigma_y = \sigma_0 + \frac{k_y}{\sqrt{d}}$$

As with their previous test, Parrikar *et al* witnessed brittle failure transition to graceful failure with increasing temperature, with the propensity for graceful failure increasing with increasing grain size. They determined that the strength of Ti_2AlC is governed by the dislocation pile-up on grain boundaries between soft and hard grains that in turn leads to high-stress concentrations and fracture. The compressive strength decreases with increasing grain size under dynamic loading due to grain boundary sliding being insignificant. A comparison of the post-mortem

results of both the quasi-static and dynamic tests can be found in Figures 9 and 10 in the Parrikar *et al* study, which generally shows two or three brittle fragments at lower temperatures and barrelling at high temperatures for quasi-static tests, while under dynamic loading conditions, numerous small fragments are formed at lower temperatures and at higher temperature much of the sample stays together, although multiple cracks are formed. CG Ti_2AlC tested at 1100°C retained its integrity and did not fragment. The fracture surface micrograph of the medium grained sample loaded to 1100°C can be found in *Figure 3.23(a, b)*, where a combination of cleavage fracture, delamination and kinking of grains is evident. The graceful failure at high temperatures is a result of delamination of grains and the kinking of grains leading to higher energy absorption. The secondary intergranular cracks seen in the CG microstructure subjected to 900°C (*Figure 3.23(c)*) could be responsible for the early transition to graceful failure due to them facilitating the kinking of grains [97,99].

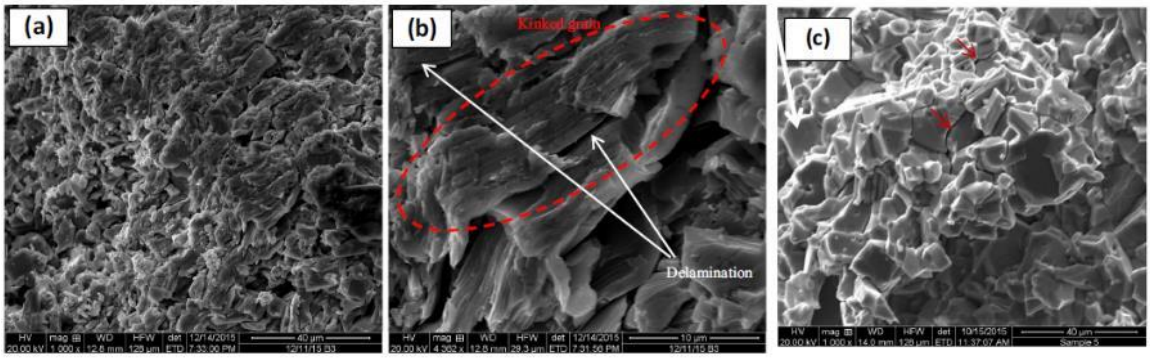

Figure 3.23: a and b) *Fracture surfaces of the MG specimen subjected to 1100°C, showing:* ***(a)*** *grain refinement, and* ***(b)*** *grain kinking and delamination. c) fracture surface of the CG specimen subjected to 900°C, showing secondary intergranular cracks [99]*

3.6.3.2 Gleeble testing

Despite the previously outlined papers covering similar areas of interest to this thesis, there are limits to the equipment, namely the split Hopkinson bar, that stop it from fully representing the aims of this thesis. Despite this, some papers have made use of a Gleeble dynamic system, similar to the equipment used for this work. As previously touched upon, Zhou *et al* deformed polycrystalline Ti_2AlC under compression using the Gleeble 1500 universal testing machine at a strain rate of $1x10^{-4}s^{-1}$. They reported that Ti_2AlC is damage tolerant at room temperature and that the samples shear fractured upon failure. At higher temperatures of up to 1200°C Ti_2AlC was found to deform plastically, with them determining that the BDTT was between 1000 and 1050°C. Scanning electron microscopes were utilised after testing, which helped them declare

that at high temperatures below the BDTT the deformation was a combination of cavities formation and intergranular sliding and that due to the availability and mobility of a sufficient number of dislocation systems, the deformation at temperature above the BDTT was mainly plastic flow [20].

Zhang *et al* reported on the strain-rate dependent compression deformation behaviour of the Ti_3AlC_2 MAX phase at temperatures between 1000 and 1200°C and strain rates between 10^{-2} and 10^{-5} s^{-1}. A Gleeble 3800 thermomechanical simulator, similar to the one used for this thesis, was used to determine the deformation behaviour. When subjected to strain rates of 10^{-2} and 10^{-3} at 1000°C the samples deformed non-plastically before failing in a brittle manner. However it was realised that as the temperature increases and strain rate decreases, Ti_3AlC_2 exhibits limited plasticity, as evidenced at 1200°C with a strain rate of 10^{-4}, where the true plastic strain was recorded as only 3%, after which strain softening following a short strain hardening regime occurs. It was postulated that this softening was due to formation of localized microvoids and microcracks. Upon decreasing the strain rate further to 10^{-5} s^{-1}, strain hardening instead of softening was witnessed, with the plastic strain reaching a value as high 27%. This hardening was thought to stem from the dislocation reactions, formation of hexagonal dislocation networks and dislocation entanglements among the dislocations, dislocation walls, and dislocation networks. The exceptional compressive plasticity at a strain rate of 10^{-5} s^{-1} at 1200°C was attributed to the initiation of nonbasal slip systems. The dislocations or dislocation walls on basal planes can cross-slip onto nonbasal planes, or double cross-slip onto other basal planes [100].

3.6.4 Thermal shock resistance

Due to the high melting point and excellent high temperature mechanical properties, ceramics are ideally suited for high temperature applications. However, the inherent brittleness of these conventional high temperature ceramics makes them more susceptible to thermal shock. After thermal shock, most ceramics show catastrophic drops in mechanical properties, such as flexural strength and elastic modulus. During quenching, the surface layer of the specimen cools down while the core portions remain at higher temperatures, causing a transient tensile

stress to form on the surface, resulting in the damage of the samples. The transient tensile stress can be determined by:

$$\sigma_t = \frac{\alpha E \Delta T}{1 - v}$$

where α is the coefficient of thermal expansion, E the elastic modulus, ΔT the temperature difference and v the Poisson's ratio. Increasing the quench temperature gives rise to higher transient thermal stress. The damage degree of thermal shock therefore becomes more serious with increasing quench temperatures [101].

The behaviour of the MAX phase ceramics in response to thermal shock, however, is unique. The retained strengths of water-quenched MAX phase samples increase with increasing quenching temperatures above a critical quench temperature. While there has been a limited amount of work on the mechanical testing of the MAX phases, and the thermo-mechanical testing in particular, there has been even less work that has examined this thermal shock behaviour.

First observed by Barsoum and El-Raghy in their paper on the characterisation of Ti_3SiC_2, they attributed the unique behaviour to a high fracture toughness [22]. It was also later observed in Ti_3AlC, Nb_2AlC and $(Ti, Nb)_2AlC$, among others [15,91,102,103]. El-Raghy *et al* determined that the response of Ti_3SiC_2 to thermal shock depends on the grain size, with CG samples quenched from 1400°C in ambient temperature water showing no detrimental effects in the post-quench flexural strengths. The strengths were also found to not be a function of quench temperature and that they actually get slightly stronger when quenched from 1400°C. FG samples behaved differently in that their post-quenching strengths gradually decrease over a 500°C range from ~600°C [89]. Barsoum *et al* and Bao *et al* ascribed this behaviour to the formation of oxide layers during thermal shock experiments which would produce compressive stresses on the surface layer of samples, while Ganguly *et al* attributed the behaviour to the formation of kink bands of substrate [1,15,89,103,104]. Wang *et al* estimated that this phenomenon was caused by the closing up of the surface flaws at high temperatures [75]. However, these mechanisms had one common problem in that they were not confirmed by experiments.

Zhang *et al* proposed a new explanation in their paper on the abnormal thermal shock behaviour of both Ti_3SiC_2 and Ti_3AlC_2. *Figure 3.24(a, b)* displays the variation in residual flexural strength of both MAX phases. As the thermal shock experiments were carried out in air, oxide layers such as rutile TiO_2 and Al_2O_3 formed on the sample surface during the heating process. Compressive stresses would be generated in the surface layer after cooling, seeming to benefit the flexural strength. This mechanism, however, was excluded as the oxide layers did not contribute to the flexural strength of as-quenched specimens at room temperature. They therefore determined that residual strength at ambient temperatures only depends on the strength of the substrates. *Figure 3.24(c)* shows the retained strength vs numbers of quenching for samples quenched from 1200°C. The substrate response to thermal shock indicated to Zhang *et al* that thermal shock could not improve the strength of the substrates. The quench strengthening behaviour is therefore not due to the fact that water quenching could increase the strength of the substrates. The damage from thermal shock was also evaluated via the elastic modulus measurement, which demonstrated the elastic modulus response to thermal shock followed the same trend as the retained strength. This trend is that the less damage, the more retained strength. The degree of damage of substrates was strongly influenced by the transient tensile stress σ. It is therefore important to understand the variation of the transient tensile stress imposed on the substrates in order to understand the phenomenon [101].

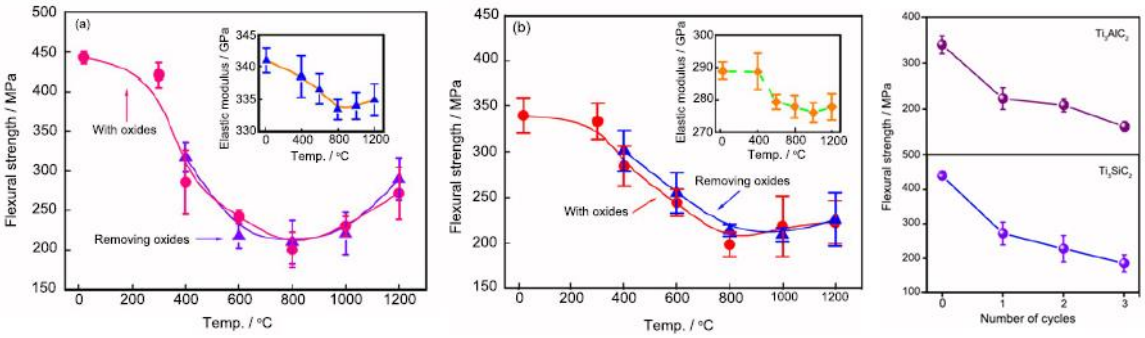

Figure 3.24: a and b) *Residual function as a function of quench temperatures of as-quenched* ***(a)*** *Ti_3SiC_2, and* ***(b)*** *Ti_3AlC_2 samples.* ***(c)*** *Retained strength vs numbers of quenching for Ti_3SiC_2 and Ti_3AlC_2 quenched from 1200°C in water. [101]*

The transient tensile stress equation is based on the hypothesis of an infinitely fast quench in which the possibility of heat conduction within materials is excluded. However, in practical

cases, the surface heat transfer coefficient *h*, thermal conductivity of a material *k* and specimen size *H* should be taken into account. Upon being reduced by a factor of ψ, the transient tensile stress equation is altered to:

$$\sigma_t = \frac{\alpha E \Psi \Delta T}{1 - v}$$

where ψ is a function of Biot modulus (β)

$$\frac{1}{\Psi} \approx 1.5 + \frac{3.25}{\beta} = 0.5 \exp\left(-\frac{16}{\beta}\right)$$

$$\beta = \frac{hk}{H}$$

The altered equation now reveals that the practical transient tensile stress σ is proportional to the product of $\Psi\Delta T$ because α, E and v are materials constants. The thickness of the oxide layers would obviously increase with quench temperatures. Due to the low thermal conductivity of oxides, the surface oxide layers essentially act as an additional thermal barrier that decreases the effective cooling rate, in effect reducing the surface heat transfer coefficient *h*. The surface heat transfer coefficient is further decreased with increasing quench temperatures, which cause the thickness of the oxide layers to increase. The increase of the thickness of oxide layer reduces the product of ψΔT, however an increase in quench temperatures increases ΔT, which increases the product of ψΔT. The damage degree of the substrate therefore decreased with quench temperature, accounting for the quench strengthening, a deduction further confirmed by FEM [101,105,106].

Three major facts generally contribute to the excellent thermal shock resistance of the MAX phases, and Ti_3SiC_2, Ti_3AlC_2 and Ti_2AlC in particular: (1) They are damage tolerant, therefore showing excellent thermal shock resistance due to the significant resistance to crack propagation; (2) Their thermal conductivities are higher than conventional brittle ceramics, being desirable for high thermal shock resistance; (3) These ceramics are ductile at high temperatures, with ductility inhibiting thermal failure [47,54].

In a later paper, Bhattacharya *et al* tested the thermal shock effects on dynamic deformation mechanisms in Ti_2AlC. They determined the suitability of the material for structural

applications under extreme environmental conditions by heat treating in a furnace with a fixed heating rate of 20°C/min before subjecting it to thermal shock followed by high strain rate loading using the SHPB setup. At higher quenching temperatures (thermal gradients 530°C and 880°C), kink bands and grain buckling were observed for purely thermal loads, apart from a change in surface morphology due to the formation of oxides. When the specimens were then thermally shocked, they displayed lesser heterogeneities in displacement fields, different values of elastic-inelastic transition and failure stress, with increasing quenching temperatures. Despite an increase in temperature systematically leading to a decrease in local heterogeneities, no particular trend was observed for the transition and/or failure stress. As can be seen in *Figure 3.25*, the retained strength increased from 0-200°C, decreased from 200-500°C before finally increasing again from 500-900°C. The specimens with a greater amount of thermal shock behaved differently in that they failed at relatively higher elongations, which they ascribed to the formation of kink bands due to thermal stresses [107].

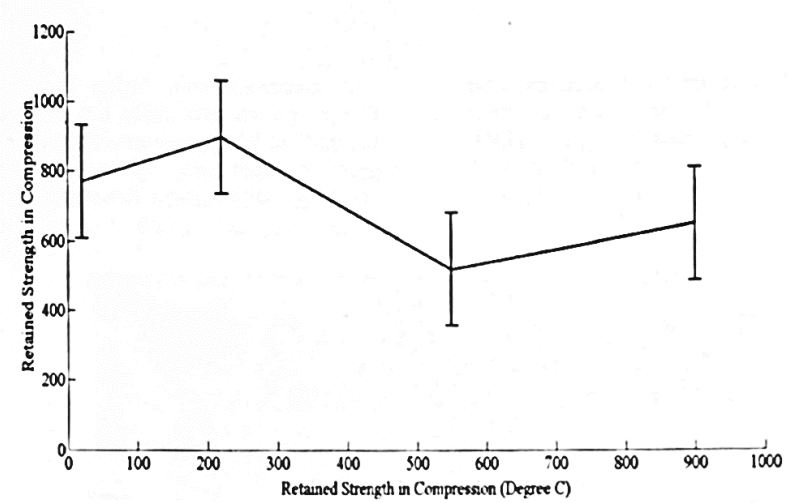

Figure 3.25: *Fracture strength vs Quenching temperature with standard deviation error bars for Ti_2AlC tested using SHPB at 5300 s^{-1}, showing little statistical variation in the fracture strength in high strain rate compression up to 900°C [107]*

The Gleeble 3500 dynamic system used for this work has the ability to study the mechanical properties of a material after thermal shock under a mechanical stress. Using a Gleeble 3500, Adamaki *et al* subjected commercial Ti_2AlC to combined thermal shock and mechanical loading to determine its mechanical properties following thermal shock. They found that the material retained its mechanical properties after thermal shock at 1200°C and a cooling rate of

90°C/sec; even when subjected to stresses of up to 150 MPa. This was further confirmed when studying the microstructure of the sample, which indicated no significant changes or defects following the thermal shock [108]. The paper by Adamaki *et al* used gas, or air, quenching, Bao *et al* performed similar quenching conditions by quenching Ti_3AlC_2 in air, where it was found that the retained strength was enhanced with increasing temperature difference [103].

Bai *et al* determined the thermal shock behaviour Ti_2AlC by heating samples to temperatures of from 200°C to 1400°C before quenching them in various cycles and testing their retained strengths afterwards using a flexural strength test. They determined that the post quench strength shows features consistent with the kinetic propagation of "short initial cracks" [107]. They related the lack of a discontinuous decrease in retained strength to the micro-scale plastic deformation associated with mobile basal dislocations. When they increased quench times to 5 cycles, there was a decrease in the retained flexural strength with a lower rate of decrease compared to the first quench. Upon quenching at 300°C and above, they found voids after the pullout of grains- features absent on the un-quenched samples -which indicated a weakening of bonding among grains and the induced damage around the grain boundary during thermal shock [109].

3.7 Applications

The unique properties of the MAX phases make them an attractive material to use for a variety of applications. The list is long, but some of the high temperature applications include its use for heating elements, high temperature foil bearings and gas burner nozzles, while some papers have also suggested its use within the nuclear industry [15].

However, as this thesis is more directed towards the high temperature aerospace applications it would be prudent to examine what structural ceramics are currently used within the industry. Within the field of aerospace, ceramics have been used in the space shuttles for many years, however recently they are increasingly being used in commercial and military aircraft. One of the primary aspects that's making ceramics more popular to use is that they are generally lighter than metals, however the costs of working with advanced ceramics means that a clear advantage over metals must be established by using them [110]. Structural ceramics are lighter

than most metals and are stable at temperatures substantially above high grade technical plastics. Conventional structural ceramics, such as the binary ceramics SiC, Si_3N_4, Al_2O_3, SiO_2, ZrO_2 etc. are currently widely used in the aerospace industry due to their low density, good corrosion resistance, high fracture toughness and high strength at high temperatures [111–113]. As an example, Silicon Nitride produced by 3M has been used as an insulator in jet engine igniters in applications where aluminium oxide insulators fail [113]. Other applications of structural ceramics include thermal protection systems in rocket exhaust cones, insulating tiles for the space shuttles and missile nose cones [110]. Technical ceramics have also been used for various parts of a jet engine for over 30 years, however the drive for better fuel efficiency has led to the development of SiC/SiC composites for use as turbine blades in jet engines. Currently, cooling channels within the jet engine are needed to stop metal alloy blades from melting. However, if the blades were made of ceramics or ceramic composites, which can deal with temperatures in excess of 1500°C, the engine could run at higher temperatures, hence increasing energy efficiency.

However, the relatively short lifetime until failure of these ceramics means that they are of limited use when using them in extreme environments. This is mainly due to the accumulation of damage, which can ultimately lead to the rapid and catastrophic failure of the ceramic components. These ceramics are also known to be hard and brittle and difficult to machine with traditional cutting tools, unlike the MAX phases, which are well known for their good machinability. As has already been expanded upon widely in this chapter, the MAX phases have an unusual set of properties that combine some of the advantageous properties of some of the ceramics discussed in this section and of metals [114].

An emerging problem within the field of aerospace is that of environmental degradation in turbines via gas phase embrittlement, oxidation and low temperature hot corrosion (LTHC) of advanced disk alloys in the high pressure turbine stage. Due to the surface of the disk and blade attachment points representing some of the most highly stressed areas of a turbine, any coating or improvement of the material would significantly lessen the chance of a potential failure. The Al containing MAX phases have the potential of excellent oxidation resistance due to the formation of Al_2O_3 scales, with Ti_2AlC exhibiting among the highest oxidation resistance. Smialek *et al* of NASA Glenn research centre vacuum diffusion bonded MAX phase coatings

in the form of thin Cr_2AlC wafers to an advanced turbine disk alloy, LSHR, at 1100°C [94,115]. They postulated that this MAX phase could be used as a potential coating due to its strain tolerance, which was in turn due to microlaminate kinking its relatively high CTE and good Type I hot corrosion resistance. Despite the detrimental effects of an NiAl reaction zone, Cr_7C_3 depletion zone and σ-phase formation in the LSHR alloy, they determined that Cr_2AlC MAX phase coatings were relatively stable with Ni-base super alloys in 800°C cycling [94]. They further explored these coatings and found that Cr_2AlC was also mechanically compatible at 1100°C or above (100h) but not for very long. This, they believed, set limits on Cr_2AlC as a high temperature thermal barrier coating (TBC) on Ni-based super alloys, but could improve corrosion resistance in lower temperature applications.

While design rules for the thermo-mechanical performance of ceramics for aerospace applications have been hard to come by, a set of design requirements of ultra-high-temperature ceramics (UHTCs) within the field of hypersonic applications were published by Squire *et al* [112]. They suggested that some key aspects that make UHTC property measurements more useful for analysts and designers are: 1) the temperature dependence of a materials properties, especially the thermal conductivities, specific heat, emissivity, tensile modulus and thermal expansion coefficients; 2) measurement techniques should be referenced to standard tests, whenever possible; 3) Measurements should always be reported with well-defined errors; 4) Isotropy and homogeneity of the UHTC materials should be confirmed, or failing that, the orientation of test specimens relative to the manufacturing process.

3.8 Literature Review Summary

Reviewing the literature, it is clear that the MAX phases are at an exciting part in their history and development. From their discovery in the 60's, through the major breakthroughs in the mid to late 90's to the present day, the MAX phases have always surprised with their unique amalgamation of properties of both metals and ceramics.

From examining the literature, a few of the aims stated at the beginning of the thesis can be further expanded and possibly be subject to further experiments. The lack of heating regimes explored in the literature suggests this could be an area that could be further examined in

relation to thermal properties and the residual stress effects of then either cooling slowly or thermally shocking the samples.

The amount of strain and strain rate applied has been explored in one paper in relation to the Ti_3AlC_2 MAX phase, so another avenue of interest would be to determine the effects of different strains and strain rates on the two MAX phases studied for this work using the Gleeble 3500. The effect of different strains at different temperatures and under different heating regimes could also be another area of interest. From the literature it was apparent that while many papers had tested the dynamic thermomechanical capabilities of Ti_2AlC, less had tested Ti_3SiC_2.

The review of aerospace applications and thermo-mechanical performance of such applications led to the determination that there is a lack of a cohesive test of a materials properties at such high temperatures using equipment such as the Gleeble 3500. Therefore, a set of design rules to test the high strain rate resistance of materials for aerospace applications using the Gleeble 3500 could be developed.

In general, an overarching comparison of the two MAX phases studied in this literature, Ti_2AlC and Ti_3SiC_2, will be undertaken. This should involve not only the mechanical testing of the materials but also the investigation of the materials microstructure both before and after this mechanical testing, any residual internal stresses, deformation mechanisms and domain formation via a variety of electron microscopy and XRD techniques.

Chapter 4 - Experimental Procedure

4.1 Material Composition and Properties

As previously stated in the literature review, two different MAX phases have been investigated for this study; Ti_2AlC and Ti_3SiC_2. The material was obtained from Kanthal (Sanvik, Sweden), under the commercial names of Maxthal 211 (Ti_2AlC) and Maxthal 312 (Ti_3SiC_2) [16]. Table 1 shows the phase compositions of these materials recorded by Lambrinou *et al* [116].

Table 1: Composition (wt%) of Maxthal 211 and 312 MAX phase Ceramic materials [115]

MAX phase	Composition (wt%)		
MAXTHAL 211 (Ti_2AlC)	55% Ti_2AlC	38% Ti_3AlC_2	7% $TiAl_3$
MAXTHAL 312 (Ti_3SiC_2)	90% Ti_2SiC_2	10% TiC	…

They documented more properties of these Maxthal MAX phases. The density of the 211 MAX phase was recorded as 4.02g/cm^3, with a theoretical density of 98%. Ti_3SiC_2 also had a theoretical density of 98% and a density of 4.42g/cm^3. The grain sizes could be described as coarse grained for the Ti_2AlC based MAX phase at 50-100μm and fine grained for the Ti_3SiC_2 MAX phase, with a grain size of 5-10μm. The Young's modulus values generally compare favourably to the 'pure' Ti_2AlC or Ti_3SiC, with values of 277 GPa and 322 GPa respectively reported in the literature and 265 ± 4 and 325 ± 5 GPa for their Maxthal counterparts. There are, however, slight differences in the hardness values, with pure Ti_2AlC generally possessing a HV of 5 ± 0.5 GPa, while Maxthal 211 has a HV of 3.2 ± 0.5 GPa. However, there are values below this general figure, with Wang and Zhou reporting a HV of 2.8 GPa for Ti_2AlC MAX phase with a grain size of ≈50μm, similar to Maxthal 211 [17,18,27,116]. The Vickers hardness value for Maxthal 312 was recorded as 3.8 ± 0.4 GPa, comparing more favourably to Ti_3SiC_2 than Maxthal 211, with values of 5 ± 1 GPa [15,116].

Before being machined to the correct sample size, each grade came in cylindrical rods of dimensions ≈206mm in height and 62mm in diameter and 197mm in height and 54mm in diameter for Ti_2AlC and Ti_3SiC_2 respectively. Using an electrical discharge machine (EDM),

≈15mm slices were cut before cylindrical uniaxial compression samples of dimensions 15mm/10mm were cut and then lightly ground using P1200 grinding paper to remove any oxide layer in preparation for the welding of thermocouples. Each cut sample was given a code to determine where it had been cut from within the material, i.e. samples cut from the centre were given codes 1A-1D, while samples cut from the outer perimeter of the cylindrical slice were given codes from 2A (left), 2B (right) to 6A and 6B. The primary reason that this was done was to assess the homogeneity of the starting block of material.

4.2 High Strain Rate Testing

The need to test the high strain rate resistance of a material in the context of aerospace applications is extremely important. High strain rate tests such as an impact test can demonstrate whether a material can withstand the ingestion of debris in situations such as a bird strike while a jet engine runs at high temperatures. To the best of the authors knowledge, there are no set design rules for the impact testing of ceramic aerospace components using such small samples, however numerous papers have impact tested aircraft components. Zhang *et al* tested the ballistic penetration resistance of Titanium alloy TC4 engine casings by using air guns, shooting at velocities ranging from 50 to 500 m/s, defined as moderate velocity. They noted that a limitation of this approach is that impact tests cannot simulate the dynamics of a released rotating blade, but can give valuable information about casing design, such as the potential failure modes, deflection, and critical impact velocity [117]. Roberts *et al* impact tested a ceramic composite for use as an aircraft engine fan case, determining that the panels of such composites could approach that of metals. The protective ceramic surface layer was seen as a promising approach for preventing fibre shear failure on the impact surface but not for limited delamination. Some of the composites reached impact velocities of approaching 200 m/s [118].

The primary aim of this thesis is to test and evaluate the high strain rate response of novel MAX phase ceramics. Conventional materials high strain rate testing can include impact testing, which involves utilising standardised impact testing techniques such as the Charpy and Izod tests. These measure the impact energy, or notch toughness of a material by releasing a swinging pendulum onto a supported sample. The problem with this technique, however, is that the results are more qualitative and are of little use for design purposes. They also cannot

perform tests at high temperatures and under a constant or increasing mechanical load [98]. The Gleeble 3500 utilised in this thesis, however, can test a materials mechanical properties at very high loading rates and at high temperatures. It also has the ability to test these properties under a vacuum. Therefore, while not being a conventional test of a materials impact resistance, the Gleeble 3500 can still test the MAX phases resistance to high speed impacts, something which could occur in the potential applications of the materials.

4.2.1 Gleeble 3500 Thermomechanical Simulation System

The Gleeble 3500 is a dynamic testing machine that possesses the capability to test and provide experimental data for a plethora of thermal and mechanical events that a material may be exposed to over its lifetime. It is these abilities that allow the Gleeble system to be used for the high temperature thermo-mechanical testing that is the basis of this project. An example of the Gleeble 3500 thermo-mechanical simulation unit can be found in *Figure 4.1*.

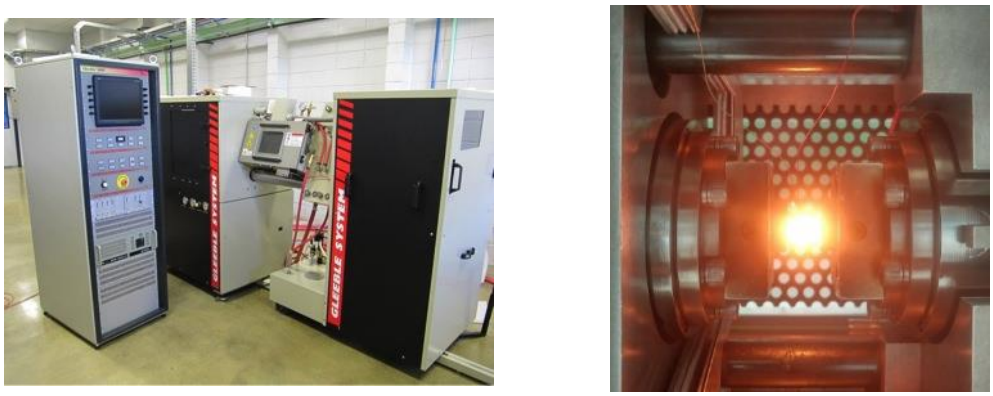

Figure 4.1: *An example of Dynamic Systems Inc.'s Gleeble 3500 thermo-mechanical simulation unit, together with an image of the Gleeble 3500 in uniaxial compression*

The Gleeble 3500 can heat specimens at rates of up to 10,000°C/second using its direct resistance heating system. High thermal conductivity grips hold the specimen, making it also capable of high cooling rates. An optional quenching system can achieve even higher cooling rates. As previously touched upon when discussing the thermo-mechanical testing of the MAX phases, the SHPB method has been used in the past to test a materials response to high temperature and/or high strains. The Gleeble 3500 system possesses more control over this technique and allows the operator to program changes from one control mode to another during a test using 'quiksim' software [119].

To achieve thermal control of the sample, thermocouples are spot welded to the approximately the centre of each of the tested samples. Type K thermocouples, which operate in the temperature range 95-1260°C, were used with Ti_2AlC and Ti_3SiC_2 samples. Mechanical control is realised through both computer control of stroke and force and the monitoring and analysis of deformation parameters directly from the sample.

4.2.2 Uniaxial Compression Testing

The Gleeble 3500 was used in uniaxial compression mode to test the high temperature thermo-mechanical performance of the MAX phases. This involved compressing ≈10 mm ø by 15 mm long cylindrical MAX phase specimens between two well lubricated tungsten carbide anvils (ISO-T) at high temperatures of up to 1200°C and at high strain rates. In order to perform a compression test, uniform deformation and temperature during the compression must be maintained. The direct resistance heating system works by constantly maintaining an isothermal plane across the diameter of the cylindrical specimen during both heating and cooling. A schematic diagram of the anvil setup can be found in *Figure 4.2*, while a basic model of the test is displayed in *Figure 4.3*.

Before each test could be started, the sample was first prepared by welding thermocouples to the centre, as demonstrated in *Figure 4.3*. Tantalum foil is then applied to the end of each specimen to both reduce friction when the sample spreads under compression and to avoid welding of the sample to the anvils. Nickel paste is added to lightly lubricate the contact between the tantalum foil and the tungsten carbide anvils.

Each uniaxial compression test was performed under partial vacuum conditions. A vacuum pump attached to the Gleeble was used to create an inert gas atmosphere in the main Gleeble chamber. This partial vacuum has an effect in reducing the level of oxidation that would have occurred on the sample surface, thereby also helping with the welding conditions.

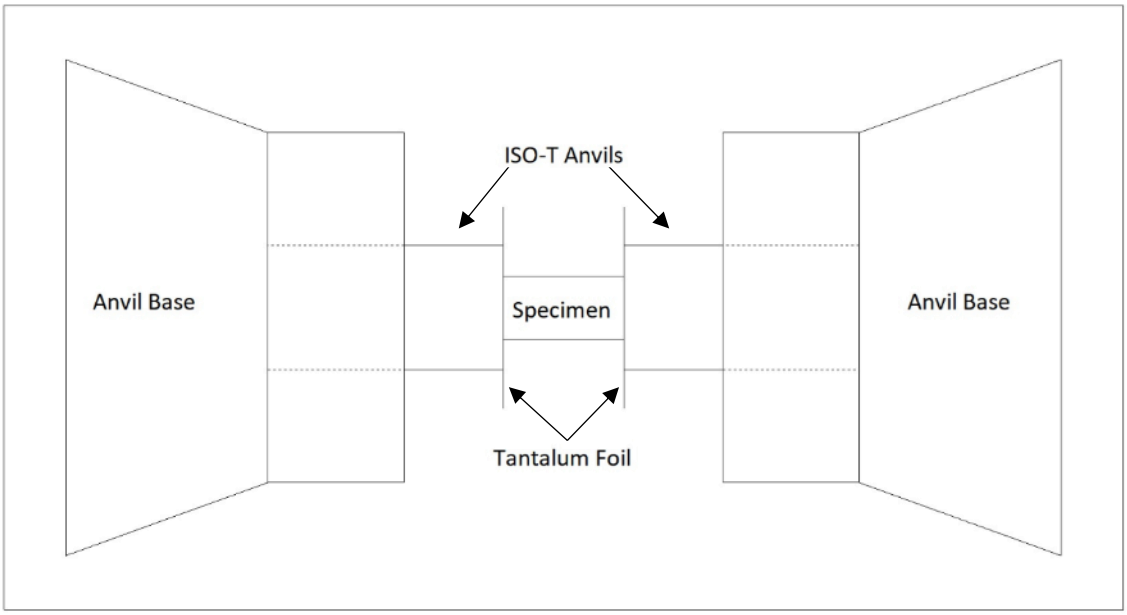

Figure 4.2: *Schematic diagram of the Gleeble system set-up in Uniaxial Compression mode*

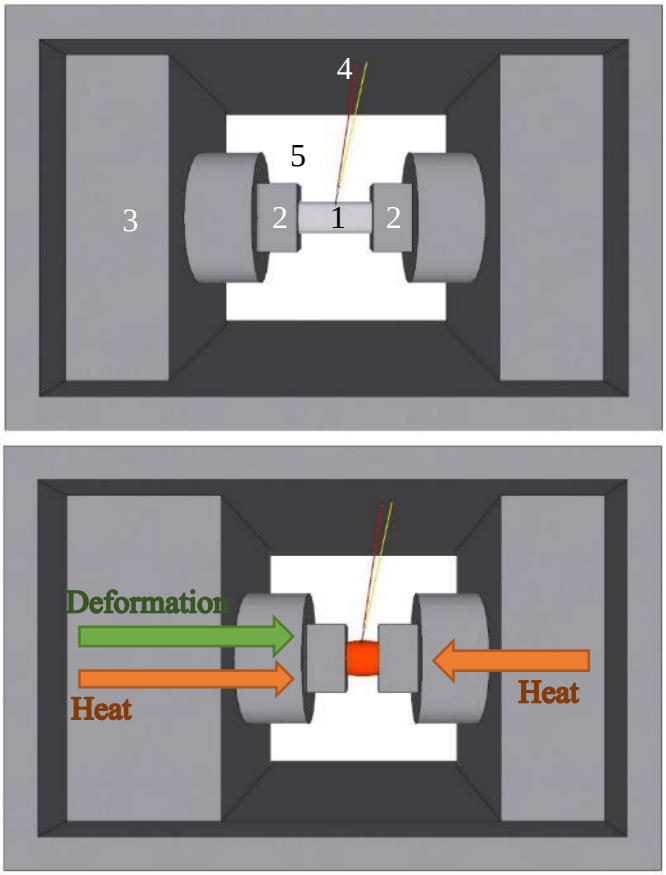

Figure 4.3: *A basic model of the Gleeble system while in Uniaxial Compression mode. The first image shows the set-up before deformation and heat have been applied.* ***1)*** *Specimen,* ***2)*** *ISO-T Anvils,* ***3)*** *Power Ram,* ***4)*** *Thermocouples,* ***5)*** *Gleeble Chamber. The second image shows the heat being applied to the test specimen via the ISO-T tungsten carbide anvils from both horizontal directions, while the power ram deforms the sample from the left hand anvil.*

As referred to in Section 4.2.1, mechanical control of the Gleeble is carried out by the computer control of both stroke and force parameters. The stroke can be defined as a large transducer in the Load Unit which measures position displacement of the moving (left) shaft. The stroke is one of the two primary methods in which the displacement or deformation of the sample during testing can be measured or controlled. The more accurate way to measure strain in the Gleeble is by using the Lengthwise Strain Gauge (L-Gauge) system. The L-Gauge is an extensometer used to measure the distance between the anvils and is mounted on both shafts inside the Gleeble vacuum chamber. The L-Gauge can record both the strain each sample is subjected to and also accurately control the amount of strain applied to a sample. In contrast, the stroke control mode offers a faster deformation rate than the L-Gauge control mode, but has a lower precision and lower resolution. In addition to its inability to perform and record very high deformation rates, strain gauges such as the L-Guage can be sensitive to extreme temperatures and can over time lose their accuracy due to conditions such as fatigue.

For the high temperature, high strain rate tests that were undertaken for this work, the L-Gauge was used to apply the desired strain to each sample. For the quench tests, the L-Gauge was also used to calculate the strain recorded during both the quenching process and the subsequent mechanical testing. All tests were carried out using true axial stress calculations:

$$\varepsilon = ln\left(\frac{L_0 + \Delta L}{L_0}\right) \qquad \sigma = \frac{Force}{\left[\frac{\frac{\pi \cdot (d_0)^2}{4} \cdot L_0}{L_0 + \Delta L}\right]}$$

4.3 Sample Preparation/Ceramography

Upon the completion of uniaxial compression tests in the Gleeble, the samples were removed and prepared ready for electron microscopy. This process involved first cutting each sample along its length using an ATM Brilliant 220 precision wet abrasive cutting machine before mounting with ether resin or Bakelite. In addition to the samples tested in the Gleeble, 'as received' samples, which had not undergone any mechanical testing, were also mounted and prepared for electron microscopy investigations.

Table 4.2 outlines the grinding and polishing stages following mounting of the samples. Each sample was ground and polished on successively finer grades of paper. Selected specimens were then etched using a mixture of $HF:HNO_3:H_2O$ at a ratio of 1:1:1 to further reveal their microstructure. Following the final polishing and etching stages, selected specimens were then inserted into a plasma cleaner to ensure that they were free from any residual debris that may have gathered on the surface at this stage.

Table 4.2: Grinding and polishing stages

Stage	Surface	Lubricant	Particle Size	Speed
Grinding	SiC Paper	Water	P120	150
			P320	
			P600	
			P1200	
			P4000	
Polishing	Chemicloth	Colloidal Silica	0.06 μm	

4.4 SEM- Scanning Electron Microscopy

Scanning Electron Microscopes (SEM) were used to help quantify the effects of the different thermo-mechanical sequences on the microstructure and nanostructure of the materials. Two SEMs were utilised in Swansea University, a Carl Zeiss Evo LS25 and a Jeol Field Emission JSM-7800F. To gain micrographs in which to compare general microstructures and deformation and fracture mechanisms of the samples, systematic magnifications were recorded between 100x and 4000x using both secondary and backscattered electron detectors on the Carl Zeiss Evo LS25, an example of which can be found in *Figure 4.4.*

As some samples had been mounted in nonconductive epoxy resin, they had to be covered with conductive carbon and copper sticky tape before being inserted into the SEM. This ensures that the samples have a good earthing circuit.

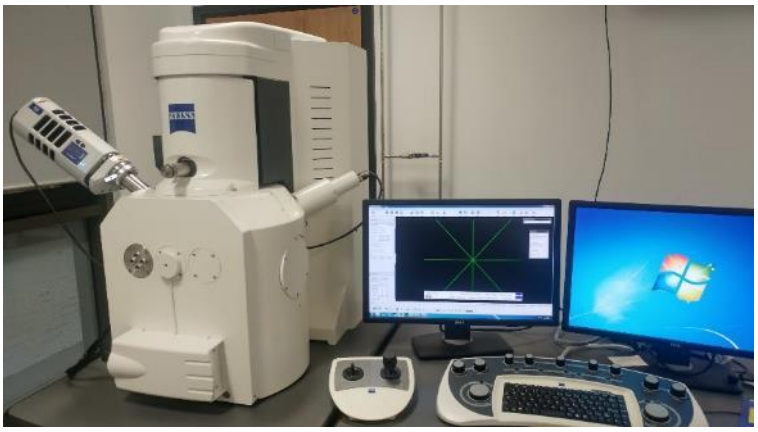

Figure 4.4: *Swansea University's Carl Zeiss EVO LS25 scanning electron microscope, with attached EDS detector*

4.4.1 EDS- Energy Dispersive X-ray Spectroscopy

Energy dispersive X-ray spectroscopy (EDS) was used to determine the elemental composition of the materials. This identification technique was carried out using Oxford Instruments Aztec EDS analysis software on both the Carl Zeiss Evo LS25 and Jeol JSM-7800F. To undertake both the spot microanalysis and map methods, the accelerating voltage used was 15-20 kV while the probe current was set to 500 pA. EDS was also utilised to determine the location of the different phases that make up each MAX phase grade.

4.4.2 EBSD- Electron Backscatter Diffraction

A Jeol JSM-7800F was used to undertake electron backscatter diffraction (EBSD) imaging of each sample. Due to the changes in crystallographic orientation that is caused by kink bands (KB) and dislocation walls (DW) within individual grains, EBSD can be a useful tool when attempting to analyse the evolution of deformation in the polycrystalline MAX phase samples. These KBs and DWs can be easily identified by EBSD when using inverse pole figures to analyse the misorientations. EBSD also helped determine the coherency of the phases and how they deform during different rates of deformation [120,121]

Figure 4.5: *Swansea University's Jeol JSM-7800F field emission scanning electron microscope with attached EDS and EBSD detectors*

The EBSD detector was used in conjunction with Oxford Instruments Aztec analysis software to help characterise the microstructure following the uniaxial compression of the samples. As a high tilt is required to perform EBSD analysis, the sample was tilted 70° once inside the vacuum chamber of the SEM. All scans were performed using an accelerating voltage of 20 kV at either 4x4 or 8x8 binning.

4.5 XRD- X-Ray Diffraction

An X-ray Diffractometer is a tool that allows the user to understand the crystal structure of a material. The Bruker B8 Discover machine, like the one found in *Figure 4.6*, that was utilised for this work uses a Cu K_α radiation source and was useful in phase identification and quantification. The test was performed under operating conditions of 40 kV and 40 mA. Each sample was mounted and cleaned before being inserted on the stage. Diffraction patterns were taken from both as received samples and those that were subjected to thermomechanical testing. For both materials, the spectra were acquired in the 10° - 90° 2θ range with a step size of 0.04°.

Figure 4.6: *The Bruker B8 Discover XRD used to undertake X-Ray Diffraction analysis of the MAX phase ceramics samples.*

Chapter 5 - Original Ti_3SiC_2 and Ti_2AlC MAX phase Characterisations

5.1 Introduction

Prior to mechanical testing, the microstructures of both as received MAX phases were characterised using various microanalytical tools. In this chapter, the results of this characterisation are presented. The MAXthal grades of MAX phase studied for this work were manufactured using the Cold Isostatic Pressing (CIP) method.

5.2 Microstructure Characterisation of As-Received MAX phases

The backscattered (BS) scanning electron images of both MAX phases are presented in *Figures 5.1 and 5.2* using JEOL 7800F SEM. When comparing the two microstructures it is immediately clear that, for the most part, the Ti_2AlC MAX phase has a substantially larger grain size than the Ti_3SiC_2 MAX phase, something which has been explored quantitatively in Section 5.5. The grain sizes of the minor secondary phases have also been explored in Section 5.5. The general microstructure of the as received (AR) MAX phases have been explored in the current section, with the elemental analysis being discussed in Section 5.3.

It is clear from *Figure 5.1,* that the Ti_2AlC MAX phase constitutes of 3 main phases. The exact number of existing phases is further confirmed by image analysis tool, ImageJ. It seems that the Ti_2AlC MAX phase exhibited a homogenous microstructure in terms of phase and size distributions. As indicated in *Figure 5.1*, the observed phases in the Ti_2AlC material consists of a (i) grey phase matrix, within which is the (ii) predominant elongated lighter phase, with a (iii) darker phase largely forming on the grain boundaries of the elongated grains and scattered around the general microstructure. Also noteworthy is the obvious layered structure to the elongated lamellar type grains, a hallmark of the MAX phases, as indicated by a solid red elliptical shape in *Figure 5.1*. Using ImageJ, the volume fraction percentages of each constituent phase were estimated, where it was found the elongated lighter phase made up around 84%, the grey phase 14% and the scattered dark phase accounting for about 2%. In the micrograph presented, it's almost certain, before any elemental characterisation is undertaken, that the phase that makes up 84% of the microstructure is Ti_2AlC in this alloy. Moreover, compared to its Ti_3SiC_2 counterpart, the amount of porosity appears to be relatively low. It

must be noted that in some ImageJ analysis of electron images like the one shown in a *Figure 5.3* that a potential 4th phase was identified, being very similar in characteristics and colour to the elongated major phase. When adjusted accordingly, ImageJ can pick up this 4th phase accounting for approximately 30% of the microstructure, with the primary phase now accounting for about 58%, with remaining phases being roughly similar in fraction. Considering the closeness in image morphology, it is reasonable to assume that this 4th phase would have a similar elemental composition to the primary Ti_2AlC phase, with the most likely candidate being Ti_3AlC_2, as recorded by Lambrinou *et al* [115].

The microstructure of Ti_3SiC_2 MAX phase appears slightly more complex than the Ti_2AlC MAX phase. As indicated in *Figure 5.2*, two major phases can be seen, together with 1 or perhaps 2 minor phases. The majority of the microstructure is made up of a fine, light in colour, relatively elongated and lamellar phase. The second major phase is scattered throughout the microstructure and is slightly darker in contrast compared to the first phase. One of the minor phases is seen to predominantly lie on the grain boundaries of both major phases, it being much whiter in colour compared to the other phases. It was rather difficult to identify the second minor phase, which is the darkest of the phases that have a similar colour contrast as the porosity. Furthermore, porosity is much more noticeable in this MAX phase than the Ti_2AlC MAX phase, which should have an impact on the materials performance when subjected to the high temperature compression testing. The volume fraction percentage of each constituent phase can be found in *Table 5.1*. The table shows that nearly three quarters of the microstructure is made up of the major phase, in this case most likely Ti_3SiC_2. The remaining quarter is mostly made up of the second major phase, with small contributions from the minor phases.

Although identifying the exact phases and their volume fractions in such complex microstructure is very difficult, the overall findings of this are in general agreement with the work carried out on the Kanthal MAX phases by Lambrinoue *et al* [115]. The manufacturing process of this material was through cold isostatic pressing (CIP). They also found that Ti_3AlC_2 could be found in the Ti_2AlC MAX phase produced by Kanthal, while the Ti_3SiC_2 phase compositions are relatively similar to the variations they found, in there being a not insignificant concentration of a minor, secondary phase.

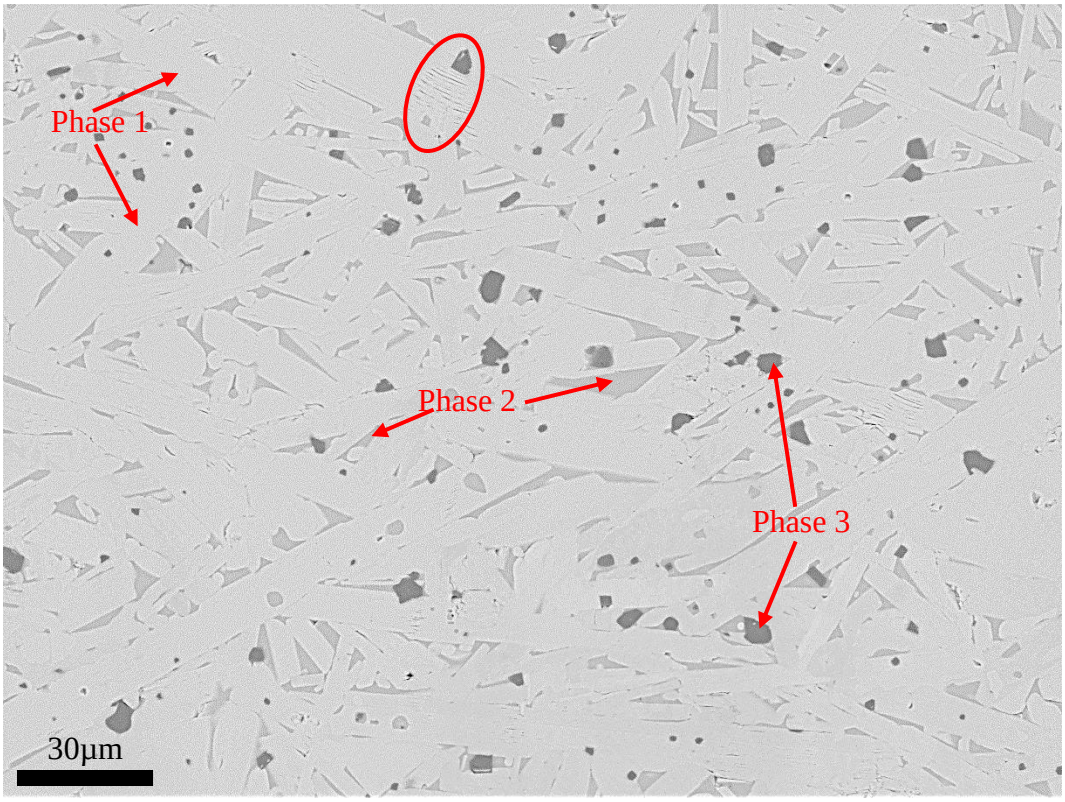

Figure 5.1: *SEM image showing the microstructure of As-Received (AR) Ti_2AlC MAX phase. The layered structure can be seen in the red ellipse.*

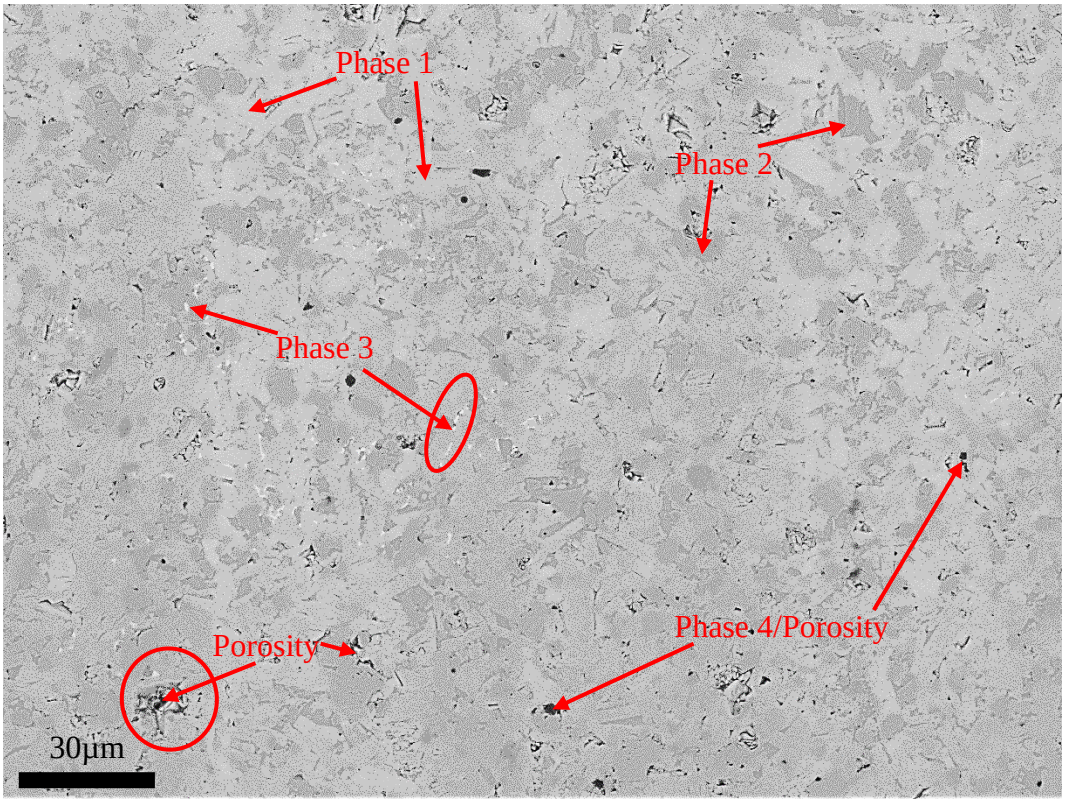

Figure 5.2: *SEM Image showing the microstructure of AR Ti_3SiC_2 MAX phase. An example of the minor white phase can be seen in the red ellipse. An example of the porosity can be seen within the red circle.*

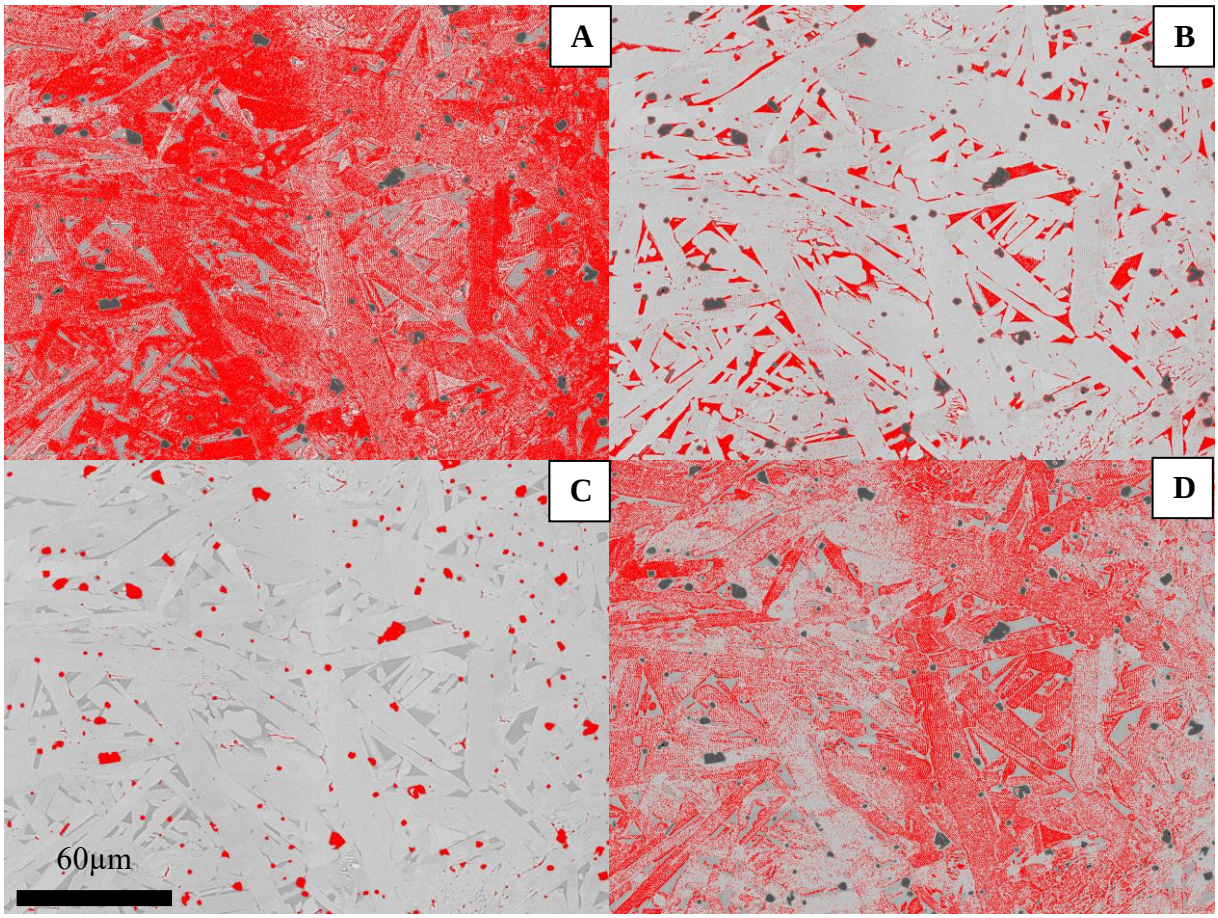

Figure 5.3: *Images of the ImageJ phase volume fraction analysis when taking into consideration the potential presence of a fourth phase of similar image morphology to the primary major phase:* ***(a)*** *Phase 1,* ***(b)*** *Phase 2,* ***(c)*** *Phase 3,* ***(d)*** *Potential phase 4.*

Table 5.1: *Volume Fraction of identified constituent phases for both MAX phases calculated using ImageJ*

MAX phase	**Volume Fraction (%)**			
	Phase 1	**Phase 2**	**Phase 3**	**Phase 4**
Ti_2AlC	84	14	2	N/A
Ti_2AlC (No.2)	58.71	7.92	2.1	31.27
Ti_3SiC_2	73.75	23.75	1.5	1

5.3 Chemical Analysis of the Materials

EDS was used to determine the elemental composition of the MAX phase ceramics used in this study as well as the composition and location of the constituent phases in both MAX phases.

5.3.1 Ti_2AlC MAX phase

Figure 5.3 shows a backscattered electron micrograph of the microstructure of Ti_2AlC, together with the EDS elemental mappings of Ti, Al, C and O and the spectrum of the whole microstructure, which also shows the chemical composition of the whole EDS map. Several EDS spectra from individual points were also obtained to determine the chemical composition of each phases. The results of the composition of several of these points and also the overall composition of the Ti_2AlC EDS map can be found in *Table 5.2*. The constituent elements of Ti, Al and C were found to contribute 68.2wt%, 21.3wt% and 10.1wt% respectively to the overall chemical composition of the Ti_2AlC MAX phase material. In order to identify the individual phases in each materials, it was clear from the elemental maps, that the elongated grains of the primary phase have a substantial concentration of Ti when compared to the other elements, Al and C, although both Al and C are still present, as proven by both the elemental maps and the spectra taken on these elongated grains. The major secondary phase is the matrix in between the large elongated grains, and it shows a very high concentrations of Al, especially when compared to the elongated grains of the primary phase. The concentration of C appears to be generally quite uniform throughout the microstructure, with the elongated grains showing slightly higher concentrations than the matrix. The elemental map of O shows that this element is being identified within the darker phase that was earlier identified using ImageJ, suggesting either porosity and/or the presence of an oxide phase such as Al_2O_3. The presence of Al_2O_3 in the MAX phases is not uncommon, with Hossein-Zadeh *et al* recording such a phase in their SPS production of V_4AlC_3. The formation of this phase has been attributed to the presence of O at the surface of the powders and/or the fact that the processing conditions can introduce O to the system [122,123]. Several spectra were taken on the elongated phase, the elemental compositions of a selection of these points can be found in *Table 5.2*. Most of the spectra taken on the elongated phases have a similar elemental composition of around 73% Ti, 16% Al and 11% C, which supports the theory that the vast majority of these elongated grains are Ti_2AlC. The spectra that show small deviations in this elemental composition could be the areas of the potential 4th phase, Ti_3AlC_2. Spectra 12 and 15 were taken at areas in between the elongated

phases, with these areas being seen to possess much higher amounts of Al than the elongated phase. The similar Ti and Al contents could suggest the presence of a TiAl intermetallic phase, as previously reported by Adamaki *et al.* [108,124]. The small, darker phase regions that were picked up as pockets of O in the elemental maps were also subjected to Point and ID analysis using the Oxford EDS software. These are Spectra 6, 7 and 14. As mentioned previously, this area could be porosity, but the very low Ti and C counts and the high Al and O counts also bring the possibility that this area could be pockets of Al_2O_3, or a similar Al rich or oxide phase.

Table 5.2: *Spectrum percentages and overall composition of the AR Ti_2AlC sample*

Element	**Spectrum**													
	1	**4**	**5**	**6**	**7**	**8**	**10**	**11**	**12**	**13**	**14**	**15**	**16**	**Overall Comp (wt%)**
Ti	73.2	70.7	44.4	1.1	33	73.4	70.3	72.4	46.8	72.4	56.1	73.9	72.7	68.2
Al	14.6	19.4	52.7	50.4	27.1	14	20.1	16.4	50	16.2	16.8	13.9	16.3	21.3
C	12.2	9.8	2.8	1.4	7.7	12.6	9.6	11.2	3.3	11.3	7.6	12.2	11	10.1
O				47.1	32.1						19.4			

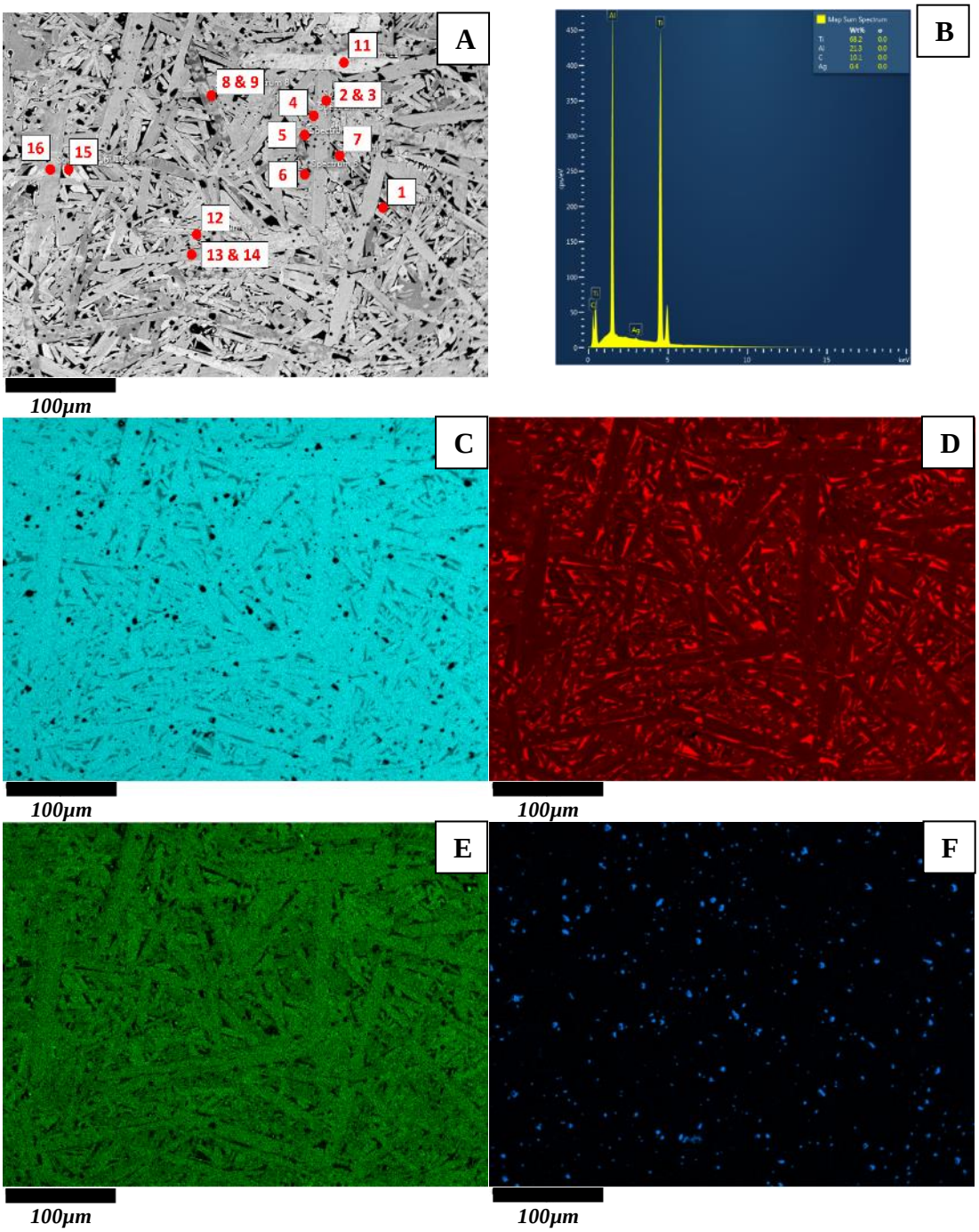

Figure 5.3: ***a)*** *Electron Image of Ti_2AlC,* ***b)*** *Spectrum of the EDS Elemental Maps, showing the relative composition of each element,* ***c-f)*** *EDS Elemental Maps of Ti, Al, C and O respectively.*

5.3.2 Ti_3SiC_2 MAX phase

The EDS data collected for Ti_3SiC_2 can be found in *Figure 5.4* and *Table 5.3*. A backscattered SEM image together with the locations of the Point and ID spectra can be found in *Figure 5.4a*. The elemental maps, together with overall spectrum and elemental composition prove the high compositions of the expected elements of Ti, Si and C throughout the microstructure. The overall elemental composition of this material can be found in *Figure 5.4e* and *Table 5.3*, where it was found that the contributions were as follows: 70.9wt% Ti, 13.7wt% Si and 15.4 C. These elemental fractions also confirm the presence of slightly more C than Si, something that would be expected in the overall composition of the Ti_3SiC_2 MAX phase material. The amount of porosity in this image seems higher than in the previous SEM image of the same material in *Figure 5.2*. When superimposing each elemental map on the electron image map it is apparent that the areas that are the brightest on the Ti elemental map appear as very dark areas on the Si map. With regards to the C elemental map, the brighter areas of this map appear to correspond to the same bright areas as the Ti map, giving weight to thought that these areas are in fact the TiC phase that was previously in the work carried out on the Kanthal MAX phases by Lambrinoue *et al* [115]. When comparing these elemental maps to the electron image it's apparent that they line up with the second major phase that constituted about a quarter of the overall microstructure in the previous SEM image, which appeared grey in image texture. The majority of the remaining general microstructure has concentrations of each element that would correspond to the Ti_3SiC_2 phase. The areas that appear bright on the Si elemental map correspond approximately to a dark phase seen on the SEM image, suggesting a phase rich in Si. When studying the Point and ID spectra, the points taken on the white grains (1-7) have a composition not too dissimilar to the overall composition of the microstructure in consisting of approximately 72% Ti, 13% Si and 15% C. These grains can therefore be confirmed with relative certainty as the main Ti_3SiC_2 phase of the microstructure. Spectra 3, 4 and 6 show quite rich in both Ti and Si, with smaller amounts of C, suggesting that this phase could be a minor TiSi phase. Spectrum 5, taken on the grey grains, are very rich in C, with small amounts of Ti and negligible amounts of Si. The phase identified here could therefore be the TiC phase proposed earlier in this section.

Table 5.3: *Point Spectrum wt% and overall composition of the Ti_3SiC_2 AR sample*

Element	**Spectrum (wt%)**							**Overall Comp (wt%)**
	1	**2**	**3**	**4**	**5**	**6**	**7**	
Ti	71.4	71.5	63.4	56.1	10.7	48	71.6	70.9
Si	13.5	12.8	28.5	37.3	0.9	44.9	13.5	13.7
C	15.1	15.6	8.2	6.6	88.5	7.2	14.9	15.4

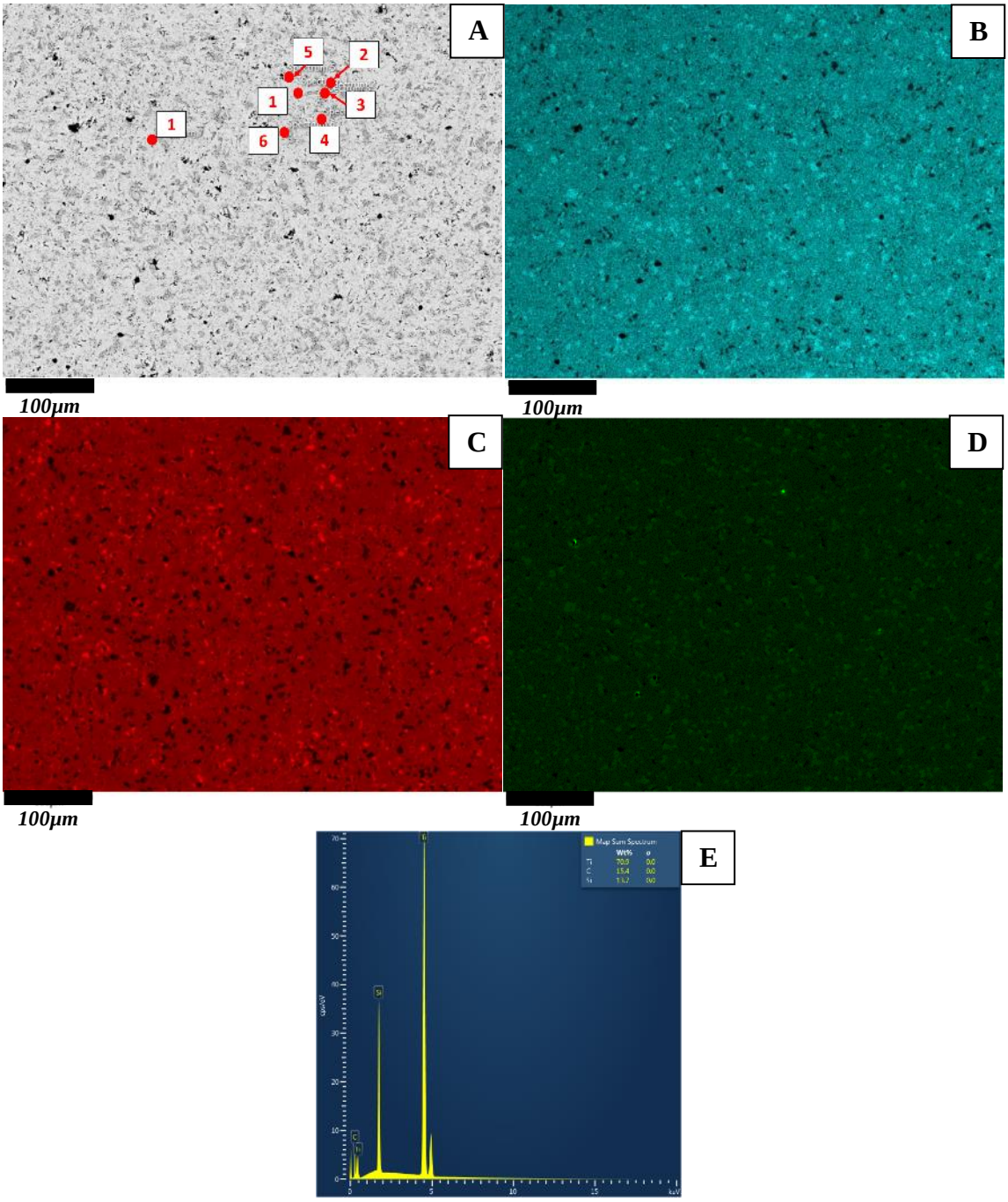

Figure 5.4: a) *Electron Image of* Ti_3SiC_2, ***b-d)*** *EDS Elemental Maps of Ti, Si and C respectively,* ***e)*** *Spectrum of the EDS Elemental Maps*

5.4 Phase Identification using XRD

X-ray diffraction technique was utilised on as received Ti_2AlC and Ti_3SiC_2 for phase identification and to validate the exact phases present in each material. Using the MAUD XRD refinement software, the peaks of the XRD spectra were identified.

Figure 5.5 shows the XRD spectrum taken for Ti_2AlC, where the presence of the dominant Ti_2AlC phase is confirmed, together with a few secondary phases. There is some debate as to what phases the peaks represent, with Adamaki *et al* suggesting that the secondary phases are TiC and $AlTi_3$, whereas Lapauw *et al* suggest that the peaks that would otherwise be TiC are in fact Ti_3AlC_2 and that the intermetallic AlTi phase is actually Ti_2Al_5. The presence of a TiAl intermetallic phase is further confirmed by Wang *et al.* [108,125,126]. It should be noted that according to Lapauw *et al.* and Wang *et al.* that 2 of the 3 phases that they found are MAX phases (Ti_2AlC and Ti_3AlC_2). There were several other peaks that were possibility identified as Al_2O_3, while some peaks were not identified, suggesting that these peaks belong to a phase that is very similar in composition to the other phases present in this MAX phase. Using the quantitative phase analysis tool within MAUD, when it was considered that the Ti_2AlC MAX phase material consisted of 4 phases, the volume fraction of the phases were estimated as 50% Ti_2AlC, 35% Ti_3AlC_2, 14% TiAl and 1% Al_2O_3, which is relatively comparable to what was found using ImageJ when studying the SEM images of the Ti_2AlC MAX phase microstructure in *Figures 5.1 and 5.3*.

The XRD spectrum for the as received Ti_3SiC_2 sample is shown in *Figure 5.6*. This analysis, backed up by the findings of Laupauw *et al.* and Lambrinou *et al.*¸ when they showed that Ti_3SiC_2 is the dominant phase, with TiC as a minor secondary phase [116,125]. Several peaks that were not either Ti_3SiC_2 or TiC were also picked up by the XRD, which could account for the minor phases identified when studying the micrographs through ImageJ and the EDS data. The quantitative phase analysis tool within MAUD estimated that the volume fraction of the phases were ~80% Ti_3SiC_2 and ~20% TiC, which is similar to the fractions found using the ImageJ and EDS analysis software.

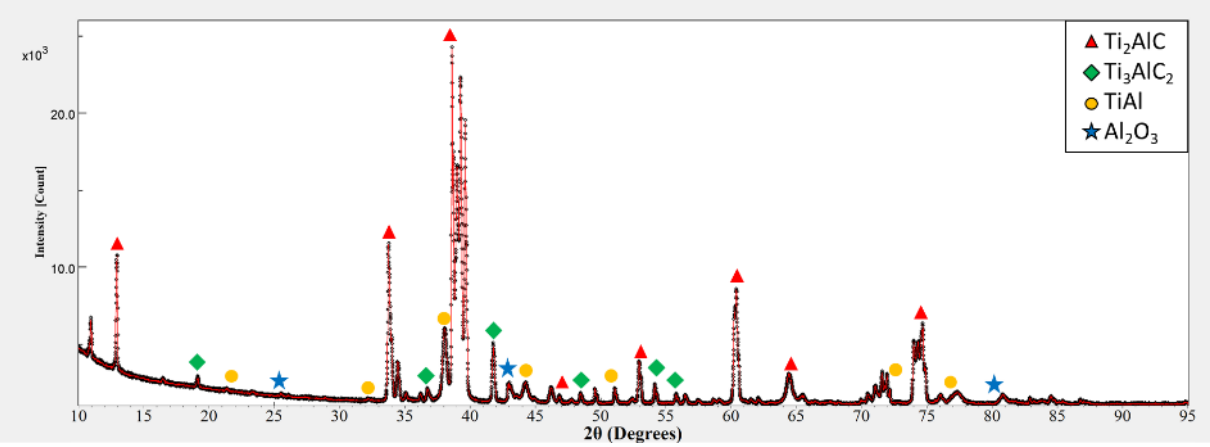

Figure 5.5: *XRD spectrum for the nominally Ti_2AlC Maxthal 211, showing the phases present in the material. Note the peaks that have not been identified, suggesting minor phases that are close in composition and formula to the ones identified*

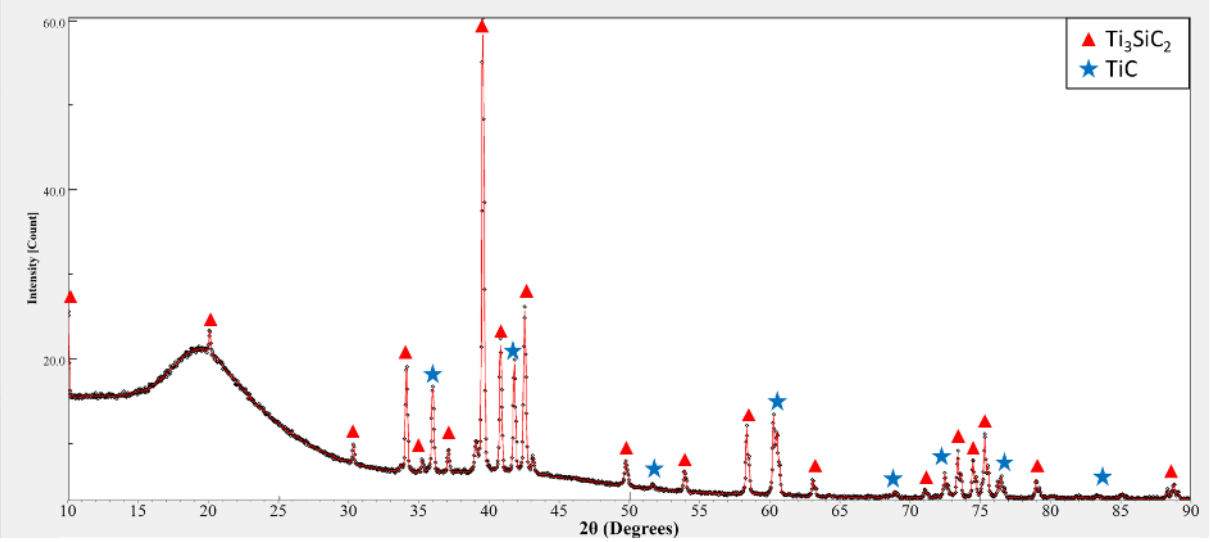

Figure 5.6: *XRD spectrum for the nominally Ti_3SiC_2 Maxthal 312, showing the phases present in the material*

5.5 EBSD Analysis of both MAX phase Materials

5.5.1 Grain Morphology (Size and Shape) Analysis

As previously stated in Section 5.2, when comparing the grain sizes of Ti_2AlC and Ti_3SiC_2, the substantial grain size differences between the two MAX phases studied for this project is immediately evident.

As shown in *Figure 5.7* although there is a substantial presence of small grains of the Ti_2AlC phase, the Ti_2AlC grains are generally quite large and are substantially bigger than the largest grains of the Ti_3SiC_2 phase in the Ti_3SiC_2 MAX phase material. The high percentage of very small grains measured could simply be as a result of the way the material is produced, which is by cold isostatic pressing, or by the grain boundary threshold used for the EBSD and grain analysis. The small grains could also represent sub grains and misindexing of the diffraction patterns during the EBSD scan. *Figure 5.7* also shows the grain area, grain diameter and aspect ratio of the separate phases exhibited in each alloy. For the EBSD and grain analysis the secondary phases were identified as TiAl for Phase 2 and Al_2O_3 for Phase 3. These phases are unsurprisingly, due their nature as minor secondary phases, of much smaller area and diameter than the larger, primary Ti_2AlC phase. The highest grain diameter recorded for Ti_2AlC was around 65µm, compared to around 9µm for the TiAl phase and 7µm for the Al_2O_3 phase. Of note when analysing the grain area and diameter for the Ti_2AlC phase is the extremely wide range of grain sizes, something which is to be expected when a material has a relatively coarse microstructure, nonetheless it is very different when compared to the other secondary phases within the Ti_2AlC MAX phase and Ti_3SiC_2 MAX phase materials. The aspect ratios for the Ti_2AlC MAX phase were found to be consistently above 1 for each phase, with the greater proportion of high aspect ratios unsurprisingly coming from the lamellar Ti_2AlC phase, despite the highest aspect ratio being anomalously found in the TiAl phase. When comparing the number of neighbouring grains for each phase, its apparent that, with some anomalous Ti_2AlC grains excepted, the phases have roughly the same amount of neighbouring grains as each other. Maps showing the grain area and grain diameter of the primary Ti_2AlC phase can be found in *Figure 5.8*. The maps have been split into two, with one showing the relatively small sub grains and the other the elongated lamellar grains.

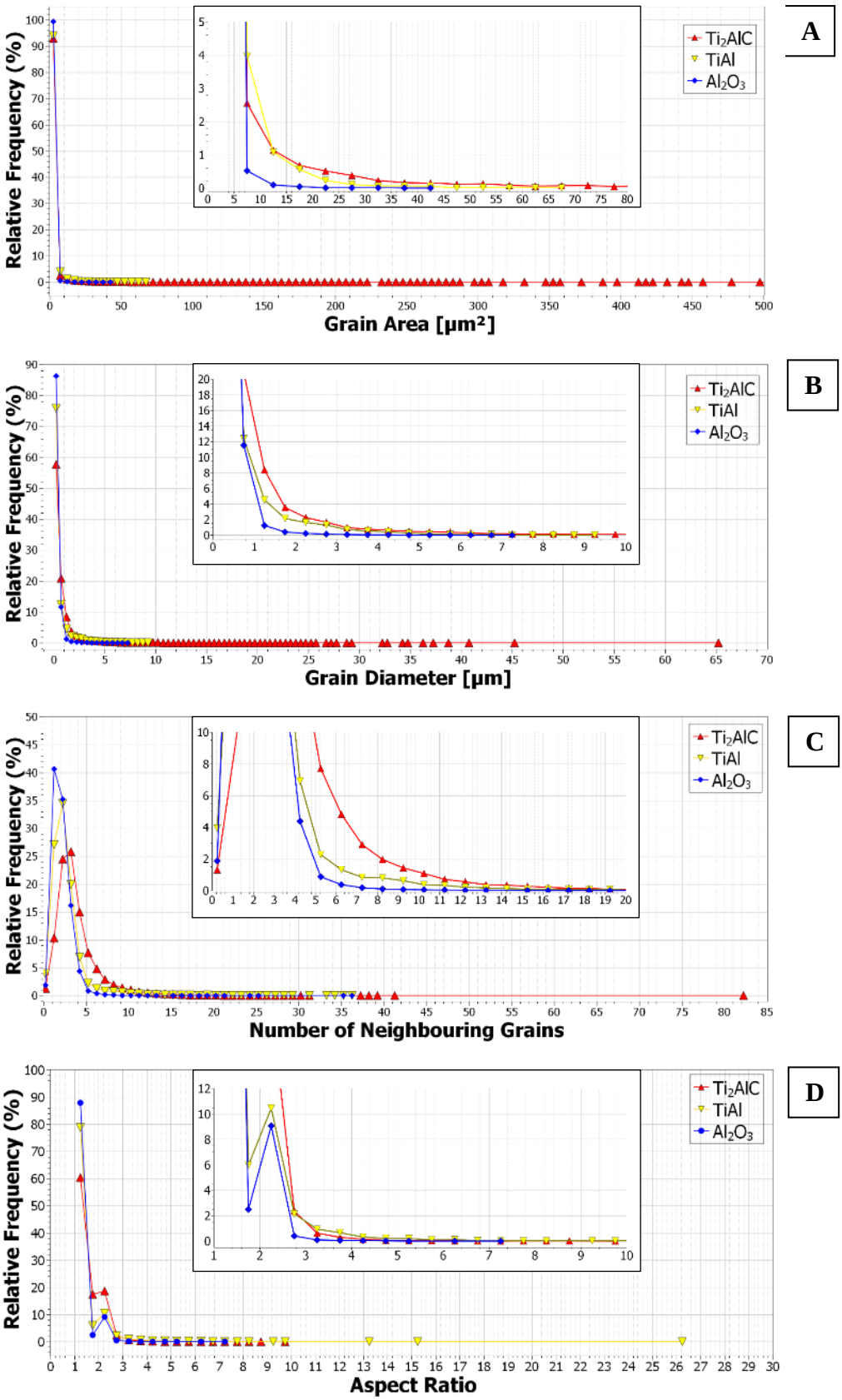

Figure 5.7: *Grain Size Analysis graphs of the Ti_2AlC MAX phase material, comparing the separate phases.* ***(a)*** *Grain Area,* ***(b)*** *Grain Diameter,* ***(c)*** *Number of Neighbouring Grains and* ***(d)*** *Aspect Ratio.*

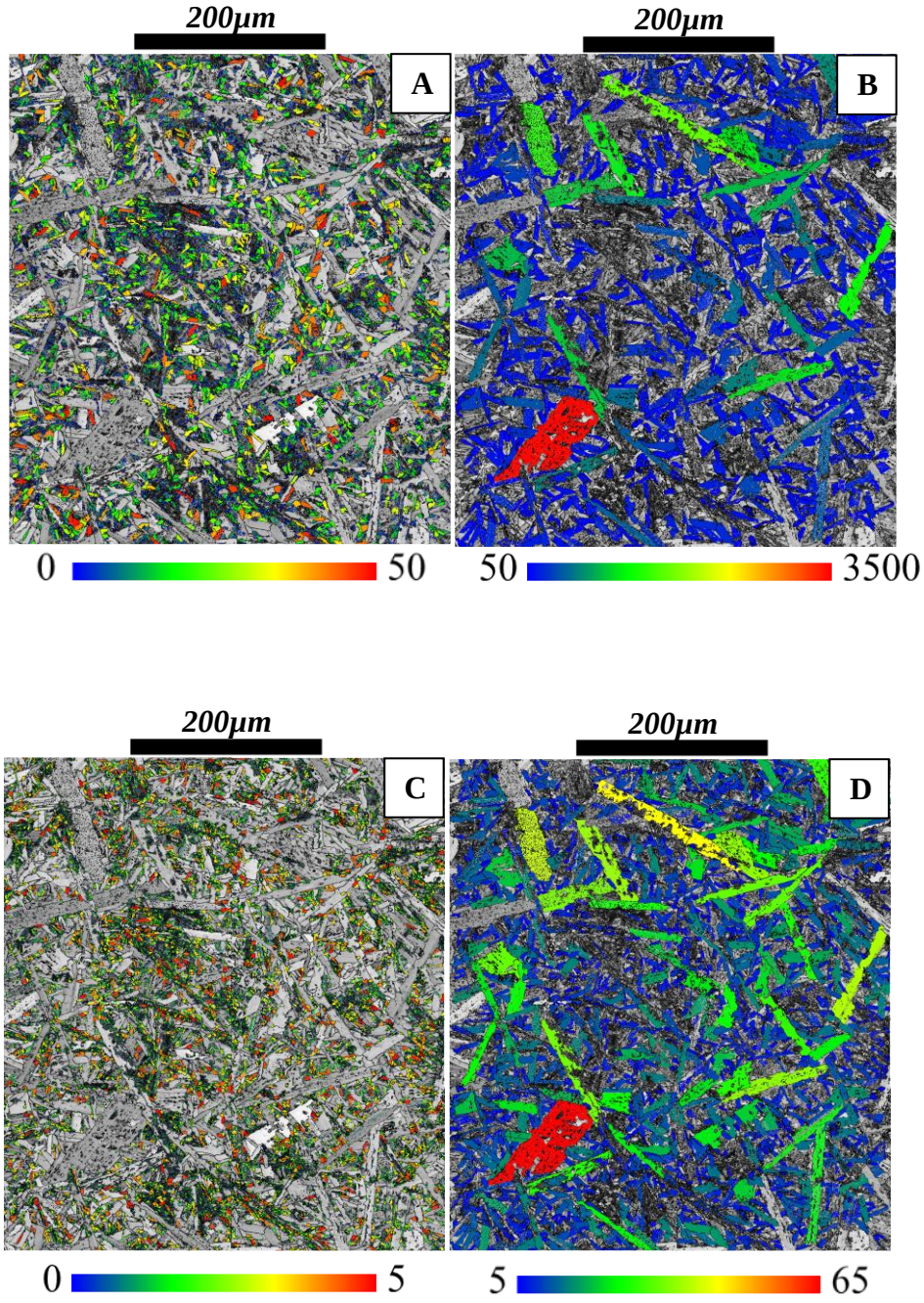

Figure 5.8: *(**a & b**) Grain Area maps for the major Ti_2AlC phase.* ***(a)*** *The grain areas up to 50µm^2* ***(b)*** *The grains that have an area of 50µm^2 and more.* ***(c & d)*** *Maps showing the Grain Diameter for the major Ti_2AlC phase.* ***(c)*** *The grains with a diameter up to 5µm,* ***(d)*** *The grains with a diameter greater than 5µm.*

Figure 5.9 shows the grain size analysis for the Ti_3SiC_2 MAX phase. As previously stated earlier in this section, when the primary Ti_3SiC_2 phase is compared to the Ti_2AlC MAX phase, it is evident that the grain area and diameter is substantially smaller. The largest grain in diameter recorded for the Ti_3SiC_2 phase was about 15µm, compared to about 65µm for Ti_2AlC. Unlike the Ti_2AlC material, the grain sizes and diameter of the secondary phase, TiC, are not significantly smaller than the primary Ti_3SiC_2 phase, with the largest TiC grains measuring about 11µm. As seen in the Ti_2AlC MAX phase, the aspect ratios of both major phases are greater than 1, indicating that the phases are generally elongated in shape. In *Figure 5.10* the maps show the grain area and the grain diameter of the primary Ti_3SiC_2 phase. Note how the grain shapes of all the grains, and in particular the primary Ti_3SiC_2 phase are generally quite different to the Ti_2AlC phase, with a very small amount of very elongated, lamellar grains.

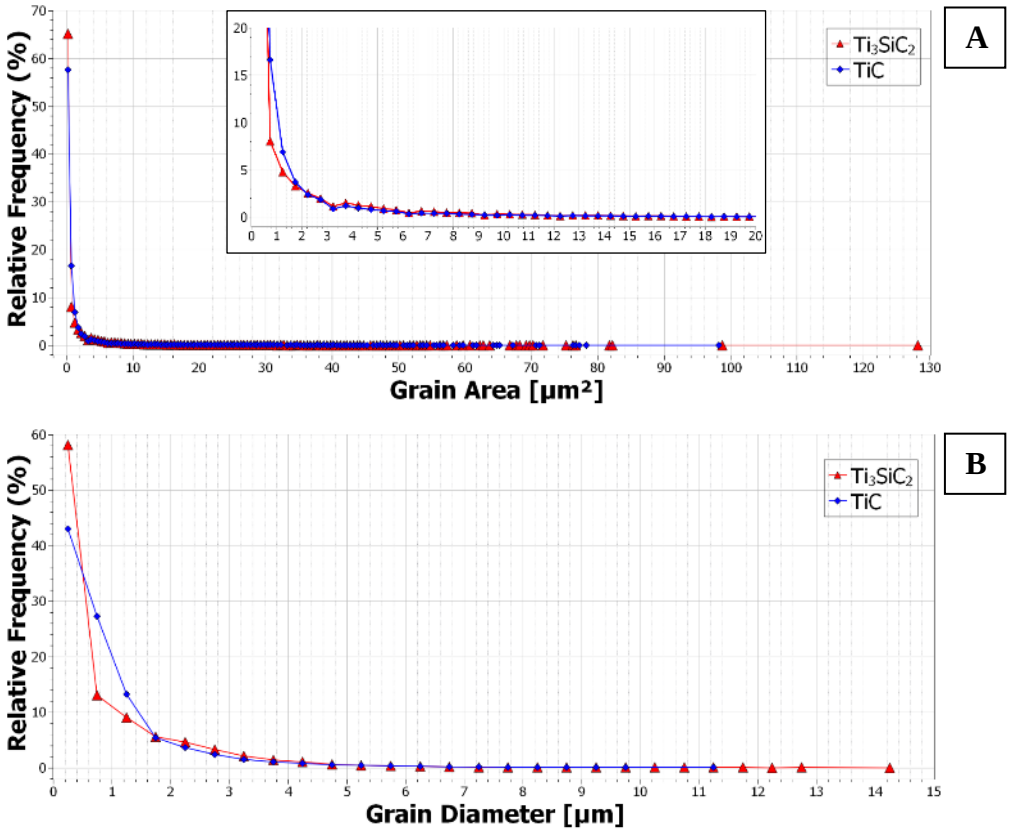

Figure 5.9i: *Grain Size Analysis graphs for all phases of the Ti_3SiC_2 MAX phase material:* ***(a)*** *Grain Area,* ***(b)*** *Grain Diameter*

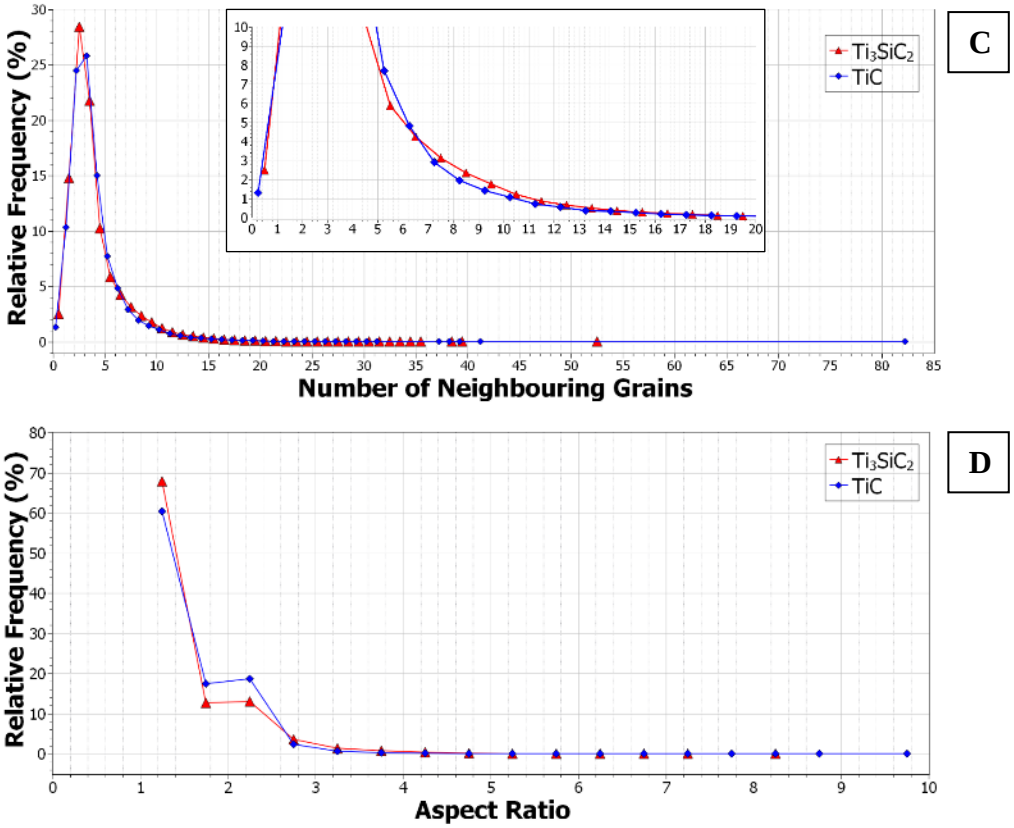

Figure 5.9ii: *Grain Size Analysis graphs for all phases of the Ti_3SiC_2 MAX phase material:* ***(c)*** *Number of Neighbouring Grains and* ***(d)*** *Aspect Ratio.*

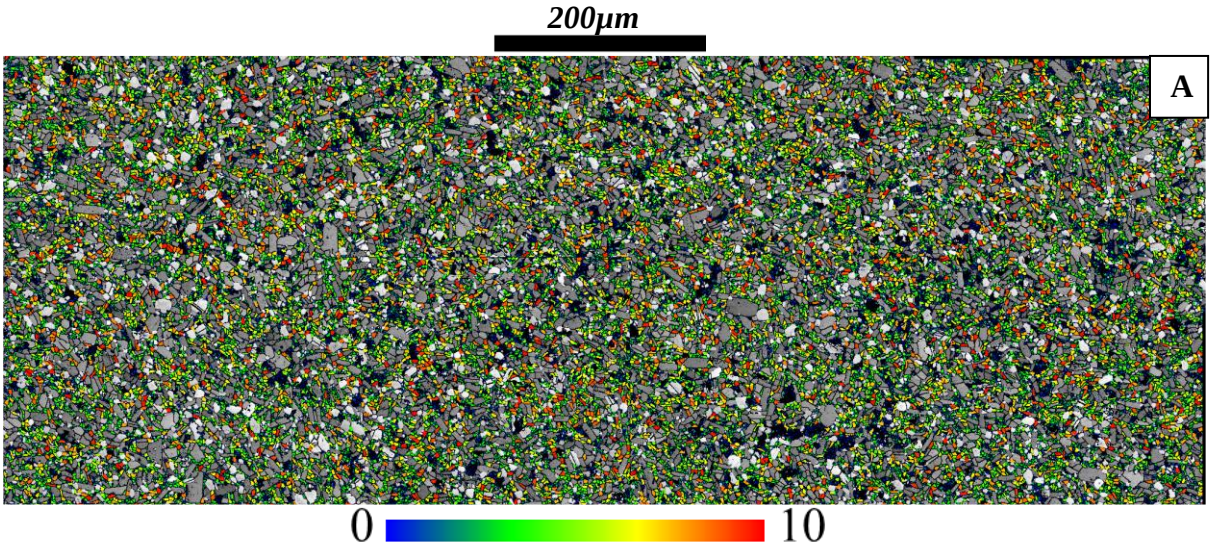

Figure 5.10i: (a & b) *Ti_3SiC_2 Maps showing the grain area for the grains of the Ti_3SiC_2 phase* ***(a)*** *The Ti_3SiC_2 grains with a grain area up to 10µm^2*

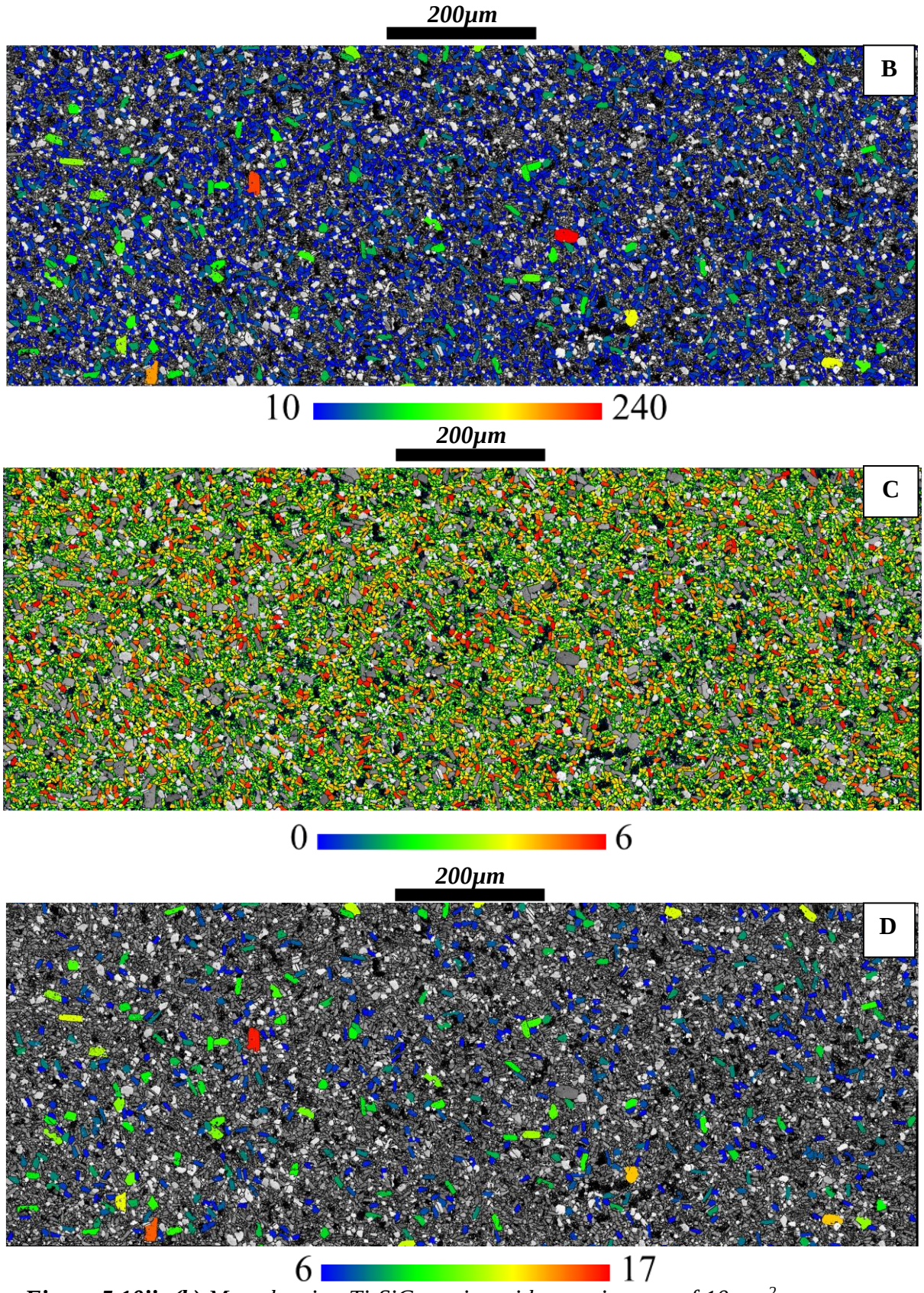

Figure 5.10ii: (b) *Map showing Ti_3SiC_2 grains with a grain area of 10 µm^2 or greater* ***(c & d)*** *EBSD grain analysis maps of Ti_3SiC_2 MAX phase showing the grain diameter for the Ti_3SiC_2 phase., **(c)** grains with a diameter up to 6µm, **(d)** map of those grains with a diameter greater than 6µm.*

5.5.2 Detailed Phase, Orientation and Grain Boundary Characterisations

Several maps were created using the data collected by the EBSD software, some of which are presented here. *Figures 5.11 and 5.12* show the EBSD maps taken of the Ti_2AlC AR sample while *Figures 5.13 and 5.14* show the maps for the Ti_3SiC_2 AR sample.

Figure 5.11a shows the band contrast map of the Ti_2AlC MAX phase. When comparing this map to the electron images discussed earlier in this chapter, it is evident that the microstructure appears more complex, with the large elongated lamellar grains being identified as possessing numerous subgrains within them, validating what was found in the previous section on the grain size analysis of the materials. *Figure 5.11b* shows a map of the phases that were used to map the EBSD data. The phases that were used were Ti_2AlC, TiAl and Al_2O_3. The volume fractions of these phases that were used for the EBSD analysis can be found in *Table 5.4*. Due to the relatively high amount of nonindexed areas, the phase fractions do not directly correlate to the phases identified using ImageJ, although if these nonindexed areas are assumed to be porosity caused by the deformation of the samples during production or a potential 4^{th} phase of similar image morphology to that of Ti_2AlC then the fractions are not too far away from what was measured using ImageJ. From the phase map, the Ti_2AlC phase is seen to be by far the most dominant phase within the microstructure, however there are pockets of the phase identified as TiAl appearing, as expected, in between the larger Ti_2AlC grains and in some case within the Ti_2AlC grains. The final secondary phase, in this case identified as Al_2O_3, is found to be located within the darker areas of the band contrast, corresponding with the dark phases identified in the SEM images discussed earlier in Section 5.2. This phase, like the dark phases identified earlier, is scattered randomly throughout the microstructure. As previously stated in this section, the relatively high amount of unindexed areas could suggest either a phase that has not been identified and/or the presence of some porosity. The IPF map in *Figure 5.11c* shows the measured orientation and the IPF colour keys. The map allows a greater understanding of the preferred orientation of each grain and phase. From the map, it appears that the grains have a largely random texture, something which is further proved when plotting the orientations in the colour key of the IPF. The grain boundaries were also identified by 4 separate colours in *Figure 5.12*, with the low angle grain boundaries (LAGBs) being between 2 and 10^o and identified by red. The medium grain boundaries (MAGBs) are represented in blue for the 10-20^o and green for 20-40^o, while yellow was used to signify the high angle grain boundaries

(HAGBs) >40°. The histograms in *Figure 5.13 and 5.14* show the data for the grain boundaries between the different phases. From this, it can be seen that the misorientation angles of the boundaries between the Ti_2AlC grains are constant across the graph, indicating that the orientations are distributed uniformly throughout the microstructure. The TiAl-TiAl grain boundaries were recorded as being of a non-random distribution, with higher amounts of low angle grain boundaries, with the Ti_2AlC-TiAl grain boundaries having a peak at 10°-20° but generally having a behaviour similar to the Ti_2AlC-Ti_2AlC grain boundaries, with the misorientations having a uniform distribution throughout the microstructure within ± 5°. The Ti_2AlC-Al_2O_3 grain boundaries had a substantial number of medium misorientation angles, with the peaks at 30°-40°. The Al_2O_3-Al_2O_3 and Al_2O_3-TiAl grain boundaries behave in a similar manner, both generally possessing high angle grain boundaries, although the distribution is close to the random (Mackenzie) profile.

Table 5.4: *Phase Volume Fractions measured by EBSD for the Ti_2AlC MAX phase*

Phase	Volume Fraction(%)	Symmetry
Ti_2AlC	70	6/mmm
TiAl	4.3	4/mmm
Al_2O_3	1.6	-3ml
Nonindexed	24.1	N/A

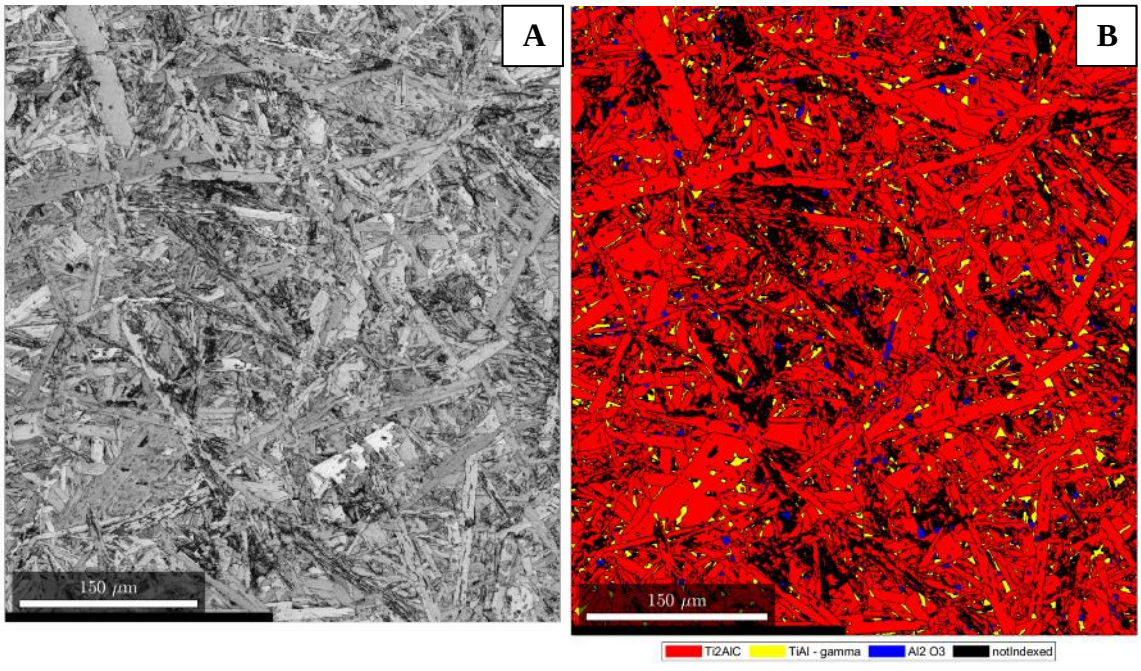

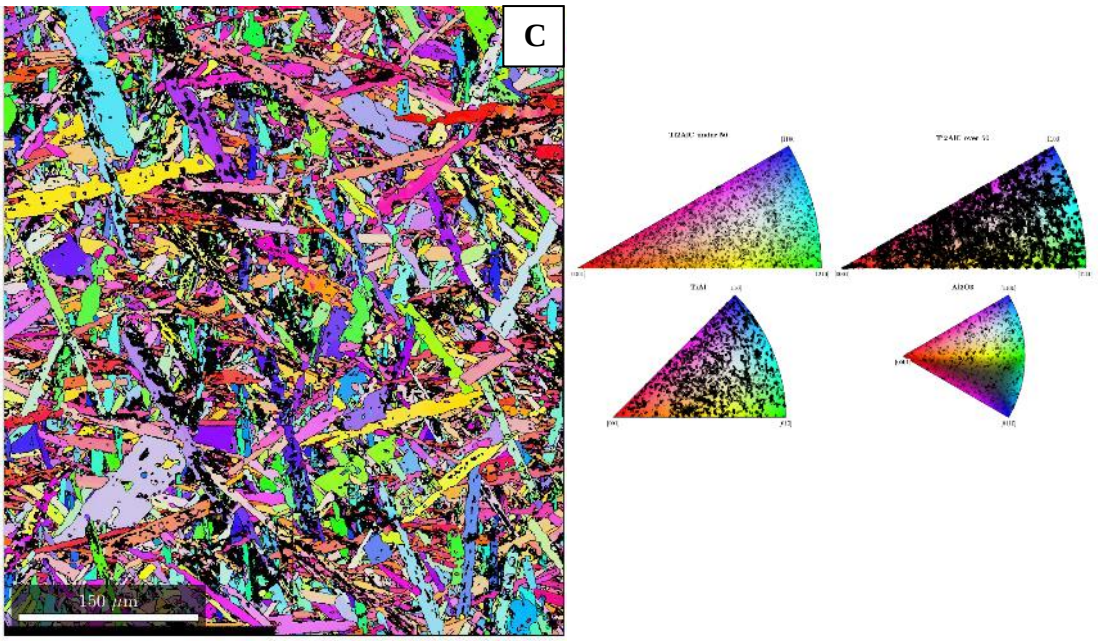

Figure 5.11: *EBSD Maps taken of the Ti_2AlC control, AR sample.* ***a)*** *Band Contrast,* ***b)*** *Phase Map,* ***c)*** *IPF-Y Orientation Map, with colour key (The two Ti_2AlC colour keys are for a grain area of under or above 50μm^2)*

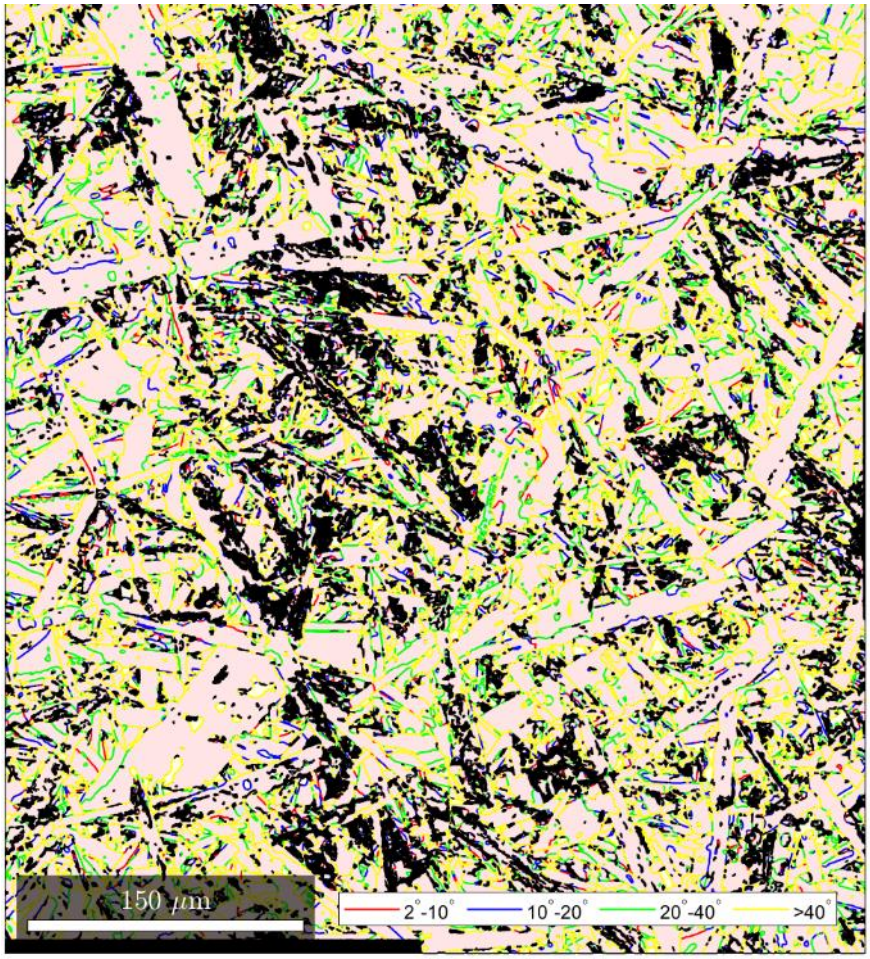

Figure 5.12: *Grain Boundaries and Grain Boundary angle Map for all phases*

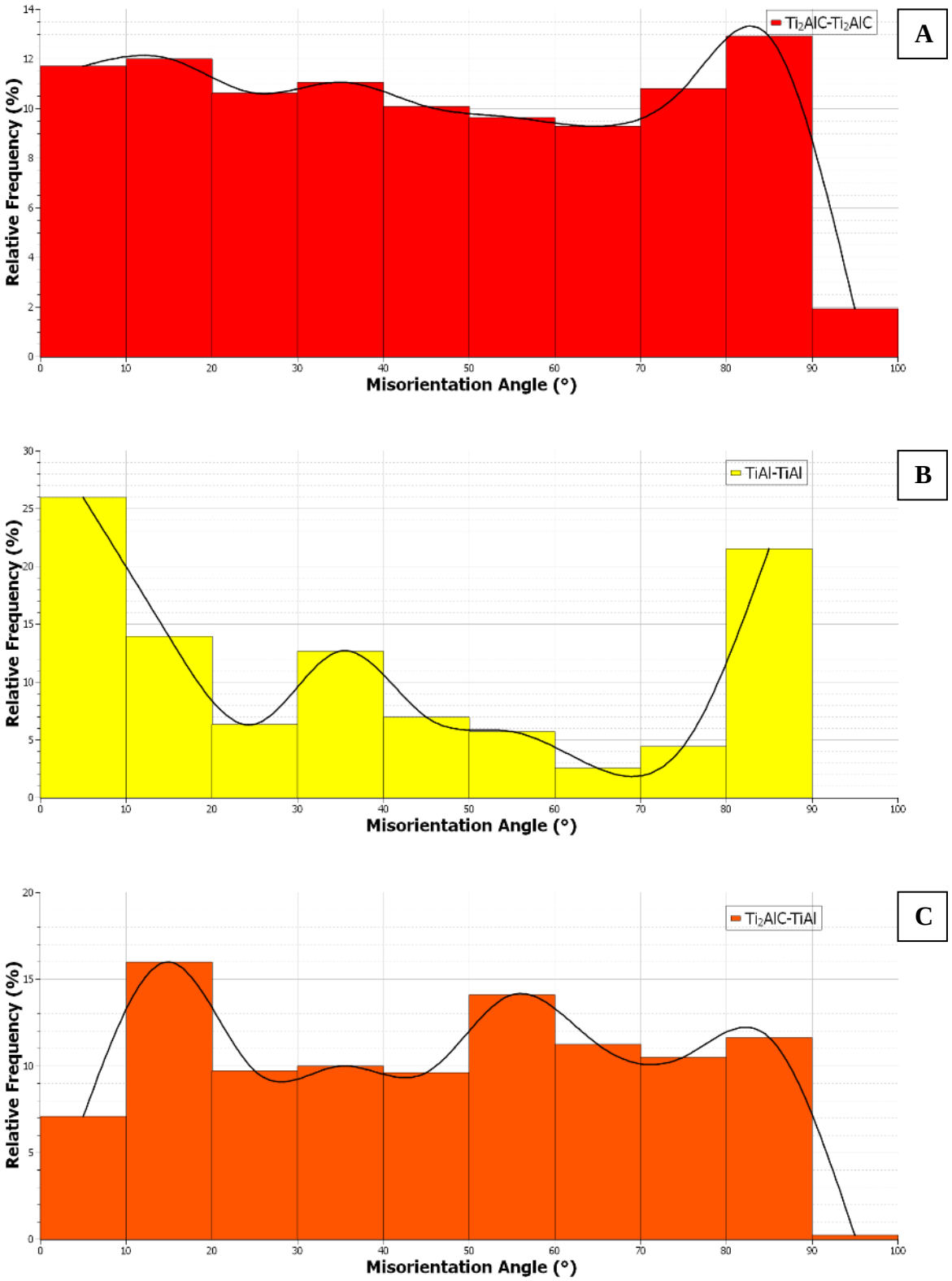

Figure 5.13: *Histograms showing the spread of the grain boundary angles from phase to phase.* ***(a)*** *Ti_2AlC-Ti_2AlC,* ***(b)*** *TiAl-TiAl,* ***(c)*** *Ti_2AlC-TiAl*

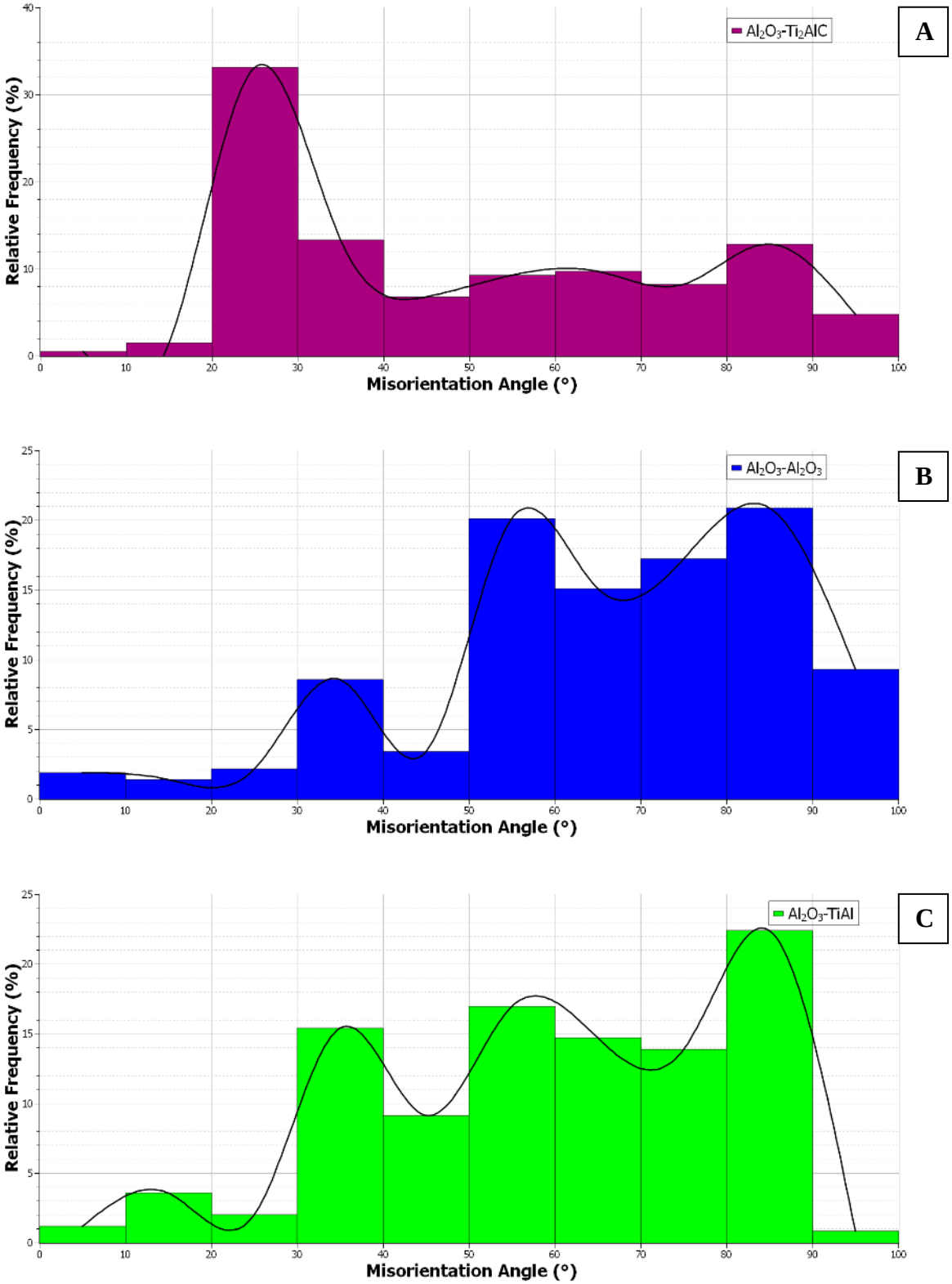

Figure 5.14: *Histograms showing the spread of the grain boundary angles from phase to phase.* ***(a)*** *Al_2O_3-Ti_2AlC,* ***(b)*** *Al_2O_3-Al_2O_3,* ***(c)*** *Al_2O_3-TiAl*

The Ti_3SiC_2 EBSD data can be found in *Figures 5.15 and 5.16.* From the band contrast map, their appears, as was proposed in Section 5.2, two distinct major phases. In this case, a dark phase and a bright phase. The EBSD phase map has been used to characterise these two phases as Ti_3SiC_2 and TiC respectively. The other phases proposed when using ImageJ appeared to take up such a small fraction that EBSD phase classification would have been difficult. In general, the major Ti_3SiC_2 phase is seen to form randomly around the microstructure, although there are small pockets where there are higher concentrations of the brighter, TiC phase. Whereas it was difficult to index some areas of the Ti_2AlC MAX phase, the Ti_3SiC_2 MAX phase is generally well indexed, although there are several areas that have not been indexed. In a similar manner to the Ti_2AlC MAX phase, these areas could either be phases that have not been identified and/or areas of porosity. Due to the high amounts of porosity previously identified using the electron image, it is more likely that these areas are porosity. The IPF map in *Figure 5.15c* shows that, like the Ti_2AlC MAX phase material, the orientation of both phases is largely random in the AR sample, as proved by the IPF colour key in *Figure 5.15c*. The grain boundaries of the Ti_3SiC_2 MAX phase were also split into the same parameters as Ti_2AlC, in that LAGBs were 2-10^o, MAGBs were 10-20^o and 20-40^o and HAGBs were >40^o. The map of the grain boundaries can be found in *Figure 5.16* while the histograms of the grain boundaries between the phases can be found in *Figures 5.17 and 5.18.* In a similar manner to the Ti_2AlC-Ti_2AlC grain boundaries, the primary Ti_3SiC_2 grains had a distribution of grain boundary misorientation angles that were constant throughout the microstructure, where no one type of grain boundary angle was seen to be dominant. The TiC-TiC grain boundaries were found to be higher angle in nature, with the highest proportion of grains falling on or around a grain boundary angle of 60^o. The misorientation angles of the Ti_3SiC_2-TiC grain boundaries appear to have a random, Mackenzie profile.

Table 5.5: *Phase Volume Fractions measured by EBSD for the Ti_2SiC_2 MAX phase*

Phase	Volume Fraction(%)	Symmetry
Ti_3SiC_2	62	6/mmm
TiC	15	m-3m
Nonindexed	23	N/A

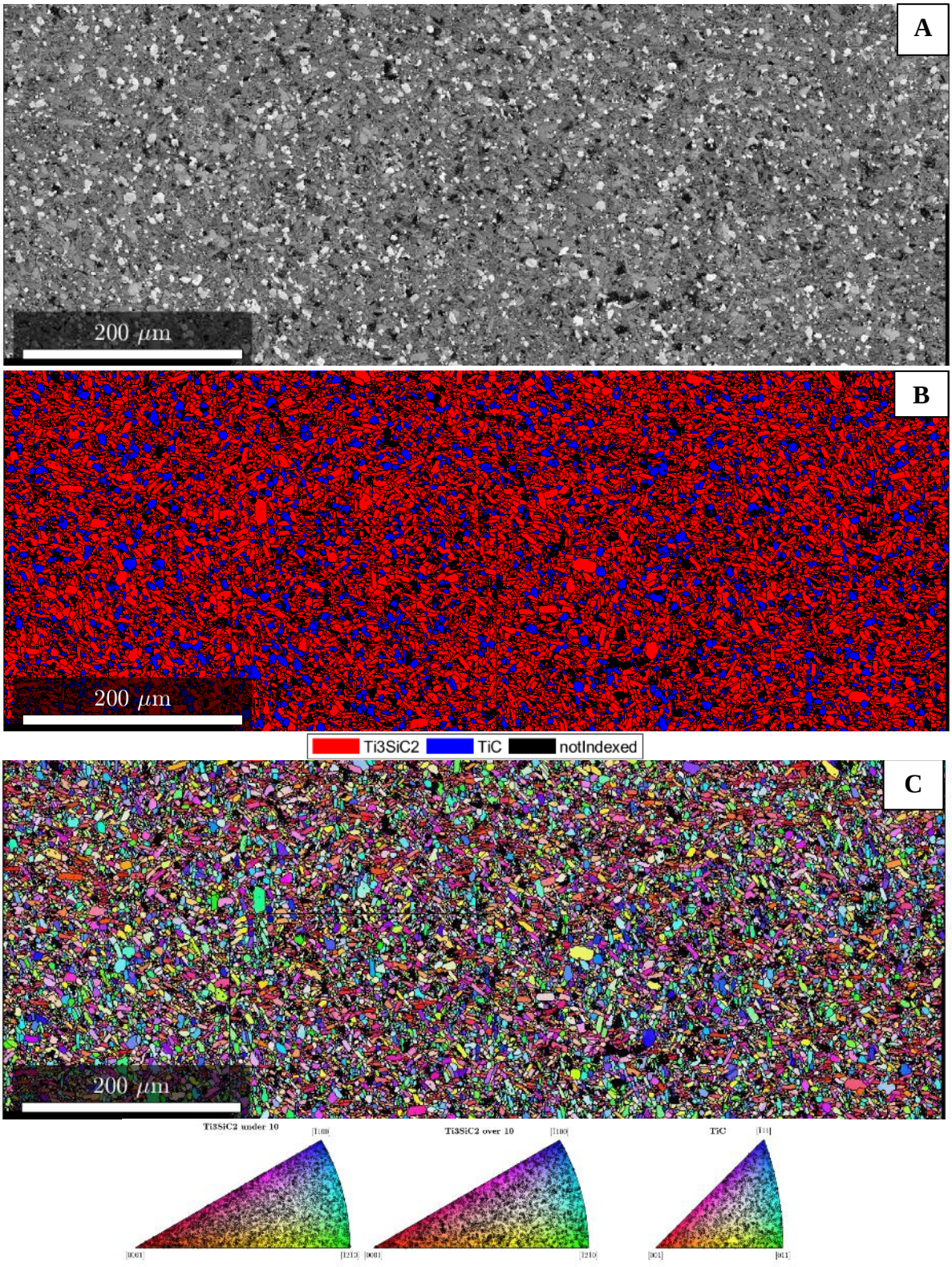

Figure 5.15: *EBSD Maps taken of the Ti_2 control, AR sample.* ***a)*** *Band Contrast,* ***b)*** *Phase Map,* ***c)*** *IPF-Y Orientation Map, with colour keys (The two Ti_2AlC colour keys are for a grain area of under or above 50μm^2)*

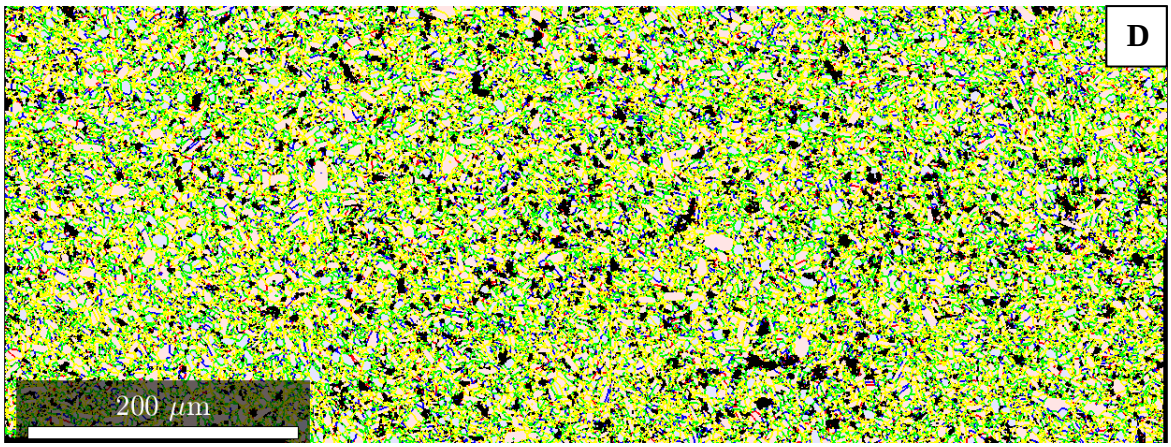

Figure 5.16: *Grain Boundary Angle map for all phases and the histograms showing the spread of the grain boundary angles from phase to phase.*

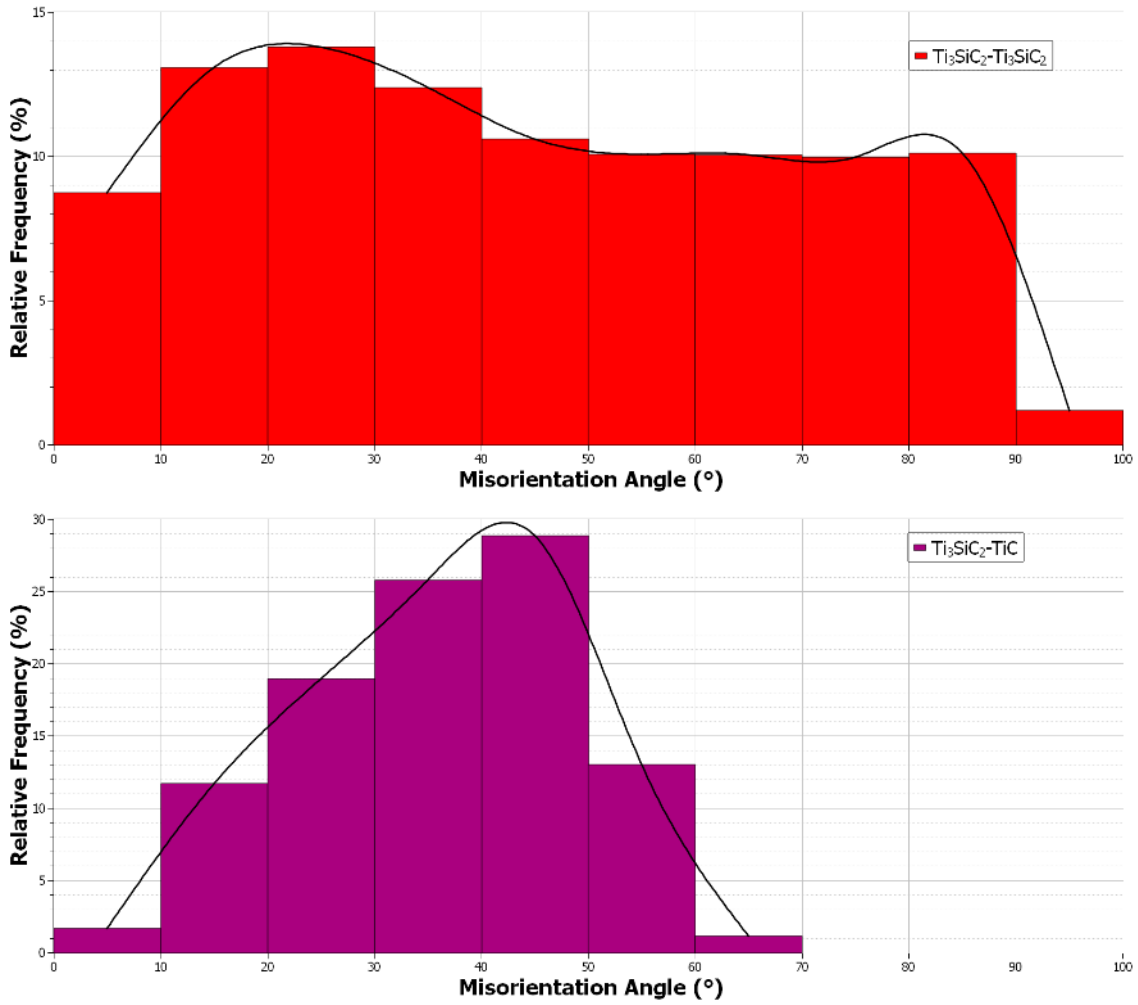

Figure 5.17: *Histograms showing the spread of the grain boundary angles from phase to phase for* ***(a)*** *Ti_3SiC_2-Ti_3SiC_2,* ***(b)*** *Ti_3SiC_2-TiC*

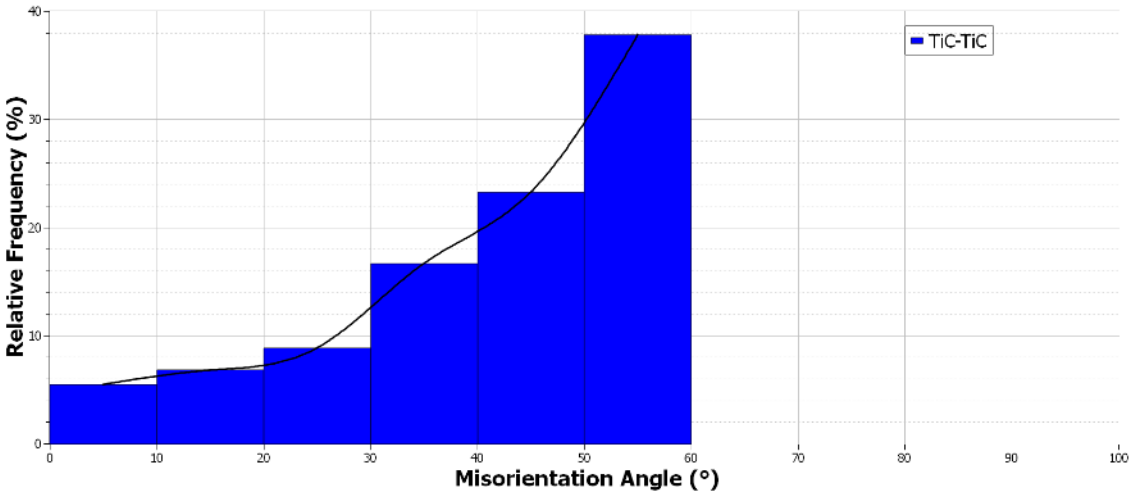

Figure 5.18: *Histogram showing the spread of the grain boundary angles between grains of the TiC phase.*

5.6 Summary and Conclusions

In this chapter, the microstructure of both Ti_2AlC and Ti_3SiC_2 have been characterised and their grain size and shape and EBSD data were analysed. The SEM images collected for both materials showed an obvious difference in microstructure, with only a few important similarities. The grain size of the largest grains found in Ti_2AlC were found to be several times larger than the largest grains found in Ti_3SiC_2, although the shape of these grains was found to be relatively similar in being an elongated lamellar. Numerous smaller grains and subgrains were also found in both MAX phases, with these grains belonging to both the major Ti_2AlC and Ti_3SiC_2 phases, and also the secondary phases identified in both materials. The presence of multiple minor secondary phases in both materials agrees with previous studies of similar material.

The EDS data showed that, as was expected, the Ti_2AlC and Ti_3SiC_2 MAX phases are rich in their constituent MAX elements (M=Ti, A=Al or Si, and X=C). Of note in the Ti_2AlC sample were the areas high in Ti and Al between the large grains, an area that could otherwise be described as the matrix. It was assumed that this area would be a TiAl intermetallic phase. The spectrum taken on this phase showed that it had a chemical composition of approximately 47wt% Ti, 50wt% Al and 3.3wt% C, which further led credence to this assumption. Due to their dominance of the microstructure the large, elongated phases were assumed to be the primary Ti_2AlC phase, something which was confirmed by the spectra taken on these grains,

which had a composition of approximately 73wt% Ti, 15wt% Al and 12% C. The other phase was found to possess high amounts of Al and potentially O. The overall chemical composition of Ti_2AlC was recorded as approximately 68wt% Ti, 22wt% Al and 10wt% C. The overall chemical composition of the Ti_3SiC_2 MAX phase was recorded as 70.9wt% Ti, 13.7wt% Si and 15.4wt% C, which is in general agreement with the structure of the 312 MAX phases, which contain more M and X layers than A layers. The primary Ti_3SiC_2 phase was recorded as having a similar composition to the overall microstructure, with approximate make up of 72wt% Ti, 13wt% Si and 15wt% C. The minor secondary phase, later identified as TiC, was found to compose of negligible amounts of Si and higher amounts of Ti and C. The spectrum taken on one grain of this phase had a composition of 10wt% Ti and 89wt% C.

XRD spectra for both MAX phases were analysed to help establish the phases present. The Ti_2AlC MAX phase was determined by the spectra to contain at least 3 potential phases, with some peaks not belonging to any of the identified phases. The chemical compositions found using EDS and the micrograph analysis using ImageJ could further confirm that the phases not identified have a similar chemical structure to the major phases previously identified in this study, namely the primary Ti_2AlC phase and the secondary phases TiAl and Al_2O_3. Ti_3AlC_2 was proposed as one of the phases that was similar in both composition and structure to one of the previously identified phases, namely Ti_2AlC. With this phase included, the composition of the Ti_2AlC MAX phase was recorded as 50% Ti_2AlC, 35% Ti_3AlC_2, 14% TiAl and 1% Al_2O_3. The peaks of the Ti_3SiC_2 MAX phase were assigned to more phases than the Ti_2AlC alloy, with Ti_3SiC_2 and TiC being, as expected, the predominant phases. Ti_3SiC_2 and TiC were recorded as constituting 80wt% and 20wt% of the microstructure respectively. Despite this, there were a few peaks that were left unassigned, potentially belonging to the minor phases that were identified using the ImageJ and EDS software.

As mentioned previously in this section and in Section 5.5.1, the grain sizes of the Ti_2AlC and Ti_3SiC_2 MAX phases was the one major difference in their appearance. The large grains of the Ti_2AlC MAX phase were identified as Ti_2AlC and were found to be 4 times larger than the largest Ti_3SiC_2 grains in the Ti_3SiC_2 MAX phase alloy. The grain shapes of the most prevalent phases are relatively similar, being roughly elongated and lamellar in nature. Due to the smaller grain size of the Ti_3SiC_2 MAX phase, this material would be expected to have a higher ultimate

compressive strength than the Ti_2AlC material. In materials with smaller grains, these grains can behave as obstacles to the dislocation movement. This, in turn, can cause more strain hardening, meaning that smaller grain materials such as Ti_3SiC_2 have more strength than larger grain materials. In materials with large grains like Ti_2AlC a dislocation can travel further without being stopped by a grain boundary, indicating the potential for extensive plastic flow and lower ultimate compressive strengths. This type of strengthening is known as Hall-Petch strengthening.

The reasoning for the large difference in grain size is most likely due to differences in the processing route of both MAX phases. The final grain size of a dense ceramic is governed by many processing variables, with the starting powder size and sintering time and temperature being the most important [127]. Grain size increases with increasing temperature due to the enhancement of diffusion rate with increasing temperature, leading to the assumption that Ti_2AlC was sintered at higher temperature and for a longer period than the Ti_3SiC_2 material [98]. The starting powder size was also likely to have been much larger in the case of the Ti_2AlC material as opposed to the Ti_3SiC_2 material.

The EBSD analysis of the Ti_2AlC MAX phase alloy showed that the phases Ti_2AlC, TiAl and Al_2O_3 were all easily indexed within the microstructure. The nonindexed areas of black in the microstructure could potentially be areas of another phase or porosity. The same is mostly true for the Ti_3SiC_2 MAX phase, which is well indexed, except a few areas that seem to be porosity rather than another phase. Both microstructures appear random in texture and orientation distribution, as proven by the IPF colour keys for the both materials IPF maps. With regards to the grain boundaries, the boundaries between the major phases, namely between Ti_2AlC and Ti_2AlC and between Ti_3SiC_2 and Ti_3SiC_2 appear to behave quite similar in that the misorientation angles are constant across the graph, indicating that the orientations are distributed evenly throughout the microstructure. In both MAX phases, the grain boundaries between the primary phase and the minor phases (i.e. Ti_2AlC-TiAl), and also between the minor phases (i.e. TiC-TiC) either have a prevalence towards a specific type of grain boundary or have a random, Mackenzie type profile. LAGBs are characterised as consisting of an array of dislocations, with their structure being a function of the misorientation.

Chapter 6 - The Effect of Deformation Temperature and Strain Rate on the Mechanical Behaviour of the MAX phases

6.1 Introduction

In this chapter, the results of high temperature mechanical testing of both MAX phase materials used in the current project are presented. The high temperature mechanical testing of these materials was conducted using the Gleeble 3500 Thermomechanical Simulator, a machine discussed in more depth in Chapter 4.2. The results of the high temperature mechanical tests and the high temperature quench tests are presented in this chapter, while also briefly discussing the ramifications these results could have on the microstructures of the MAX phases, something that will be explored in greater depth in Chapter 7.

6.2 Compression Testing Conditions and Parameters

Various parameters were used to test the MAX phases response to high temperature mechanical testing. The samples were tested at 3 different high temperatures, 1000°C, 1100°C and 1200°C, as well as a room temperature (RT) test in the Gleeble for comparison purposes. The heating rate of 5°C/s was used for all high temperature tests. 5 different strain rates were utilised to test any variation in mechanical response at the different temperatures. One example of this type of heating cycle can be found in *Figure 6.1*. The samples were also photographed following each high temperature compression test to show the effect the testing conditions had on the 10 × 15mm cylindrical samples. Each sample was given a code following a test, the details of the coding system can be found in *Table 6.1*.

Table 6.1: *Coding System for High Temperature Mechanical Testing Samples and High Temperature Quenching Samples*

Sample Coding System	Example	Temperature	Strain Rate/ Compressive Load Stress
TXX-SR *XX=Temperature(°C)* *SR=Strain Rate*	T11-3	1100°C	1×10^{-3}/s
QXX-SY *XX=Temperature(°C)* *Y=Compressive Load Stress(MPa)*	Q12-S150	1200°C	150 MPa

The MAX phases were also subjected to quench tests in air to determine their performance after thermal shock. The samples were heated to either 1000°C or 1200°C, held at these temperatures for 2 minutes before being quenched at a cooling rate of 60°C/s under a compressive load stress. The samples were then tested under compression at room temperature to determine if quenching the materials had had a detrimental effect on their mechanical properties. Examples of the heating and cooling regimes can be found in Section 6.4. The coding system for the quenched samples can be found in *Table 6.1*.

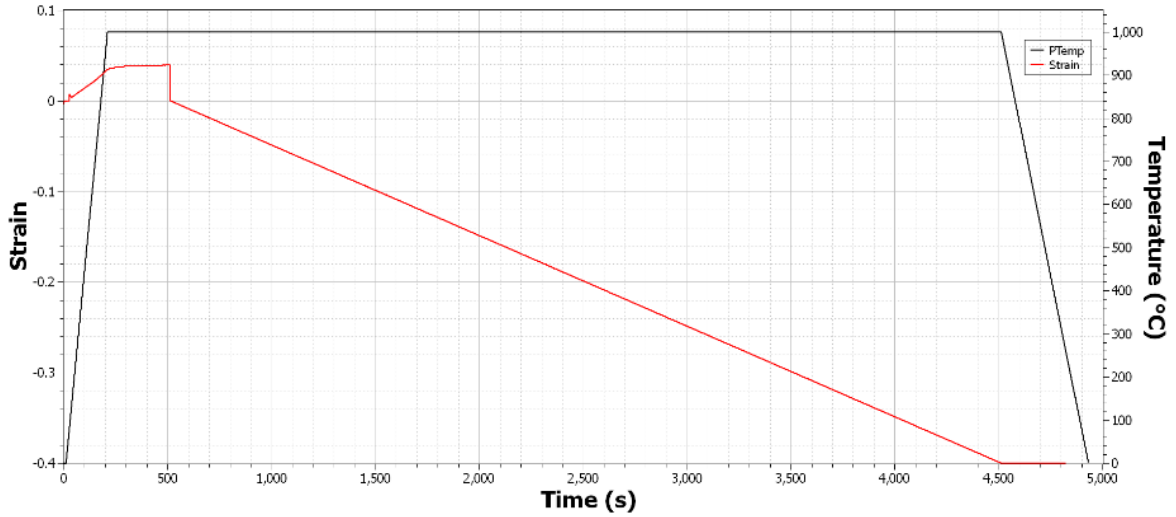

Figure 6.1: *A typical high temperature mechanical test regime, showing the initial heating rate to the highest temperature, at which the sample is held for 5 mins to attain equilibrium before the material is strained at a certain strain rate. In the case of this test, the material is subjected to a strain of 0.4 at a strain rate of 1×10^{-4}/s at a temperature of 1000°C.*

6.3 High Temperature Mechanical Testing results

Sample Code	Example	Temperature	Strain Rate
TRT-S	T11-3	1100	1×10^{-3}/s

6.3.1 Ti_2AlC MAX phase

The current section will outline the results of the high temperature mechanical testing of both MAX phases. The performance of Ti_2AlC at the different temperatures has been set out in *Figures 6.2 - 6.9*, while the performance of the Ti_3SiC_2 MAX phase under the same temperatures can be found in *Figures 6.10 - 6.17*.

6.3.1.1 Ti_2AlC MAX phase Compression at Room Temperature

The stress-strain curves for the Ti_2AlC sample tested at room temperature can be found in *Figure 6.2*. As shown in the figure, the two samples were strained to -0.1 at the slowest strain rates; 1×10^{-3}/s and 1×10^{-4}/s, with both stress-strain curves showing great similarity. The peak compressive stress is recorded as 500 MPa, while the strain to failure was approximately -0.04 for both samples. In terms of both strain and time, the samples failed very abruptly upon the application of the mechanical load. The curves do not show any plasticity, with both samples rupturing straight after the yield point. The stress drop recorded as the sample failed could be explained by the sampling rate of the test rather than any evidence of ductility. The other mechanical properties of the samples at room temperature can be found in *Table 6.2*. The Young's Modulus of both samples were 23±1 GPa, while the yield stresses were similar to the UCS of both samples.

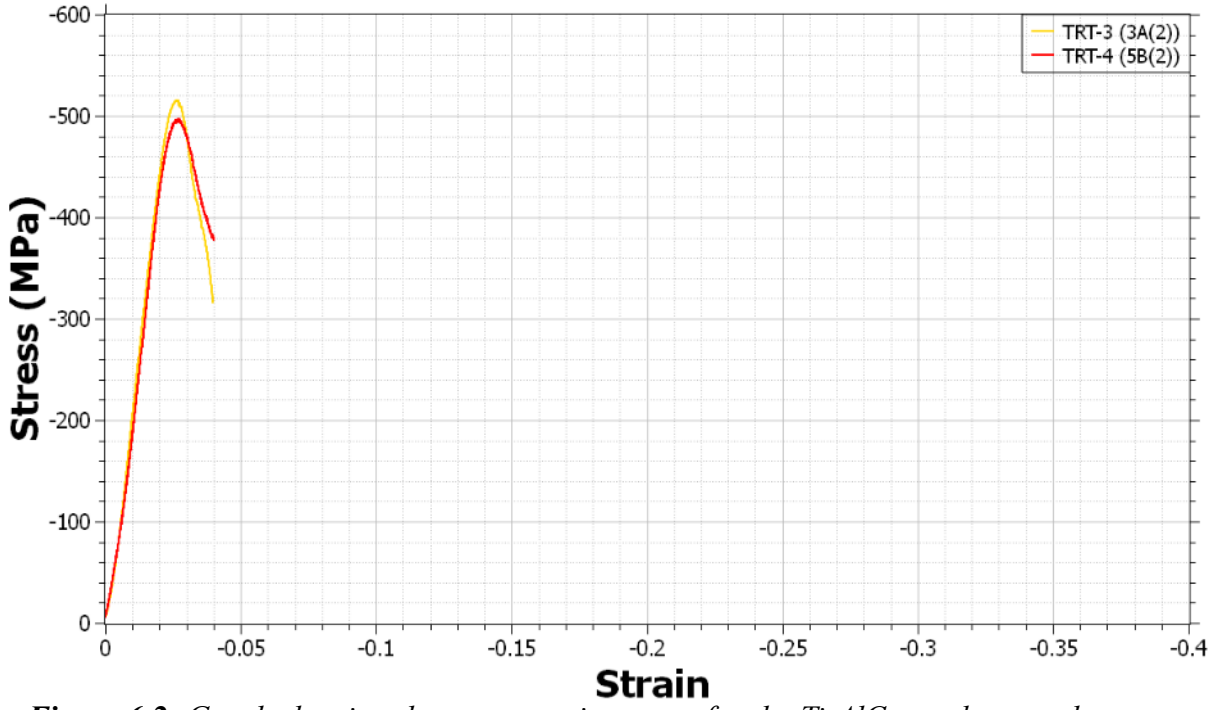

Figure 6.2: *Graph showing the stress-strain curves for the Ti_2AlC samples tested at room temperature and under a strain rate of 1×10^{-3}/s and 1×10^{-4}/s*

Table 6.2: *Mechanical Properties of Ti_2AlC samples tested at 1000°C and under strain rates of 1×10^{-3}/s and 1×10^{-4}/s*

Test	Ultimate Comp Stress (MPa)	Young's Modulus (GPa)	Yield Stress (MPa) (0.02 Proof Stress)	Compression (%)
TRT-3	-515.65	23.26	-513.13	-3.97
TRT-4	-497.7	22.08	-490.87	-4.00

Following the room temperature compression tests, both samples were removed from the Gleeble chamber and photographed. These images can be found in *Figure 6.3* and show the appearance of the samples following failure. The brittle nature of material failure is immediately evident in these images, with numerous cracks noticeable throughout both samples and, in the case of the TRT-3 sample, breaking into numerous separate pieces. The direction of the main crack in the TRT-4 sample is approximately ~45° to the compression axis, as highlighted by the red ellipse in *Figure 6.3b*. If the test had been carried out to a higher strain of, for example, 0.4, then both samples would likely have been crushed even further and split into several more pieces, as has been evidenced in the literature [99]. The brittleness of ceramic materials at room temperature is caused by their general low resistance against crack propagation. These observations are evidence that at room temperatures the Ti_2AlC MAX phase samples failed in a very brittle manner, something which has been noted consistently in previous studies on the mechanical properties of the Ti_2AlC MAX phase [1].

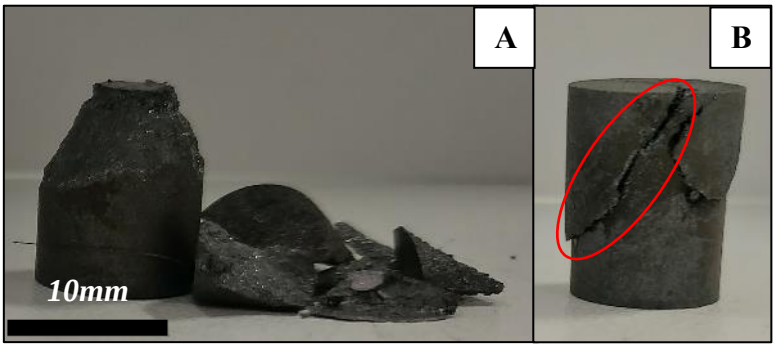

Figure 6.3: *Pictures of the Ti_2AlC samples following their room temperature compression testing using the Gleeble.* ***(a)*** *TRT-3,* ***(b)*** *TRT-4, with the crack ~45° to the loading direction highlighted with red ellipse*

6.3.1.2: Ti_2AlC MAX phase compression at 900°C

Figure 6.4 shows the stress-strain curves for the T_2AlC samples tested at 900°C. The mechanical properties of the tests can be found in *Table 6.3*. Similar to the testing undertaken for the samples at 1000°C, two strain rates were tested; 1×10^{-3}/s and 1×10^{-4}/s. The peak compressive strengths recorded are within 50 MPa for both samples, with the T09-3 sample having the slightly higher compressive strength of -355.86 MPa. The compressive strain to failure was recorded as ~6% for both samples. The behaviour of the samples is analogous to that of the samples tested at room temperature in that the samples both failed abruptly after reaching their yield points, not showing any plasticity thereafter. The Young's Modulus of both samples were significantly lower than those recorded for the samples tested at room

temperature at ~8 and 9 GPa respectively for the T09-3 and T09-4 samples. The yield stresses were very close to the UCS of both samples.

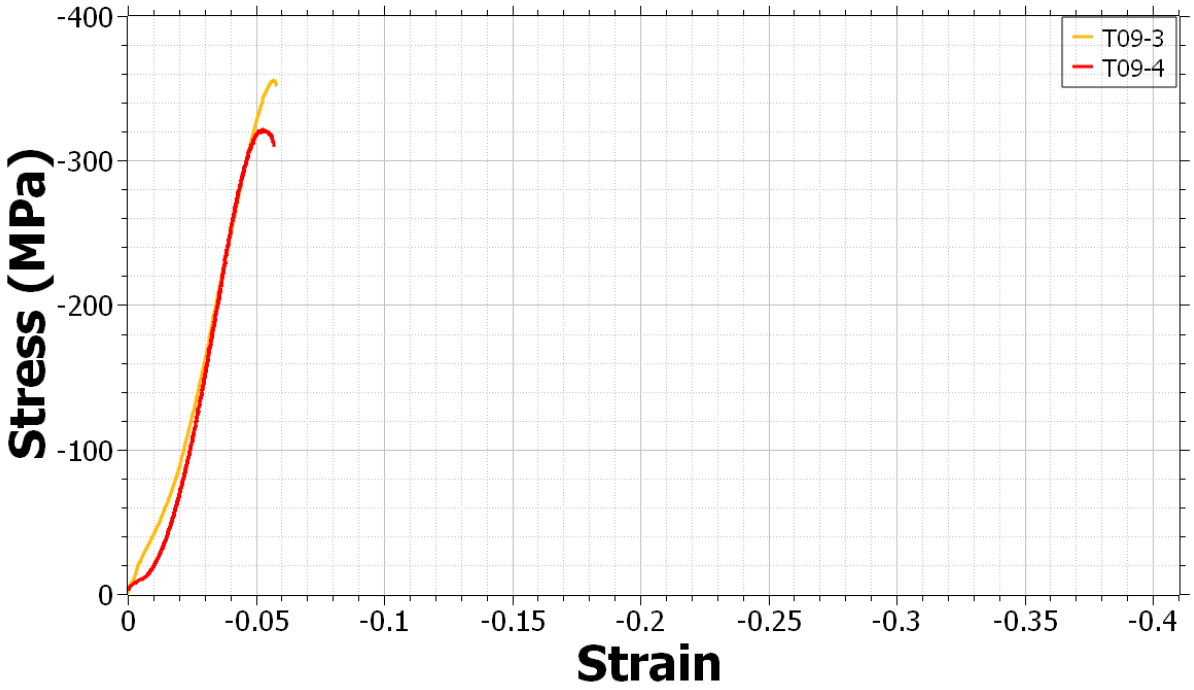

Figure 6.4: *Graph showing the stress-strain curves for the Ti_2AlC samples tested at 900°C and under a strain rate of 1×10^{-3}/s and 1×10^{-4}/s*

Table 6.3: *Mechanical Properties of Ti_2AlC samples tested at 900°C and under strain rates of 1×10^{-3}/s and 1×10^{-4}/s*

Test	Ultimate Comp Stress (MPa)	Young's Modulus (GPa)	Yield Stress (MPa) (0.02 Proof Stress)	Compression (%)
T09-3	-355.86	7.784	-352	-5.81
T09-4	-321.84	8.86	-318	-5.71

The images of the samples upon the completion of the test can be found in *Figure 6.5*. Like the samples tested at room temperature, the brittle nature of failure was immediately evident for both samples, with a large crack that is approximately 45° to the compression axis. These cracks are highlighted on *Figures 6.5* by red ellipses. Smaller cracks can be seen emanating from the larger crack. Both samples also appeared to stay together, despite the catastrophic crack through each of them. The effect of temperature could therefore be said to slightly improve the fracture mechanics of the samples tested in that the samples do not fracture into

several pieces or succumb to numerous cracks, like that seen in the samples tested at room temperature.

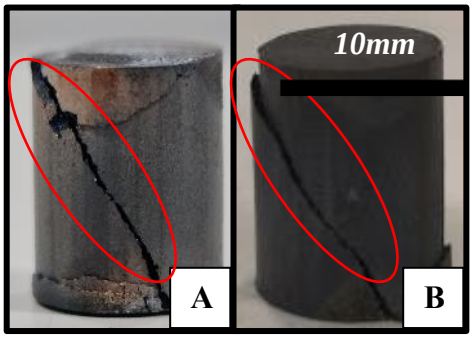

Figure 6.5: *Pictures of the Ti_2AlC samples following their room temperature compression testing using the Gleeble.* ***(a)*** *T09-3,* ***(b)*** *T09-4, with the crack ~45° to the loading direction highlighted with red ellipse*

6.3.1.2 Ti_2AlC MAX phase Compression at 1000°C

The stress-strain curves of Ti_2AlC samples tested at 1000°C can be found in *Figure 6.6*. It is evident that all samples tested at the faster strain rates of 1/s through to 1×10^{-3}/s failed abruptly in a brittle manner upon reaching their peak compressive stresses, showing no signs of strain softening or hardening. The mechanical properties of each sample can be found in *Table 6.4*. The peak stresses of all samples tested at this temperature are all in a similar region of between 320-380 MPa, which is approximately 100 MPa lower than the samples tested at room temperature. The Young's Modulus for samples tested at under the two fastest strain rates, T10-0 and T10-1 was recorded as being 12±0.5 GPa. For the T10-2 and T104 samples, the Young's Modulus is slightly higher at values of 16.08 and 15.39 respectively. The T10-3 sample having a slightly anomalous value of 9 GPa. The yield stress values of samples that had negligible to non-existent plasticity were very close to UCS of those samples. However, the sample that did show plasticity, T10-4, did have a slight difference, with a yield stress ~20 MPa less that the UCS. The T10-4 sample behaves differently in that it exhibits a short strain hardening region before reaching a peak stress very similar to the peak stresses for the failed samples. After reaching the yield point there appears to be a lengthy period of strain softening until ~0.2 strain, the softening modulus of this period being recorded as -297.8 MPa. After 0.2 strain, moderate amounts of hardening were noted, having a hardening modulus of 97.12 MPa. The sample then seems to soften once again right before the end of the test, having a softening modulus of -170.9 MPa. It must be noted that the test was completed at 0.4 strain and the sample was air cooled to room temperature.

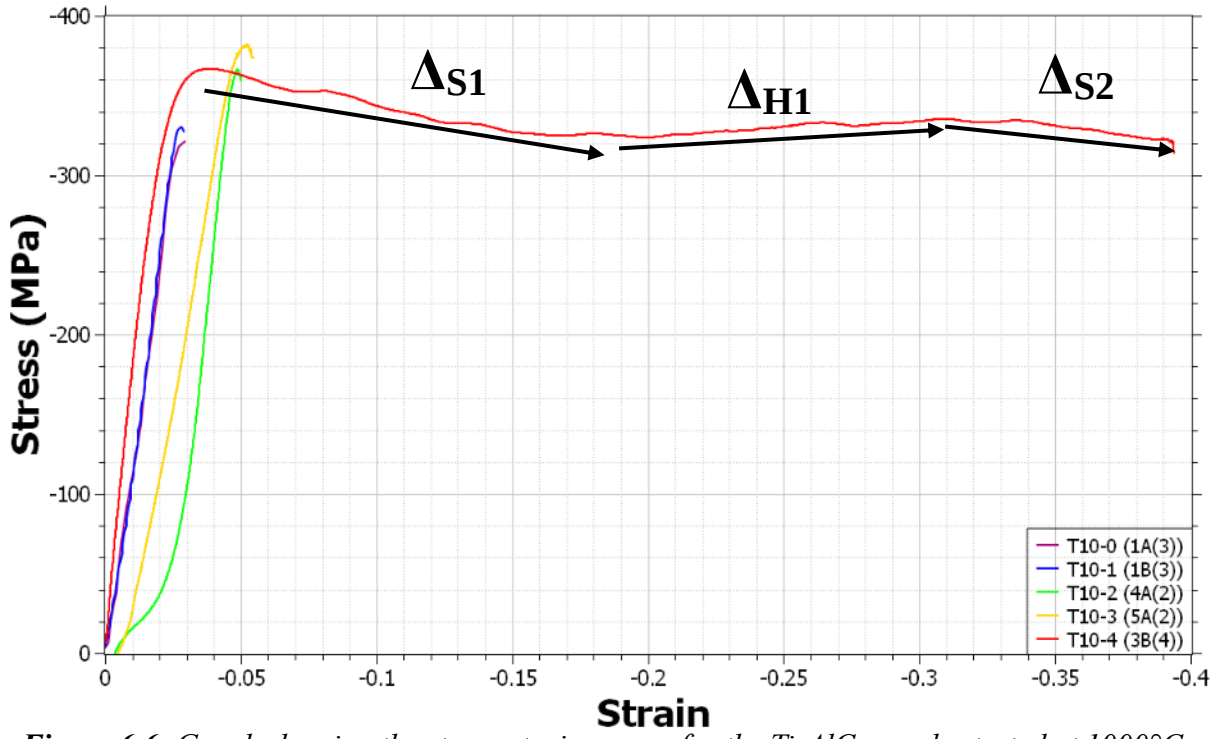

Figure 6.6: *Graph showing the stress-strain curves for the Ti_2AlC samples tested at 1000°C and under strain rates between 1/s and 1×10^{-4}/s*

Table 6.4: *Mechanical Properties of Ti_2AlC samples tested at 1000°C and under strain rates between 1/s and 1×10^{-4}/s*

Test	Ultimate Comp Stress (MPa)	Young's Modulus (GPa)	Yield Stress (MPa) (0.02 Proof Stress)	Compression (%)	Softening Rate Δ_{S1} | Δ_{S2}		Hardening Rate Δ_{H1}
T10-0	-321.05	12.04	-319.92	-6.55	-		-
T10-1	-330.22	12.37	-329.08	-2.91	-		-
T10-2	-366.93	16.08	-366.89	-5.01	-		-
T10-3	-382.55	9.00	-379.4	-5.44	-		-
T10-4	-369.06	15.39	-350	-40	-297.8	-170.9	97.12

The images of some of the samples following their tests can be found in *Figure 6.7*. Upon removing each sample from the Gleeble it was evident that the samples tested under the 4 fastest strain rates (1/s - 1×10^{-3}/s) appeared to have behaved and deformed in a very similar manner, in that they exhibited a large crack that was ~45° to the compression axis that went from the top to the bottom of each sample. These cracks are highlighted on *Figures 6.7a-d* by red ellipses. Another aspect of note was that despite the samples cracking at relatively low strains, each sample stayed together, in that the bulk of the sample either side of the ~45° crack did not fall apart into several pieces. Like the samples tested at 900°C , it could be said that

the increasing temperatures improve the fracture mechanics of the samples tested at the faster strain rates so that the samples do not fracture into several pieces or succumb to numerous cracks, like that seen in the samples tested at room temperature. The sample tested at the slowest strain rate, T10-4, is, has already been discussed, the only sample to exhibit ductility at this temperature and the image of it can be found in *Figure 6.7d*. This image shows that the T10-4 sample experienced significant barrelling during the test. Highlighted within the yellow ellipse in *Figure 6.7d* are cracks on the outside of the sample, indicating that the material has failed, but not in the same way as the other samples tested at this temperature. The oxide layer for the T10-4 is very different compared to the samples that were tested at a quick strain rates, perhaps indicative of the effect the length of the test has on the oxide layer of the samples.

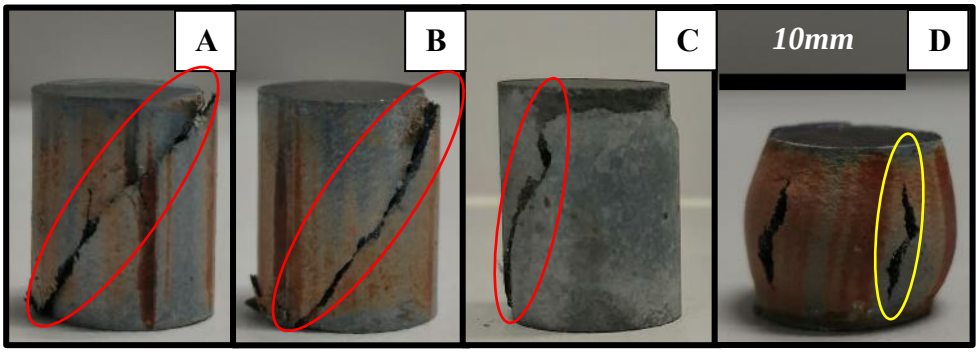

Figure 6.7: *Pictures of the Ti_2AlC samples following their high temperature compression tests at 1000°C.* ***(a)*** *T10-0,* ***(b)*** *T10-1,* ***(c)*** *T10-3,* ***(d)*** *T10-4. Cracks ~ 45° to the loading direction highlighted with the red ellipse. Outer surface cracks of T10-4 highlighted with yellow ellipse*

6.3.1.3 Ti_2AlC MAX phase Compression at 1100°C

Figure 6.8 shows the stress-strain curves for the Ti_2AlC samples tested at 1100°C. It is evident once again that in general the peak stress for each strain rate has decreased with increasing temperature and decreasing strain rates. The sample that produces the highest peak stress is the sample tested at fastest strain rate, 1/s, with progressively lower peak stresses as the strain rate gets slower. The peak compressive stress of the 1/s sample is -500 MPa, which is anomalously much higher than other peak stresses recorded at high temperature for Ti_2AlC, which are within the -250 MPa to -400 MPa range. The samples tested at strain rates of 1×10^{-1}-1×10^{-3}/s have peak stresses that fall into the -320 MPa to -380 MPa range, with the samples subjected to strain rates up to 1×10^{-2}/s failing in a brittle manner once again, cracking abruptly at approximately -0.03 strain. The samples tested at the two slowest strain rates, 1×10^{-3}/s and at 1×10^{-4}/s, behave in a ductile manner, with both samples having a linear elastic regime and then showing significant periods of strain softening after reaching their peak stresses. Both samples

also do not fail upon the conclusion of the test at -0.4 strain. As shown in *Table 6.5*, the sample subjected to the slowest strain rate has the lowest peak stress of the high temperature tests taken at 1100°C, with a stress of approximately -260 MPa. The Young's Modulus is seen to follow a general trend of getting higher with the faster strain rates, T11-1 and T11-2 being the mild contradictions to this rule. The highest Young's Modulus recorded was 29.18 GPa, for T11-0 sample, while 8.99 GPa was the lowest recorded, for the T11-4 sample. As was seen for the tests at 1000°C, the yield stress for the samples that failed in a brittle manner were very close to their respective UCS's, while those that behaved in a ductile manner have a much lower yield stress than UCS's. Both T11-3 and T11-4 have substantial periods of strain softening, and their softening moduli were recorded as -545 MPa and -441.1 respectively.

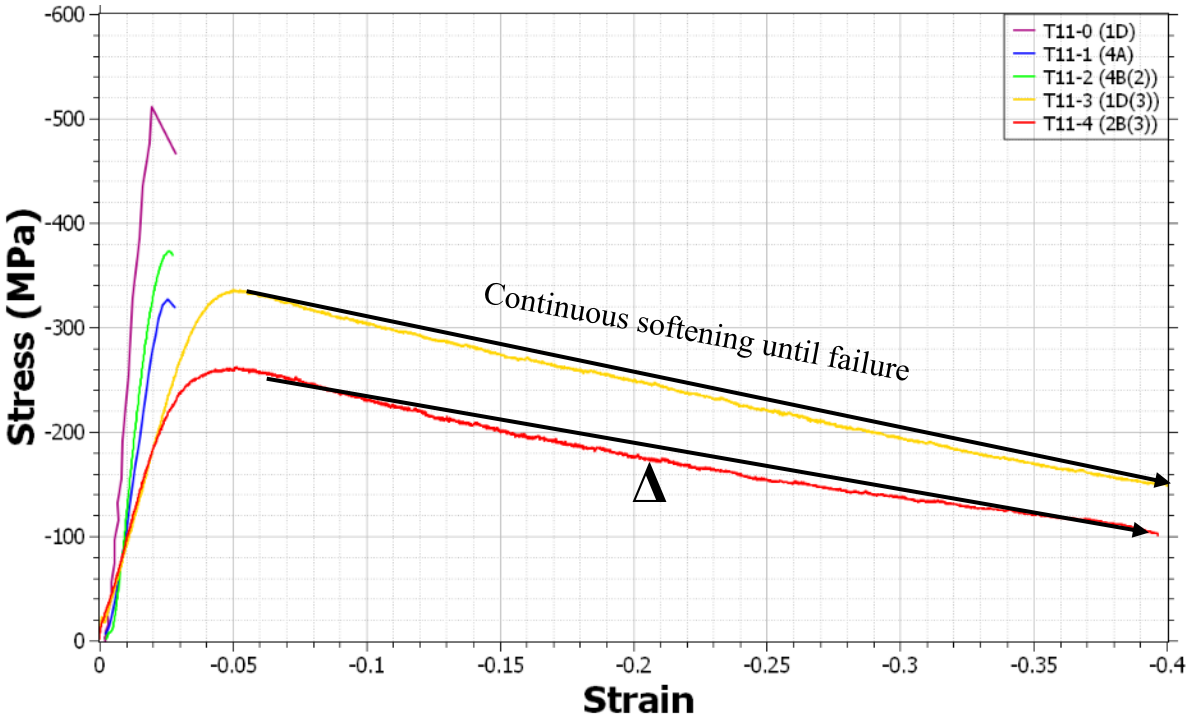

Figure 6.8: *Graph showing the stress-strain curves for the Ti_2AlC samples tested at 1100°C and under strain rates between 1/s and $1x10^{-4}$/s*

Table 6.5: *Mechanical Properties of Ti_2AlC samples tested at 1100°C and under strain rates between 1/s and 1×10^{-4}/s*

Test	Ultimate Comp Stress (MPa)	Young's Modulus (GPa)	Yield Stress (MPa) (0.02 Proof Stress)	Compression (%)	Softening Rate Δ
T11-0	-493.49	29.18	-489.20	-2.85	-
T11-1	-317.10	15.08	-316.00	-3.09	-
T11-2	-360.16	19.90	-347.90	-2.73	-
T11-3	-332.66	11.40	-308.35	-39.58	-545.04
T11-4	-261.74	8.99	-213.23	-40.00	-441.1

The images of some of the samples following compression at 1100°C can be found in *Figure 6.9*. Once again it can be seen that the samples tested at the fastest strain rates exhibit the same crack ~45° to the loading direction as the samples tested at fast strain rates at lower temperatures. Like the samples tested at 1000°C, despite the crack going straight through the sample at ~45° to the loading direction, the sample generally stays together with both pieces of the sample either side of the ~45° crack not breaking away. As mentioned previously, ductility is exhibited for the two samples that were subjected to the slowest strain rates, T11-3 and T11-4. The images for these samples in *Figure 6.9c-d* show the same type of barrelling that was witnessed in the T10-4 sample tested at 1000°C. Like the T10-4 sample, small outer surface cracks are once again witnessed on the T11-3 sample, with these highlighted by the yellow ellipse in *Figure 6.9c*. These cracks are not apparent on the T11-4 sample. The oxide layer appears different depending on the length of the test, with the shorter, T11-1 test showing none of the reddish colouring of the T11-3 and T11-4 samples.

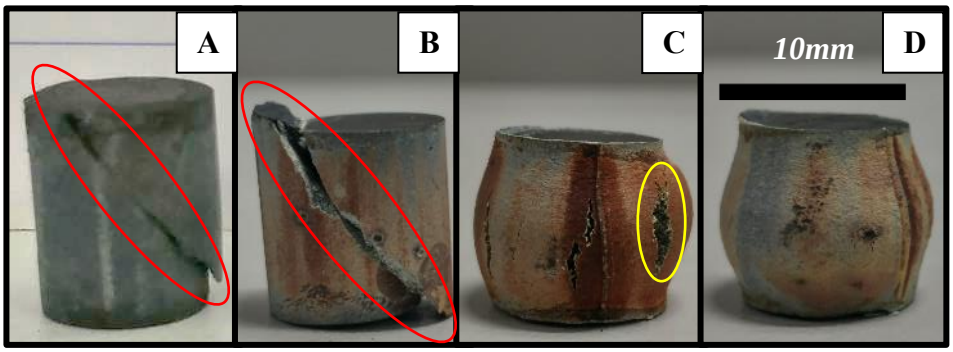

Figure 6.9: *Pictures of the Ti_2AlC samples following their high temperature compression tests at 1100°C.* ***(a)*** *T11-1,* ***(b)*** *T11-2,* ***(c)*** *T11-3,* ***(d)*** *T11-4*

6.3.1.4 Ti2AlC MAX phase Compression at 1200°C

The previously identified trend of peak stress generally increasing with increasing strain rates can once again be observed in *Figure 6.10.* The exception to this rule can be seen in the stress-strain curves for the Ti_2AlC samples tested at the fastest strain rates of 1/s and 1×10^{-1}/s, although these samples have a peak compressive stress in the similar -250 MPa to -350 MPa range as the sample tested at 1×10^{-2}/s. The slower strain rates do follow this trend, however. The trend of peak stress for each sample decreasing with the increase in temperature also applies to the samples tested at 1200°C. It's also worth noting that, like the samples tested at 1100°C, the peak stress decreases by approximately -125 MPa with the slower strain rates. The highest peak stress recorded at this temperature was -350 MPa for the sample subjected to a strain rate of 1×10^{-2}/s, a strain rate that had yielded brittle behaviour up until this temperature. The peak stresses for the samples subjected to strain rates of 1×10^{-3}/s and 1×10^{-4}/s was recorded as ~-225 MPa and ~-100 MPa respectively. The tests on samples subjected to strain rates between 1×10^{-2}/s and 1×10^{-4}/s all have a relatively similar shape to their stress-strain curves, with all 3 samples lasting until the end of the test at 0.4 strain. The rest of the mechanical properties can be found in *Table 6.6.* The Youngs's Modulus for the samples tested at this temperature are generally lower than those calculated at lower temperatures, with the T12-2 sample having the highest value of 10.63 GPa and T12-3 the lowest of 7.24 GPa. The yield stresses are close to each sample's UCS at this temperature, especially for the slowest strain rates. Another trend observed under slower strain rates at this temperature is the tendency for the strain softening rate to decrease, as can be seen in the extreme sense for the sample tested at 1×10^{-4}/s. The rate of softening also changes at ~0.225 for the T12-2 and T12-3 samples. For the T11-2 sample, the first period of softening has a softening modulus of -978.8 MPa while the second softening moduli was recorded as -553.1 MPa. There were similar rates of change between the softening moduli for the T12-3 sample, with the first softening moduli recorded as -608.2 MPa and the second as -275.3 MPa. The softening moduli for T12-4 was recorded as being -170.09 MPa.

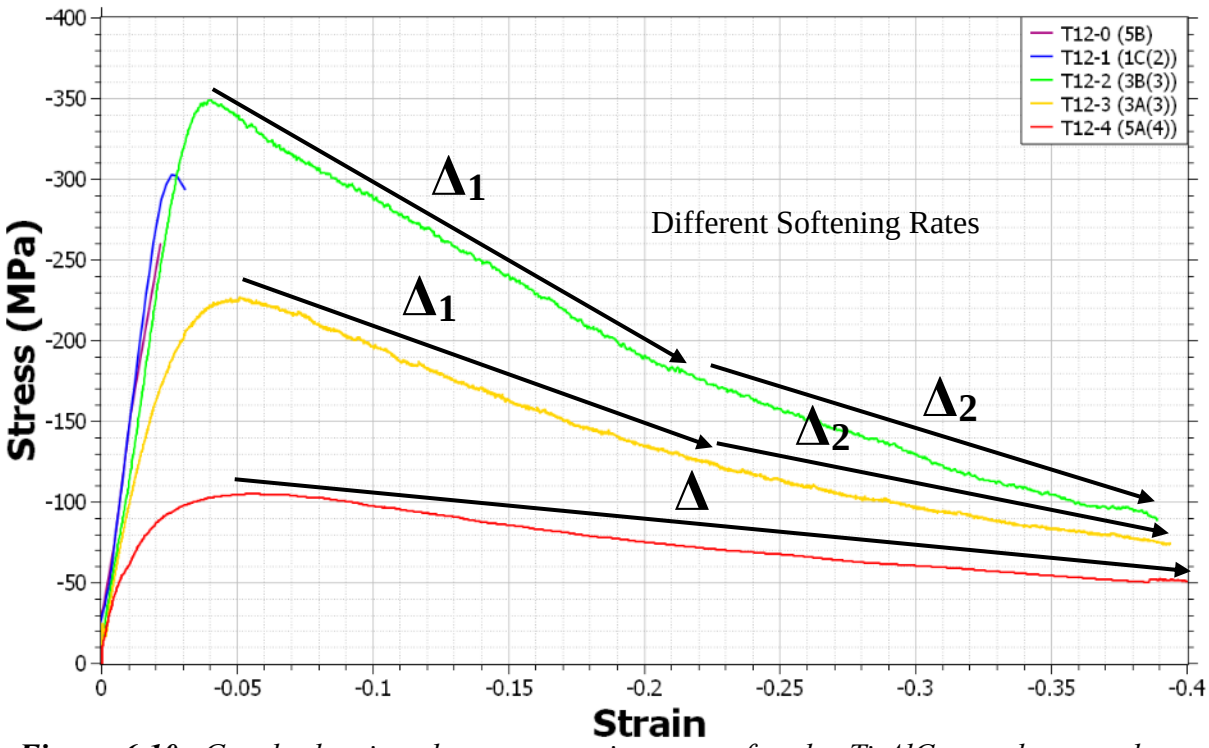

Figure 6.10: *Graph showing the stress-strain curves for the Ti_2AlC samples tested at 1200°C and under strain rates between 1/s and 1×10^{-4}/s*

Table 6.6: *Mechanical Properties of Ti_2AlC samples tested at 1200°C and under strain rates between 1/s and 1×10^{-4}/s*

Test	Ultimate Comp Stress (MPa)	Young's Modulus (GPa)	Yield Stress (MPa) (0.02 Proof Stress)	Compression (%)	Softening Rate Δ_1 | Δ_2	
T12-0	-259.30	8.51	-	-2.20	-	
T12-1	-302.52	9.79	-300.90	-3.08	-	
T12-2	-348.893	10.63	-333.95	-39.06	-978.7	-533.1
T12-3	-227.92	7.24	-227.31	-39.97	-608.2	-275.3
T12-4	-113.70	7.48	-113.70	-39.99	-170.09	

The images taken upon the completion of each high temperature compression test can be found in *Figure 6.11*. As has already been established, the samples that were subjected to the faster strain rates and exhibit no plastic deformation fail in a brittle manner and are the ones with cracks ~45° to the loading direction, as highlighted by the red ellipse in *Figures 6.11a-b*. The samples at 1200°C that succumbed to this fate were T12-0 and T12-1, with both samples exhibiting this crack once again from the top of the sample through to the bottom. Minor fragments of each sample also cracked off but in general both samples, like other Ti_2AlC samples tested at high temperature did not break apart, with both parts of the sample either side

of the ~45° crack staying attached. Minor cracks propagating from these major cracks could also be witnessed, with these highlighted with an orange ellipse. The samples that were found to show ductility when studying the stress-strain curves, T12-2, T12-3 and T12-4, showed significant amounts of barrelling when their images taken post-testing were examined (*Figures 6.11c-e)*. Of note are the number of outer surface cracks increasing with faster strain rates, with the sample tested at the slowest strain rate, T12-4, exhibiting no obvious surface cracks. T12-2, the sample that was subjected to the fastest strain rate but still showed signs of ductility displayed both major and minor surface cracks, as highlighted by the yellow ellipse in *Figure 6.11c*. This shows a general trend of the slower the strain rate, the less likely cracks, both major and minor, are to form in the Ti_2AlC MAX phase.

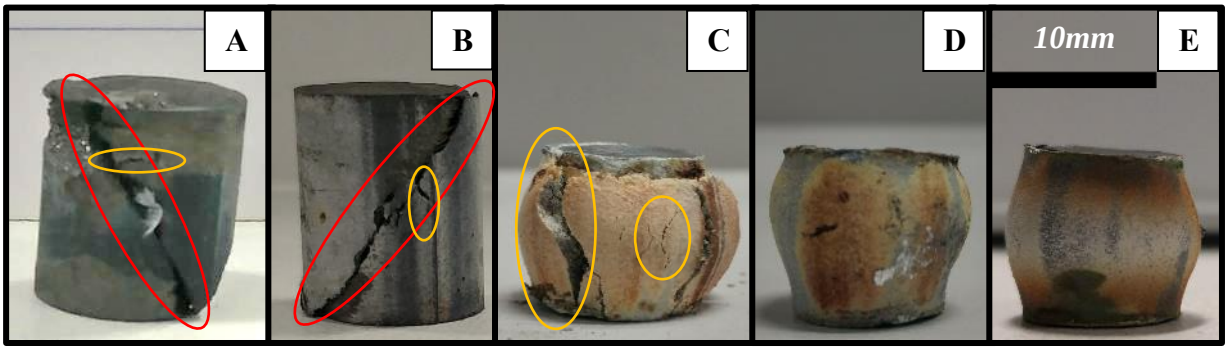

Figure 6.11: *Pictures of the Ti_2AlC samples following their high temperature compression tests at 1200°C.* ***(a)*** *T12-0,* ***(b)*** *T12-1,* ***(c)*** *T12-2,* ***(d)*** *T12-3,* ***(e)*** *T12-4*

6.3.2 Ti_3SiC_2 MAX phase

6.3.2.1 Ti_3SiC_2 MAX phase Compression at Room Temperature

The Ti_3SiC_2 samples were compressed in the Gleeble at room temperature before any high temperature testing to establish the effect of temperature on the materials properties. The results for the tests taken at room temperature with the strain rates of 1×10^{-3}/s and 1×10^{-4}/s, the slowest strain rates used for the mechanical testing of the MAX phases in this work, can be found in *Table 6.7* and the stress-strain curves in *Figure 6.12*. Both samples behave in a near identical manner, with a very linear elastic regime until the point of failure at approximately -480±10 MPa and at strain of -0.02. The Young's Modulus of both samples are relatively similar at 28±2 GPa. There is no yield point or any strain softening or hardening for the samples tested under these conditions, with both samples failing after being compressed ~2%. Just like their Ti_2AlC counterparts tested under the same conditions, the observations seen are an indication that these

samples fail in a very brittle manner when subjected to even the slowest of strain rates at room temperature.

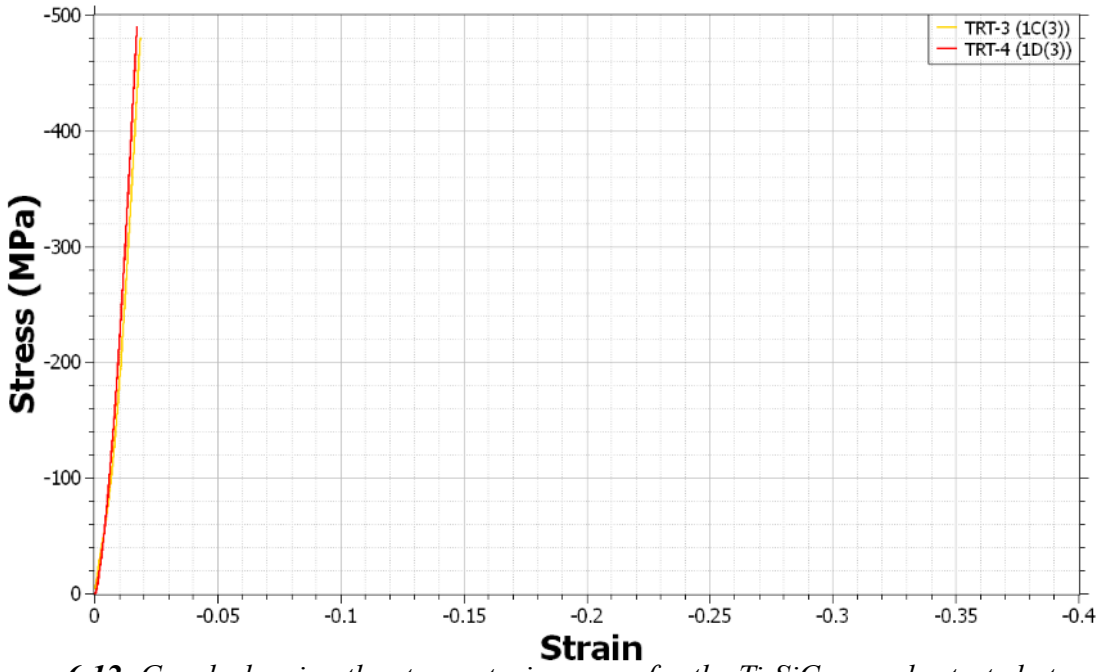

Figure 6.12: *Graph showing the stress-strain curves for the Ti_3SiC_2 samples tested at room temperature and under a strain rate of 1×10^{-3}/s and 1×10^{-4}/s*

Table 6.8: *Mechanical Properties of Ti_3SiC_2 samples tested at Room Temperature and under strain rates of 1×10^{-3}/s and 1×10^{-4}/s*

Test	Ultimate Comp Stress (MPa)	Young's Modulus (GPa)	Yield Stress (MPa) (0.02 Proof Stress)	Compression (%)
TRT-3	-472.91	26.35	-	-1.87
TRT-4	-483.20	29.80	-	-1.74

The brittle nature of failure is further proved when studying the images in *Figure 6.13*, taken after both samples were removed from the Gleeble chamber. Unlike the Ti_2AlC samples that were tested under the same conditions, the Ti_3SiC_2 samples break into several small pieces, with only one part of the disintegrated TRT-3 and TRT-4 samples, highlighted with the red ellipse, showing any sign of not failing completely. Of note is the angular nature to broken pieces, although the inner surfaces of the broken samples are relatively smooth when studied more carefully. The observed brittle failure of the Ti_3SiC_2 MAX phase material at room temperature under similar testing parameters as those used here has also been consistently witnessed in previous studies on their mechanical behaviour.

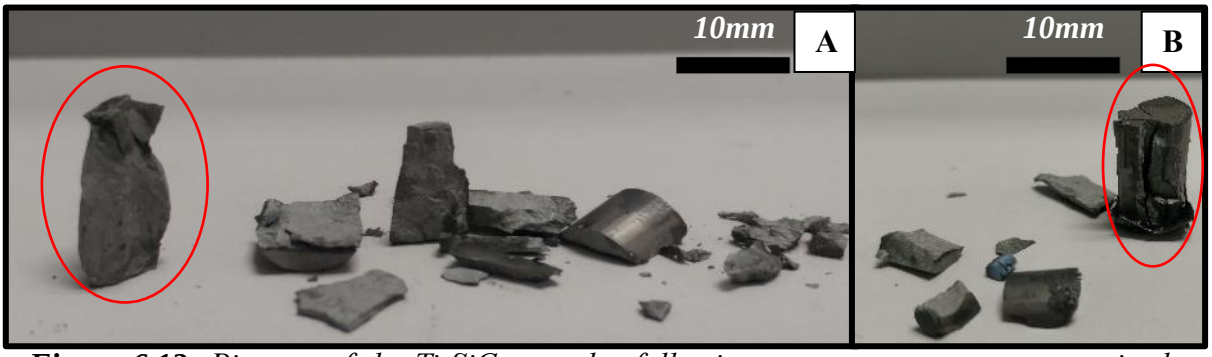

Figure 6.13: *Pictures of the Ti_3SiC_2 samples following tests at room temperature in the Gleeble.* ***(a)*** *TRT-3,* ***(b)*** *TRT-4. Red ellipses showing the parts of the sample which didn't break apart into several pieces.*

6.3.2.2 Ti_3SiC_2 MAX phase Compression at 900°C

Like the sample tested at room temperature, only the two slowest strain rates were used when testing the performance of the Ti_3SiC_2 MAX phases at 900°C. The stress-strain curves of the samples tested at this temperature can be found in *Figure 6.14* and the mechanical properties derived from this data can be found in *Table 6.9.* Unlike the samples tested at room temperature, the peak stresses were not similar, with T09-4 having the higher peak stress of -744 MPa, compared to T09-3 with a peak stress of -537 MPa. T09-4 has a Young's Modulus more than twice as big as that of the T09-3 sample. Both samples behaved in a linear elastic manner and succumbed to instant brittle failure upon reaching their peak stresses. The T09-3 sample compressed 7.46% before failure, while the T09-4 sample compressed 5.46%.

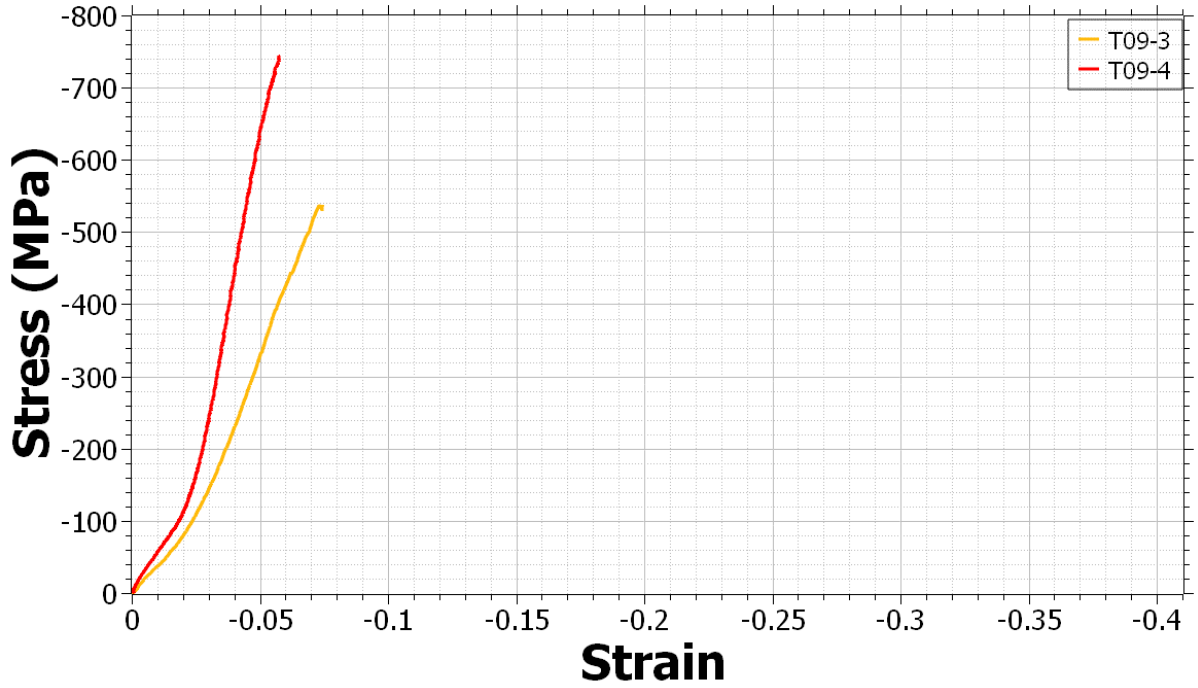

Figure 6.14: *Graph showing the stress-strain curves for the Ti_3SiC_2 samples tested at 900°C under a strain rate of 1×10^{-3}/s and 1×10^{-4}/s*

Table 6.9: *Mechanical Properties of Ti3SiC2 samples tested at 900°C and under strain rates of 1×10-3/s and 1×10-4/s*

Test	Ultimate Comp Stress (MPa)	Young's Modulus (GPa)	Compression (%)
T09-3	-537.56	7.80	-7.45
T09-4	-744.21	18.99	-5.76

Images of the samples tested at 900°C can be found in *Figure 6.15*. Both samples can be seen to have cracked into several pieces, with the T09-3 sample staying together slightly more than the T09-4 sample, albeit with numerous internal and external cracks. The behaviour of both samples is similar to that of the Ti_3SiC_2 samples tested at room temperature. The brittle nature of failure at this temperature further proves that the brittle to ductile transition temperature for Ti_3SiC_2 is higher than 900°C.

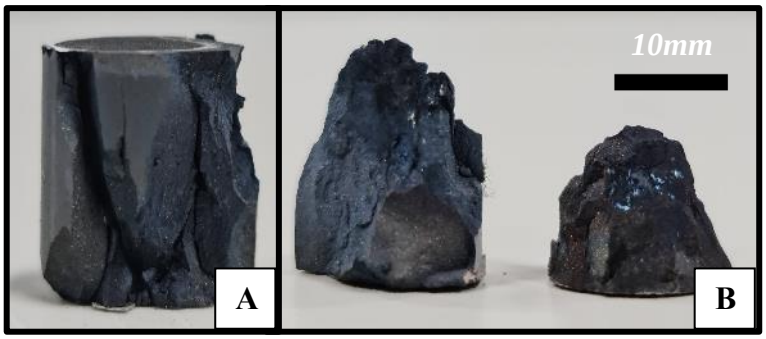

Figure 6.15: *Pictures of the Ti_3SiC_2 samples following tests at 900°C in the Gleeble.* ***(a)*** *T09-3,* ***(b)*** *T09-4.*

6.3.2.3 Ti_3SiC_2 MAX phase Compression at 1000°C

The stress-strain curves of the samples tested at 1000°C can be found in *Figure 6.16.* The peak stresses of the samples tested at this temperature are generally around -700 MPa, with the sample tested at 1/s behaving anomalously by reaching a stress of -512 MPa at a strain to failure of -0.04. The samples tested at the fastest strain rates (1/s-1×10^{-3}/s) behaved in a linear elastic manner and succumbed to brittle failure upon reaching their ultimate compressive stresses. The samples that were tested to a strain of -0.1 at strain rates between 1×10^{-1}/s and 1×10^{-3}/s all failed at around -0.04 strain with peak stresses in the range of -670-720 MPa. This behaviour is similar to the Ti_2AlC samples tested at this temperature, where all the strain rates yielded very similar peak stresses. The Young's Modulus of all the samples can be found in *Table 6.10*. The lowest Young's Modulus is for the T10-0 sample, while the highest Young's Modulus was for the T10-3 sample. The other Young's Modulus values are relatively similar at 15±2 GPa. The sample that was tested at the slowest strain rate behaved in a very similar

manner to that of Ti_2AlC, in that it was the only sample that showed ductility, with the sample not failing upon the completion of the test at 0.4 strain. The yield stress of the T10-4 sample was found to be much less than its UCS, with a value of -585.20 MPa. This yield point was followed by a short period of strain hardening and significant period of strain softening. The Strain hardening region can be split into two sections, the first hardening moduli being 7327 MPa and the second 1572 MPa. The softening moduli can also be split into two sections, with the first -1934 MPa and the second moduli much smaller at -689.2 MPa.

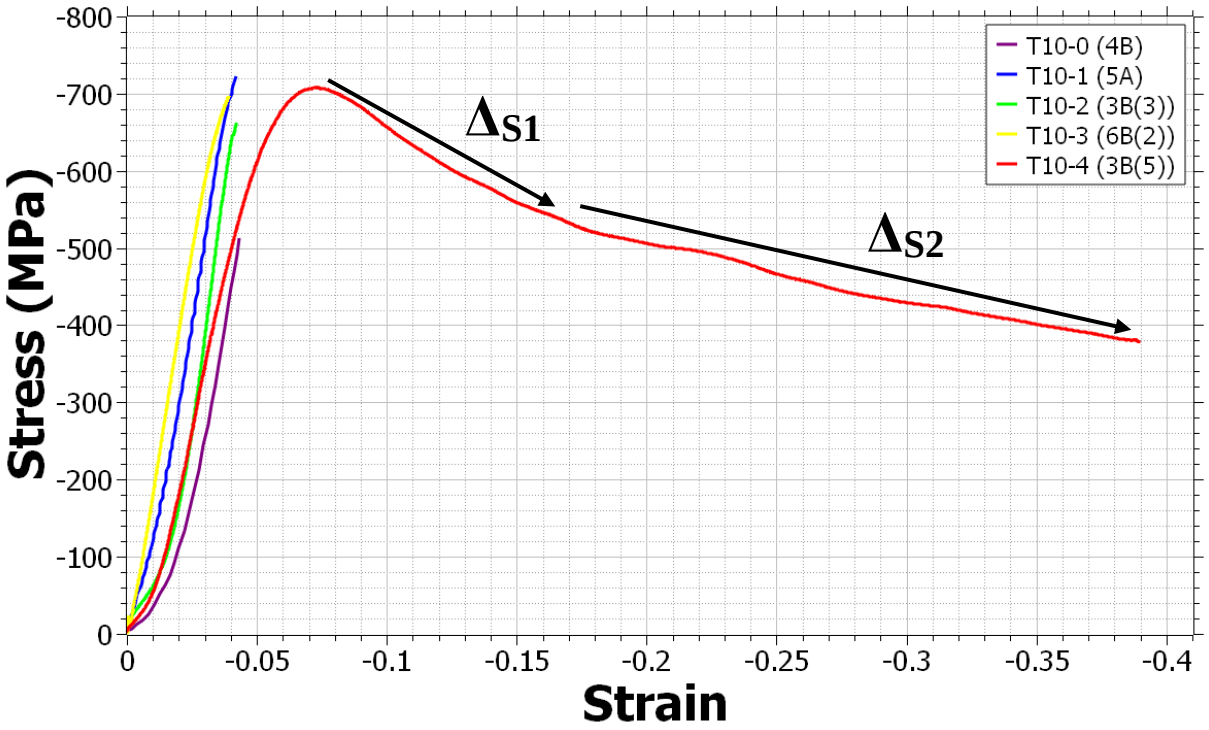

Figure 6.16 *Graph showing the stress-strain curves for the Ti_3SiC_2 samples tested at 1000°C and under strain rates between 1/s and 1×10^{-4}/s*

Table 6.10: *Mechanical Properties of Ti_3SiC_2 samples tested at 1000°C and under strain rates between 1/s and 1×10^{-4}/s*

Test	Ultimate Comp Stress (MPa)	Young's Modulus (GPa)	Yield Stress (MPa) (0.02 Proof Stress)	Compression (%)	Softening Rate Δ	
T10-0	-512.59	11.81	-	-4.34	-	
T10-1	-723.20	17.72	-	-4.21	-	
T10-2	-662.08	16.68	-	-4.21	-	
T10-3	-696.79	19.76	-	-3.93	-	
T10-4	-724.43	13.72	-585.20	-39.96	-1934	-698.2

The images of the samples following compression testing at 1000°C can be found in *Figure 6.17*. Unlike the Ti_2AlC samples tested under the same conditions, the performance of the Ti_3SiC_2 when subjected to the faster strain rates at 1000°C is very similar to that of the samples tested at room temperature in that rather than staying together the sample breaks into several pieces. This is true for all samples tested at this temperature except the sample that showed ductility, T10-4. A crack ~45° to the loading direction is a feature that was previously identified in some of the Ti_2AlC samples and is seen again in the T10-0 sample, as highlighted with a red ellipse. The other samples that failed showed no obvious feature, with these samples exhibiting relatively smooth fracture surfaces on their generally angular fractured pieces. The sample that showed ductility, T10-4, behaved in a similar manner to its Ti_2AlC counterpart in showing significant barrelling and cracks on its outer surface, as highlighted with the yellow ellipse.

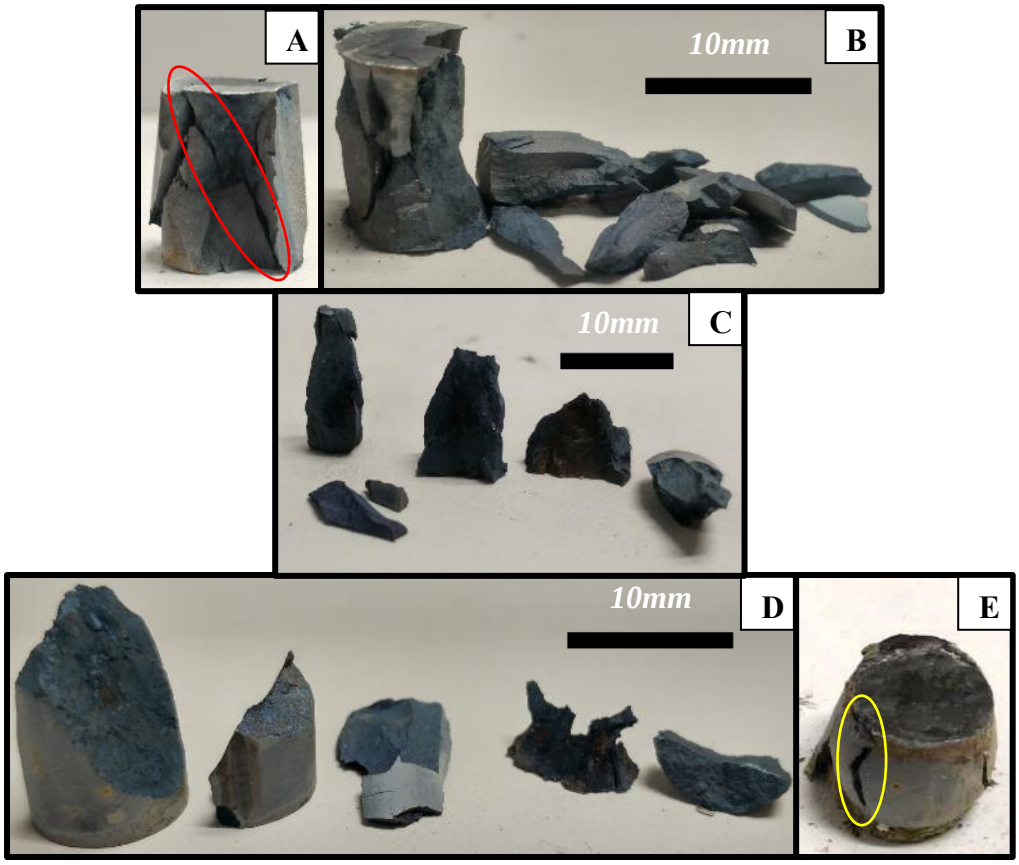

Figure 6.17: *Pictures of the Ti_3SiC_2 samples following their high temperature compression tests at 1000°C.* ***(a)*** *T10-0,* ***(b)*** *T10-1,* ***(c)*** *T10-2,* ***(d)*** *T10-3,* ***(e)*** *T10-4. Red ellipse highlighting the crack ~45° to the loading direction and the yellow ellipse highlighting the small surface cracks*

6.3.2.4 Ti_3SiC_2 MAX phase Compression at 1100°C

The trend that has been observed so far in both MAX phases, namely that in general the peak stress for each strain rate decreases with increasing temperature, is once again on show in *Figure 6.18,* showing the stress-strain curves for the Ti_3SiC_2 samples tested at 1100°C. The previously observed trend of faster strain rates providing the highest peak stresses for a given temperature is not applicable to the samples tested at this temperature, with the sample tested at the fastest strain rates of 1/s and 1×10^{-1}/s giving very similar peak stresses of ~-380 MPa before failing abruptly at this stress and at a strain to failure of -0.02. The sample tested in the mid-range of the strain rates, 1×10^{-2}/s, performed slightly better in that it reached a strain of -0.03 and a peak stress of ~-620 MPa at failure. The abrupt failures of the samples at fast strain rates are proof of the materials brittle performance under these conditions. This peak stress is close to the ultimate peak stress witnessed at this temperature for Ti_3SiC_2 of ~-675 MPa for the sample tested at 1×10^{-3}/s. The samples tested 1×10^{-3}/s and 1×10^{-4}/s were the only samples that showed ductility until the end of their respective tests. The peak stress for the sample tested at the slowest strain rate of is approximately 200 MPa lower than that of the sample tested at 1×10^{-3}/s. All samples tested at this temperature show a linear elastic regime until their peak stresses, upon which they either fail, as is the case for the samples tested at the 3 fastest strain rates, or continue onto a short period of strain hardening followed by a lengthy period of strain softening until the completion of the test, as is the case for the samples tested at the 2 slowest strain rates. The Young's Modulus for the samples can be seen in *Table 6.11*. All samples appeared to have a very similar linear elastic region judging from the shapes of the stress-strain curves in *Figure 6.18*. This was proved to be the case, with the Young's Modulus being 17±3 GPa for all samples. Similar to tests at other temperatures at the faster strain rates for the Ti_3SiC_2 MAX phase, there are no easily defined yield points. The samples that did show ductility had yield stresses much lower than their respective UCS'S. For both the T11-3 and T11-4 samples, there is a short period of strain hardening following the yield point, with the hardening regions of both samples having two different hardening rates. The first hardening moduli of T11-3 was recorded as 12918 MPa, with the second moduli being much lower at 3140 MPa. Similarly, for the T11-4 sample, the first hardening moduli is higher than the second. Following the UCS for both T11-3 and T11-4, there is a long period of strain softening which, like the hardening moduli, can be split into two softening rates. For T11-3, the first softening moduli was recorded as -3203 MPa and the second as -1037 MPa. The softening moduli of T11-4 is much lower, with the first moduli -1012 MPa and the second as -389.1 MPa.

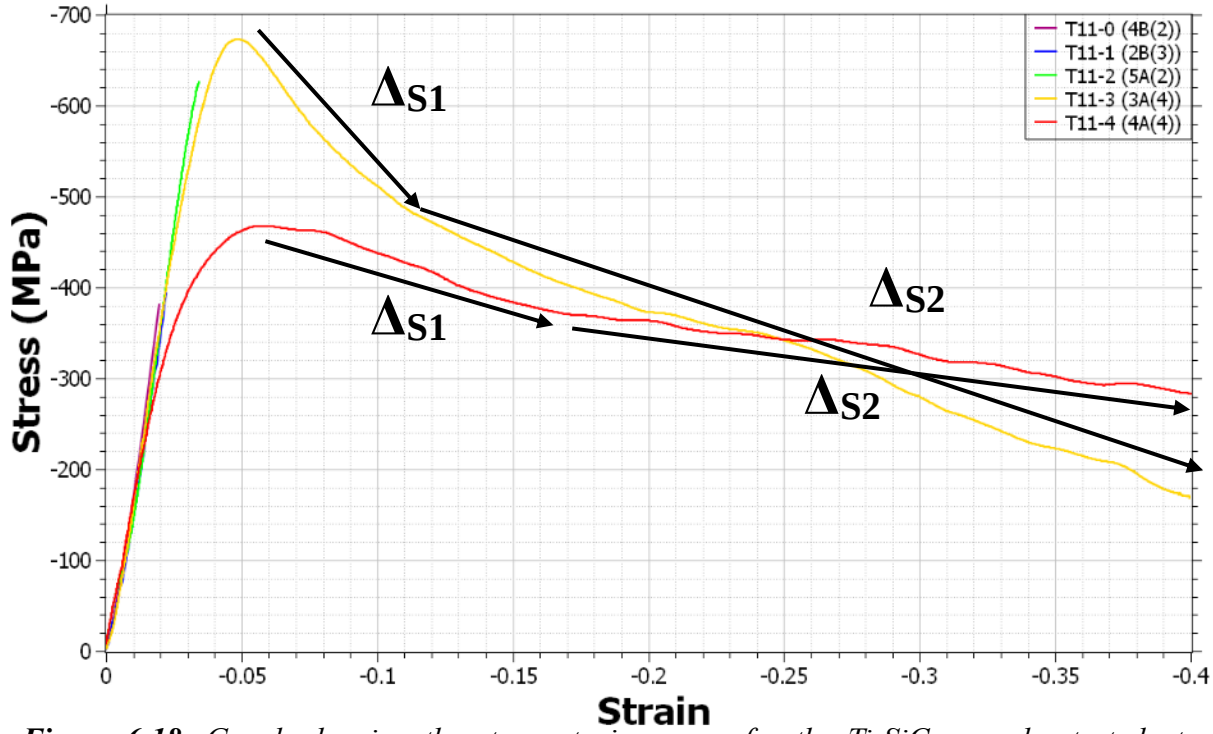

Figure 6.18: *Graph showing the stress-strain curves for the Ti_3SiC_2 samples tested at 1100°C and under strain rates between 1/s and 1×10^{-4}/s*

Table 6.11: *Mechanical Properties of Ti_3SiC_2 samples tested at 1100°C and under strain rates between 1/s and 1×10^{-4}/s*

Test	Ultimate Comp Stress (MPa)	Young's Modulus (GPa)	Yield Stress (MPa) (0.02 Proof Stress)	Compression (%)	Softening Rate Δ_{S1} | Δ_{S2}	
T11-0	-376.18	18.20	-	-4.09	-	
T11-1	-388.68	17.45	-	-2.27	-	
T11-2	-614.06	18.88	-	-3.41	-	
T11-3	-679.07	19.38	-594.30	-39.99	-3203	-1037
T11-4	-471.68	15.27	-368.85	-39.95	-1012	-389.1

Figure 6.19 shows the images taken upon removing each sample from the Gleeble chamber. These images show that the Ti_3SiC_2 samples fail in a similar manner to those tested at 1100°C by breaking into numerous pieces when subjected to the 3 fastest strain rates, confirming the brittle nature of the Ti_3SiC_2 MAX phase under those conditions. Like those samples tested at 1000°C, the surfaces of each angular fractured piece appear relatively smooth. As was the case in the Ti_2AlC samples tested under these conditions, the T11-3 and T11-4 samples exhibited

significant barrelling and in the case of the T11-4 sample considerable amounts of cracking on the outer surface on the sample, as highlighted with the yellow ellipse. This is contrary to the trend witnessed for Ti_2AlC where it was found that the slower the strain rate, the less cracks that appear. The colour of the oxide layer appears to change with decreasing strain rates. The samples tested at strain rates from 1/s to 1×10^{-2}/s appear to show little to no oxide layer, while the slowest strain rate samples seem to exhibit a moderate amount of yellowish oxide layer.

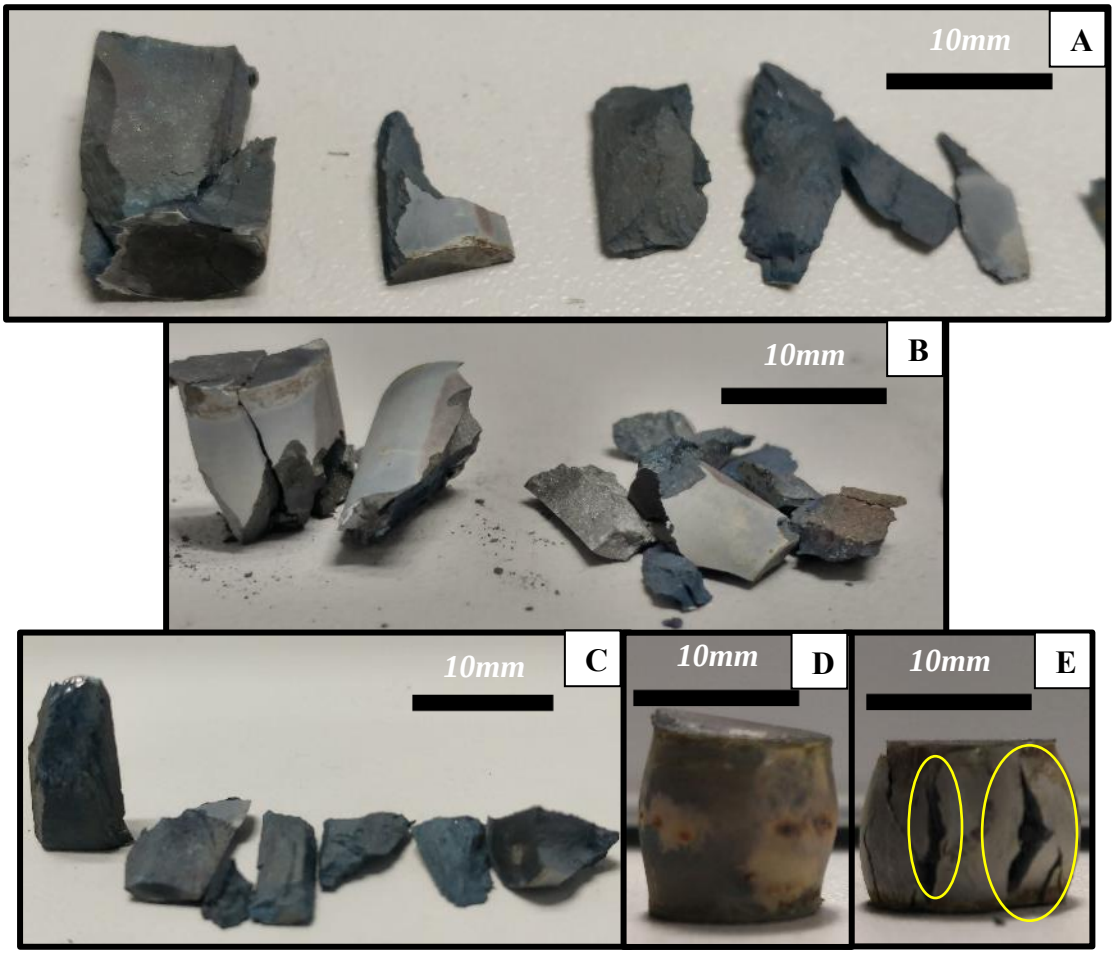

Figure 6.19: *Pictures of the Ti_3SiC_2 samples following their high temperature compression tests at 1100°C.* ***(a)*** *T11-0,* ***(b)*** *T11-1,* ***(c)*** *T11-2,* ***(d)*** *T11-3,* ***(e)*** *T11-4. Yellow ellipse highlighting the surface cracks on the T11-4 sample*

6.3.2.5 Ti_3SiC_2 MAX phase Compression at 1200°C

The stress-strain curves for the samples tested at 1200°C can be found in *Figure 6.20*. It is immediately clear from studying the curves that all tests undertaken at this temperature produced very inconsistent results, suggesting that this material is more unstable at this temperature than the Ti_2AlC samples. As also laid out in *Table 6.12*, the samples that were tested at 1/s and 1×10^{-1}/s, once again yielded very similar peak stresses of ~-500 MPa. Like was witnessed for the Ti_3SiC_2 samples tested at lower temperatures, the fastest strain rates generally do not show an obvious yield point, the exception being -484.25 MPa recorded for the T12-0 sample. Also, like the tests conducted at 1100°C, the fastest strain rates do not provide the highest peak stresses, which was found in one of the samples tested at 1×10^{-2}/s. This sample failed abruptly at a stress of -650 MPa and at a strain to failure of ~-0.035. As further proof of the unstable nature of Ti_3SiC_2 at this temperature, a repeat test at a strain rate of 1×10^{-2}/s showed that the material could deform in a ductile manner. The ductile T12-2 sample was able to reach a strain of ~-0.2 before the test had to be stopped and showed signs strain softening after reaching its peak stress of -575 MPa. The softening rates of this sample can be found in *Table 6.10*. The first softening moduli was recorded as -5262.9 MPa, while the following softening moduli were much smaller at -3177.2 MPa and -397.1 MPa. The samples tested at the two slowest strain rates gave very different shaped curves to that of the Ti_2AlC samples tested under the same conditions. The sample tested at 1×10^{-3}/s started yielding at a stress of -298.4 MPa before reaching a peak stress of -320 MPa. Following this there is a lengthy period of strain softening until 0.3 strain, after which the sample seems to exhibit some strain hardening until the end of the test. Like previous tests, the softening rate is seen to change during the test. The first softening moduli was measured as -1175.8 MPa, with a second period of strain softening starting at ~0.2 strain and having a smaller softening modulus of -376.2 MPa. The hardening modulus towards the end of the test was recorded as 627.8 MPa. The performance of the sample tested at 1×10^{-4}/s is further proof of the materials instability at this temperature, which appears to show significant ductility but also a nonlinear elastic region and substantial strain hardening regime until -0.25 strain. After the yield point of -112.7 MPa, five different hardening rates were noted, following by periods of both strain softening and hardening. As can be seen from *Table 6.13*, the hardening modulus decreases and then increases again twice until the onset of strain softening at the UCS of 515.29 MPa. The sample was also found to strain soften at two different rates from this point, with the first softening modulus having a value of -1565 MPa, which is much lower than the second softening modulus of -5249.1 MPa. Following this period of strain softening, the sample once again hardens at

two different rates before softening until the completion of the test. The Young's Modulus of all samples tested at this temperature generally followed a trend of decreasing with decreasing strain rate, the exception to this being the brittle T12-2 sample which, at 19.59 GPa, was the highest recorded at 1200°C. Excepting the brittle T12-2 sample, the highest Young's Modulus recorded was 14.49 for the T12-0 sample and the lowest being 6 for the T12-4 sample.

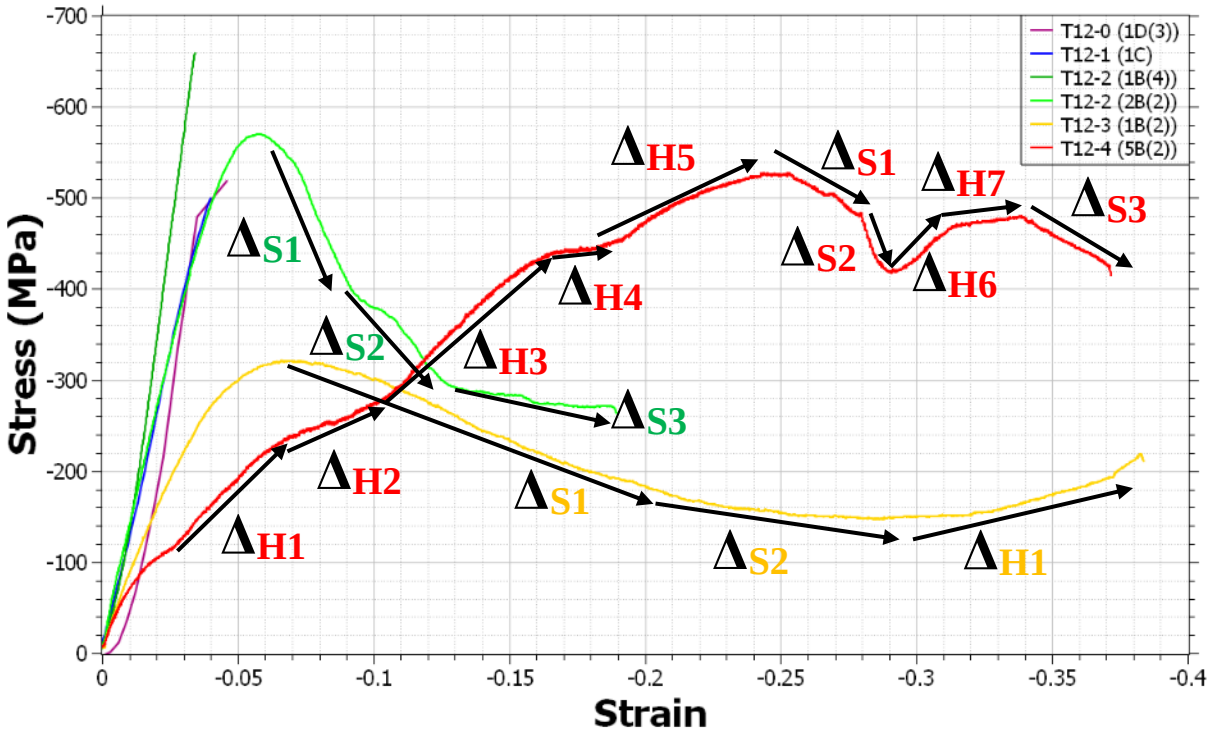

Figure 6.20: *Graph showing the stress-strain curves for the Ti_3SiC_2 samples tested at 1200°C and under strain rates between 1/s and 1×10^{-4}/s.*

Table 6.12: *Mechanical Properties of Ti_3SiC_2 samples tested at 1100°C and under strain rates between 1/s and 1×10^{-4}/s*

Test	Ultimate Comp Stress (MPa)	Young's Modulus (GPa)	Yield Stress (MPa) (0.02 Proof Stress)	Compression (%)
T12-0	-548.62	14.49	484.25	-4.59
T12-1	-491.83	12.42	-	-3.99
T12-2	-646.10	19.59	-	-3.42
T12-2	-560.08	12.45	-488.50	-19.40
T12-3	-318.42	6.70	-298.40	-38.89
T12-4	-515.29	6.00	-112.70	-38.89

Table 6.13: *Hardening and Softening Moduli of Ti_3SiC_2 samples tested at 1100°C and under strain rates between 1×10^{-2}/s and 1×10^{-4}/s*

Test	Softening Modulus (MPa)			Hardening Modulus (MPa)						
	Δ_{S1}	Δ_{S2}	Δ_{S3}	Δ_{H1}	Δ_{H2}	Δ_{H3}	Δ_{H4}	Δ_{H5}	Δ_{H6}	Δ_{H7}
T12-2	-5262.9	-3177.2	-397.1	-	-	-	-	-	-	-
T12-3	-1175.8	-376.2	-	627.8	-	-	-	-	-	-
T12-4	-1565	-5249.1	-1552.6	2910	1156	2676.4	328.8	1221	2298.4	354.9

The images of the Ti_3SiC_2 samples following testing at 1200°C can be found in *Figure 6.21*. As was found when studying the stress-strain curves in *Figure 6.16* it was apparent from the images that the samples subjected to the fastest strain rates, T12-0 and T12-1, failed in a catastrophically brittle manner, breaking into several pieces with numerous cracks inside the samples also visible, as highlighted by the red ellipses in *Figure 6.21a-b*. The samples that showed ductility, T12-2-T12-4 show the signature barrelling of both MAX phases at this temperature. The T12-2 sample shown in *Figure 6.21c* is the sample that showed ductility before it failed at 0.2 strain. Like was seen multiple times in the Ti_2AlC MAX phase, a crack approximately ~ 45° to the loading direction can be seen, as highlighted with the yellow ellipse, along with numerous smaller cracks on the outer surface of the sample. The T12-3 and T12-4 samples see significant barrelling but no cracks on the outer surface, fitting a trend which was previously witnessed happening throughout the Ti_2AlC MAX phase: The slower the strain rate, the less likely cracks are to form on the outer surface of the specimen. The different colours of the oxide layers for each sample were also noted, with the T12-4 sample having a dark, reddish appearance compared to the pinkish colour of the T12-2 and T12-3 samples.

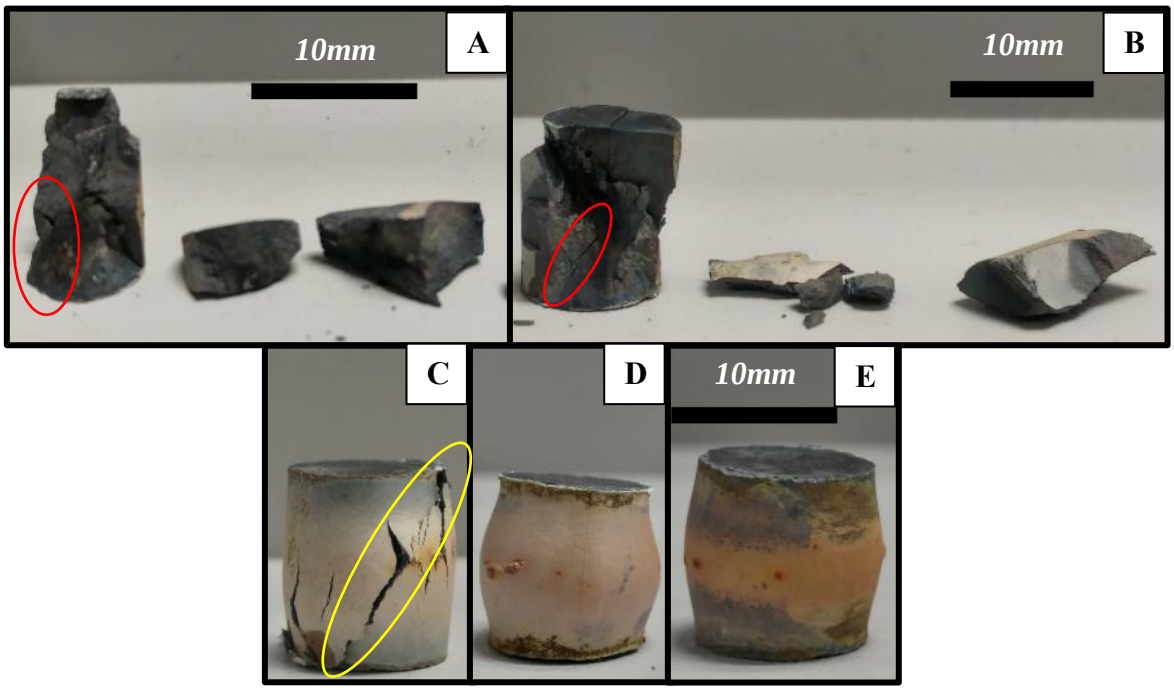

Figure 6.21: *Pictures of the Ti_3SiC_2 samples following their high temperature compression tests at 1200°C.* ***(a)*** *T12-0,* ***(b)*** *T12-1,* ***(c)*** *T12-2 (2B(2)),* ***(d)*** *T12-3,* ***(e)*** *T12-4. Red ellipse highlighting areas of very small cracks and the yellow ellipse highlighting the crack ~45° to the loading direction.*

6.4 The Effect of High Temperature Quenching on Deformation Mechanisms of MAX phases

As discussed in the literature review in Chapter 3, the properties of the MAX phases following thermal shock is of great interest when proposing their future use for potential applications. The high temperature quenching tests undertaken for this study have explored the effect of thermal shock under mechanical stress on both Ti_2AlC and Ti_3SiC_2 MAX phases. Two temperatures were chosen, 1000°C and 1200°C, to study the effects of quenching from different starting temperatures. These temperatures were chosen as previous studies have found areas of interest in the 1000-1200°C temperature region when quenching the MAX phases. The MAX phases studied for this work have previously been found to start exhibiting ductile behaviour and potential phase changes in this region[108]. The loading conditions proposed are also of interest when considering these MAX phases for use in high temperature applications, such as in aerospace components, where similar conditions could occur. The heating ramp before thermal shock and the quenching regime of the quenching tests can be found in *Figures 6.22-6.26* for the Ti_2AlC samples quenched at 1000°C and in *Figures 6.28-6.33* for those tested at 1200°C. The heating and quenching regimes for the Ti_3SiC_2 samples can be found in *Figure 6.35-6.39* for those tested at 1000°C and in *Figures 6.41-6.46* for those tested at 1200°C. The effect of thermal shock on the mechanical properties following each test has been explored in Section 6.4.3.

6.4.1 Ti_2AlC High Temperature Quenching Trials

The thermal profile of the Ti_2AlC samples thermally shocked at a starting temperature of 1000°C while subjected to a compressive stresses of either 0, 50, 150 or 200 MPa can be found in *Figures 6.22-6.26*. The strain was recorded as well as the heating and cooling regime to detect any effect the regime could have on the mechanical properties of the samples during each test. All samples were heated to 1000°C at a rate of 5°C/sec and maintained at this temperature for 2 minutes to attain equilibrium. Each sample was then rapidly cooled by quenching with air at a cooling rate of ~60°/sec.

Figures 6.28-6.33 show the thermal profile of the Ti_2AlC samples being subjected to thermal shock at a temperature of 1200°C under a compressive stress of between 0 and 200 MPa. The

heating and quenching rates were the same as those at 1000°C. For both the 1000°C and 1200°C quenching tests the cooling rate decreased as it got closer to room temperature. Upon the completion of the tests the temperature of the samples quenched from 1000°C was recorded as approximately 300°C and 400°C when quenched from 1200°C. After this point the samples air cooled to room temperature.

In *Figures 6.22-6.26* nothing of note was recorded during the heating regime of all of the samples quenched at 1000°C. All samples heated to 1000 successfully, while the strain only performed slightly differently for the Q10-S0 sample, which was recorded as at ~0.02 upon the completion of the heating of the sample, compared to the other samples which had a strain of between 0.03 and 0.04. Upon the application of compressive stresses, a general trend can be seen that the strain decreases with the reduction in temperature. The largest reduction in strain can be seen for the Q10-S200 sample, where the strain was recorded as ~0 at the end of the test. The strain profiles of each of the quenching regimes also show no major deviations from the standard curve.

The images of the samples after they were quenched at 1000°C can be found in *Figure 6.27*. As can be seen, the colouring of the samples are slightly different post quench, perhaps more of an indication of sample preparation rather than any consequences of the quench. Each sample remained intact when concurrently quenched and compressively stressed at this temperature.

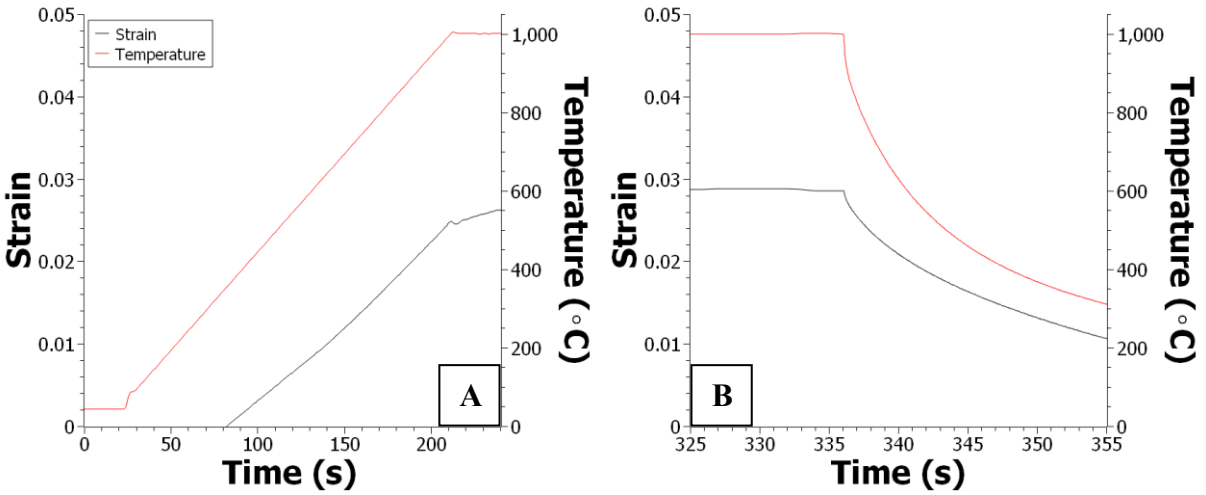

Figure 6.22: (a) *Heating and* ***(b)*** *quenching regime of a Ti_2AlC sample heated to 1000°C and then quenched under no load stress. Sample code: Q10-S0*

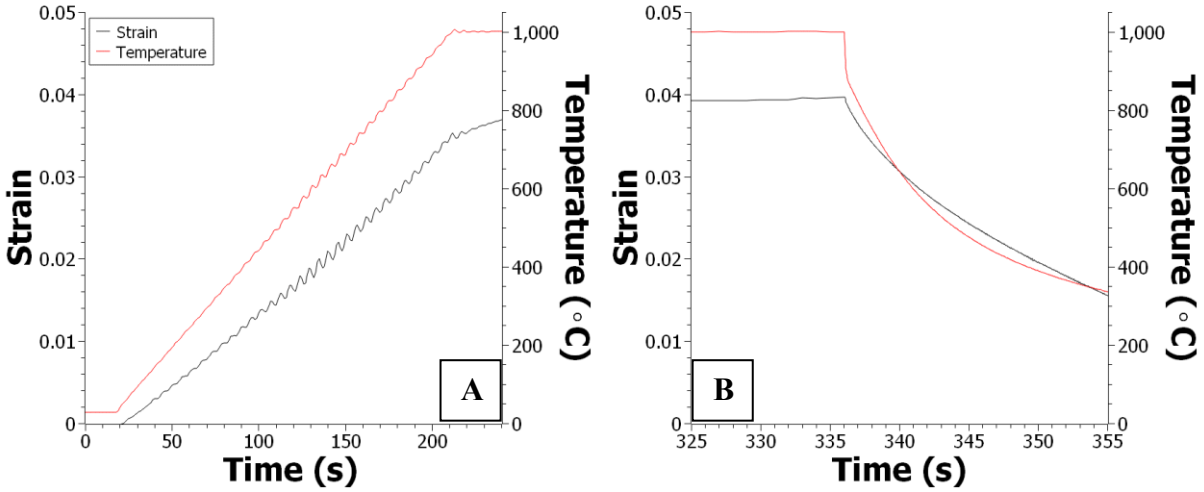

Figure 6.23: (a) *Heating and* ***(b)*** *quenching regime of a Ti_2AlC sample heated to 1000°C and then quenched under a load stress of 50MPa. Sample code: Q10-S50*

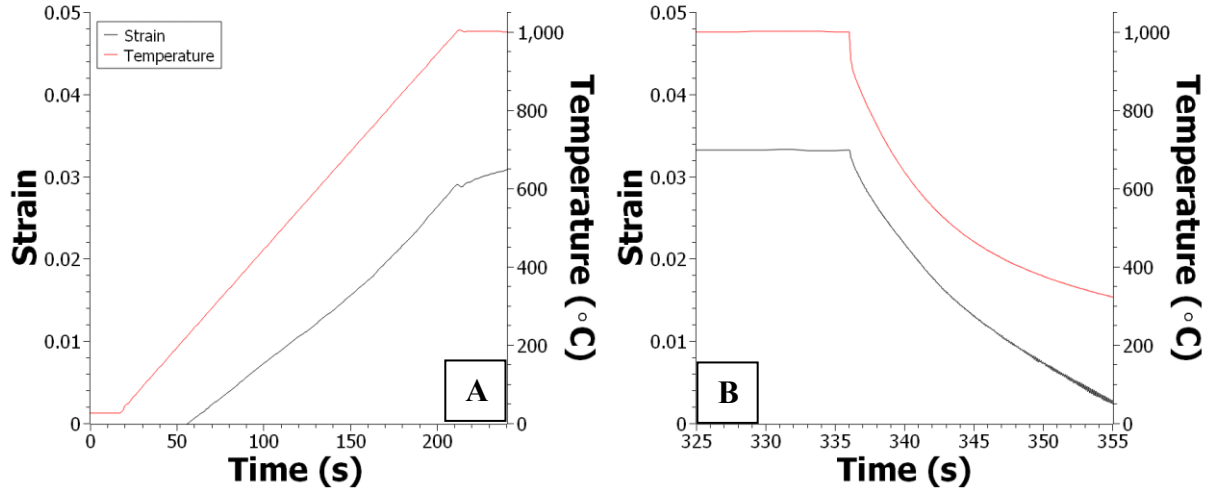

Figure 6.24: (a) *Heating and* ***(b)*** *quenching regime of a Ti_2AlC sample heated to 1000°C and then quenched under a load stress of 100MPa. Sample code: Q10-S100*

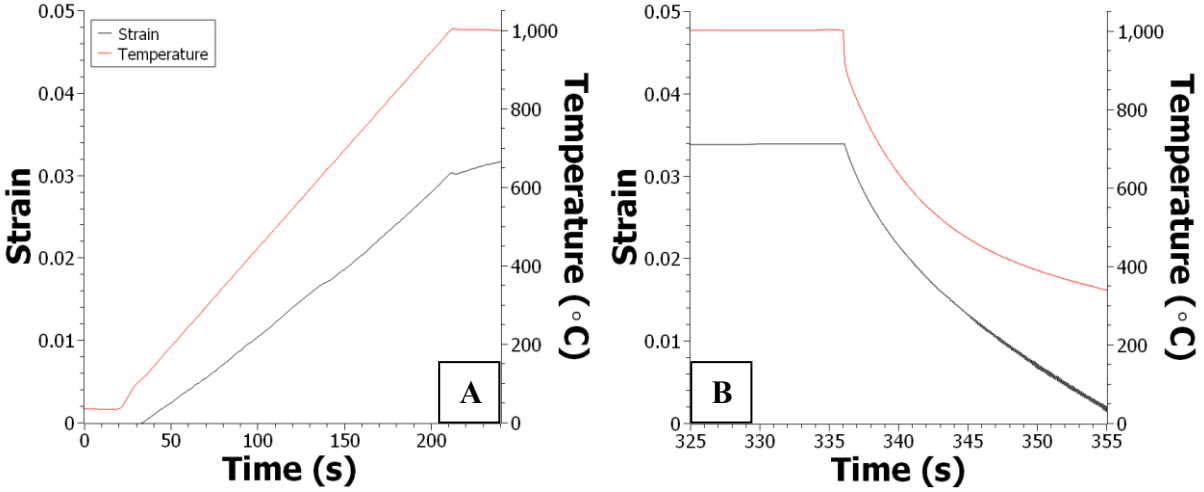

Figure 6.25: (a) *Heating and* ***(b)*** *quenching regime of a Ti_2AlC sample heated to 1000°C and then quenched under a load stress of 150MPa. Sample code: Q10-S150*

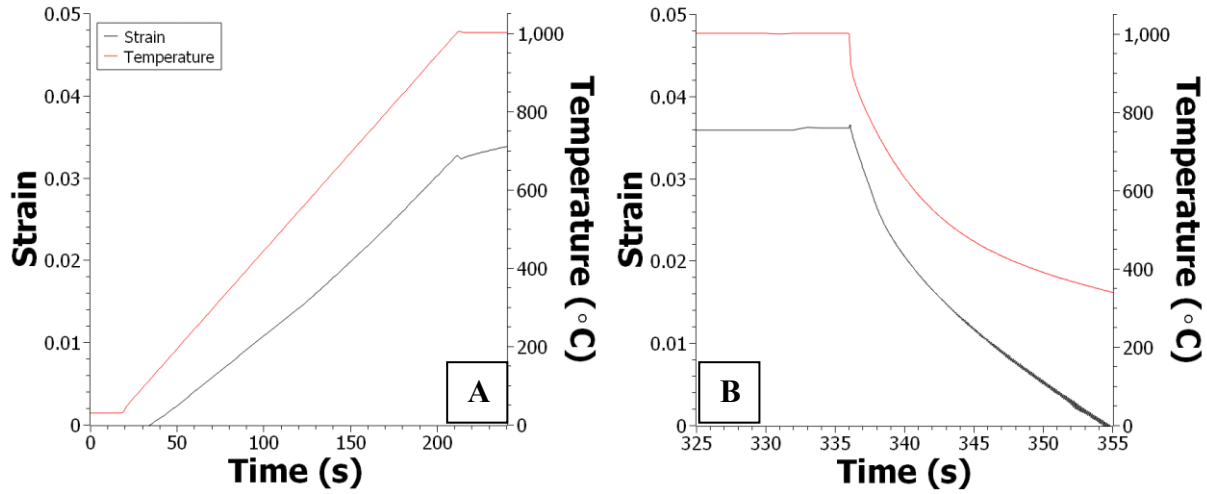

Figure 6.26: ***(a)*** *Heating and* ***(b)*** *quenching regime of a Ti_2AlC sample heated to 1000°C and then quenched under a load stress of 200MPa. Sample code: Q10-S200*

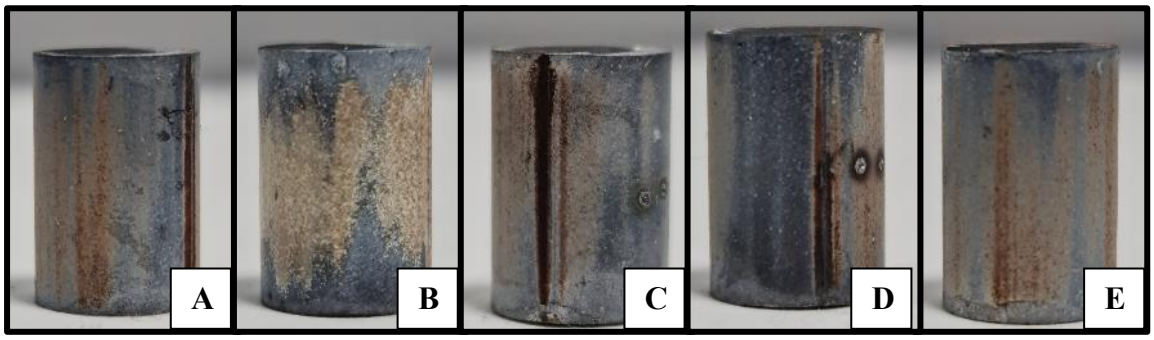

Figure 6.27: *Pictures of the Ti_2AlC samples thermally shocked at 1000°C:* ***(a)*** *Q10-S0,* ***(b)*** *Q10-S50,* ***(c)*** *Q10-S100,* ***(d)*** *Q10-S150,* ***(e)*** *Q10-S200.*

Figure 6.28 shows the temperature and strain profiles recorded during heating and quenching of sample Q12-S0, which was quenched from 1200°C with no load stress applied. Nothing of note is recorded when studying the strain slope in *Figure 6.28a*, although there is a slight change in the slope immediately after the cooling starts in *Figure 6.28b*. The sample was recorded as having a strain of ~0.025 at the completion of the test. As was discussed previously in the introduction to this section, the sample starts to cool at the previously set cooling rate of 60°C/sec until ~700°C, when the cooling rate decreases. This decrease in the cooling rate means that the final recorded temperature for the sample at end of the test was ~425°C.

More Ti_2AlC samples were then subjected to similar heating and quenching cycles in the Gleeble. These samples were quenched under a compressive stress of either 50, 100, 150 or 200 MPa. *Figures 6.29-6.33* show the results of these tests and, in general, a trend can be seen that the strain decreases with the reduction in temperature, potentially due to the application of

the additional loads. The Q12-S200 sample witnesses the greatest reduction in strain from the beginning of its quenching regime, with a final strain recorded of ~0.007.

Small changes in the strain slope can be seen for each sample at approximately 1000°C as the sample is quenched, as indicated by the green ellipse in *Figures 6.29-6.33*. This could be an indication of the brittle-to-ductile transition temperature (BDTT) for the Ti_2AlC MAX phase that was proposed by Zhou *et al* [20]. They found that the temperature where the deformation mechanism changes was approximately 1050°C. This type of reaction to quenching from high temperature was previously witnessed by Adamaki *et al* where they surmised that due to the availability and mobility of dislocation systems such as cavities formation, grain rotation and intergranular sliding at high temperatures, the deformation can occur more plastically [108]. The absence of this feature from the 1000°C quench tests could be further evidence of the transition temperature in action during the higher temperature quenching from 1200°C.

Unlike the samples quenched at 1000°C, 2 of the samples tested at 1200°C under the higher stress conditions did start to crack on the outside surface. These samples were the only quenched samples to exhibit any form of obvious deformation and can be found in *Figure 6.34* The cracked parts are highlighted with a red ellipse. All other Ti_2AlC samples subjected to this type of quenching regime remained intact following their tests.

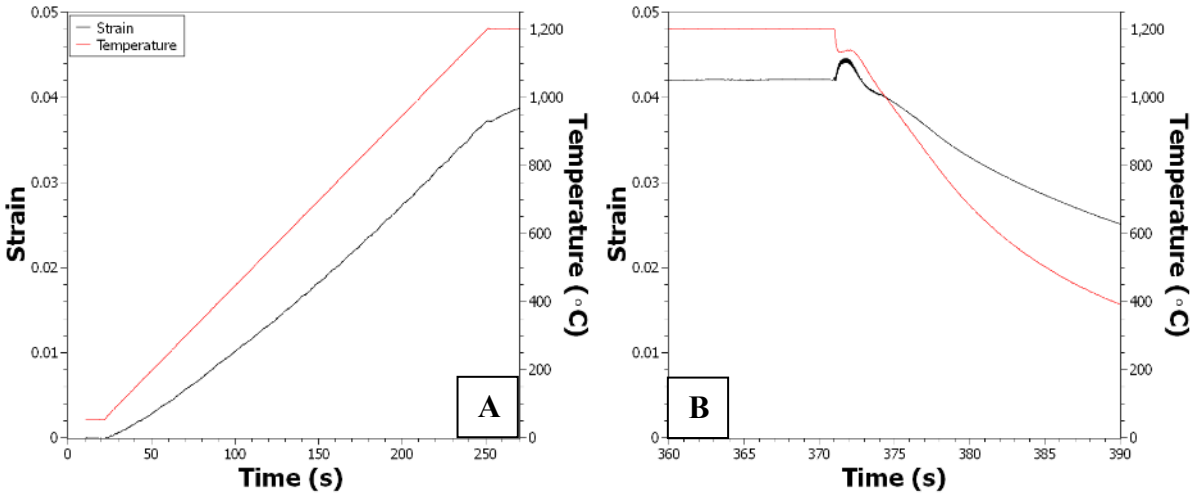

Figure 6.28: (a) *Heating and* ***(b)*** *quenching regime of a Ti_2AlC sample heated to 1200°C and then quenched under no load stress. Sample code: Q12-S0*

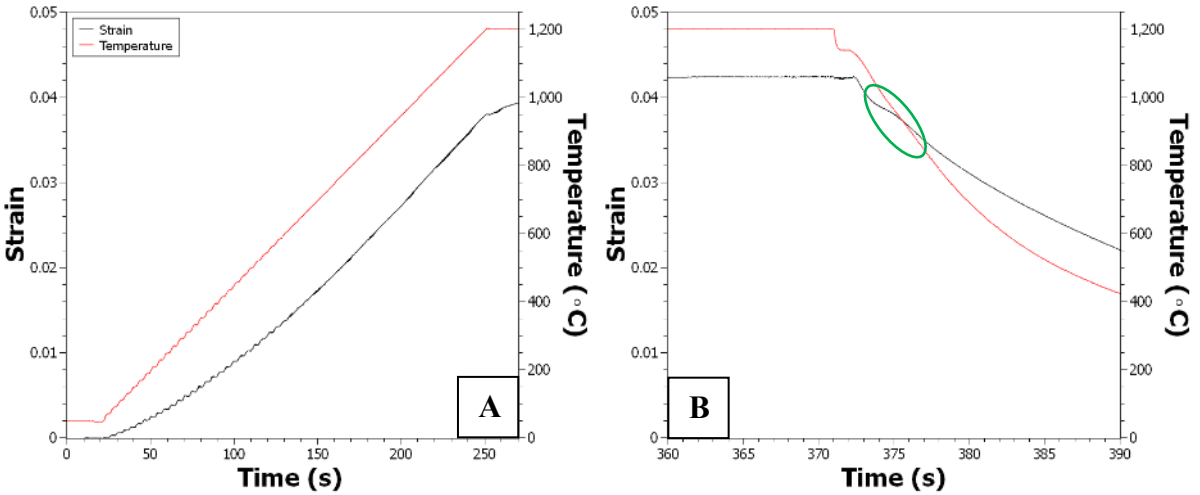

Figure 6.29: (a) *Heating and* ***(b)*** *quenching regime of a Ti_2AlC sample heated to 1200°C and then quenched under a compressive load stress of 50MPa. Sample code: Q12-S50*

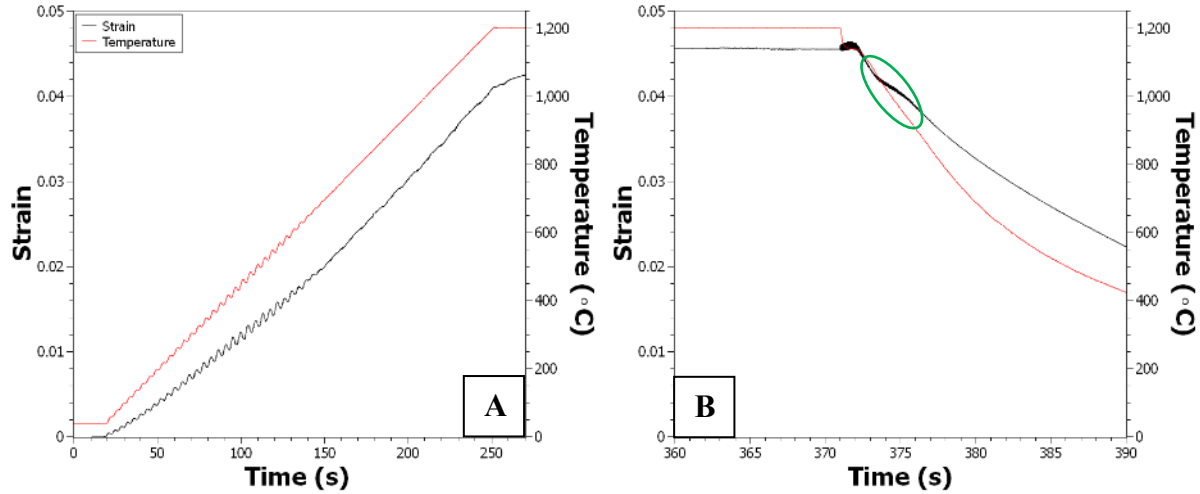

Figure 6.30: (a) *Heating and* ***(b)*** *quenching regime of a Ti_2AlC sample heated to 1200°C and then quenched under a load stress of 100MPa. Sample code: Q12-S100a*

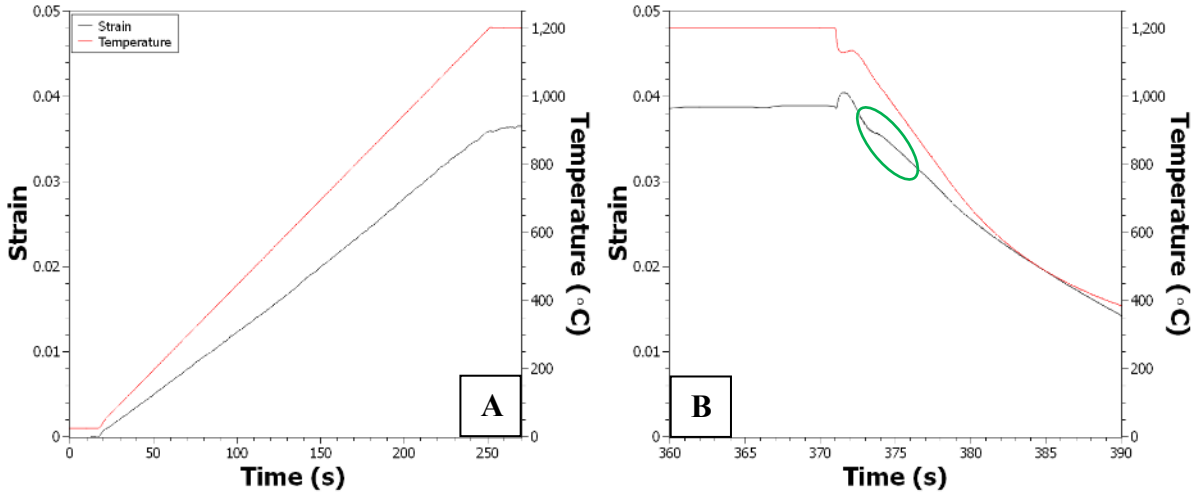

Figure 6.31: (a) *Heating and* ***(b)*** *quenching regime of a Ti_2AlC sample heated to 1200°C and then quenched under a load stress of 100MPa. Sample code: Q12-S100b*

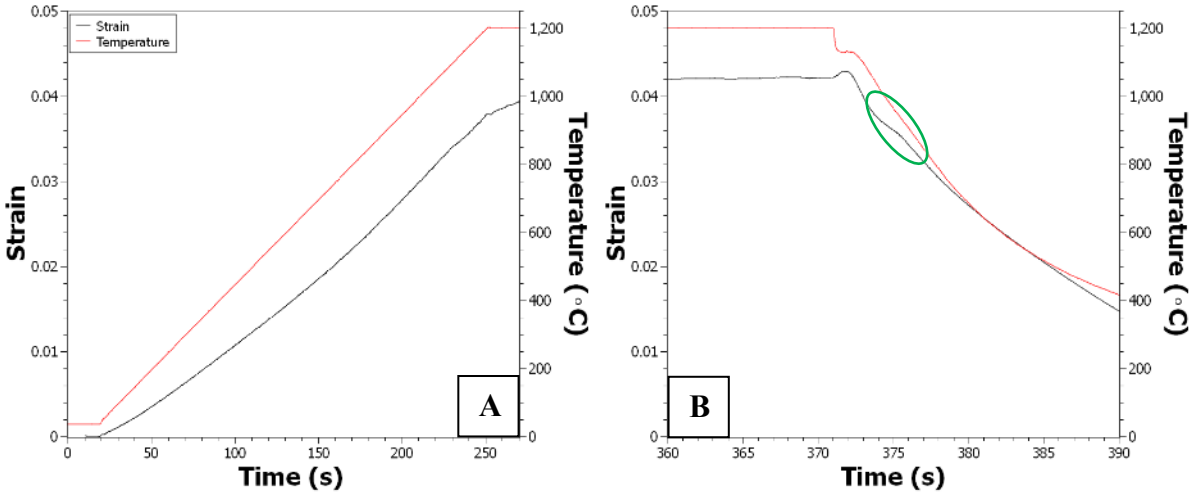

Figure 6.32: ***(a)*** *Heating and* ***(b)*** *quenching regime of a Ti_2AlC sample heated to 1200°C and then quenched under a load stress of 150MPa. Sample code: Q12-S150*

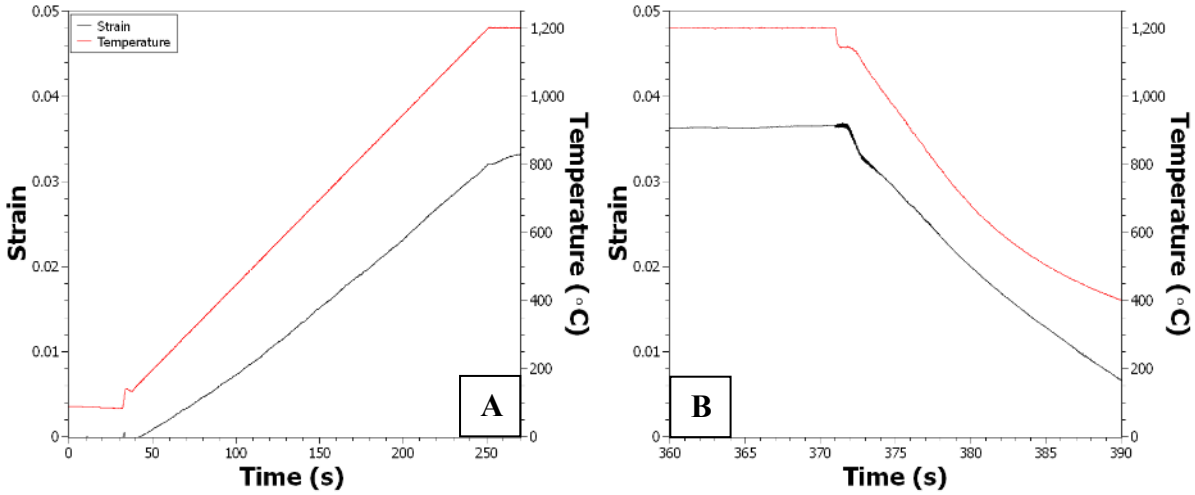

Figure 6.33: ***(a)*** *Heating and* ***(b)*** *quenching regime of a Ti_2AlC sample heated to 1200°C and then quenched under a load stress of 200MPa. Sample code: Q12-S200*

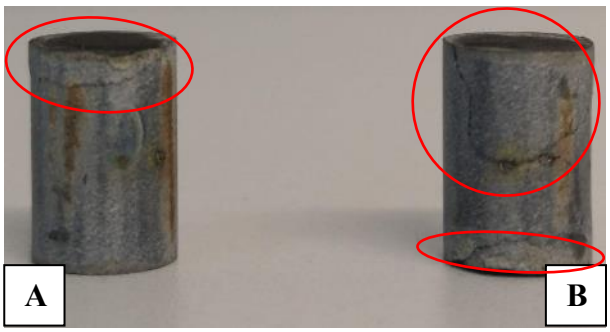

Figure 6.34: *The only samples tested under quench and load conditions to show any form of failure.* ***(a)*** *Q12-S150b* ***(b)*** *Q12-S200b. Cracked parts highlighted with red ellipse*

6.4.2 Ti_3SiC_2 High Temperature Quenching Trials

The Ti_3SiC_2 MAX phase samples were also thermally shocked from the two different temperatures of 1000°C and 1200°C while concurrently being subjected to compressive stresses of between 0 and 200 MPa.

The thermal and strain profile of the samples tested at 1000°C can be found in *Figures 6.35-6.39*. Each sample had a very similar heating regime to the target temperature and were all found to have quenched to ~400°C by the end of the 20 seconds of quenching. The strains recorded for each sample at the end of the heating regime was within a range of between 0.03 and 0.04 strain.

The quenching regime of Q10-S0, the sample subjected to no compressive stresses, can be found in *Figure 6.35b.* The strain profile of this sample does not see any major features, with the test finishing with the strain recorded as ~0.02. The strain slope on the Q10-S50 sample does show some changes, as highlighted by the green ellipse in *Figure 6.36.* A similar feature was also found in *Figure 6.39,* also highlighted by a green ellipse. These changes in strain could be an indication of a phase change or a change in deformation mechanism [108]. With the exception of the Q10-S150 sample, a general trend of a greater reduction in strain with increasing compressive stress can be seen.

The images of the Ti_3SiC_2 MAX phase samples following thermal shock can be found in *Figure 6.40*. Most of the samples have a similar appearance to each other, with the only exception being the Q10-S200 sample which has a small crack on the outer surface, as shown by the red ellipse in *Figure 6.36e.*

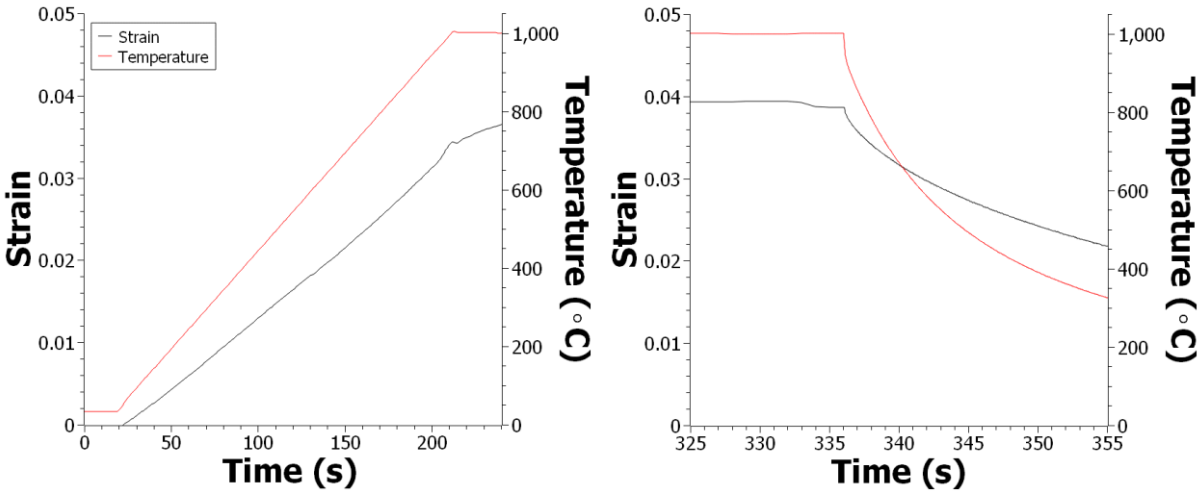

Figure 6.35: (a) *Heating and* ***(b)*** *quenching regime of a Ti_3SiC_2 sample heated to 1000°C and then quenched under no load stress. Sample code: Q10-S0*

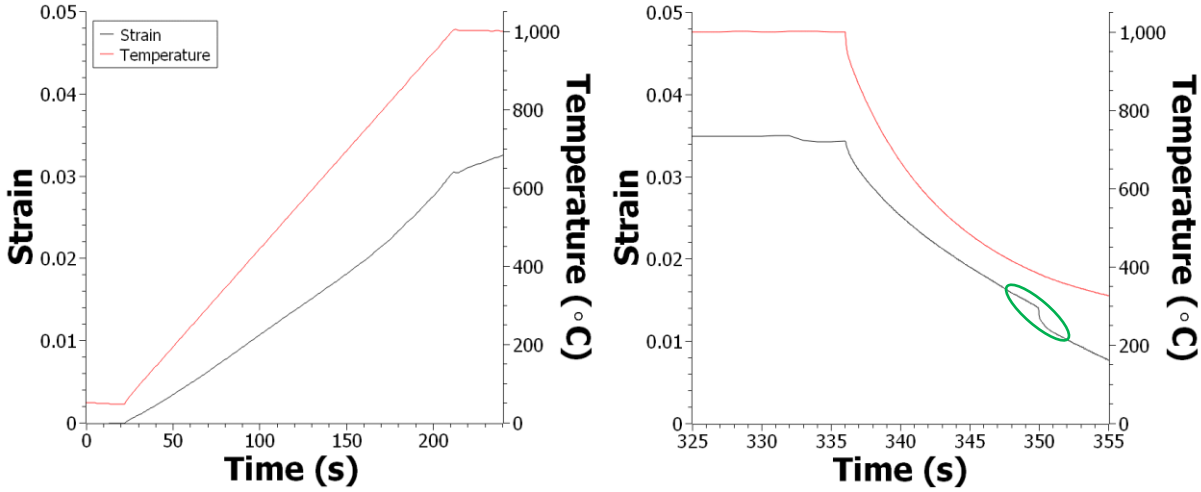

Figure 6.36: (a) *Heating and* ***(b)*** *quenching regime of a Ti_3SiC_2 sample heated to 1000°C and then quenched under a load stress of 50MPa. Sample code: Q10-S50*

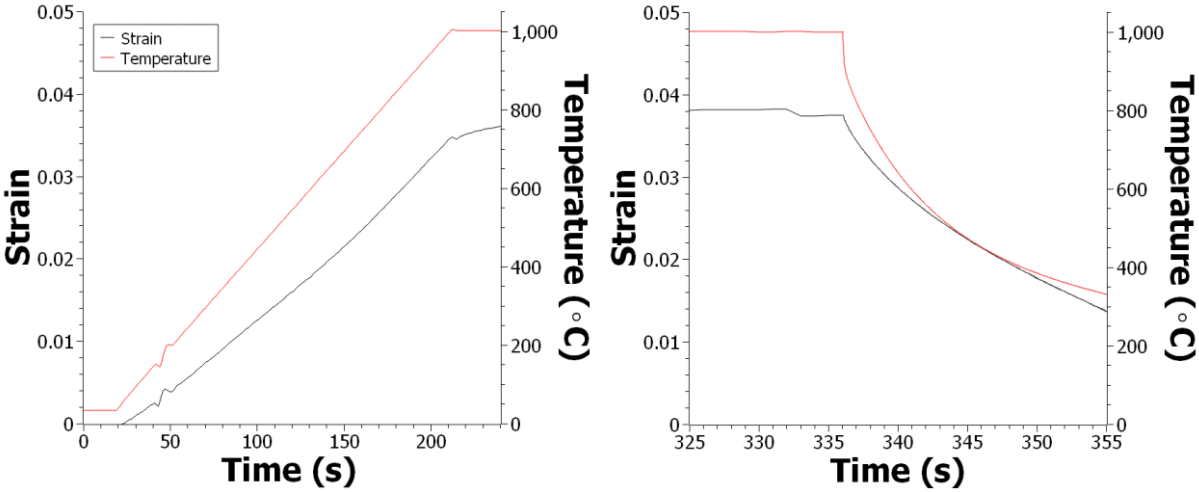

Figure 6.37: (a) *Heating and* ***(b)*** *quenching regime of a Ti_3SiC_2 sample heated to 1000°C and then quenched under a load stress of 100MPa. Sample code: Q10-S100*

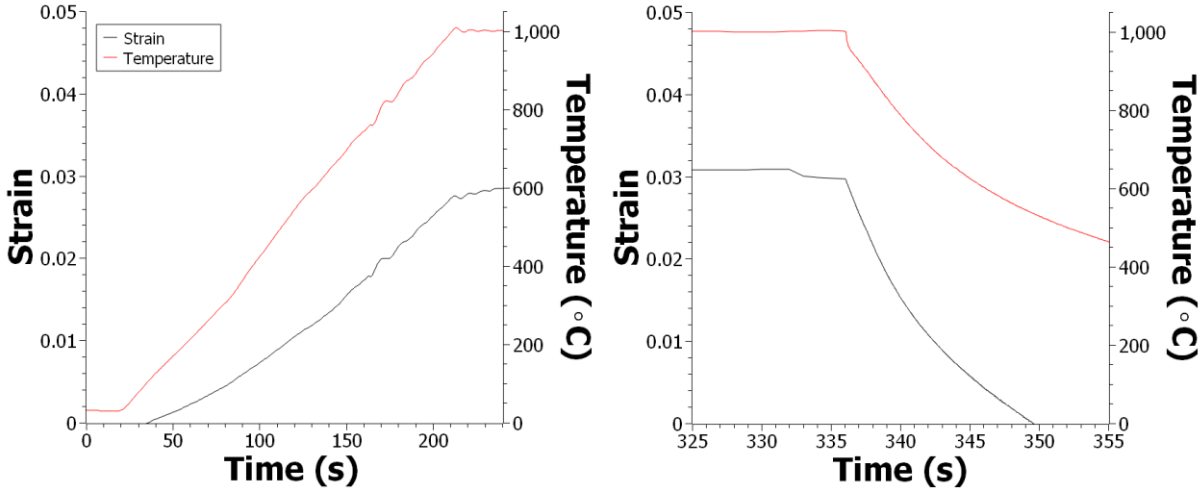

Figure 6.38: ***(a)*** *Heating and* ***(b)*** *quenching regime of a Ti_3SiC_2 sample heated to 1000°C and then quenched under a load stress of 150MPa. Sample code: Q10-S150*

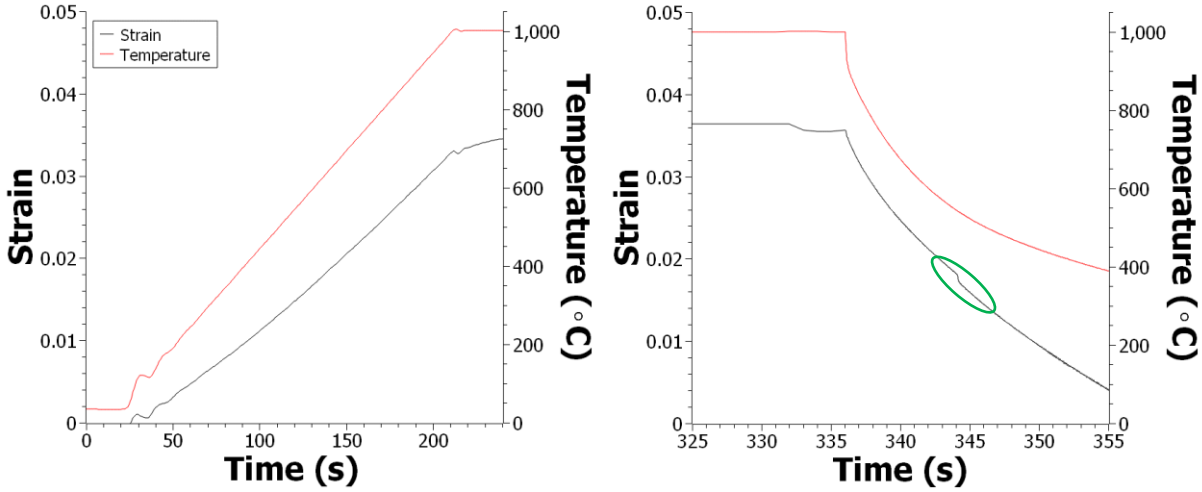

Figure 6.39: ***(a)*** *Heating and* ***(b)*** *quenching regime of a Ti_3SiC_2 sample heated to 1000°C and then quenched under a load stress of 200MPa. Sample code: Q10-S200*

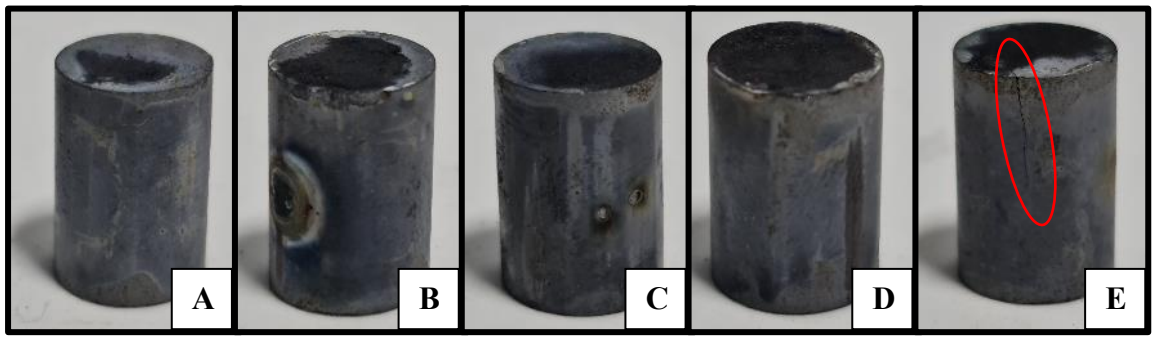

Figure 6.40: *Pictures of the Ti_3SiC_2 samples thermally shocked at 1000°C:* ***(a)*** *Q10-S0,* ***(b)*** *Q10-S50,* ***(c)*** *Q10-S100,* ***(d)*** *Q10-S150,* ***(e)*** *Q10-S200.*

The thermal profile of the Ti_3SiC_2 samples subjected to thermal shock at 1200°C while under the compressive load stress of either 0, 50 or 100 MPa can be found in *Figure 6.41-6.45*. While quench tests under a compressive stress of 150 MPa and 200 MPa were also carried out, the thermocouple detached upon the application of the stress. Despite this, the strain data was recorded as the samples completed their 20 seconds of quenching from 1200°C and these can be found in *Figures 6.44 and 6.45.*

When comparing the Ti_3SiC_2 MAX phase with that of the Ti_2AlC MAX phase under the highest loads at this temperature, the same general trend of strain decreasing with the reduction in temperature was also witnessed for this MAX phase alloy, once again this could be explained by the application of the additional stresses. The final strain recorded for the samples quenched while stressed at 150 MPa and 200 MPa was noticeably lower than the lower stressed samples, giving a final strain for both samples of ~0.015.

Like their Ti_2AlC MAX phase counterparts, the strain slopes for the Ti_3SiC_2 MAX phase are generally free from any noticeable features during the heating stage up to 1200°C. The strain slopes in the cooling stage do show some small changes, as highlighted by the green ellipses on *Figures 6.41 and 6.43*. These could be, as was expected for the Ti_2AlC sample, an indication of the BDTT deformation mechanism. In thermal shock tests undertaken by El-Raghy *et al*, they believed that the BDTT for Ti_3SiC_2 occurred at ~1200°C. They surmised that this transition was attributable to one of two sources: (i) activation of a new, not yet determined slip system in the Ti_3SiC_2 phase, in addition to slip on the basal planes; or (ii) an increase in the ease of kinking and accompanying lattice rotation of individual grains as a result of thermal activation [89].

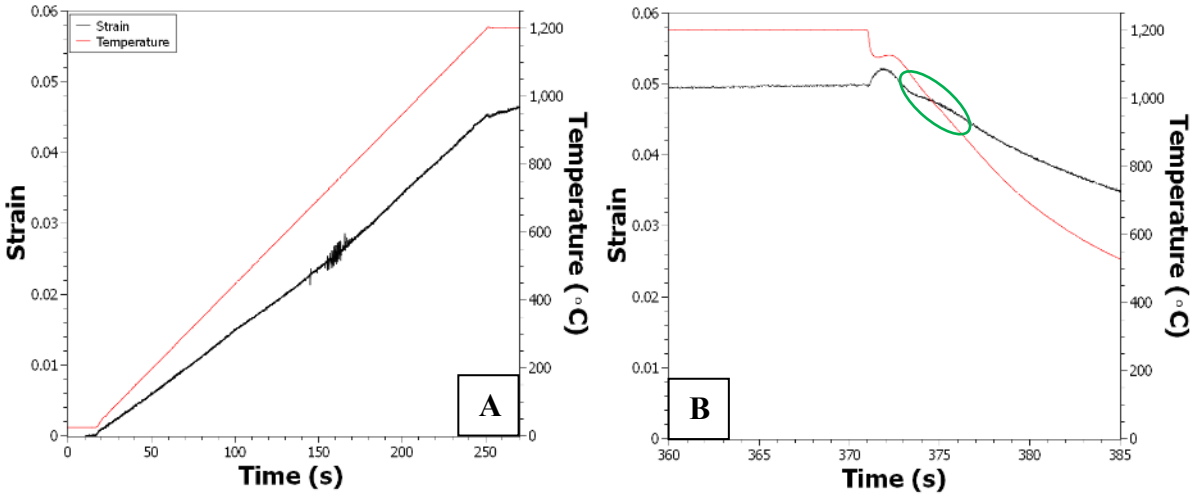

Figure 6.41: (a) *Heating and* ***(b)*** *quenching regime of a Ti_3SiC_2 sample heated to 1200°C and then quenched under no load stress. Sample code: Q12-S0*

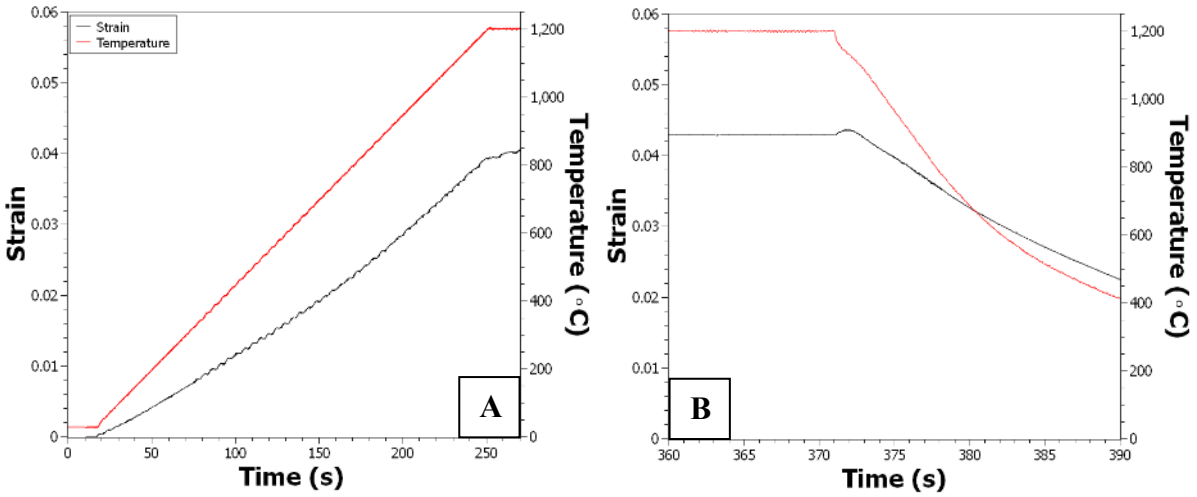

Figure 6.42: (a) *Heating and* ***(b)*** *quenching regime of a Ti_3SiC_2 sample heated to 1200°C and then quenched under a load stress of 50MPa. Sample code: Q12-S50*

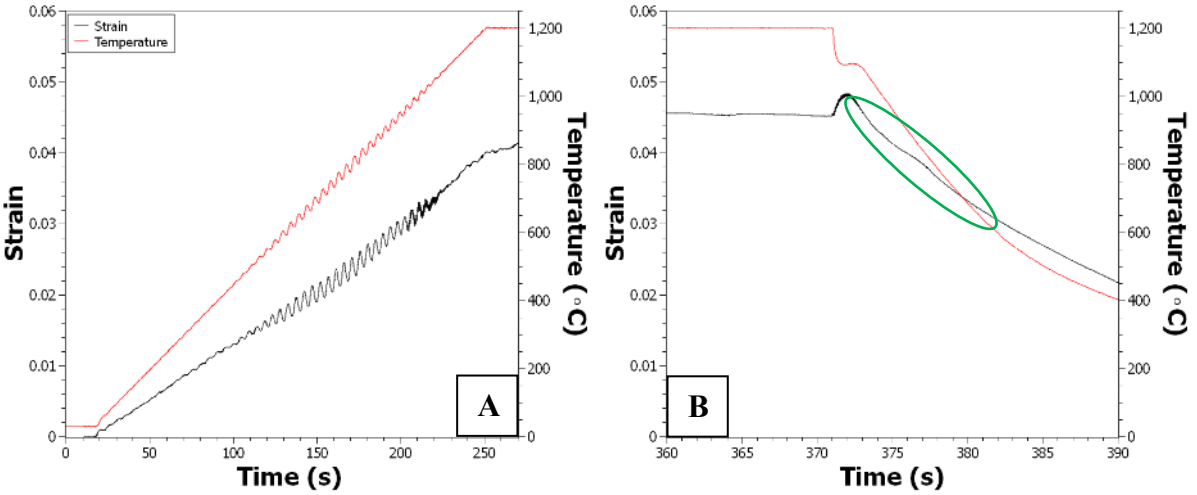

Figure 6.43: (a) *Heating and* ***(b)*** *quenching regime of a Ti_3SiC_2 sample heated to 1200°C and then quenched under a load stress of 100MPa. Sample code: Q12-S100*

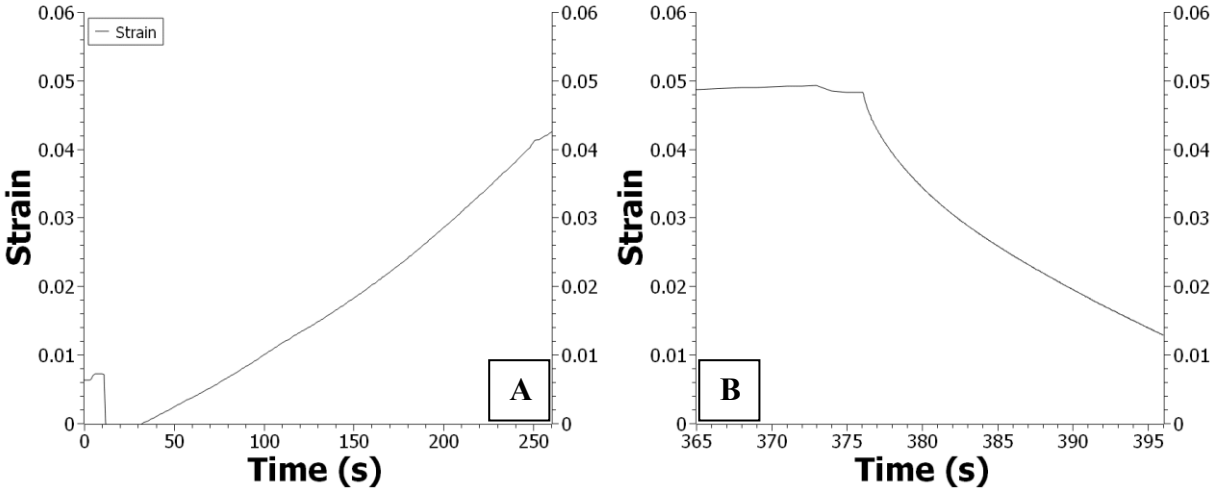

Figure 6.44: *Strain profile of the* ***(a)*** *Heating and* ***(b)*** *quenching regime of a Ti_3SiC_2 sample heated to 1200°C and then quenched under a load stress of 150MPa. Sample code: Q12-S150*

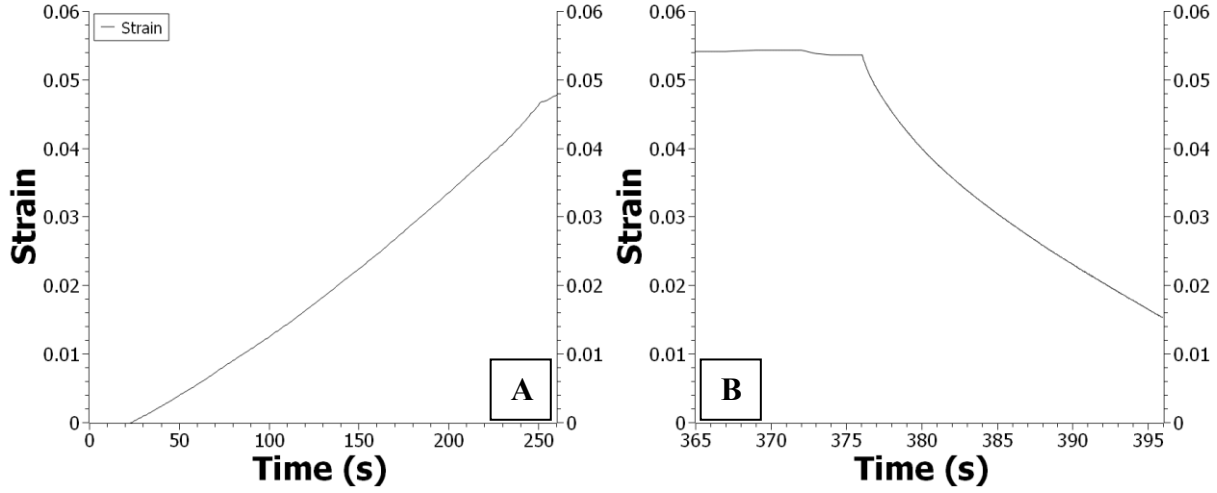

Figure 6.45: *Strain profile of the* ***(a)*** *Heating and* ***(b)*** *quenching regime of a Ti_3SiC_2 sample heated to 1200°C and then quenched under a load stress of 200MPa. Sample code: Q12-S200*

6.4.3 Mechanical Properties of Ti_2AlC and Ti_3SiC_2 MAX phases following Thermal Shock

To better understand the effect of thermal shock on the mechanical properties of the Ti_2AlC and Ti_3SiC_2 MAX phases, Room Temperature compression tests were performed on the samples following their subjection to thermal shock. All of these room temperature compression tests were carried out at a strain rate of 1/s.

The stress-strain graphs for the Ti_2AlC samples quenched at 1000°C can be found in *Figure 6.46*, with the mechanical properties derived from this data shown in *Table 6.14*. With the exception of the Q10-S100 sample, a general trend of the ultimate compressive stress increasing with the increase in compressive load stress when quenching was found. This could suggest that the thermal shock conditions might have an effect on the ultimate compressive stress of the Ti_2AlC mechanical properties at this temperature. As previously stated, the only outlier was the stress recorded for the Q10-S100 sample, which at -323.49 MPa was significantly lower than the stress recorded for Q10-S0 at -384.13 MPa. A short period of further compression followed after the UCS before all samples failed catastrophically at 3-4.5% compression.

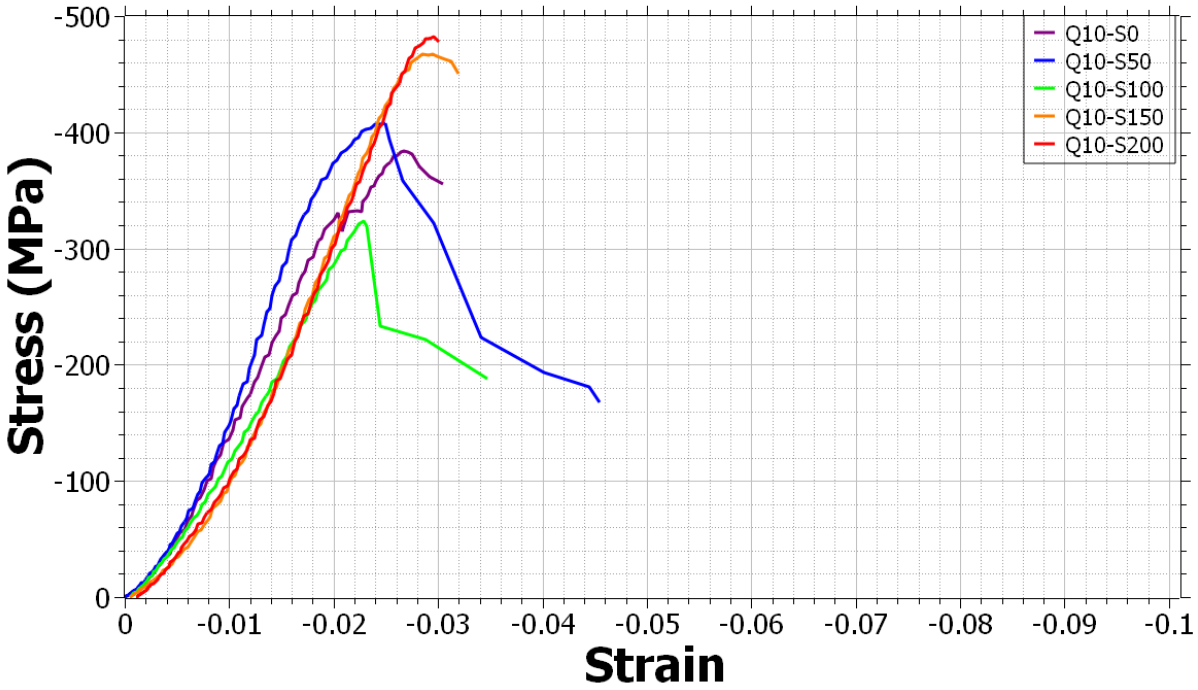

Figure 6.46: *Graph showing the stress-strain curves for the Ti_2AlC samples tested at room temperature and under strain rate of 1/s*

Table 6.14: *Room Temperature Mechanical Properties of quenched Ti_2AlC samples*

Test	Ultimate Comp Stress (MPa)	Young's Modulus (GPa)	Yield Stress (MPa) (0.02 Proof Stress)	Compression (%)
Q10-S0	-384.13	15.86137	-	-3.53006
Q10-S50	-408.21	18.76624	-	-4.48361
Q10-100	-323.49	14.88348	-	-3.46793
Q10-150	-467.31	17.64753	-	-3.19633
Q10-200	-482.4	18.01693	-	-3.01051

The images of the Ti_2AlC samples quenched at 1000°C following their room temperature compression tests can be found in *Figure 6.47.* Like the samples tested at faster strain rates at all temperatures that were not quenched, a 45° crack through the sample can be seen. The obvious lack of any plastic deformation is also apparent. Small cracks emanating from this large crack can also be seen, especially in the sample quenched while being subjected to a compressive stress of 200 MPa.

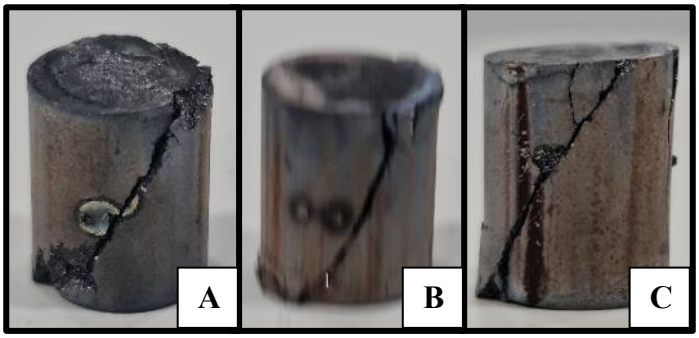

Figure 6.47: *Pictures of the Ti_2AlC samples thermally shocked at 1000°C following their room temperature compression tests.* ***(a)*** *Q10-S0,* ***(b)*** *Q10-S100,* ***(c)*** *Q10-S200*

The stress-strain graphs for the Ti_2AlC samples quenched at 1200°C can be found in *Figure 6.48,* while the mechanical properties derived from this data can be found in *Table 6.15.* The ultimate compressive stress of all of the samples falls within a 50 MPa range of between -390 to -420 MPa, suggesting thermally shocking Ti_2AlC from 1200°C does not have a significant effect on this aspect of the MAX phases mechanical properties. The UCS of the samples tested was generally followed by a short period of further compression before the ultimate failure of the samples, with the compression generally being around 5%.

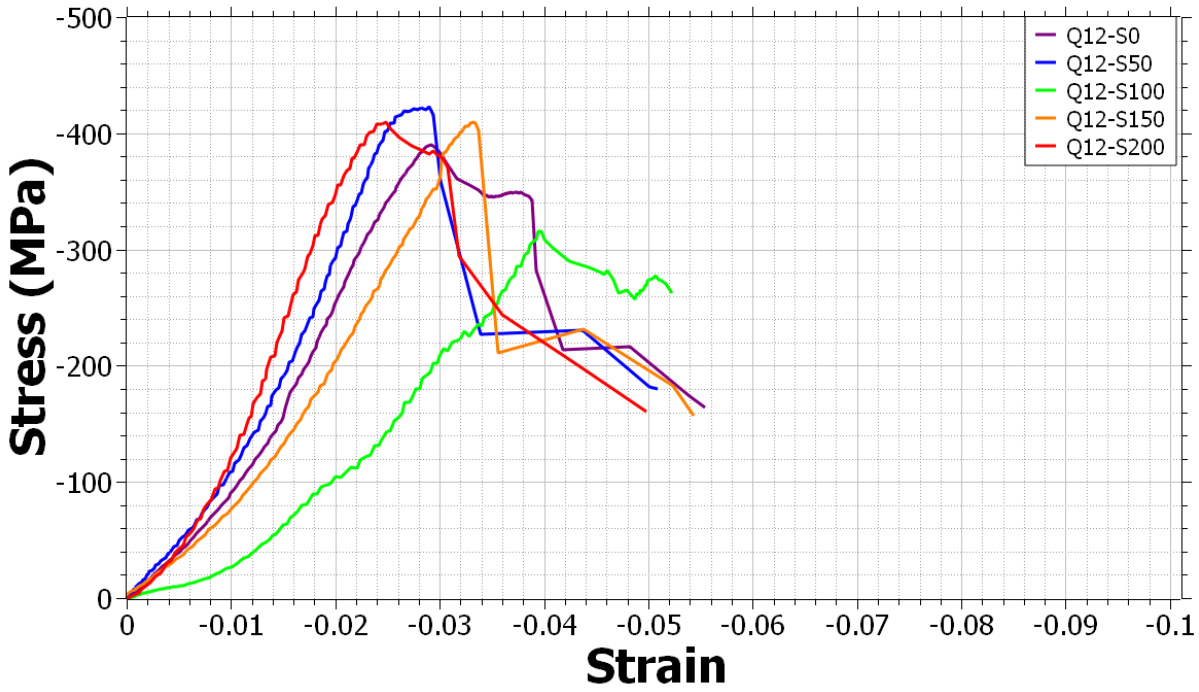

Figure 6.48: *Graph showing the stress-strain curves for the Ti_2AlC samples tested at room temperature and under strain rate of 1/s*

Table 6.15: *Room Temperature Mechanical Properties of quenched Ti_2AlC samples*

Test	Ultimate Comp Stress (MPa)	Young's Modulus (GPa)	Yield Stress (MPa) (0.02 Proof Stress)	Compression (%)
Q12-S0	-390.31	9.34	-380.37	-5.55
Q12-S50	-422.49	15.56	-422.27	-5.09
Q12-100	-315.66	7.99	312.22	-5.1
Q12-150	-409.42	12.90	-397.34	-5.43
Q12-200	-409.85	19.14	-400.12	-4.9

Figure 6.49 shows the images taken of the quenched Ti_2AlC samples following the compression tests. Like the samples quenched at 1000°C, these images generally portray a similar picture to the one seen in the samples tested at the faster strain rates at all temperatures that were not quenched, namely the 45° crack through the sample and the lack of any form of plastic deformation. The 45° crack feature is particularly prevalent in the samples subjected to higher stresses upon quenching: Q12-S150 and Q12-S200. The samples that were quenched at lower stresses perform slightly different in that there are two 45° cracks on the surface of those samples.

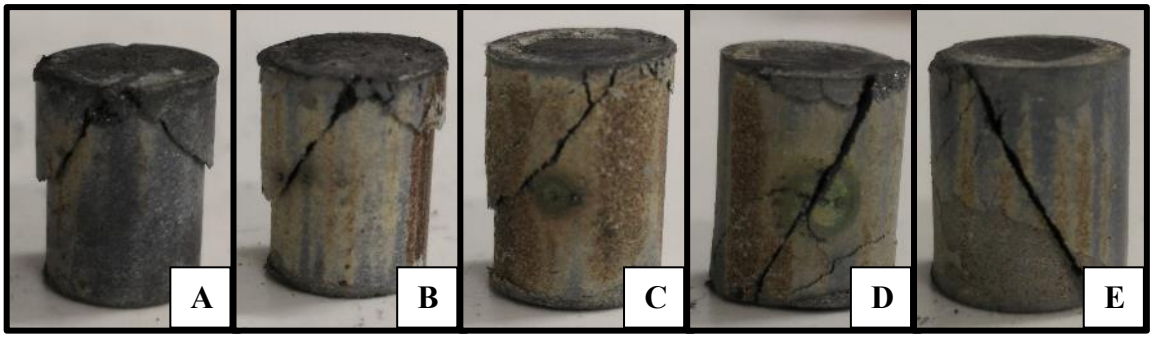

Figure 6.49: *Pictures of the Ti_2AlC samples thermally shocked at 1000°C following their room temperature compression tests.* ***(a)*** *Q12-S0,* ***(b)*** *Q12-S50,* ***(c)*** *Q12-S100,* ***(d)*** *Q12-S150,* ***(e)*** *Q12-S200.*

Figure 6.50 shows the stress-strain curves of the Ti_3SiC_2 compression tested at room temperature following their quenching at 1000°C. The mechanical results derived from this data has been outlined in *Table 6.16.* A non-linear elastic region is evident from the Q10-S0, Q10-S100 and Q10-S150 samples. These samples, together with the Q10-S50 sample, have a ultimate compressive stress of between -317 and -367 MPa, with the Q10-200 sample showing a significantly higher UCS of -568 MPa. With the exception of the Q10-S50 sample, all samples fractured catastrophically at their UCS points.

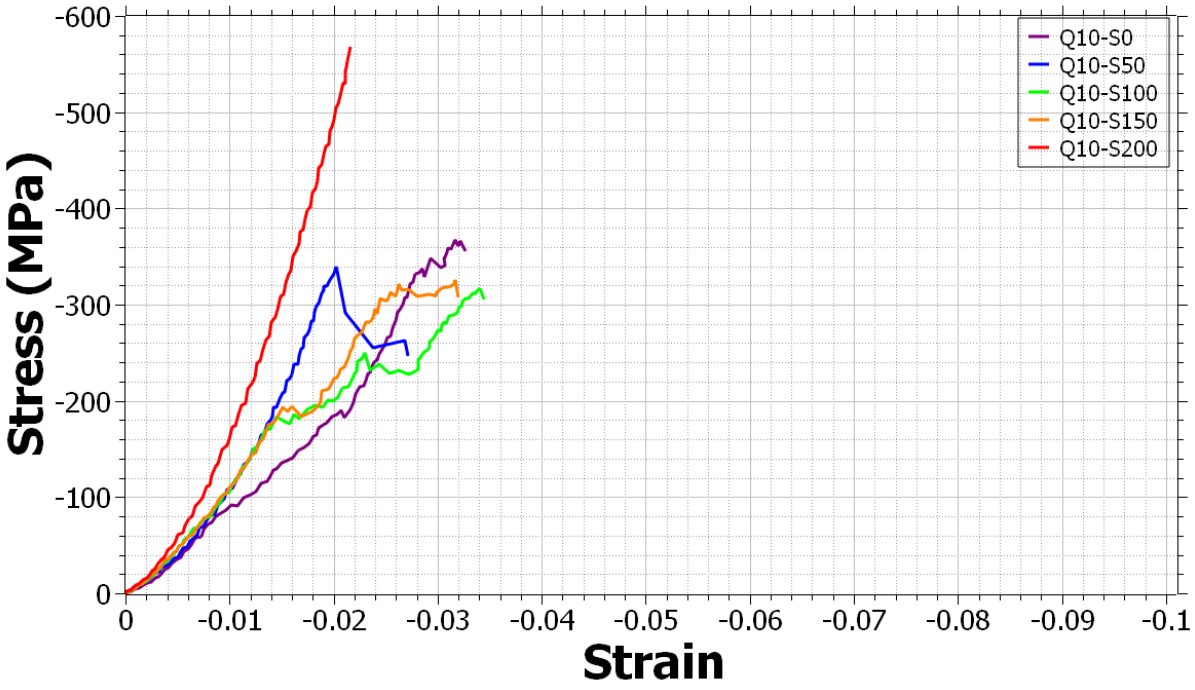

Figure 6.50: *Graph showing the stress-strain curves for the Ti_3SiC2 samples tested at room temperature and under strain rate of 1/s*

Table 6.16: *Room Temperature Mechanical Properties of quenched Ti_3SiC2 samples*

Test	Ultimate Comp Stress (MPa)	Young's Modulus (GPa)	Yield Stress (MPa) (0.02 Proof Stress)	Compression (%)
Q10-S0	-366.977	11.80281	-	-3.2728
Q10-S50	-339.391	16.07306	-	-2.91252
Q10-100	-317.397	9.050698	-	-3.44257
Q10-150	-325.305	11.3407	-	-3.19555
Q10-200	-568.418	26.68414	-	-2.16412

Figure 6.51 shows the images of room temperature compression tested Ti_3SiC_2 samples which were quenched at 1000°C. Like those seen in the quenched Ti_2AlC samples, the images are very similar to those seen when conducting high strain rate tests at both room and high temperature. All samples were found to disintegrate upon failure, once again indicating the brittle nature of these ceramics at room temperature. Of note is the almost ripple like features that can be found macroscopically on the fracture surface of the Q10-S0 and Q10-S100 samples, as highlighted by the red ellipses.

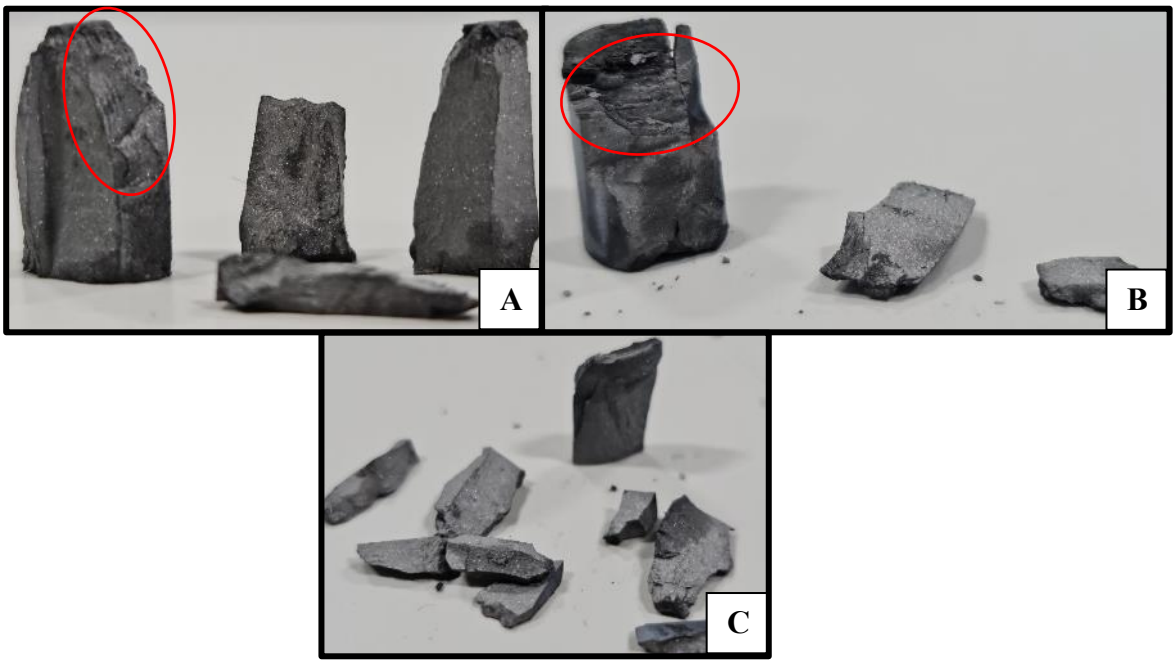

Figure 6.51: *Pictures of the thermally shocked Ti_3SiC2 samples following their room temperature compression tests.* ***(a)*** *Q10-S0,* ***(b)*** *Q10-S100,* ***(c)*** *Q10-S200*

The stress-strain curves for the Ti_3SiC_2 samples are shown in *Figure 6.52. Table 6.17* shows the mechanical data derived from this stress-strain data. The ultimate compressive stresses of each sample falls between 310 and 440 MPa, showing a larger range than that seen in Ti_2AlC. The highest UCS recorded, -441.58 MPa, was for the sample subjected to a stress of 50 MPa when being quenched, with the lowest being that of the sample that was quenched under a stress of 100 MPa. The sample that wasn't subjected to any stress upon quenching behaved slightly differently in that its UCS occurred following a period of yielding. All samples fractured at their UCS points. The Young's Modulus for Q12-S50 was calculated as being double that of both Q12-SO and Q12-S100. Apart from the Q12-S150 sample, each sample was noted to have a nonlinear elastic regime before failing abruptly at the peak stresses.

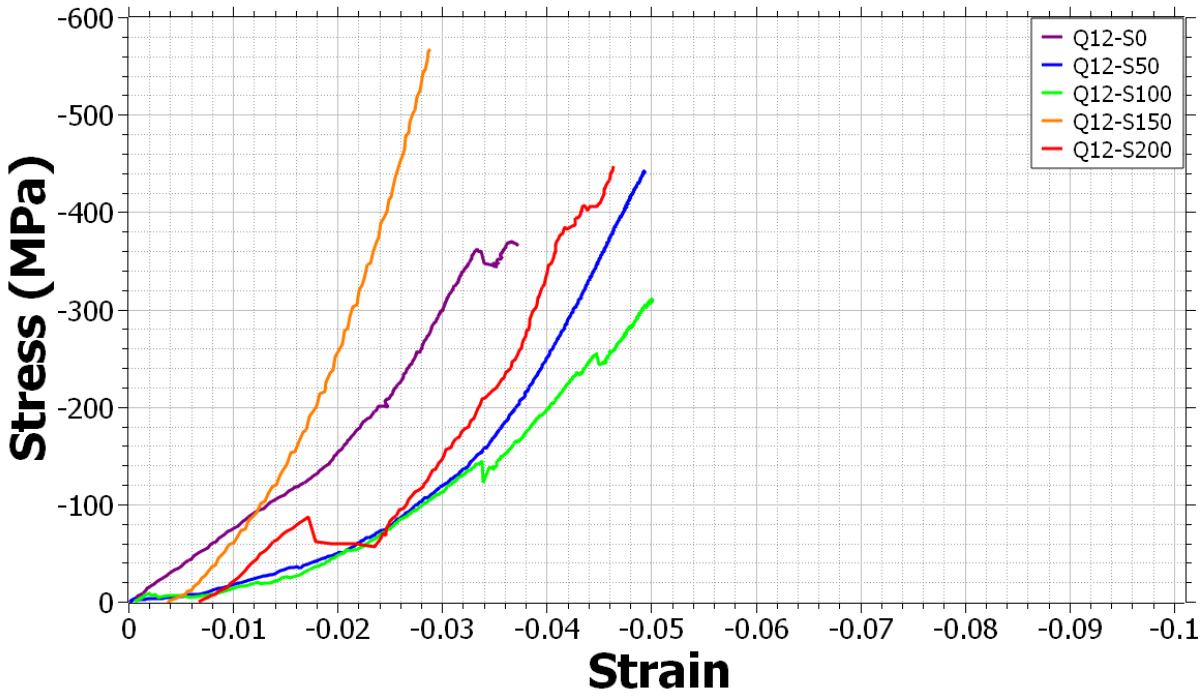

Figure 6.52: *Graph showing the stress-strain curves for the Ti_3SiC2 samples tested at room temperature and under strain rate of 1/s*

Table 6.17: *Room Temperature Mechanical Properties of quenched Ti_3SiC_2 samples*

Test	Ultimate Comp Stress (MPa)	Young's Modulus (GPa)	Yield Stress (MPa) (0.02 Proof Stress)	Compression (%)
Q12-S0	-404.38	10.14	-347.70	-5.01
Q12-S50	-441.58	19.66	-	-4.94
Q12-S100	-310.45	10.14	-	-5.00
Q12-S150	-567.39	22.68	-	-2.85
Q12-S200	-446.74	17.10	-	-4.61

The images of the compression tested quenched Ti_3SiC_2 samples can be found in *Figure 6.53.* The images are very similar to those seen when compression testing the Ti_3SiC_2 samples at high strain rates at both room and high temperature, namely the very brittle nature to the failure and the samples splitting into several pieces. However, the Q12-S100 sample seems to have maintained its integrity better than the samples quenched under different stresses.

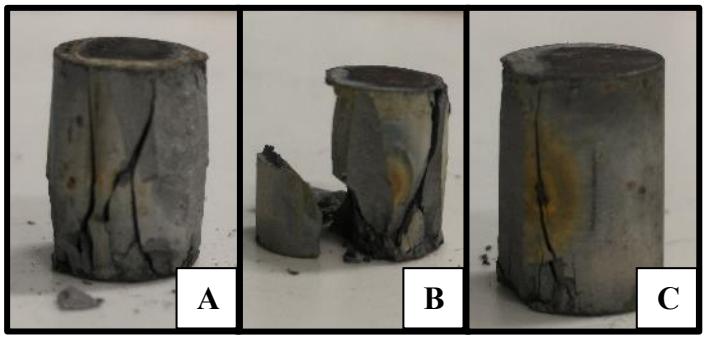

Figure 6.53: *Pictures of the thermally shocked Ti_3SiC_2 samples following their room temperature compression tests.* ***(a)*** *Q12-S0,* ***(b)*** *Q12-S50,* ***(c)*** *Q12-S100*

6.5 Summary and Conclusions

The results of the high temperature testing of the Ti_2AlC and Ti_3SiC_2 MAX phases have been investigated in this chapter. Microstructural studies in subsequent chapters have further explored the microstructure and deformation mechanisms of the Ti_2AlC and Ti_3SiC_2 MAX phases following their high temperature compression tests. A summary of each materials response to different strain rates and temperature can be found in *Figures 6.54-6.55*. These figures show the ultimate compressive strength (UCS) reached at each strain rate and temperature. There are two general trends seen for the Ti_2AlC MAX phase in *Figure 6.54*: (i) The slower the strain rate, the lower the UCS; and (ii) for each strain rate, the higher the temperature, the lower the UCS. These trends are generally satisfied, except for the sample tested under the very fastest strain rate at 1100°C, which was recorded as having a peak stress of ~-500 MPa. The samples tested with the medium range strain rate of 1×10^{-2}/s also see a minor deviation from the trend, although the results at all temperatures under this strain rate are within a stress value of ~50 MPa. The slower strain rates follow the previously stated trends, with the peak stress of each temperature roughly equidistant by ~150 MPa for the samples tested at 1×10^{-4}/s. Increasing the strain rate for a given temperature generally has an effect in decreasing the ductility of the MAX phases. This could be attributed to an increase in the internal stresses within the sample. At slower strain rates and higher temperatures, dynamic recovery mitigates internal stresses and may halt crack nucleation and therefore produce improved ductility. At both high and room temperature, if the MAX phase grains are highly oriented and/or the deformation is confined, the MAX phase material can exhibit significant ductility, mostly due to the formation of shear bands [15].

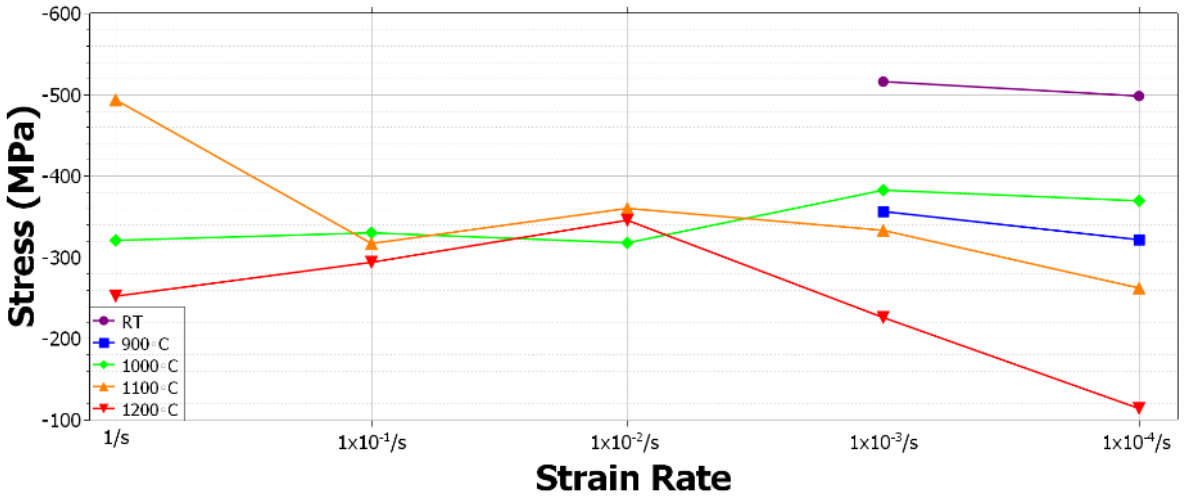

Figure 6.54: *Graph comparing the ultimate compressive strengths at different temperatures of the Ti_2AlC samples by strain rate*

The response of the Ti_3SiC_2 by strain rate and temperature is summarised in *Figure 6.55*. When compared to the response of Ti_2AlC in *Figure 6.54*, it can be asserted that the results of Ti_3SiC_2 when subjected to different strain rates at various temperatures are more incoherent. The UCS fluctuates across the range of strain rates for most temperatures at which the sample was tested. As was mentioned in Section 6.3.1.1, the UCS for most strain rates at 1000°C are generally within 75 MPa of each other, excepting the UCS of the T10-0 sample. This is similar to the response of the Ti_2AlC samples, which were also within ~75 MPa for most of the range of strain rates. For the slowest strain rate, the UCS of both of the samples tested at room temperature were found to be ~-475 MPa, which is much lower than that of the samples tested at 1000°C and about the same as the samples tested under the slowest strain rate conditions at 1100°C and 1200°C. This is generally the opposite of what would usually be expected for the fine grained Ti_3SiC_2 material, where samples fail at stresses sometimes exceeding 1 GPa [17,95,128]. One reason for this is the production method of the MAX phase samples used here, creating a sample that perhaps doesn't have the density or purity of the samples tested in previous studies or the testing conditions [96]. It is likely that, despite the microstructure of the bulk sample being determined to be generally homogenous, that small chemical composition variations have affected the generated microstructure and the overall phase distribution across the samples. The biggest UCS fluctuations for the Ti_3SiC_2 MAX phase are for the samples tested at 1100°C and 1200°C.

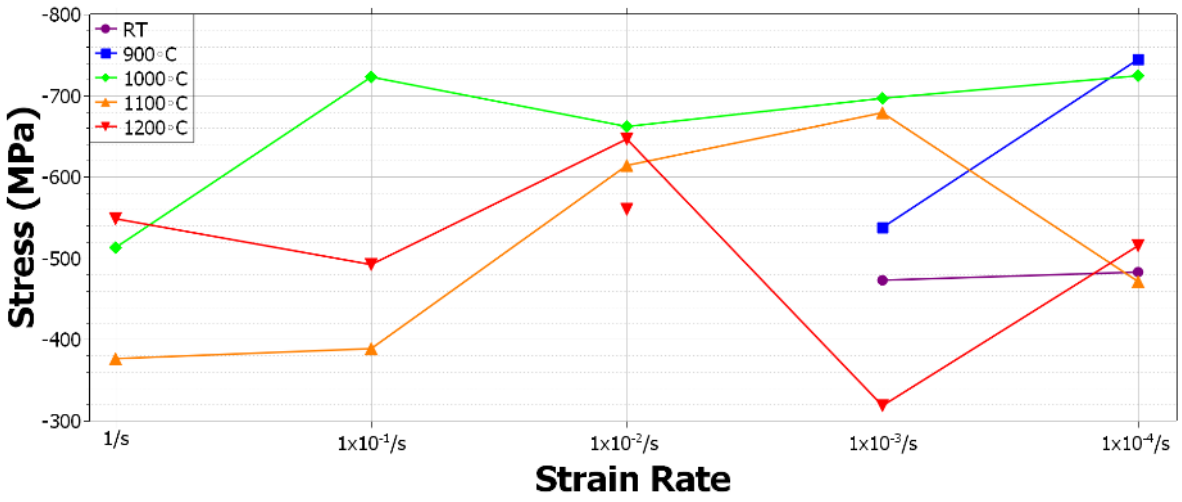

Figure 6.55: *Graph comparing the ultimate compressive strengths at different temperatures of the Ti_3SiC_2 samples by strain rate*

The photographs taken of each sample upon the completion of their tests were helpful in proving the failure mechanisms of the samples under the different strain rates and temperatures. For both MAX phases, the room temperature failure was found to be brittle. As previously stated, materials started to exhibit significant plastic deformation in the form of barrelling as the temperature was increased and the strain rate decreased. The barrelling shape that is present when a material is ductile is as a result of the mechanics of a compression test. The material spreads in the lateral direction and increases the samples cross sectional area. The sample generates a frictional force when held between the anvils, which opposes the lateral spread. This frictional force is not constant across the entire cross section of the specimen, with the edges of the sample that are connected to the anvil having a higher frictional force than the centre of the sample. The faster the strain rate, the less time the frictional force has in order to develop a barrelling shape to the sample. The stress/strain distribution relationship across a barrelled sample is generally inverse to the frictional force. A sample which has barrelled generally possesses a triaxial strain state, with higher levels of strain witnessed at the centre of the sample as opposed to the sample edges. Wang *et* al found that both temperature and strain rate have an effect on the barrelling of a material. They found that the effect of barrelling decreases as the temperature increases. They attributed this to the softening of material at elevated temperatures, which increases material flow behaviour. They found that strain rate had a more complex relationship with barrelling. At a constant friction coefficient and temperature, barrelling at first increases when the strain rate is increased, and attributed this to strain hardening. However as the strain rate was increased further the softening of stress-strain curves occurs [129].

As was discussed in the literature review in Chapter 3, the temperature at which the MAX phases start behaving in a ductile manner varies depending on the processing route and the MAX phase studied. For the Ti_2AlC and Ti_3SiC_2 MAX phases, the BDTT was generally found to be between 1000°C and 1100°C, with it also being strain rate sensitive. Several reasons for this behaviour have been given in Section 6.4, where changes in the strain slope during the quenching of both MAX phases were proposed as proof of a change in the failure mechanism.

At lower strain rates, plastic deformation can generally be treated as isothermal, where the temperature remains constant throughout the test, but conditions transition to adiabatic as the

strain rate is increased. Adiabatic heating is a process which takes place when the energy used for deforming a material turns into heat, but this heat cannot dissipate fast enough to its surroundings, so the temperature of the material increases. This increase in temperature can cause thermal softening, microstructural evolution and can change the active deformation mechanisms of the material. Consequently, adiabatic heating has a strong effect on the mechanical response of the material.[130–133]

As can be seen from the photographs of the samples following each test. For Ti_2AlC, the higher the temperature and slower the strain rate, the more likely a sample is not to show any evidence of cracking on the outer surface. At slightly faster strain rates and lower temperatures cracking does occur on the outer surface of samples that still failed in a ductile manner. This is particularly the case when studying the photographs of the samples tested at a strain rate of 1×10^{-4}/s at different temperatures, where increasing the temperature has an effect in halting the nucleation of external cracks until 1200°C, where no cracks appear. A similar relationship can also be seen in the Ti_3SiC_2 samples, particularly when studying the photographs of the samples tested at 1200°C, which show no external cracking on the surface. The orientation of these external cracks is seen to be generally parallel to the compression direction.

A comparison of the ultimate compressive strengths of both quenched MAX phases can be seen in *Figures 6.56 and 6.57.* In *Figure 6.56* it can be seen that increasing the compressive load stress while quenching from 1000°C has a small effect on the UCS of Ti_2AlC. With the exception of the Q10-S100 sample, the UCS gradually increased with increasing compressive load stress. No obvious trend can be seen for the Ti_3SiC_2 samples. The UCS of each sample is ~-350 MPa, with the exception of the Q10-S200 sample, which has a significantly higher UCS of ~-575 MPa.

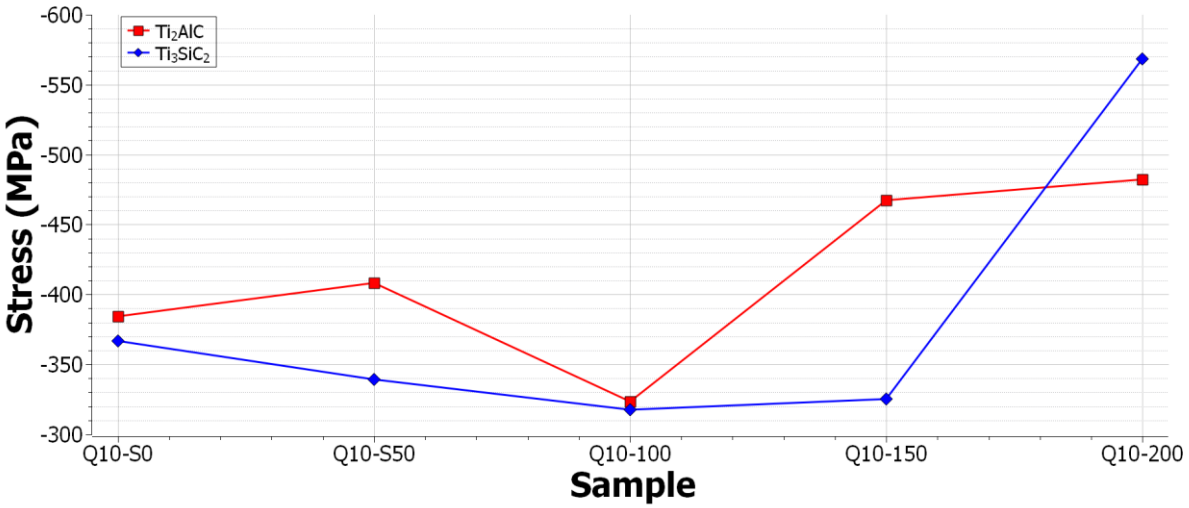

Figure 6.56: *Graph comparing the ultimate compressive strength of both MAX phases quenched at 1000°C under different compressive load stress conditions.*

Figure 6.57 shows the UCS's of the MAX phases quenched at 1200°C under different compressive load stress conditions. Unlike the Ti_2AlC samples quenched from 1000°C, it appeared that increasing the compressive load stresses during quenching did not have a significant effect on the UCS of either MAX phase. Like the samples quenched at 1000°C, the lowest recorded UCS's were for the Q12-S100 samples. The highest UCS was recorded for the Ti_3SiC_2 Q12-S150 sample.

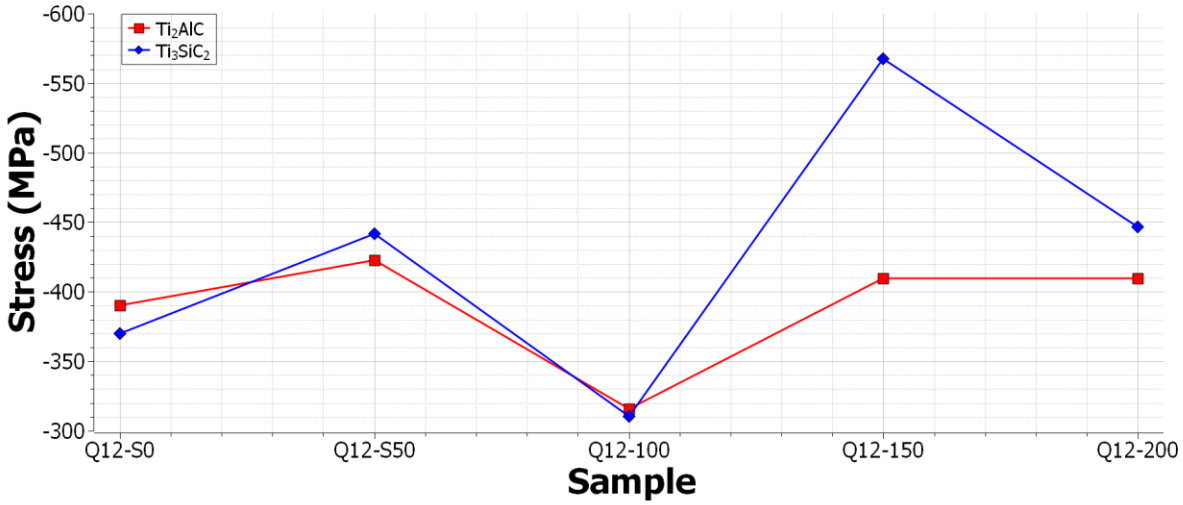

Figure 6.57: *Graph comparing the ultimate compressive strength of both MAX phases quenched at 1200°C under different compressive load stress conditions.*

Chapter 7 - Microstructural Characterisation of the MAX phases Following Mechanical Deformation

7.1 Introduction

The characterisation of the microstructure and nanostructure of both MAX phase materials are presented in this chapter. Following both room and high temperature mechanical testing of these materials, each sample was prepared and examined using the scanning electron microscopes Carl Zeiss Evo LS25 and Jeol Field Emission JSM-7800F. These SEMs were utilised, in conjunction with attached EBSD and EDS detectors, to help determine the deformation mechanisms present and the effect of the mechanical testing on overall microstructure and texture of both MAX phase materials.

7.2 Grain Morphology (Size and Shape) Analysis Post Deformation

7.2.1 Microstructural Analysis of Ti_2AlC Samples Compression Tested at both Room and High Temperatures

7.2.1.1 Microstructural Analysis of Samples Tested at Room Temperature

The microstructures of both Ti_2AlC samples tested at room temperature can be found in *Figures 7.1 and 7.2*. From first observations, the microstructures of the samples tested at strain rates of 1×10^{-3}/s and 1×10^{-4}/s appear heavily deformed. The locations of the SEM images have been outlined in *Figures 7.1 and 7.2*, also showing the samples orientation with respect to the compression direction. The micrograph of *Figure 7.1a* was taken at the 'tip' of the broken sample while *Figure 7.1b* was taken at the left centre edge of the sample. As seen in *Figure 6.3a*, the sample broke into several pieces rather than staying together, hence the unusual shape to the SEM sample. The lamellar structure of the Ti_2AlC MAX phase is evident in both samples in *Figures 7.1b and 7.2b*, with kinks in the lamellar structure being particularly evident in *Figure 7.2b*.

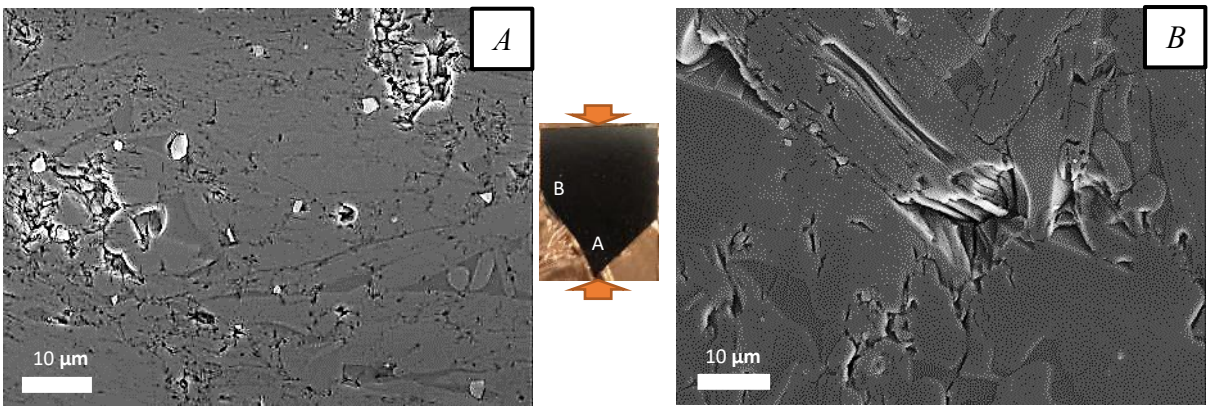

Figure 7.1: *Electron Micrographs of the TRT-3 sample, compression tested at room temperature at a strain rate of 1×10^{-3}/s.* ***B)*** *Lamellar microstructure particularly evident*

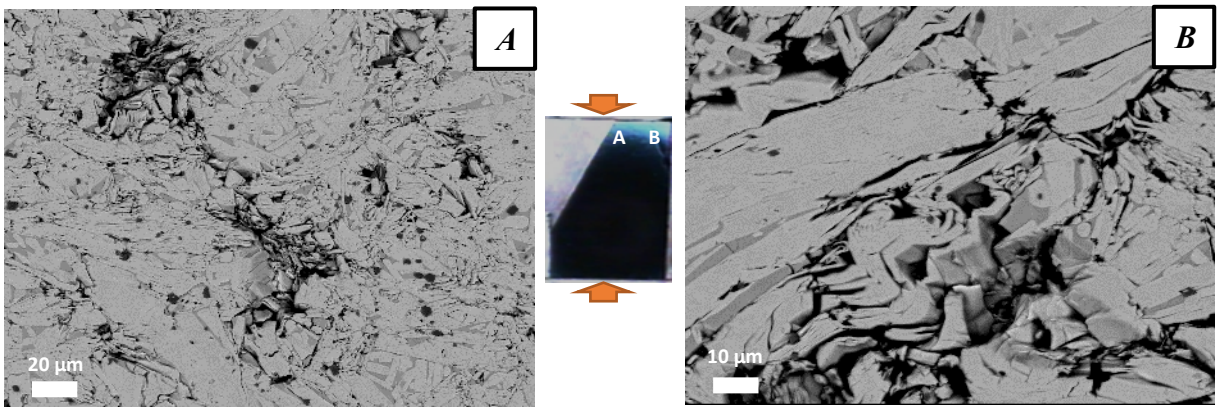

Figure 7.2: *Electron Micrographs of the TRT-4 sample, compression tested at room temperature at a strain rate of 1×10^{-4}/s.* ***A)*** *High levels of deformation at the tip of the sample,* ***B)*** *Evidence of kinking and delaminations*

7.2.1.2 Microstructural Analysis of Samples Tested at 1000°C

Like the samples tested at room temperature, most of the tests conducted at 1000°C yield sample microstructures that also exhibit a heavily deformed microstructure. Significant transgranular and intergranular cracks can be seen throughout the microstructure, with *Figures 7.3D and 7.5A* in particular showing this formation. It must be noted that the T10-1 sample was cut in a different direction to the T10-0 and T10-2 samples with regards to the substantial crack/breakage that was previously noted in the post deformation photographs of the samples in Chapter 6 (i.e. the red ellipse in *Figure 6.7A)*. *Figure 7.4* shows the different cutting axis/direction for each sample. Evidence of kinking is also found in *Figure 7.3A and 7.6A.* The microstructure within the close proximity of the large cross-sample crack is much more heavily deformed than the rest of the microstructure, as can be seen when comparing the microstructure around the large crack (*Figures 7.5 and 7.6),* with images which were taken at the sample corners and do not show significant cracking or delamination (*Figures 7.3B and C).* As has been shown in the post deformation images of the samples in Chapter 6, the samples that failed in a predominantly ductile manner, such as T10-4, did not show any significant crack across the width or length of the specimen, rather areas that were substantially more deformed than others. Evidence of this can be seen when comparing *Figure 7.7A*, an image taken at the sample edge that was in contact with the ISO-T compression anvil, with *Figures 7.7B, C and D*, taken respectively at the right edge, centre and bottom right edge in contact with the anvil. These later figures show that high deformation damage occurs at areas that were not in direct, substantial contact with the anvil, showing grains that are highly deformed, kinking and delaminating. In contrast, the shape of the grains in *Figure 7.7A* appears to be relatively similar to the shape of the grains in the as received sample seen in *Figure 5.1*, with no kinking or delamination in them. This phenomenon could be explained by low levels of strain close to the surface, something which was seen by Buckingham *et al* in their study of forging a nickel based superalloy (*Figure 7.8)*. This so-called ‘dead zone’ that was found in their forging trials (using a very similar set up to the high temperature compression testing of this work) can vary in size depending on the testing parameters, but is typically shaped as a cone, within which the deformation levels are generally low. [134]

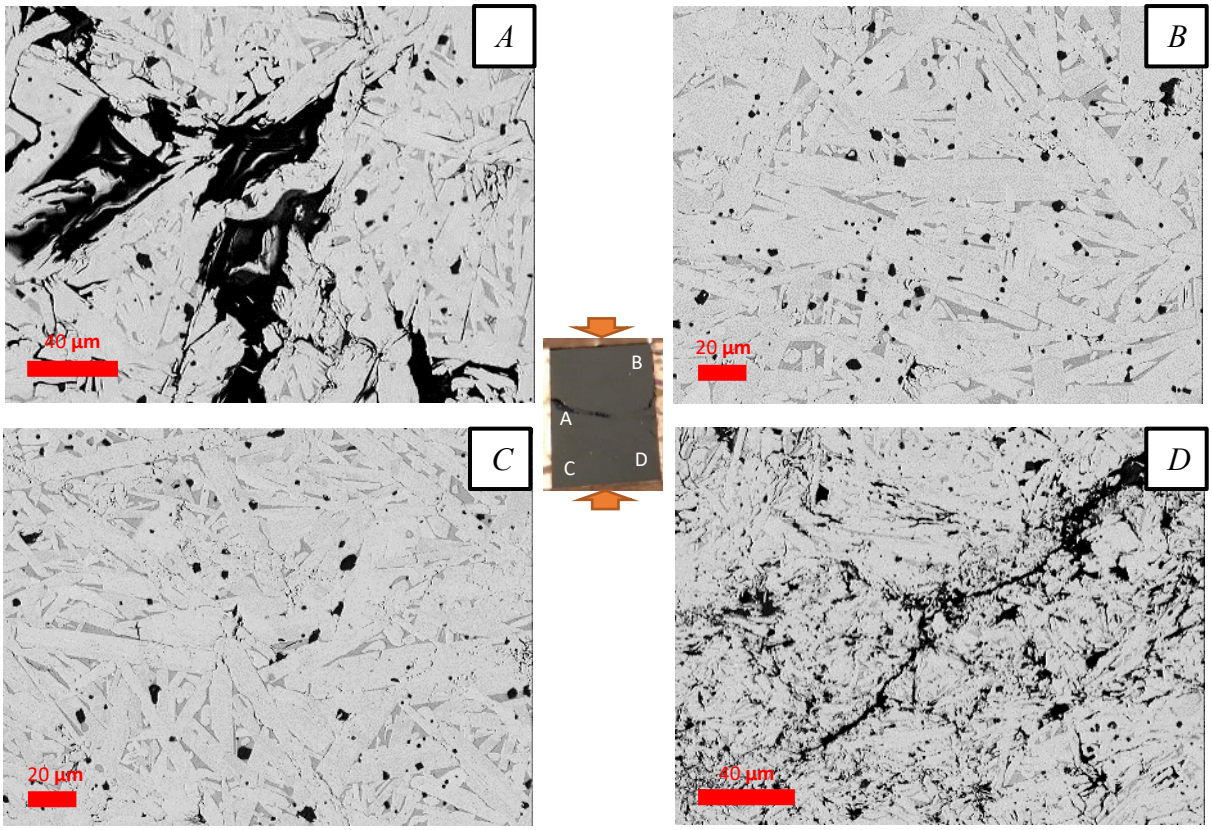

Figure 7.3: *Electron Micrographs of the T10-0 sample, compression tested at 1000°C at a strain rate of 1/s.* ***A)*** *Delaminated Ti_2AlC grain,* ***B & C)*** *No major cracks or delaminations at the edges of the sample.* ***A & B)*** *Transgranular and intergranular cracks are particularly evident*

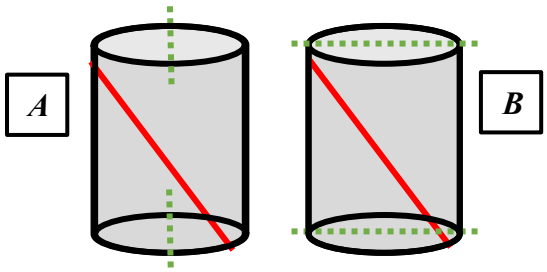

Figure 7.4: *Diagram showing the cutting direction (green dotted line) with relation to the large external crack/sample breakage seen following brittle failure of the Ti_2AlC MAX phase.* ***A)*** *Samples such as T10-0, with a large, roughly horizontal crack from one side to the other of the cross section, were cut in a way outlined in* ***Figure 7.4A****, with the cut going through only a small part of the large crack/breakage.* ***B)*** *Samples such as T10-1, where the cross section has a large crack going through the sample 45° to the loading direction, were cut in a way as shown in* ***Figure 7.4B.***

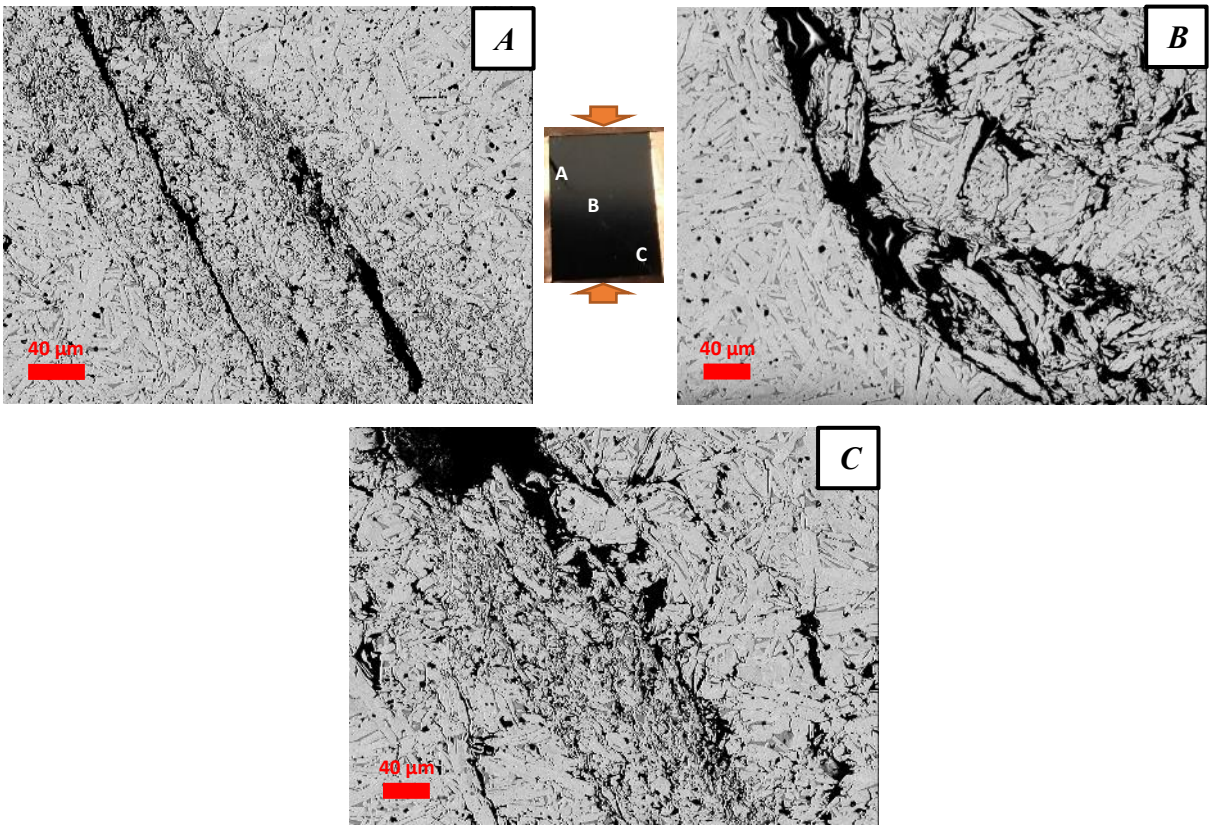

Figure 7.5: *Electron Micrographs of the T10-1 sample, compression tested at 1000°C at a strain rate of 1×10^{-1}/s showing high levels of deformation close to the major crack.*

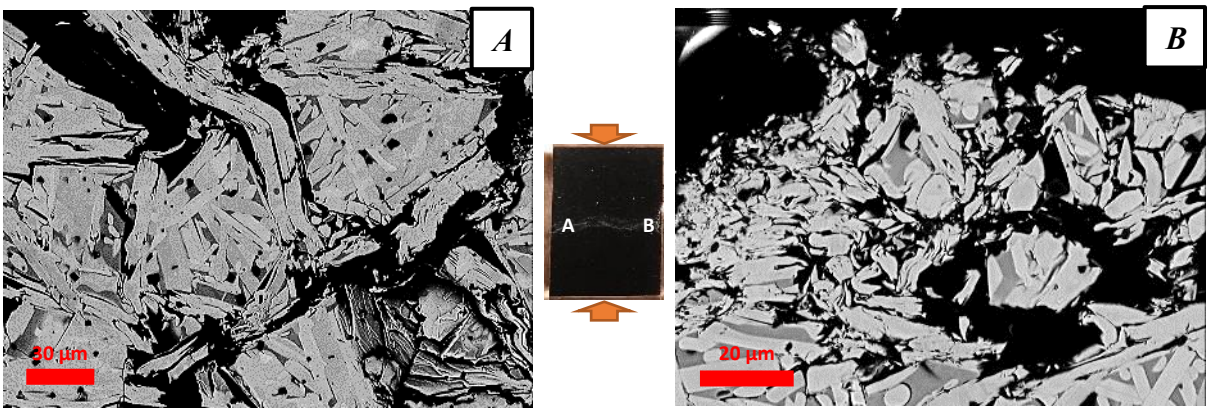

Figure 7.6: *Electron Micrographs of the T10-2 sample, compression tested at 1000°C at a strain rate of 1×10^{-2}/s.* ***A)*** *Kinked grain,* ***B)*** *High levels of deformation at the major crack*

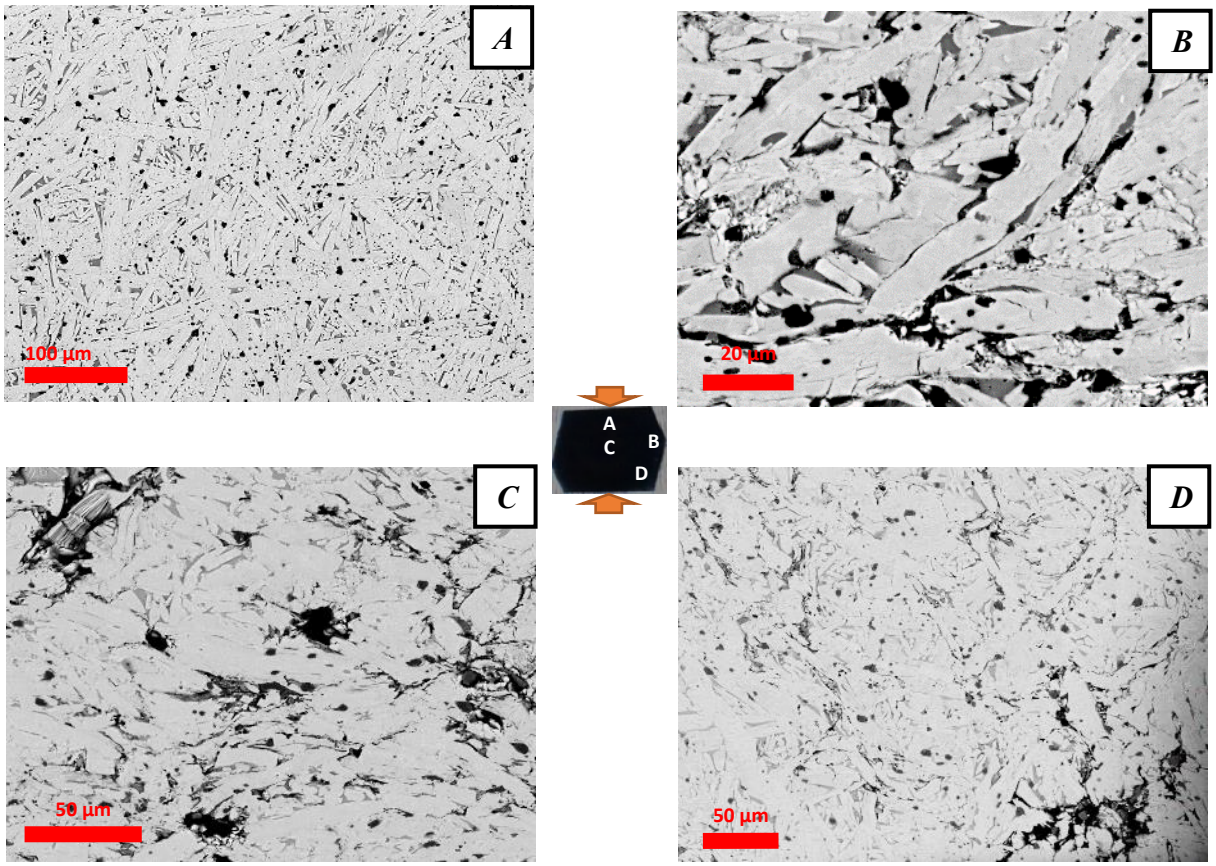

Figure 7.7: *Electron Micrographs of the T10-4 sample, compression tested at 1000°C at a strain rate of 1×10^{-4}/s.* ***A)*** *A potential deformation 'dead zone' close to the sample edge, where the grains generally retain their original shape,* ***B, C & D)*** *High levels of deformation, showing delaminated grains.*

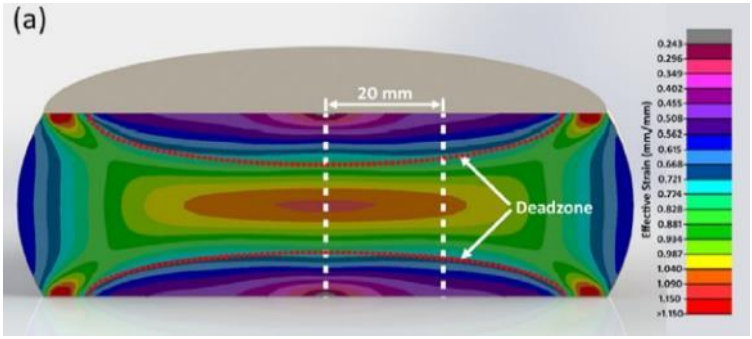

Figure 7.8: *A Deform 2D effective strain map created by Buckingham et showing the visual contours of strain distribution throughout forging of a cylindrical nickel alloy compression specimen.* [134]

7.2.1.3 Microstructural Analysis of Samples Tested at 1100°C

As has been established in Chapter 6, the higher the testing temperature and the slower strain rate, the more ductile the Ti2AlC MAX phase becomes. The large T-shaped cracks throughout the cross section of the microstructure for the T11-0 and T11-2 samples are further evidence of the brittle nature of the Ti2AlC MAX phase under the high strain rate conditions. The clearest evidence yet of kinking and delamination of the Ti2AlC MAX phase under these conditions can be found in *Figure 7.9C*, which also shows the layered structure of the MAX phase in general. *Figure 7.10A* was taken at the intersection between the substantial T crack/breakage, and a significant amount of deformation around this intersection can be seen. T11-3, the sample that failed in a ductile manner, like the other low strain rate samples tested at lower temperatures, exhibits a significant amount of deformation throughout the microstructure, in particular at the corners and the sides. As can be seen both from the photograph of the sample surface and the selection of micrographs in *Figure 7.11*, each corner of the sample has a large, wide crack, something that was also witnessed on the outer surface of the samples in *Figure 6.7C.* These cracks, or large voids created by the compression of the sample, are generally at an angle 45° to the compression axis.

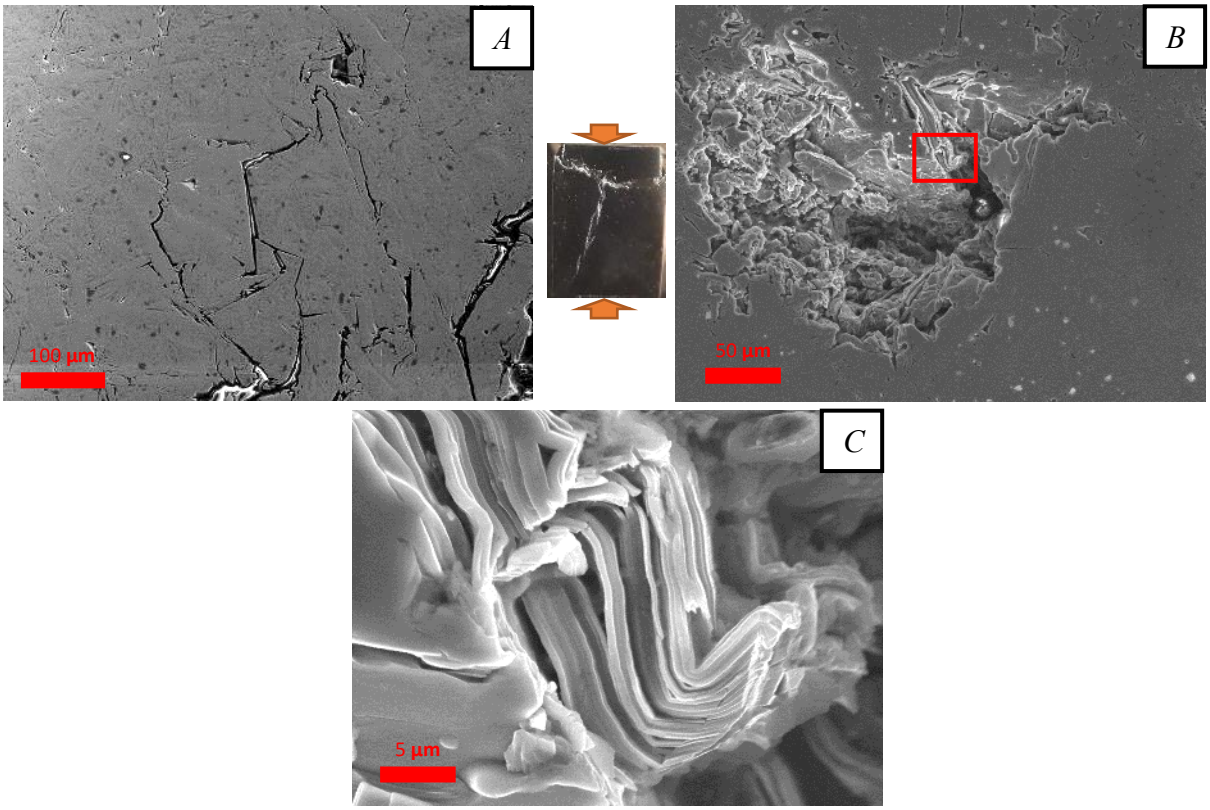

Figure 7.9: *Electron Micrographs of the T11-0 sample, compression tested at 1100°C at a strain rate of 1/s.* ***A)*** *Distinctive intergranular cracks,* ***B)*** *Lamellar structure evident within a small area of cracking,* ***C)*** *Magnified area of* ***(B)*** *showing the kinks and lamellar structure*

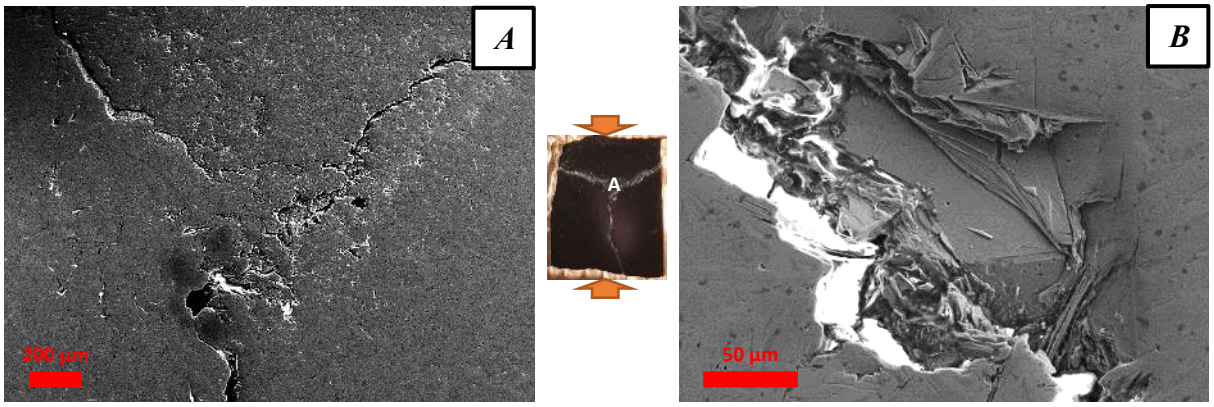

Figure 7.10: *Electron Micrographs of the T11-2 sample, compression tested at 1100°C at a strain rate of 1×10^{-2}/s.* ***A)*** *'Junction' of the major T crack propagating throughout the sample.* ***B)*** *Magnified area of the T area showing the a very flat lamellar structure*

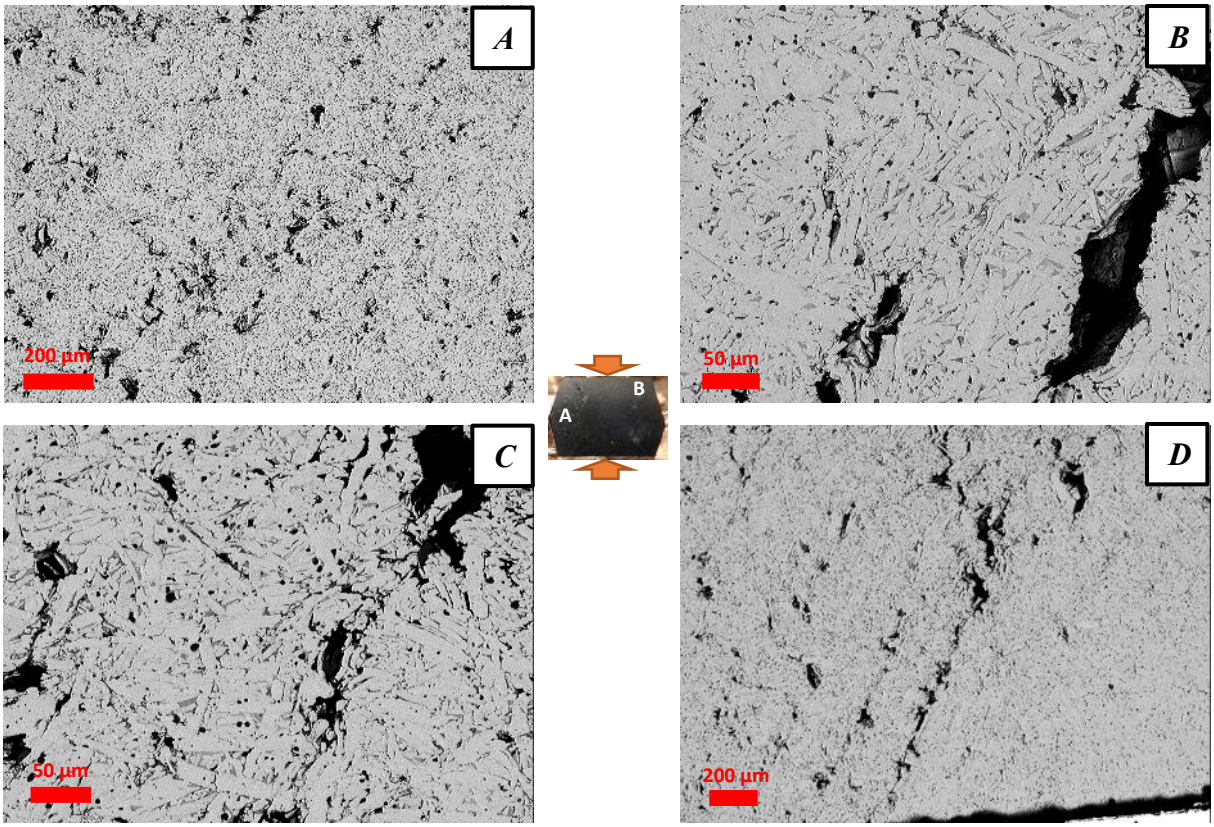

Figure 7.11: *Electron Micrographs of the T11-3 sample, compression tested at 1100°C at a strain rate of 1×10^{-3}/s.* ***A-D)*** *High levels of deformation at every corner of the sample.*

7.2.1.4 Microstructural Analysis of Samples Tested at 1200°C

Most of the samples tested at 1200°C have a microstructure similar to the samples that failed in a ductile manner in the lower temperature tests with a highly delaminated structure being the typical feature of the T12-2, T12-3 and T12-4 samples. The exception, as would be expected, is from the sample that failed in a brittle manner (T12-0). The fracture surface of the T12-0 sample was also taken, with the surface being that of the '45° crack' that was created

when the samples failed in a brittle manner. For most tests the sample stayed together but for the T12-0 test of this sample, both parts of the sample either side of the 'crack' detached, allowing inspection of the fracture surface. The lamellar structure was once again evident in these images, as was the large crack in *Figure 7.12B.* Both trans and intergranular cracks can be seen in *Figure 7.12C,* with the transgranular cracks generally running through the length of the long Ti_2AlC grains. *Figures 7.13B & C* and *Figure 7.15C* respectively show areas of the microstructure of the T12-2 and T12-3 samples that have an unusually fine appearance when compared to the rest of the microstructure. The large voids or cracks 45° to the compression axis that were previously seen in the samples tested at 1100°C have also occurred in the ductile samples at this temperature, with the microstructure in the areas around the voids showing higher levels of deformation than other areas of the microstructure. Evidence of grain bending of the Ti_2AlC grains was also found in *Figures 7.16A & B* of the T12-4 sample. In *Figure 7.16,* high levels of deformation in the larger Ti_2AlC phase grains was also witnessed.

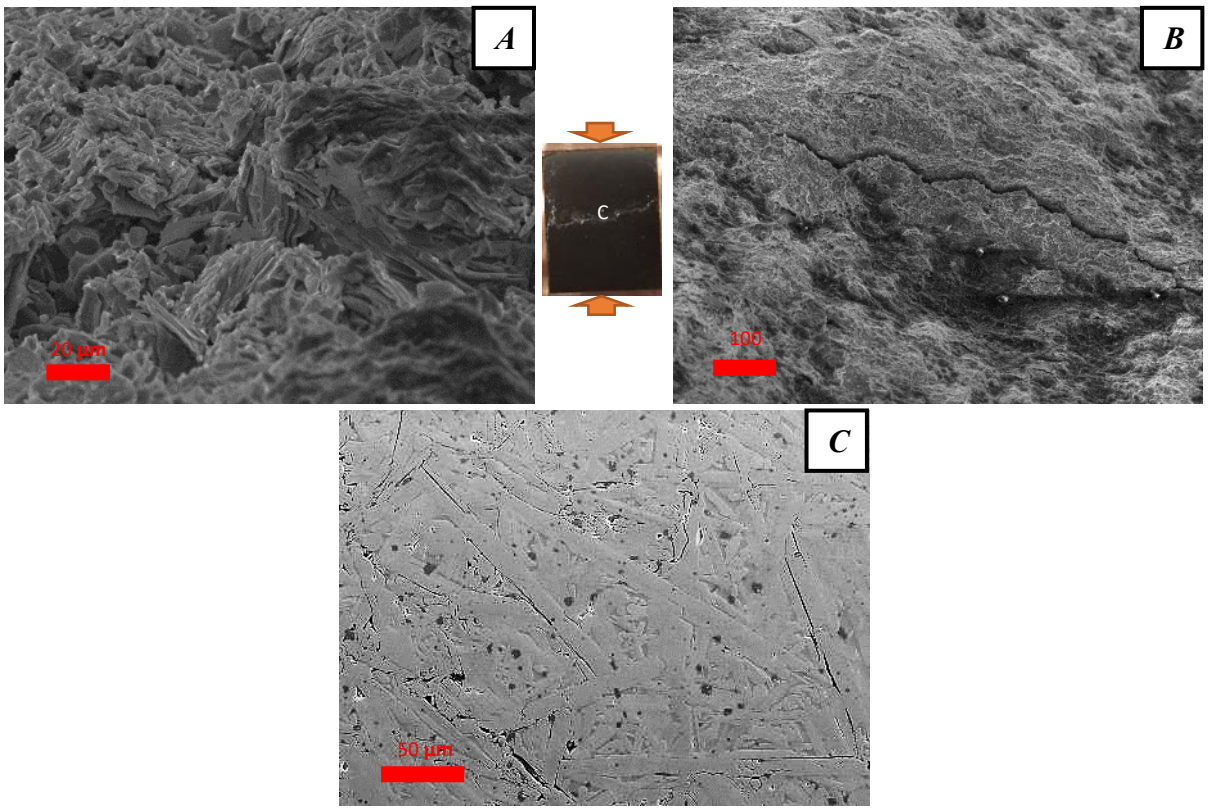

Figure 7.12: A & B) *Fracture surface electron micrographs of the T12-0 sample, compression tested at 1200° at a strain rate of 1/s.* ***C)*** *Electron micrograph showing the microstructure of the same sample*

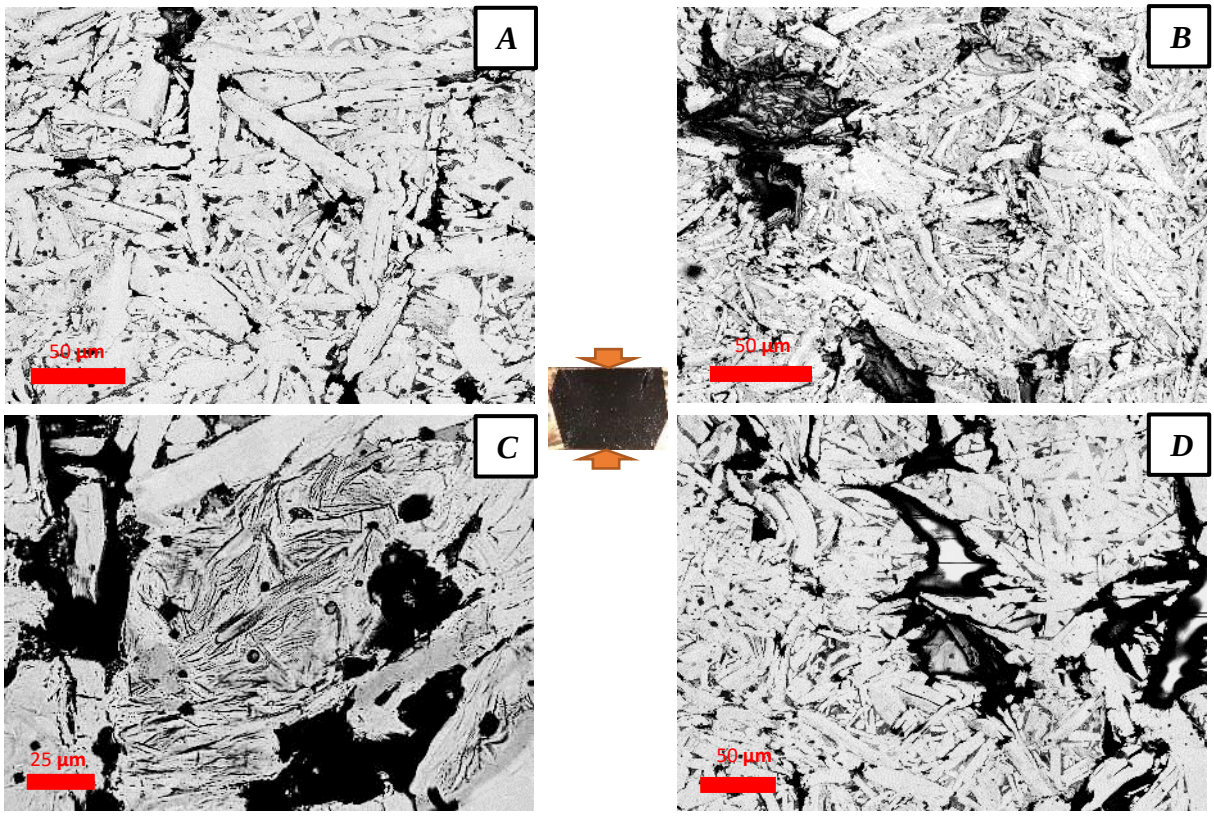

Figure 7.13: *Electron Micrographs of the T12-2 sample, compression tested at 1200°C at a strain rate of 1×10^{-2}/s.* ***A-D)*** *High levels of deformation* ***B & C)*** *Areas of very fine grains amongst the elongated Ti_2AlC grains.*

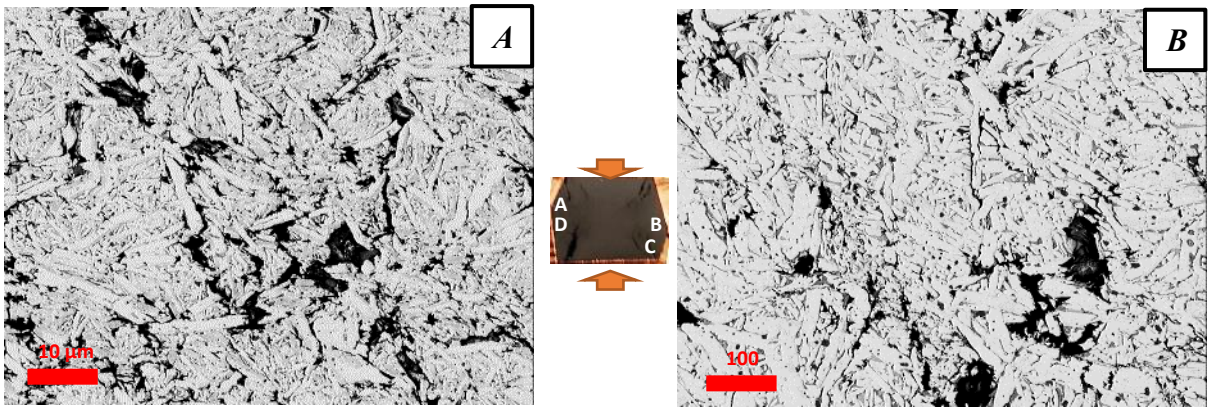

Figure 7.14: *Electron Micrographs of the T12-3 sample, compression tested at 1200°C at a strain rate of 1×10^{-3}/s.* ***A-D*** *High levels of deformation throughout the microstructure.*

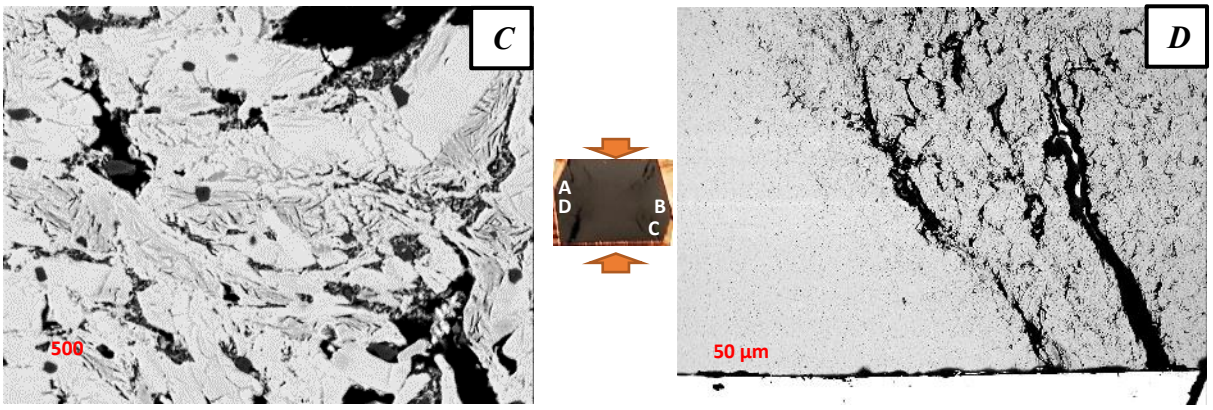

Figure 7.15: *Electron Micrographs of the T12-3 sample, compression tested at 1200°C at a strain rate of 1×10^{-3}/s.* ***C)*** *Similar to T12-2, an area with a very fine structure.* ***D)*** *Large*

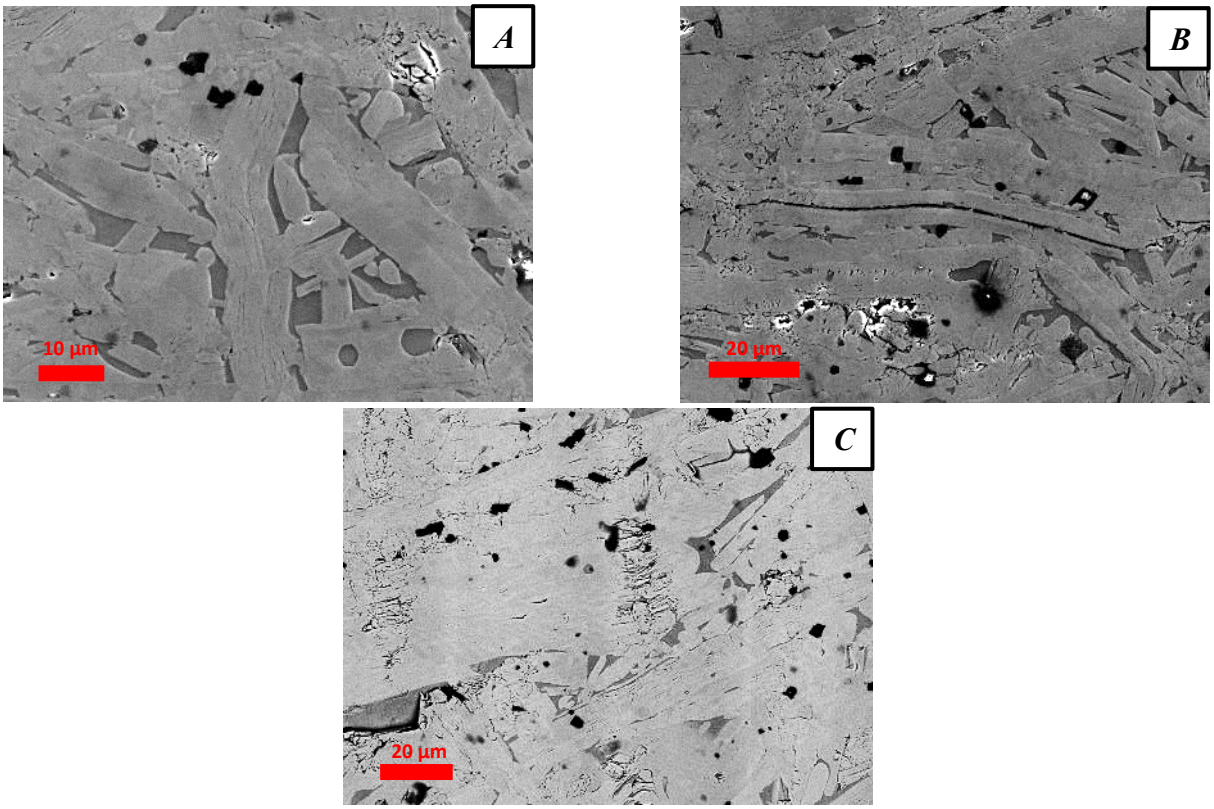

Figure 7.16: *Electron Micrographs of the T12-4 sample, compression tested at 1200°C at a strain rate of 1×10^{-4}/s* ***A)*** *Kinked Ti_2AlC grain* ***B)*** *Long transgranular crack through elongated Ti_2AlC grain.* ***C)*** *Small cracks at the edge of a large Ti_2AlC grain*

7.2.2 Microstructural Analysis of Ti_3SiC_2 Samples Compression Tested at both Room and High Temperatures

7.2.2.1 Microstructural Analysis of Samples Tested at Room Temperature

Figures 7.17 and 7.18 show the microstructures of the Ti_3SiC_2 samples tested at room temperature. As was outlined in the images of the Ti_3SiC_2 samples post deformation in Section 6.3.2 of Chapter 6, the samples that failed in a brittle manner generally disintegrated into several smaller pieces. This resulted in microstructural samples of varying shapes and sizes, as opposed to the majority of the Ti_2AlC samples, which generally maintained their integrity and cracked into two or three pieces. Both the microstructures of the TRT-3 and TRT-4 samples showed evidence of substantial deformation throughout their respective structures, as particularly evidenced in *Figures 7.17B & 7.18C*. Kinking and delaminating of the major Ti_3SiC_2 phase was also found in the TRT-3 sample, as seen in *Figure 7.17A.* An obvious difference between the two MAX phases when tested under room temperature conditions is the plethora of cracks and the direction of these cracks in the Ti_3SiC_2 MAX phase. Whereas the Ti_2AlC MAX phase samples tested at room temperature had a few areas of minor cracks, the cracks in the TRT-3 and TRT-4 Ti_3SiC_2 samples can be seen to propagate throughout the whole microstructure and form 'branches' of cracks that are interconnected with other larger crack formations.

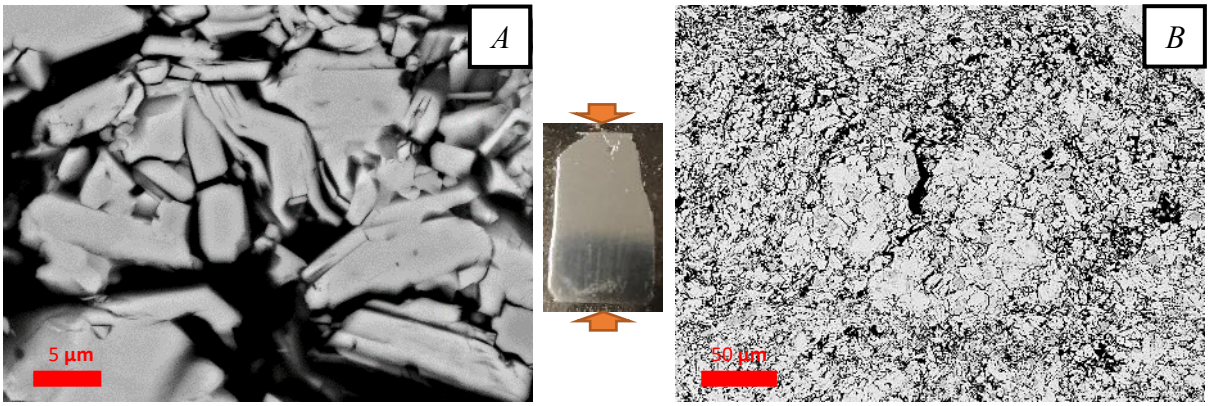

Figure 7.17: *Electron Micrographs of the TRT-3 sample, compression tested at room temperature at a strain rate of 1×10^{-4}/s.* ***A)*** *Kinked Ti_3SiC_2 grain,* ***B)*** *Very high levels of deformation, with numerous transgranular and intergranular cracks.*

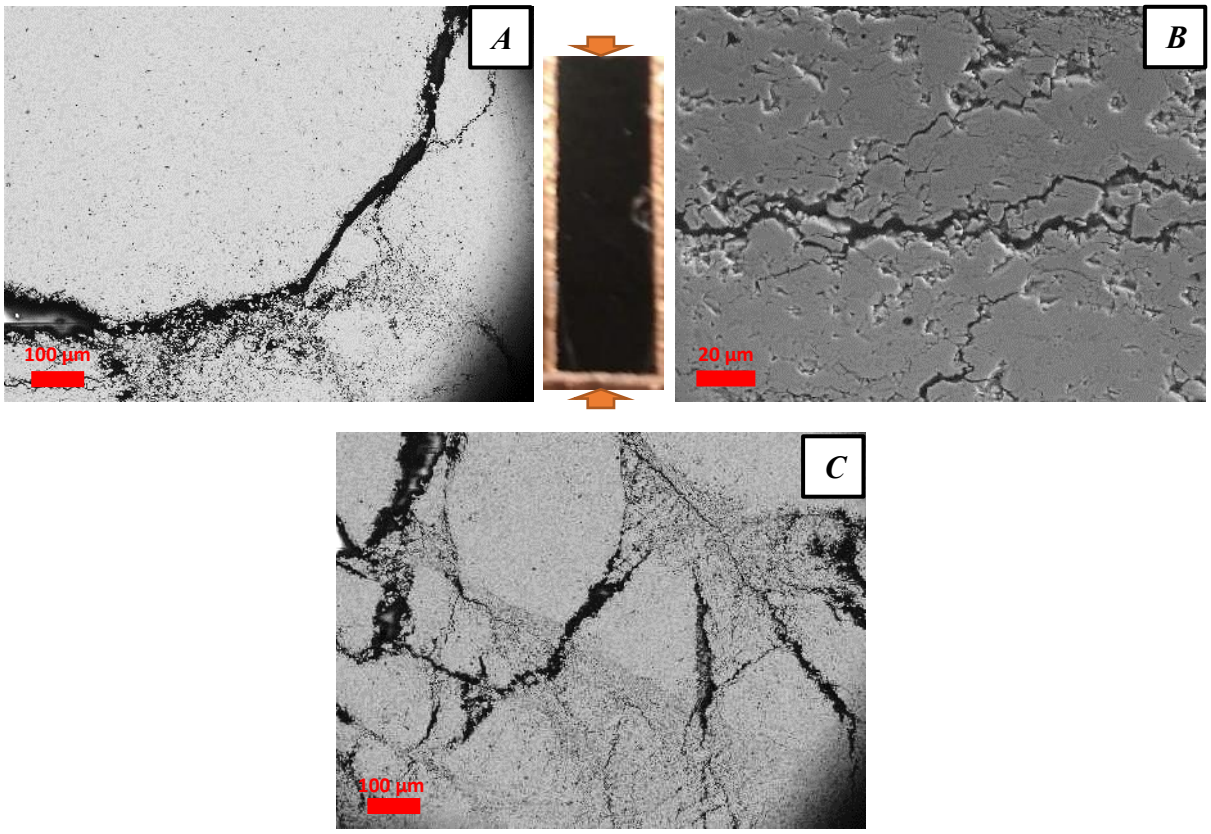

Figure 7.18: *Electron Micrographs of the TRT-4 sample, compression tested at room temperature at a strain rate of 1×10^{-4}/s* ***A)*** *Large crack emanating through the microstructure,* ***B)*** *Intergranular cracks,* ***C)*** *'Branches' of cracks interconnected with other large crack formations*

7.2.2.2 Microstructural Analysis of Samples Tested at 1000°C

The microstructure of the Ti_3SiC_2 samples deformed at 1000°C can be found in *Figures 7.19-7.22*. *Figures 7.19A & B* show the typical intergranular cracks found in a Ti_3SiC_2 sample that deformed in a brittle manner, with the cracks propagating throughout the fine grained microstructure. As previously mentioned, the Ti_3SiC_2 samples that deformed in a brittle manner broke into several pieces and the fracture surface of two of those pieces were investigated, as shown in *Figures 7.19C & D.* From *Figure 7.19C*, a small crack can be seen on the tip of the fracture surface. Further evidence of the brittle nature to the failure of this specimen could be found in the presence of cone shaped features on the fracture surface of another piece of the sample in *Figure 7.19D*. The aforementioned intergranular cracks were also found in the T10-2 sample, as shown in *Figure 7.20.* For the sample which did not fail in a catastrophically brittle manner, T10-4, no major differences in the microstructure were found when comparing it with the samples that did fail in a brittle style. Intergranular cracks were still prevalent, although some transgranular cracks can be seen in *Figure 7.22C.* Also of note was the presence of a

large phase that appeared to be inside a crack, as seen at the top of *Figure 7.22B* and in *Figure 7.22C*. As seen in *Figure 7.22B*, most of the large cracks are filled in with non-conductive resin, so the presence of a conductive substance within the crack seen in *Figure 7.22C* was a surprise. Other features noted from the T10-4 sample include the small crack propagating from the vertical crack in *Figure 7.22A* and the crack that connects the two much larger cracks in *Figure 7.22B*.

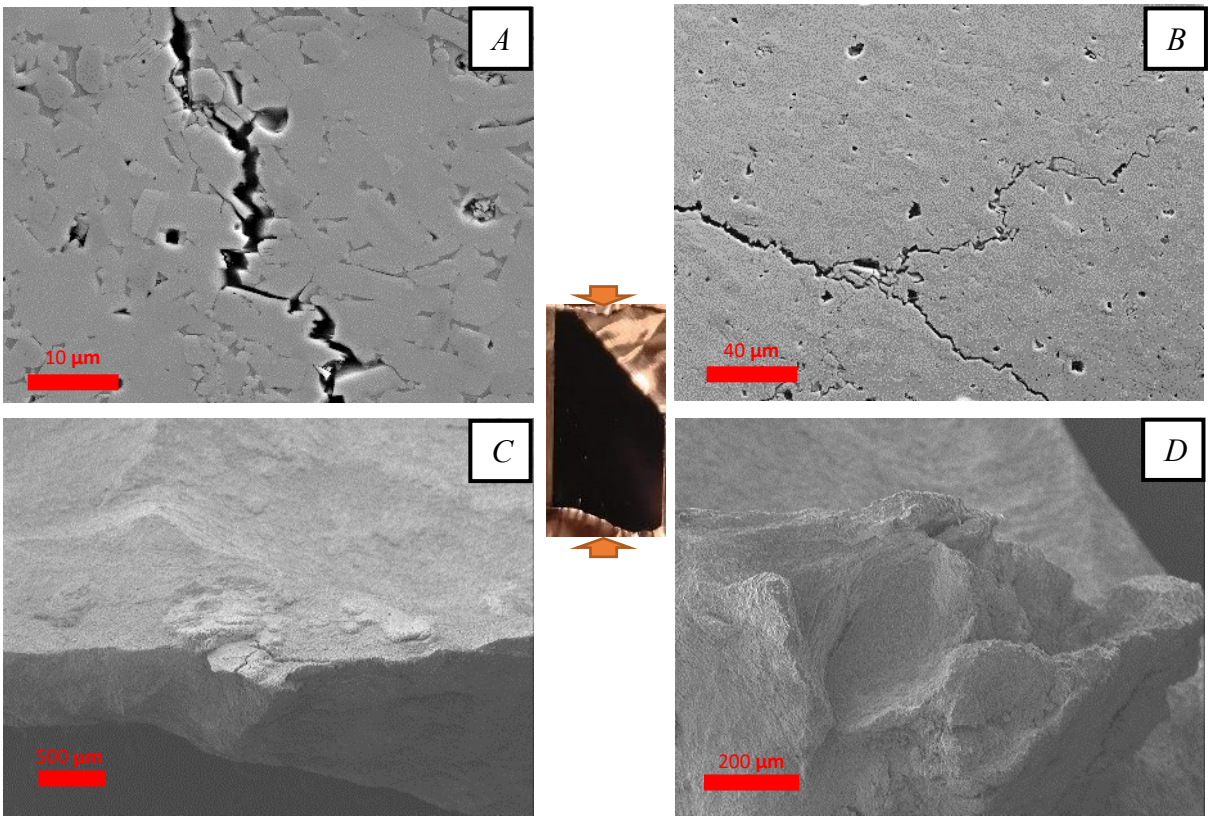

Figure 7.19: *Electron Micrographs of the T10-0 sample, compression tested at 1000°C at a strain rate of 1/s* ***A & B)*** *Transgranular cracks,* ***C & D)*** *Fracture surface of the T10-0 sample,* ***C)*** *Small crack at tip of fracture surface,* ***D)*** *Cup and cone shaped feature on the fracture surface*

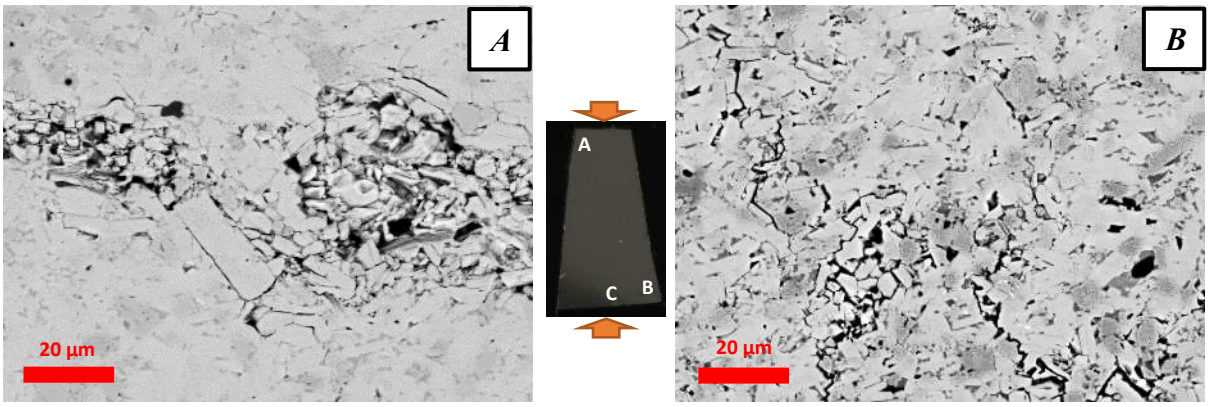

Figure 7.20: *Electron Micrographs of the T10-2 sample, compression tested at 1000°C at a strain rate of* 1×10^{-2}*/s* ***A)*** *Deformed area,* ***B)*** *Intergranular cracks*

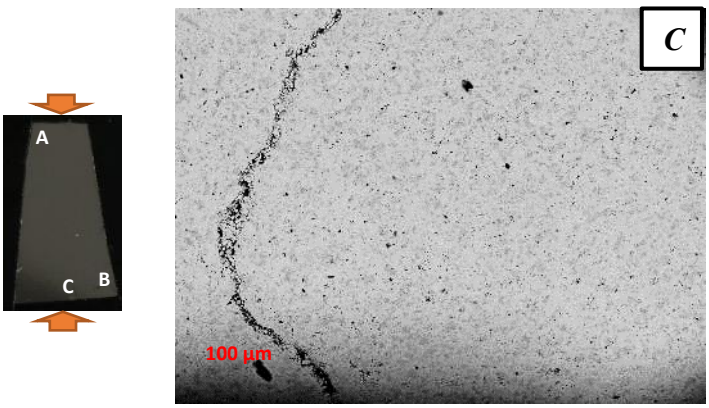

Figure 7.21: C) C) *Large crack propagating through at the bottom edge of the sample*

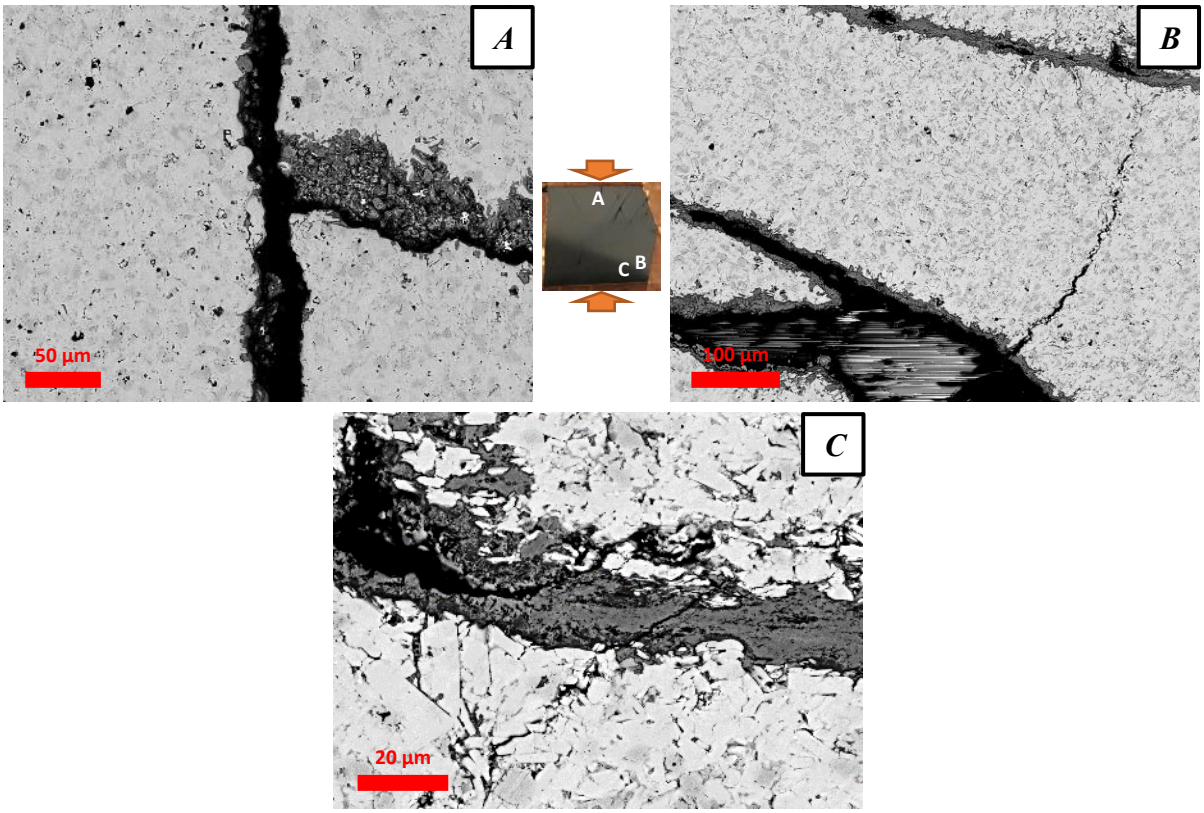

Figure 7.22: *Electron Micrographs of the T10-4 sample, compression tested at 1000°C at a strain rate of 1×10^{-4}/s* ***A)*** *Small crack emanating from a larger, vertical crack* ***B)*** *Small crack connected to two larger cracks,* ***C)*** *Potential small conductive secondary phase within a large crack*

7.2.2.3 Microstructural Analysis of Samples Tested at 1100°C

High levels of deformation were found at the edge of the T11-1 sample (*Figure 7.23A)*, while significantly less deformation was recorded at the bottom centre of the same sample (*Figure 7.23B)*. A similar feature was also noted in the Ti_2AlC samples, in particular those tested at

1000°C. The deformation noted composed of two large cracks of similar shape propagating from one large crack to the bottom edge of the sample. A similar feature to that found in the T10-4 sample of a vertical intergranular crack with horizontal cracks branching off of it was found in the T11-2 sample in *Figure 7.24*. The fracture surface of a separate piece of the same sample was also found to possess a large crack at the tip of the cone, similar to the T10-0 sample. Substantial levels of deformation were recorded in the microstructure of the T11-4 sample, with both transgranular and intergranular cracks prevalent throughout the microstructure of the sample. *Figure 7.25A* and its inset of *Figure 7.25B* once again show cracks that branch out directly perpendicular to the compression direction. The cracks in these figures also showed the extremely fine nature to the microstructure. The vertical Ti_3SiC_2 grain in *Figure 7.25C* is almost directly parallel to the compression direction and as such, a large amount of both intergranular and transgranular cracks were found. Evidence of kinking within this grain was also noted.

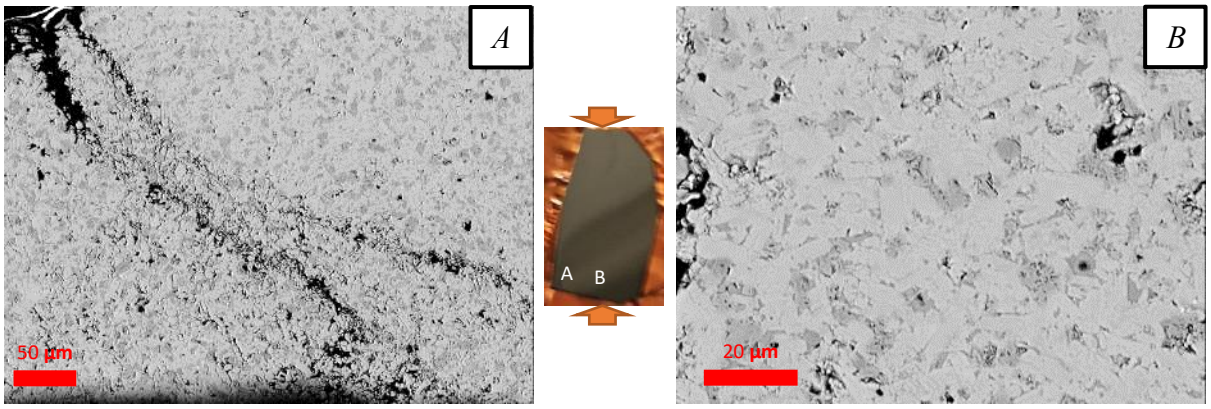

Figure 7.23: *Electron Micrographs of the T11-1 sample, compression tested at 1100°C at a strain rate of 1×10^{-1}/s* ***A)*** *High levels of deformation in the corner of the sample,* ***B)*** *Potential 'dead zone' at the bottom edge of the sample, with the microstructure having a similar appearance to the as-received sample*

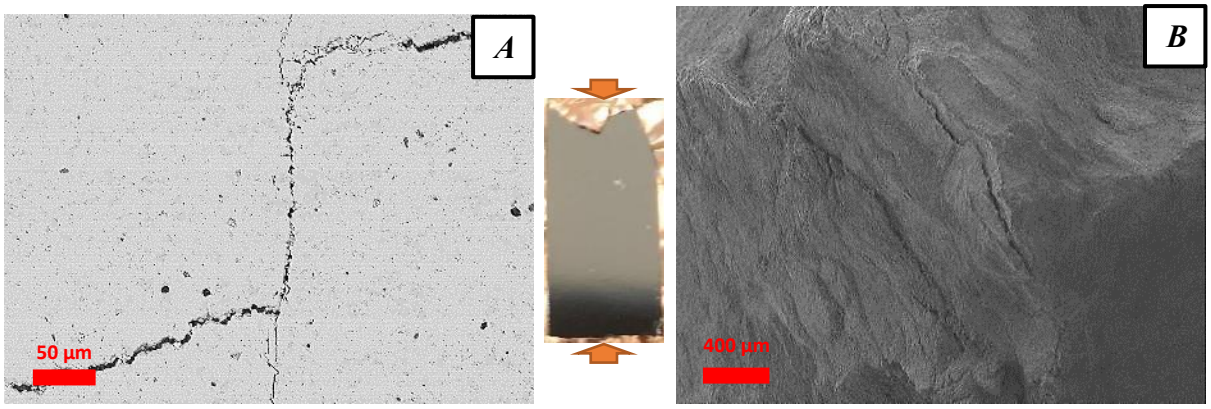

Figure 7.24: *Electron Micrographs of the T11-2 sample, compression tested at 1100°C at a strain rate of 1×10^{-2}/s* ***A)*** *vertical intergranular crack with horizontal cracks branching off* ***B)*** *Fracture surface showing a small crack at the tip of the 'cone' of the sample*

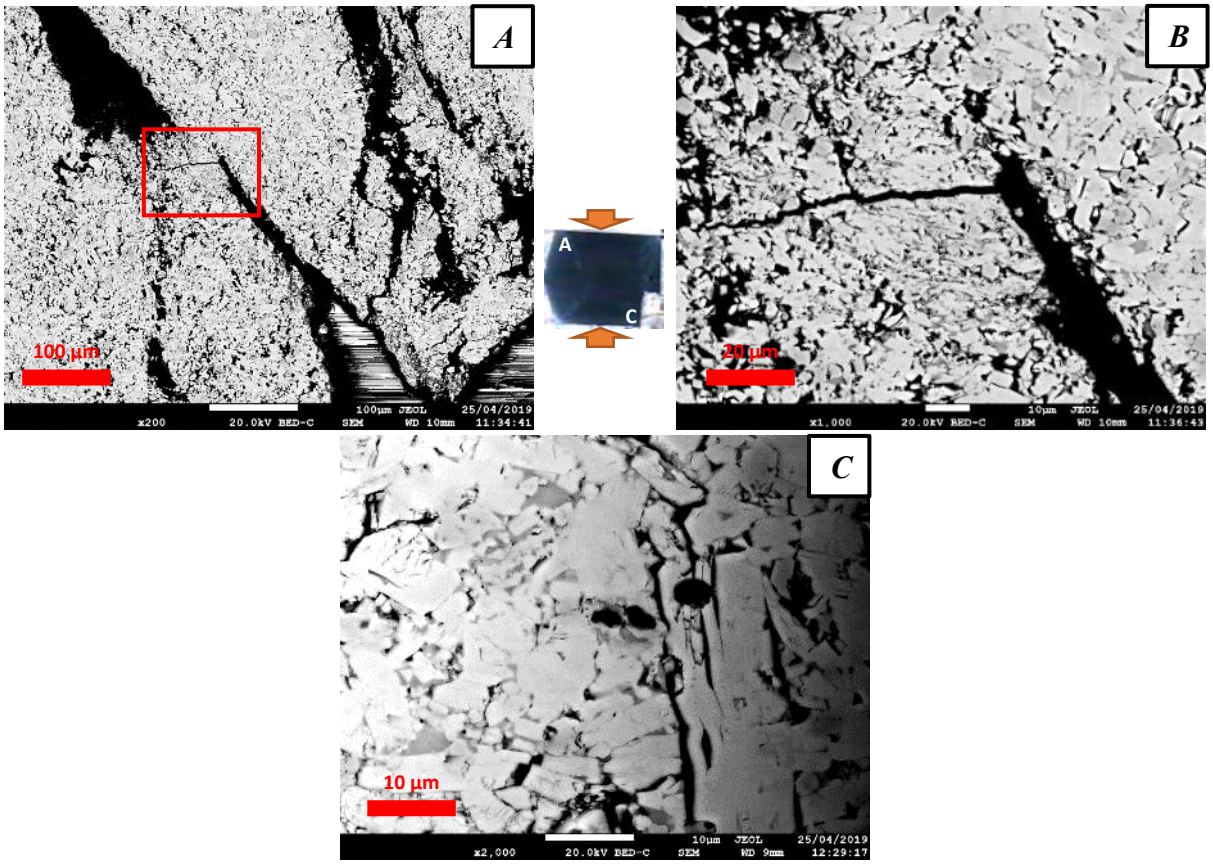

Figure 7.25: *Electron Micrographs of the T11-4 sample, compression tested at 1100°C at a strain rate of 1×10^{-4}/s.* ***A)*** *Extremely fine microstructure,* ***B)*** *Inset of (A) showing a crack branching out perpendicular to compression direction.* ***C)*** *Vertical Ti_3SiC2 grain almost directly parallel to compression direction showing kinking and intergranular and transgranular cracks*

7.2.2.4 Microstructural Analysis of Samples Tested at 1200°C

The microstructure of the Ti_3SiC_2 samples tested at 1200°C can be found in *Figures 7.26-7.28*. As previously shown in Section 6.3.2.4, the samples tested at a strain rate of 1/s or 1×10-1/s at 1200°C failed in a catastrophically brittle manner while the other samples tested at slower strain rates didn't break apart into pieces, with their final form resembling an almost barrel shape, as further evidenced in the images of the cross sections of the samples shown in *Figures 7.26-7.28. Figure 7.26* shows both the microstructure and fracture surface of pieces of the T12-1 sample. As shown in in *Figure 7.26A*, large, straight cracks were once again found in microstructure, while also being found in the fracture surface in *Figure 7.28D*. Whereas the T12-1 sample appeared to display pockets of areas of high levels of deformation, the T12-2 and T12-3 samples show a highly deformed microstructure of similar levels to that found in the T11-4 sample. Transgranular and intergranular cracks are evident in *Figures 7.27 and 7.28*. Also of note is the appearance of voids and/or cracks forming parallel to the compression direction in *Figure 7.27B*.

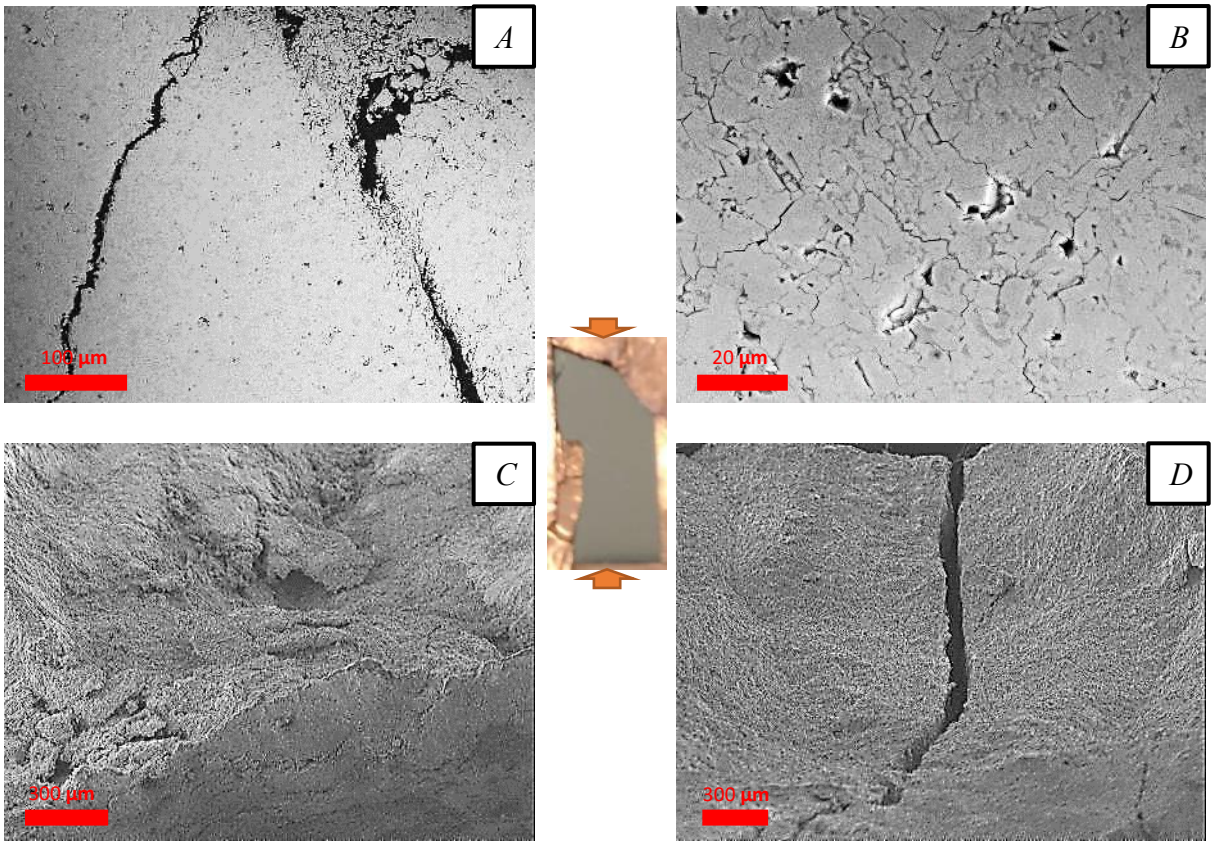

Figure 7.26: *Electron Micrographs of the T12-1 sample, compression tested at 1200°C at a strain rate of 1×10^{-1}/s* ***A)*** *Large straight cracks through the microstructure,* ***B)*** *Localised area of intergranular cracks,* ***C & D)*** *Fracture surface images showing large cracks throughout the microstructure.*

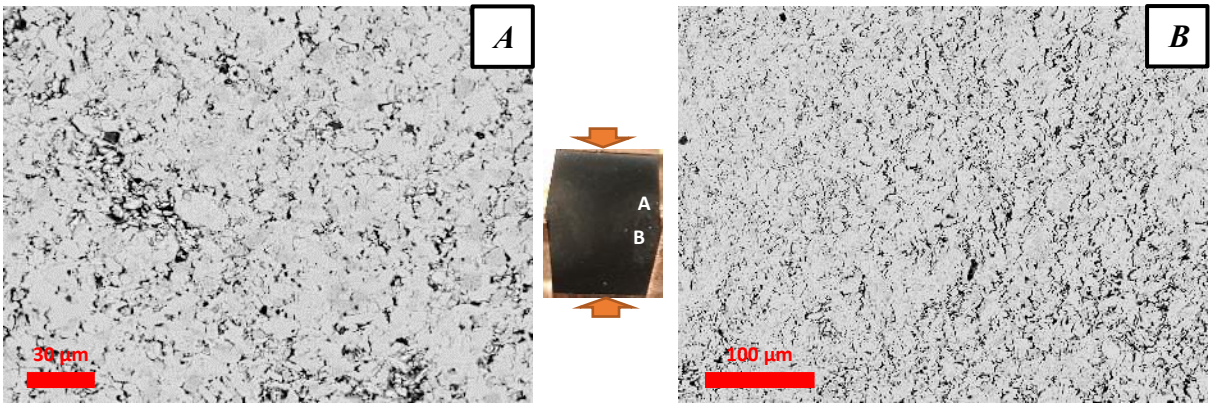

Figure 7.27: *Electron Micrographs of the T12-2 sample, compression tested at 1200°C at a strain rate of 1×10^{-2}/s. Transgranular and intergranular cracks at the edge of the sample*

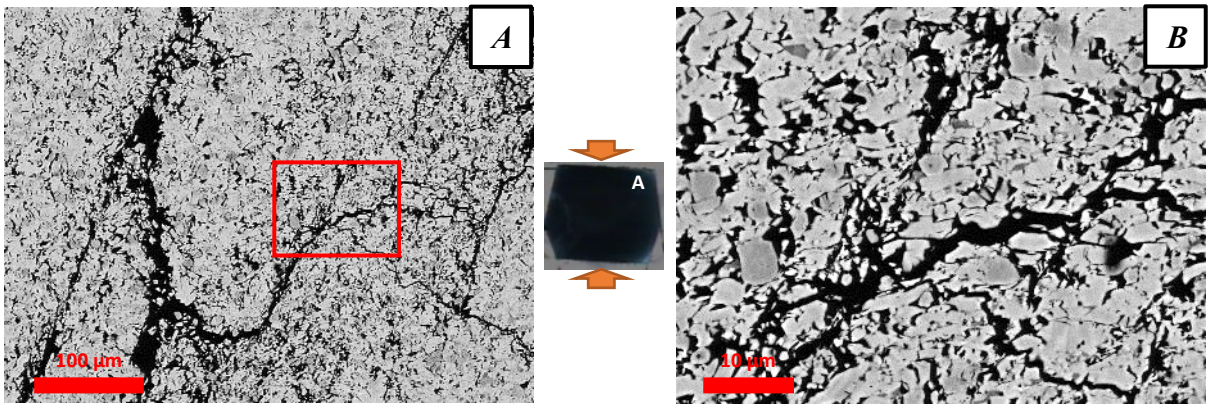

Figure 7.28: *Electron Micrographs of the T12-3 sample, compression tested at 1200°C at a strain rate of 1×10^{-3}/s.* ***A)*** *Voids and/or cracks forming parallel to the compression direction,* ***B)*** *Inset of (A)*

7.2.3 Summary

In this section of the chapter, the microstructure of the Ti_2AlC and Ti_3SiC_2 samples have been studied and analysed. It has already been established in Chapter 5 that, despite their crystal structural similarities, the microstructures of both materials are quite different, with Ti_2AlC generally having a coarser grain size than Ti_3SiC_2. Despite this difference, the microstructures of each material do share some features in their response to both room temperature and high temperature compression testing.

The microstructures of both Ti_2AlC and Ti_3SiC_2 following room temperature compression testing confirm what has previously been found in various sources, with substantial deformation throughout each microstructure and evidence of kinking and delaminations

present amongst the highly deformed zones [75,80,90,97,135]. As previously stated in Chapter 6, both materials did not retain their integrity after room temperature compression testing, although whereas Ti_2AlC samples broke into several large pieces, the Ti_3SiC_2 samples disintegrated upon failure, creating numerous pieces both large and small.

As the testing temperature was increased, the samples retained their integrity slightly better than when tested at room temperature, with this especially being the case for the Ti_2AlC samples. The Ti_2AlC samples tested at the faster strain rates were found to generally break into 2 large pieces or retain their general integrity with a large shear crack 45° to the compression direction. The areas around these large cracks generally were areas of highest deformation and both transgranular and intergranular cracks could be seen around these areas of each Ti_2AlC sample tested under these high strain rate, high temperature conditions. Kinking and heavily delaminated areas were also recorded under these conditions.

Intergranular cracks were found to be particularly prevalent in the Ti_3SiC_2 samples which were tested under high strain rates and high temperatures. Unlike the Ti_2AlC samples, certain areas throughout each Ti_3SiC_2 sample suffered from high levels of deformation, with cracks both large and small seen emanating from several points in the microstructure. Cracks branching off in several directions from larger cracks were also recorded, while the fracture surfaces of some of the samples tested at higher strain rates showed evidence of cup and cone formations, as well as several cracks.

As previously established in Chapter 6, as the strain rate was decreased at the higher temperatures, the more ductile both MAX phases behave. This was further confirmed in the microstructure of each sample deformed under these conditions. For both MAX phases these samples generally did not show any significant large crack across the width or length of the specimen but rather areas which were substantially more deformed than other areas. For several samples tested at the slowest strain rates, it was seen that micrographs taken of the sample edges in contact with the compression anvil showed grains that were generally of a similar size and shape to that of the as received sample. Micrographs taken at edges of each sample not in contact with the compression anvil did show grains that were highly deformed, kinked and

delaminated. This behaviour was attributed to a potential ‘dead zone’, where deformation levels are generally low. Other features recorded for these samples that failed in a more ductile manner included grain bending and voids within the areas of high deformation at the corners and sides of each sample. Transgranular cracks were generally more prevalent throughout the samples of both MAX phases tested under these conditions, although intergranular cracks were still recorded.

7.3 EBSD Analysis of Ti_2AlC and Ti_3SiC_2 Samples Compression Tested at both Room and High Temperatures

Following standard scanning electron microscopic inspection of the Ti_2AlC and Ti_3SiC_2 MAX phases, both sets of materials were examined via EBSD using the JEOL 8700F SEM. The data was then analysed and maps were created using the MTEX MATLAB software. EBSD is a helpful tool when analysing the evolution of deformation in the MAX phases due to its ability to locate kink bands and dislocation walls. These features can result in changes in the crystallographic orientation, or misorientation, within individual grains and can be easily identified when analysing misorientations on inverse pole figure (IPF) maps.

For each sample, the data collected was presented in the form of several maps. These maps included a phase map of each sample, an IPF map in the Y (compression) direction, and a map of the misorientation angles. Also produced were band contrast images from the areas of each sample selected for analysis. A map and histogram of the grain boundary misorientation angle was also produced for each sample.

7.3.1 EBSD Analysis of Ti_2AlC Samples Compression Tested at both Room and High Temperatures

7.3.1.1 EBSD analysis of Ti_2AlC samples tested at Room Temperature

The EBSD maps in *Figures 7.29 & 7.30* represent the data collected for the TRT-3 Ti_2AlC sample. IPF maps of the as-received Ti_2AlC MAX phase microstructure in *Figure 5.11c* from Chapter 5 showed that the grains have a largely random texture before being tested, something which was further proved when plotting the orientations in the colour key of the IPF. The IPF map of the TRT-3 and TRT-4 samples can be found in *Figures 7.29b and 7.31b* respectively. *Figure 7.33* shows a plot of the orientations of each grain on the colour key of each phase. From this it can be deduced that, similar to the as-received sample, the TRT-3 sample has a more random orientation for all the phases. The TRT-4 sample, however, appears to have much more orientation than the TRT-3 sample. The Ti_2AlC phase, for all grain sizes, has a preferred orientation to the [0001] direction, while the orientation of the TiAl and Al_2O_3 phases appear to be more random.

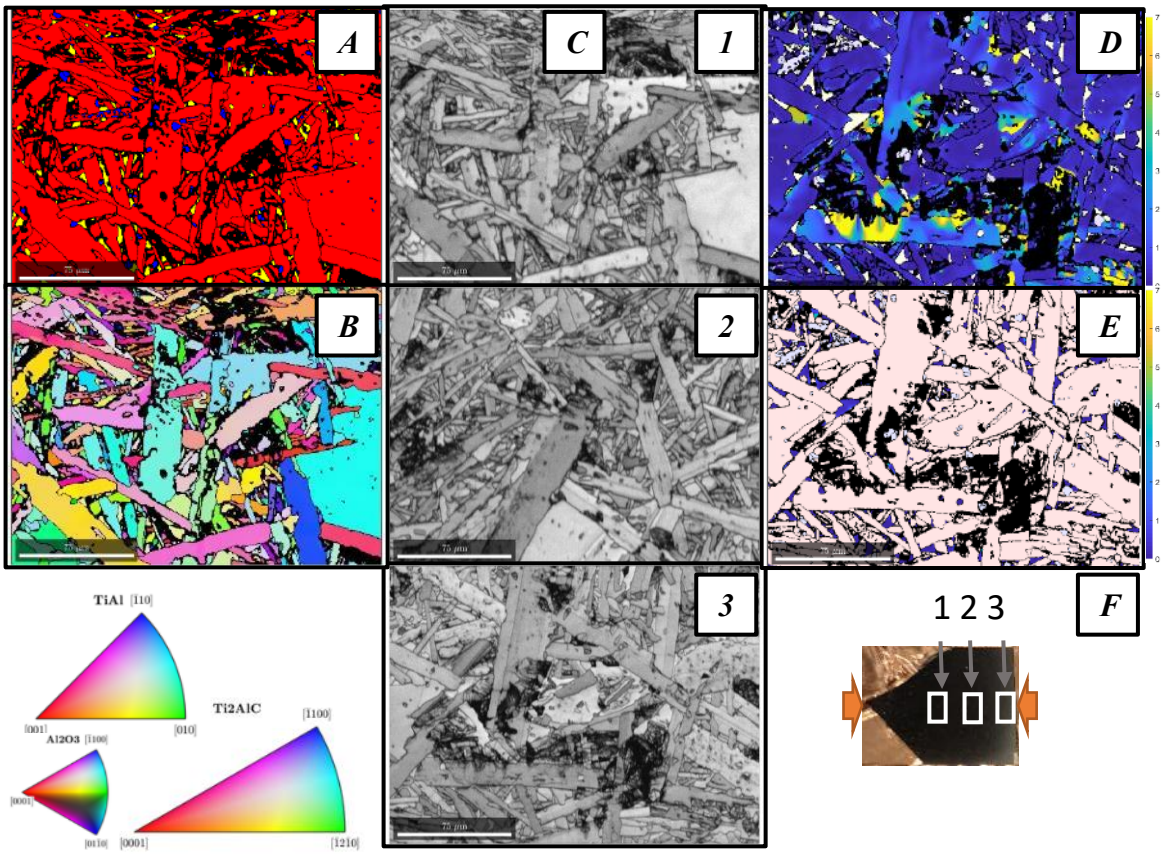

Figure 7.29: *EBSD Maps of the TRT-3 Ti_2AlC Sample:* ***A)*** *Phase Map, (R=Ti_2AlC, Y=TiAl, B=Al_2O_3),* ***B)*** *IPF-Y Map,* ***C)*** *Band Contrast showing Sites 1-3,* ***D-E)*** *Misorientation Angles,* ***F)*** *Map locations*

Like the colour coding of the grain boundaries in *Figure 5.12*, each set of grain boundaries were identified by 4 separate colours for the data in *Chapter 7*. The low angle grain boundaries (LAGBs) being between 2 and 10° and identified by red. The medium angle grain boundaries (MAGBs) are represented in blue for the 10-20° and green for 20-40°, while yellow was used to signify the high angle grain boundaries (HAGBs) >40°. The histograms in *Figures 7.30A &B and 7.32A & B* show the data for the grain boundaries between the different phases. For both samples, the misorientation angles of the boundaries between the Ti_2AlC grains are constant across the graph, indicating that the orientations are distributed uniformly throughout the microstructure. For the TRT-3 sample, the TiAl-TiAl grain boundaries were recorded as being of a non-random distribution, with high amounts of the grain boundaries falling in between the two ranges of 20°-30° (MAGBs) and also 80°-90° (LAGBs). The TRT-4 sample was also found to have a non-random distribution for the grains boundaries between these

phases, with peaks recorded between 2° and 20° (LAGBs and MAGBs) and also 80°-90° (HAGBs) were recorded for the TRT-4 sample. The Ti_2AlC-TiAl grain boundaries for both samples have a uniform distribution throughout the microstructure within ± 10°. For both samples, the Ti_2AlC-Al_2O_3 grain boundaries had a substantial number of medium misorientation angles, with the peaks at 20°-30°. The Al_2O_3-Al_2O_3 and Al_2O_3-TiAl grain boundaries behave in a similar manner for both samples, with the distribution close to the random (Mackenzie) profile.

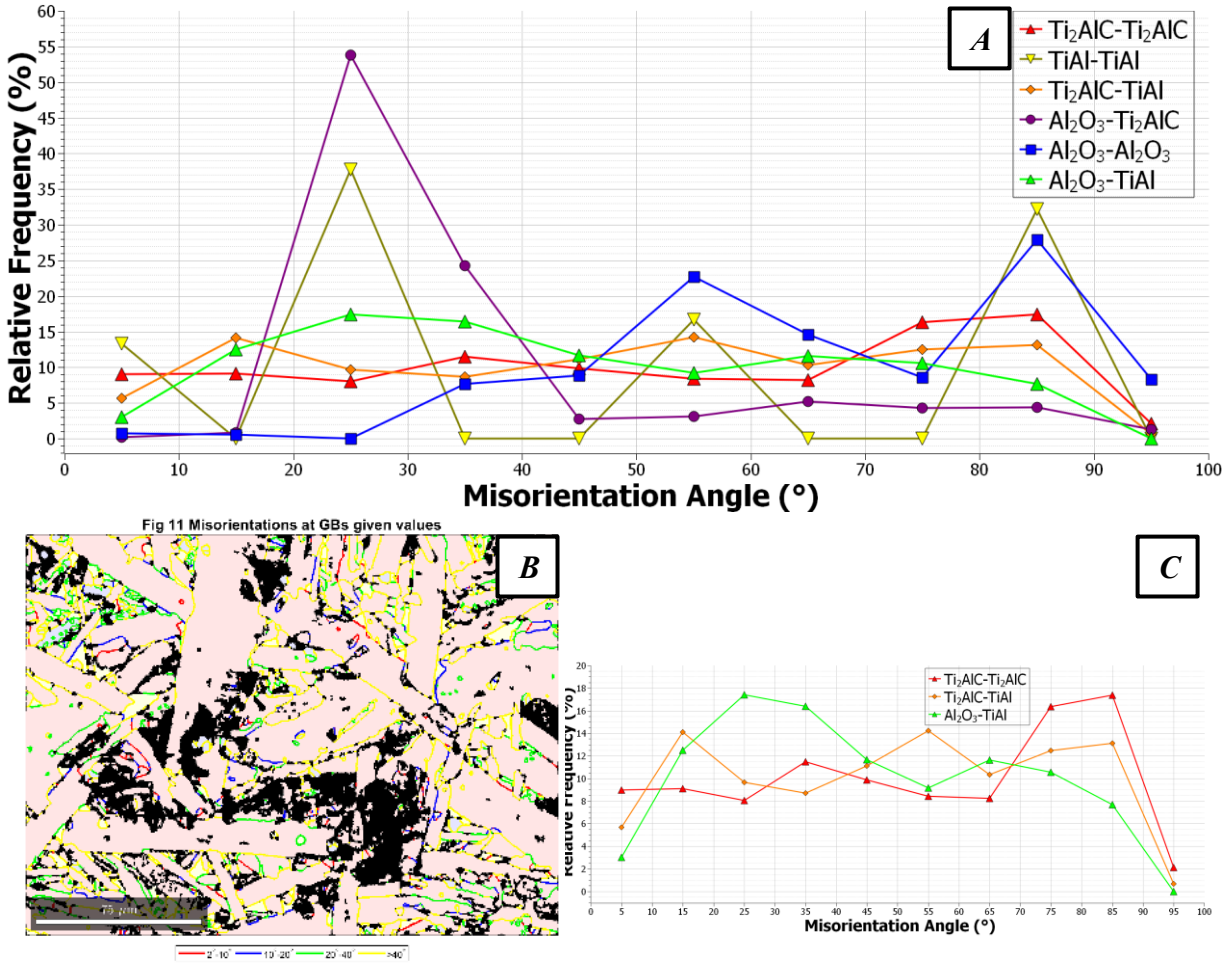

Figure 7.30: A) *Line graph showing an average of the grain boundary misorientation angles across the recorded sites, with the grain boundaries between each phase shown;* ***B)*** *EBSD map showing the misorientation angles of the grain boundaries in Site 3 of the TRT-3 Ti_2AlC sample;* ***C)*** *Inset of A, showing the data for the Ti_2AlC-Ti_2AlC, Ti_2AlC-TiAl and Al_2O_3-TiAl grain boundaries.*

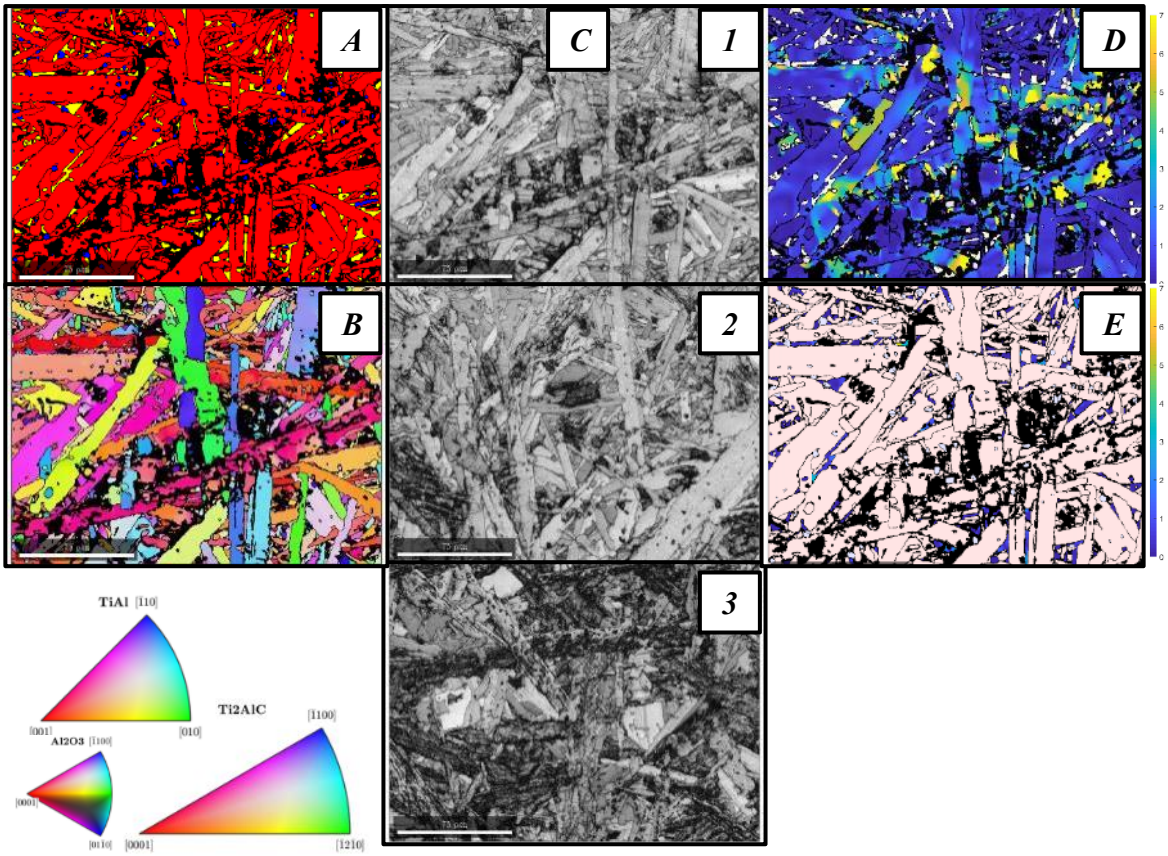

Figure 7.31: *EBSD Maps of the TRT-4 Ti_2AlC Sample:* ***A)*** *Phase Map, (R=Ti_2AlC, Y=TiAl, B=Al_2O_3),* ***B)*** *IPF-Y Map,* ***C)*** *Band Contrast showing Sites 1-3,* ***D-E)*** *Misorientation Angles of Site 1*

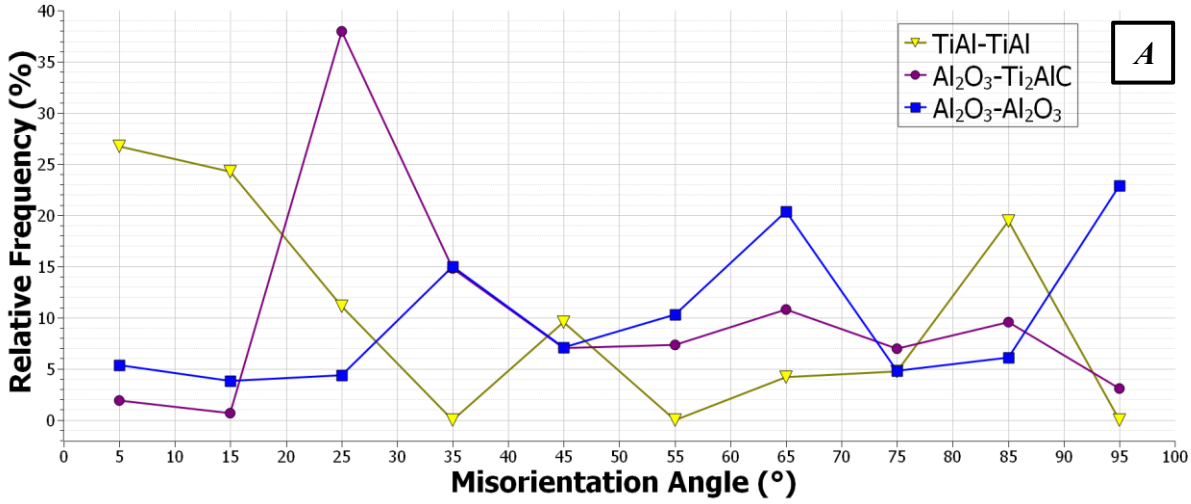

Figure 7.32i: A) *Line graph showing an average of the grain boundary misorientation angles across the recorded sites. Graph shows the grain boundaries between phases that produced the highest peaks*

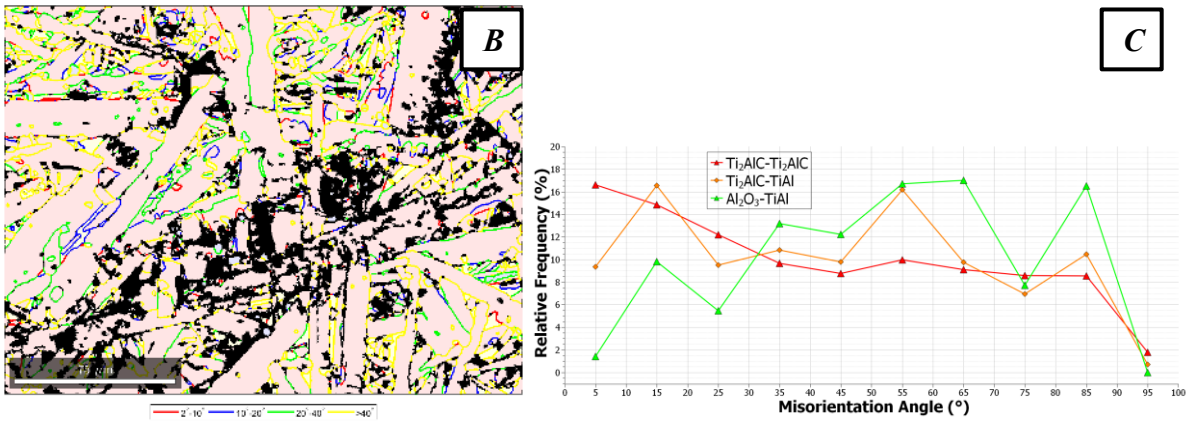

Figure 7.32ii: B) *EBSD map showing the misorientation angles of the grain boundaries in Site 1 of the TRT-4 Ti_2AlC sample;* ***C)*** *Same line graph as* ***A****, showing the grain boundaries between phases that produced the lowest peaks.*

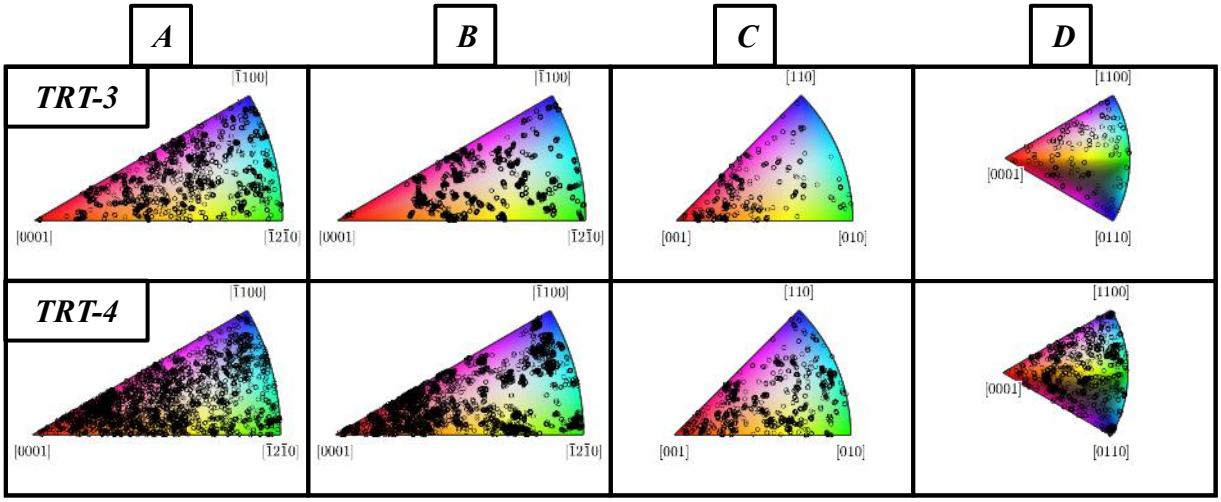

Figure 7.33: *Y-direction Inverse Pole Figure keys of the separate phases found in the Ti_2AlC MAX phase deformed at Room Temperature, with the orientation spread of the separate grains superimposed.* ***IPF Keys: A)*** *Ti_2AlC grains with a grain area of under 50μm^2,* ***B)*** *Ti_2AlC grains with a grain area of over 50μm^2,* ***C)*** *TiAl grains,* ***D)*** *Al_2O_3 grains*

7.3.1.2 EBSD analysis of Ti_2AlC samples tested at 1000°C

The EBSD data collected for the Ti_2AlC samples tested at 1000°C can be found in *Figures 7.34-7.40*. As has already been established in previous sections, each sample tested at 1000°C under the faster strain rates failed in a brittle manner, with most samples generally splitting into two pieces, with the large crack running through the sample 45° to the loading direction being the predominant macroscopic feature. This brittle nature of failure invariably means that the microstructure of the sample is, for the most part, similar to that of the as-received samples. From the band contrast images in *Figures 7.34C and 7.35C*, it is evident that the grain shape of the T10-0 and T10-2 samples is similar to that of the as received sample. The IPF maps of each sample tested at the fastest strain rate can be found in *Figures 7.34B and 7.35B*, while the plot of the orientation of each grain on the IPF colour keys can be found in *Figure 7.40*. From these figures it can be seen that there is generally a random orientation for all phases for both the T10-0 and T10-2 samples.

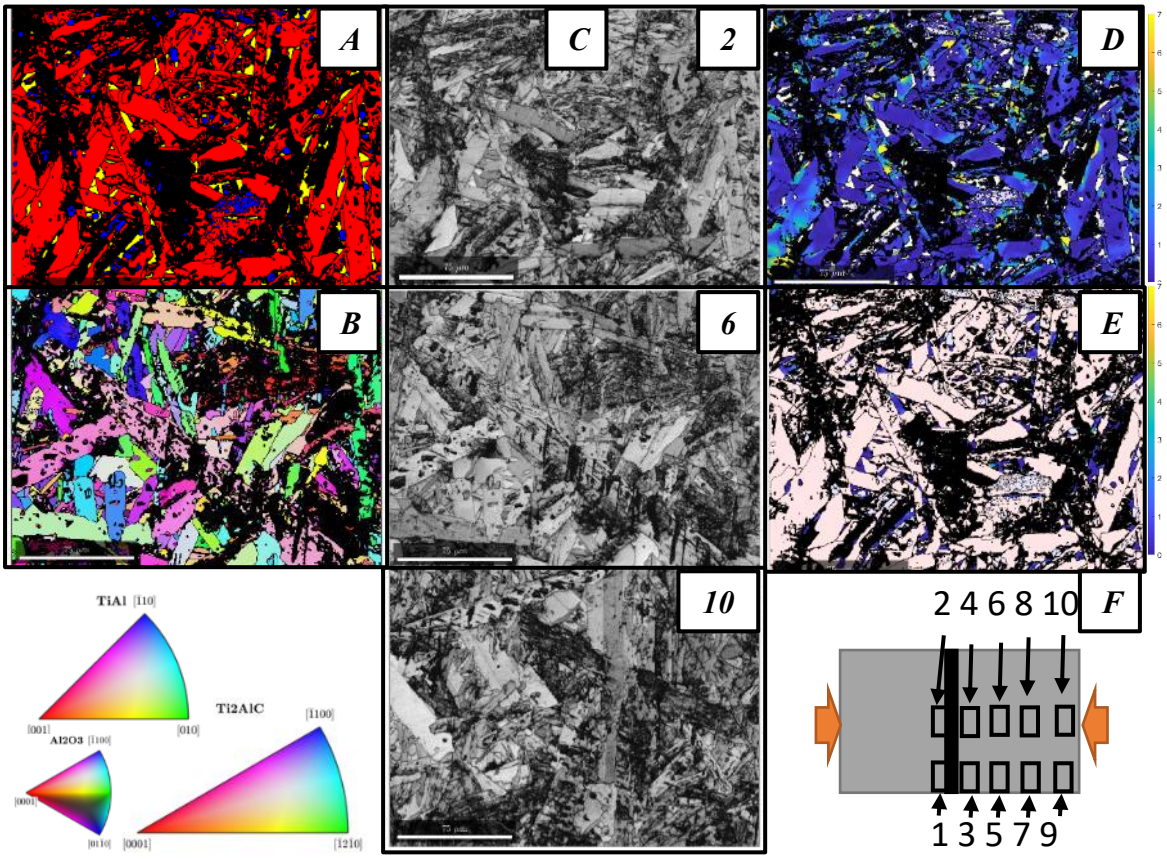

Figure 7.34: *EBSD Maps of the T10-0 Ti_2AlC Sample:* ***A)*** *Phase Map, (R=Ti_2AlC, Y=TiAl, B=Al_2O_3),* ***B)*** *IPF-Y Map,* ***C)*** *Band Contrast showing Sites 2, 6 and 10,* ***D-E)*** *Misorientation Angles of Site 2,* ***F)*** *Map locations*

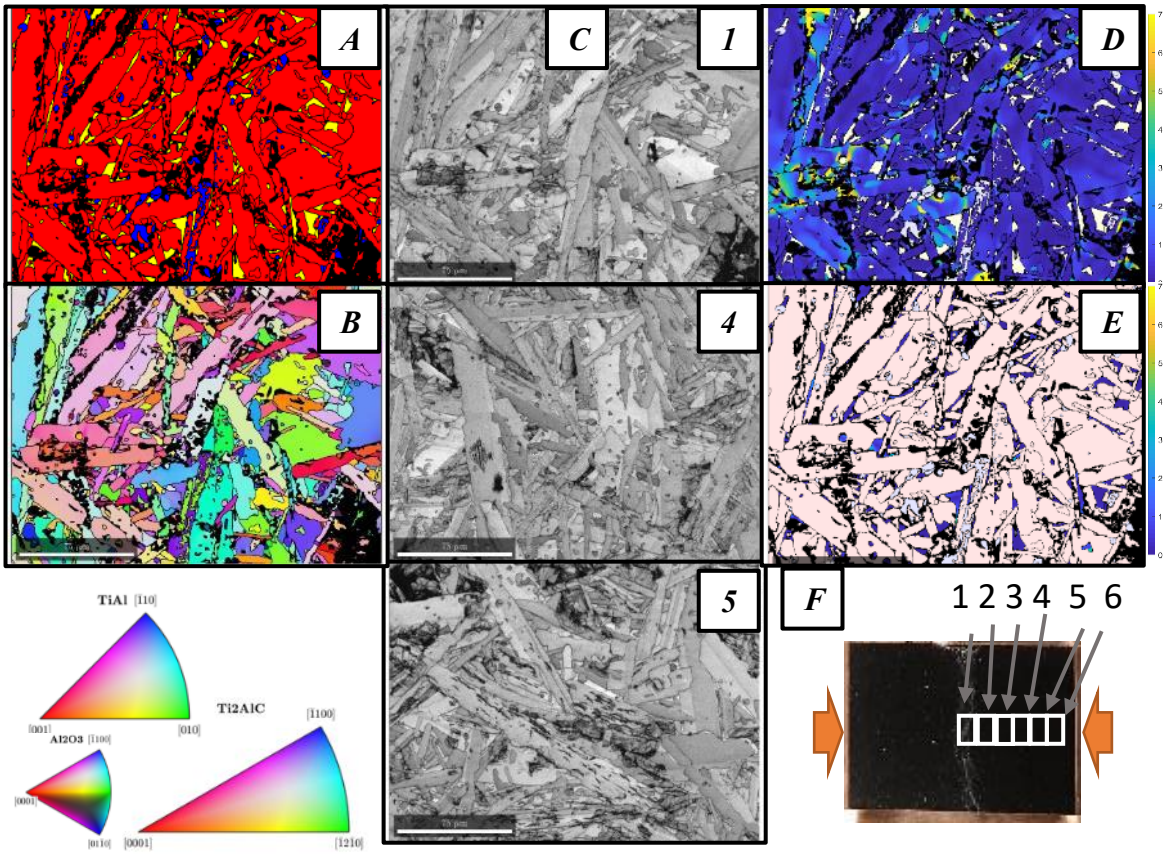

Figure 7.35: *EBSD Maps of the T10-2 Ti_2AlC Sample:* ***A)*** *Phase Map, (R=Ti_2AlC, Y=TiAl, B=Al_2O_3),* ***B)*** *IPF-Y Map,* ***C)*** *Band Contrast showing Sites 1-3,* ***D-E)*** *Misorientation Angles of Site 1,* ***F)*** *Map locations*

The grain boundaries misorientation angle data for the T10-0 and T10-2 samples is presented in *Figures 7.36 and 7.37*. For both samples, the misorientation angles of the boundaries between the Ti_2AlC grains are constant across the graph, indicating that the orientations are distributed uniformly throughout the microstructure. A uniform distribution is also present for the grain boundaries between the Ti_2AlC and TiAl phases for both samples. There is a non-random distribution for the boundary misorientation angles between the TiAl grains for both samples, with the majority of grains having a high angle grain boundary of between 80°-90°. The misorientation angles between Al_2O_3 grains for both samples were also found to have a non-random distribution, with a noticeable peak between 50°-60° for both. The Al_2O_3-TiAl grain boundaries for the T10-0 sample appear more uniform than those of the T10-2 sample, which have a slight random, Mackenzie distribution.

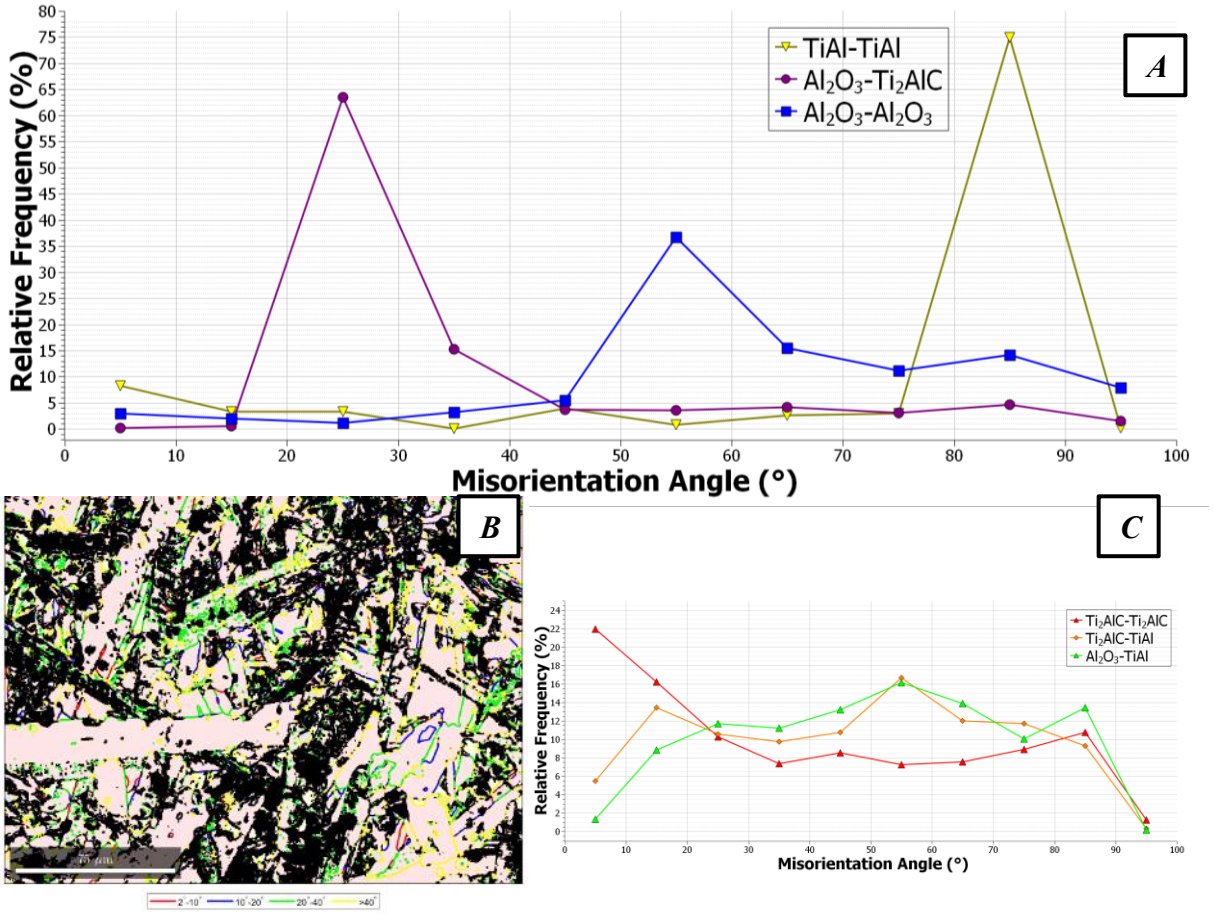

Figure 7.36: A) *Line graph showing an average of the grain boundary misorientation angles across the recorded sites. Graph shows the grain boundaries between phases that produced the highest peaks;* ***B)*** *EBSD map showing the misorientation angles of the grain boundaries in Site 3 of the T10-0 Ti_2AlC sample;* ***C)*** *Same line graph as* ***A****, showing the grain boundaries between phases that produced the lowest peaks.*

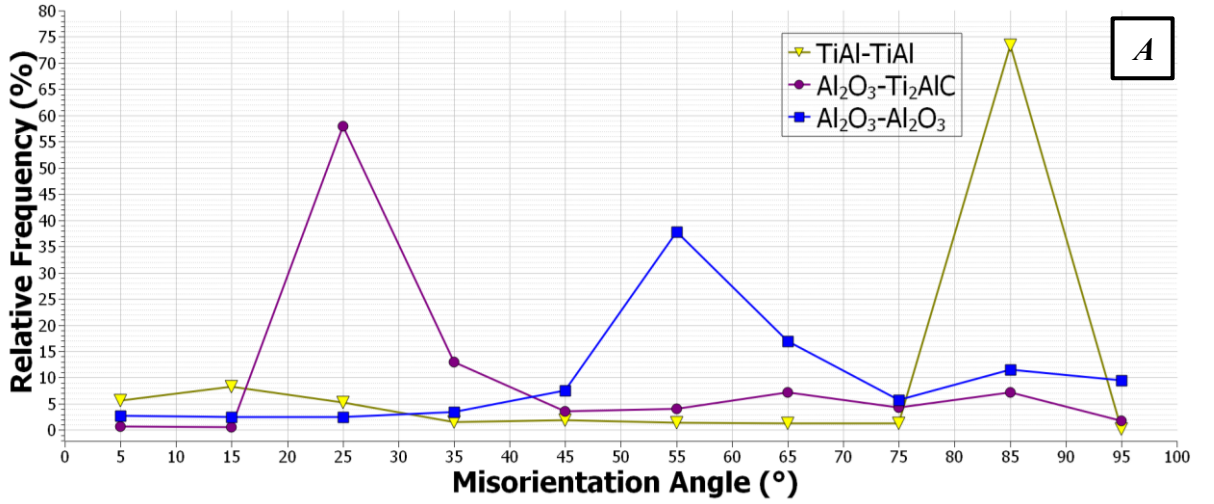

Figure 7.37i: A) *Line graph showing an average of the grain boundary misorientation angles across the recorded sites. Graph shows the grain boundaries between phases that produced the highest peaks*

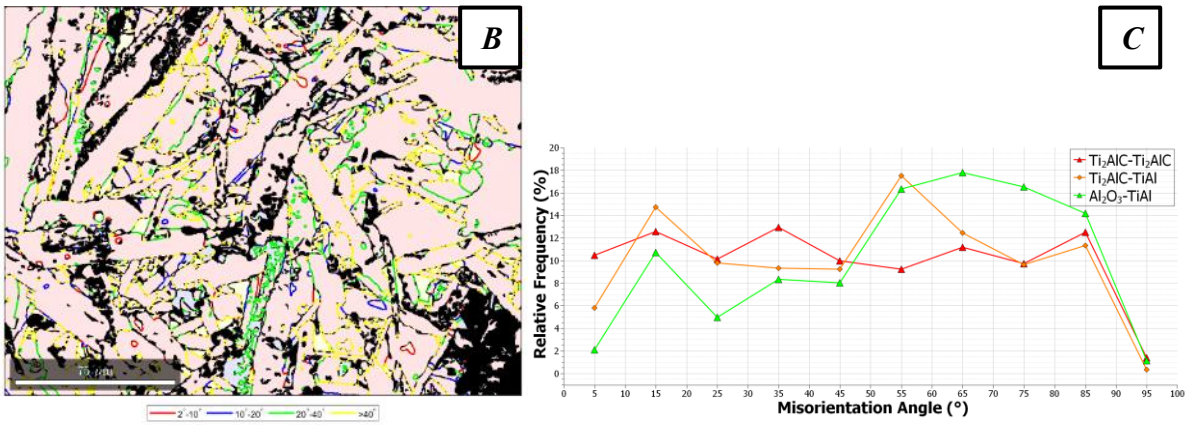

Figure 7.37ii: B) *EBSD map showing the misorientation angles of the grain boundaries in Site 1 of the T10-2 Ti_2AlC sample;* ***C)*** *Same line graph as* ***A****, showing the grain boundaries between phases that produced the lowest peaks.*

The EBSD maps for the T10-4 sample can be found in *Figures 7.38 and 7.39*. The changed microstructure is immediately evident when studying the phase and band contrast maps. The size and shape of the Ti_2AlC grains in particular is significantly different from the earlier tests, with the larger grains breaking down into numerous smaller grains. This is especially true for the map taken closest to the centre of the sample, while the map closest to the compression anvil has a microstructure more in common with the as-received sample. Also of note is the TiAl phase being almost entirely absent from the phase map in *Figure 7.38A.* The IPF map in *Figure 7.38B* shows that the colour in each grain is much less uniform than both the as received sample and the samples that failed in a brittle manner. The IPF colour key interpolated with a plot of the orientation of each grain can be found in *Figure 7.40.* This colour key not only confirms the relative lack of TiAl when compared to the previous samples tested at 1000°C (*Figure 7.40C),* but also that the Ti_2AlC grains with a grain area over $50\mu m^2$ have an orientation to the [0001] direction. This feature is not as obvious for the Ti_2AlC grains under $50\mu m^2$, which appear slightly more randomly orientated than the larger grains.

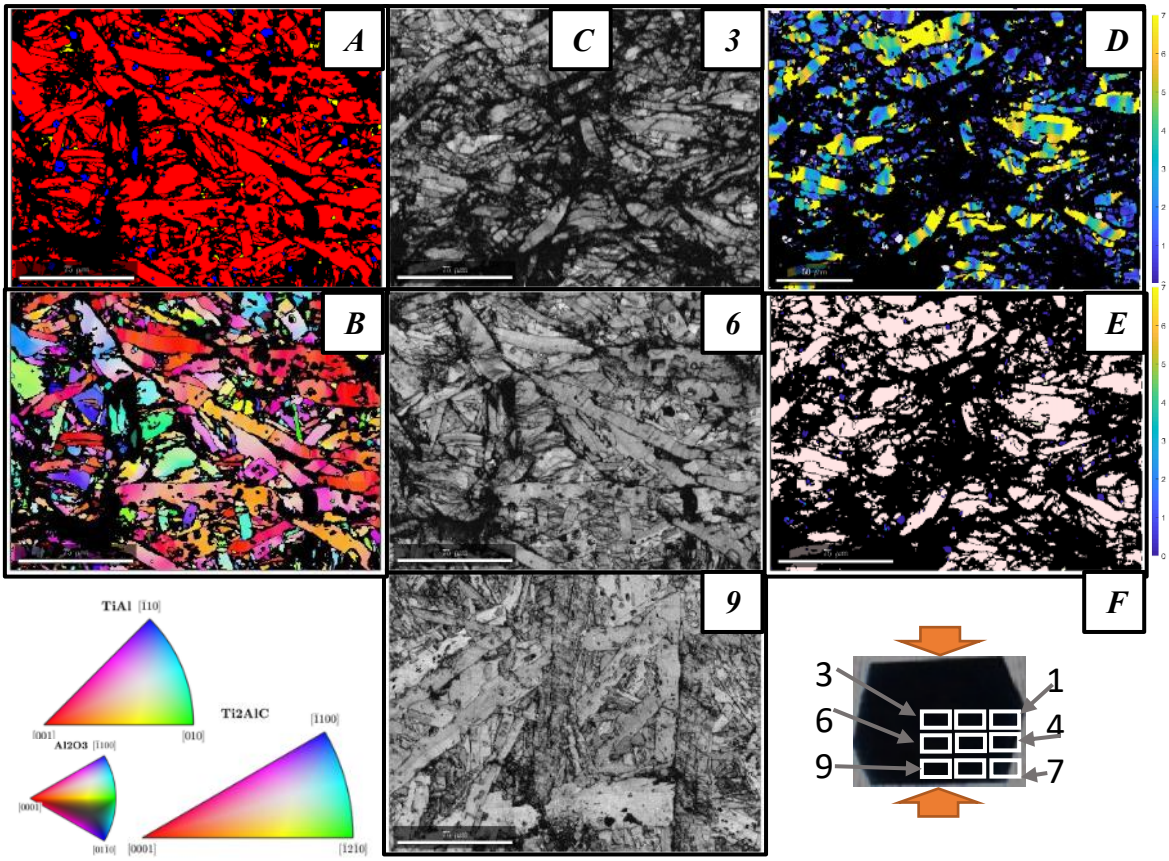

Figure 7.38: *EBSD Maps of the T10-4 Ti_2AlC Sample:* ***A)*** *Phase Map, (R=Ti_2AlC, Y=TiAl, B=Al_2O_3),* ***B)*** *IPF-Y Map,* ***C)*** *Band Contrast showing Sites 1-3,* ***D-E)*** *Misorientation Angles of Site 1,* ***F)*** *Map locations*

The grain boundary misorientation angles of the T10-4 sample are shown in *Figure 7.39*. From the histogram it is evident that the majority of the grain boundaries possess a non-random distribution, with only the boundaries between the Al_2O_3 grains and the Al_2O_3 and TiAl grains showing a random, Mackenzie distribution. For the boundaries between the Ti_2AlC grains, the majority fall into the misorientation angles of between 2°-10° (LAGBs) and 10°-20° (MAGBs). Like the T10-0 and T10-2 samples, the TiAl-TiAl and Al_2O_3-Ti_2AlC grain boundaries have the majority of their misorientation angles in the 80°-90° (HAGBs) and 20°-30° (MAGBs) regions respectively. The TiAl-Ti_2AlC grain boundaries also have a non-random distribution, having generally high angle grain boundaries, with a peak between 50°-60°.

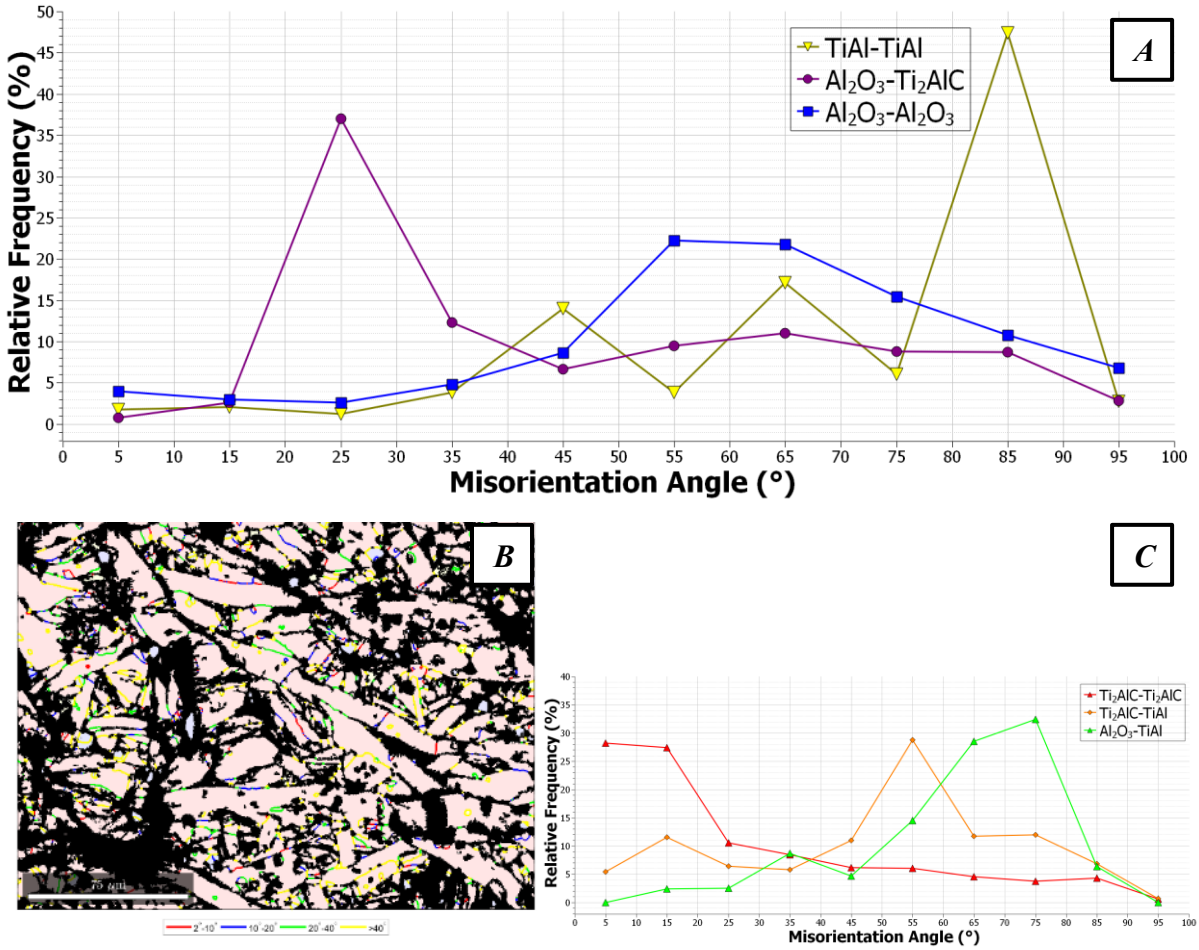

Figure 7.39: A) *Line graph showing an average of the grain boundary misorientation angles across the recorded sites. Graph shows the grain boundaries between phases that produced the highest peaks;* ***B)*** *EBSD map showing the misorientation angles of the grain boundaries in Site 2 of the T10-4 Ti_2AlC sample;* ***C)*** *Same line graph as* ***A****, showing the grain boundaries between phases that produced the lowest peaks.*

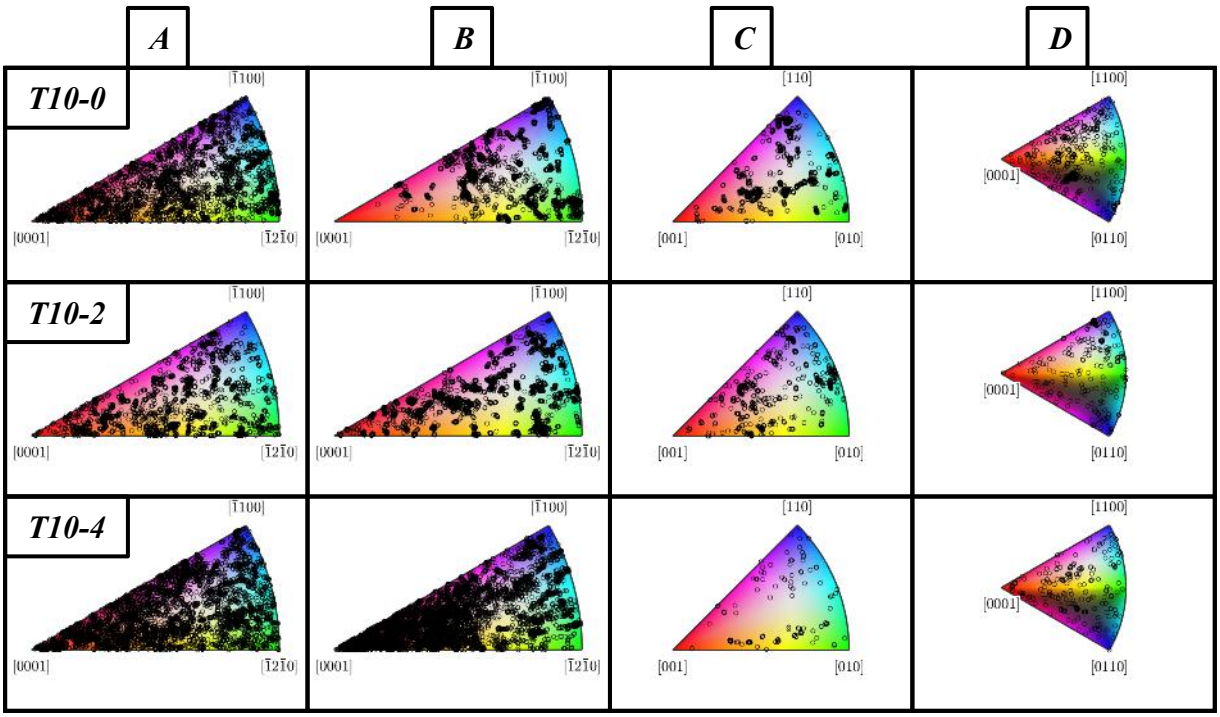

Figure 7.40: *Y-direction Inverse Pole Figure keys of the separate phases found in the Ti_2AlC MAX phase deformed at 1000°C, with the orientation spread of the separate grains superimposed.* ***Tests: 1)*** *T10-0,* ***2)*** *T10-2,* ***3)*** *T10-4.* ***IPF Keys: A)*** *Ti_2AlC grains with a grain area of under 50µm^2,* ***B)*** *Ti_2AlC grains with a grain area of over 50µm^2,* ***C)*** *TiAl grains,* ***D)*** *Al_2O_3 grains*

7.3.1.3 EBSD analysis of Ti_2AlC samples tested at 1100°C

Figures 7.41-7.47 show the EBSD data for the samples tested at 1100°C. Like the samples tested at 1000°C, the samples tested at the faster strain rates, T11-0 and T11-2, show a microstructure not too dissimilar from the as-received sample. When studying the phase maps of T11-0 and T11-2 in *Figures 7.41A and 7.42A* it can be seen that the overall grain shape, with elongated Ti_2AlC grains amongst a TiAl matrix, with small areas of Al_2O_3 grains is reminiscent to that of the as-received sample. The band contrast images are similar, although there is a more deformed microstructure in the T11-2 sample. When comparing the IPF maps of the T11-0 and T11-2 samples it can be seen that the colour in each grain is still generally quite uniform across the microstructure, independent of phase. The IPF colour key of these two samples in *Figure 7.47* shows that the Ti_2AlC grains smaller than $50\mu m^2$ have more orientation to the [0001] direction than the larger grains. For the other phases, the orientation of each grain is still seen to be random.

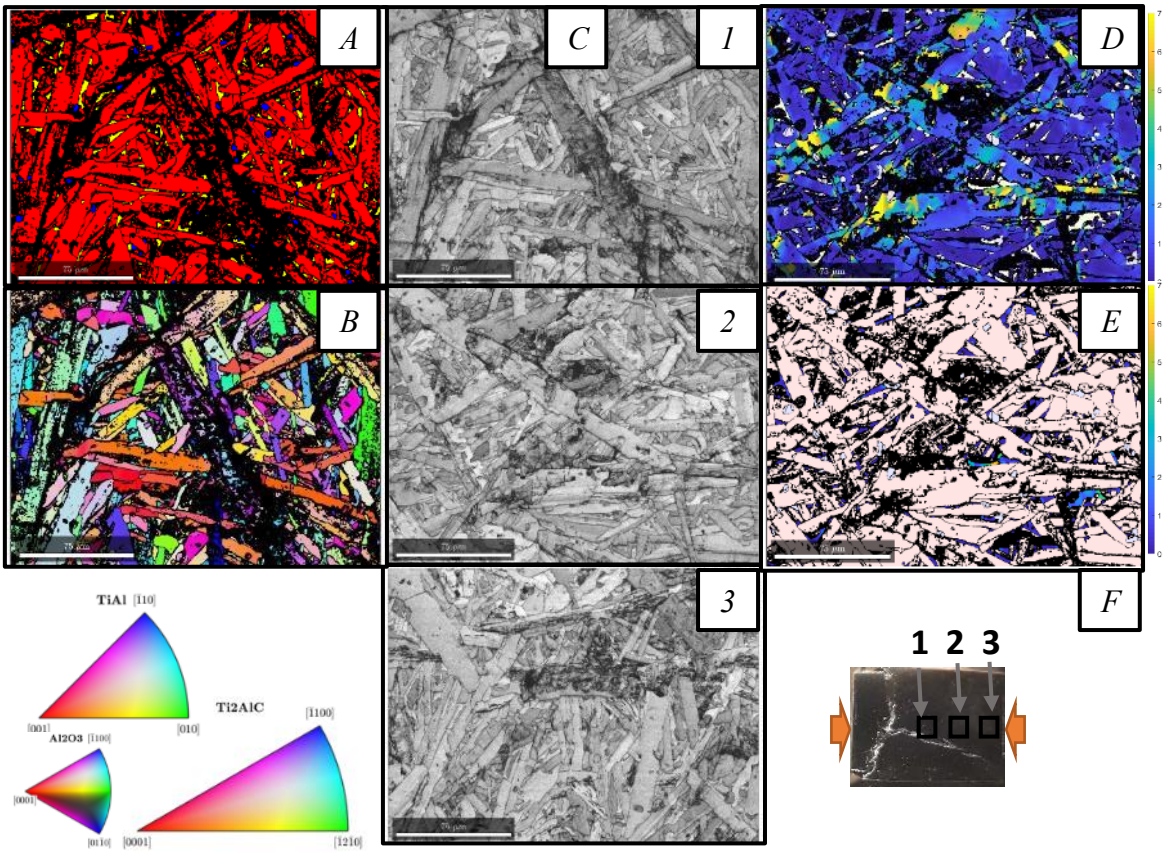

Figure 7.41: *EBSD Maps of the T11-0 Ti_2AlC Sample:* ***A)*** *Phase Map, (R=Ti_2AlC, Y=TiAl, B=Al_2O_3),* ***B)*** *IPF-Y Map,* ***C)*** *Band Contrast showing Sites 1-3,* ***D-E)*** *Misorientation Angles of Site 2,* ***F)*** *Map locations*

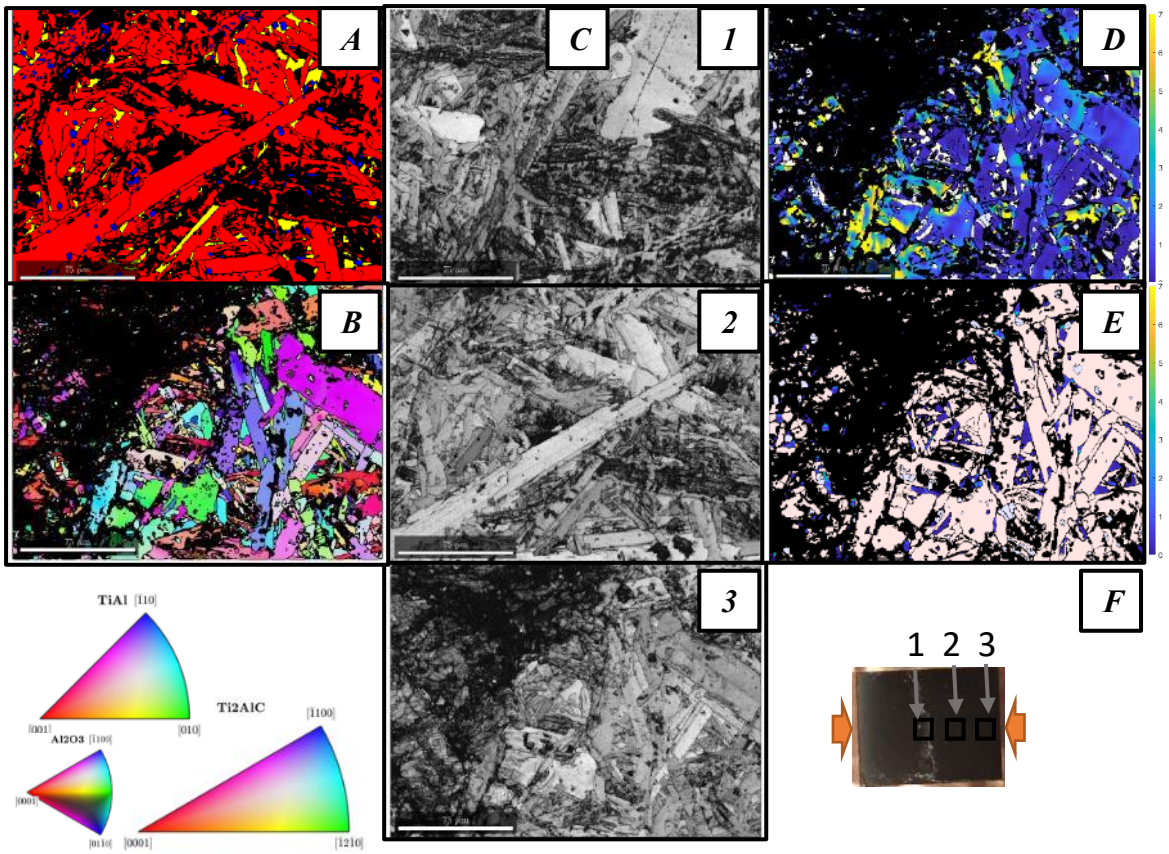

Figure 7.42: *EBSD Maps of the T11-2 Ti_2AlC Sample:* ***A)*** *Phase Map, (R=Ti_2AlC, Y=TiAl, B=Al_2O_3),* ***B)*** *IPF-Y Map,* ***C)*** *Band Contrast showing Sites 1-3,* ***D-E)*** *Misorientation Angles of Site 3,* ***F)*** *Map locations*

Figures 7.43 and 7.34 show the grain boundaries misorientation angle data for the T10-0 and T10-2 samples. Both samples have a very similar profile with regards to their grain boundary misorientation angles. A uniform distribution was found to be present in both samples for the boundaries between the Ti_2AlC grains and also between the Ti_2AlC and TiAl grains. For both samples a non-random distribution for the boundary misorientation angles between the TiAl grains was found, with the peaks suggesting a high angle grain boundary of between 80°-90°. The boundaries between the Al_2O_3 grains show an random Mackenzie type distribution for both samples, although peaks at 60°-70° and 50°-60° (both HAGBs) for the T11-0 and T11-2 samples respectively suggest a slightly less random distribution than has been seen before. The misorientation angles between the Al_2O_3 and Ti_2AlC grains for both samples were found to have a generally non-random distribution, with a noticeable peak between 20°-30° (MAGB) for both, although the relatively small peak for the T11-0 sample suggests a slightly more uniform distribution. The Al_2O_3-TiAl grain boundaries for both samples have a more random, Mackenzie type distribution

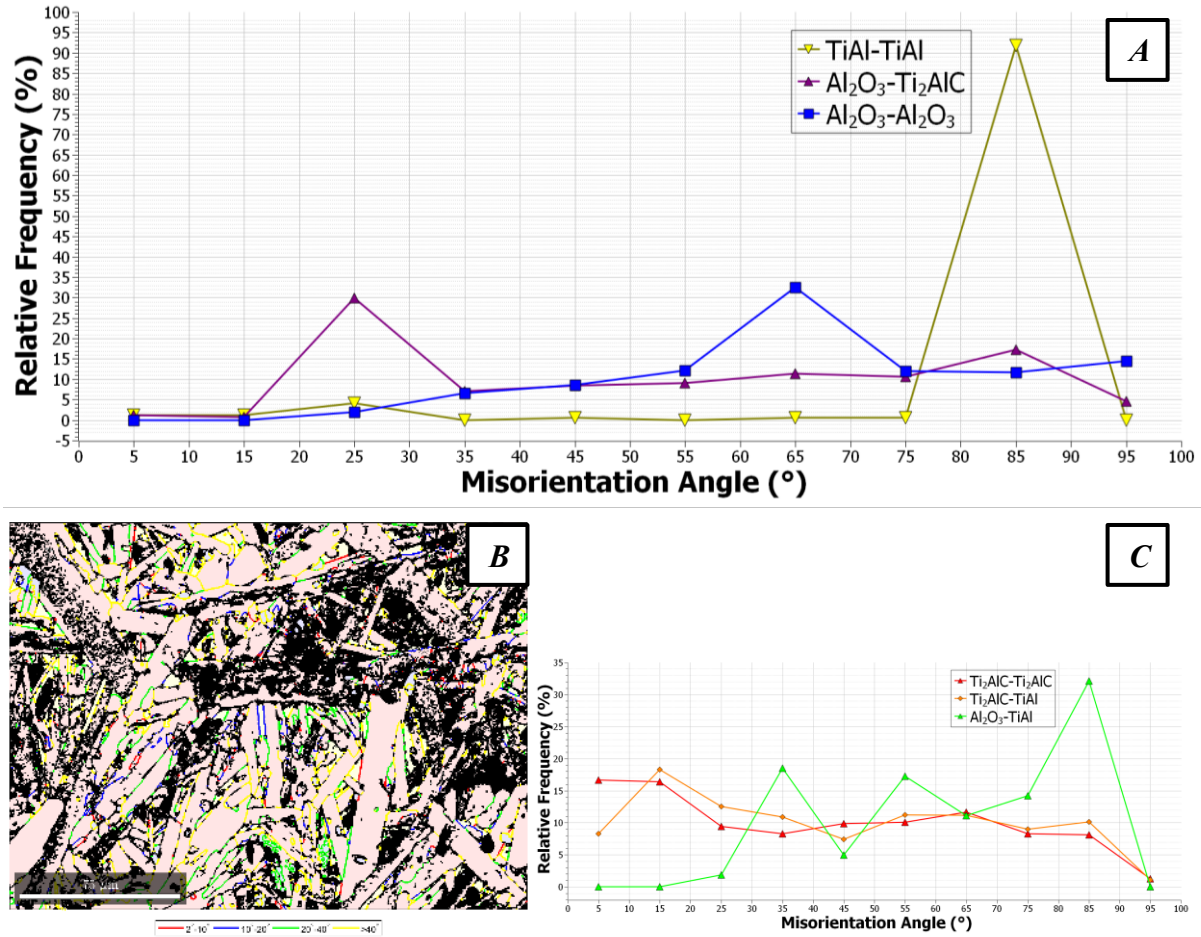

Figure 7.43: ***A)*** *Line graph showing an average of the grain boundary misorientation angles across the recorded sites. Graph shows the grain boundaries between phases that produced the highest peaks;* ***B)*** *EBSD map showing the misorientation angles of the grain boundaries in Site 3 of the T11-0 Ti_2AlC sample;* ***C)*** *Same line graph as* ***A****, showing the grain boundaries between phases that produced the lowest peaks.*

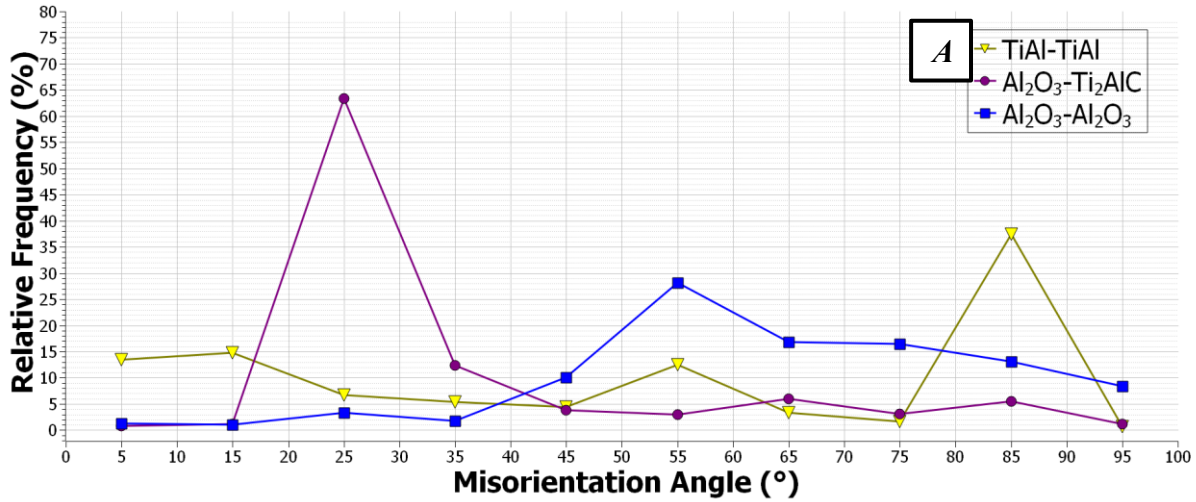

Figure 7.44i: ***A)*** *Line graph showing an average of the grain boundary misorientation angles across the recorded sites. Graph shows the grain boundaries between phases that produced the highest peaks*

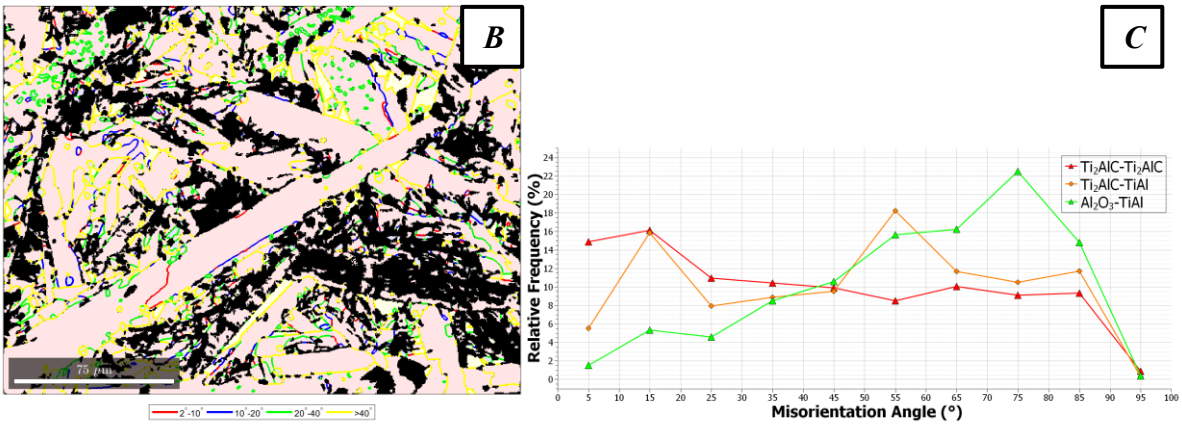

Figure 7.44ii: B) *EBSD map showing the misorientation angles of the grain boundaries in Site 2 of the T11-2 Ti_2AlC sample;* ***C)*** *Same line graph as* ***A****, showing the grain boundaries between phases that produced the lowest peaks.*

The EBSD maps for the T11-4 sample can be found in *Figures 7.45 and 7.46*. Similar to the T10-4 sample also tested with the slowest strain rate, the size and shape of the grains within the microstructure is substantially different to the T11-0 and T11-2 samples. The large Ti_2AlC grains previously seen are seen to break down into numerous smaller grains. This feature is particularly evident in maps taken closer to the centre of the sample, as can be seen in the band contrast maps in *Figure 7.45C*. From *Figure 7.45C(3)* it can be seen that in general, the closer to the surface of the sample that was in contact with the compression anvil, the less deformed the microstructure. Like the T10-4 sample, the TiAl phase is almost completely absent from the phase map in *Figure 7.45A*. *Figure 7.45B* shows the IPF map of the T11-0 sample, in which it can be seen that the colour in each individual grain, regardless of phase, is substantially less uniform than seen in the T11-0 or T11-2 samples. The IPF colour keys in *Figure 7.47* show that the Ti_2AlC grains smaller than 50µm^2 generally have an orientation to the [0001] direction. For Ti_2AlC grains larger than 50µm^2 most appear to have an orientation to the [0001] direction, although a small number of grains also appear to orient to both the $[\bar{1}2\bar{1}0]$ and the $[\bar{1}100]$ directions.

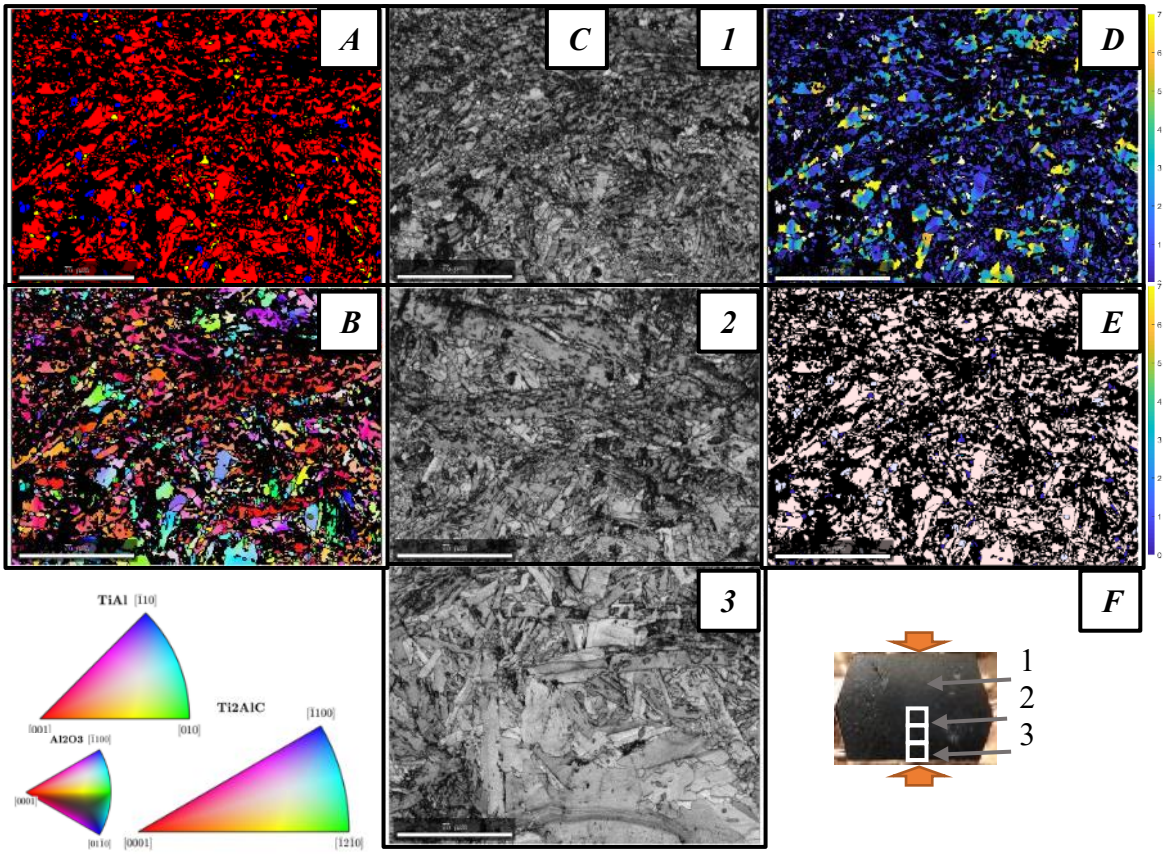

Figure 7.45: *EBSD Maps of the T11-4 Ti_2AlC Sample:* ***A)*** *Phase Map, (R=Ti_2AlC, Y=TiAl, B=Al_2O_3),* ***B)*** *IPF-Y Map,* ***C)*** *Band Contrast showing Sites 1-3,* ***D-E)*** *Misorientation Angles of Site 1,* ***F)*** *Map locations*

The grain boundary misorientation angles of the T11-4 sample are shown in *Figure 7.46*. Like the T10-4 samples, it is evident from the histogram that the majority of the grain boundaries possess a non-random distribution. For the boundaries between the Ti_2AlC grains, the majority fall into the misorientation angles of between 2°-10° (LAGBs) and 10°-20° (MAGBs). The TiAl-TiAl grain boundaries have the majority of their misorientation angles in the 80°-90° region, although there are also substantial amounts of grain boundaries that have a misorientation angle of 2°-20° (LAGBs and MAGBs). A substantial number of the Al_2O_3-TiAl grain boundaries have a misorientation angle between 40°-50°, also suggesting a non-random distribution. The Al_2O_3-Ti_2AlC grain boundaries have the majority of their misorientation angles in the 20°-30° (MAGBs) region. The TiAl-Ti_2AlC grain boundaries generally have a uniform distribution, while the boundaries between the Al_2O_3 grains have the Mackenzie distribution.

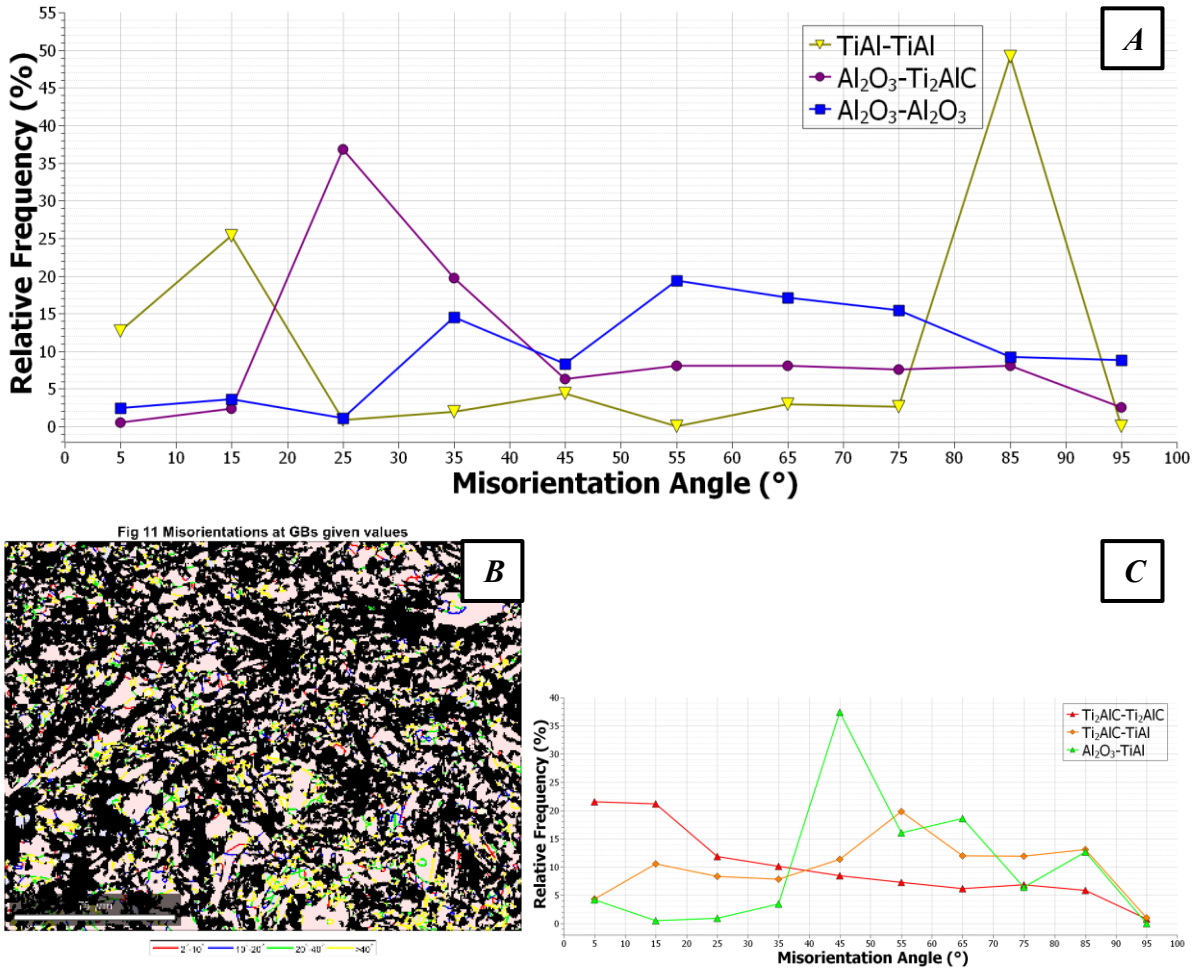

Figure 7.46: A) *Line graph showing an average of the grain boundary misorientation angles across the recorded sites. Graph shows the grain boundaries between phases that produced the highest peaks;* ***B)*** *EBSD map showing the misorientation angles of the grain boundaries in Site 1 of the T11-4 Ti_2AlC sample;* ***C)*** *Same line graph as* ***A****, showing the grain boundaries between phases that produced the lowest peaks.*

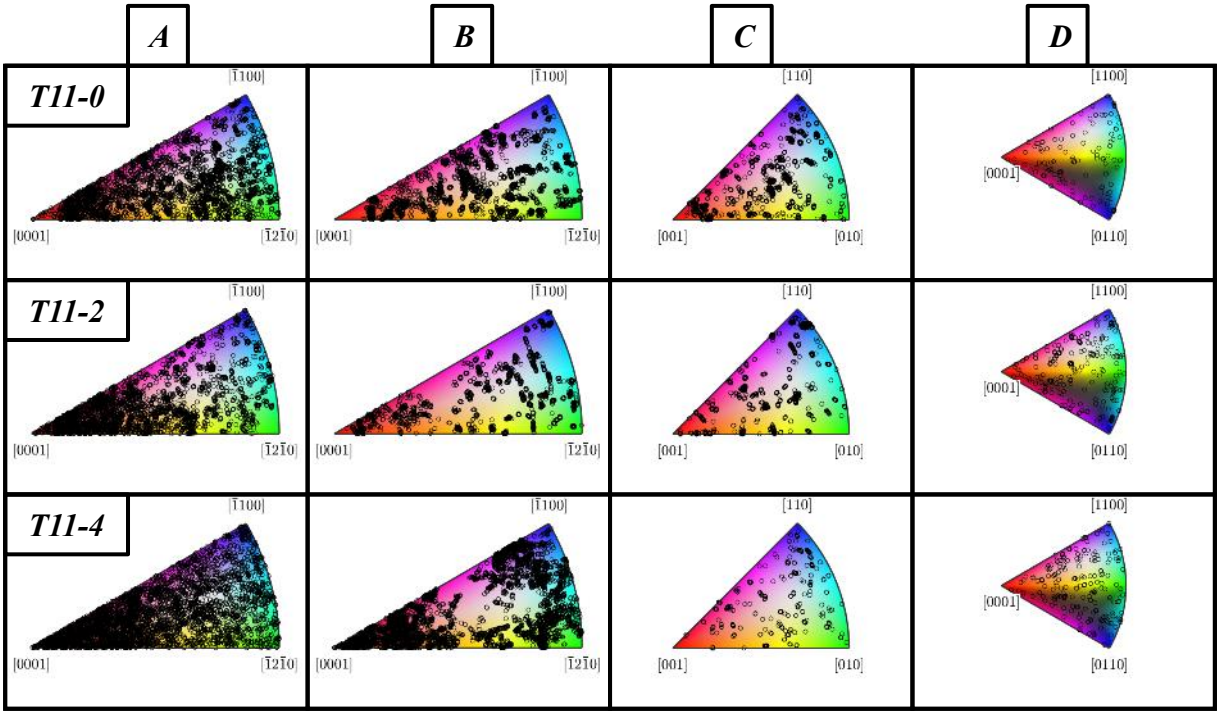

Figure 7.47: *Y-direction Inverse Pole Figure keys of the separate phases found in the Ti_2AlC MAX phase deformed at 1100°C, with the orientation spread of the separate grains superimposed.* ***IPF Keys: A)*** *Ti_2AlC grains with a grain area of under 50µm^2,* ***B)*** *Ti_2AlC grains with a grain area of over 50µm^2,* ***C)*** *TiAl grains,* ***D)*** *Al_2O_3 grains*

7.3.1.4 EBSD analysis of Ti_2AlC samples tested at 1200°C

Figures 7.48-7.54 show the EBSD data for the Ti_2AlC samples tested at 1200°C. The maps for the T12-0 sample can be found in *Figure 7.48*. The T12-0 sample, in addition to the T12-1 sample, were the samples tested at this temperature that failed in a brittle manner, and has a grain morphology very similar to the other samples tested at faster strain rates at lower temperatures. This is further evident when comparing the microstructure of the sample to the T12-2 and T12-4 samples, which appear much more compact and with significantly less large straight, elongated Ti_2AlC grains. The IPF map of the T12-0 sample shows that the colour in each grain is not quite as uniform as samples tested under the same strain rate conditions at lower temperatures. The IPF colour key in *Figure 7.53* shows that all grains for the T12-0 sample have a random orientation, regardless of grain size or phase.

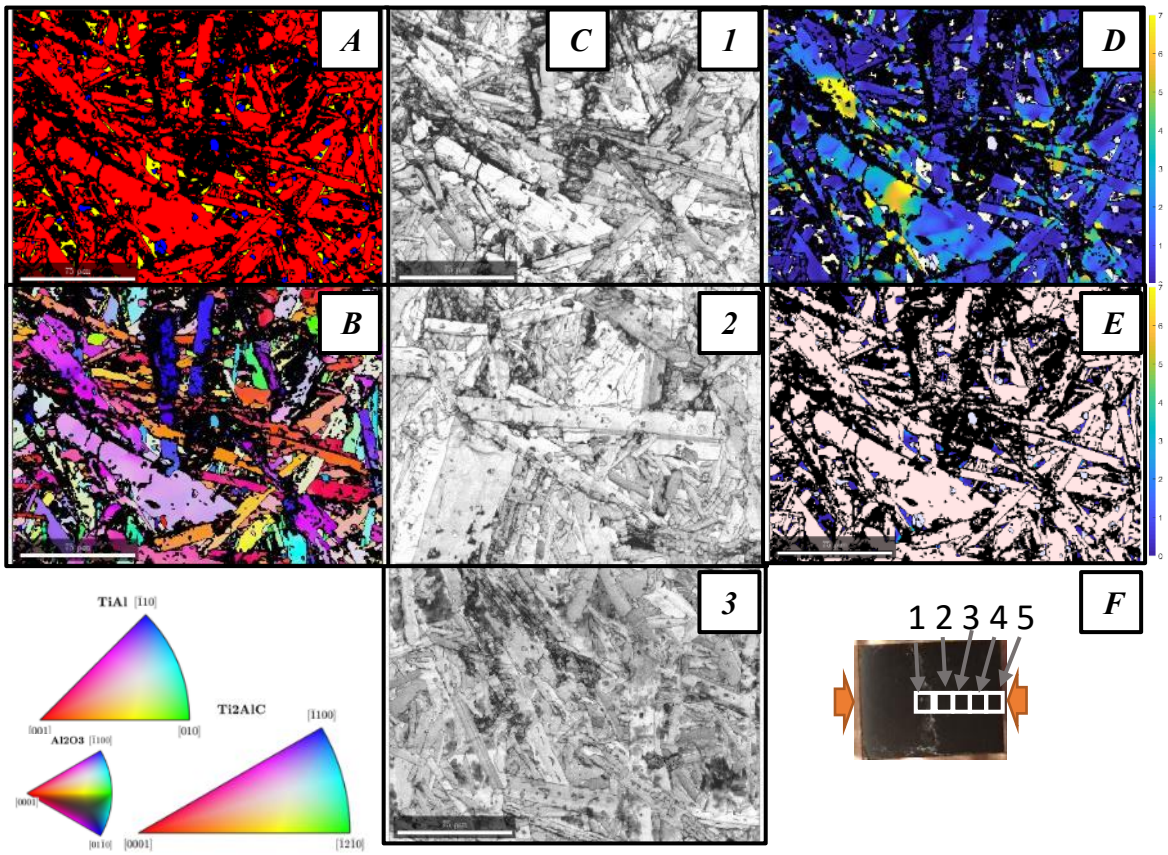

Figure 7.48: *EBSD Maps of the T12-0 Ti_2AlC Sample:* ***A)*** *Phase Map, (R=Ti_2AlC, Y=TiAl, B=Al_2O_3),* ***B)*** *IPF-Y Map,* ***C)*** *Band Contrast showing Sites 1-3,* ***D-E)*** *Misorientation Angles of Site 1,* ***F)*** *Map locations*

The grain boundary misorientation angle data for the T12-0 sample can be found in *Figure 7.49*. The Ti_2AlC-Ti_2AlC, Ti_2AlC-TiAl and Al_2O_3-TiAl grain boundaries all appear to have to have a generally uniform distribution to their misorientation angles, while the grain boundaries between the Al_2O_3 grains appear to have a random Mackenzie profile. The misorientation

angles of the boundaries between both the TiAl grains and the boundaries between the Al_2O_3 and Ti_2AlC grains are non-random, with them having HAGBs in the region of 80°-90° and MAGBs of between 20°-30° respectively.

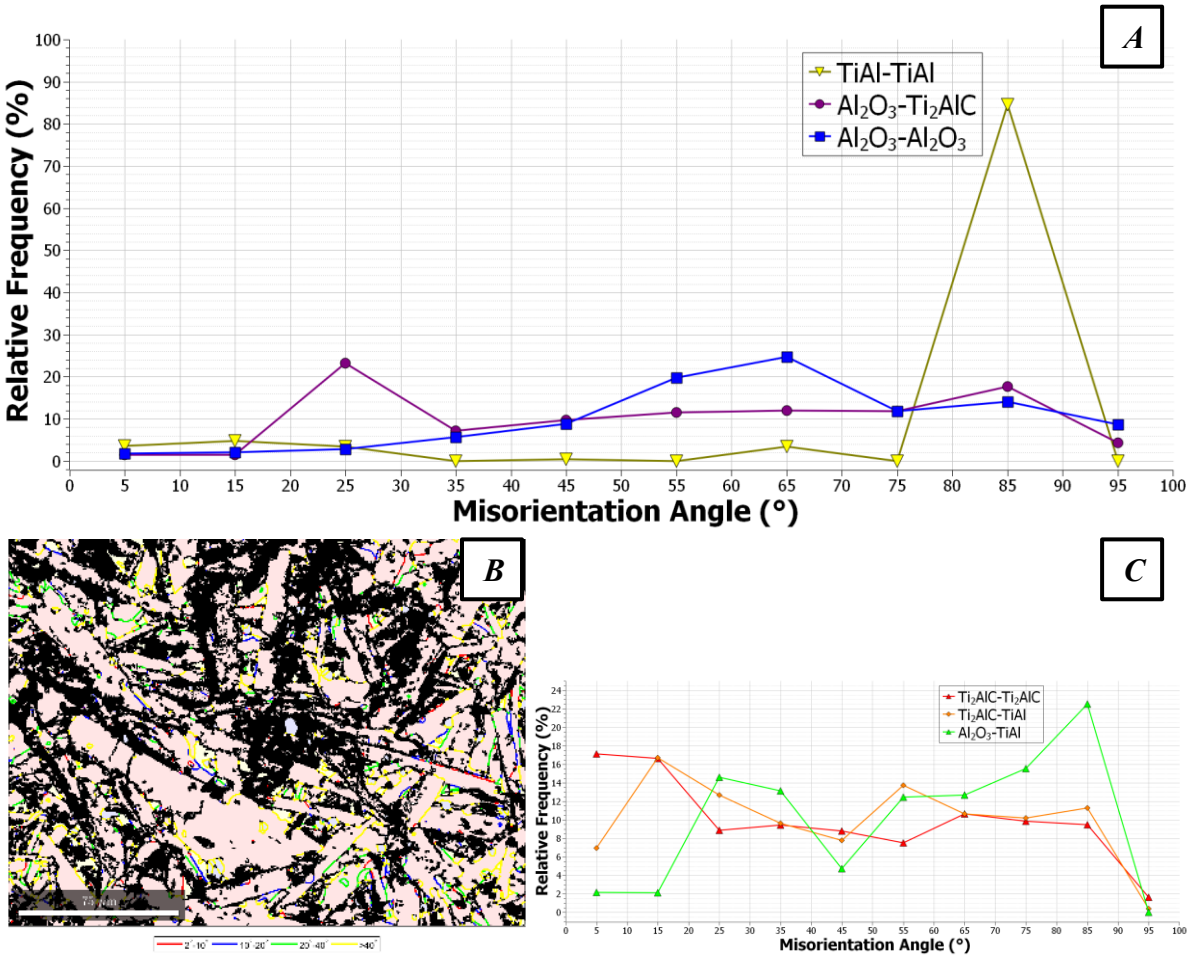

Figure 7.49: A) *Line graph showing an average of the grain boundary misorientation angles across the recorded sites. Graph shows the grain boundaries between phases that produced the highest peaks;* ***B)*** *EBSD map showing the misorientation angles of the grain boundaries in Site 1 of the T12-0 Ti_2AlC sample;* ***C)*** *Same line graph as* ***A****, showing the grain boundaries between phases that produced the lowest peaks.*

Comparing the EBSD data for the T12-2 and T12-4 samples in *Figures 7.50-7.52* it can be seen that features which were also witnessed for the T10-4 and T11-4 samples are on display here as well. These features being the relative lack of the TiAl phase when compared to the samples tested at faster strain rates, the generally compact microstructure and the number of large Ti_2AlC grains that have deformed into numerous smaller grains. The IPF maps for both samples and their related IPF colour keys, are also characterised by grains orientating to the [0001] direction for all Ti_2AlC grain sizes. The two other phases have a random orientation in both samples.

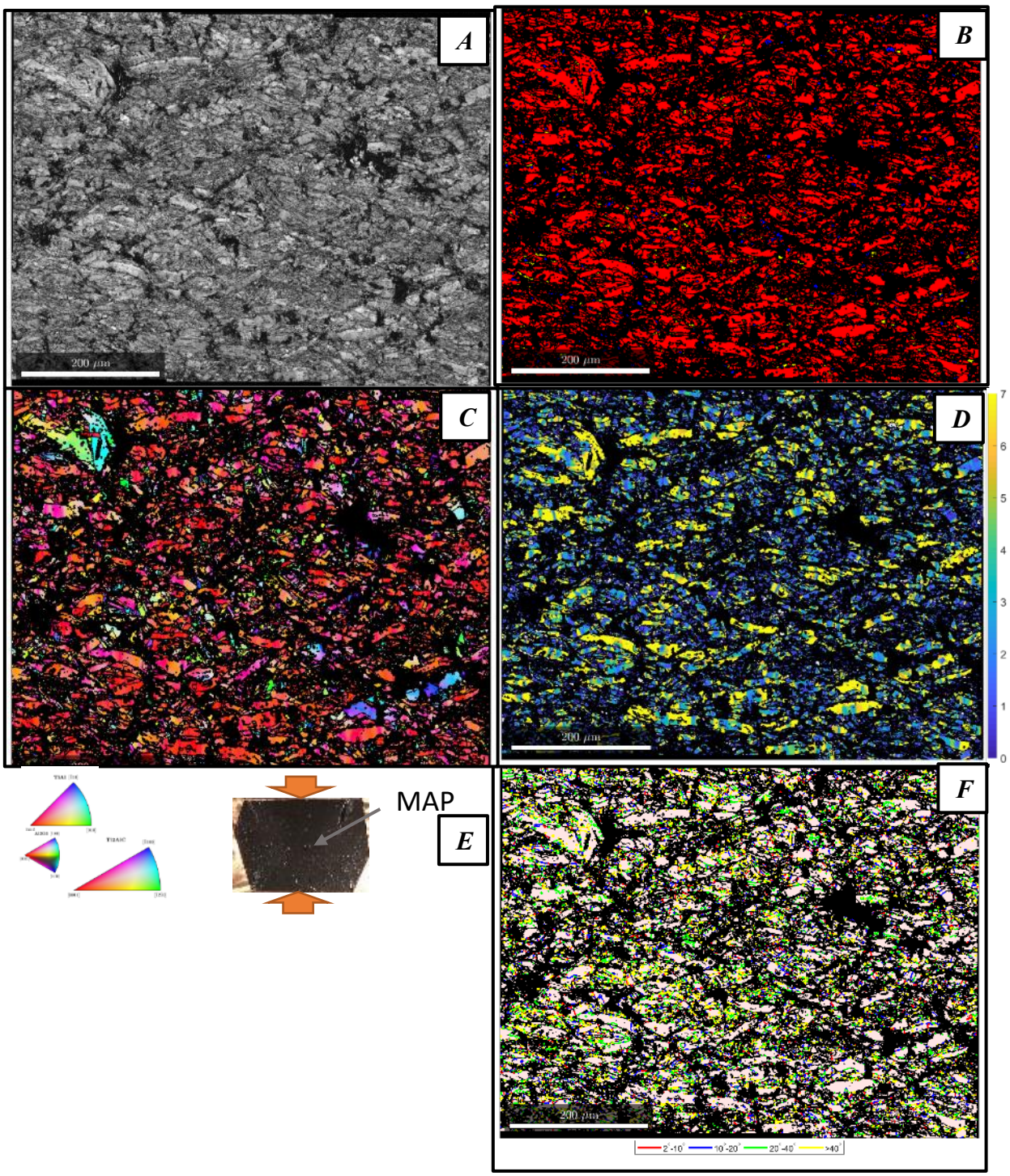

Figure 7.50i: *EBSD Maps of the T12-2 Ti_2AlC Sample:* ***A)*** *Phase Map, (R=Ti_2AlC, Y=TiAl, B=Al_2O_3),* ***B)*** *IPF-Y Map,* ***C)*** *Band Contrast showing Sites 1-3,* ***D)*** *Misorientation Angles,* ***E)*** *Map location,* ***F)*** *EBSD map showing the misorientation angles of the grain boundaries in Site 1 of the T12-0 Ti_2AlC sample.*

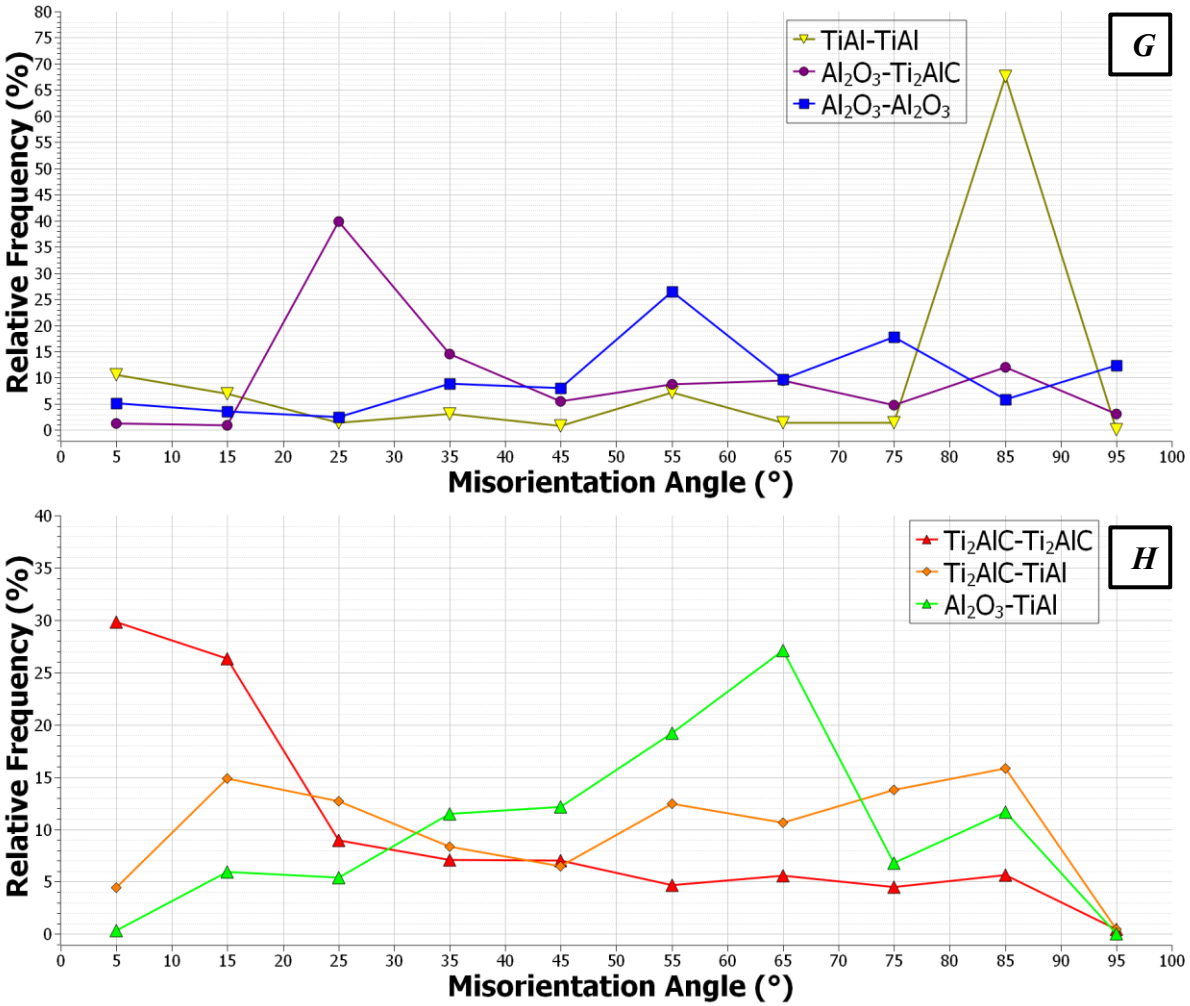

Figure 7.50ii: G) *Line graph showing an average of the grain boundary misorientation angles across the recorded sites. Graph shows the grain boundaries between phases that produced the highest peaks;* ***H)*** *Same line graph as* ***A****, showing the grain boundaries between phases that produced the lowest peaks*

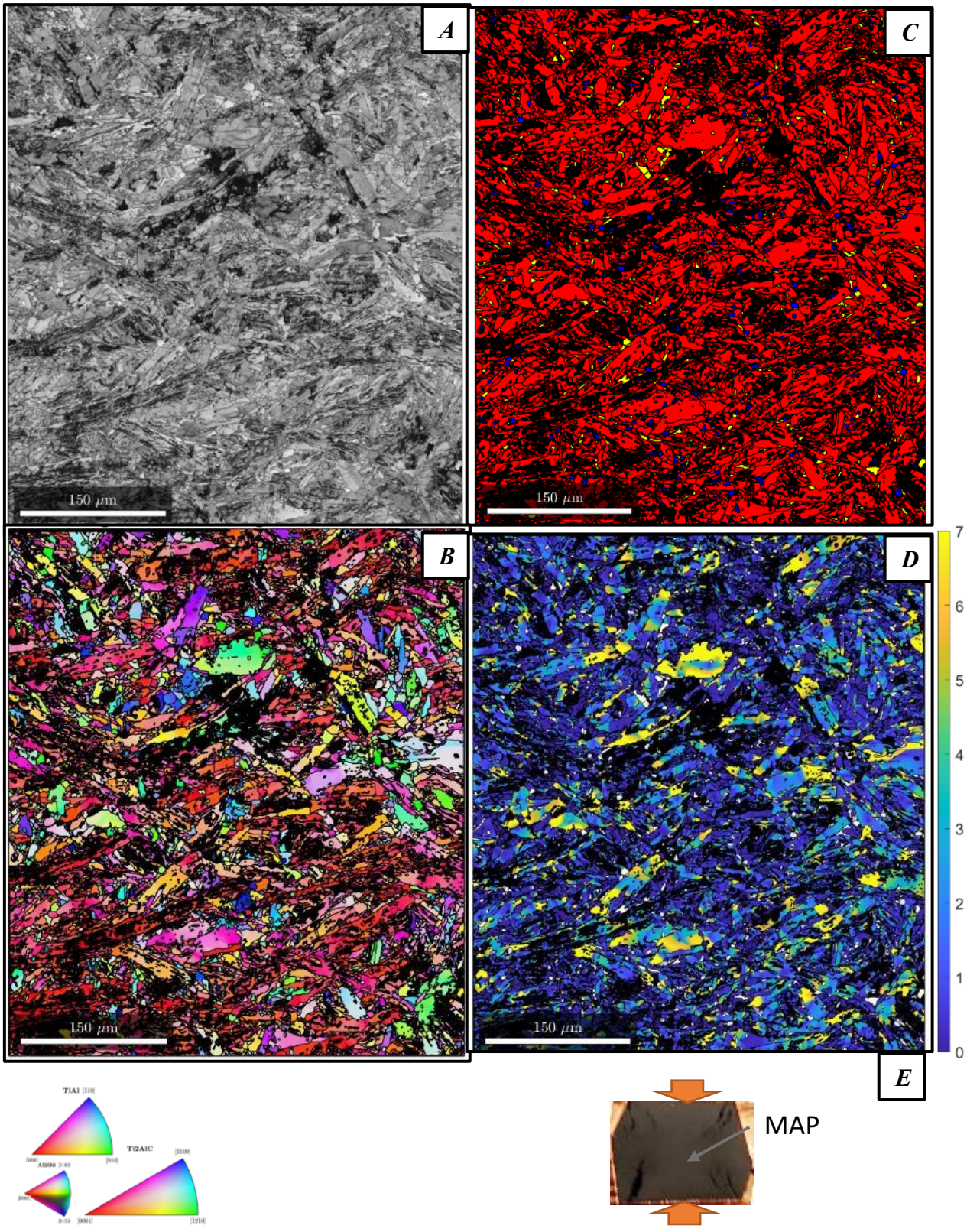

Figure 7.51: *EBSD Maps of the T12-4 Ti_2AlC Sample:* ***A)*** *Phase Map, (R=Ti_2AlC, Y=TiAl, B=Al_2O_3),* ***B)*** *IPF-Y Map,* ***C)*** *Band Contrast showing Sites 1-3,* ***D)*** *Misorientation Angles,* ***E)*** *Map location*

As can be seen from the histograms in *Figures 7.50F and 7.52*, the grain boundary misorientation angles for both the T12-2 and T12-4 samples are very similar. For both samples, the Ti_2AlC-Ti_2AlC, TiAl-TiAl and Al_2O_3-Ti_2AlC grain boundaries were found to have a non-random distribution with regards to misorientation angle. The boundaries between the Ti_2AlC grains for both samples were seen as being close to uniform, although the misorientation angle peaks for both samples were in the LAGB and MAGB range of 2°-20°. Like for most of the Ti_2AlC samples, the peak for the boundaries between the TiAl grains was between a misorientation angle between 80°-90° (HAGB), while the peak for the Al_2O_3-Ti_2AlC grain boundaries was between 20°-30° for both samples. The misorientation angle for the boundaries between the Ti_2AlC and TiAl grains was determined to be uniform, while both the Al_2O_3-Al_2O_3 and Al_2O_3-TiAl grain boundaries were found to have a random, Mackenzie distribution.

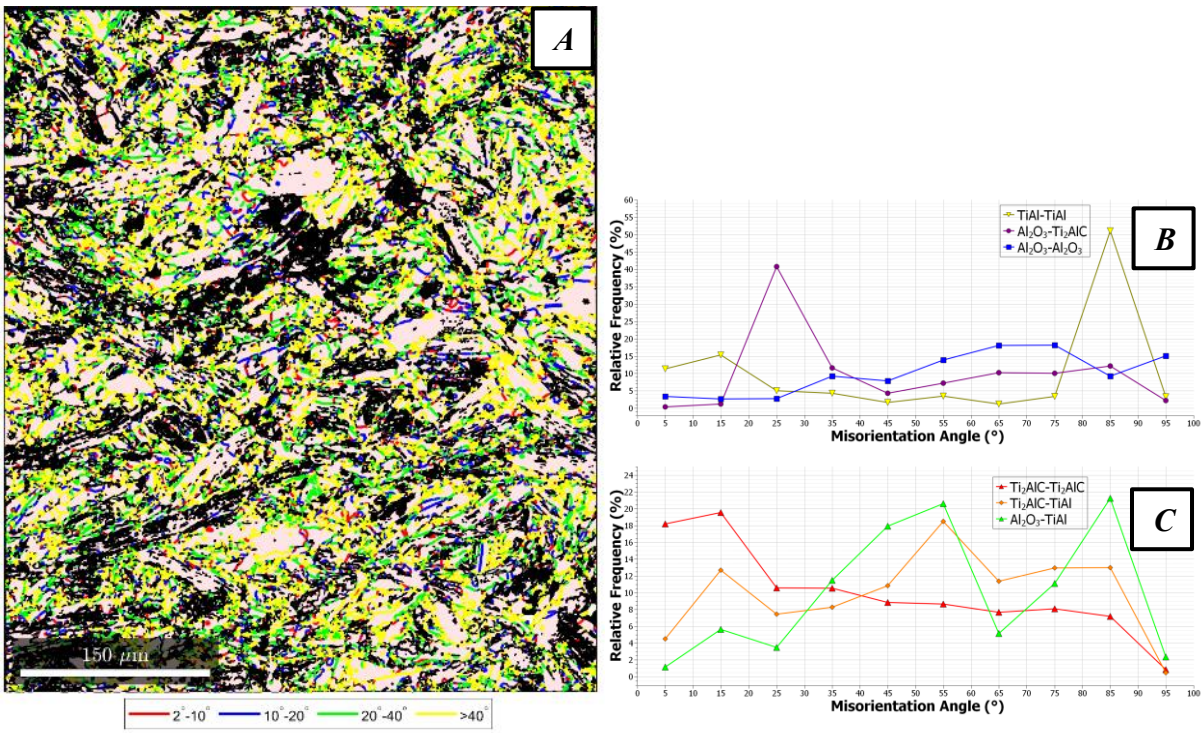

Figure 7.52: A) *EBSD map showing the misorientation angles of the grain boundaries in Site 3 of the T10-0 Ti_2AlC sample;* ***B)*** *Line graph showing an average of the grain boundary misorientation angles across the recorded sites. Graph shows the grain boundaries between phases that produced the highest peaks;* ***C)*** *Same line graph as* ***B****, showing the grain boundaries between phases that produced the lowest peaks.*

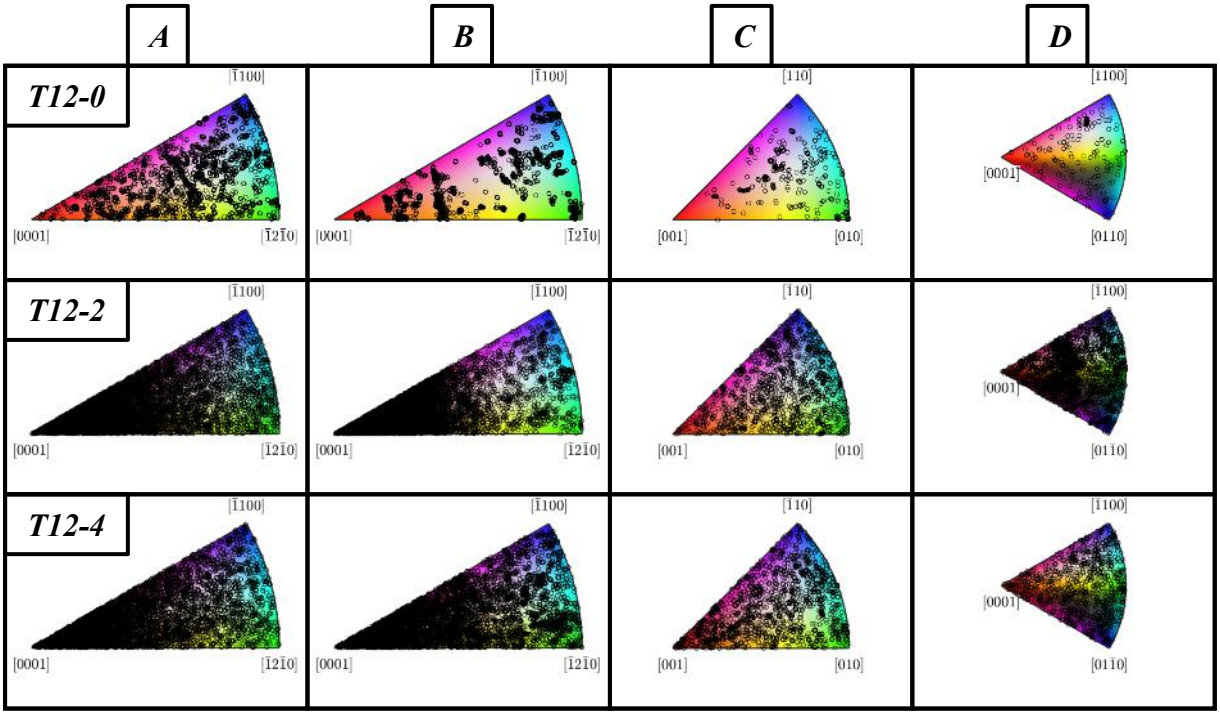

Figure 7.53: *Y-direction Inverse Pole Figure keys of the separate phases found in the Ti_2AlC MAX phase deformed at 1200°C, with the orientation spread of the separate grains superimposed.* ***IPF Keys: A)*** *Ti_2AlC grains with a grain area of under 50µm^2,* ***B)*** *Ti_2AlC grains with a grain area of over 50µm^2,* ***C)*** *TiAl grains,* ***D)*** *Al_2O_3 grains*

7.3.2 EBSD Analysis of Ti_3SiC_2 Samples Compression Tested at both Room and High Temperatures

7.3.2.1 EBSD analysis of Ti_3SiC_2 samples tested at Room Temperature

Figures 7.54 and 7.55 represent the EBSD data collected for the room temperature compression tests of Ti_3SiC_2. The EBSD graphs for the TRT-3 sample can be found in *Figure 7.54*, in which it can be seen that apart from the two large cracks running through Site 3 in *Figure 7.54C(3)*, the microstructure is largely unchanged from that of the as-received sample seen in *Figure 5.15* in Chapter 5. The porosity that was found in the as-received samples is also evident for both the TRT-3 and TRT-4 samples. The EBSD graphs for the TRT-4 sample can be found in *Figure 7.55*. The IPF maps of both samples tested at room temperature show that, like the as-received microstructure, the grains have a largely random texture regardless of phase. This is further confirmed by the IPF colour key with the orientations of each grain overlayed onto it in *Figure 56*, with the colour keys split into both Ti_3SiC_2 and TiC grains smaller and larger than 10µm. For both samples, the grain boundary misorientation data can be found in *Appendix 1*, where it can be seen that for both samples, both the Ti_3SiC_2-TiC and TiC-TiC grain boundaries have a random, Mackenzie profile, while the misorientation is uniform for the Ti_3SiC_2-Ti_3SiC_2 grain boundaries.

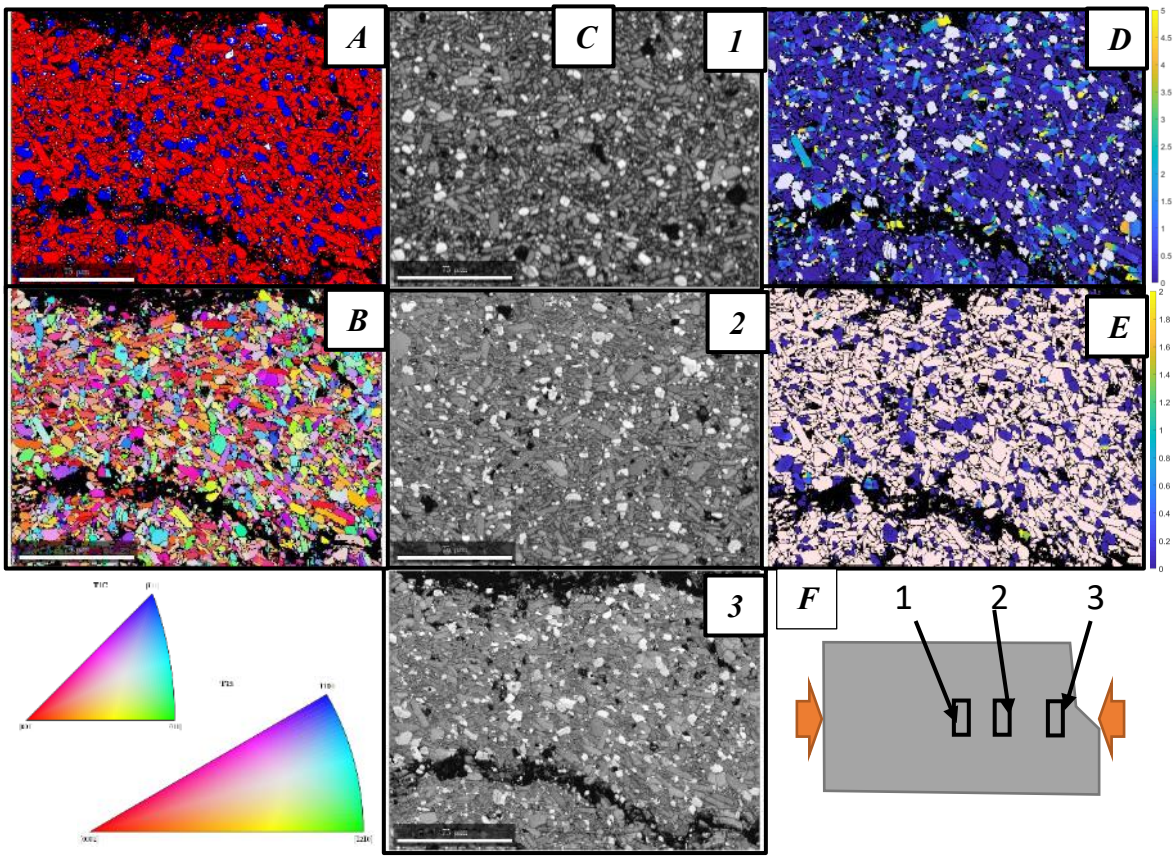

Figure 7.54: *EBSD Maps of the TRT-3 Ti_3SiC_2 Sample:* ***A)*** *Phase Map, (R=Ti_3SiC_2, B=TiC),* ***B)*** *IPF-Y Map,* ***C)*** *Band Contrast showing Sites 1-3,* ***D-E)*** *Misorientation Angles of Site 3,* ***F)*** *Map locations*

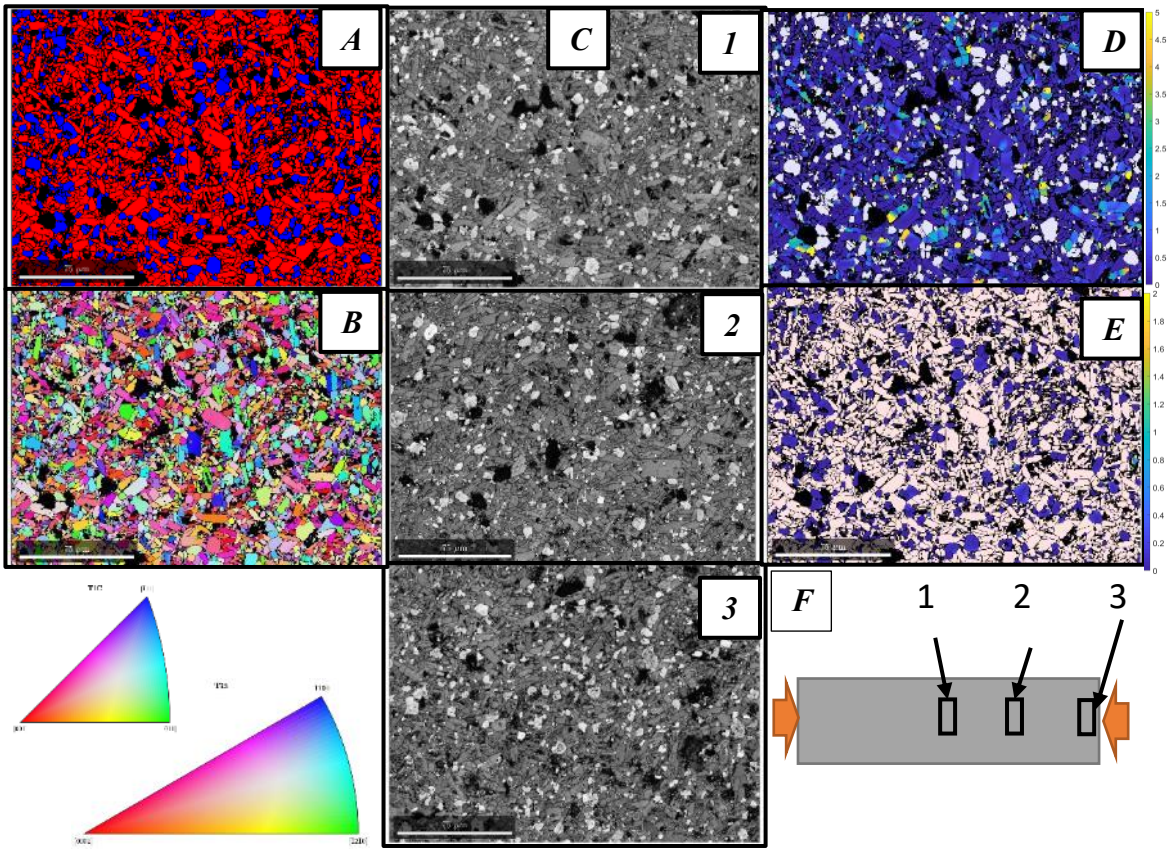

Figure 7.55: *EBSD Maps of the TRT-4 Ti_3SiC_2 Sample:* ***A)*** *Phase Map, (R=Ti_3SiC_2, B=TiC),* ***B)*** *IPF-Y Map,* ***C)*** *Band Contrast showing Sites 1-3,* ***D-E)*** *Misorientation Angles of Site 1,* ***F)*** *Map locations*

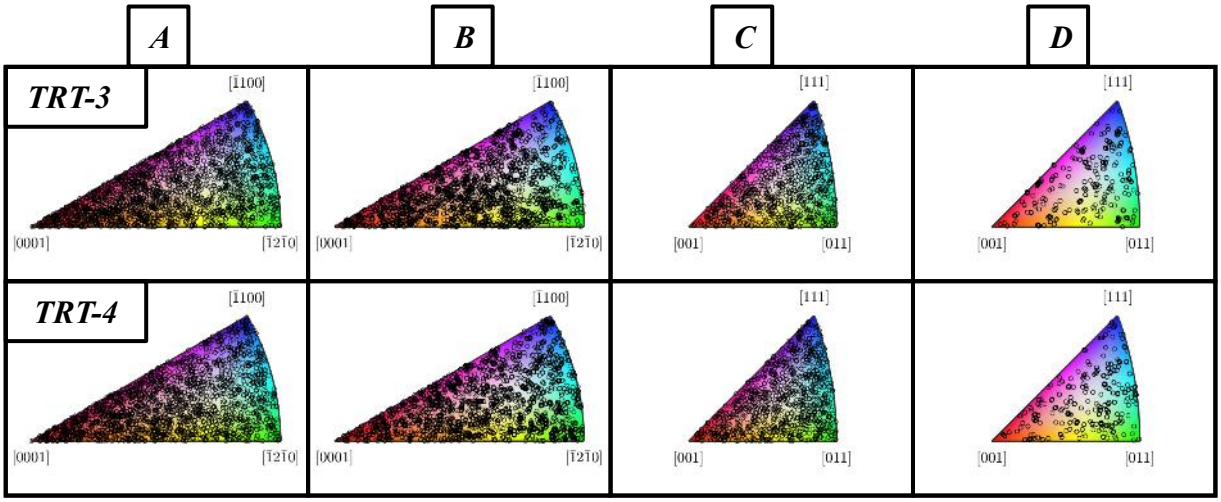

Figure 7.56: *Y-direction Inverse Pole Figure keys of the separate phases found in the Ti_3SiC_2 MAX phase deformed at Room Temperature, with the orientation spread of the separate grains superimposed.* ***IPF Keys: A)*** *Ti_3SiC_2 grains with a grain area of under 10μm^2,* ***B)*** *Ti_3SiC_2 grains with a grain area of over 10μm^2,* ***C)*** *TiC grains with a grain area of under 10μm^2,* ***D)*** *TiC grains with a grain area of over 10μm^2*

7.3.2.2 EBSD analysis of Ti_3SiC_2 samples tested at 1000°C

The EBSD maps derived from the data collected for the Ti_3SiC_2 samples tested at 1000°C can be found in *Figures 7.57-7.60*. Each sample tested at the strain rates between 1/s to 1×10^{-3}/s at 1000°C failed in a brittle manner, while the sample tested at 1×10^{-4}/s showed ductility, as previously established in Chapters 5 and 6. Similar to what was seen in the Ti_2AlC sample tested under the same conditions, the grain morphology of the T10-0 sample seen in *Figure 7.57* is similar to that of the as-received Ti_3SiC_2 sample. However, with slower strain rates, the microstructure appears to become more deformed, with this particularly evident in the T10-4 sample seen in *Figure 7.59*. The IPF maps of the T10-0 and T10-2 samples can be found in *Figures 7.57B and 7.58B* respectively, while the plot of the orientation of each grain on the IPF colour keys can be found in *Figure 7.60*. From these figures it can be seen that there is generally a random orientation for both phases for the T10-0 and T10-2 samples, with the exception of the T10-2 Ti_3SiC_2 grains smaller than $10\mu m^2$, which has a slight orientation to the [0001] direction.

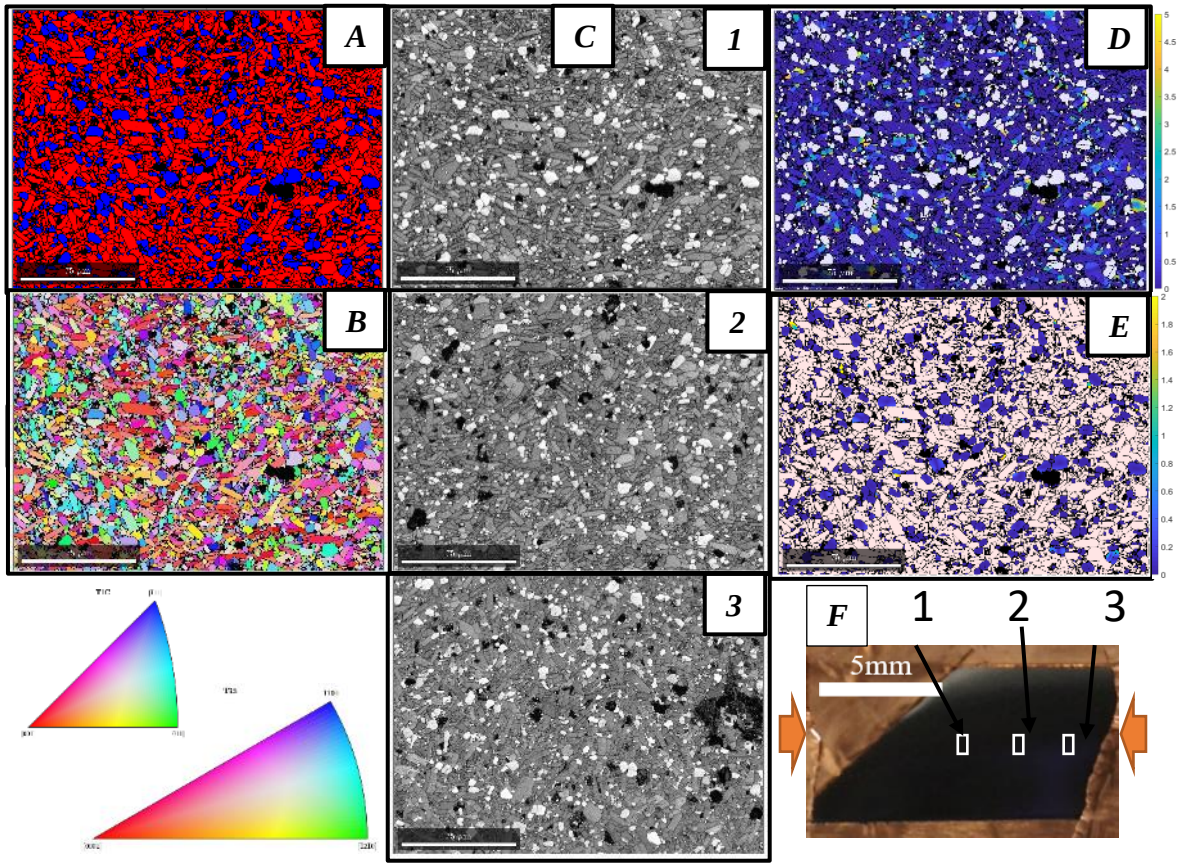

Figure 7.57: *EBSD Maps of the T10-0 Ti_3SiC_2 Sample:* ***A)*** *Phase Map, (R=Ti_3SiC_2, B=TiC),* ***B)*** *IPF-Y Map,* ***C)*** *Band Contrast showing Sites 1-3,* ***D-E)*** *Misorientation Angles of Site 1,* ***F)*** *Map locations*

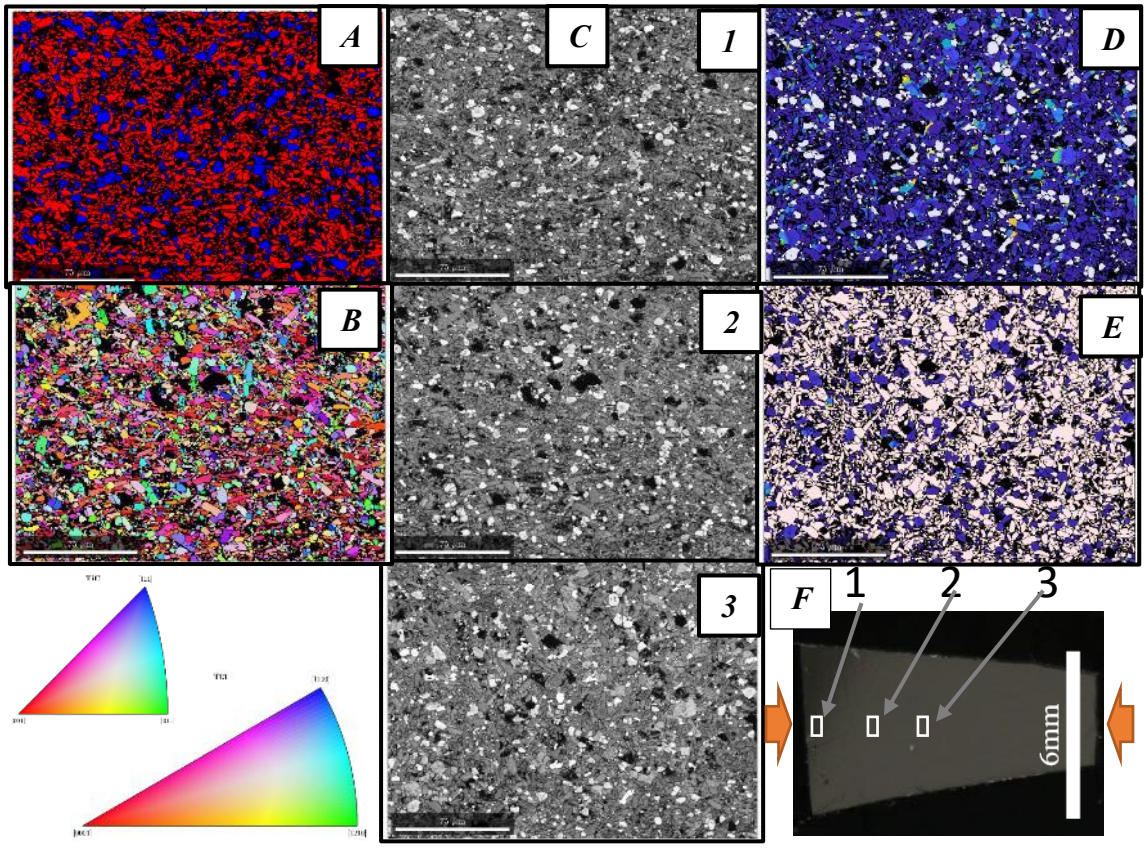

Figure 7.58: *EBSD Maps of the T10-2 Ti_3SiC_2 Sample:* ***A)*** *Phase Map, (R=Ti_3SiC_2, B=TiC),* ***B)*** *IPF-Y Map,* ***C)*** *Band Contrast showing Sites 1-3,* ***D-E)*** *Misorientation Angles of Site 3,* ***F)*** *Map locations*

As previously witnessed in the Ti_2AlC samples, when a MAX phase sample fails in a ductile manner, the centre of that sample is significantly more deformed than the outer edges of the sample. As seen in the band contrast image and IPF map in *Figures 7.59B & C(2)*, taken at the centre of the specimen, this was found to be the case for the T10-4 sample. The IPF map and its related colour key in *Figure 7.60* show that while the TiC phase has a random orientation regardless of grain size, the grains of the Ti_3SiC_2 phase have a much higher orientation in one direction. All grains of the Ti_3SiC_2 phase have an orientation to the [0001] direction, although this orientation is slightly more random in grains smaller than $10\mu m^2$ than grains larger than $10\mu m^2$.

The grain boundary misorientation data for all samples tested at 1000°C can be found in *Appendix 1*, where it can be seen that for all samples that both the Ti_3SiC_2-TiC and TiC-TiC grain boundaries have a random, Mackenzie profile, while the misorientation is uniform for the Ti_3SiC_2-Ti_3SiC_2 grain boundaries.

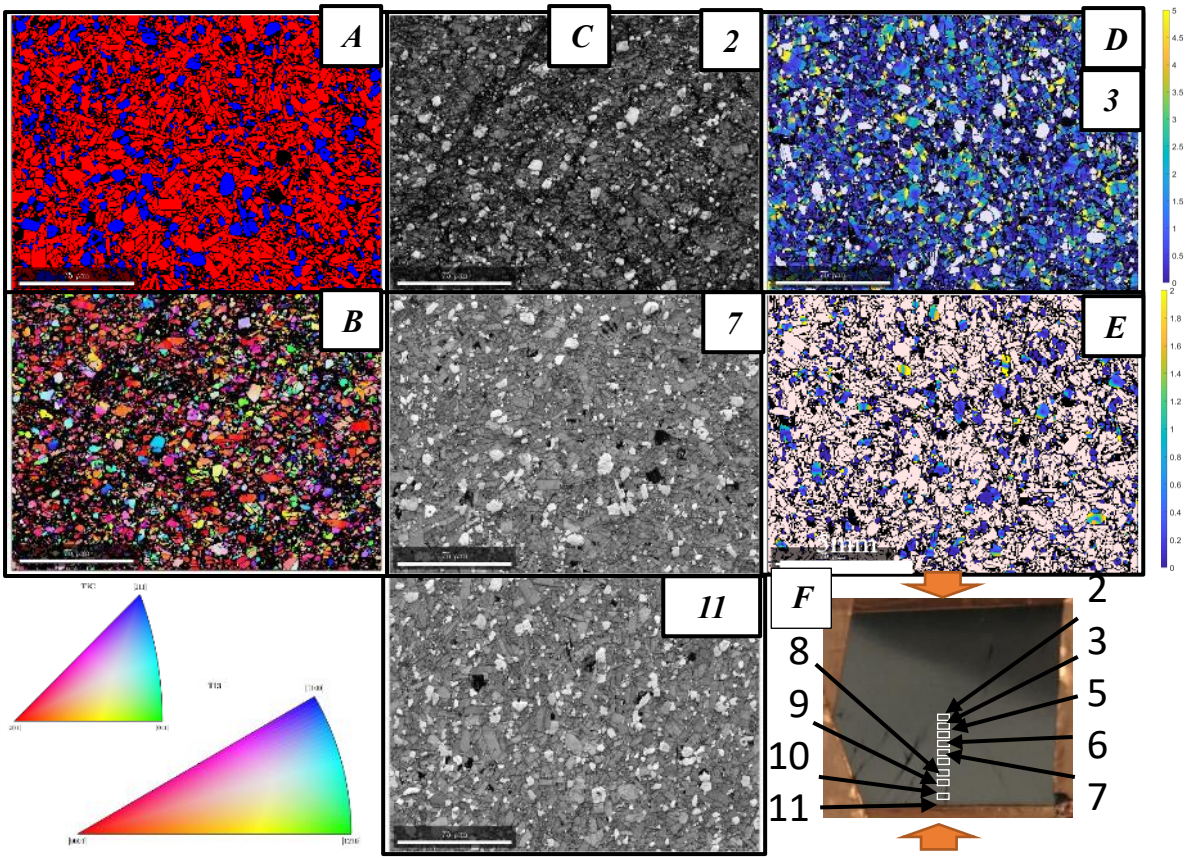

Figure 7.59: *EBSD Maps of the T10-4 Ti_3SiC_2 Sample:* ***A)*** *Phase Map, (R=Ti_3SiC_2, B=TiC),* ***B)*** *IPF-Y Map,* ***C)*** *Band Contrast showing Sites 2, 7 and 11,* ***D-E)*** *Misorientation Angles of Site 3,* ***F)*** *Map locations*

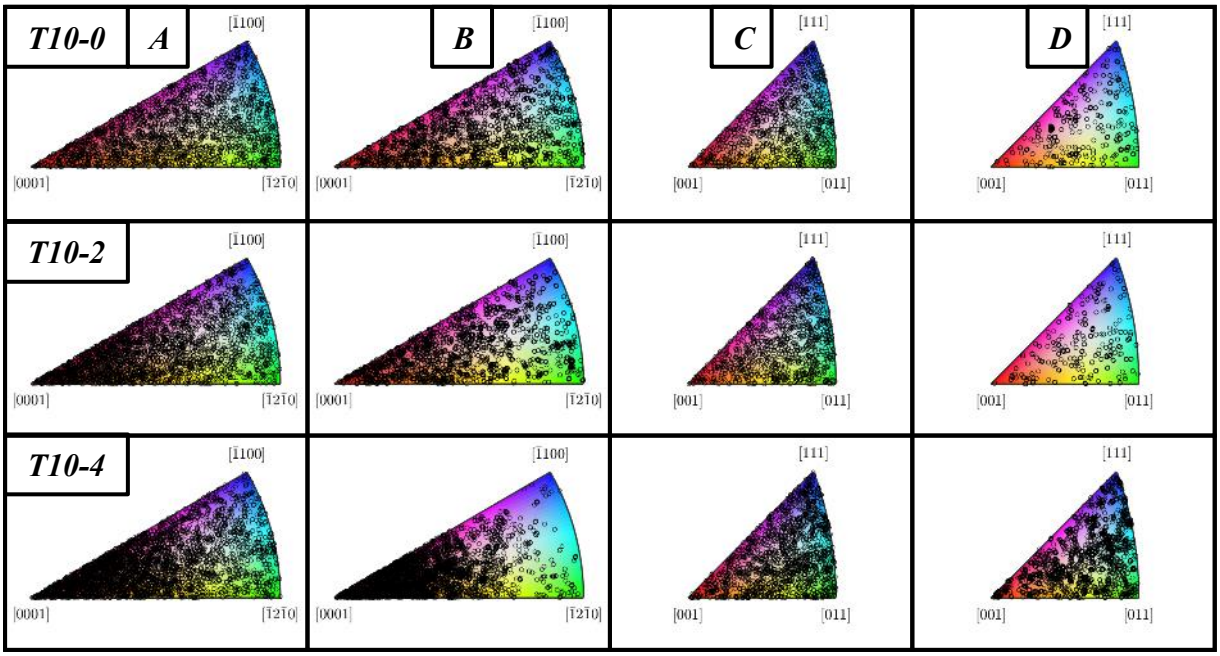

Figure 7.60: *Y-direction Inverse Pole Figure keys of the separate phases found in the Ti_3SiC_2 MAX phase deformed at 1000°C, with the orientation spread of the separate grains superimposed.* ***IPF Keys: A)*** *Ti_3SiC_2 grains with a grain area of under 10μm^2,* ***B)*** *Ti_3SiC_2 grains with a grain area of over 10μm^2,* ***C)*** *TiC grains with a grain area of under 10μm^2,* ***D)*** *TiC grains with a grain area of over 10μm^2*

7.3.2.3 EBSD analysis of Ti_3SiC_2 samples tested at 1100°C

Figures 7.61-7.64 show the EBSD maps for the Ti_3SiC_2 samples at 1100°C. The EBSD data for the T11-0 sample can be found in *Figure 7.61*, while *Figure 7.62* shows the data for the T11-2. When comparing the IPF maps of the T11-0 and T11-2 samples it can be seen that the colour in each grain is still generally quite uniform across the microstructure, independent of phase. This is further confirmed when studying the related IPF colour keys in *Figure 7.64*, on which the orientation of each grain was plotted. A generally random orientation for both phases can be seen for both samples under these testing conditions.

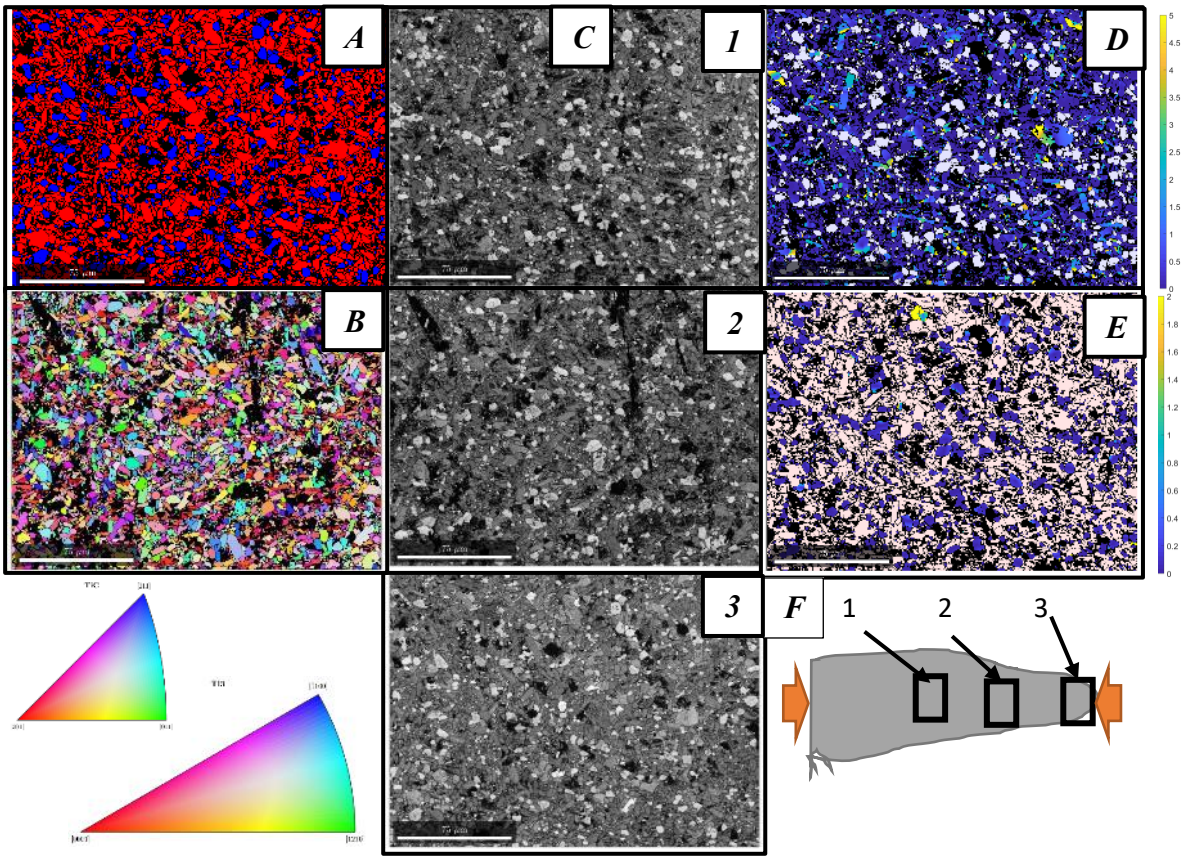

Figure 7.61: *EBSD Maps of the T11-0 Ti_3SiC_2 Sample:* ***A)*** *Phase Map, (R=Ti_3SiC_2, B=TiC),* ***B)*** *IPF-Y Map,* ***C)*** *Band Contrast showing Sites 1-3,* ***D-E)*** *Misorientation Angles of Site 1,* ***F)*** *Map locations*

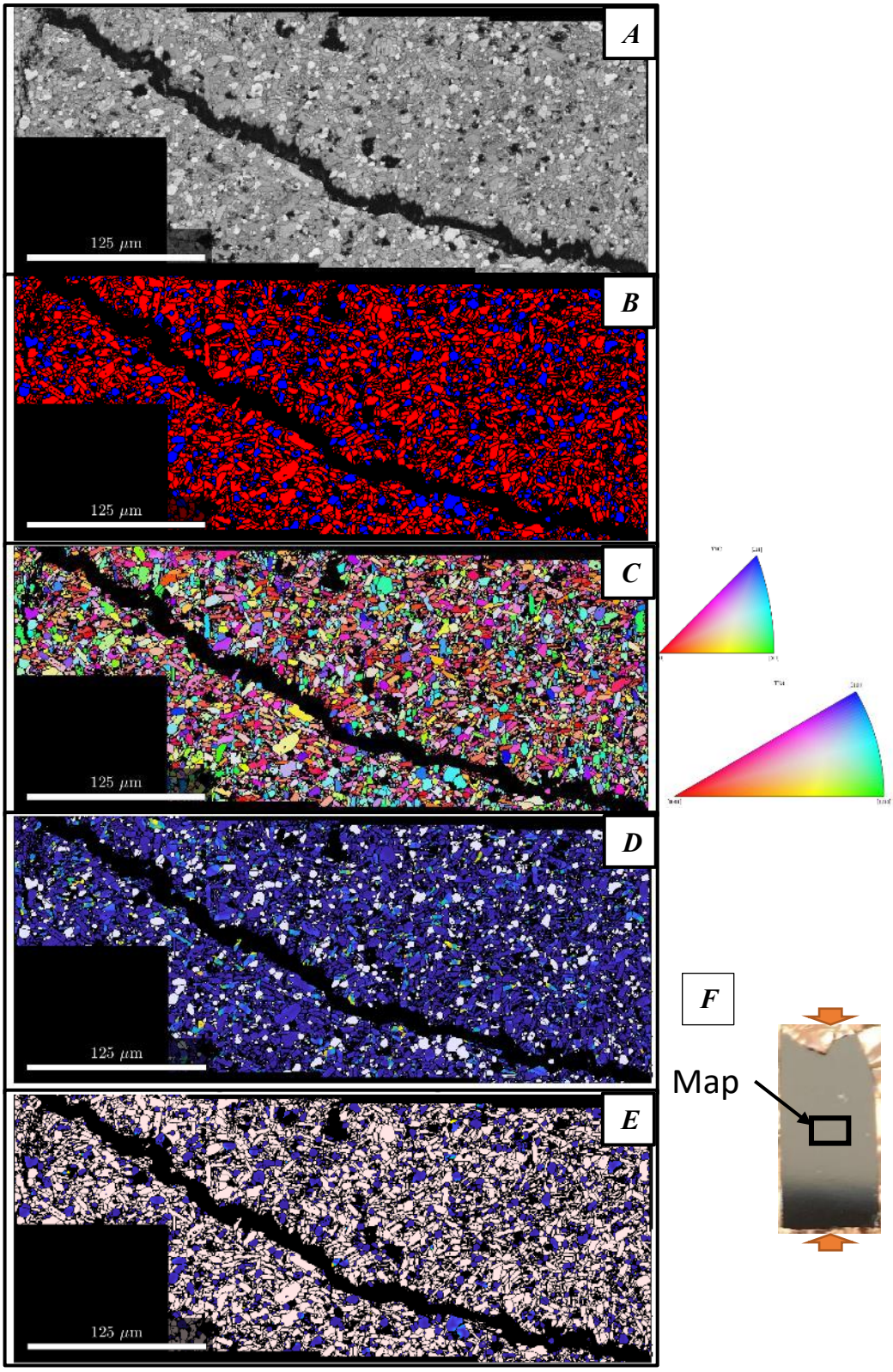

Figure 7.62: *EBSD Maps of the T11-2 Ti_3SiC_2 Sample:* ***A)*** *Phase Map, (R=Ti_3SiC_2, B=TiC),* ***B)*** *IPF-Y Map,* ***C)*** *Band Contrast,* ***D-E)*** *Misorientation Angles,* ***F)*** *Map locations*

The EBSD maps for the T11-4 sample can be found in *Figure 7.63*. As previously seen for samples tested at a strain rate of 1×10^{-4}/s, the grain morphology appears different to samples tested at faster strain rates; a generally finer microstructure, especially with regards to the Ti_3SiC_2 phase is evident from the band contrast images and the phase map. The IPF map in *Figure 7.63B* also shows a relative lack of colour uniformity when compared with the samples tested at faster strain rates. The IPF colour key in *Figure 7.64* shows that while the TiC grains have a random orientation, the Ti_3SiC_2 grains are more orientated to the [0001] orientation. This is especially true for grains larger than $10\mu m^2$.

The grain boundary misorientation data for all samples tested at 1100°C can be found in *Appendix 1*, where it can be seen that for all samples that both the Ti_3SiC_2-TiC and TiC-TiC grain boundaries have a random, Mackenzie profile, while the misorientation is uniform for the Ti_3SiC_2-Ti_3SiC_2 grain boundaries.

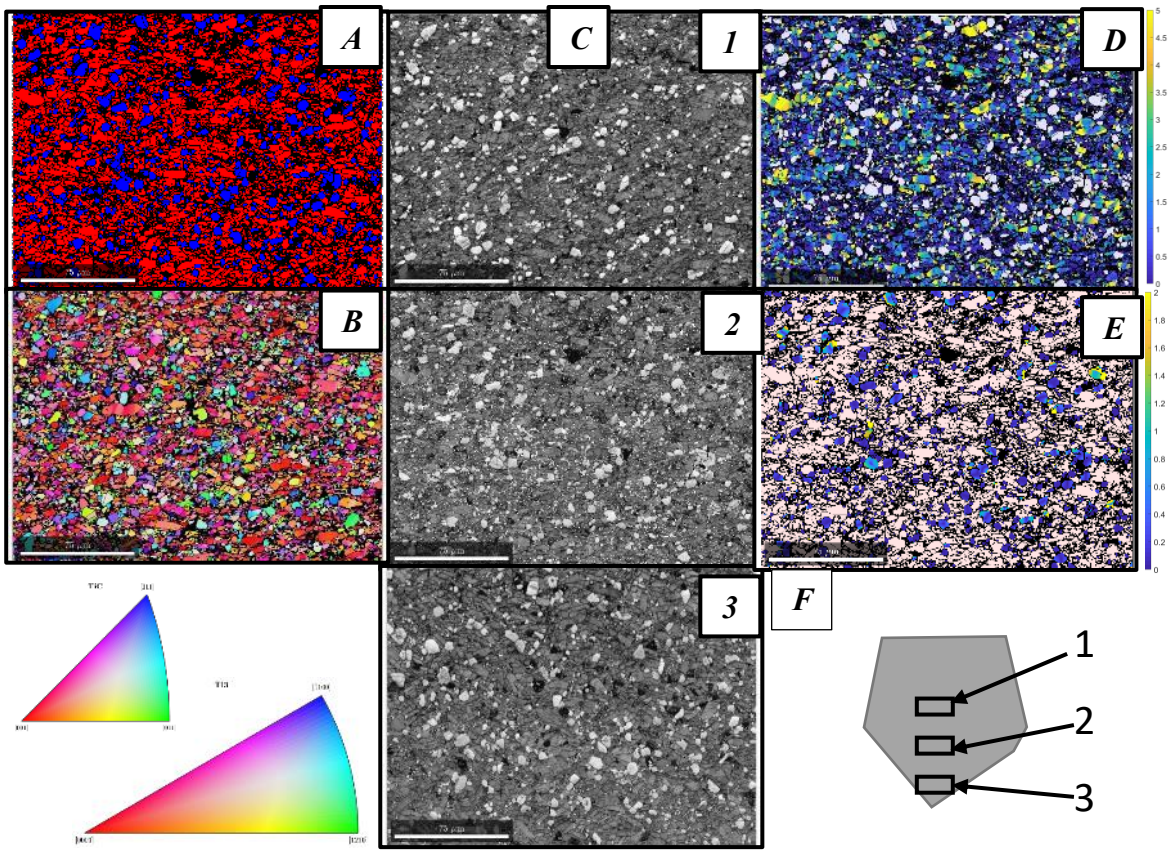

Figure 7.63: *EBSD Maps of the T11-4 Ti_3SiC_2 Sample:* ***A)*** *Phase Map, (R=Ti_3SiC_2, B=TiC),* ***B)*** *IPF-Y Map,* ***C)*** *Band Contrast showing Sites 1-3,* ***D-E)*** *Misorientation Angles of Site 2,* ***F)*** *Map locations*

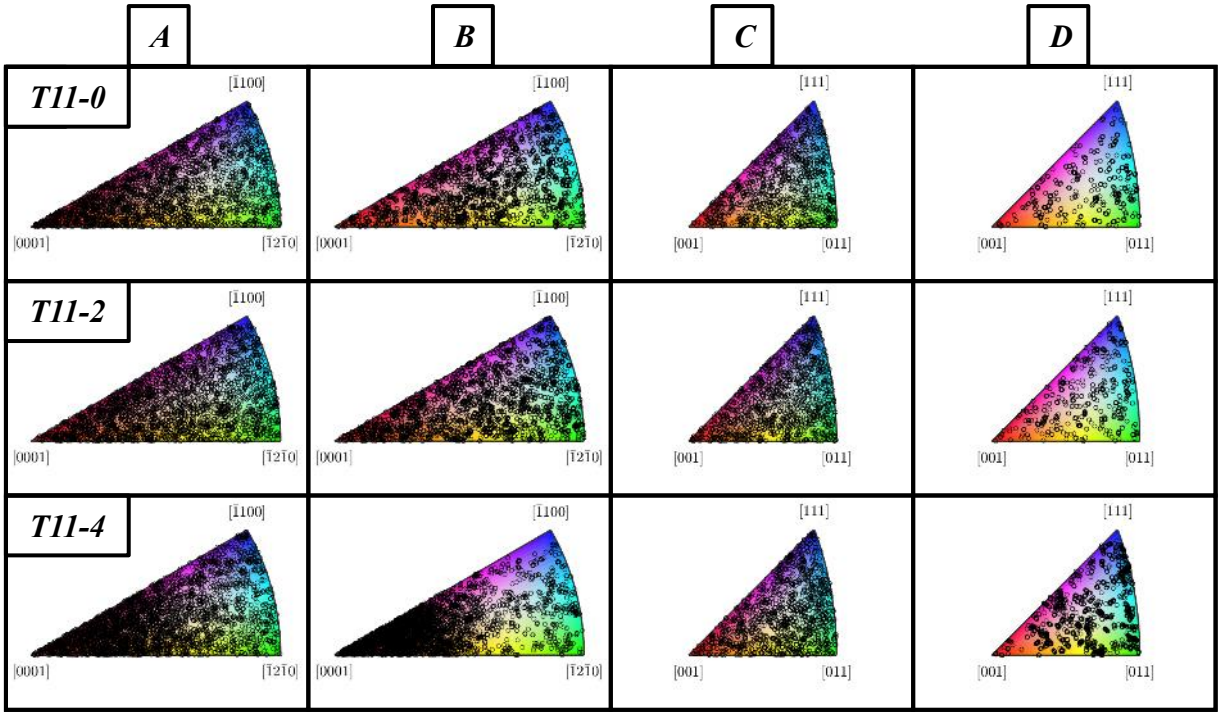

Figure 7.64: *Y-direction Inverse Pole Figure keys of the separate phases found in the Ti_3SiC_2 MAX phase deformed at 1100°C, with the orientation spread of the separate grains superimposed.* ***IPF Keys: A)*** *Ti_3SiC_2 grains with a grain area of under 10µm^2,* ***B)*** *Ti_3SiC_2 grains with a grain area of over 10µm^2,* ***C)*** *TiC grains with a grain area of under 10µm^2,* ***D)*** *TiC grains with a grain area of over 10µm^2*

7.3.2.4 EBSD analysis of Ti_3SiC_2 samples tested at 1200°C

The EBSD data for the samples tested at 1200°C can be found in *Figures 7.65-68*. As can be seen in *Figure 7.65*, the T12-0 sample shows the hallmarks of previous samples tested at the fastest strain rate, namely a microstructure generally devoid of any noticeable features. As can be seen from the band contrast images taken at different sites across the sample, the compression test does not seem to have a considerable effect on the microstructure, indicating the brittle nature to the failure of the sample. The IPF map of the sample, shown in *Figure 7.65B*, shows that colour in each grain is generally very uniform. When studying the IPF colour key interpolated with the orientation of each individual grain it can be seen that the orientation of all phases, regardless of grain size is generally random. The grain boundary misorientation data for the T12-0 sample can be found in *Appendix 1*, where it can be seen that the boundaries between the Ti_3SiC_2 and TiC grains and the boundaries between the TiC grains have a random, Mackenzie profile, while the misorientation is uniform for the Ti_3SiC_2-Ti_3SiC_2 grain boundaries.

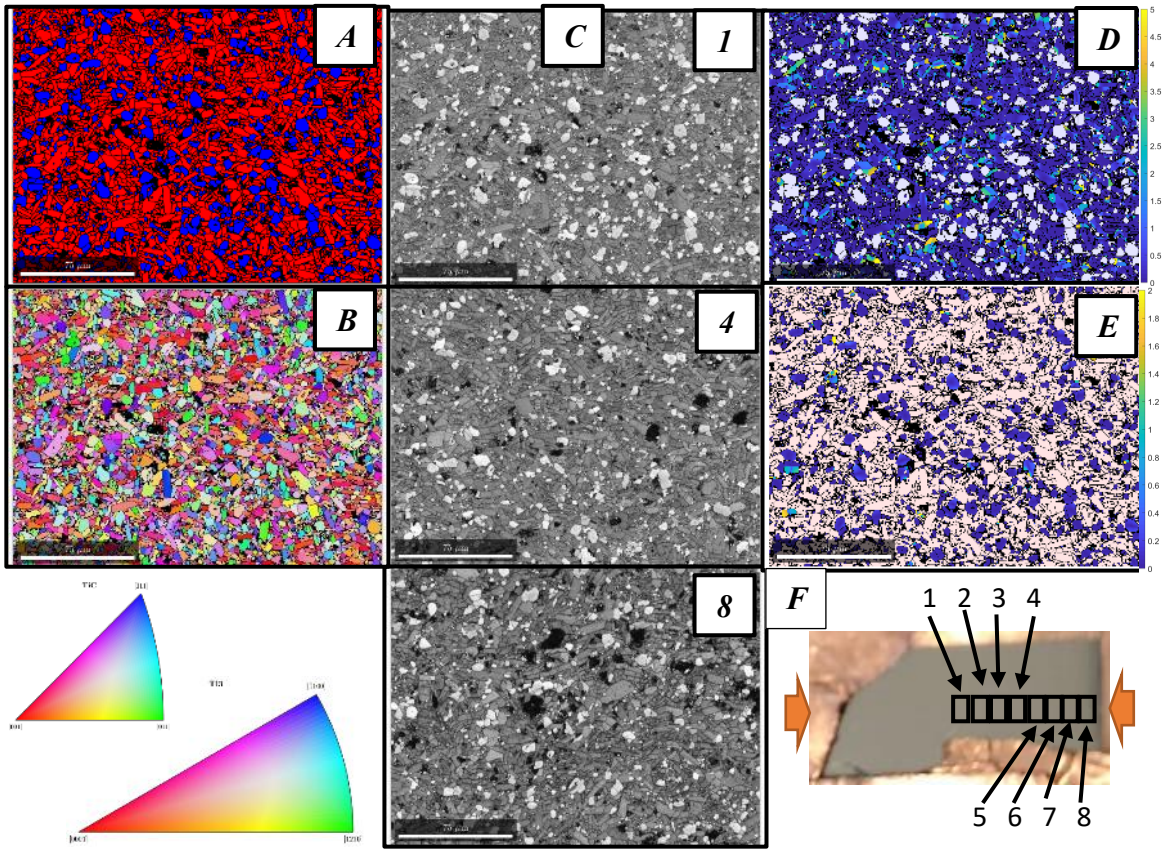

Figure 7.65: *EBSD Maps of the T12-0 Ti_3SiC_2 Sample:* ***A)*** *Phase Map, (R=Ti_3SiC_2, B=TiC),* ***B)*** *IPF-Y Map,* ***C)*** *Band Contrast showing Sites 1-3,* ***D-E)*** *Misorientation Angles of Site 1,* ***F)*** *Map locations*

As shown in Chapter 6, both the T12-2 and T12-4 samples have been found to have failed in a ductile manner. It is therefore reasonable to compare these two samples, with both showing similar features following their EBSD analysis. For both samples, areas of greater porosity can be seen from maps taken near the centre of the sample (Site 1 for T12-2 and Site 2 for T12-4), while the microstructure also appears distinctly finer than that of the T12-0 sample When studying the IPF maps of both samples it can be seen that the colour uniformity previously seen for the T12-0 sample is no longer applicable for the T12-2 and T12-4 sample. The IPF colour key in *Figure 6.68* also reveals that while the TiC phase has random orientation irrespective of grain size for both samples, the Ti_3SiC_2 does have an orientation to the [0001] direction. This orientation is more prevalent in the grains larger than $10\mu m^2$ for both samples.

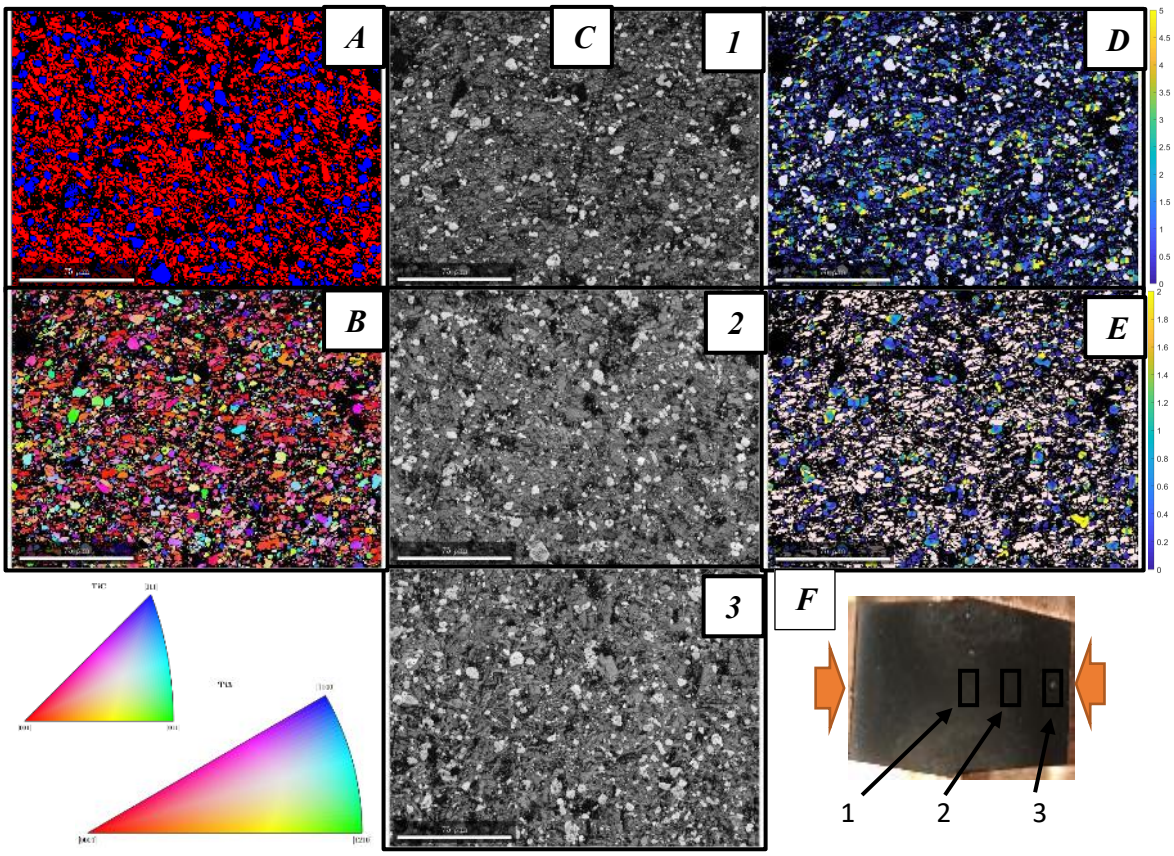

Figure 7.66: *EBSD Maps of the T12-2 Ti_3SiC_2 Sample:* ***A)*** *Phase Map, (R=Ti_3SiC_2, B=TiC),* ***B)*** *IPF-Y Map,* ***C)*** *Band Contrast showing Sites 1-3,* ***D-E)*** *Misorientation Angles of Site 1,* ***F)*** *Map locations*

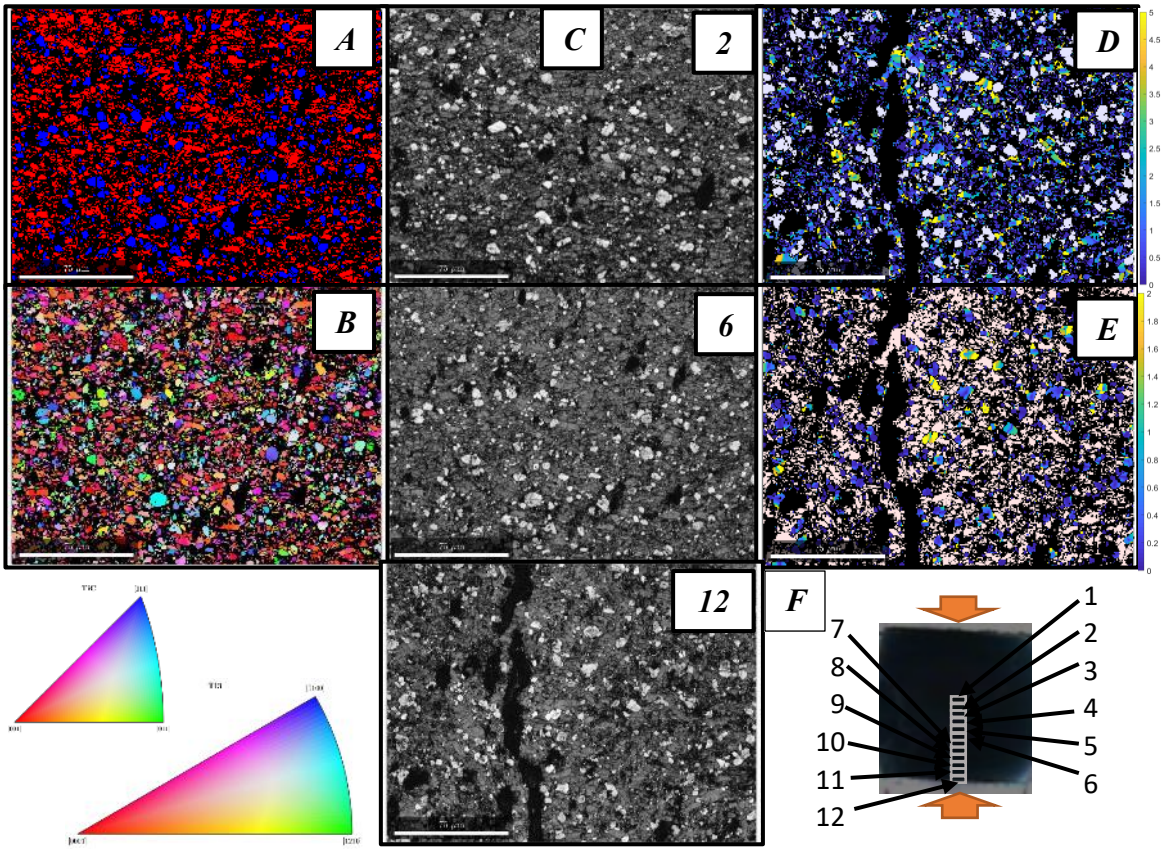

Figure 7.67: *EBSD Maps of the T12-4 Ti_3SiC_2 Sample:* ***A)*** *Phase Map, (R=Ti_3SiC_2, B=TiC),* ***B)*** *IPF-Y Map,* ***C)*** *Band Contrast showing Sites 2, 6 and 12,* ***D-E)*** *Misorientation Angles of Site 12,* ***F)*** *Map locations*

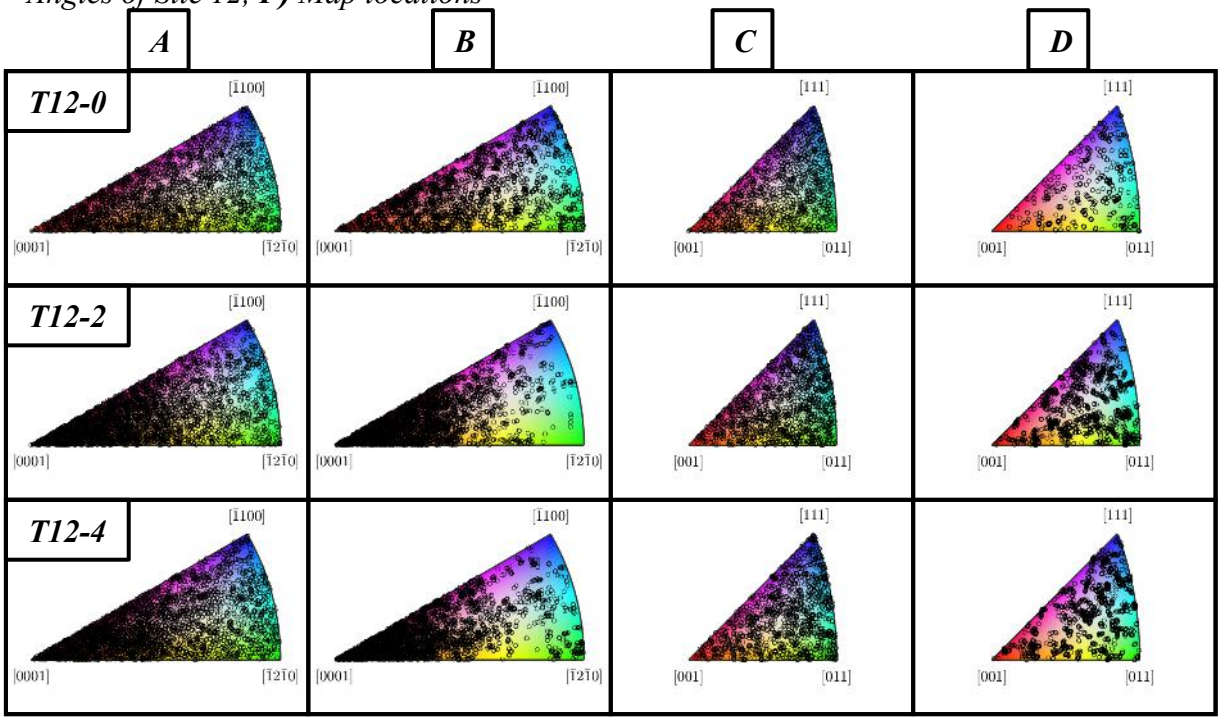

Figure 7.68: *Y-direction Inverse Pole Figure keys of the separate phases found in the Ti_3SiC_2 MAX phase deformed at 1200°C, with the orientation spread of the separate grains superimposed.* ***IPF Keys: A)*** *Ti_3SiC_2 grains with a grain area of under 10μm^2,* ***B)*** *Ti_3SiC_2 grains with a grain area of over 10μm^2,* ***C)*** *TiC grains with a grain area of under 10μm^2,* ***D)*** *TiC grains with a grain area of over 10μm^2*

The grain boundary misorientation data for all samples tested at 1200°C can be found in *Appendix 1*. Like all of the Ti_3SiC_2 samples tested, the grain boundary misorientation angles between the Ti_3SiC_2-TiC and TiC-TiC grains have a random, Mackenzie profile. However, the boundaries between the Ti_3SiC_2 grains in the T12-2 and T12-4 samples have a slightly non-random profile. While the profile is still generally uniform, there are peaks at 2°-20°, indicating a slightly low angle grain boundary between the Ti_3SiC_2 grains.

7.3.3 Summary

In this section of Chapter 7, the EBSD results of the Ti_2AlC and Ti_3SiC_2 samples have been studied and analysed. As was established in Chapter 5, the MAX phases used for this work were found to have multiple secondary phases and all of these, as well as the primary phase (Ti_2AlC or Ti_3SiC_2) were found to have a largely random texture before being tested.

The EBSD results for both MAX phases under room temperature compression conditions revealed no major changes to the orientation of either the primary phases or the secondary phases, with the exception of the TRT-4 Ti_2AlC sample, where it was recorded that for all grain sizes, the Ti_2AlC phase generally favoured the [0001] direction. The grain boundary misorientation between the grains of the major phases (Ti_2AlC-Ti_2AlC or Ti_3SiC_2-Ti_3SiC_2) either have a random, Mackenzie profile or are uniform. The grains between the Ti_2AlC phase and its secondary phases and amongst the secondary phases appear to favour MAGBs or HAGBs.

The samples for both MAX phase materials tested under high strain rate conditions at 1000°C were found to have a largely random texture, with only the Ti_3SiC_2 grains smaller than 10µm for the T10-2 sample having a slight orientation to the [0001] direction. However, the primary phase for the T10-4 samples for both MAX phases were recorded as having a significant orientation to the [0001] direction. The secondary phases for both MAX phases still retained a random texture. The Ti_2AlC T10-4 sample was the only sample for this aforementioned MAX phase that had a different grain boundary misorientation angle behaviour to the samples tested at room temperature. This sample showed that the grain boundaries between the grains of the Ti_2AlC phase generally had low angle misorientation angles of between 2-10°, while the relationship between some of the secondary phases also favoured the MAGBS or HAGBs. The

behaviour of the grain boundaries for each testing condition for the Ti_3SiC_2 MAX phase at this temperature were all the same, with the Ti_3SiC_2-Ti_3SiC_2 boundaries having a uniform distribution and Ti_3SiC_2-TiC and TiC-TiC grain boundaries having a random, Mackenzie profile.

From the IPF maps it was found that colour throughout each grain in the maps of the T11-0 and T11-2 Ti_2AlC samples tested at 1100°C were generally uniform. It was also found that the smaller grains have more of an orientation to the [0001] direction than the larger grains, while for the secondary phases the orientation of each grain was still random. The same colour uniformity across each grain was also seen for the Ti_3SiC_2 samples under the same testing conditions, although orientation for both phases was seen to be random. The band contrast images for the T11-4 samples show further evidence of a deformation 'dead zone', where the deformation is minimal at the edge of the sample in connection with the compression anvil. The colour uniformity in each grain is also absent from this sample. The smaller grains generally had an orientation to the [0001] direction, with the larger ones also mostly having an orientation to the [0001] direction, although other grains do have an orientation to the $[\bar{1}2\bar{1}0]$ and the $[\bar{1}100]$ directions. The same change in colour uniformity could be seen in the T11-4 Ti_3SiC_2 samples, which also had the Ti_3SiC_2 grains orientated to the [0001] direction. For the faster strain rates, the behaviour of the grain boundaries is similar to the samples tested 1000°C, while the T11-4 sample once again sees the grain boundaries between the Ti_2AlC grains having an LAGB relationship. This was also true for the grains between the TiAl phase. The Ti_3SiC_2--TiC and TiC-TiC grain boundaries have a random, Mackenzie profile, while the misorientation is uniform for the Ti_3SiC_2-Ti_3SiC_2 grain boundaries.

The T12-0 Ti_2AlC sample was found to have a generally random orientation, regardless of grain size or phase, while the T12-2 and T12-4 samples failed in a ductile manner, having similar EBSD maps to the T10-4 and T11-4 samples. The grains in both of these samples generally orientate to the [0001] direction for all Ti_2AlC grain sizes. Similar behaviour was found in the Ti_3SiC_2 samples, where the grains in the T12-0 sample had a generally random orientation. The Ti_3SiC_2 phase in both the T12-2 and T12-4 samples were found to have an orientation to the [0001] direction, with the orientation being more prevalent in the grains larger than $10\mu m^2$ for both samples, while the TiC phase was once again found to be random. Whereas

the Ti_2AlC T12-0 sample had a similar grain boundary misorientation relationship to the other samples compression tested at a high strain rate, the T12-2 and T12-4 samples once again having LAGBs for the boundaries between the Ti_2AlC grains. The T12-2 and T12-4 Ti_3SiC_2 samples are the only Ti_3SiC_2 samples recorded as having a slightly different grain boundary misorientation angle relationship. While both still have a profile that is generally uniform, the peaks between the Ti_3SiC_2 grains are at 2-20°, indicating a slightly low angle grain boundary. The LAGBs that were recorded in the EBSD data for both MAX phases are features that have been reported before in the MAX phases. They can generally be seen as evidence of kink bands and dislocation walls.

In general it was found that for both MAX phases, samples which were tested at slower strain rates, and therefore to higher strains, had a greater orientation to the [0001] direction than samples tested at faster strain rates and which ultimately failed at lower strains. This is an indication of the substantially more deformed microstructure of the samples tested at slower strain rates.

7.4 GND Analysis of Ti_2AlC and Ti_3SiC_2 following high temperature compression testing

To further understand the deformation mechanisms involved in the testing of the MAX phases at high temperatures, the Geometrically Necessary Dislocation (GND) density of each sample was also calculated.

Within crystalline materials, plastic deformation is generally accepted to be accommodated by dislocation multiplication, annihilation, movement (glide and climb) and interactions between microstructural features such as grain boundaries or secondary phases. Both Nye and Kroner suggested that there are two types of dislocations: geometrically necessary dislocations (GNDs) and statistically stored dislocations (SSDs). GNDs can be defined as representing the excess dislocations stored within a Burgers circuit and also contribute to the curvature of the lattice. Within SSDs however, there is no curvature of the crystal lattices at sufficiently larger enough scales, with these dislocations consisting of dipoles, multiples and loops within the Burgers circuit [136,137].

Deformation in a crystal lattice gives rise to changes in interplanar angles. This corresponds to the movements of features contained within diffraction patterns. Using cross-correlation methods, these movements can be measured and then related to both the elastic strain and lattice rotations, which are measured with respect to the reference pattern within each grain on a polycrystalline sample map. Due to the comparably negligible contribution from the elastic strain, only the lattice curvature is used when calculating the GND of a sample. The total dislocation density consists of the individual dislocation densities from each dislocation slip system [136–140]. Both Ti_2AlC and Ti_3SiC_2 are hexagonal crystals, so the GNDs for these are assumed to be either pure edge dislocations (36 types) or pure screw dislocations (9 types), giving 55 GND types in total for the primary phase of each MAX phase material. As the TiC phase has an FCC crystal structure, the GNDs for this phase are assumed to be either pure edge (12 types) or pure screw (6 types).

7.4.1 GND comparison of Ti_2AlC and Ti_3SiC_2 and their constituent phases

Figures 7.69-78 show the mean GND per pixel and GND Density per grain values distributed across each MAX phase sample for their separate phases, with Site, or Map 1 being the centre of the sample, and Site 10 (for Ti_2AlC samples) or Site 12 (for Ti_3SiC_2 samples), being the bottom edge of the sample, in connection with the compression anvil. The results for each sample are coloured with regards to their testing temperature, with samples tested at 1000°C having a shade of red, samples tested at 1100°C a shade of green and samples tested at 1200°C a shade of blue. The GNDs were calculated using the MTEX Matlab software [141,142]. The units for all graphs are: $\rho_{GND(m^{-2})}$

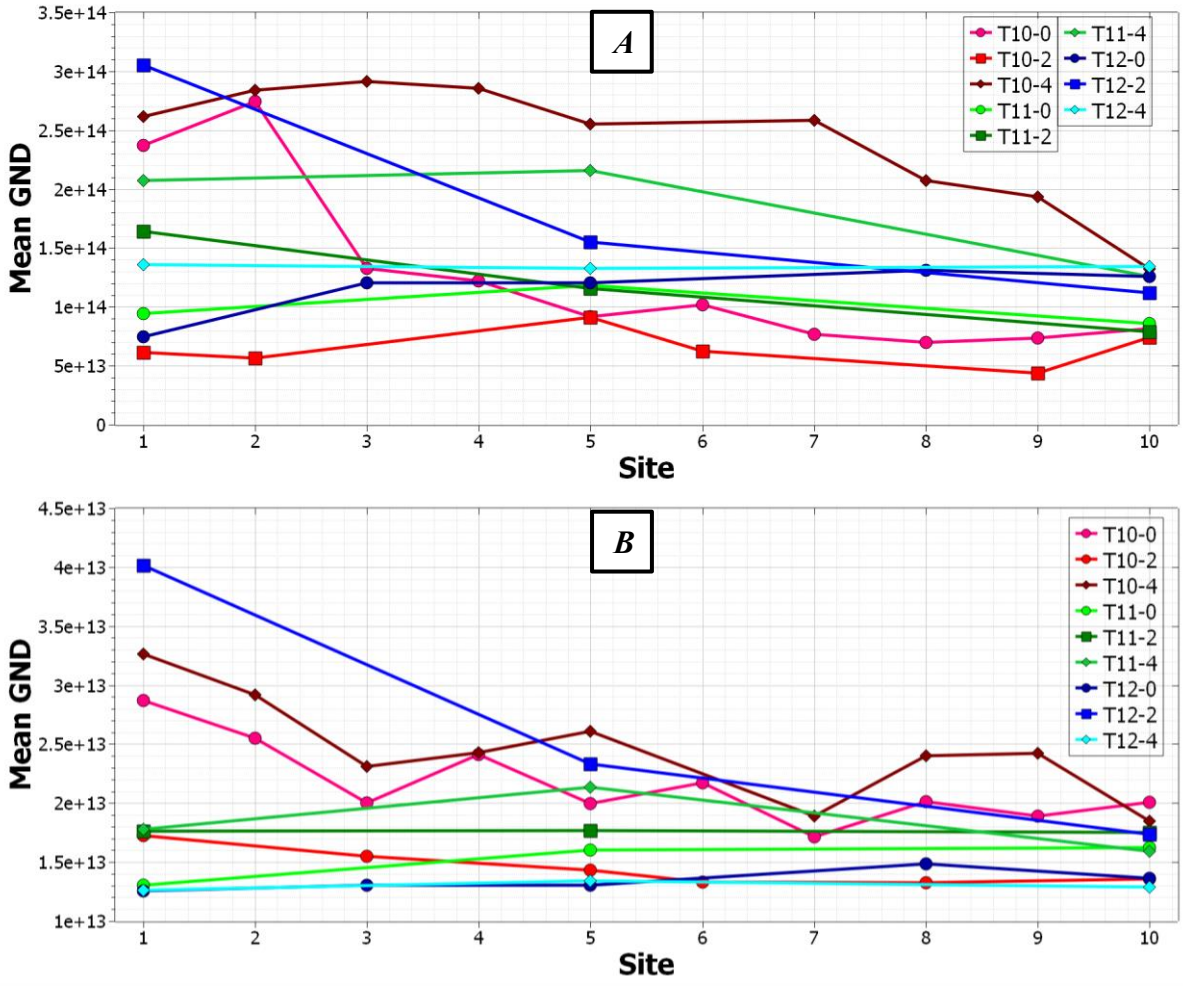

Figure 7.69i: *The mean GND values distributed across each Ti_2AlC sample for the separate phases:* ***A)*** *Ti_2AlC;* ***B)*** *Al_2O_3, with Site 1 being the centre of the sample and Site 10 being the bottom edge of each sample (in connection with the compression anvil).*

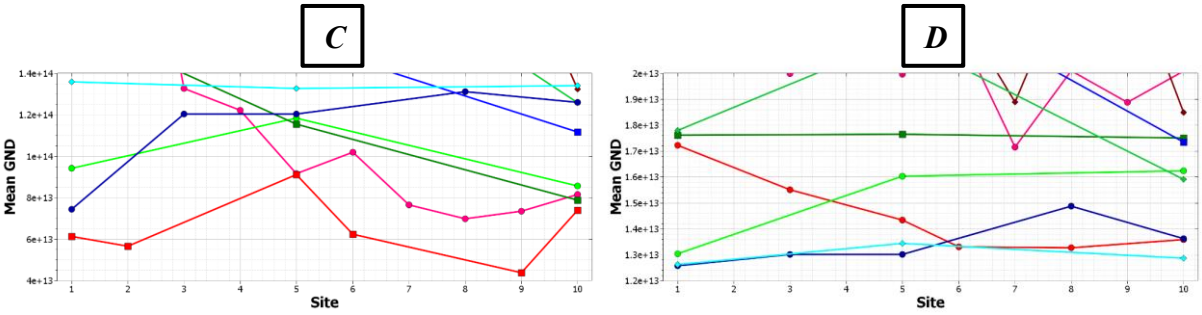

Figure 7.69ii: *The mean GND values distributed across each Ti_2AlC sample for the separate phases:* ***C)*** *Inset of A;* ***D)*** *Inset of B*

The graphs of the mean GND per pixel values for the Ti_2AlC samples can be found in *Figures 7.69 and 7.70.* From *Figure 7.69* it can be seen that, in general, the sites closest to the centre of the sample have a higher GND value than sites situated close to the sample edge which was in contact with the compression anvil. *Figure 7.70* shows the average of each EBSD site for each sample with respect to their mean GND. As seen in *Figure 7.69* and further outlined in *Figure 7.70*, samples tested to a strain rate of 1×10^{-4}/s generally have the highest GND value regardless of temperature, while the samples tested at 1/s generally have the lowest, with the only noticeable exception being mean GND values for the Al_2O_3 phase in the T12-4 sample. The mean GND for the control sample was also measured and this has a similar value to the samples tested at the fastest strain rate of 1/s.

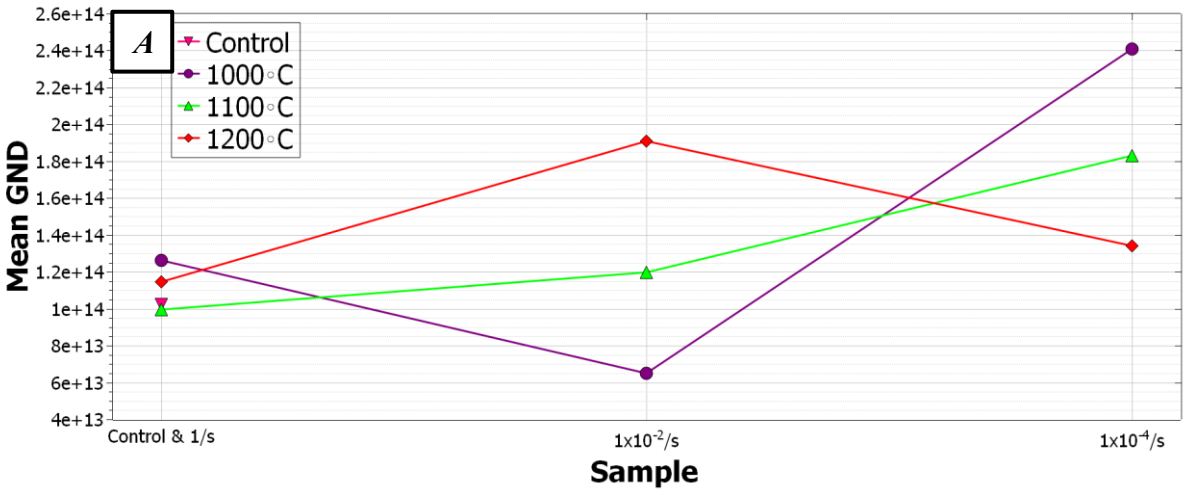

Figure 7.70i: *Graph showing the average mean GND for each Ti_2AlC sample* **A)** Ti_2AlC phase. *Average of each EBSD data site*

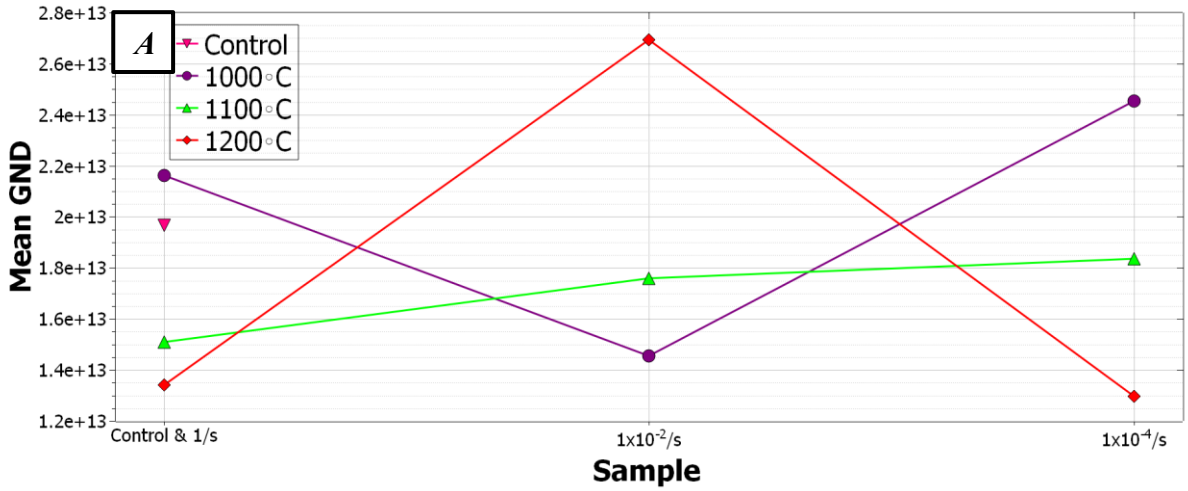

Figure 7.70ii: *Graph showing the average mean GND for each Ti_2AlC sample* **B)** Al_2O_3 phase. *Average of each EBSD data site*

Figures 7.71 and 7.72 show the mean GND data for the Ti_3SiC_2 samples. *Figure 7.71* shows the distribution of the mean GND values by EBSD map site location. As previously seen in the Ti_2AlC samples, the sites close to the centre of the samples have the highest mean GND values, while the sites near the edge in connection with the compression anvil have the lowest mean GND values. As seen in *Figure 7.72*, unlike the 2 phases in the Ti_2AlC samples, both of the main phases in the Ti_3SiC_2 MAX phase sample; Ti_3SiC_2 and TiC, follow a near identical pattern with regards to their average mean GND across every site for each sample. The as received control sample and the samples compression tested at the fastest strain rates of 1/s and 1×10^{-2}/s generally have a very low mean GND compared to the samples tested at 1×10^{-4}/s, regardless of temperature. The only exception is the T12-2 sample, although it should be noted that this sample did deform in a ductile manner similar to the samples tested at 1×10^{-4}/s.

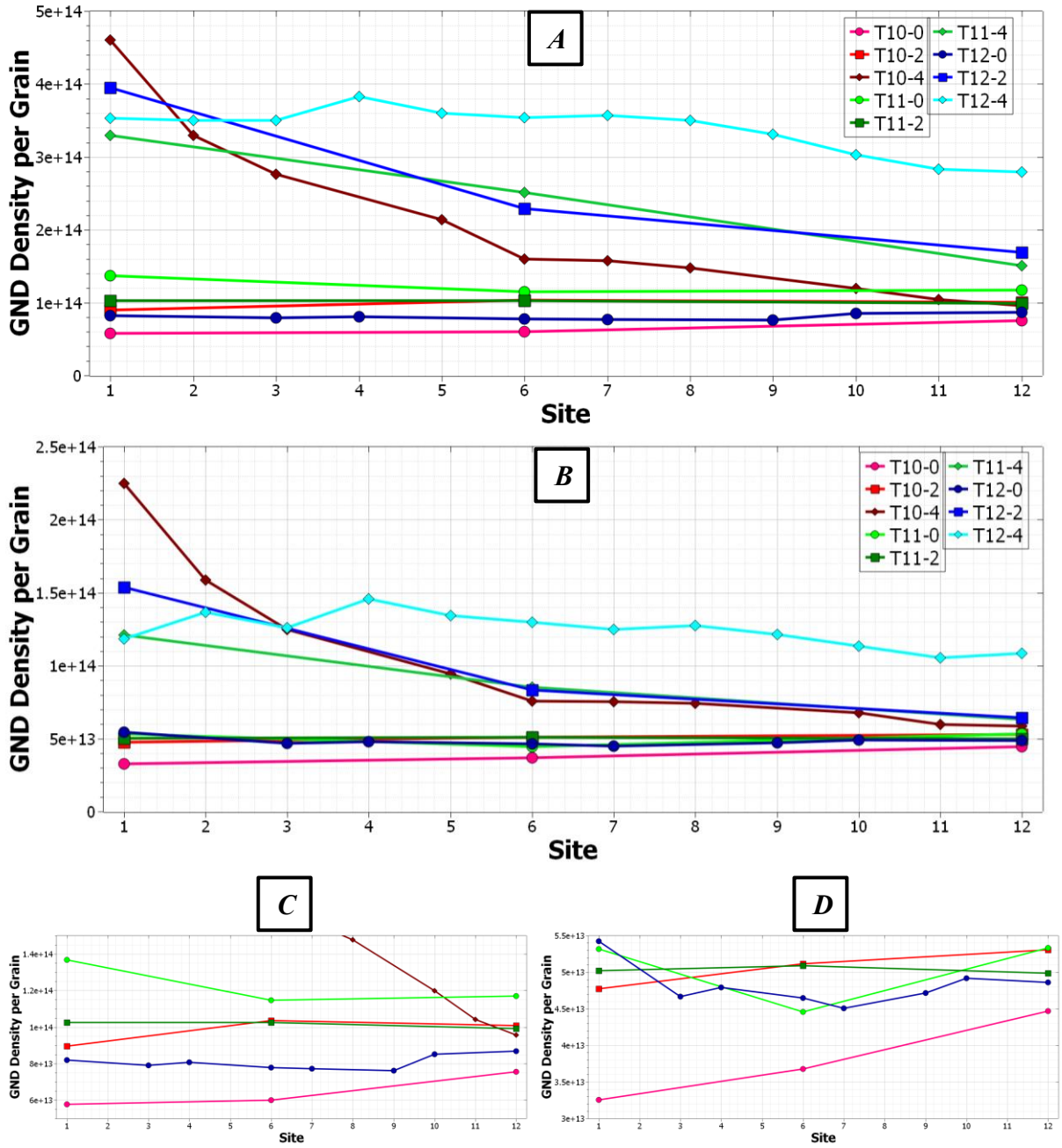

Figure 7.71: *The mean GND values distributed across each Ti_3SiC_2 sample for the separate phases:* ***A)*** *Ti_3SiC_2,* ***B)*** *TiC,* ***C)*** *Inset of A;* ***D)*** *Inset of B, with Site 1 being the centre of the sample and Site 12 being the bottom edge of each sample (in connection with the compression anvil).*

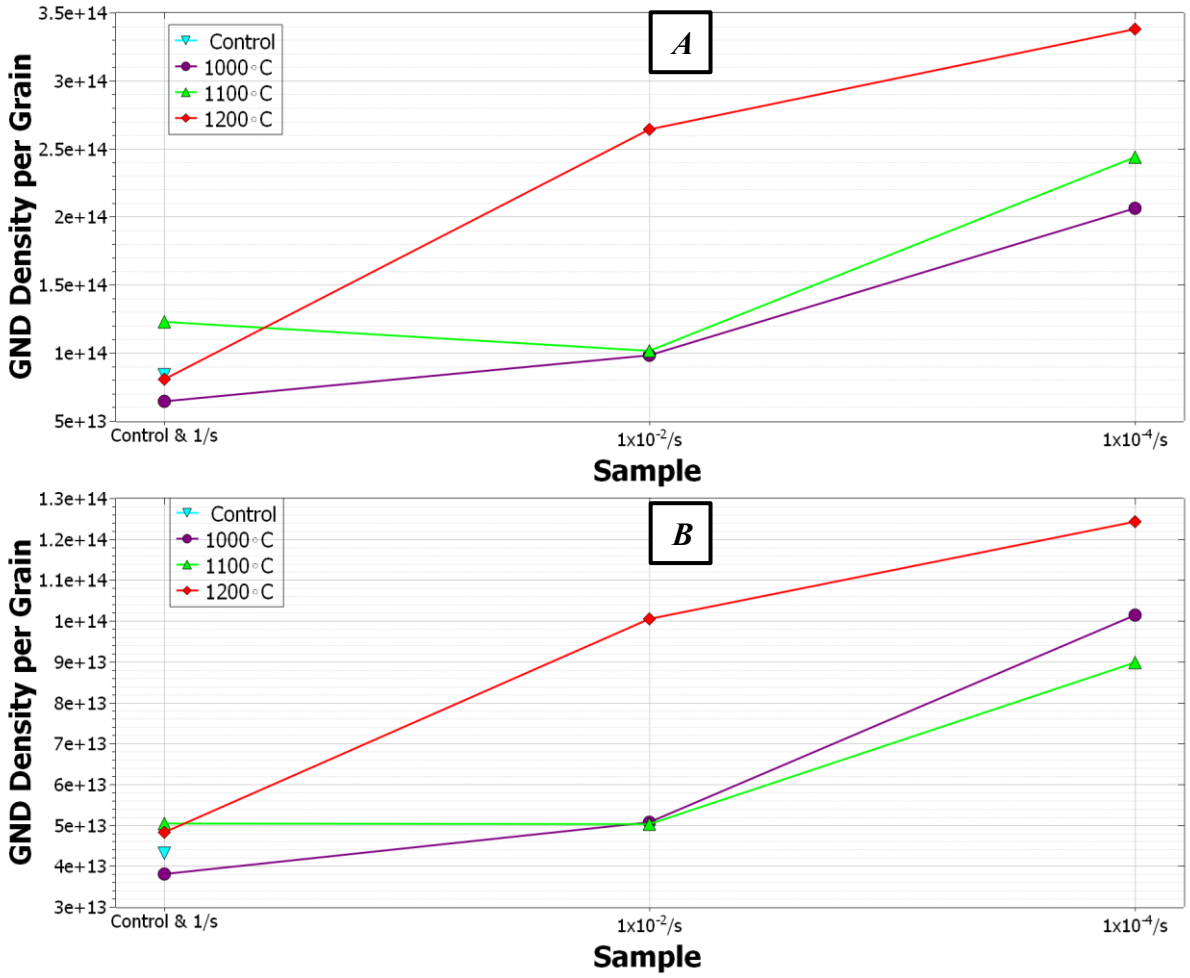

Figure 7.72: *Graph showing the average mean GND for each Ti_3SiC_2 sample* **A)** Ti_3SiC_2 phase and **B)** TiC phase. *Average of each EBSD data site*

Figures 7.73-76 show the GND density per grain values for both the Ti_2AlC and Ti_3SiC_2 samples. From *Figure 7.73* it can be seen that unlike the mean GND values for Ti_2AlC, the GND density distribution across the Ti_2AlC samples is slightly more uniform for both of the phases recorded here, with the sites near the centre of each sample not having a significantly higher GND density than those nearer the sample edge. *Figure 7.74* shows the average GND density across each sample. For both phases, the average GND density across every site for each sample is random when compared to the average mean GND.

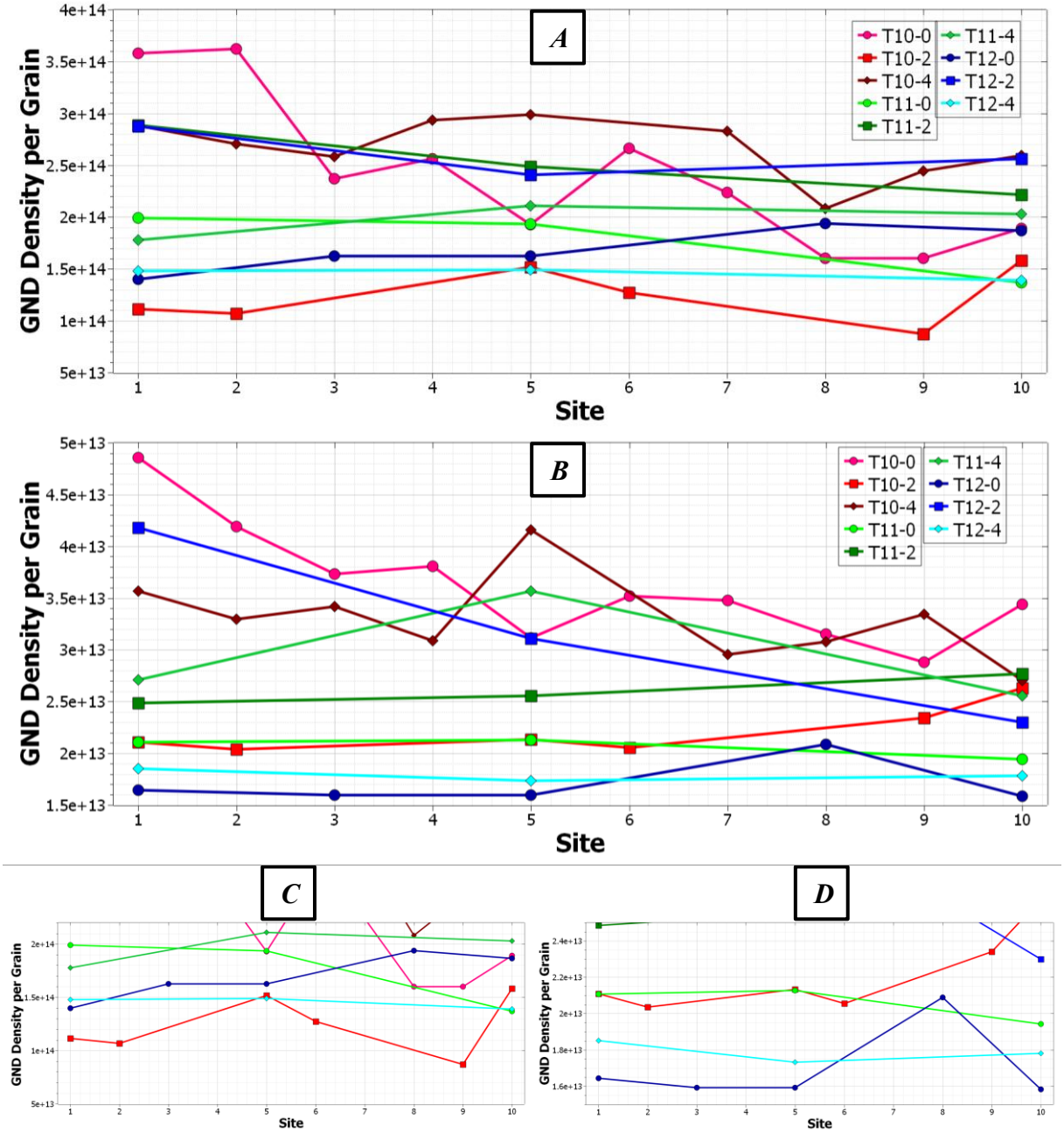

Figure 7.73: *The GND density per grain values distributed across each Ti_2AlC sample for the separate phases:* ***A)*** *Ti_2AlC,* ***B)*** *Al_2O_3,* ***C)*** *Inset of A,* ***D)*** *Inset of B, with Site 1 being the centre of the sample and Site 10 being the bottom edge of each sample (in connection with the compression anvil).*

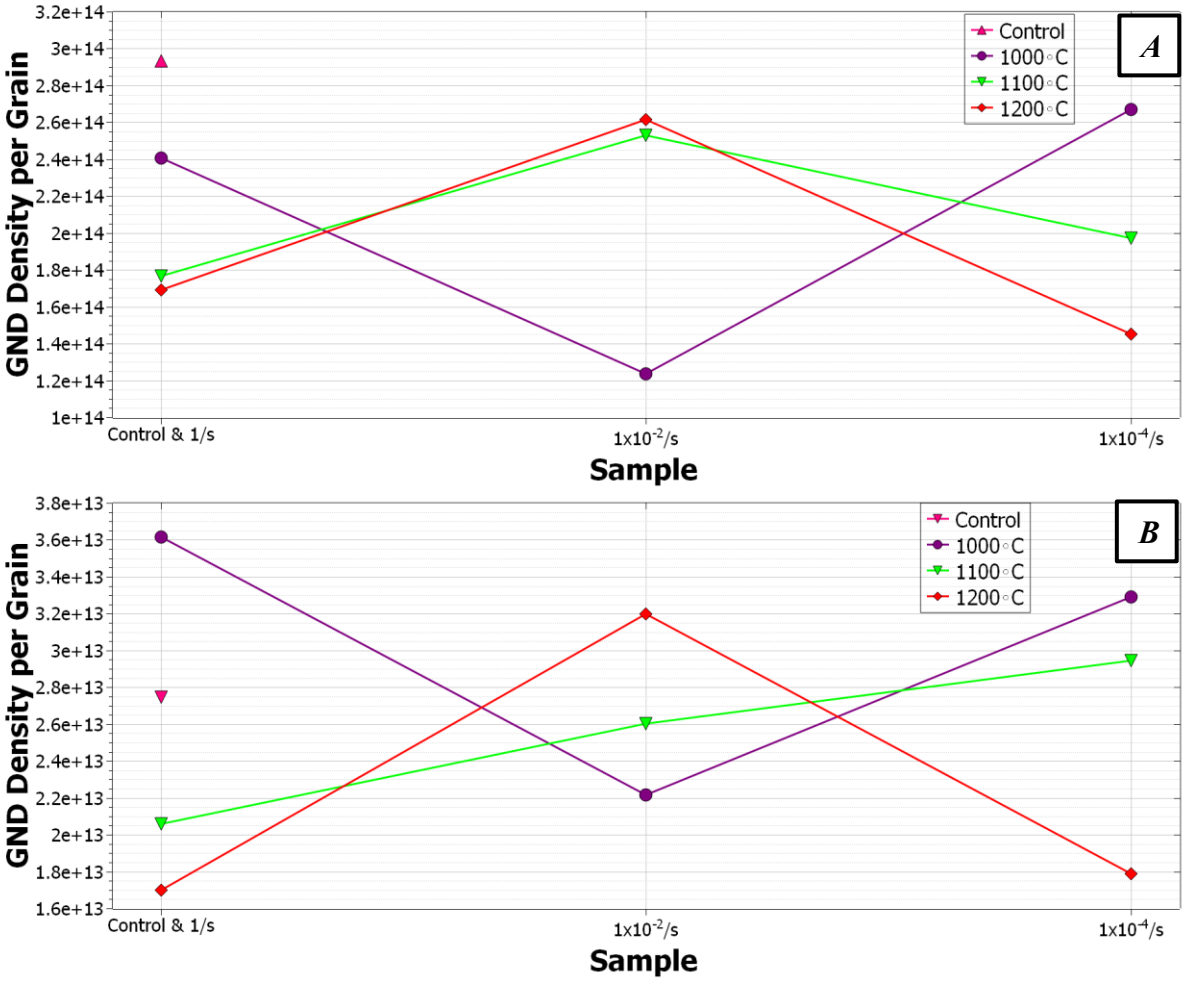

Figure 7.74: *Graph showing the average GND density per grain for each Ti_2AlC sample* **A)** Ti_3SiC_2 phase and **B)** TiC phase. *Average of each EBSD data site*

GND Density per grain distribution maps for the Ti_2AlC phase can be found in *Figure 7.75*. The figure shows the Site 1 (centre of the sample) density distributions for samples tested at all temperatures under both the fastest *(A-C)* and slowest *(D-F)* strain rates (1/s and 1×10^{-4}/s respectively). As shown in *Figure 7.73*, Site 1 was found to be generally the location with the highest GND density distribution.

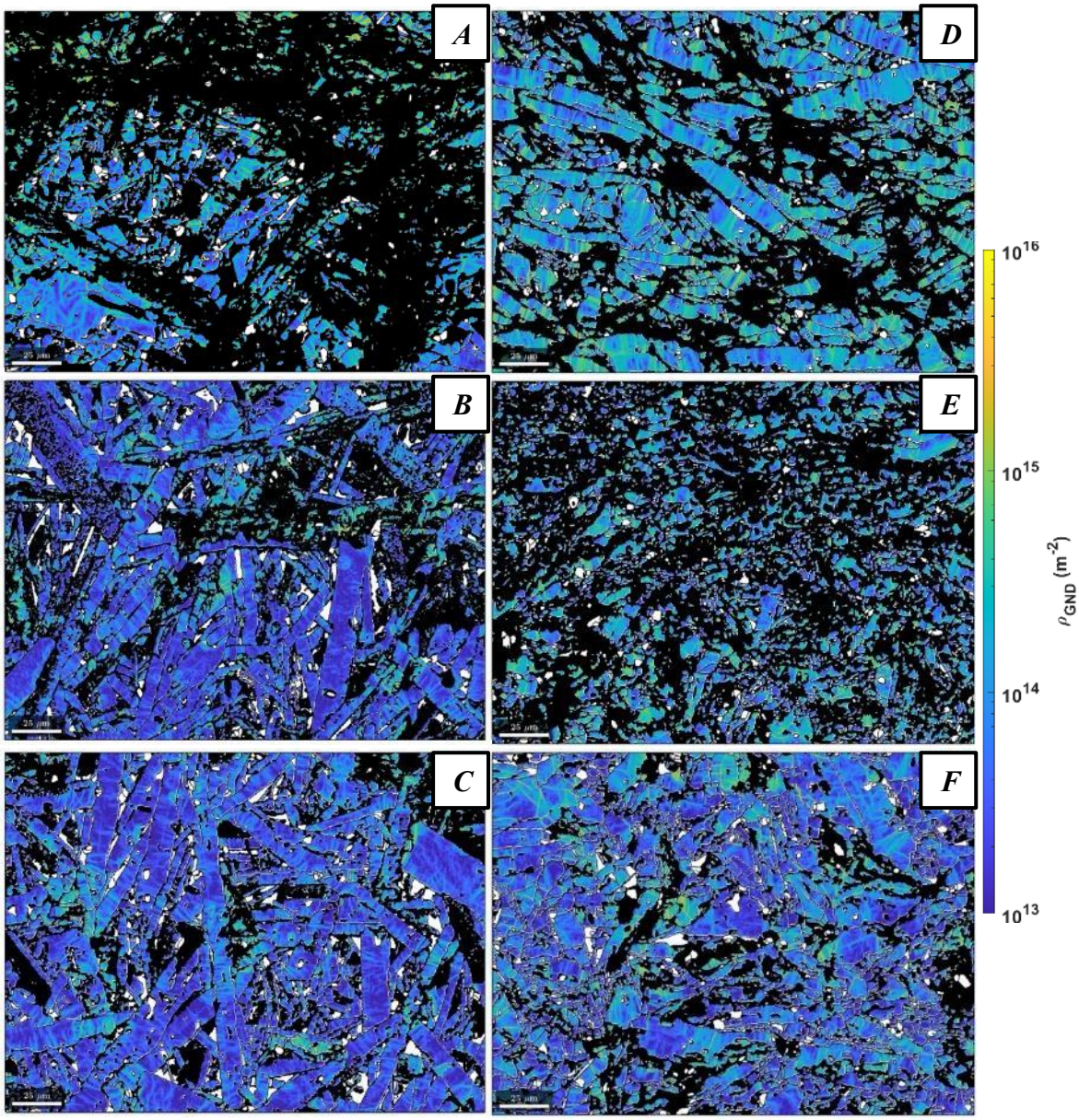

Figure 7.75: *EBSD maps showing the total GND density distributions for the Ti_2AlC phase at Site 1 (the centre of each sample) for the following Ti_2AlC samples:* ***A)*** *T10-0,* ***B)*** *T11-0,* ***C)*** *T12-0,* ***D)*** *T10-4,* ***E)*** *T11-4,* ***F)*** *T12-4.*

Figures 7.76-78 show the GND density per grain for the Ti_3SiC_2 samples. Unlike the GND density data for the Ti_2AlC samples, *Figure 7.76* shows a more established trend of the GND density being higher in the centre of the samples and lower in the sites mapped closer to the sample edge in contact with the compression anvil. As seen in *Figure 7.77*, showing the average GND density of every site across each sample, both the Ti_3SiC_2 and TiC phase behave in a very similar manner. Like what was seen in the average mean GND values in *Figure 7.72*, the samples tested under a strain rate of 1×10^{-4}/s have the highest GND density values for both phases at all temperatures, while the samples tested under strain rate conditions of 1/s or $1\times10^{-}$

^{2}/s have a comparatively low average GND density very similar to that of the as-received control sample, with the ductile T12-2 once again being the exception.

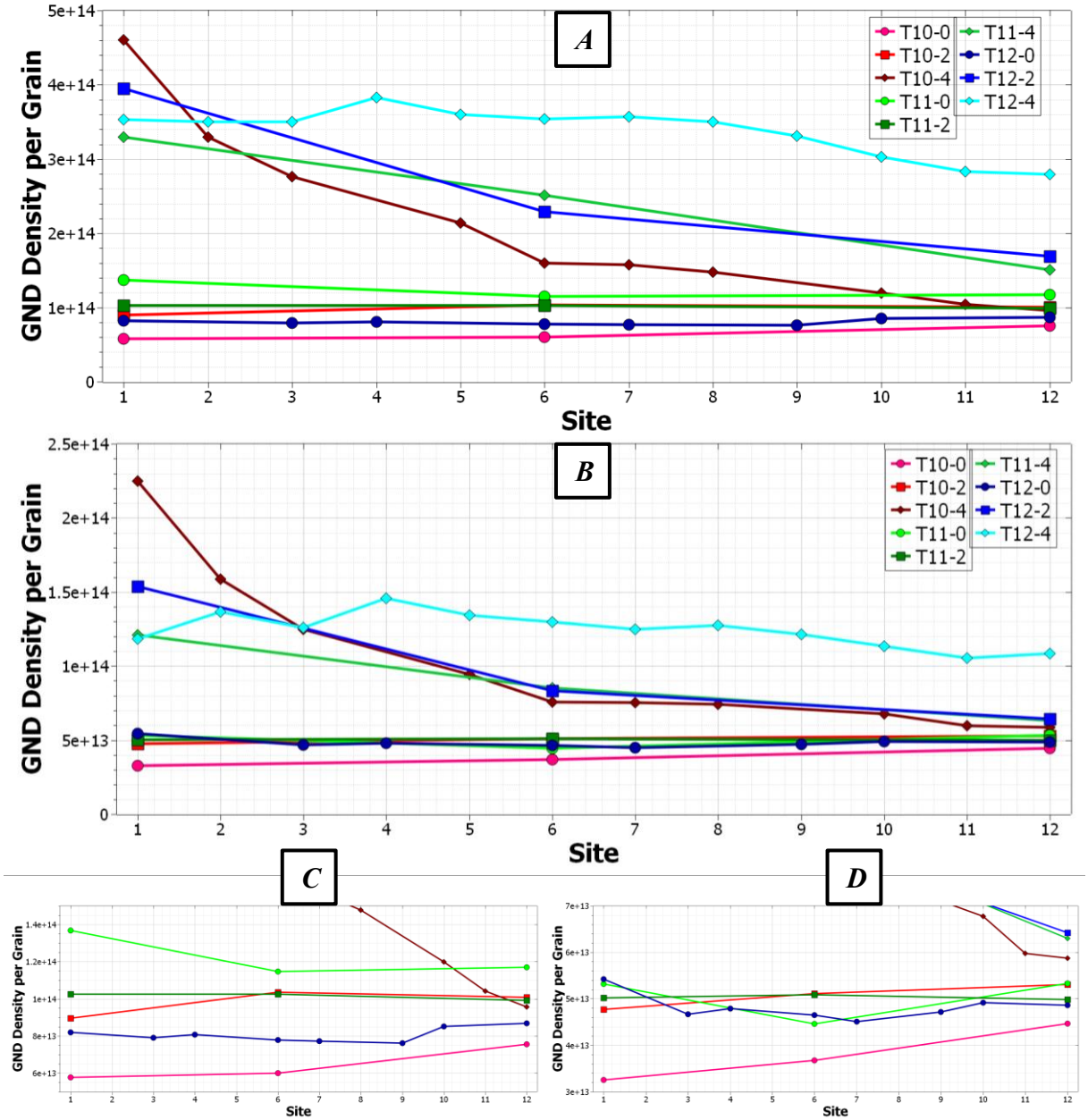

Figure 7.76: *The GND density per grain values distributed across each Ti_3SiC_2 sample for the separate phases:* ***A)*** *Ti_3SiC_2,* ***B)*** *TiC,* ***C)*** *Inset of A,* ***D)*** *Inset of B, with Site 1 being the centre of the sample and Site 12 being the bottom edge of each sample (in connection with the compression anvil).*

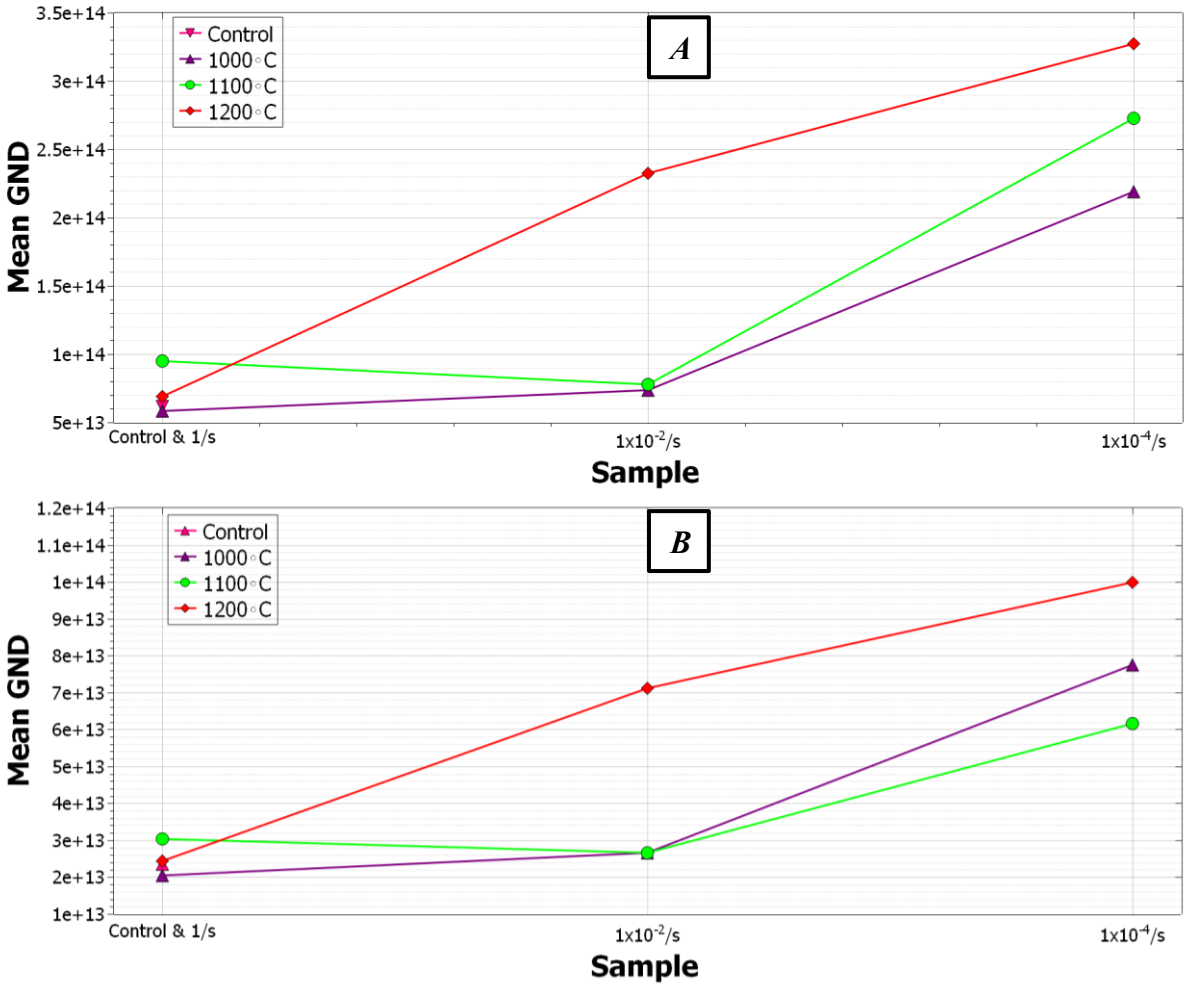

Figure 7.77: *Graph showing the average GND density per grain for each Ti_3SiC_2 sample* **A)** Ti_3SiC_2 phase and **B)** TiC phase. *Average of each EBSD data site*

Figure 7.78 shows the GND Density per grain distribution maps for Site 1 (centre of each sample) of both the Ti_3SiC_2 and TiC phases within the Ti_3SiC_2 MAX phase. The maps shown in the figure are of the samples which were recorded as having the highest relative GND Density per grain, namely all the samples tested at the slowest strain rate (1×10^{-4}/s) for each temperature. Of note when comparing the GND distributions of the different phases is the direction of the area of high density. In the Ti_3SiC_2 grains, the GNDs appear to be going parallel to the loading direction, while in the TiC grains, the GNDs appear to be more evenly distributed throughout each grain and not favouring one direction over another. The high levels of deformation resulted in a high amount of non-indexing for the T10-4 and T12-4 EBSD maps, this feature is particularly prevalent in the T11-4 sample (*Figure 7.78 C & D).*

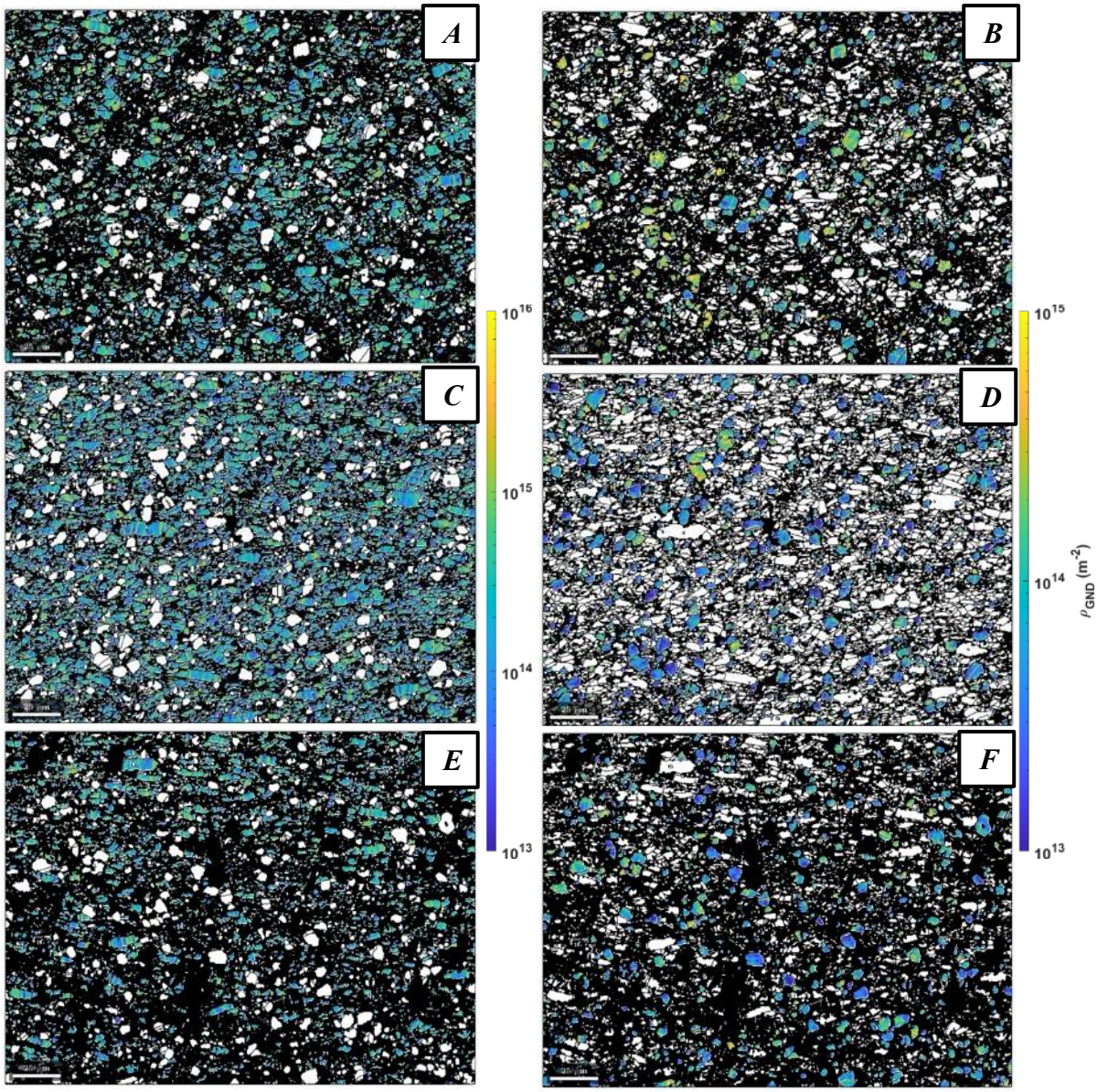

Figure 7.78: *EBSD maps showing the total GND density distributions for the Ti_3SiC_2 phase (**A, C & D**) and TiC phase (**B, D & F**) at Site 1 (the centre of each sample) for the following Ti_3SiC_2 samples: **A & B)** T10-4, **C & D)** T11-4, **E & F)** T12-4.*

7.4.2 Analysis of the Basal and Non-Basal GNDs for the Ti_2AlC and Ti_3SiC_2 phases

As has already been established, the primary phase of both of the MAX phase materials have 55 total GND types due to the variety of slip systems that could be activated within a hexagonal crystal, namely Basal, Prismatic and Pyramidal. The GND types for both the MAX phases were split into either basal or non-basal GNDs and the results of these findings can be found in *Figures 7.79-7.82.*

The graphs in *Figure 7.79 & 80* show the average mean GND density per pixel for both the fastest and slowest strain rates for each testing temperature for both MAX phases. A noticeable feature that was witnessed is that the basal GND densities are substantially greater than the non-basal GND densities for both materials, with the basal GND densities being approximately 1×10^{30} and the non-basal GND densities being approximately 1×10^{14}. Anomalous peaks for the basal GNDs were noted for both the T11-4 and T12-0 samples for both materials, with the trend otherwise being that of lower GND densities for the samples tested at faster strain rates than the samples tested at slower strain rates. This trend is more noticeable for the non-basal GNDs for both materials, although the mean GND densities decrease with increasing temperature in Ti_2AlC and increase with increasing temperature for the Ti_3SiC_2 samples.

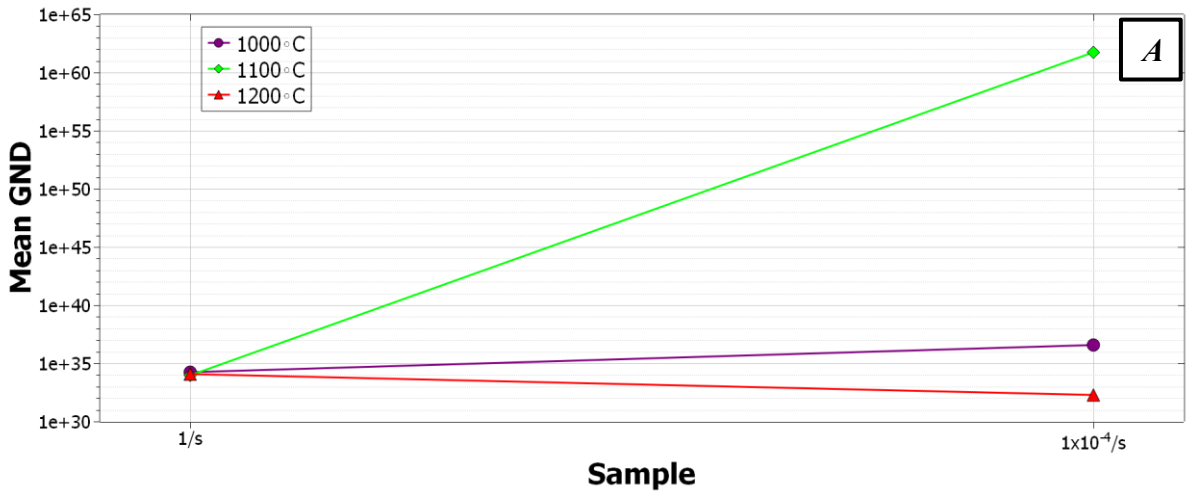

Figure 7.79i: *Graph showing the average mean GND density per pixel for the fastest and slowest strain rates for each temperature for the Ti_2AlC phase in the Ti_2AlC samples* **A)** Basal GND types. *Average of each EBSD data site*

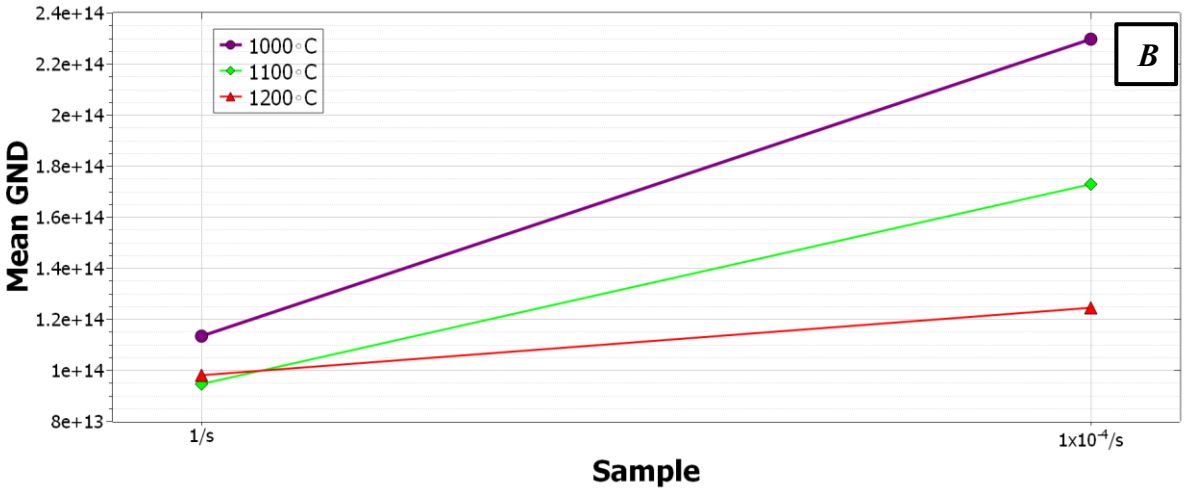

Figure 7.79ii: *Graph showing the average mean GND density per pixel for the fastest and slowest strain rates for each temperature for the Ti_2AlC phase in the Ti_2AlC samples*:* ***B)*** *Non-Basal GND types. *Average of each EBSD data site*

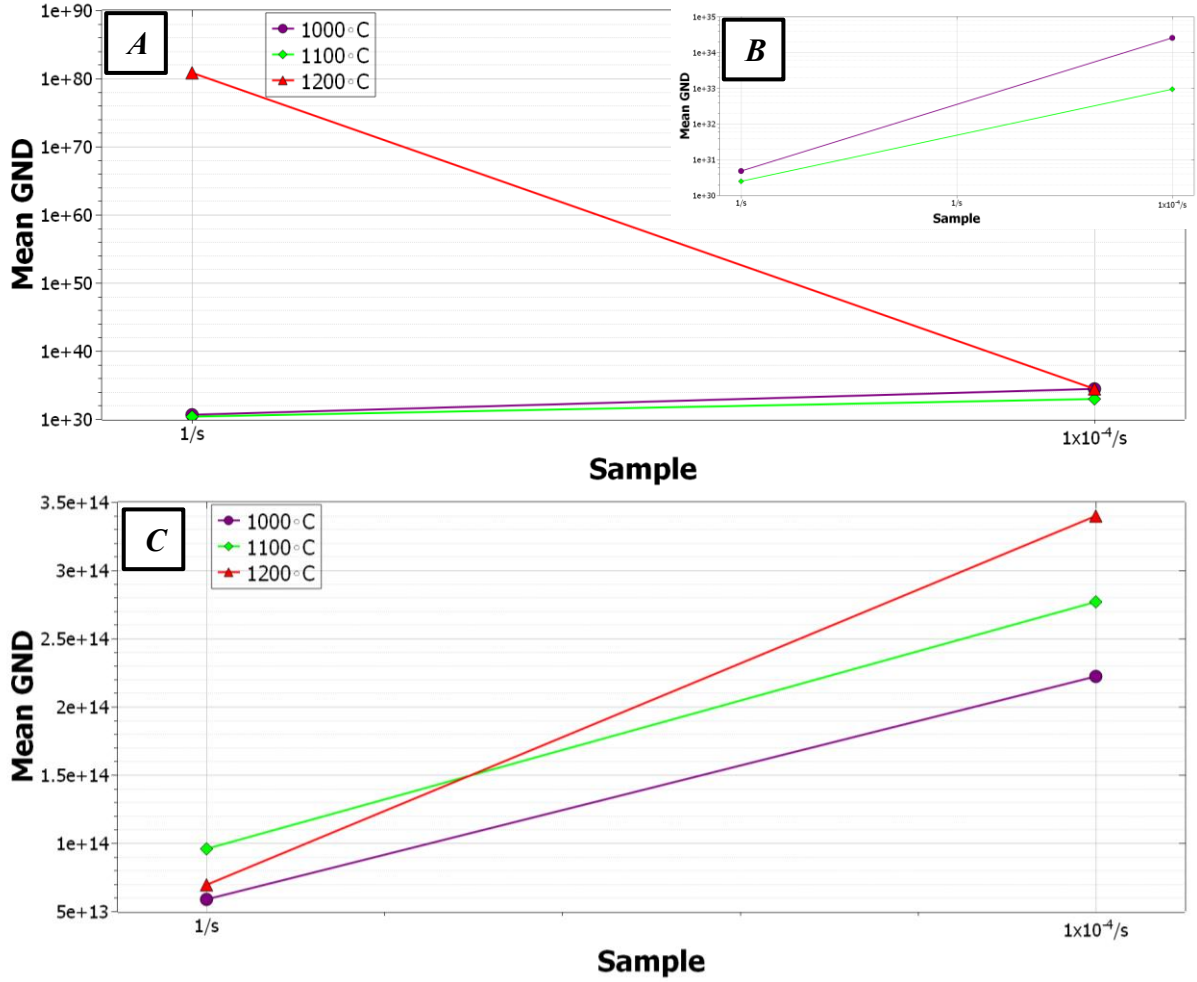

Figure 7.80: *Graph showing the average mean GND density per pixel for the fastest and slowest strain rates for each temperature for the Ti_3SiC_2 phase in the Ti_3SiC_2 samples* **A)** Basal GND types, **B)** Inset of A, and **C)** Non-Basal GND types. *Average of each EBSD data site*

Similar trends were seen in the *Figures 7.81 & 82* showing the average GND density per grain, with the basal GND densities being a substantial order of magnitude greater than those of the non-basal GND densities. The decrease and increase of non-basal GND densities for the Ti_2AlC and Ti_3SiC_2 materials respectively with regards to increasing temperature was also witnessed.

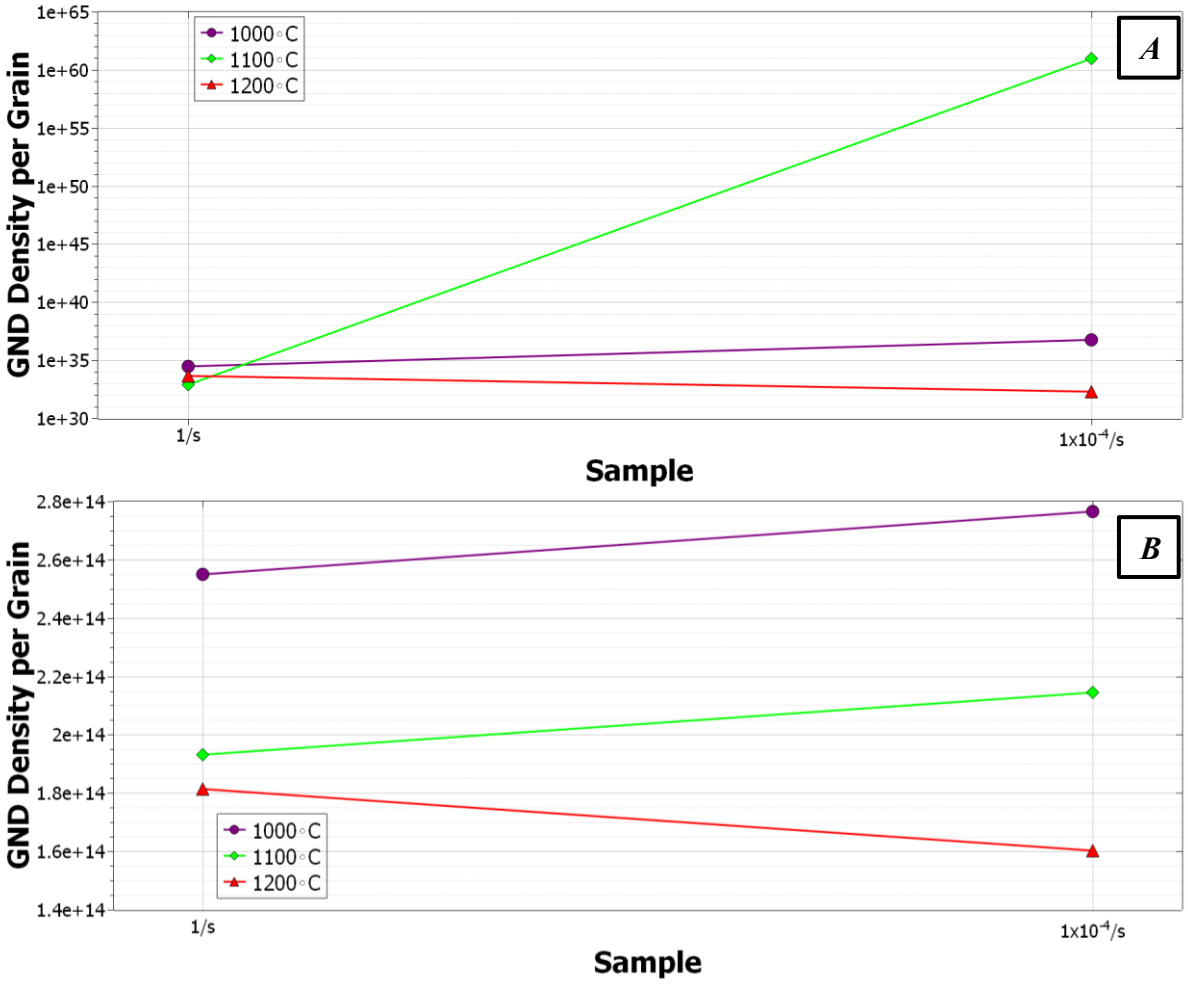

Figure 7.81: *Graph showing the average GND density per grain for the fastest and slowest strain rates for each temperature for the Ti_2AlC phase in the Ti_2AlC samples* **A)** Basal GND types and **B)** Non-Basal GND types. *Average of each EBSD data site*

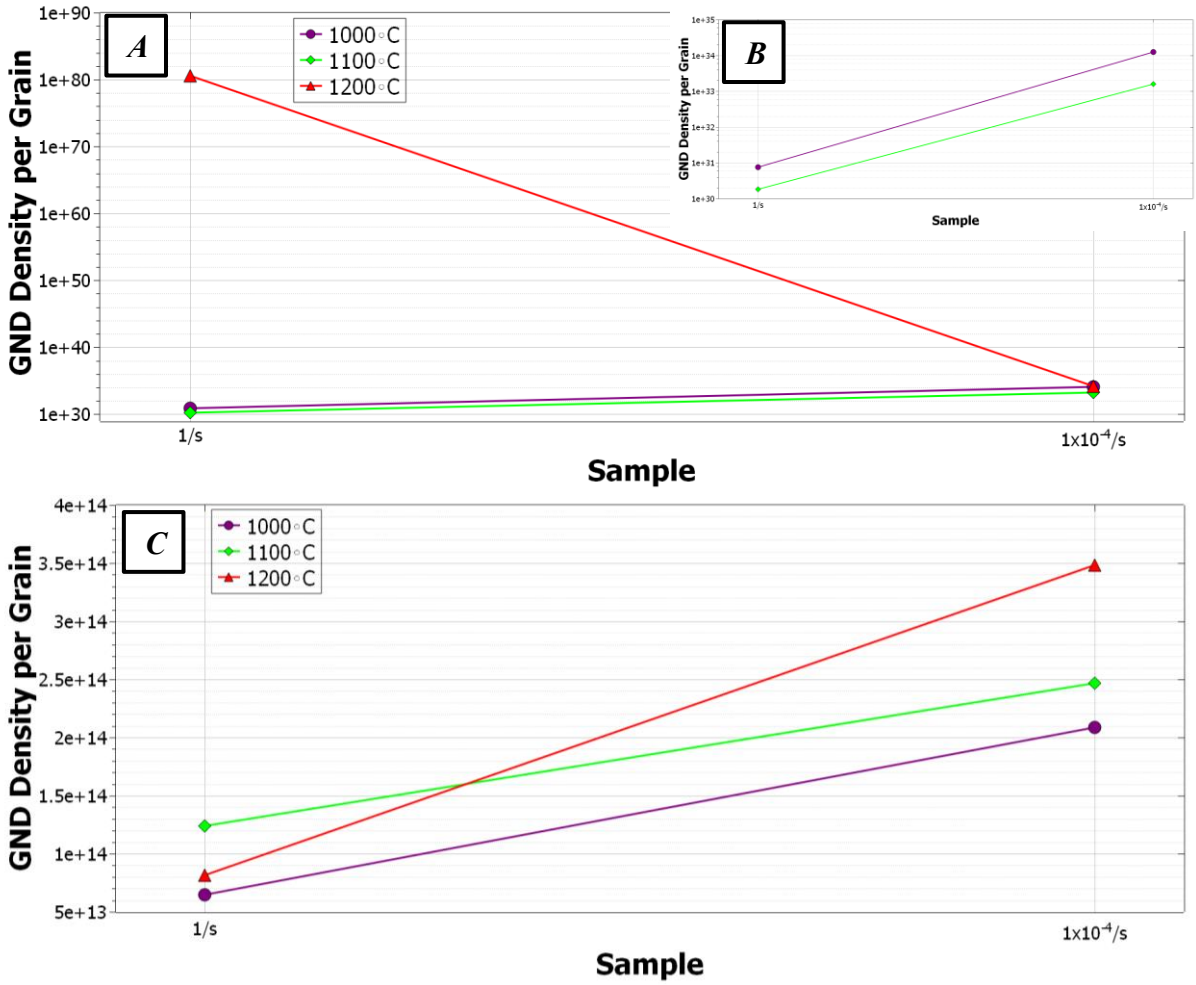

Figure 7.82: *Graph showing the average GND density per grain for the fastest and slowest strain rates for each temperature for the Ti_3SiC_2 phase in the Ti_3SiC_2 samples* **A)** Basal GND types, **B)** Inset of A, and **C)** Non-Basal GND types. *Average of each EBSD data site*

GND EBSD maps of both MAX phases comparing the basal and non-basal densities can be found in *Figures 7.83 & 7.84*. It is evident in *Figure 7.83A* that the grains that appear to be more heavily deformed in the Ti_2AlC T10-0 sample are areas with a very high basal GND density. The same area in the non-basal GND density map does not have any significant change in density. Similar trends were also seen in the Ti_2AlC T12-4 sample in *Figures 7.83C & D.* Like the GND maps in Section 7.4.1, the maps displayed here are from Site 1, with this being the area in which the highest total GND density values were recorded for each sample.

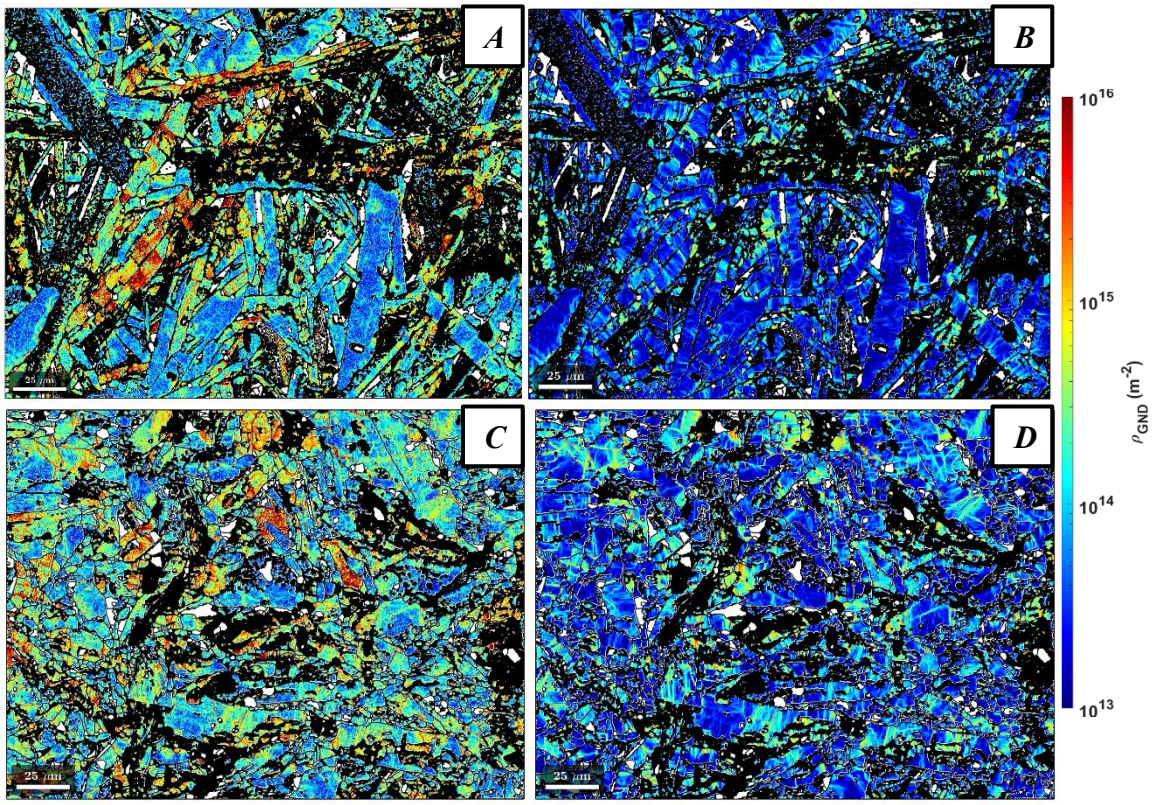

Figure 7.83: *EBSD maps showing the total GND density distributions for the basal GNDs (**A & C**) and non-basal GNDs (**B & D**) at Site 1 (the centre of each sample) for the following Ti_2AlC samples: **A & B)** T11-0, **C & D)** T12-4.*

Figure 7.84 shows the total GND density distributions for both the basal and non-basal GNDs of the Ti_3SiC_2 T10-0 and T11-4 samples. The maps for both samples were taken from Site 1, the closest site to the centre of the sample, where the highest GND density values have generally been recorded. The effect of strain rate and temperature is immediately evident when comparing *Figure 7.84A* and *Figure 7.84C*, where the basal GND densities are far higher in the T11-4 sample than in the T10-0 sample. Whereas the non-basal GND densities are still high in the T11-4 sample, they are not substantially higher than those found in the T10-0, something further evidenced in *Figure 7.82B*.

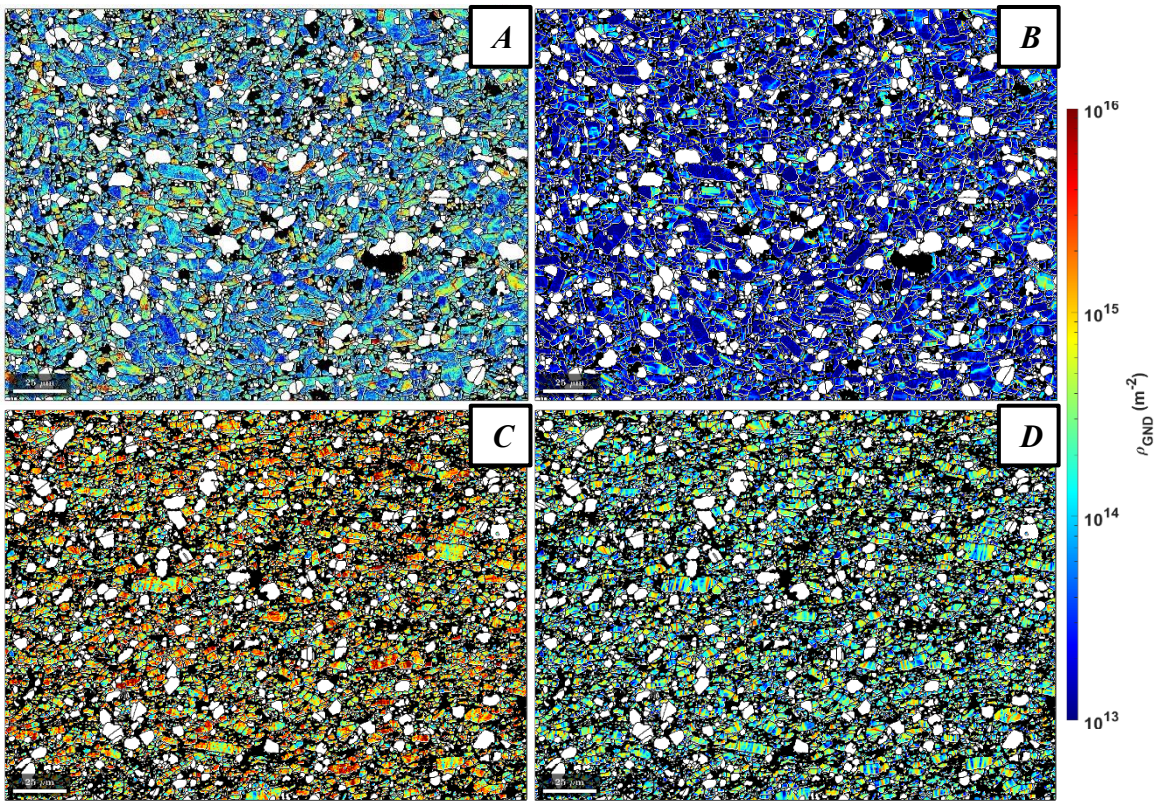

Figure 7.84: *EBSD maps showing the total GND density distributions for the basal GNDs (**A & C**) and non-basal GNDs (**B & D**) at Site 1 (the centre of each sample) for the following Ti_3SiC_2 samples: **A & B)** T10-0, **C & D)** T11-4.*

Chapter 8 - General Discussion

The experimental work presented in Chapters 5-7 has investigated the Ti_2AlC and Ti_3SiC_2 MAX phases and their response to high temperature thermo-mechanical testing. The original microstructure of both MAX phases were studied in Chapter 5, where it was established that the Ti_2AlC MAX phase tested here has a much coarser grain size than the Ti_3SiC_2 MAX phase. The presence of secondary phases within both MAX phase materials was also noted, which were attributed to the manufacturing process of the original MAX phase material studied for this work. When studying the results of both the room temperature and high temperature compression tests it was evident that the grain size relationship between the two MAX phases studied here agreed with the Hall-Petch relationship. The Hall-Petch relationship is well established in correlating the grain size with material strength. This relationship predicts that materials with fine grains usually have a higher UCS than materials with coarse grains. This relationship is most prominent when studying the two primary phases of Ti_2AlC and Ti_3SiC_2, with these phases making up a considerable part of their respective MAX phase materials.

Figure 8.1 compares the coarse grained Ti_2AlC with the fine grained Ti_3SiC_2 and the effect of temperature on their respective compressive strengths. It is evident from the graph that the Ti_3SiC_2 material is generally the stronger of the two materials over most strain rates and temperatures. Bhattacharya *et al* have previously tested the high strain rate response of Ti_3SiC_2 and they surmised that the scatter in peak stress values were as a result of variations in microflaws and impurity phase concentrations [96]. This could be the case for the Ti_3SiC_2 MAX phase tested for this work, as it was found to contain a secondary phase in the form of TiC, potentially acting as a catalyst for the stress variations. Parrikar *et al* surmised that the strength of Ti_2AlC is governed by the dislocation pileups on grain boundaries between soft grains that in turn leads to high stress concentrations and fracture. They also proposed that kinking and delamination of grains during high temperature testing was the reason for the ductile nature of failure of the samples they tested [99].

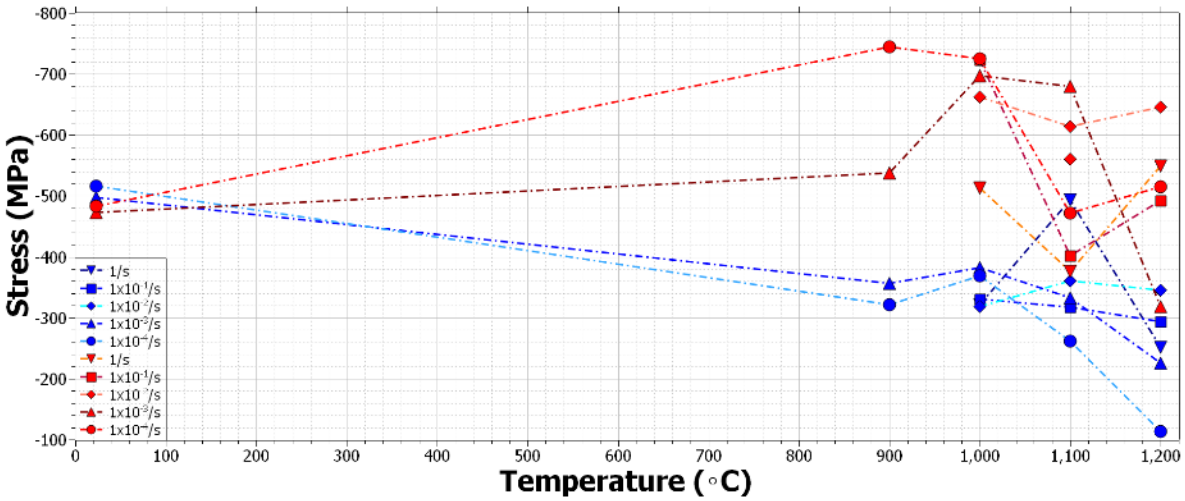

Figure 8.1: *Effect of temperature on the UCS of fine grained Ti_3SiC_2 (red) and coarse grained (blue) MAX phase materials.*

Figure 8.2 shows the effect that temperature and strain rate has on the ductility of both MAX phases. Both MAX phases have a similar relationship in that they reach ductility under the same strain rate and temperature conditions, with the Ti_2AlC MAX phase showing the more coherent relationship of the two materials. As previously mentioned in Chapter 6, each test at the slower strain rates were programmed to stop at 0.4 strain, although it is evident that for the highest temperature tests in particular that increasing the final strain would have seen even greater ductility for the samples.

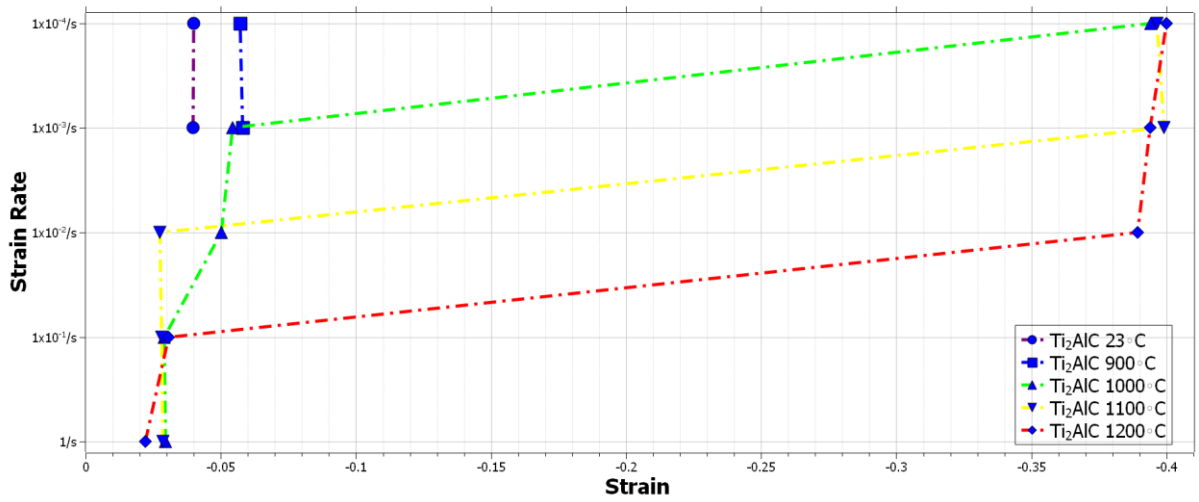

Figure 8.2i: *Effect of temperature and strain rate on the ductility of coarse grained Ti_2AlC MAX phase materials.*

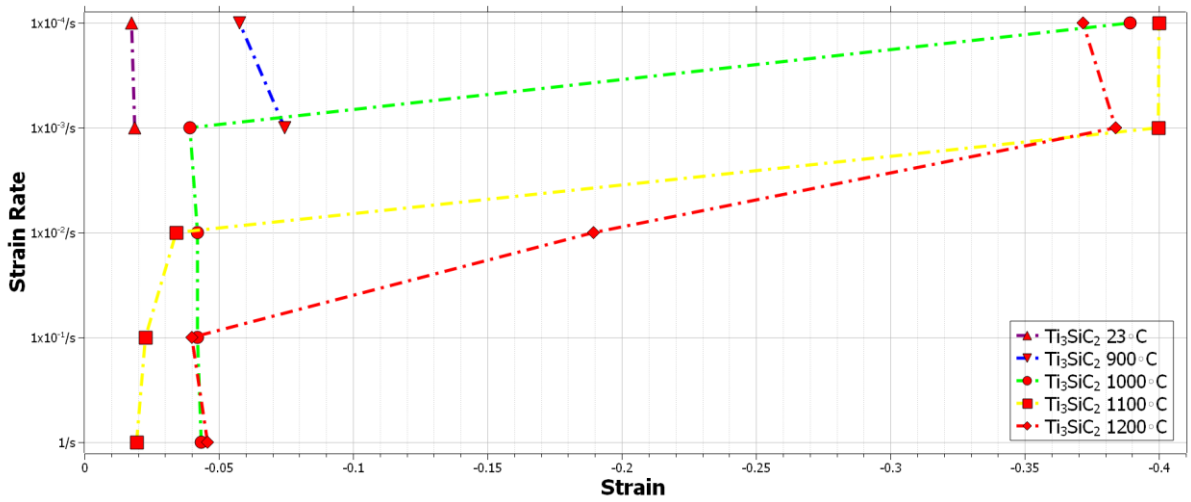

Figure 8.2ii: *Effect of temperature and strain rate on the ductility of fine grained Ti_3SiC_2 MAX phase materials.*

The stress-strain response of the samples that failed in a ductile manner were found to generally exhibit three main stages, as indicated by regions I, II and III in *Figure 8.3*, a subset of *Figure 6.14:* (i) A linear elastic regime; (ii) a brief hardening regime; and (iii) a long softening regime until the end of the test. This response has also been witnessed in several other similar tests on these two MAX phase materials [100]. The longer hardening regimes that were sometimes witnessed for the MAX phases, the Ti_3SiC_2 in particular, were explained by El Raghy *et al* as due to damage initiation early in the elastic regime resulting in initially localised plastic deformation. [17,76].

In previous studies Ti_2AlC has been recorded as being damage tolerant but fracturing in a shear manner under room temperature compressive loads. This was theorised by Zhou *et al* as being due to an insufficient number of dislocation systems at room temperature, which in turn leads to kinking and delamination of the laminated Ti_2AlC grains, basal plane dislocation slip and the formation of voids and cavities within the vicinity of the main crack. At high temperatures below the BDTT, deformation was found to still be a combination of cavities formation, with grain rotating and intergranular sliding also occurring at this stage. At temperatures above the BDTT, plasticity was thought to occur due to availability and mobility of dislocation systems [20,108]. The activation of new slip systems, an increase in the ease of kinking due to thermal activation and the presence of viscous grain boundary films were theories proposed as reasons for the BDTT in Ti_3SiC_2 [89].

As was detailed in the literature review in Section 3.6.4, there are generally three major contributing factors to the excellent thermal shock resistance of the MAX phases: (1) They are damage tolerant, therefore showing excellent thermal shock resistance due to the significant resistance to crack propagation; (2) Their thermal conductivities are higher than conventional brittle ceramics, being desirable for high thermal shock resistance; (3) These ceramics are ductile at high temperatures, with ductility inhibiting thermal failure [47,54].

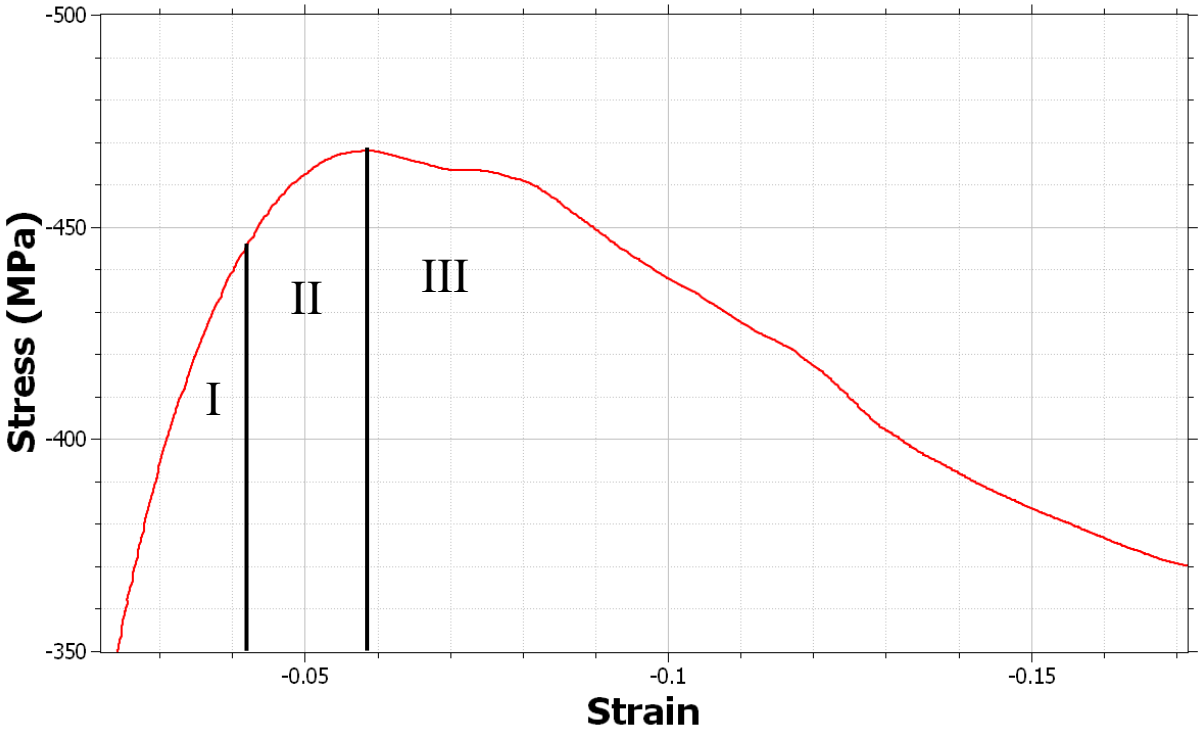

Figure 8.3: *Subset of Figure 6.14 showing the three stages of the stress-strain curve for the Ti_3SiC_2 sample tested at 1100°C and under a strain rate of 1×10^{-4}/s.*

The schematic in *Figure 8.4* can help summarise the response of the MAX phases at both room temperature and at the fastest strain rates at the higher temperatures. It was found that the main crack formed in the Ti_2AlC MAX phase propagated ~45° to the compression direction and that the damage was generally confined to the immediate vicinity of the crack, as best shown in *Figure 7.3*. With regards to the Ti_3SiC_2 MAX phase, as previously stated in Chapters 6 and 7, the samples tested at both room temperature and the faster strain rates at higher temperatures generally disintegrated into several pieces, and cracks could be seen throughout the microstructure at several angles, as opposed to the large main crack witnessed for the Ti_2AlC samples. The formation of voids and cavities, as well as the branching and deflection of both

the main and minor cracks were seen in both MAX phases. Grain pull-out of all the phases in both the Ti_2AlC and Ti_3SiC_2 materials could also be seen. The kinking and delamination of both Ti_2AlC and the Ti_3SiC_2 grains seen here in the samples that failed in a brittle manner is something that has been witnessed before in the literature [20,90]. Delaminating cracks being confined within laminated Ti_2AlC grains, as shown in *Figure 7.2A* is evidence of the ability Ti_2AlC has in confining damage. At both room temperature and under the conditions at high temperature which allow a brittle failure, it was found that the main deformation modes and resultant damage confinement was the formation of voids/cavities and crack branching, and the kinking, delaminating and pull-out of the MAX phase grains [143][28].

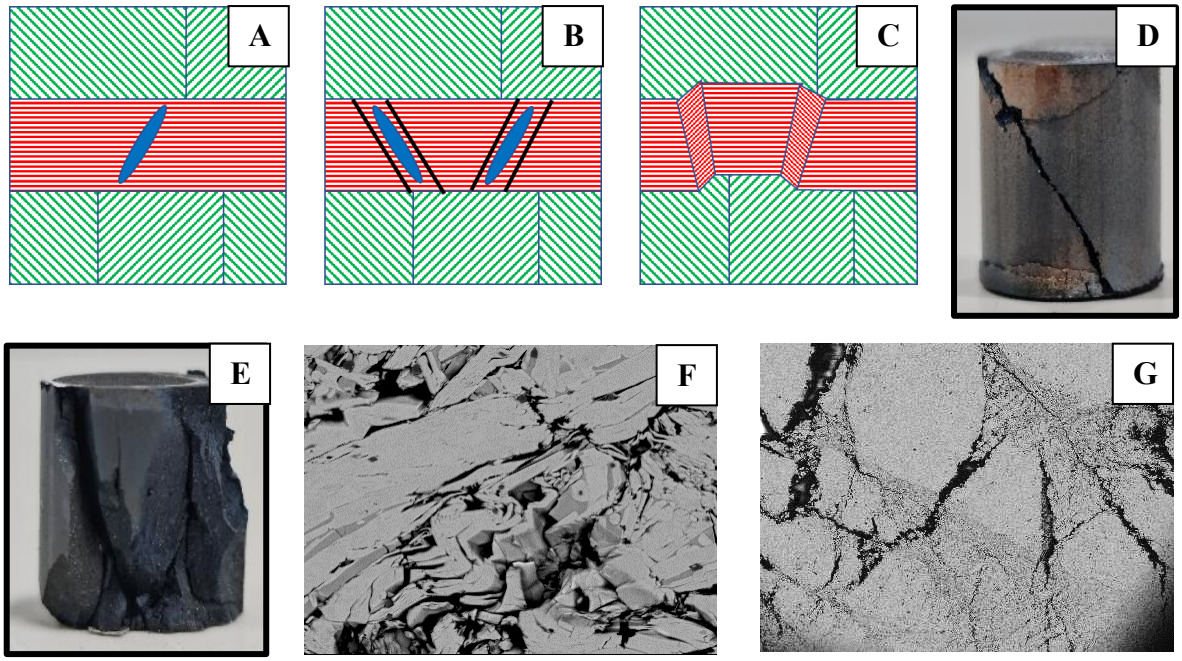

Figure 8.4i: *Schematic showing the deformation mechanisms present in both MAX phases after testing under fast strain rate conditions at both low and high temperatures.* ***A-C)*** *Schematic showing the formation of incipient kink bands within a grain that eventually form kinks like those seen in F;* ***A)*** *An IKB forming within a grain, halted at the grain boundary;* ***B)*** *At higher stresses and/or temperatures, mobile dislocation walls can form upon the devolution of IKBs;* ***C)*** *The formation and subsequent collapse of several MDWs can lead to the formation of kink bands and boundaries;* ***D & E)*** *Pictures of Ti_2AlC and Ti_3SiC_2 samples after testing;* ***F)*** *Micrograph showing kinks and delamination in Ti_2AlC;* ***G)*** *Micrograph showing the substantial cracking in Ti_3SiC_2 grains*

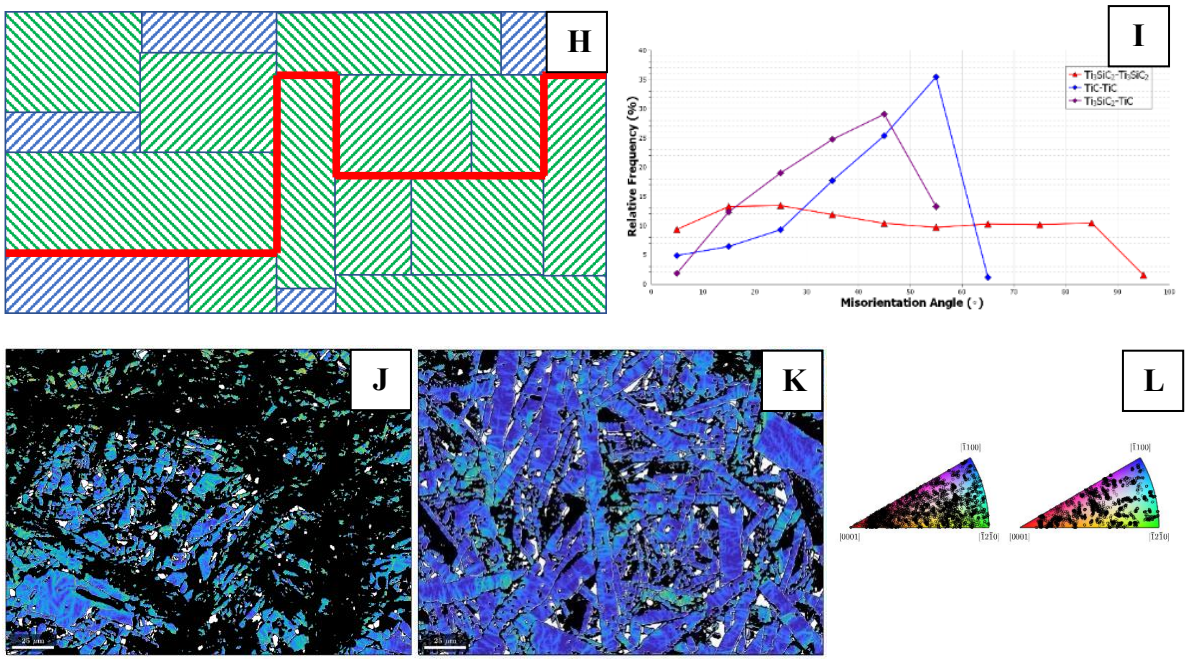

Figure 8.4ii: *Schematic showing the deformation mechanisms present in both MAX phases after testing under fast strain rate conditions at both low and high temperatures.* ***H)*** *Schematic showing intergranular cracking, the most prevalent grain cracking mechanism in samples under these conditions;* ***I)*** *Typical grain boundary misorientation angles for* Ti_3SiC_2 *under these conditions, note the generally uniform relationship for the* Ti_3SiC_2*-*Ti_3SiC_2 *grain boundaries;* ***J & K)*** *EBSD maps showing the total GND density distributions for the* Ti_2AlC *phase in the T10-0 and T12-0 samples;* ***L)*** *IPF keys of the* Ti_2AlC *phase for the T11-0 sample*

As previously mentioned in Chapter 6 and 7, there is a similarity to the sample failure and the microstructure of the samples that failed at room temperature and the samples tested at the fastest strain rates at elevated temperatures. For the Ti_2AlC samples in particular, upon increasing the testing temperature up to 1000°C, the samples still shear fractured, although unlike the samples tested at room temperature these samples maintained their integrity. The Ti_3SiC_2 samples did not maintain their integrity at either room temperature or at elevated temperature under the faster strain rates. Cavities, intergranular and transgranular cracks were found to be features of the microstructures of the samples that failed in a ductile manner, as seen in *Figure 8.5.*

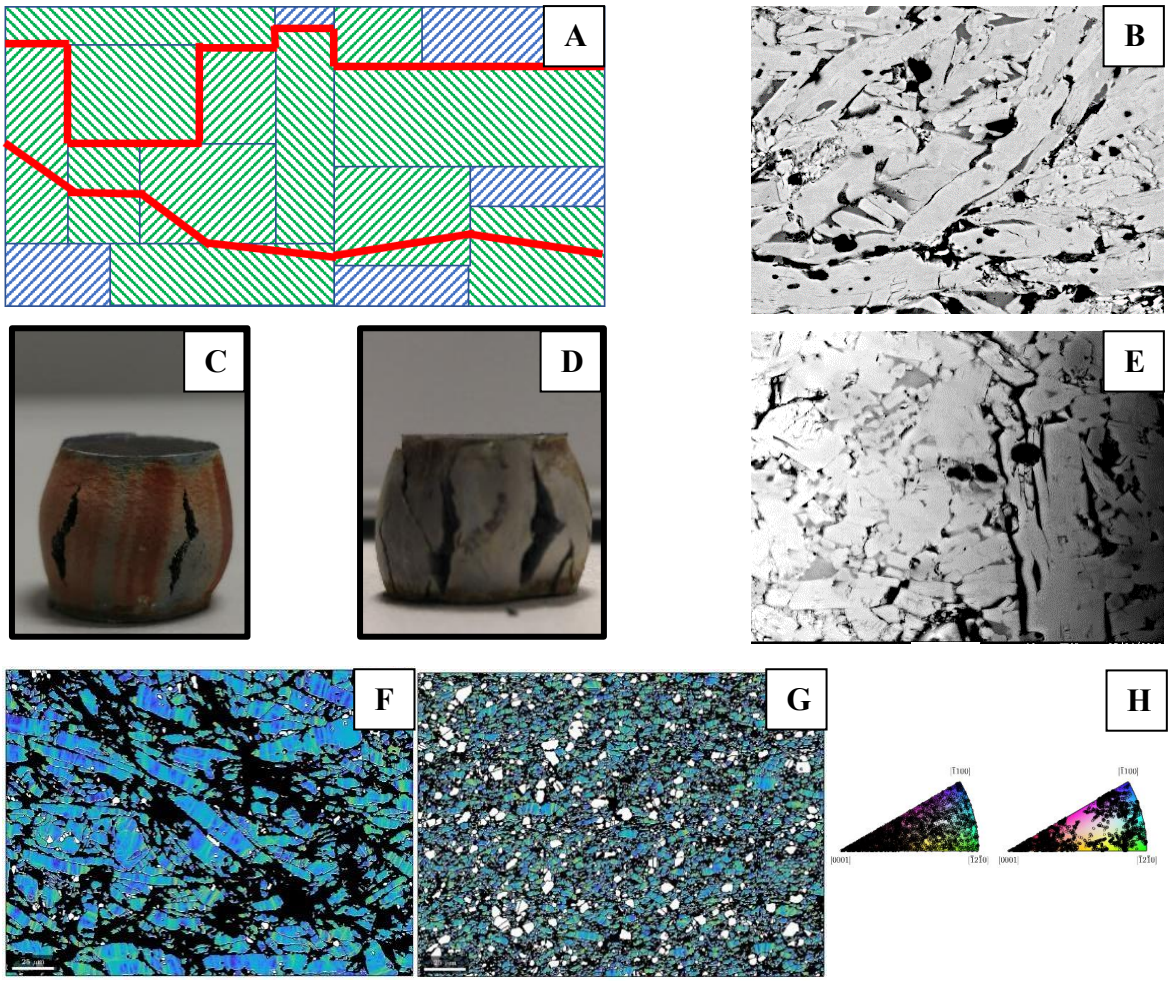

Figure 8.5: *Schematic showing the deformation mechanisms present in both MAX phases after testing under slow strain rate conditions at low-medium range high temperatures.* ***A)*** *Schematic showing the main deformation mode under these conditions: Intergranular and Transgranular cracking;* ***B)*** *Micrograph showing kinks and grain bending in Ti_2AlC grains;* ***C & D)*** *Pictures of Ti_2AlC and Ti_3SiC_2 samples after testing;* ***E)*** *Micrograph showing the substantial Transgranular and Intergranular cracking in Ti_3SiC_2 grains, parallel to the loading direction;* ***F & G)*** *EBSD maps showing the total GND density distributions for the Ti_2AlC phase (F) and Ti_3SiC_2 phase (G) in the T10-4 and T11-4 samples respectively;* ***H)*** *IPF keys of the Ti_2AlC phase for the T11-4 sample*

Using the Cerius[2] computer program based on the Donnay-Harker theory, Zhou *et als* simulations showed that the hexagonal surfaces of Ti_2AlC were parallel to {200} and the side surfaces parallel to the {100} planes of Ti_2AlC [20,144]. As has been established in Chapters 2 and 4, laminated Ti_2AlC grains are made up of thin hexagonal slices of micro-lamellae. In Ti_3SiC_2 these hexagonal slices are wormed when the growth rate on {002} is slowest among that of {002}, {100} and {101} surfaces [54,145]. The hexagonal slices in Ti_3SiC_2 were also found to be weakly bonded, resulting in the occurrence of easy shear slip. Macro-fracture is also suppressed by the weak boundaries deflected incipient surface cracks away from the

directional tensile stress trajectory, in turn increasing its resistance to damage [146]. Ti_2AlC was also thought by Zhou *et al* to be weakly bonded, allowing for the easy shear slip and delamination that was found in Chapter 7. Under room temperature conditions, the kinking and delaminating of laminated Ti_2AlC grains, together with intergranular fracture, were found by both Zhou *et al* and in this work to be the main deformation mode of Ti_2AlC under compression. Due to the relative structural and crystallographic similarities between Ti_2AlC and Ti_3SiC_2, a number of theories proposed for Ti_3SiC_2 can generally be seen to be applicable to Ti_2AlC and *vice versa*. Shear band formation by dislocation arrays, cavities and the creation of dislocation walls and kink boundaries, buckling and delaminations of Ti_3SiC_2 grains was proposed by Barsoum *et al* as the main deformation modes for Ti_3SiC_2 [89,90]. It is also well established that at room temperature, only basal places dislocations are mobile, with a slip trace of basal plane dislocation observed previously in Ti_3SiC_2 [20,90].

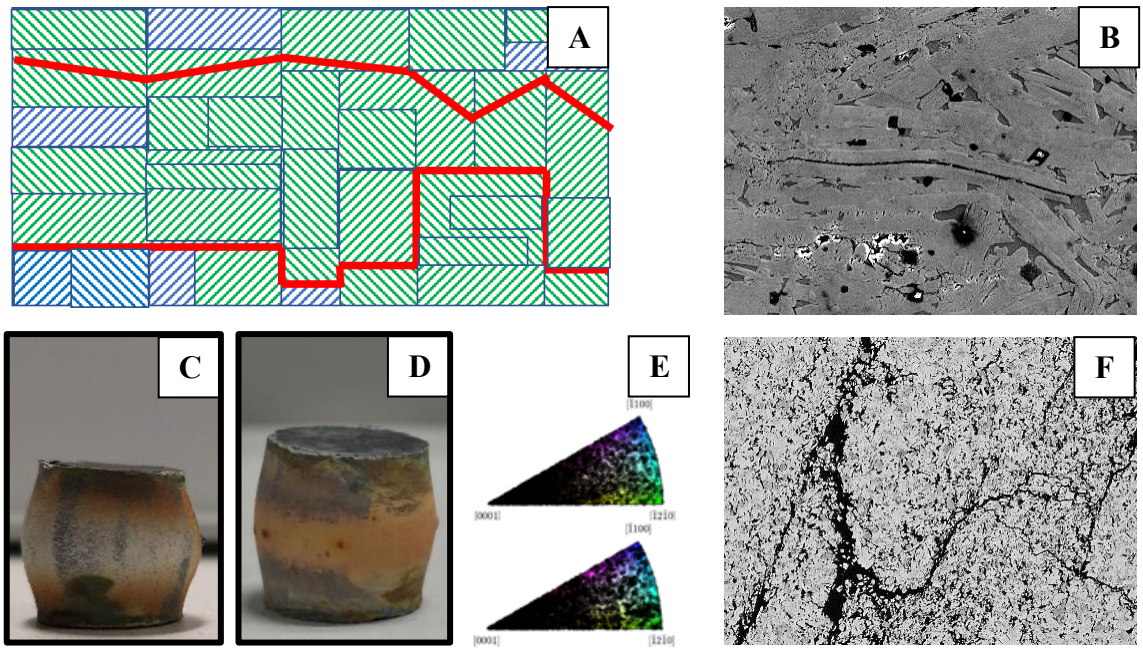

Figure 8.6i: *Schematic showing the deformation mechanisms present in both MAX phases after testing under slow strain rate conditions at high temperatures.* ***A)*** *Schematic showing the main deformation mode under these conditions: Intergranular and Transgranular cracking, with the large laminated grains breaking up into smaller grains;* ***B)*** *Micrograph showing grain bending and Transgranular cracking in Ti_2AlC grains;* ***C & D)*** *Pictures of Ti_2AlC and Ti_3SiC_2 samples after testing, note the lack of outer surface cracks;* ***E)*** *IPF keys of the Ti_2AlC phase for the T12-4 sample;* ***F)*** *Micrograph showing the substantial Transgranular and Intergranular cracking in Ti_3SiC_2 grains.*

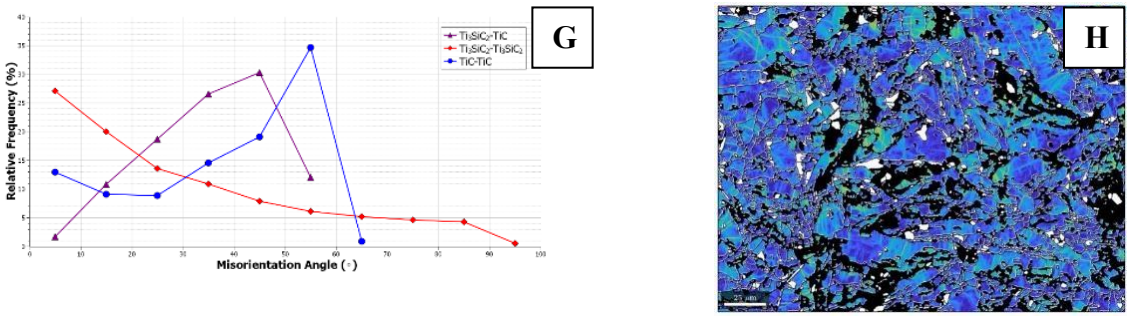

Figure 8.6ii: *Schematic showing the deformation mechanisms present in both MAX phases after testing under slow strain rate conditions at high temperatures.* ***G)*** *Graph showing the grain boundary misorientation angles in the Ti_3SiC_2 tested under these conditions, note the increased amount of LAGBs for the Ti_3SiC_2-Ti_3SiC_2 grains compared to the faster strain rate conditions;* ***H)*** *EBSD map showing the total GND density distributions for the Ti_2AlC phase in the T12-4 sample.*

As outlined in both Chapter 6 and 7, and summarised in *Figures 8.5 and 8.6*, the increase in temperature leads to the MAX phases performing differently once subjected to compressive loads. Whereas kinking and delaminating and intergranular shear fracture was observed for samples tested at room temperature, for samples tested at 1000°C and above and at the lower strain rates, the failure is mixed mode intergranular and transgranular in nature. Unlike previous studies by Zhou *et al*, where the layered nature of the MAX phase disappears upon deforming the samples at high temperature, the layered nature of the microstructure was still found to be prevalent throughout every sample tested for this work. As well as the cavities and transgranular cracks seen by Zhou *et al*, they also witnessed the rotation of grains and, at temperatures above 1100°C, evidence of plastic flow. It has been established in literature that the BDTT of a material is controlled by the mobility of dislocations and that therefore the deformation mechanisms at temperatures above the BDTT can be attributed to the availability and mobility of sufficient dislocation systems [20,147].

The shape of the stress-strain graphs in Chapter 6 and summarised in this chapter show in general that the amount of strain decreases below 1000°C and increases above this temperature, but that this increase is strongly dependent on the strain rate. The shape and slope of the stress-strain curves is similar to the flow stress behaviour observed by Sun *et al* in Ti_3SiC_2. However, due to the strain rate dependence, their theory of this behaviour being explained by the Kear-Wilsforf mechanism was not held to be valid [148]. Both MAX phases studied for this work have been known to exhibit anisotropic and laminated MAX phase grains, which are made up

of several thin hexagonal slices. At room temperature the grains kink and delaminate and are also susceptible to shear slip and buckling. These factors contribute to the large compressive strain that the MAX phases suffer from at room temperature. At high temperatures, however, the bonding between the thin hexagonal slices is stronger, inhibiting the slip of the hexagonal slices and thus resulting in less compressive strain. A sufficient number of mobile dislocations are available at temperatures above the BDTT, with the compressive strain increasing [20].

Chapter 9 - Conclusions

The aim of this work was to investigate the high temperature thermo-mechanical performance of high-density MAX phase ceramics. The two MAX phases which were used for this work were the Kanthal produced MAXthal 211 and MAXthal 312, which are the commercial names for the Ti_2AlC and Ti_3SiC_2 based MAX Phases respectively. A microstructural characterisation was undertaken of each MAX phase before they were subjected to high temperature compression testing. The main conclusions when comparing the microstructures are:

- The Ti_2AlC based MAX phase has a substantially larger grain size than the Ti_3SiC_2 MAX phase, with the largest Ti_2AlC grains being approximately 4 times larger than the relatively fine grained Ti_3SiC_2. The grain shapes of the large Ti_2AlC and Ti_3SiC_2 phases were found to be relatively similar, being roughly elongated and lamellar in nature.
- Using microscopy, XRD and EDS techniques it was determined that both MAX phases had secondary phases present in their structure. The secondary phases present in Ti_2AlC included TiAl and Al_2O_3, while TiC was the secondary phase detected in the Ti_3SiC_2 MAX phase.
- For both MAX phases, the grains appeared to have a random texture and orientation, with the grains not favouring one predominant direction. Misorientation angles between the major phase grain boundaries were recorded as being quite uniform, while grain boundaries between the other phases either have a prevalence towards an LAGB, HAGB or have a random, Mackenzie type profile.

After the characterisation of the as received samples, the high temperature mechanical properties of both MAX phases were tested. Several samples of both MAX phase were subjected to a variety of heating and mechanical testing regimes to determine the effect of deformation temperature and strain rate had on the MAX phases. The temperatures at which samples were tested were room temperature (23°C), 900°C, 1000°C, 1100°C and 1200°C, while the strain rates used ranged from 1/s to 1×10^{-4}/s. The general trends witnessed were:

- For Ti_2AlC, the slower the strain rate, the lower the ultimate compressive stress, and also, for each strain rate, the higher the temperature, the lower the ultimate compressive stress.
- The results of Ti_3SiC_2 when subjected to different strain rates at various temperatures were more incoherent. Relatively low UCS at room temperature suggested that small

chemical compositional variations during processing could have affected the overall microstructure and phase distribution.

- The fine grained Ti_3SiC_2 generally has a higher UCS than Ti_2AC for the same testing conditions, showing an example of the Hall-Petch relationship with regards to grain size. The highest UCS recorded for Ti_3SiC_2 was ~-740 MPa (T09-4), while the highest for Ti_2AlC was ~-510 MPa for the TRT-3 sample.
- The Ti_2AlC samples which failed in a brittle manner mostly retained their integrity after fracturing, with the main indication of failure being a large crack/breakage 45° to the compression direction. This feature was found on the majority of Ti_2AlC samples tested at the faster strain rates.
- The Ti_3SiC_2 samples which failed in a brittle manner generally disintegrated into several pieces.
- Both MAX phases exhibited significant plastic deformation in the form of barrelling as the temperature was increased and the strain rate decreased, with the transition temperature recognised as being around 1000°C.

High temperature quenching trials were also undertaken to investigate the effect of thermal shock on the MAX phases. Each thermal shock test involved heating the sample to its testing temperature and then air quenching it while being subjected to a mechanical load of between 0-200 MPa. After the quenching trials each sample was compression tested to determine the effect quenching while under different loads had on the UCS of each sample. The main results of these tests established that:

- The majority of the samples maintained their integrity following the application of a load while being thermally shocked, with the only exception being the Ti_2AlC samples of Q12-S150 and Q12-S200.
- With the exception of the Q10-S100 samples for both MAX phases, the samples quenched from 1000°C do see a slight increase in their recorded UCS after being quenched under a compressive load. The Q10-S200 samples for both MAX phases have their highest recorded UCSs.
- The change in compressive loads during quenching did not have a significant effect on the samples quenched from 1200°C, although both MAX phases recorded similar values for each test.

The microstructure of both MAX phases were studied following the thermo-mechanical trials in the Gleeble. When comparing the response of both MAX phases to both room and high temperature compression testing, several trends were established:

- At room temperature, areas of substantial deformation revealed evidence of kinking and delaminations, with Ti_3SiC_2 showing substantially more deformation than Ti_2AlC
- In Ti_2AlC, areas around the large cracks that were 45° to the compression direction were the areas with the highest levels of deformation, with both transgranular and intergranular cracks in evidence. At the high strain rates at high temperature, kinking and heavily delaminated areas were also recorded.
- Intergranular cracks are particularly prevalent in Ti_3SiC_2 samples tested under high strain rate, high temperature conditions. Cracks branching between cracks were also seen for both large and small cracks.
- Fracture surfaces of Ti_3SiC_2 samples tested at higher strain rates showed evidence of cup and cone formation, as well as several cracks.
- No large, cross sample cracks for the samples tested under slower strain rate conditions at higher temperatures were recorded.
- Areas of both MAX phase samples that were in contact with the compression anvil showed very little deformation. This was attributed to a deformation 'dead zone', where deformation levels are generally low in areas in direct contact with a compression anvil at high temperature.
- The areas of high deformation were recorded as being at the corners and sides of both MAX phase samples that were tested at high strain rate, high temperature conditions. Grain bending and voids within these areas were witnessed, while transgranular cracks were generally more prevalent in both MAX phases, although intergranular cracks were still recorded.

Electron backscatter diffraction (EBSD) was also utilised to investigate the microstructure following thermo-mechanical testing. The main results of these investigations established that:

- The faster strain rates samples for all temperatures generally have a very similar overall microstructure and texture to the as received samples previously investigated. This being that for each phase of both MAX phases their texture is generally random.

- The grain boundary misorientation angles of the Ti_2AlC samples tested at a faster strain rate generally fall into 3 categories: either random (Mackenzie), uniform, or with peaks indicating a generally medium angle or high angle grain boundary.
- For both MAX phase materials, the samples tested at a slower strain rates generally had a favourable orientation to the [0001] direction. The likelihood of a sample fulfilling this trend increased with increasing temperature.
- The grain boundaries of the Ti_2AlC samples tested at slower strain rates at high temperature behaved differently to those at slower strain rates. The boundaries between the Ti_2AlC grains were found to generally have LAGBs of between 2-10°, while the relationship between the secondary phases also yielded grain boundaries that adhered to MAGB or HAGB relationships.
- For the majority of the Ti_3SiC_2 samples, the grain boundary misorientation angles between the Ti_3SiC_2-TiC and TiC-TiC grains have a random, Mackenzie profile, while the boundaries between each Ti_3SiC_2 grain are generally uniform. The exception to this rule was witnessed in the T12-2 and T12-4 samples, which had a more LAGB relationship than the other samples.

A further EBSD study on the GND of both materials following high temperature compression testing was also undertaken. The results of these investigations found that:

- For both materials, the GND density was found to generally be higher in EBSD map sites closest to the centre of each sample.
- Samples tested at the slowest strain rate of 1×10^{-4}/s generally have the highest GND density regardless of temperature, with samples tested at 1/s having the lowest.
- Ti_3SiC_2 and TiC phases were found to behave in an almost identical manner with regards to their GND densities, despite their structural differences.
- Basal GND densities are substantially greater in number than the non-basal GND densities for both materials.
- Higher GND densities for samples tested at slower strain rates.
- GND densities increased with increasing temperature for Ti_3SiC_2 samples, with Ti_2AlC densities decreasing with the increase in temperature.
- High GND density areas are located around broken or kinked Ti_2AlC grains.

To summarise, an in depth comparison study has been undertaken on the Ti_2AlC and Ti_3SiC_2 MAX phases. The microstructure and high temperature compression study revealed a Hall-Petch relationship with regards to grain size and the UCS of the materials studied. The high temperature compression studies also determined that the deformation behaviour of both MAX phases was dependent on strain rate and temperature. Microstructural studies of the mechanically tested samples revealed several features, including kinked grains, delaminations, microvoids, microcracks and both transgranular and intergranular cracks. Using EBSD, the microstructure was also found to be highly orientated to the [0001] direction at the slowest strain rates, while the presence of dislocation walls were proposed in the form of LAGBs. A deformation 'dead zone' was also proposed in areas of each sample closest to the compression anvil, while the GND study revealed higher GND densities with increasing strain rate and temperature for Ti_3SiC_2 samples, with the opposite being true of Ti_2AlC samples.

Chapter 10 – Future Work

Due to time constraints and access to the relevant equipment, not all the work which was planned at the beginning of the PhD turned out to be possible. Therefore, there is scope for continuing the work presented in this thesis. Some ideas for any potential further work include:

- Investigations into multi-hit tests of the MAX phases, as well as potentially replicating these tests on materials similar to the MAX phases, such as MXenes.
- Further EBSD analysis, particularly on the samples which were quenched.
- A more in depth GND analysis to further understand the relationships between the different phases.
- TEM analysis of both the fracture surfaces and general microstructure to further understand the dislocations present and the deformation mechanisms involved.
- Electrical measurements, to determine whether the electrical properties of the MAX phases change once subjected to thermo-mechanical testing.

References

1. Barsoum MW. The Mn+1AXn Phases: A New Class of Solids. Prog Solid State Chem. 2000 Jan 1;28(1–4):201–81.
2. Jeitschko W, Nowotny H. Die Kristallstruktur von Ti3SiC2-ein neuer Komplexcarbid-Typ. Monatshefte für Chemie. 1967;
3. Nowotny VH. Strukturchemie einiger Verbindungen der Übergangsmetalle mit den elementen C, Si, Ge, Sn. Prog Solid State Chem. 1971;
4. Jeitschko W, Nowotny H, Benesovsky F. Kohlenstoffhaltige ternare Verbindungen (H-Phase). Monatshefte für Chemie. 1963;
5. Jeitschko W, Nowotny H, Benesovsky F. Kohlenstoffhaltige ternare Verbindungen (V-Ge-C, Nb-Ga-C, Ta-Ga-C, Ta-Ge-C, Cr-Ga-C und Cr-Ge-C). Monatshefte für Chemier Chemie. 1963;
6. Jeitschko W, Nowotny H, Benesovsky F. Ti2AlN, eine stickstoffhaltige H-Phase. Monatshefte für Chemie. 1963;
7. Jeitschko W, Nowotny H, Benesovsky F. Die H-Phasen: Ti2CdC, Ti2GaC, Ti2GaN, Ti2InN, Zr2InN und Nb2GaC. Monatshefte für Chemier Chemie. 1964;
8. Jeitschko W, Holleck H, Nowotny H, Benesovsky F. Phasen mit aufgefülltem Ti2Ni-Typ. Monatshefte für Chemier Chemie. 1964;95(3):1004–6.
9. Reiffenstein E, Nowotny H, Benesovsky F. Strukturchemische und magnetochemische Untersuchungen an Komplexcarbiden. Monatshefte für Chemie. 1966;
10. Beckmann O, Boller H, Nowotny H, Benesovsky F. Einige Komplexcarbide und-nitride in den Systemen Ti-{Zn, Cd, Hg}-{C, N} und Cr-Ga-N. Monatshefte für Chemie. 1969;
11. Beckmann O, Boller H, Nowotny H. Neue H-Phasen. Monatshefte für Chemie. 1968;99(4):1580–3.
12. Sun ZM. Progress in research and development on MAX phases: a family of layered ternary compounds. Int Mater Rev. 2011;56(3):143–66.
13. Palmquist JP, Li S, Persson PO., Emmerlich J, Wilhelmsson O, Högberg H, et al. Mn+1AXn phases in the Ti-Si-C system studied by thin-film synthesis and ab initio calculations. Phys Rev B - Condens Matter Mater Phys. 2004;
14. Barsoum MW, El-Raghy T. The MAX phases: Unique new carbide and nitride materials: Tertiary ceramics are soft and machinable, yet heat-tolerant, strong and lighweight. Am Sci. 2001;89(4):334–43.
15. Barsoum MW. MAX phases: Properties of machinable ternary carbides and nitrides. MAX Phases: Properties of Machinable Ternary Carbides and Nitrides. 2013.
16. Maxthal ceramic engineering material. [cited 2018 Oct 12]; Available from: https://www.kanthal.com/en/products/furnace-products-and-heating-systems/refractory-material/
17. Barsoum MW, Ali M, El-Raghy T. Processing and characterization of Ti2AlC, Ti2AlN, and Ti2AlC0.5N0.5. Metall Mater Trans A Phys Metall Mater Sci. 2000;31(July):1857–65.
18. Barsoum MW, Brodkin D, El-Raghy T. Layered machinable ceramics for high temperature applications. J Name Scr Mater J Vol 36; J Issue 5; Other Inf PBD 1 Mar 1997. 1997;
19. Wang XH, Zhou YC. Layered Machinable and Electrically Conductive Ti2AlC and Ti3AlC2 Ceramics: a Review. J Mater Sci Technol. 2010;26(5):385–416.
20. Zhou YC, Wang XH. Deformation of polycrystalline Ti2AIC under compression. Mater Res Innov. 2001;5(2):87–93.
21. Zhou Y, Sun Z. Electronic structure and bonding properties of layered machinable Ti2AlC and Ti2AlN ceramics. Phys Rev B Condens Matter Mater Phys.

2000;61(19):570–3.
22. Barsoum MW, El-Raghy T. Synthesis and characterization of a remarkable ceramic: Ti3SiC2. Vol. 79, Journal of the American Ceramic Society. 1996. p. 1953–6.
23. Barsoum M. MAX Phases & Bulk Layered Solids [Internet]. [cited 2018 Oct 12]. Available from: http://max.materials.drexel.edu/research-areas/max-phases/
24. Mauchamp V, Hug G, Bugnet M, Cabioc'h T, Jaouen M. Anisotropy of Ti2AlN dielectric response investigated by ab initio calculations and electron energy-loss spectroscopy. Phys Rev B. 2010;81(3):035109.
25. Magnuson M, Mattesini M, Wilhelmsson O, Emmerlich J, Palmquist J. Electronic structure and chemical bonding in Ti 4 SiC 3 investigated by soft x-ray emission spectroscopy and first principle theory. Phys Rev B. 2006;74:205102.
26. Yanagida H, Kōmoto K, Miyayama M. The Chemistry of Ceramics. Wiley; 1996. 263 p.
27. Ivchenko VI, Lesnaya MI, Nemchenko VF, Kosolapova TY. Some physical properties of ternary compounds in the system Ti-Al-C. Sov Powder Metall Met Ceram. 1976 May;15(5):367–9.
28. Wang X, Zhou Y. Solid-Liquid Reaction Synthesis and Simultaneous Densification of Polycrystalline Ti 2 AlC. Zeitschrift für Met. 2002;93(1):66–71.
29. Bai Y, He X, Li Y, Zhu C, Zhang S. Rapid synthesis of bulk Ti2AlC by self-propagating high temperature combustion synthesis with a pseudo-hot isostatic pressing process. J Mater Res. 2009;24(8):2528–35.
30. Kopeliovich D. Methods of shape forming ceramic powders [Internet]. SubsTech. [cited 2018 Oct 12]. Available from: http://www.substech.com/dokuwiki/doku.php?id=methods_of_shape_forming_ceramic_powders
31. Zhou WB, Mei BC, Zhu JQ, Hong XL. Rapid synthesis of Ti2AlC by spark plasma sintering technique. Mater Lett. 2005;59(1):131–4.
32. Łopaciński M, Puszynski J, Lis J. Synthesis of Ternary Titanium Aluminum Carbides Using Self-Propagating High-Temperature Synthesis Technique. J Am Ceram Soc. 2001;84(12):3051–3.
33. Zhou A, Wang CA, Ge Z, Wu L. Preparation of Ti3AlC2 and Ti2AlC by self-propagating high-temperature synthesis. J Mater Sci Lett. 2001;20(21):1971–3.
34. Khoptiar Y, Gotman I, Gutmanas EY. Pressure-assisted combustion synthesis of dense layered Ti 3AlC2 and its mechanical properties. J Am Ceram Soc. 2005;88(1):28–33.
35. Yeh CL, Shen YG. Combustion synthesis of Ti3AlC2from Ti/Al/C/TiC powder compacts. J Alloys Compd. 2008;466(1–2):308–13.
36. Yeh CL, Shen YG. Effects of TiC and Al4C3addition on combustion synthesis of Ti2AlC. J Alloys Compd. 2009;470(1–2):424–8.
37. Yeh CL, Shen YG. Effects of using Al4C3as a reactant on formation of Ti3AlC2by combustion synthesis in SHS mode. J Alloys Compd. 2009;473(1–2):408–13.
38. Liu G, Chen K, Zhou H, Guo J, Ren K, Ferreira JMFF. Layered growth of Ti2AlC and Ti3AlC2 in combustion synthesis. Mater Lett. 2007;61(3):779–84.
39. Hashimoto S, Takeuchi M, Inoue K, Honda S, Awaji H, Fukuda K, et al. Pressureless sintering and mechanical properties of titanium aluminum carbide. Mater Lett. 2008;62(10–11):1480–3.
40. SUNDBERG M, LINDGREN K, EL-RAGHY T, BARSOUM M. A METHOD OF PRODUCING A METAL-CONTAINING SINGLE-PHASE COMPOSITION. WO/2003/000618, 2003.
41. EL-RAGHY T, BARSOUM, Michel W, SUNDBERG M, PETTERSSON H. PROCESS FOR FORMING 312 PHASE MATERIALS AND PROCESS FOR SINTERING THE

SAME. WO/2001/046083, 2001.
42. Gouma PI, Davey SJ, Loretto MH. Microstructure and mechanical properties of a TiAl-based powder alloy containing carbon. Mater Sci Eng A. 1998;
43. Appel F, Oehring M, Wagner R. Novel design concepts for gamma-base titanium aluminide alloys. Intermetallics. 2000;
44. Lin ZJ, Zhuo MJ, Zhou YC, Li MS, Wang JY. Microstructural characterization of layered ternary Ti2AlC. Acta Mater. 2006;54(4):1009–15.
45. Chien F-R, Nutt SR, Cummings D. Defect structures in single crystal TiC. Philos Mag A. 1993 Aug;68(2):325–48.
46. Nickl J., Schweitzer K., Luxenberg P. Gasphasenabscheidung im system Ti-Si-C. J Less Common Met. 1972;
47. Zhang HB, Bao YW, Zhou YC. Current status in layered ternary carbide Ti3SiC2, a review. J Mater Sci Technol. 2009;25(1):1–38.
48. Goto T, Hirai T. Chemically vapor deposited Ti3SiC2. Mater Res Bull. 1987;
49. Lis J. Reaction sintering phenomena of self-propagating high-temperature synthesis-derived ceramic powders in the Ti-Si-C system. Solid State Ionics. 1997;103:59–64.
50. Riley DP, Kisi EH, Phelan D. SHS of Ti3SiC2: Ignition temperature depression by mechanical activation. J Eur Ceram Soc. 2006;26(6):1051–8.
51. Arunajatesan S, Carim AH. Synthesis of Titanium Silicon Carbide. J Am Ceram Soc. 1995 Mar 1;78(3):667–72.
52. Abu MJ, Mohamed JJ, Ahmad ZA. Synthesis of high purity titanium silicon carbide from elemental powders using arc melting method. Int J Refract Met Hard Mater. 2014;47:86–92.
53. Zhimei S, Yi Z, Yanchun Z. Synthesis of Ti3SiC2 powders by a solid-liquid reaction process. Scr Mater. 1999 Jun;41(1):61–6.
54. Zhou Y, Sun Z, Chen S, Zhang Y. In-situ hot pressing/solid-liquid reaction synthesis of dense titanium silicon carbide bulk ceramics. Mater Res Innov. 1998 Nov 13;2(3):142–6.
55. Yongming L, Wei P, Shuqin L, Jian C, Ruigang W, Jianqiang L. Synthesis of high-purity Ti3SiC2 polycrystals by hot-pressing of the elemental powders. Mater Lett. 2002;52(4–5):245–7.
56. Gao NF, Li JT, Zhang D, Miyamoto Y. Rapid synthesis of dense Ti3SiC2 by spark plasma sintering. J Eur Ceram Soc. 2002;22(13):2365–70.
57. Zhang ZF, Sun ZM, Hashimoto H. Rapid synthesis of ternary carbide Ti3SiC2 through pulse-discharge discharge sintering technique from Ti/Si/TiC powders. Metall Mater Trans A Phys Metall Mater Sci. 2002;33(11):3321–8.
58. Zhang ZF, Sun ZM, Hashimoto H, Abe T. A new synthesis reaction of Ti3SiC2 through pulse discharge sintering Ti/SiC/TiC powder. Scr Mater. 2001;45(12):1461–7.
59. Li J. Fabrication of highly dense Ti3SiC2 ceramics by pressureless sintering of mechanically alloyed elemental powders. J Mater Sci. 2003;8:2661–6.
60. El-Raghy T, Barsoum MW. Processing and Mechanical Properties of Ti3SiC2: I , Reaction Path and Microstructure Evolution. J Am Ceram Soc. 1999;80(10):2849–54.
61. Wu E, Kisi EH, Kennedy SJ, Studer AJ. In Situ Neutron Powder Diffraction Study of Ti 3 SiC 2 Synthesis. J Am Ceram Soc. 2001;8884:2281–8.
62. Wu E, Kisi EH, Riley DP, Smith RI. Intermediate Phases in Ti3SiC2 Synthesis from Ti/SiC/C Mixtures Studied by Time-Resolved Neutron Diffraction. J Am Ceram Soc. 2002;85(12):3084–6.
63. Zhou YC, Wang XH, Sun ZM, Chen SQ. Electronic and structural properties of the layered ternary carbide Ti3AlC2. J Mater Chem. 2001;11(9):2336–40.
64. Barsoum MW, Salama I, El-Raghy T, Golczewski J, Seifert HJ, Aldinger F, et al.

Thermal and electrical properties of Nb2AlC, (Ti, Nb)2AlC and Ti2AlC. Metall Mater Trans A Phys Metall Mater Sci. 2002 Sep;33(9):2775–9.
65. Li JF, Sato F, Watanabe R. Synthesis of Ti3SiC2 polycrystals by hot-isostatic pressing of the elemental powders. J Mater Sci Lett. 1999;18(19):1595–7.
66. Barsoum MW, Yoo H, Polushina IK, Rud VY, Rud Y V. Electrical conductivity, thermopower, and Hall effect of Ti3AlC2,Ti4AlN3, and Ti3SiC2. Phys Rev B. 2000;62(15):194–8.
67. Bai Y, He X, Zhu C, Chen G. Microstructures, Electrical, Thermal, and Mechanical Properties of Bulk Ti2AlC Synthesized by Self-Propagating High-Temperature Combustion Synthesis with Pseudo Hot Isostatic Pressing. J Am Ceram Soc. 2012;95(1):358–64.
68. Hettinger JD, Lofland SE, Finkel P, Meehan T, Palma J, Harrell K, et al. Electrical transport, thermal transport, and elastic properties of M2AlC (M=Ti, Cr, Nb, and V). Phys Rev B - Condens Matter Mater Phys. 2005;72(11):2–7.
69. Kulikov NI. McMillan-Hopfield factor and ideal resistivity of transition metals. J Phys F Met Phys. 1978;8(6).
70. Finkel P, Barsoum MW, Hettinger JD, Lofland SE, Yoo HI. Low-temperature transport properties of nanolaminates Ti3AlC2 and Ti4AlN3. Phys Rev B - Condens Matter Mater Phys. 2003 Jun 23;67(23):1–6.
71. Yoo H-I, Barsoum MW, El-Raghy T. Ti3SiC2 has negligible thermopower. Nature. 2000 Oct 5;407(6804):581–2.
72. Scabarozi T, Ganguly A, Hettinger JD, Lofland SE, Amini S, Finkel P, et al. Electronic and thermal properties of Ti3Al(C0.5,N0.5)2, Ti2A(C0.5,N0.5) and Ti2AlN. J Appl Phys. 2008;104(7):073713.
73. Barsoum MW, Radovic M. Elastic and Mechanical Properties of the MAX Phases. Annu Rev Mater Res. 2011;41(1):195–227.
74. Duval P, Ashby MF, Anderman I. Rate-controlling processes in the creep of polycrystalline ice. J Phys Chem. 1983 Oct;87(21):4066–74.
75. Wang X., Zhou Y. Microstructure and properties of Ti3AlC2 prepared by the solid–liquid reaction synthesis and simultaneous in-situ hot pressing process. Acta Mater. 2002;50(12):3143–51.
76. Barsoum MW, Farber L, El-Raghy T. Dislocations, kink bands, and room-temperature plasticity of Ti3SiC2. Metall Mater Trans A Phys Metall Mater Sci. 1999;30(7):1727–38.
77. Farber L. Transmission electron microscopy study of a low-angle boundary in plastically deformed Ti3SiC2. Philos Mag Lett. 1999 Apr;79(4):163–70.
78. Barsoum MW, Zhen T, Kalidindi SR, Radovic M, Murugaiah A. Fully reversible, dislocation-based compressive deformation of Ti3SiC2 to 1 GPa. Nat Mater. 2003;2(2):107–11.
79. Frank FC, Stroh AN. On the Theory of Kinking. Proc Phys Soc Sect B. 1952 Oct 1;65(10):811–21.
80. Zhen T, Barsoum MW, Kalidindi SR. Effects of temperature, strain rate and grain size on the compressive properties of Ti3SiC2. Acta Mater. 2005;53(15):4163–71.
81. Fraczkiewicz M, Zhou AG, Barsoum MW. Mechanical damping in porous Ti3SiC2. Acta Mater. 2006;54(19):5261–70.
82. Sun ZM, Murugaiah A, Zhen T, Zhou A, Barsoum MW. Microstructure and mechanical properties of porous Ti3SiC2. Acta Mater. 2005;53(16):4359–66.
83. Zhou AG, Barsoum MW, Basu S, Kalidindi SR, El-Raghy T. Incipient and regular kink bands in fully dense and 10 vol.% porous Ti2AlC. Acta Mater. 2006;54(6):1631–9.
84. Barsoum MW, Zhen T, Zhou A, Basu S, Kalidindi SR. Microscale modeling of kinking

nonlinear elastic solids. Phys Rev B - Condens Matter Mater Phys. 2005;71(13):3–10.
85. Zhou AG, Basu S, Barsoum MW. Kinking nonlinear elasticity, damping and microyielding of hexagonal close-packed metals. Acta Mater. 2008;56(1):60–7.
86. Zhou AG, Barsoum MW. Kinking nonlinear elastic deformation of Ti3AlC2, Ti2AlC, Ti3Al(C0.5,N0.5)2 and Ti2Al(C0.5,N0.5). J Alloys Compd. 2010;498(1):62–70.
87. Zhang ZF, Sun ZM. Shear fracture behavior of Ti3SiC2 induced by compression at temperatures below 1000 °C. Mater Sci Eng A. 2005;408(1–2):64–71.
88. Zhou AG, Brown D, Vogel S, Yeheskel O, Barsoum MW. On the kinking nonlinear elastic deformation of cobalt. Mater Sci Eng A. 2010;527(18–19):4664–73.
89. El-Raghy T, Barsoum MW, Zavaliangos A, Kalidindi SR. Processing and Mechanical Properties of Ti3SiC2: II, Effect of Grain Size and Deformation Temperature. J Am Ceram Soc. 1999;82(10):2855–60.
90. Barsoum MW, El-Raghy T. Room-temperature, ductile carbides. Metall Mater Trans A Phys Metall Mater Sci. 1999;30(2):363–9.
91. Tzenov N V., Barsoum MW. Synthesis and Characterization of Ti3AlC2. J Am Ceram Soc. 2004;83(4):825–32.
92. Bei GP, Laplanche G, Gauthier-Brunet V, Bonneville J, Dubois S. Compressive behavior of Ti3AlC2 and Ti 3Al0.8Sn0.2C2 MAX phases at room temperature. J Am Ceram Soc. 2013;96(2):567–76.
93. Bao YW, Chen JX, Wang XH, Zhou YC. Shear strength and shear failure of layered machinable Ti3AlC2 ceramics. J Eur Ceram Soc. 2004;24(5):855–60.
94. Smialek JL, Garg A. Microstructure and Oxidation of a MAX Phase / Superalloy Hybrid Interface. Nasa Tm 2014-216679. 2014;(July):1–19.
95. Sun Z, Zhang Z, Hashimoto H, Abe T. Ternary Compound Ti3SiC2: Part II. Deformation and Fracture Behavior at Different Temperatures. Vol. 43, Materials Transactions. 2002.
96. Bhattacharya R, Benitez R, Radovic M, Goulbourne NC. High strain-rate response and deformation mechanisms in polycrystalline Ti2AlC. Mater Sci Eng A. 2014;598:319–26.
97. Naik Parrikar P, Benitez R, Gao H, Radovic M, Shukla A. Mechanical response of fine grained Ti2AlC under extreme thermo-mechanical loading conditions. Mater Sci Eng A. 2016;658:176–84.
98. Callister W, Rethwisch D. Materials science and engineering: an introduction. Vol. 94, Materials Science and Engineering. 2007. 266–267 p.
99. Naik Parrikar P, Benitez R, Gao H, Radovic M, Shukla A. The Effect of Grain Size on Deformation and Failure of Ti2AlC MAX Phase under Thermo-Mechanical Loading. Exp Mech. 2017;57(5):675–85.
100. Zhang H, Wang X, Wan P, Zhan X, Zhou Y. Insights into Higherature Uniaxial Compression Deformation Behavior of Ti3AlC2. J Am Ceram Soc. 2015;98(10):3332–7.
101. Zhang HB, Zhou YC, Bao YW, Li MS. Abnormal thermal shock behavior of Ti3SiC2 and Ti3AlC2. J Mater Res. 2006;21(09):2401–7.
102. Salama I, El-Raghy T, Barsoum MW. Synthesis and mechanical properties of Nb2AlC and (Ti,Nb)2AlC. J Alloys Compd. 2002;347(1–2):271–8.
103. Bao YW, Wang XH, Zhang HB, Zhou YC. Thermal shock behavior of Ti3AlC2from between 200 °C and 1300 °C. J Eur Ceram Soc. 2005;25(14):3367–74.
104. Ganguly A, Zhen T, Barsoum MW. Synthesis and mechanical properties of Ti3GeC2 and Ti3(SixGe1-x)C2 (x = 0.5, 0.75) solid solutions. J Alloys Compd. 2004;376(1–2):287–95.
105. Glenny E, Royston MG. TRANSIENT THERMAL STRESSES PROMOTED BY THE

RAPID HEATING AND COOLING OF BRITTLE CIRCULAR CYLINDERS. Farnborough; 1958 Jun.
106. Gupta JK. Resistance to crack propagation in ceramics subjected to thermal shock. J Mater Sci. 1973 Jan;8(9):1283–6.
107. Bhattacharya R, Goulbourne NC. Thermal Shock Effects on Dynamic Deformation Mechanisms in Ti2AlC. ASME International Mechanical Engineering Congress and Exposition, Proceedings (IMECE) American Society of Mechanical Engineers Digital Collection; Oct 8, 2012 p. 165–85.
108. Adamaki V, Minster T, Thomas T, Fourlaris G, Bowen CR. Study of the mechanical properties of Ti2AlC after thermal shock. Mater Sci Eng A. 2016;667:9–15.
109. Bai Y, Kong F, He X, Li N, Qi X, Zheng Y, et al. Thermal shock behavior of Ti2AlC from 200°C to 1400°C. J Am Ceram Soc. 2017;100(9):4190–8.
110. de Lorgeril F. Advanced Ceramics in the Aerospace Industry [Internet]. Ceramic Industry. 2016 [cited 2018 Oct 15]. Available from: https://www.ceramicindustry.com/articles/95338-advanced-ceramics-in-the-aerospace-industry/
111. Raj R. Fundamental Research in Structural Ceramics for Service Near 2000°C. J Am Ceram Soc. 1993 Sep 1;76(9):2147–74.
112. Squire TH, Marschall J. Material property requirements for analysis and design of UHTC components in hypersonic applications. J Eur Ceram Soc. 2010;30(11):2239–51.
113. Durable ceramic material for the aerospace industry Take it to the limit. 3M ™ Silicon Nitride for Aerospace Applications. 2016.
114. Ji-Zheng D. Advances in Science and Technology of MAX Phase. 2012. 1–429 p.
115. Smialek JL. Unusual Oxidative Limitations for Al-MAX Phases. NASA/TM—2017-219444. 2017. 1–29 p.
116. Lambrinou K, Lapauw T, Vleugels J. Exploring the Potential of MAX Phases for Select Applications in Extreme Environments. MatISSE/JPNM Work. 2015;1–32.
117. Zhang T, Chen W, Guan Y, Gao D. Study on titanium alloy TC4 ballistic penetration resistance part I: Ballistic impact tests. Chinese J Aeronaut. 2012;25(3):388–95.
118. Roberts GD, Revilock DM, Binienda WK, Nie WZ, Mackenzie S Ben, Todd KB. Impact testing and analysis of composites for aircraft engine fan cases. J Aerosp Eng. 2002;15(April):19.
119. Gleeble 3500-GTC [Internet]. Dynamic Systems for Materials Research. [cited 2018 Oct 15]. Available from: https://www.gleeble.com/products/gleeble-systems/gleeble-3500.html
120. Benitez R, Kan WH, Gao H, O'Neal M, Proust G, Radovic M. Room temperature stress-strain hysteresis in Ti2AlC revisited. Acta Mater. 2016;105:294–305.
121. Barcelo F, Doriot S, Cozzika T, Le Flem M, Béchade JL, Radovic M, et al. Electron-backscattered diffraction and transmission electron microscopy study of post-creep Ti3SiC2. J Alloys Compd. 2009;488(1):181–9.
122. Hossein-Zadeh M, Mirzaee O, Mohammadian-Semnani H. An Investigation into the microstructure and mechanical properties of V4AlC3 MAX phase prepared by spark plasma sintering. Ceram Int. 2019 Jan 7;
123. Ghasali E, Yazdani-rad R, Asadian K, Ebadzadeh T. Production of Al-SiC-TiC hybrid composites using pure and 1056 aluminum powders prepared through microwave and conventional heating methods. J Alloys Compd. 2017;
124. WANG P, MEI B, HONG X, ZHOU W, Ping WG, Xiao H. Synthesis of Ti2ALC by hot pressing and its mechanical and electrical properties. Trans Nonferrous Met Soc China. 2007 Oct 1;17(5):1001–4.
125. Lapauw T, Vanmeensel K, Lambrinou K, Vleugels J. A new method to texture dense

Mn+1AXn ceramics by spark plasma deformation. Scr Mater. 2016;111:98–101.
126. Wang K, Li M, Liang Y, Wang J, He L, Du S, et al. Interface modification of carbon fibers with TiC/Ti2AlC coating and its effect on the tensile strength. Ceram Int. 2018 Nov 22;
127. Lee WE, Rainforth WM. Ceramic Microstructures: Property Control by Processing. 1st ed. London: Chapman & Hall; 1994. 590 p.
128. Benitez R, Gao H, O'Neal M, Lovelace P, Proust G, Radovic M. Effects of microstructure on the mechanical properties of Ti2AlC in compression. Acta Mater. 2018;143:130–40.
129. Wang X, Li H, Chandrashekhara K, Rummel SA, Lekakh S, Van Aken DC, et al. Inverse finite element modeling of the barreling effect on experimental stress-strain curve for high temperature steel compression test. J Mater Process Technol. 2017;243:465–73.
130. Sorini C, Chattopadhyay A, Goldberg RK. Effects of Adiabatic Heating on the High Strain Rate Deformation Response of Triaxially Braided Polymer Matrix Composites. Earth Sp 2018 Eng Extrem Environ - Proc 16th Bienn Int Conf Eng Sci Constr Oper Challenging Environ. 2018;768–81.
131. Vazquez-Fernandez NI, Soares GC, Smith JL, Seidt JD, Isakov M, Gilat A, et al. Adiabatic Heating of Austenitic Stainless Steels at Different Strain Rates. J Dyn Behav Mater. 2019 Sep 15;5(3):221–9.
132. Soares GC, Patnamsetty M, Peura P, Hokka M. Effects of Adiabatic Heating and Strain Rate on the Dynamic Response of a CoCrFeMnNi High-Entropy Alloy. J Dyn Behav Mater. 2019 Sep 15;5(3):320–30.
133. Klitschke S, Trondl A, Huberth F, Liewald M. Adiabatic heating under various loading situations and strain rates for advanced high-strength steels. IOP Conf Ser Mater Sci Eng. 2018 Sep 1;418(1):012123.
134. Buckingham RC, Argyrakis C, Hardy MC, Birosca S. The effect of strain distribution on microstructural developments during forging in a newly developed nickel base superalloy. Mater Sci Eng A. 2016;654:317–28.
135. Lankford J, Predebon WW, Staehler JM, Subhash G, Pletka BJ, Anderson CE. The role of plasticity as a limiting factor in the compressive failure of high strength ceramics. Mech Mater. 1998;29(3–4):205–18.
136. Jiang J, Britton TB, Wilkinson AJ. Measurement of geometrically necessary dislocation density with high resolution electron backscatter diffraction: Effects of detector binning and step size. Ultramicroscopy. 2013;125:1–9.
137. Nye JF. Some geometrical relations in dislocated crystals. Acta Metall. 1953 Mar 1;1(2):153–62.
138. Wilkinson AJ, Meaden G, Dingley DJ. High-resolution elastic strain measurement from electron backscatter diffraction patterns: New levels of sensitivity. Ultramicroscopy. 2006 Mar 1;106(4–5):307–13.
139. Britton TB, Wilkinson AJ. High resolution electron backscatter diffraction measurements of elastic strain variations in the presence of larger lattice rotations. Ultramicroscopy. 2012 Mar 1;114:82–95.
140. Wilkinson AJ, Meaden G, Dingley DJ. High resolution mapping of strains and rotations using electron backscatter diffraction. 2013;
141. Pantleon W. Resolving the geometrically necessary dislocation content by conventional electron backscattering diffraction. Scr Mater. 2008 Jun 1;58(11):994–7.
142. Geometrically Necessary Dislocations [Internet]. MTEX. [cited 2021 Jun 19]. Available from: https://mtex-toolbox.github.io/GND.html
143. El-Raghy T, Chakraborty S, Barsoum MW. Synthesis and characterization of Hf2PbC, Zr2PbC and M2SnC (M = Ti, Hf, Nb or Zr). J Eur Ceram Soc. 2000;20(14–15):2619–

25.
144. Berkovitch-Yellin Z. Toward an ab Initio Derivation of Crystal Morphology. J Am Chem Soc. 1985;107(26):8239–53.
145. Zhou Y, Sun Z. Crystallographic relations between Ti3SiC2 and TiC. Mater Res Innov. 2000;3(October):286.
146. Low IM. Vickers contact damage of micro-layered Ti3SiC2. J Eur Ceram Soc. 1998;18(6):709–13.
147. Gumbsch P, Riedle J, Hartmaier A, Fischmeister HF. Controlling factors for the brittle-to-ductile transition in tungsten single crystals. Science (80-). 1998;282(5392):1293–5.
148. Sun Z, Zhou Y, Zhou J. The anomalous flow behaviour in the layered Ti3SiC2 ceramic. Philos Mag Lett. 2000;

Appendix

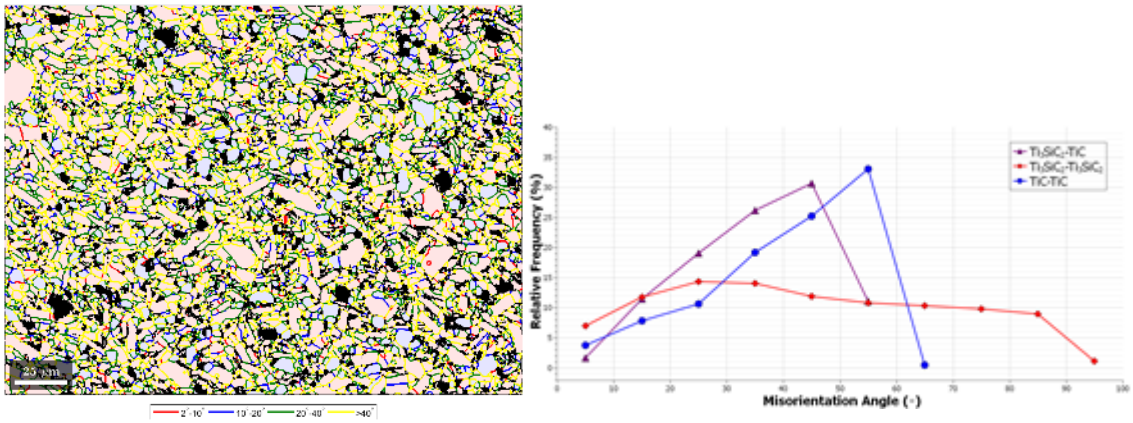

Figure 10.1: A) *EBSD map showing the misorientation angles of the grain boundaries in Site 2 of the TRT-3 Ti_3SiC_2 sample,* ***B)*** *Line graph showing an average of the grain boundary misorientation angles across the recorded sites, with the grain boundaries between each phase shown.*

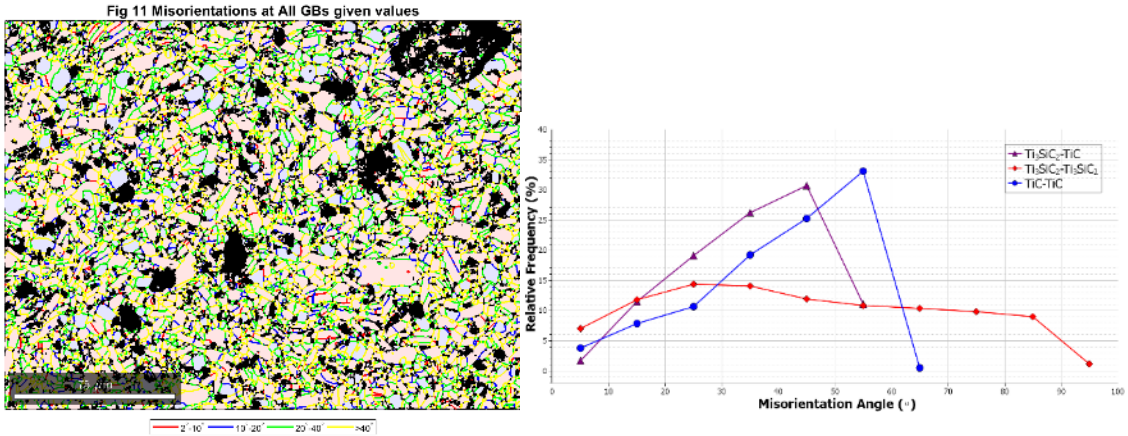

Figure 10.2: A) *EBSD map showing the misorientation angles of the grain boundaries in Site 2 of the TRT-4 Ti_3SiC_2 sample,* ***B)*** *Line graph showing an average of the grain boundary misorientation angles across the recorded sites, with the grain boundaries between each phase shown.*

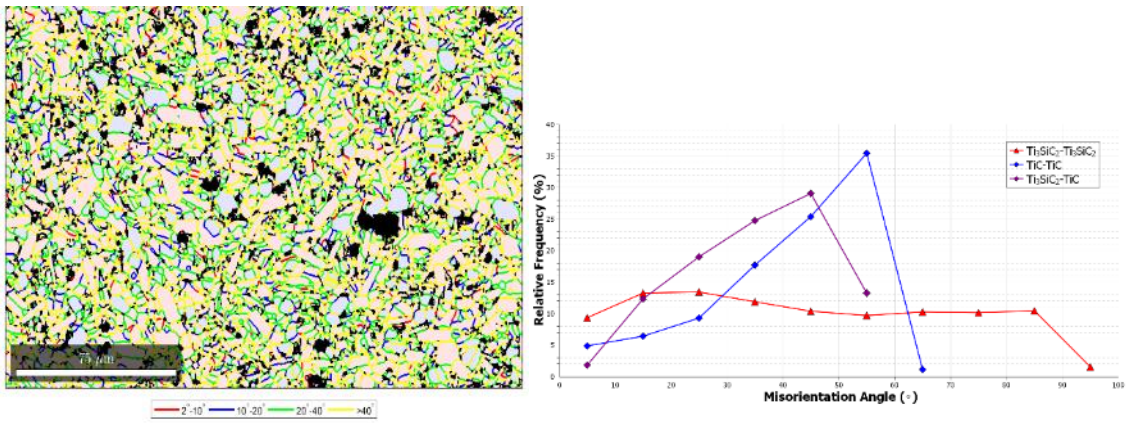

Figure 10.3: A) *EBSD map showing the misorientation angles of the grain boundaries in Site 1 of the T10-0 Ti_3SiC_2 sample,* ***B)*** *Line graph showing an average of the grain boundary misorientation angles across the recorded sites, with the grain boundaries between each phase shown.*

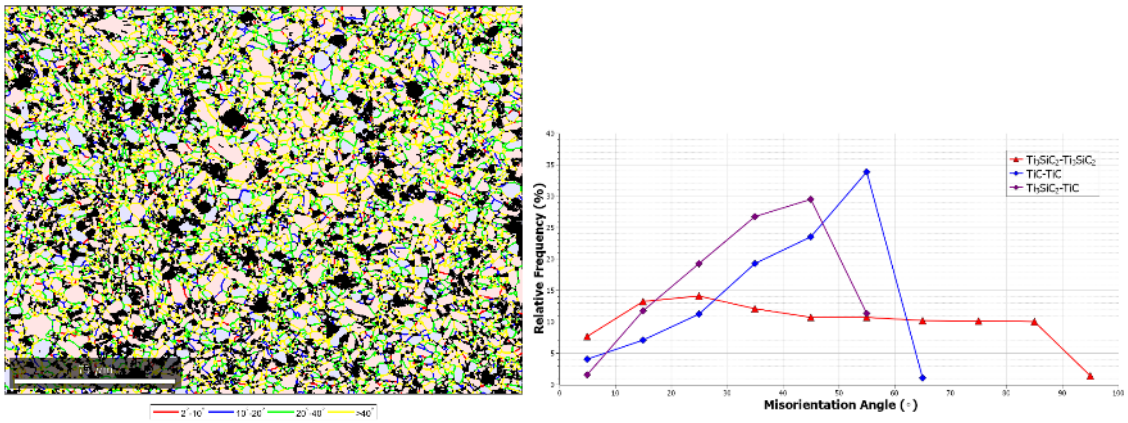

Figure 10.4: ***A)*** *EBSD map showing the misorientation angles of the grain boundaries in Site 2 of the T10-2 Ti_3SiC_2 sample,* ***B)*** *Line graph showing an average of the grain boundary misorientation angles across the recorded sites, with the grain boundaries between each phase shown.*

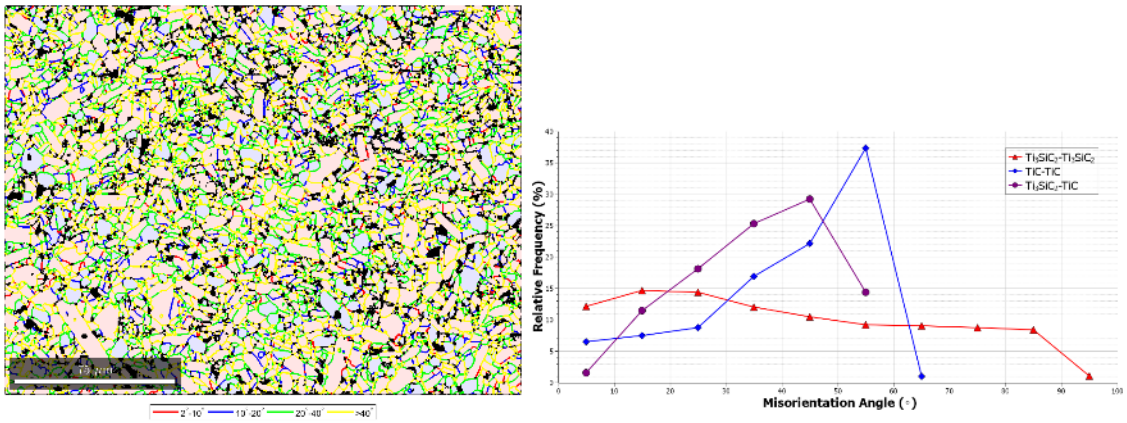

Figure 10.5: ***A)*** *EBSD map showing the misorientation angles of the grain boundaries in Site 3 of the T10-4 Ti_3SiC_2 sample,* ***B)*** *Line graph showing an average of the grain boundary misorientation angles across the recorded sites, with the grain boundaries between each phase shown.*

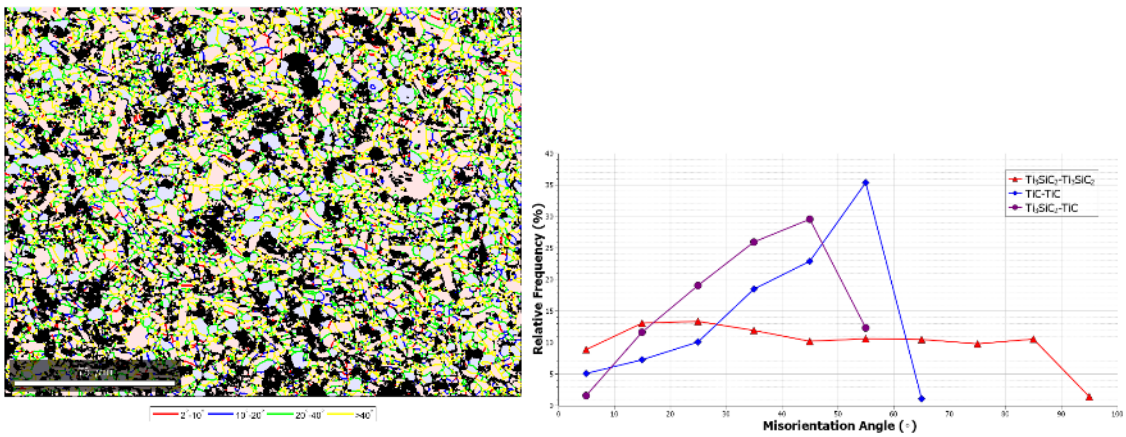

Figure 10.6: ***A)*** *EBSD map showing the misorientation angles of the grain boundaries in Site 1 of the T11-0 Ti_3SiC_2 sample,* ***B)*** *Line graph showing an average of the grain boundary misorientation angles across the recorded sites, with the grain boundaries between each phase shown.*

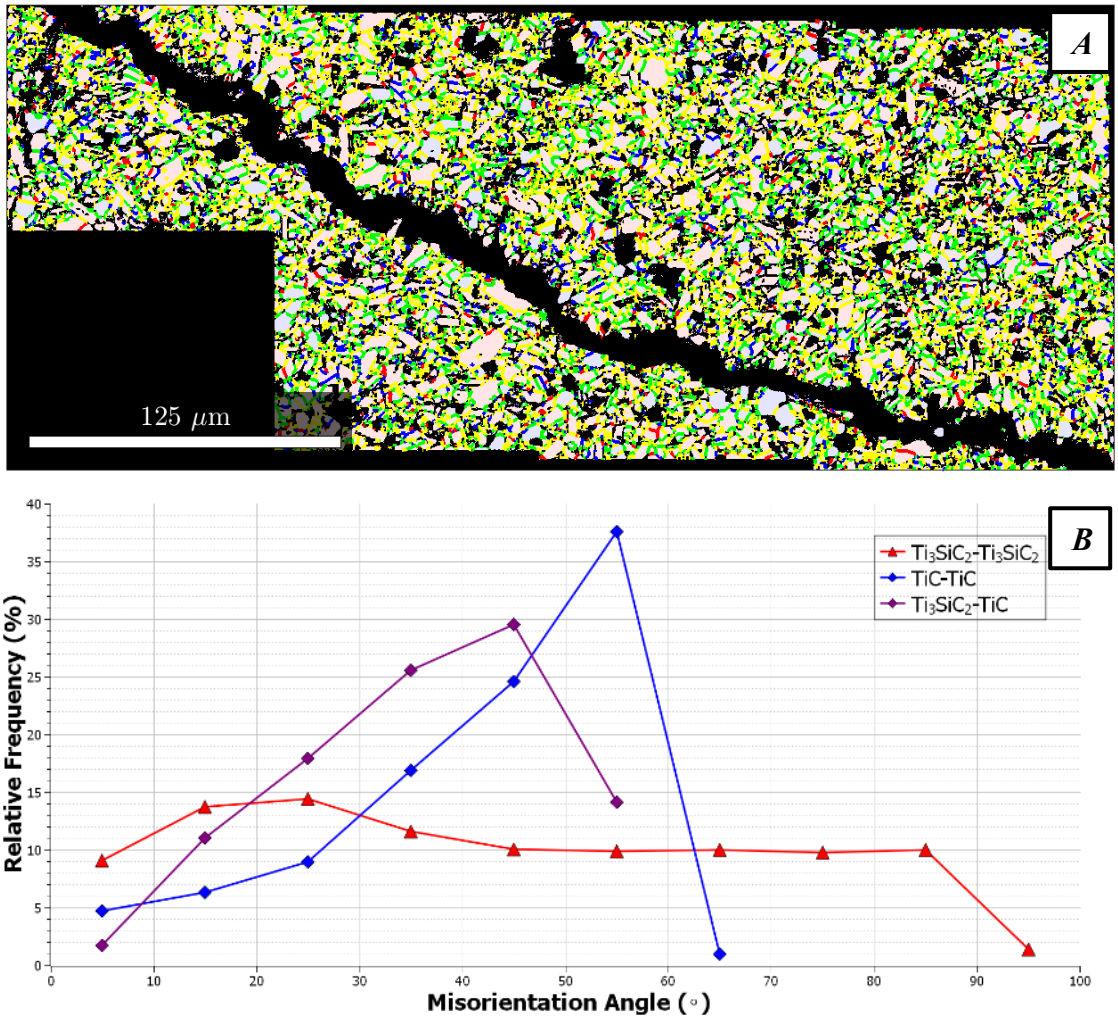

Figure 10.7: A) *EBSD map showing the misorientation angles of the grain boundaries in the T11-2 Ti_3SiC_2 sample,* ***B)*** *Line graph showing an average of the grain boundary misorientation angles across the recorded sites, with the grain boundaries between each phase shown.*

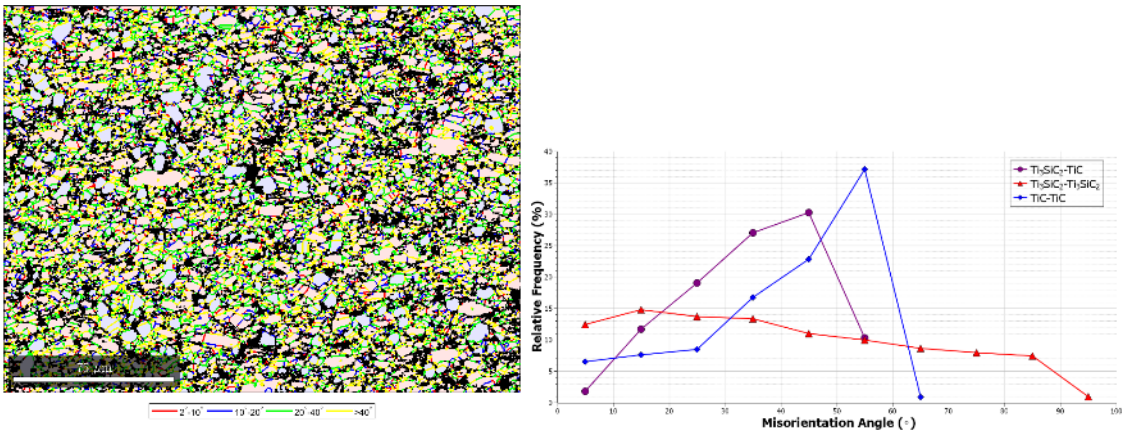

Figure 10.8: A) *EBSD map showing the misorientation angles of the grain boundaries in Site 1 of the T11-4 Ti_3SiC_2 sample,* ***B)*** *Line graph showing an average of the grain boundary misorientation angles across the recorded sites, with the grain boundaries between each phase shown.*

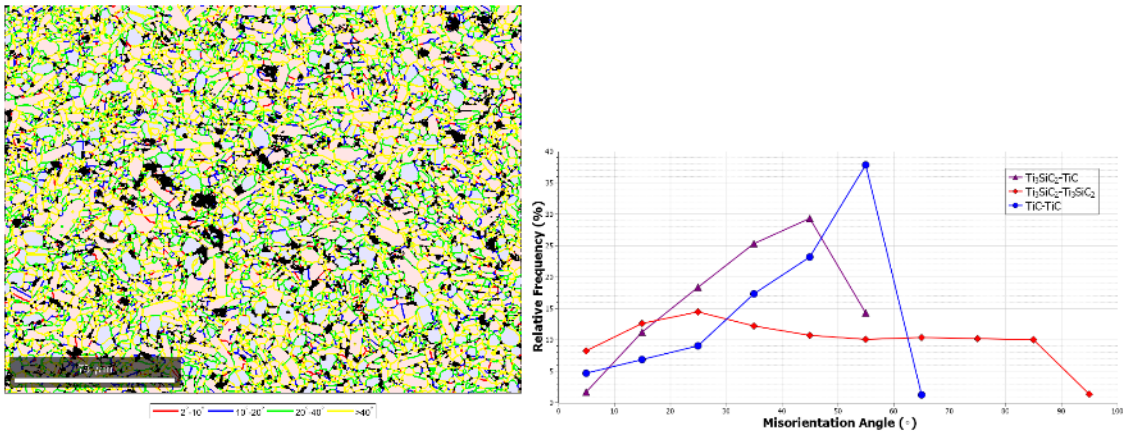

Figure 10.9: ***A)*** *EBSD map showing the misorientation angles of the grain boundaries in Site 1 of the T12-0 Ti_3SiC_2 sample,* ***B)*** *Line graph showing an average of the grain boundary misorientation angles across the recorded sites, with the grain boundaries between each phase shown.*

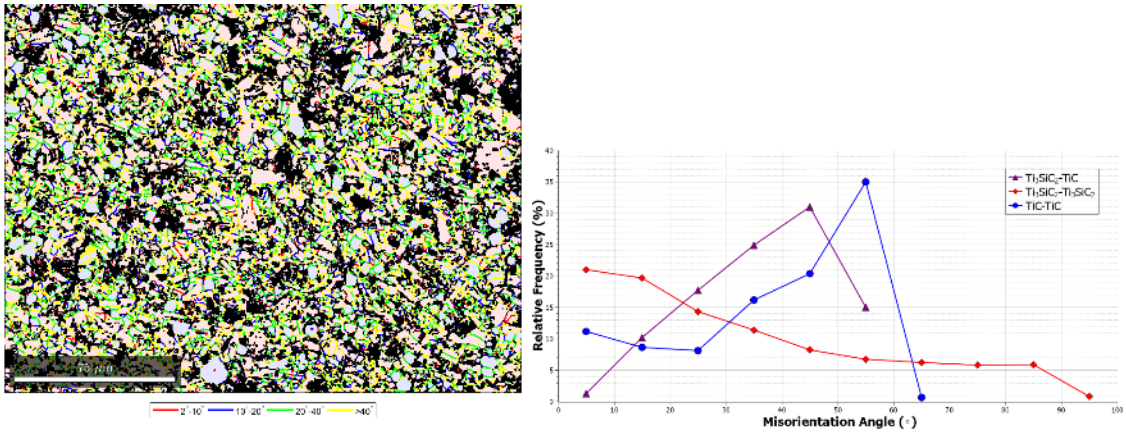

Figure 10.10: ***A)*** *EBSD map showing the misorientation angles of the grain boundaries in Site 2 of the T12-2 Ti_3SiC_2 sample,* ***B)*** *Line graph showing an average of the grain boundary misorientation angles across the recorded sites, with the grain boundaries between each phase shown.*

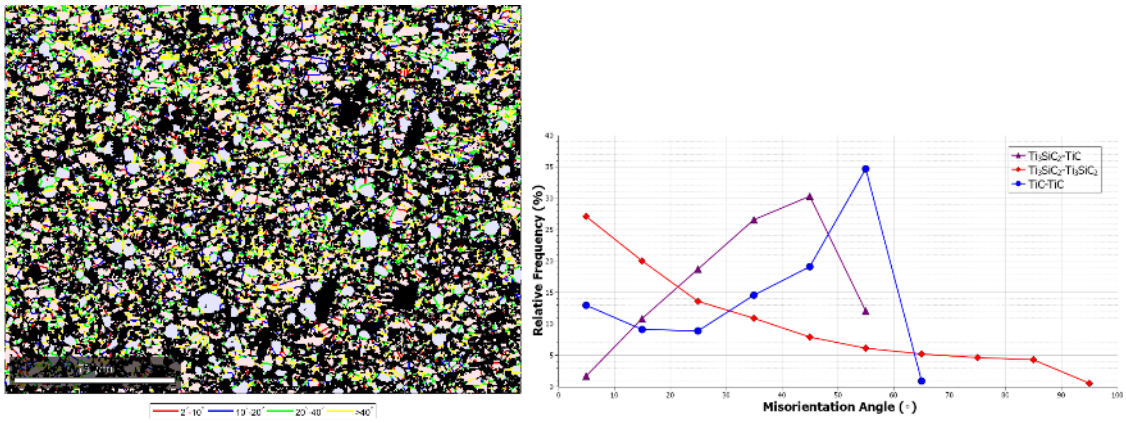

Figure 10.11 ***A)*** *EBSD map showing the misorientation angles of the grain boundaries in Site 6 of the T12-4 Ti_3SiC_2 sample,* ***B)*** *Line graph showing an average of the grain boundary misorientation angles across the recorded sites, with the grain boundaries between each phase shown.*